JOURNAL OF CONDENSED MATTER NUCLEAR SCIENCE

Experiments and Methods in Cold Fusion

Proceedings of ICCF24 Solid State Energy Summit, Mountain View, California, USA, July 25–28, 2022

VOLUME 38, May 2024

Preface

Anthropocene Institute was pleased to sponsor ICCF24 Solid-State Energy Summit, the conference where industry leaders took a critical look at the field of lattice-enabled nuclear reactions (LENR), such as solid-state atomic and fusion reactions. On behalf of the "cold fusion" community, I was honored to serve as the conference chair.

The conference focused on observations, results, and theory, with an eye toward satisfying increased interest in practical fusion from the investment and research communities. The conference took place at the Computer History Museum (CHM) in Mountain View, CA, in July 2022. ICCF24 had approximately 150 in-person attendees, with an additional online attendance of 150.

Distinguished speakers, among others, included: Nobuo Tanaka, Former Executive Director of the International Energy Agency; Florian Metzler, Research Scientist at MIT Industrial Performance Center; Matt Trevithick, Partner at DCVC; Steve Katinsky, Co-Founder and Director LENRIA Corporation; Huw Price, Distinguished Professor Emeritus and Philosopher of Science; Oliver Barham, Project Manager, Naval Surface Warfare Center Indian Head; Theresa Benyo, PhD, Principal Investigator, NASA; Peter Shannon, Founder, Radius Mobility; and David Nagel, Research Professor, George Washington University.

A few of the highlights from the conference included:

- The pre-announcement of the ARPA-E FOA on LENR. Dr. Scott Hsu, a former Program Director at ARPA-E announced at ICCF24 that ARPA-E would issue a new Exploratory Topic to solicit applications for financial assistance in pursuit of diagnostic evidence of LENR reactions that are convincing to the wider scientific community.
- NASA Glenn Research Center Principal Investigator Theresa Benyo's presentation on "The History of LENR Research at NASA Glenn Research Center." The decade-long project, first known as the Advanced Energy Conversion Project, is now called the Lattice Confinement Fusion (LCF) Project. NASA got involved in this work because they do "a lot of missions in extreme environments that require novel power sources." Benyo stated that "LCF may be the key to harnessing fusion within a compact system," by eliminating highly enriched uranium; reducing safety, security and supply concerns; being compact and controllable; having near zero radioactive waste.
- Brillouin Energy Corp's public demonstration of its high-tech boiler system, which uses ordinary hydrogen to produce scalable heat on demand, holds the promise of lowering the cost of, and reducing the carbon footprint of hot water boilers and radiant heaters for residential and commercial applications.

There were too many high points to mention all of them, so I encourage you to explore the conference proceedings and important links below.

For More Information on the Technical Talks

David Nagel was Chair of the Technical Review Committee. The book of abstracts for the Technical Program is available on the ICCF24 website. Many of the technical talks are available on the ICCF24 YouTube channel. The Short Course videos are available on the ICCF24 YouTube channel playlist and include:

- Introduction and Issues (David Nagel)
- Electrochemical Loading (Michael McKubre)
- Hot Gas Loading (Shinya Narita) - Plasma Loading (Lawrence Forsley)

- Calorimetry and Heat Data (Edmund Storms)
- Transmutation Data (Jean-Paul Biberian)
- Materials Challenges (Ashraf Imam)
- Theoretical Considerations (Peter Hagelstein)
- Commercialization (Steve Katinsky)
- Applications and Impacts (Jed Rothwell)

Also, check out these important ICCF24 links:

- Abstracts of oral presentations.
- Videos of presentations, short course talks, some posters, and other material.

Thanks to everyone involved in the solid state fusion community for persevering in the face of doubt, staying curious and determined, and continuing the advancement of the ultimate source of inexpensive, carbon-free, energy. For too long the issues of unstable isotopes have stalemated innovation in nuclear energy. This community has been the most creative in finding ways to unlock nuclear binding energy without a giant machine.

Regards,
Carl Page, Co-Founder and President, Anthropocene Institute

J. Condensed Matter Nucl. Sci. 38 (2024) 1–362

 ISSN 2227-3123

JOURNAL OF CONDENSED MATTER NUCLEAR SCIENCE

Volume 38 2024

CONTENTS

RESEARCH ARTICLES

J. Condensed Matter Nucl. Sci. 38 (2024) 1–12

Research Article

Reproduction of Excess Heat of Pd-B Cathode Measured by Seebeck Calorimeter

Wu-Shou Zhang*

Institute of Chemistry, Chinese Academy of Sciences, Beijing 100190, China

Abstract

Clear excess power from a Pd-B rod cathode provided by Melvin H. Miles was measured with a Seebeck calorimeter during D_2O electrolysis. A reflux open-electrolytic cell, with the advantage of small constant power of D_2O evaporation in electrolysis ($P_{vapor} = 0.00979I$ at 25°C, the working temperature of calorimeter) was used and the calorimetry was therefore simplified. It was verified that pre-electrolysis of the cathode in open cell under high current and high temperature is an effective activation method for excess heat production in subsequent electrolysis. However, only the second activation gave the maximum excess power of 0.15 W with input power of 3 W and more activation was useless. After checking past results on excess heat of Pd plate samples in our lab, it is also found that the activation of cathode must be limited to a couple of times. On the other hand, after a long duration of intermittent electrolysis, the volume of the Pd-B electrode increased very little, meeting the requirement of volume expansion of excess-heat-producing Pd samples discovered by Edmund Storms.
 ISSN 2227-3123

Keywords: Excess heat, Heavy water, Pd-B rod, Reflux open-electrolytic cell, Activation, Excess volume.

1. Introduction

It is well known that excess heat occurring in Pd/D_2O systems was first found in open-electrolytic cells by using isoperibolic calorimetry (IPC) by Fleischmann and Pons [1], [2] and reproduced afterwards in closed-electrolytic cells with mass flow calorimetry (MFC, e.g., the method used by McKubre et al. [3]) and Seebeck envelope calorimetry (SEC, e.g., Storms [4]). Since then, Melvin H. Miles and his co-workers have been studying excess heat in open Pd/D_2O electrolytic cells with IPC, in detail, for more than 30 years [5]–[8]. Miles and Imam reported that Pd-B rod can give reproduceable excess heat [7]. During the satellite meeting of ICCF20 in 2016, Xing Zhong Li suggested me to measure excess heat with samples of Miles using our SEC, which had been shown to detect significant excess heat in closed Pd/D_2O electrolytic systems [9]–[11]. In May 2017, Miles delivered one Pd-0.25wt.%B rod and other 3 samples to me. The rod is 4.71 mm in diameter and 20.1 mm in length, volume of 350.2 mm^3, area of 3.3227 cm^2 and weight of 4.1177 g (measured with an Ohaus PX224ZH balance) as shown in the left of Fig. 1. This batch was made at

*Corresponding author: wszhang@iccas.ac.cn or zhangwushou@hotmail.com

 ISSN 2227-3123

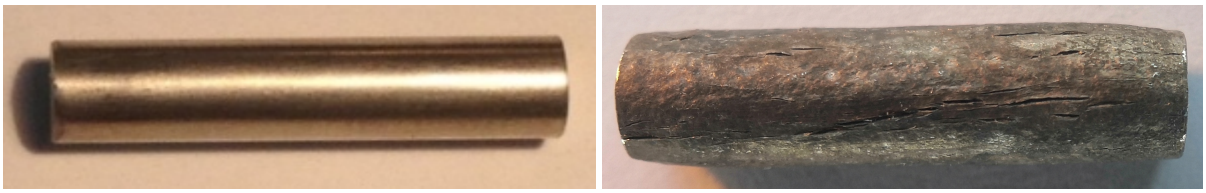

Figure 1. Pd-0.25wt.%B rod from M. H. Miles. (left) new sample; (right) the sample after electrolysis for 2,147 h (89.5 d).

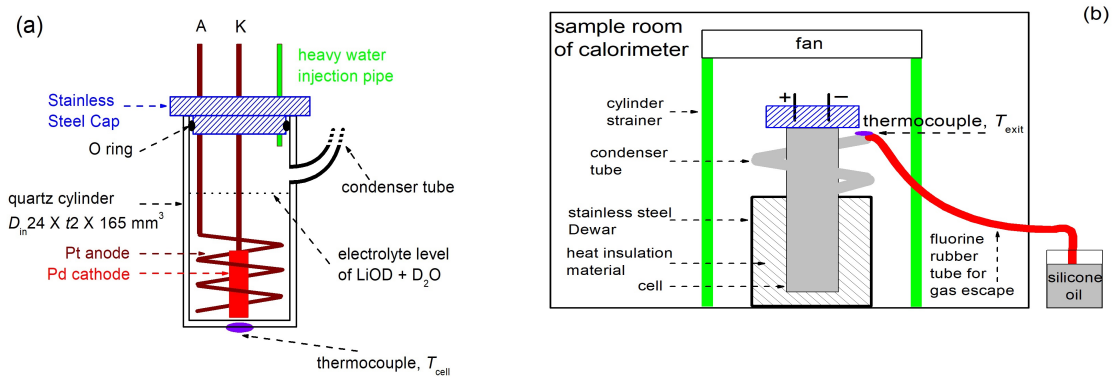

Figure 2. Schematics of Pd/D_2O reflux open-electrolytic cell (a) and the cell with calorimetric attachments (b). All components shown here are placed in a Seebeck calorimeter, as described in previous literatures [9]–[12].

NRL by M. Ashraf Imam, which had produced the maximum excess power of 0.24 W [7]. This sample became stumpy (4.62 $\sim$ 4.94 in diameter and 19.1 mm in length) with weight of 4.1156 g after a long duration of electrolysis as shown in the right of Fig. 1. At ICCF-23, the primary results of excess heat produced by this sample was reported [12]. This paper presents all results.

2. Experimental Set-Up and Calorimetry of Reflux Open-Electrolysis

2.1. Experimental Set-Up

We designed a reflux open-electrolytic cell as shown schematically in Fig. 2(a). The electrolytic cell is a quartz tube (ϕ_{in}24 mm, ϕ_{out}28 mm and h165 mm) with a curved branch tube and a stainless-steel lid. The branch tube is in a spiral shape (1 cm in tube diameter, 7 cm in spiral diameter, around 3 circles or 65 cm long). The branch tube serves as the outlet for the evolving gas and vapor, and as the condenser tube. It enters the cell at a position 9.4 cm high, which is above the waterline, as shown in Figs. 2 and 3. The anode is a spiral Pt wire (ϕ0.5 mm and l1.4 m, 99.95%, GRINM, Beijing). The electrode leads are Pt wires (ϕ1.1 mm and l18 cm each, 99.99%, GRIKIN, Beijing) covered with PTFE heat shrinkable tubes to prevent catalyzing $D_2 + O_2$ recombination. D_2O (99.8at.%) is from J&K Chemical. Li_2O powder (99.5%, Alfa Aesar) is dissolved in heavy water to make a 0.1 M LiOD solution. An injection pipe made of stainless-steel is fixed in the lid for periodic heavy water addition. Four different O-rings (not all shown in Fig. 2(a)) are used around the lid, the two leads and the injection pipe to prevent gas from escaping through the lid. A K-type thermocouple is attached to the bottom of the cell to measure temperature (T_{cell}). The top part of the cell, the lid with two leads and electrodes, is not taken part after each run. Li_2SiO_3 sediment sometimes appears on the inner wall of the

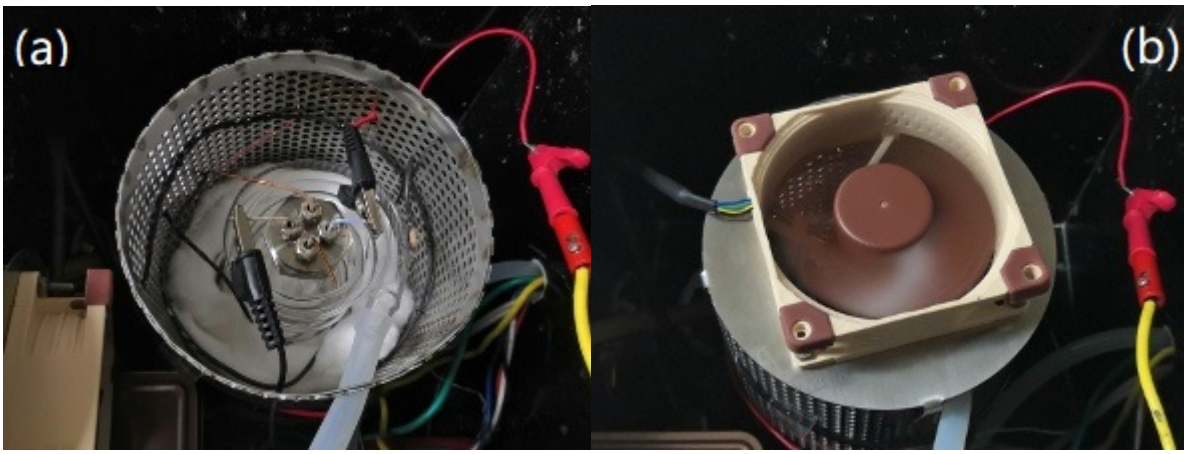

Figure 3. Photos of electrolytic cell with heat insulation (a) and fan (b) in the Seebeck calorimeter.

cell and the surfaces of two electrodes, when temperature is higher than 80°C, especially in activation experiments [12]. Then this happens, the whole cell has to be taken part and cleaned in water and ethanol, and dried in an electric constant temperature blast drying oven (80°C for 1 h).

The electrolytic cell is placed in the center of a stainless-steel Dewar (ϕ_{in}75 mm, ϕ_{out}83 mm, h_{in}103 mm and h_{out}120 mm) with cotton wool between the gap as heat insulation material to increase the cell temperature, as shown in Figs. 2(b) and 3(a). The Dewar is placed in the center of a cylinder strainer (ϕ12 cm and h23 cm), which is covered with a fan blowing the air downward to ensure even temperature distribution in the sample chamber of the SEC, as shown in Figs. 2(b) and 3. To make the heavy water vapor further condense, a fluorine rubber tube (ϕ_{in}10 mm, ϕ_{out}14 mm and l2 m) is connected to the condenser tube of the cell at one end, and another end is immersed in the silicone oil outside of the SEC to prevent contamination from air, as shown in Figs. 2(b) and 3(a). A K-type thermocouple is attached to the end of the condenser tube to monitor the temperature of the exit (T_{exit}), as shown in Figs. 2(b) and 3(a). Gases produced in electrolysis, including oxygen, deuterium and heavy water vapor, all escape through the tubes. It should be noted that T_{cell} and T_{exit} are only used for reference in the electrolysis process. The output power of the electrolytic cell (P_{SEC}) is measured by 18,796 thermocouples in a Seebeck calorimeter as reported previously [10].

To replenish heavy water consumed by electrolysis and evaporation, a syringe pump with injector was used to add heavy water into the electrolytic cell through the injection pipe shown in Fig. 2(a). It was used in the long duration electrolysis experiments, Exp. #201127 to 210322, as summarized in Table 7 in the previous work [12]. The syringe injection pump was not used after that. The purpose of this work was to find a way to activate the Pd sample, rather than continuously monitor for excess heat for a long duration, as was done in early cold fusion research. With our method, the electrolysis time was generally controlled within 48 h (except in Exp. #220222 in which it lasted 60 h).

2.2. Calorimetry of Reflux Open-Electrolysis

The excess power P_{ex} in the D_2O reflux open-electrolytic cell shown in Figs. 2 and 3 under steady state (input power is constant, i.e., $dP_{in}/dt = 0$) can be expressed as [12]

$$P_{ex} = P_{SEC} + P_{vapor} - (V_{cell} - V_{th})I \quad (1)$$

where P_{SEC} is the thermal power measured by SEC; V_{cell} is the cell voltage; $V_{\mathrm{th}} = 1.52666$ V at 25°C (the working temperature of SEC), the thermoneutral potential of heavy water ($V_{\mathrm{th}} = 1.48121$ V for light water at 25°C); I is the electrolysis current; P_{vapor} is the evaporation power and it can be expressed as

$$P_{\mathrm{vapor}} = 0.75\frac{I}{F}\frac{p}{p* - p}L_{\mathrm{D_2O}} \tag{2a}$$

$$= 0.00979I \ @\ 25°\mathrm{C} \tag{2b}$$

where F is the Faraday constant; $p^* = 1.01325$ bar, the atmosphere pressure; $L_{\mathrm{D_2O}} = 45.402$ kJ/mol, the evaporation enthalpy of heavy water at 25°C; $p = 0.02735$ bar, the evaporation pressure of heavy water at 25°C. Because p is a small value at room temperature, therefore P_{vapor} does not change prominently with p^* as in the Fleischmann-Pons-Miles situation [2], [5]–[8]. For light water, the coefficient in Eq. (2b) is 0.01104 at 25°C.

Our experimental results also indicate that only the D_2O evaporation at ambient temperature, and not the cell temperature, needs to be considered for reflux open-electrolysis. The maximum temperature increment ΔT_{exit} of the condenser-tube end (see Figs. 2(b) and 3(a)) during electrolysis was 2.6°C when the cell temperature (T_{cell}) was 96°C in Exp. #200713 (where D_2O vapor pressure is 0.83 bar at this temperature). This also verifies that the vapor is cooled to around the ambient temperature through the condenser tube. Because there is another 50 cm of rubber tube to condense the D_2O in the sample chamber of the SEC, there is no doubt about the validity of Eqs. (1) and (2). The validation of Eq. (2) is also verified by the mass change during electrolysis. As shown in the previous work [12], at 25°C, the evaporation of D_2O will induce 4.16% more mass loss than that of electrolysis alone. In most cases, the difference between the theoretical and actual mass losses in our experiments was less than 1%. For example, in Exp. #210327, electrolysis currents and times of 0.7 A × 36 h, 0.6 A × 4 h and 0.5 A × 8 h were applied successively, and a total of 9.6 ml of heavy water was added 3 times during electrolysis. The theoretical mass-loss according to this model is 12.3372 g, the actual loss was 12.3184 g, so the difference is only 0.0188 g or 0.15%.

In other words, the reflux open-electrolytic cell is an effective design to reduce the evaporation process' influence on power balance, which was the biggest uncertainty omitted or debated in the calorimetry of open electrolysis in past works [2], [5]–[8].

Because the open-electrolyzing process is usually unsteady ($\mathrm{d}P_{\mathrm{in}}/\mathrm{d}t \neq 0$), we need to use the combination of the average excess power $\overline{P}_{\mathrm{ex}}$ ($= Q_{\mathrm{ex}}/t$, the total excess heat divided by the electrolysis time) and P_{ex} of Eq. (1) to determine whether there is excess heat or not. Another approximation is to consider the change of input power over time, $\mathrm{d}P_{\mathrm{in}}/\mathrm{d}t$, the modification of excess power in Eq. (1) is approximated in the first order:

$$P'_{\mathrm{ex}} \ = \ P_{\mathrm{ex}} \ + \ C\frac{\mathrm{d}P_{\mathrm{in}}}{\mathrm{d}t} \tag{3}$$

where C is the correction coefficient, which depends on the thermal properties of the whole system (e.g. the open cell and materials around it, and the calorimeter). P'_{ex} is closer to $\overline{P}_{\mathrm{ex}}$ than P_{ex} is. However, Eq. (3) is only applied in data analysis after the data-logging is completed while the input power changes slowly and linearly with time.

In our experiments, the cell voltage and current, temperatures and calorimetric signals are all recorded on a computer, in real-time, every second.

3. Results

3.1. Calibration and Trial Results

In the last 7 years, a new technique which can eliminate most thermal noise caused by temperature fluctuation of the circulating bath of the SEC was developed in our lab [12], [13]. An example of the calibration in Exp. #210315 using this technique is shown in Fig. 4, the standard deviation is only 1.3 mW this time and is one order smaller than

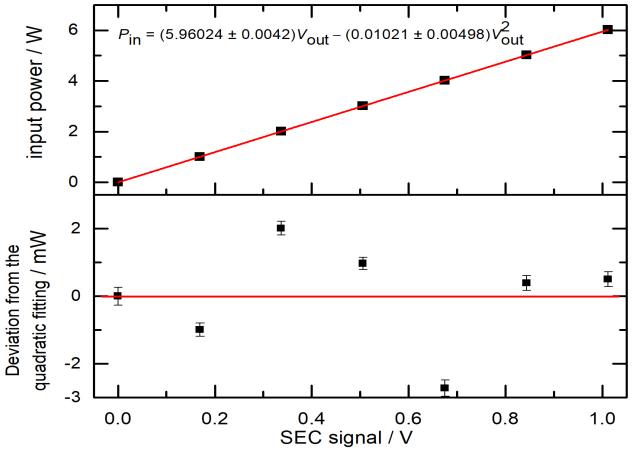

Figure 4. Calibration result of the SEC with an electric heater at 25°C in Exp. #210315.

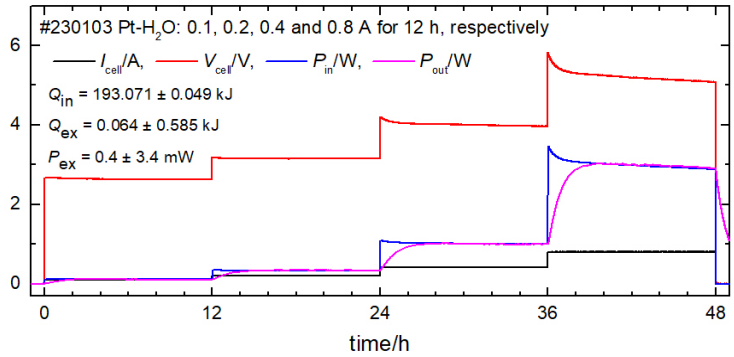

Figure 5. Zero excess heat in Exp. #230103 for Pt-H_2O reflux open-electrolysis.

before [9]–[11]. This technique ensures that the sensitivity and accuracy of the decimeter-sized sample chamber of the SEC can approach the levels of IPC of Fleischmann-Pons-Miles [2], [5]–[8].

The calorimeter was calibrated with a resistor in the electrolytic cell every month to ensure the accuracy of calorimetry. They gave the same results in the measurement error of milliwatts.

Before the report of excess heat production, some trivial results are introduced. Fig. 5 shows an example of calorimetry on Pt-H_2O system in Exp. #230103, where a Pt wire cathode (ϕ0.5 mm and l14.6 cm), a Pt plate anode (0.05 mm $\times$ 2 cm^2) and 0.1 M H_2SO_4 solution was used. The cathode and anode in previous experiments were exchanged in this run; therefore, the cathode showed no excess heat production because of no deposition [12]. The electrolytic current was stepped through 0.1, 0.2, 0.4 and 0.8 A successively, with each step applied for 12 hours. It is shown that total excess heat is 0.064 kJ, which is only 11% of the standard deviation. At 0.8 A, the instantaneous excess power $P_{ex} = 32 \pm 5$ mW, which is just a non-equilibrium effect due to $dP_{in}/dt = -16$ mW/h. Because $P'_{ex} = 0$, the correction coefficient C in Eq. (3) is 2 h/mW. In Exp. #201227 for a Pd-D_2O open-electrolytic cell, $C = -2.93$ h/mW, as shown in Fig. 15 of Ref. [12]. These two values of C are of a similar order of magnitude.

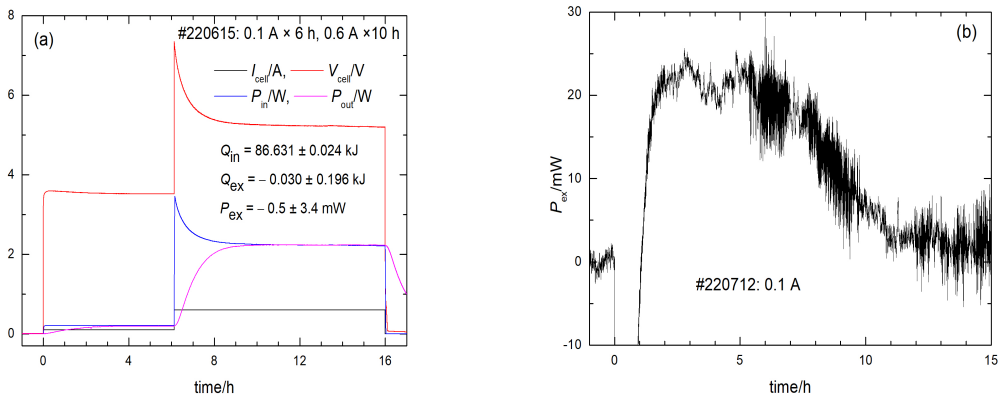

Figure 6. (a) zero excess heat in Exp. #220615; (b) formation heat of palladium deuteride in Exp. #220712.

Table 1. Effects of activation on excess power production of Pd-B rod.

#	$T_{\mathrm{activ,max}}$/°C	R	$\overline{P}_{\mathrm{ex,max}}$/mW	I/A	t/h	date range
0		1/7	21(7)	0.5-0.75	387	201223-210129
1	218	2/11	46(3)	0.17-0.7	436	210202-220206
2	94	11/12	130(2)	0.1-1.2	371	220220-220330
3	97	1/4	22(7)	0.1-0.6	86	220401-220419
4	96	6/13	43(7)	0.05-0.6	629	220421-220623
5	96	3/6	42(3)	0.1-0.7	130	220626-220709
6	96	0/2	6(2)	0.1-0.7	54	220711-220714

Note: # is the ordinal number of cathode activation, which is putting the cathode in an open cell and electrolyzing under high current (< 4 A) and high temperature for less than 11 h. The electrolyte is D_2SO_4 in #1 and LiOD heavy water solution in #2 to 6; $T_{\mathrm{activ,max}}$ is the maximum temperature of cell reached during activation; R, $\overline{P}_{\mathrm{ex,max}}$, I and t are the reproducibility, the maximum average excess power, the current applied and the total electrolysis time, respectively, in the subsequent runs of electrolysis and calorimetry.

Two other examples of zero excess heat are shown in Fig. 6, for Pd-B/D_2O electrolysis while the cathode is inactive. In the first example (Fig. 6(a)), 0.1 A was applied for 6 h and then 0.6 A was applied for 10 h in Exp. #220615. The total excess heat is -0.030 $\pm$ 0.196 kJ with the total input heat of 86.631 $\pm$ 0.024 kJ. The average excess power is -0.5 ± 3.4 mW, which is equivalent to zero within the standard deviation. At 0.6 A, the instantaneous excess power $P_{\mathrm{ex}} = 15 \pm 4$ mW and $\mathrm{d}P_{\mathrm{in}}/\mathrm{d}t = -5$ mW/h; therefore $C = 3$ h/mW as done before.

Fig. 6(b) shows another example of calorimetry from Exp. #220712, where the Pd-B cathode was heated to 80°C in an electric constant temperature blast drying oven for 1 h before calorimetry was performed, and the absorbed deuterium in previous runs was desorbed. The average excess power is 21 $\pm$ 2 mW in the first 7 h, the total excess heat is 0.602 $\pm$ 0.172 kJ, while the formation heat of palladium deuteride is 0.593 kJ (calculated as $PdD_{0.6}$ stoichiometric number). This means the excess heat in the first 10 h is only from the formation heat of palladium deuteride.

3.2. Excess Heat With Pd-B

A total of 6 runs with activation and 55 runs of calorimetry were tested for the Pd-B rod from Dec. 2020 to July 2022 as listed in Table 1. The cumulative electrolysis duration was 2,147 h (including 54 h of activation). The appearance of Pd-B rod in the fresh as-received condition, and after electrolysis, are shown in Figs. 1(a) and (b), respectively.

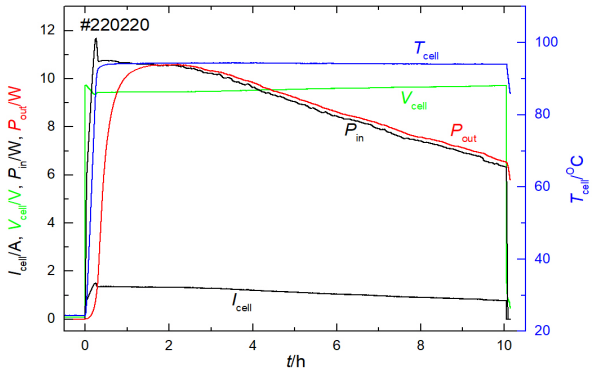

Figure 7. Electrolytic parameters in the second activation in Exp. #220220.

It is found that the Pd-B rod changed from brightness and uniform to darkness, rough and uneven due to repeated deuteriding-dedeuteriding.

In the first 7 runs of Exp. #201223 to 210129 (see also Table 7 in Ref. [12]), the Pd-B cathode was used as received and only cleaned with ethanol before the first run. However, it only produced maximum average excess power of 21 ± 7 mW in Exp. #201225 as listed in Table 1 and reported previously [12]. After that, the Pd-B cathode was treated with the activation method described before [9], [11]. Firstly, the cathode was open-electrolyzed in concentrated D_2SO_4 heavy water solution in another cell for 3.6 h on Feb. 2, 2021; the DC power was set at 4 A and 18 V; the maximum temperature of cell reached 218°C. Then the cathode was cooled naturally and cleaned. Finally, the cathode was assembled in the reflux open-cell and it was electrolyzed and conducted calorimetry. It showed more excess power than the previous series, the maximum average excess power of 46 ± 3 mW occurred in Exp. #210306 in all 11 runs (Exp. #210202 to 220206). However, the reproducibility was only 2 out of 11 tests as listed in Table 1.

On February 20, 2022, we tried a second activation run, as shown in Fig. 7. At this time, the electrolyte of 0.1 M LiOD heavy water solution and the reflux open-electrolytic cell were used; the DC power was set as 2 A and 10 V; the electrolysis duration was 10 h; the actual current decreased from 1.5 A at the beginning to 0.76 A at the end; the maximum temperature of the cell reached 94°C.

In subsequent electrolysis of Exp. #220222, average excess power of 70 ± 2 mW with average input power of 3.2 W was observed. In Exp. #220226, average excess power of 53 ± 2 mW at 0.1 A were observed ($\overline{P}_{ex}/\overline{P}_{in} = 18\%$, see Fig. 8(a)). In Exp. #220228, average excess power of 130 ± 2 mW at 0.6 A were observed ($\overline{P}_{ex}/\overline{P}_{in} = 5\%$); the total excess heat in this run was 22.488 ± 0.332 kJ as shown in Fig. 8(b).

The comparison of two experiments with and without excess power is shown in Fig. 9. In Exp. #210318 shown in Fig. 9(a), no excess power was observed while 0.7 A was applied for 36 h after first activation. In Exp. #220228 shown in Fig. 9(b), instantaneous excess power reached 0.2 W after the second activation. Another interesting point is that the temperature of cell was 82°C in both runs; however, the input power was 3.6 and 3 W in Exp. #210318 and #220328, respectively. This also indicates the excess power was produced in the latter run. Even if the linear correction of the input power is taken into account as in Eq. (3) and $C = 3$ h/mW as obtained in Section 3.1, $P'_{ex} = -4 \pm 13$ mW for the case shown in Fig. 9(a) with $dP_{in}/dt = 1.3$ mW/h (see Table 7 in Ref. [12]), and $P'_{ex} = 168 \pm 26$ mW for the case shown in Fig. 9(b) with $dP_{in}/dt = -8.5$ mW/h (see Table 2). The conclusion remains that the experiment shown in Fig. 9(b) produces significant excess power.

Excess heat results of open-electrolytic system with the Pd-B rod after the second activation, as shown in Fig. 7, are summarized in Table 2. Nearly all of runs gave excess power at different currents and different temperature, except for

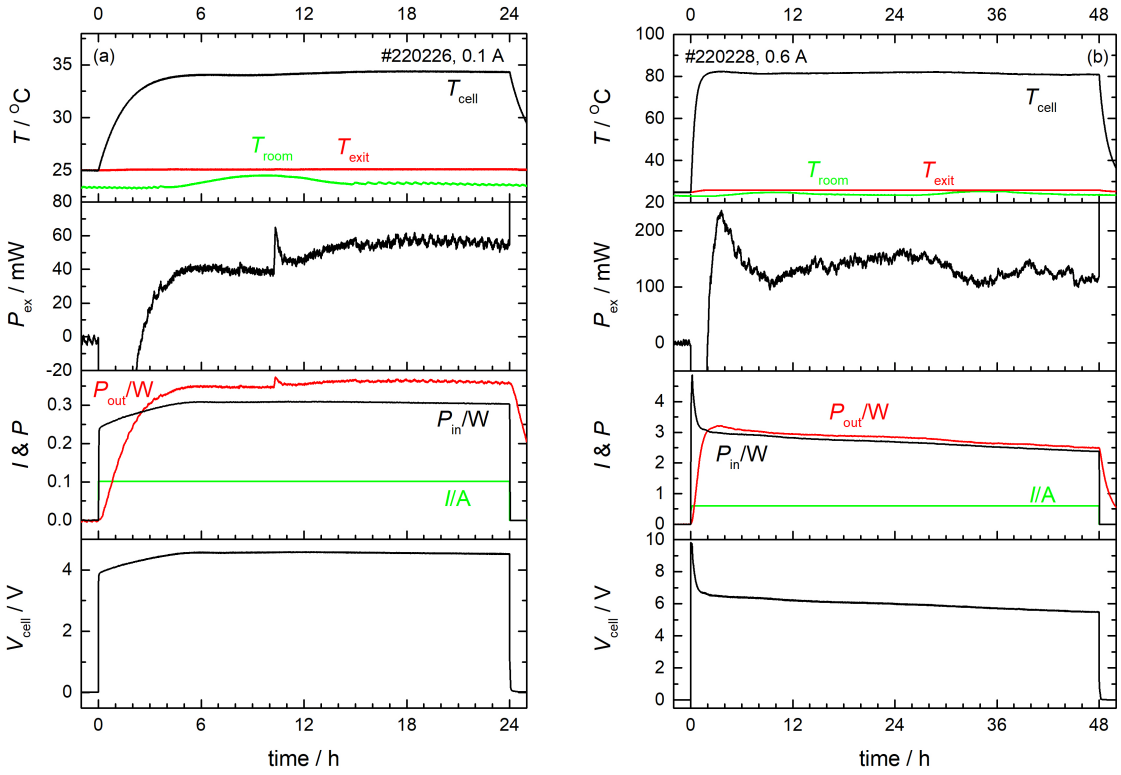

Figure 8. Electrochemical and calorimetric parameters of Pd-B/D_2O system in Exp. #220226 (a) and #220228 (b).

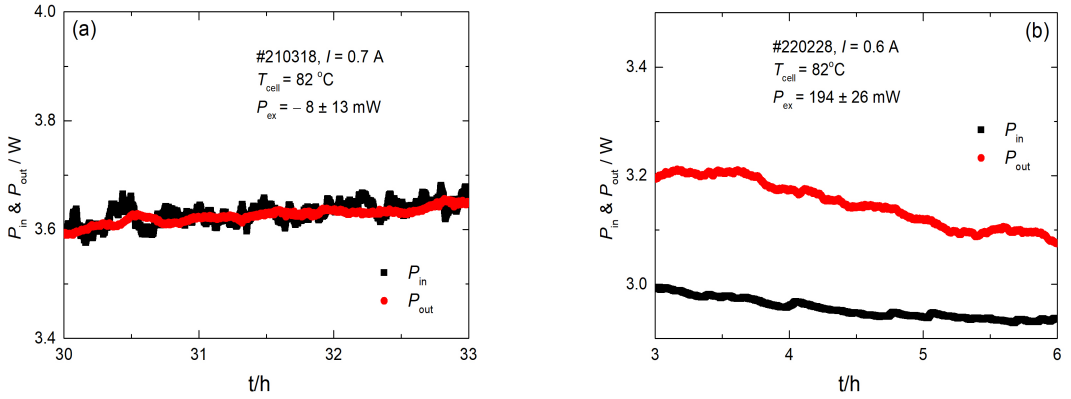

Figure 9. (a) Input and output power of Exp. #210318, no excess heat was produced, and the Pd-B cathode was inactive at that time; (b) Input and output power of Exp. #220228, sustained excess heat was produced, indicating that Pd-B cathode was active.

Table 2. Summary of excess heat in Pd-B/D_2O+LiOD reflux open-electrolytic cell after second activation.

	Integrated values				Steady values				
Exp. #	$I \times t$	Q_{in}	Q_{ex}	$\overline{P}_{ex}$	period	P_{in}	P_{ex}	dP_{in}/dt	T_{cell}
	A × h	kJ	kJ	mW	h	W	mW	mW/h	°C
220222	0.1 × 18,	838.61(15)	18.23(52)	70(20)	6 - 8	0.254(1)	32(1)	0.35	31
	0.6 × 30,				28 - 32	2.730(16)	158(8)	−16	76
	1.2 × 11,				50 - 53	9.504(16)	122(14)	−18	92
	0.6 × 13				62 - 64	3.612(3)	52(14)	36	88
220226	0.1 × 24	26.047(2)	4.62(17)	53(2)	22 - 24	0.304(0)	55(2)	−0.55	34
220228	0.6 × 48	466.67(9)	22.49(33)	130(2)	20 - 24	2.710(11)	149(6)	−8.5	82
220303	0.6 × 11		NA		4 - 6	2.986(22)	39(18)	−15	78
220304	0.6 × 48	484.61(9)	3.98(33)	23(2)	12 - 16	2.781(24)	85(16)	6.1	77
220317	0.6 × 24	272.48(5)	5.06(54)	59(6)	20 - 24	3.126(5)	53(3)	−3.6	26
220319	0.6 × 24	226.47(5)	3.34(63)	39(7)	9 - 12	2.603(4)	44(3)	−4	73
220322	0.6 × 24	241.92(5)	1.43(63)	17(7)	11 - 13	2.786(4)	6(7)	3.6	82
220324	0.6 × 24	278.01(5)	4.00(56)	46(6)	4 - 7	3.151(8)	40(3)	17	46
					22 - 24	3.305(1)	55(4)	0.56	NA
220326	0.6 × 24	329.92(6)	4.24(58)	49(7)	9 - 10	3.601(18)	−10(4)	66	41
					23 - 24	4.734(20)	-5(6)	86	47
220328	0.6 × 24	227.20(4)	3.87(50)	45(6)	22 - 24	2.511(6)	42(4)	−11	42
220330	0.6 × 24	166.44(4)	1.89(64)	22(7)	9 - 11	1.847(7)	42(5)	−12	71

Note: Q_{in} is the total input energy; Q_{ex} is the total excess heat; $\overline{P}_{ex} = Q_{ex}/t$, the average excess power.

Exp. #220303 due to a calorimetric problem. Of course, high current or high temperature will give more excess power than low current and low temperature. One example is shown in Exp. #220222 as listed in Table 2. It was found that $P_{ex} = 32$ mW at 0.1 A (31°C) and $P_{ex} = 158$ mW at 0.6 A (76°C). However, $P_{ex} = 122$ mW at 1.2 A (92°C), which is less than that at 0.6 A because the input power was overestimated due to bubble formation and unstable voltage recording, as discussed in Ref. [12]. In any case, the excess power depends mainly on the activity of the sample itself. The first several runs gave the most prominent excess power. After then, excess power decreased with time in a random manner.

After the first two activations and subsequent runs of electrolysis and calorimetry, this process was repeated 4 times from April to July 2022 as listed in Table 1. However, the excess heat was not as prominent as the second series.

4. Discussions

In previous works [9], [11], we found that 3 activation methods of (1) pre-electrolysis under high current and temperature, (2) heating in D_2SO_4 and (3) etching by aqua regia are all effective ways to make a Pd cathode produce excess heat in subsequent closed-electrolysis of D_2O. The author once believed that these activations are valid for every Pd sample every time. However, after checking our past data for Pd plates, I found that all Pd samples showed the similar behavior as the Pd-B rod here, i.e., every Pd plate can only be activated a couple of times as listed in Tables 3 to 5. Tables 3 and 4 show Pd plates of #1 and #32, respectively, for pre-electrolysis activation and subsequent runs of calorimetry in electrolysis. It is found that Pd#1 produced the maximum excess power after the first two activations and Pd#32 produced the maximum excess power after the third activation. For activation of heating in D_2SO_4, Pd#16 produced the maximum excess power after the fourth activation as listed in Table 5. For activation of etching by aqua regia, only Pd#8 showed the maximum excess power after the first activation, as listed in Table 2 in Ref. [11] and no other sample was studied systematically due to etching process being hard to control.

On the other hand, Miles and Imam discussed another possibility, i.e., a cracked sample cannot produce excess heat [7]. As shown in Fig. 1(b), there are more than a dozen axial cracks of 0.15 mm width on the cylinder surface of

Table 3. Effects of cathode activation on excess power production for Pd#1 in D_2O closed electrolysis in Ref. [9].

#	$T_{activ,max}$/°C	R	$P_{ex,max}$/mW	I/A	t/h	date range
1	110	8/15	120(16)	0.03 - 3	167	081221 - 090907
2	97	4/4	115(24)	3 - 4	30	090908 - 090812
3	98	3/8	51(24)	0.3 - 3	71	090815 - 090906
4	108	0/1	17(22)	3	8	090916
5	145	0/2	31(22)	3	19	090918 - 090919
6	127	0/1	20(15)	3	7	090922
7	114	0/12	34(24)	0.1 - 3	99	090924 - 110523

Note: # is the ordinal number of cathode activation by open-electrolysis while DC power is set as 4 A and 18 V for 5 to 7.5 h. $P_{ex,max}$ is the maximum value of excess power under stable state ($P_{ex,max}$ listed in Table 3 of Ref. [9] was only instantaneous value, which was not stable and reliable after checking). Other symbols are the same as that in Table 1.

Table 4. Effects of cathode activation on excess power production for Pd#32 in D_2O closed electrolysis in Ref. [11].

#	$T_{activ,max}$/°C	R	$P_{ex,max}$/mW	I/A	t/h	date range
1	181	0/2	39(18)	4	27	150107 - 150110
2	196	0/1	40(16)	4	15	150112
3	213	1/1	100(32)	4.2	15	150116
4	188	1/2	30(15)	3 - 4.5	24	150121 - 150309
5	171	0/4	53(23)	3.5 - 4	48	150311 - 150326

Note: # is the ordinal number of cathode activation by open-electrolysis while DC power is set as 4 A and 18 V for 2 to 3.5 h. Other symbols are the same as that in Table 3.

Table 5. Effects of cathode activation on excess power production for Pd#16 in D_2O closed electrolysis in Ref. [11].

#	$T_{activ,max}$/°C	R	$P_{ex,max}$/mW	I/A	t/h	date range
1	235	1/1	61(24)	3.3	12	131231
2	242	0/1	-12(24)	3.3	8	140102
3	244	1/1	65(24)	3.3	12	140104
4	244	2/2	117(16)	3 - 3.3	36	140107 - 140110
5	241	1/2	29(16)	3 - 3.3	24	140122 - 140123

Note: # is the ordinal number of cathode activation by heating in D_2SO_4 for 1.5 to 2 h. Other symbols are the same as that in Table 3.

the Pd-B rod after 2,147 h of electrolysis. However, cracks with a width of 0.03 mm was observed as early as Mar. 18, 2021 (prior to Exp. #210318 shown in Fig. 9(a)), the cathode had been electrolyzed for 480 h and experienced one activation procedure before that day. Although the Pd-B rod did not produce pronounced excess heat at that time, it become activated after second activation on Feb. 20, 2022, as shown in Fig. 7. We are sure that the cracking on the Pd-B rod continuously grew during deuteriding-dedeuteriding in experiments due to radial plastic stresses developed in $\alpha \leftrightarrow \beta$ phase transition. Therefore, we cannot be sure that the cracking inhibits the excess heat, at least for this sample.

After 2,147 h of intermittent electrolysis, the Pd-B rod become thin at both ends and thick in the middle, as shown in the right of Fig. 1(b). Its average diameter of 12 points is 4.848 mm, therefore the total volume is 352.6 mm^3, which is only 2.4 mm^3 or 0.7% greater than the original volume of 350.2 mm^3. Storms studied the relationship between excess volume induced by deuteriding and dedeuteriding cycles and production of excess heat of Pd cathodes [14]–[16], and found that the excess volume of less than 1% of a sample does not increase even after repeated deuteriding-dedeuteriding, while the excess volume of greater than 1% of a sample increases with repeated deuteriding-dedeuteriding. The excess volume here is only 0.7%, which is less than 1%. Storms also found that excess volume no more than 2% is important for production of excess heat [15]. This means that the Pd-B rod here is a good

sample and B additive can suppress void production and expansion during deuteriding-dedeuteriding. One possible reason is that the concentration and volume changes of D during the $\alpha \leftrightarrow \beta$ phase transition in Pd-B are smaller than that in Pd [17], [18], resulting in a reduction in the plastic stress, so the void production is also less than that of pure palladium.

This cathode contains 0.25wt.% of boron (corresponding to $PdB_{0.025}$) and the actual boron content measured by glow-discharge mass spectroscopy (GDMS) is 0.18wt.% (corresponding to $PdB_{0.018}$) [19]. However, the original density of this rod according to the mass and volume in Section 1 is 11.758 g/cm^3, which is closed to that of $PdB_{0.05}$ and is smaller than that of $PdB_{0.025}$ or $PdB_{0.018}$ [20]. Although Pd-0.5wt.%B rods were manufactured at the same time and have the same dimensions as that of Pd-0.25wt.%B, M. A. Imam confirmed that the component of this rod is the latter. The reason of this inconsistency is unknown now. On the other hand, the volume expansion of this rod after repeated deuteriding and dedeuteriding cycles is different from the result of Pd containing 500 ppm boron in Ref. [16], where the presence of B leads to an increase in excess volume. One obvious reason is that the B content here is at least 36 times higher than in Storms [16].

This sample contains 10.3 mg of B and has a mass loss of 2.1 mg after long-duration electrolysis. Because it has been subjected to high temperature (218°C) electrolysis in D_2SO_4 in the first activation experiment as discussed above, we could not determine whether the mass loss was mainly due to the loss of B or the corrosion of Pd by sulfuric acid, because the electrode could not be weighed after it was spot-welded onto its Pt lead.

5. Conclusions

We reached four conclusions: First, The Pd-B cathode provided by Miles does produce excess heat. Second, Pre-electrolysis under high current and high temperature is an effective method to activate this cathode to produce excess heat during subsequent electrolysis. Third, the activation method is only effective the first few times it is applied. After that, applying it more times is disadvantageous. This experience applies not only to this Pd-B rod, but also to all samples of Pd plates studied in our lab. Finally, this sample expanded very little after repeated absorption and desorption of deuterium, meeting Storms' requirements for good Pd samples.

Although the detailed reason of present discovery is unclear now, it is a good start to improve the reproducibility and increase the magnitude of excess heat in Pd/D_2O electrolytic systems in the future.

Acknowledgments

The author thanks Profs. Melvin H. Miles and M. Ashraf Imam for providing the sample and helpful discussions. This work was supported by NSFC (22373106, 21153003, 20973185) and 973 program of MOST in China (2009CB226113).

References

[1] M. Fleischmann, S. Pons and M. Hawkins, Electrochemically induced nuclear fusion of deuterium. *J. Electroanal. Chem.* **261** (1989) 301–308. Erratum in **263** (1989) 187–188.

[2] M. Fleischmann, S. Pons, M.W. Anderson, L.J. Li and M. Hawkins, Calorimetry of the palladium-deuterium-heavy water system. *J. Electroanal. Chem.* **287** (1990) 293–348.

[3] M.C.H McKubre, S. Crouch-Baker, R.C. Rocha-Filho, S.I. Smedley, F.L. Tanzella, T.O. Passell and J. Santucci, Isothermal flow calorimetric investigations of the D/Pd and H/Pd systems, *J. Electroanal. Chem.* **368** (1994) 55–66.

[4] E. Storms, Use of a very sensitive Seebeck calorimeter to study the Pons–Fleischmann and Letts effects. *Proc. 10th Int. Conf. Cold Fusion*, P.L. Hagelstein and S.R. Chubb (Eds.), World Scientific, New York, 2006, pp. 183–197.

[5] M.H. Miles, R.A. Hollins, B.F. Bush, J.J. Lagowski and R.E. Miles, Correlation of excess power and helium production during D_2O and H_2O electrolysis using palladium cathodes. *J. Electroanal. Chem.* **346** (1993) 99–117.

[6] M.H. Miles, The Fleischmann–Pons calorimetric methods, equations and new applications. *J. Condensed Matter Nucl. Sci.* **24** (2017) 1–14.
[7] M.H. Miles and M.A. Imam, Excess power measurements for palladium–boron cathodes. *J. Condensed Matter Nucl. Sci.* **29** (2019) 12–20
[8] M.H. Miles, The Thermoneutral potential in electrochemical calorimetry for the Pd/D_2O System. *J. Condensed Matter Nucl. Sci.* **33** (2020) 74–80.
[9] W.-S. Zhang, Characteristics of excess heat in Pd|D_2O+D_2SO_4 electrolytic cells measured by Seebeck envelope calorimetry. *Proc. 15th Int. Conf. Condensed Matter Nuclear Science*, Roma, Italy, Oct. 5–9, 2009, pp. 27–32.
[10] W.-S. Zhang, Construction, calibration and testing of a decimeter-size heat-flow calorimeter. *Thermochim. Acta* **499** (2010) 128–132.
[11] J. Gao, W.-S. Zhang, J.-J. Zhang, Effects of D/Pd Ratio and cathode pretreatments on excess heat in closed Pd|D_2O + D_2SO_4 electrolytic cells. *J. Condensed Matter Nucl. Sci.* **24** (2017) 42–59.
[12] H. Zhao, W.-S. Zhang, W.-Y. Xiao, Excess heat in a Pd(Pt)-D_2O+LiOD reflux open-electrolytic cell, Presented at ICCF-23, Xiamen, China, June 7 to 9, 2021. See: http://lenr-canr.org/acrobat/ZhaoHexcessheat.pdf.
[13] W.-S. Zhang, A device and method for thermal power measurement. China Patent 201810191597.0.
[14] E. Storms, and C. Talcott-Storms, The effect of hydriding on the physical structure of palladium and on the release of contained tritium. *Fusion Technol.* **20** (1991) 246–257.
[15] E. Storms, How to produce the Pons-Fleischmann effect. *Fusion Technol.* **29** (1996) 261–268.
[16] E. Storms, Some thoughts on the nature of the nuclear-active regions in palladium. *The Sixth Int. Conf. on Cold Fusion, Progress in New Hydrogen Energy*, Hokkaido, Japan, Oct. 13–18, 1996. Vol. 1, pp. 105–112.
[17] R. Burch and F.A. Lewis, Absorption of Hydrogen by Palladium + Boron and Palladium + Silver + Boron Alloys. *Trans. Faraday Soc.* **66** (1970) 727–735.
[18] Y. Sakamoto, Y. Tanaka, K. Baba, T.B. Flanagan. Hydrogen Solubility in Palladium-Boron Alloys. *Z. Phys. Chem. N.F.* **158** (1988) S237–251.
[19] M.A. Imam, D.J. Nagel, M.H. Miles, Fabrication and characterization of palladium–boron alloys used in LENR experiments. *J. Condensed Matter Nucl. Sci.* **29** (2019) 1–11.
[20] M. Yoshihara, R.B. McLellan, Thermodynamics of the palladium-boron-hydrogen system. *Acta Metall. Mater*. **38** (1990) 655–661.

J. Condensed Matter Nucl. Sci. 38 (2024) 13–41

Research Article

The History of LENR Research at NASA Glenn Research Center

T. L. Benyo[1],* L. Forsley[1,2], B. Steinetz[1]

[1]*NASA Glenn Research Center, USA*

[2]*Global Energy Corporation, LLC, USA*

Abstract

NASA requires novel power sources to accomplish future planetary science missions. A range of power systems will likely be required for both scientific investigations and future manned missions on the moon and Mars. NASA has successfully used radioisotope power systems for over five decades for missions throughout the solar system. For example, both the Curiosity and Perseverance, *aka* Percy, Mars rovers have "nuclear batteries". The two Voyager spacecraft that launched in 1977 continue to operate after 46 years, a little over half of the half-life of the heat source ^{238}Pu's alpha particle decay and are now in interstellar space! However, radioisotope thermoelectric generators, or RTGs, have been limited to producing less than 1 kilowatt of electrical power and usually only produce a few hundred watts. Consequently, for decades NASA has investigated fission and fusion reactors. The NASA Glenn Research Center (GRC) has had deep space power and propulsion as part of its mission portfolio beginning with Nuclear Thermal Propulsion (NTP) in the 1960s. Later, ion propulsion, (used with deep space probes and geosynchronous satellite station keeping), radioisotope power systems (used in nearly all deep space missions) and most recently the Kilopower space/fission reactor tested in 2018 were added. For the past several years, NASA Glenn researchers have been investigating an unconventional approach to initiate nuclear reactions [1]. This work has been called by various names including Low Energy Nuclear Reactions (LENR), Chemical Assisted Low Energy Nuclear Reactions (CANR-LENR), and more recently Lattice Confinement Fusion (LCF) reactions. Using a high flux of energetic electrons in an environment containing a high atomic density of nuclear fuel, such as deuterium, researchers have seen compelling evidence of condensed matter nuclear reactions, including charged particle and neutron emissions, as well as small levels of excess heat, which cannot be explained by chemical reaction processes. This paper provides a summary of the 30+ year history of LENR research at NASA Glenn Research Center from 1989 to the present and cites several reports published during that period.
 ISSN 2227-3123

Keywords: Lattice confinement fusion, LENR

*Corresponding author: Email: theresa.l.benyo@nasa.gov

© 2023 ICCF. All rights reserved. ISSN 2227-3123

1. INTRODUCTION

GRC has studied LENR or Lattice Confinement Fusion under various names since the 1989 University of Utah announcement by Drs. Fleischmann and Pons. We began with D_2 gas cycling [2] then investigated Mills' potassium-carbonate [3] and energy harvesting from sonoluminescence [4]. Later, we undertook gas cycling Pd/Ni powders, Pd/D co-deposition [5,6], x-ray [7], electron and bremsstrahlung irradiation [8, 9] following Didyk's experiments [10], glow discharge repeating Karabut's experiments [11], and plasma loading calorimetry [12]. Lipson's TiD_2 SEM irradiation [13] was repeated. We modeled [14] or measured [15] various loading and triggering mechanisms. Our later efforts began in 2014 under the Advanced Energy Conversion Project and have continued under the Lattice Confinement Fusion Project. Many of our published papers can be found through our website:

https://www1.grc.nasa.gov/space/science/lattice-confinement-fusion/

NASA GRC conducted LCF research with several organizations ranging from the Naval Surface Warfare Centers Pd/D co-deposition replications and Density Functional Theory modeling to the Department of Energy Los Alamos National Laboratory on nuclear modeling with MCNP.

To verify nuclear reactions, we have used or developed nuclear diagnostics like High Purity Germanium (HPGe) Gamma Ray Spectroscopy, Solid State Nuclear Track Detectors (CR-39), liquid scintillator alpha/beta spectroscopy, neutron scintillator [16] and moderating-type spectrometers [17]. We have used a variety of elemental and isotopic assays to determine LENR effects including optical microscopy, Scanning Electron Microscopy with Energy Dispersive X-Ray Analysis (SEM/EDX), X-Ray Photoelectron Spectroscopy (XPS) and Transmission Electron Microscopy (TEM). All these methods observe the surface of a material. By dissolving or vaporizing samples, Inductively Coupled Plasma Optical Element Spectroscopy (ICP-OES) has been used to determine elemental composition (in parts per billion) or with mass spectroscopy, isotopes (ICP/MS). Focused ion beam (FIB) is used to slice open a sample and observe the "cut" with either SEM/EDX, or Time-of-Flight Secondary Ion Mass Spectroscopy (TOF-SIMS) [18]. Notably, we have learned and documented the limitations associated with each of these methods ranging from handling contamination, background interferences, instrumental limitations including sensitivity and field of view, and sample preparation.

2. Novel Nuclear Fusion Reactions as an Energy Source

Harnessing fusion would provide humanity with nearly limitless energy. Many NASA missions require a compact, controllable power source that is unaffected by environmental concerns such as lunar dust. Novel energy producing materials could lead to a scalable novel power source, extending the state-of-the-art in specific power compared to photovoltaic-based solar cells. NASA could take advantage of a new source of power eliminating the need for high-cost radioisotopes and nuclear fission-based reactors.

For 30 years, multiple labs have observed fusion reactions suggesting Lattice Confinement Fusion (LCF). LCF may be the key to harnessing fusion within a compact, contained system. The advantages of LCF include:

- Eliminates the need for low enriched uranium (LEU), high assay low enriched uranium.(HALEU) and weapons-grade uranium (HEU).
- Reduces safety, security, and supply concerns.
- Nearly zero radioactive waste.
- Offers compact, controllable power.

Figure 1 illustrates the many long-term applications that the LCF team at NASA GRC has in mind that could take advantage of LCF reactions.

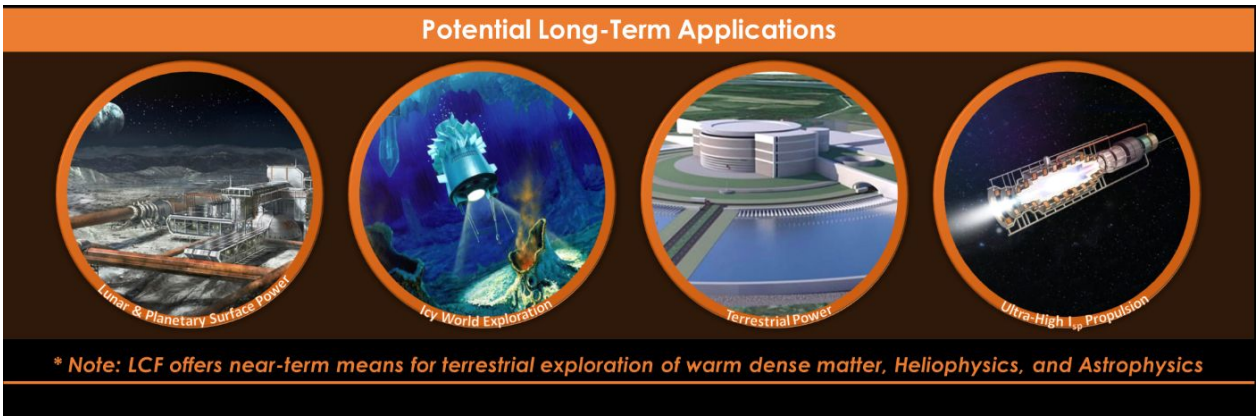

Figure 1. NASA Applications Needing Compact Controllable Power.

3. Timeline of Events

Several groups at NASA; Langley Research Center (LaRC), Marshall Space Flight Center (MSFC) and GRC followed various LENR researchers including Pons/Fleischmann, Focardi, Piantelli, Miley, Widom and Larson, Nagel, and Rossi (1989 to 2011). The NASA teams discussed and reviewed various approaches. Dennis Bushnell (Chief Scientist, NASA LaRC) met with GRC researchers Fralick, Niedra, Wrbanek, and Decker along with several GRC managers to discuss Bushnell's LENR concept. After that meeting, Bushnell invited Robert Hendricks to visit MSFC and learn about the LENR work there. Inspired by the LENR work being done at LaRC and MSFC, Robert Hendricks formed a group and with GRC R&D management approval, Mr. Hendricks (GRC) organized a LENR/Innovations Workshop held on Sept 21, 2011, at NASA GRC in Cleveland, OH. Speakers from GRC, LaRC and MSFC shared their current research. Dr. Bruce Steinetz, Dr. Theresa Benyo, and others attended with great interest. Robert Hendricks briefed GRC Center Director, Dr. Ray Lugo shortly after. Dr. Bruce Steinetz, Dr. Arnon Chait (representing Drs. Vladimir and Marianna Pines), Gus Fralick, and Dr. Lei (GRC R&D Director) attended Mr. Hendricks' briefing. Hendricks proposed a LENR research project at GRC. Dr. Lei authorized a small effort at GRC led by Dr. Steinetz and named Advanced Energy Conversion (AEC). Dr. Lugo orchestrated a briefing at NASA HQ where all NASA efforts were presented.

The AEC Project grew from a few researchers to about 25 over the years from 2011 to 2018. Dr. Steinetz met with Lawrence Forsley and Dr. Pam Mosier-Boss to discuss co-deposition papers at Navy SPAWAR in 2012. Forsley, between GEC and GRC, set up a NASA Space Act Agreement to identify high temperature Solid State Nuclear Track Detectors. A small amount of funding from the Director's Discretionary Fund (~2012–2013) under Dr. Ray Lugo's and Dr. James Free's tenures as NASA GRC Center Director grew to a large NASA Science Mission Directorate, Planetary Science Division funded effort (2014 to 2018) under Dr. James Free's and Dr. Janet Kavandi's tenures as NASA GRC Center Director. Various NASA HQ and other government agency reviews were held of the work over the active years. The AEC Project's work culminated in the *Phys Rev C* journal publication of experiment [9] and theory [14] papers in 2020.

Many individuals contributed to the success of GRC's past LENR research efforts. The diverse and talented team consisted of experimental physicists, nuclear physicists, solid state physicists, electrochemists, material scientists, research technicians, mechanical engineers, electrical engineers, plasma physicists, statisticians, mathematicians, computer scientists, data analysts, and project managers. The following paragraphs list the individuals along with their activities and contributions during our LENR research efforts.

3.1. AEC Research Scientists and Engineers

Mr. Gustave Fralick conducted experiments cycling D_2 gas in palladium (Pd) as a source of nuclear activity (compare with Celani et al). This gas cycling was one of the first non-electrochemical experiments. Mr. Fralick also investigated the possibility of the existence of sub-normal hydrogen energy levels (Niedra et al) and sonoluminescence (Wrbanek et al) sources of energy. The cycling experiments were reported in International Journal of Hydrogen Energy in 2020 (Fralick et al).

Mr. Robert Hendricks recognized the value of conducting LENR experiments at NASA and was instrumental in orchestrating a formal LENR research project at NASA GRC. His investigation in prior LENR research outside of NASA helped guide the direction of the AEC project. He conducted electrolytic wet cell slow co-deposition and x-ray irradiation experiments. As a senior technologist, Mr. Hendricks continually provided his expertise and offered guidance to all members on the team conducting LENR experiments that the NASA GRC team performed during his tenure at NASA.

Dr. Bruce Steinetz was the original Principal Investigator (PI) of the AEC Project. He advocated for the initial funding for the effort by convincing the then Center Director to provide some discretionary funding to cover initial hardware and staffing needs. Under his leadership the project grew slowly first and then rapidly later as we started to make some very interesting physics findings (anomalous heat generation, apparent nuclear transmutations, evidence of charge particle and neutron emissions). The Team grew with the addition of experts in many fields including: both theoretical and experimental physicists; solid state physicists; materials scientists; a large staff of engineers to design hardware to carry out carefully constructed experiments; and engineering technicians to implement the experimental hardware. The project continued to grow through ~2017 at which time NASA Headquarters gave us direction to verify and publish clear evidence of novel nuclear reactions, namely bremsstrahlung radiation of highly deuterated ErD_3 targets. We completed that assignment in 2018. The culminating papers (experimental and theoretical) were published in the high impact factor Journal *Phys Rev C* in April 2020. Late in 2019, Dr Steinetz was asked by management to support other pressing Agency projects so turned over the reins of the project to Dr. Theresa Benyo and Mr. Lawrence Forsley.

Dr. Arnon Chait helped launch and lead the LENR project and NASA GRC. With training and experience covering physics, engineering, and biosciences, Dr. Chait extensively published in multiple fields and is the co-inventor of LENR patents. Dr. Chait advised the AEC Team and helped develop the electron screening theory.

Dr. Vladimir Pines is a theoretical physicist instrumental in developing the electron screening theory that guided the AEC Team's experiments. Dr. Pines expertise in nuclear physics and attention to fundamental physics theories helped the AEC Team to achieve success with the bremsstrahlung irradiation studies conducted at IBA. Dr. Pines helped guide many AEC experiments with his expert knowledge in experimental nuclear physics.

Dr. Marianna Pines worked closely with Dr. Vladimir Pines and helped develop the AEC project's electron screening theory. Dr. Marianna Pines was instrumental in writing and running Mathematica codes that determined the cross sections of d-d fusion reactions with deuterated metals according to the main theory developed by Dr. Vladimir Pines. She also helped develop a novel nuclear reactor design that the AEC team tested in small scale experiments.

Dr. Theresa Benyo is the Lattice Confinement Fusion Project PI and an analytical physicist. During the AEC Project she was the nuclear diagnostics lead conducting nuclear diagnostics including gamma spectroscopy, alpha/beta detection, and half-life determination. Dr. Benyo carried out nuclear Monte Carlo and Density Functional Theory modeling and oversaw material assays. In addition, Dr. Benyo worked to merge experimental data with electron screening theory by analyzing all the nuclear diagnostic data to help explain how to orchestrate nuclear fusion reactions.

Mr. Lawrence Forsley is the senior lead experimental physicist on the NASA GRC AEC Project and the Lattice Confinement Fusion Project of which he currently serves as co-PI. Mr. Forsley assisted with planning many of the

AEC experiments and guided the team in collecting experimental data and detecting nuclear reaction products. He instituted the use of CR39 chips for charged particle and neutron detection and liquid beta scintillation for beta and tritium detection. Previously he worked on diagnostics, command, and control systems (C4I) for laser and magnetic fusion systems in the US and Germany.

Dr. Bayar Baramsai joined the AEC team in 2017 to perform neutron spectroscopy, working especially with liquid scintillators. He supported nuclear events diagnostics using pulse-shape-discrimination (PSD) and neutron unfolding codes with neutron scintillator spectrometers. He also supported the bremsstrahlung beam characterization and nuclear event rate calculations for the experiments at IBA.

Dr. Philip Ugorowski joined the AEC team in 2017 to perform neutron spectroscopy, working especially with a moderating-type neutron detector. Tests were made at Neil Armstrong Test Facility using a linear accelerator. Tests at ATF also involved scintillator panel Time-of-Flight neutron spectroscopy. Experiments using the IBA Dynamitron used the moderating-type neutron detector to precisely calibrate the gamma-ray beam energy. Dr. Ugorowski also contributed to theory discussions of LCF and experimental planning for wet-cell experiments and analysis of wet-cell data.

Dr. Wayne Jennings prepared many of the samples used in the AEC project, primarily through deuterization of rare earth metals. He also was central to characterization of pre- and post- experiment materials by SEM/EDS and ToF-SIMS.

Dr. Fred Van Keuls initially assisted Mr. Fralick with the deuterium gas cycling experiments with palladium and captured thermal output of the experiments. Dr. Van Keuls also worked at loading metals with deuterium gas for later experiments involving irradiation of deuterated metals.

Mr. Phillip Smith conducted electrolytic wet cell experiments using the slow co-deposition protocol. His no-nonsense and unbiased approach to scientific experiments enabled an unprejudiced set of LENR experiments. The results of which were worthy of publication in the "Journal of Electroanalytical Chemistry". Mr. Smith's background in fuel cells and batteries was invaluable to the AEC team.

Mr. Richard E. Martin served as the Deputy PI for the AEC project and was responsible for much of the X-ray based experiment development, testing and data acquisition.

Dr. Timothy Grey is a Plasma Physicist who supported the modeling and design of both AEC plasma rigs.

Dr. James Gilland is a Plasma Physicist who supported the modeling and design of both AEC plasma rigs.

Mr. Anthony Colozza led the design, construction and operation of the plasma test stand and the diaphragm reactor. He also coordinated the test plan for each set of experiments.

3.2. Material Science Experts

Dr. David Ellis performed material analysis of pre- and post-test samples under SEM and ToF-SIMS for the GRC programs, including the Naval Surface Warfare Center, Dahlgren Division and samples provided by Dr. Francesco Celani with INFN in Frascati, Italy. His material science expertise also assisted the AEC Team with deuteration of many metals.

Dr. Ivan Locci is a material scientist who supported the AEC Team through material analysis of many samples from AEC experiments under SEM and prepared Pd 'straw' samples with brazing techniques.

Mr. Dereck Johnson performed ICP-OES analysis on pre- and post- exposed materials for trace elements in the ppm-ppb range as well as confirmation of the bulk composition. Mr. Johnson also coordinated with outside commercial labs to arrange for analysis by techniques such as ICP-MS, GDMS, and NMR, where in-house capability did not exist.

Dr. Kathy Chuang characterized materials used during the x-ray irradiation experiments, mainly deuterated polyethylene using FTIR.

3.3. Technical Support Experts

Mr. Nicholas Penney provided invaluable technical support throughout the AEC project. Mr. Penney completed many tasks such as experimental equipment build-up, material vessels development, and LabView connectivity for capturing nuclear product detection under the electron beam and x-ray irradiation experiments.

Ms. Annette Marsolais worked with the AEC Team to help analyze data and integrate it into research efforts. Ms. Marsolais also researched the electron screening theory to help provide a link between theoreticians and other members of the team.

Mr. Michael Becks managed the Chain of Custody of experimental test samples, including documenting pedigree of raw materials, storing pre- and post-test samples, and shipped test samples and other equipment to off-site testing locations as needed. He assisted in assembling test samples, split off materials for pre- and post-test analysis, consolidated and organized test data, and was a member of the IBA test team. He documented test sample details, i.e., test sample name, masses of ingredients, configurations. Mr. Becks also provided data analysis support and software support using MCNP.

Dr. Christopher Daniels provided assistance with experimental data processing to establish proper statistics and determining experimental error.

Ms. Kristen Bury provided project management support during the project formulation phase. Ms. Bury also provided some hands-on support during the gamma irradiation experiments.

Ms. Tracey Kamm served as a research technician and assisted Dr. Benyo with nuclear diagnostics running pre- and post-test samples under various nuclear detection systems such as the alpha/beta detection system at NASA GRC.

Mr. Robbie Malcolm helped develop engineering plans and designs for many of the AEC team's experimental equipment, mainly the calorimeter apparatus.

Mr. Paul Passe is a design engineer who designed much of the Glow Discharge rig and assisted with the design of the Plasma rig.

Mr. Brian Jones operated the AEC project's Linear Accelerator (LINAC) during the gamma irradiation campaign from 2015 to 2017.

Mr. Paul Stout is an electrician who was instrumental in helping make LINAC operate and assisted in much of the electrical work that was needed to support the gamma irradiation experiments. Mr. Stout was also one of the LINAC operators.

Mr. Joseph Assion is a hardware designer who provided many of the detailed drawings for test hardware and fixtures used during the AEC experiments.

Mr. Francis Gaspare is a machinist and mechanic who fabricated several sample holders and other fixtures used during the AEC experiments.

Mr. Frank Bremenour is a technician who supported rig buildup and test sample assembly of test facilities used during the AEC experiments.

Mr. John Zang is an engineer who supported some of the early facilities design for the Igloo and LINAC installation.

Mr. Christian Maloney is an engineer who supported installation of Data Systems and remote operation capabilities for the LINAC. Mr. Maloney also served as one of the LINAC operators.

Mr. Mark Bell is an engineer who provided some initial LabView work with the buildup of the AEC calorimeter.

Ms. Marian Cronin is a systems engineer who coordinated the systems engineering work and created the work instructions for the AEC plasma rigs.

Mr. Csongor Hollohazy performed cleaning and loading of experimental disks for the AEC plasma rig.

Mr. Ian Jakupca is a direct energy conversion researcher who operated the AEC plasma rig.

Mr. Scott Panko is an electrical engineer who provided support in operating the AEC plasma rig.

Mr. Lawrence Edwards provided support in operating the AEC plasma rig.

Mr. Don Johnson served as an Electrical Engineer in support of various experimental needs during the AEC project and operated the AEC plasma rig.

Mr. Stephen J. Guzik served as an Electrician in support of various experimental needs during the AEC project.

Mr. Christopher Garcia developed LabVIEW data acquisition and control programming that assisted the operation of many AEC experiments.

Mr. Joseph Rymut is an electrical engineer who was involved with building up and running the Arc Glow Reactor experiments, the Johnson-Matthey experiments, and the Parr Reactor experiments.

Mr. Arthur Erker was instrumental in procuring the needed diagnostic and other experimental equipment for the AEC Team. Mr. Erker's background in nuclear diagnostic systems helped the AEC team a great deal with procuring the correct equipment for such a research effort.

Lori Bulat provided support with analyzing the many CR-39 chips used in the AEC experiments.

Victoria Leist provided support with analyzing the many CR-39 used in the AEC experiments. Ms. Leist also used liquid scintillator spectroscopy to analyze experimental materials.

Amy Rankin provided support with analyzing the many CR-39 chips used in the AEC experiments.

Ms. Rebecca 'Beckey' Johannsen was one of the health physics technicians that performed nuclear diagnostics on samples from the AEC Team's LINAC experiments. Ms. Johannsen was proficient at HPGe spectroscopy, liquid beta scintillation operation, and CR39 chip etching.

Ms. Karen Novak was one of the health physics technicians that performed nuclear diagnostics on samples from the AEC Team's LINAC experiments. Ms. Novak was proficient at HPGe spectroscopy and liquid beta scintillation operation.

Ms. Catherine Jensen was one of the health physics technicians that performed nuclear diagnostics (HPGe and liquid beta scintillation spectroscopy) on samples from the AEC Team's LINAC experiments. Ms. Jensen was also proficient at the logistics of shipping and receiving sensitive research equipment and samples for the AEC Team.

Mr. Christopher Blasio is NASA GRC's Radiation and Laser Safety Officer and has assisted the AEC Team with obtaining the necessary safety permits for all the experiments performed by the team. He also was responsible for conducting radiation safety training for all the AEC Team members that handled experimental materials from the AEC research activities.

Mr. Roderick Case is a health physicist and has supported the AEC Team with HPGe spectroscopy expertise and the proper handling of radioactive materials.

Ms. Jennifer Baumeister, Bastion Technologies, Principal Risk Management Facilitator. From 2016 to 2018, Ms. Baumeister ensured AEC Project Team compliance with NASA Continuous Risk Management (CRM) Procedures by tailoring the CRM section of the Project Plan, creating a Risk Board Charter, and conducting CRM training and risk identification workshops. She initiated monthly Risk Boards to guide the AEC Project team in identifying and managing technical, schedule, cost, and safety threats that may have created obstacles in meeting requirements and goals.

3.4. LENR Research Partners

Dr. Pamela Mosier-Boss is a retired analytical chemist from SPAWAR San Diego, now NIWC. Along with Stan Szpak, she was involved in the development of Pd/D co-deposition process. Her work was duplicated by the AEC Team, and she currently serves as a consultant to the LCF team. Besides her work in LENR, she had been involved in the development of sensors to map contaminant plumes in the environment as well as materials science research on thionyl chloride batteries, drag reducing polymers, polyacetylene, and hydrogen generation to inflate lighter than air vehicles.

Dr. Timothy Koeth is an assistant professor of Material Science & Engineering at the University of Maryland. He performed gamma irradiation experiments with their 3MV LINAC to replicate the gamma irradiation experiments performed at NASA GRC.

Ms. Amber Johnson is the director of the Radiation Facilities at University of Maryland and oversees the operation of the LINAC that was used to replicate NASA GRC's gamma irradiation experiments. Ms. Johnson was instrumental in orchestrating the gamma irradiation experiments at the University of Maryland with Dr. Timothy Koeth.

Dr. Lou DeChiaro, Naval Surface Warfare Centers: Indian Head and Dahlgren Division, conducted Quantum Espresso Density Functional Theory modeling of various hydrided/deuterided metals supporting co-deposition and bremsstrahlung irradiation campaigns, and parametric pumping. Dr. DeChiaro analyzed co-deposition calorimetry data from Dahlgren and Indian Head and conducted RF signal acquisition from the Indian Head DARPA co-funded HIVER Project.

Dr. Pearl Rayms-Keller, Naval Surface Warfare Center: Dahlgren Division, conducted SEM/EDX analyses of co-deposition cathodes run at Dahlgren.

Ms. Stacy Barker, Naval Surface Warfare Center: Dahlgren Division, conducted co-deposition experiments at Dahlgren using the Fast Protocol including preparing multiple cells and collecting data.

Ms. Karen Long, Naval Surface Warfare Center: Dahlgren Division, assisted and led various aspects in the design, setup, implementation, and data analysis of the NSWC Dahlgren co-deposition LENR experiments including XPS analysis.

3.5. Project Management Support

Mr. Paul Westmeyer provided support for the GRC team overseeing the AEC project and serving as the liaison between the research team and NASA HQ. Mr. Westmeyer routinely visited NASA GRC to provide hands-on support during the x-ray and gamma irradiation experimental campaigns. His interactions with members of the AEC team proved invaluable as progress was made in demonstrating d-d nuclear fusion.

Mr. Leonard Dudzsinki is a Chief Technologist for the PSD at NASA HQ. He has supported the AEC/LCF Team with countless discussions on the nuclear fusion reactions being studied and sharing our successes with the PSD management team at NASA HQ. He oversees the sustainment of NASA's deep space power capabilities and development of new power systems based on Plutonium-238.

General (ret.) David Stringer is the director of NASA's Neil Armstrong Test Facility (ATF) and was instrumental in supporting the AEC Team's build-up of the LINAC facility at ATF.

Mr. Gerald Hill was a facility manager at NASA's Plum Brook Station (now called the Neil Armstrong Test Facility) who oversaw the operation of the AEC project's LINAC housed in one of the 'bunkers' at that test facility. Mr. Hill also managed and supervised the technicians that were supporting the LINAC gamma irradiation experiments conducted by the AEC Team.

Mr. John Heese worked as the NASA Advanced Energy Conversion (AEC) integration manager from 2016 to 2018. Then, from 2019 until the present, he has been providing NASA Contractor management oversight to AEC and Lattice Confinement Fusion (LCF) related work.

Ms. Susan Jansen, Branch Chief, Thermal Systems and Transport Process, was the Task Lead for the AEC contract work from 2012 to 2018. At one time, the AEC contract employed 30 Vantage Partner employees, carried subcontracts with researchers including Larry Forsley, Vladimer Pines, Jim Gilland, Nick Penney, Frank Lynch, Edmund Storms, and support from CWRU (TOF-SIMS analysis), the University of Akron, the Ohio Aerospace Institute and Ohio State University. She managed procurements of materials and equipment, including a Linear Accelerator for Armstrong Test Facility. Ms. Jansen's goal was to supply the research team with essential personnel, materials, and equipment.

Ms. Jennifer Grof is a budget analyst and provided guidance and support for the AEC funding.

Dr. Hakimzadeh Roshanak was the project manager of AEC from 2014-2016.

Mr. John Hamley was the project manager of AEC from 2016-2017.

Mr. Carl Sandifer served as the AEC Review Manager for the project in 2016. At that time, the Science Mission Directorate (SMD) Planetary Sciences Division (PSD) desired a new energy source to enable science priorities identified in both the 2010 Planetary Science Decadal Survey and the 2014 Science Plan. The AEC Project sought to develop a safe and cost-effective heat source for power generation and in a follow-on project, would integrate this with an electric power conversion system. The intent was for the system to offer significant performance, cost, safety, and/or operability improvements compared to current or currently conceived planetary science power systems. Following the successful review, Mr. Sandifer became the AEC Project Manager from 2017-2019. In early 2017, he worked with the team to develop a research plan to address the PSD direction to focus the latest AEC project research on investigating clear evidence of sub-threshold nuclear activation using either an electron beam or photon irradiation of highly deuterated target materials, and to provide suitable experimental evidence to address the physics community scrutiny, questioning if unconventional physics had been revealed. After conducting a successful test campaign, the team evaluated and complied the data to publish two peer-reviewed papers within *Phys Rev C*, sharing our lessons learned and results to enhance the societal body of knowledge regarding the initiation of fusion reactions.

Mr. Mathew DeMinico led strategic planning, communication, and coordination for NASA's LCF as Project Manager, and supported coordination of independent review of LCF research and publications from 2020 to 2022.

Mr. Andy Presby is the current LCF Project Manager. Mr. Presby's background is in nuclear physics and his expertise with nuclear submarines lends itself well to the LCF Project. He leads diverse multi-Agency teams supporting the development of advanced nuclear in-space propulsion systems to enable fast crewed missions to Mars and exciting new robotic science missions to the outer planets.

3.6. Virtual Workshop

The AEC Project held a virtual workshop in May of 2020 [19] to announce the results of the published work which was attended by 70 LENR researchers from industry, government, and academia. During the 4-hour online workshop the AEC team presented key results from the two [9,14] *Phys Rev C* published papers. The objectives of the workshop were twofold:

(1) NASA Glenn Research Center (GRC) disseminated the key findings detailing experiments and theory to select invited external researchers and a NASA panel of reviewers. The presentations emphasized electron screening in a confined lattice which allows enhanced nuclear fusion.
(2) Identified challenges to the theory and the results through invited questions and critiques from all participants, and feedback from invited panelists. The feedback received from several participants was very positive and was used to further direct follow-on LCF research.

The AEC Project transitioned to the LCF Project with the current funded effort (July 2021 to present) where the leadership transitioned from Dr. Steinetz to Dr. Benyo. Additionally, a 2023 NASA Innovative Advanced Concepts grant was awarded to the LCF team to study accessing icy world oceans using LCF fast fission for the power source of an autonomous robotic probe.

The Appendix has figures detailing the AEC and LCF projects timelines.

4. Experiments

Many experiments were conducted by the AEC/LCF team using various methods of triggering the fusion reactions to happen. Figure 2 illustrates the types of experiments that were completed to investigate the best trigger and conditions for nuclear fusion reactions to take place.

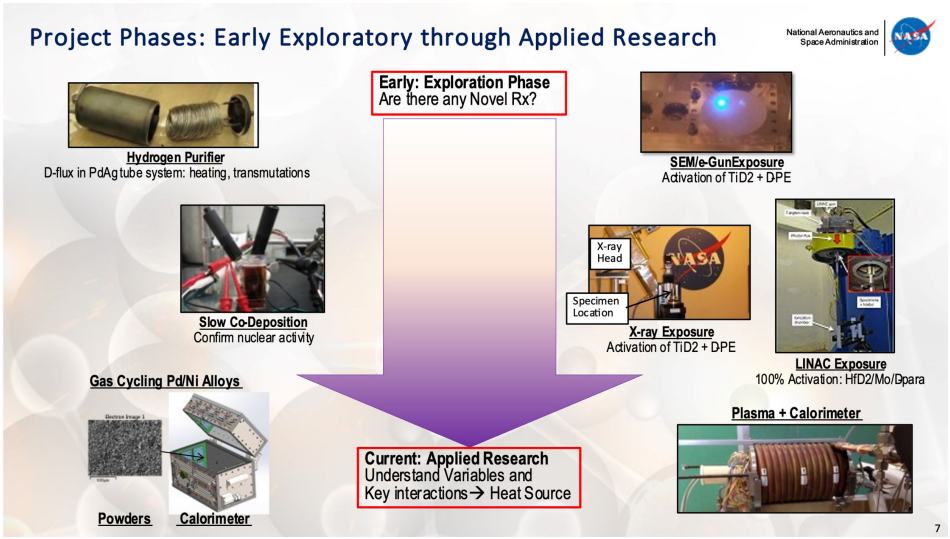

Figure 2. Exploration of LCF Through Experimentation.

5. Hydrogen Purifier

In 1989, Fralick and his NASA colleagues documented anomalous thermal behavior when performing tests with a Johnson-Matthey (JM) hydrogen purifier loaded weeks prior with deuterium gas [2]. The authors detected anomalous heating when D_2 but not when H_2 was dumped from the JM purifier and concluded that neutron activity was insufficient to satisfy the desired 3σ proof of fusion. As the JM purifier is sealed, no metallurgical analysis was pursued at that time. The actual experiment consisted of monitoring temperature and neutron counts. Fralick continued testing with the JM purifier cycling the deuterium gas at various pressures, temperatures, and rate of compression, holding at constant conditions and expansion cycling-rates, noting each cycle produced a particular anomalous behavior. During these early experiments, Fralick et al. [2] found the evidence of anomalous heat and enigmatic neutrons when the purifier was filled with D_2 at a temperature of 383 °C and a pressure of about 1.38 MPa. Several researchers in Italy (Celani), Japan (Iwamura) and China (Zhang) were inspired by this work to undertake their own gas phase explorations as noted during ICCF-23 [1].

During the experiments conducted by Fralick, the supply lines to the purifier were pumped down and the purifier was evacuated prior to running another background count. As the valve on the hydrogen purifier was cracked open to allow the gas to evacuate the pressure vessel, the temperature began to rise. He continued to open the valve slowly. By the time the valve was fully open (10 or 15 s), the temperature had increased to 400 °C before it began to decrease. During this time, the temperature control setting remained at 382 °C, and the temperature rise was much more rapid than was possible using the electric heater. The expansion should have cooled, not heated, the gas, further adding to the anomalous heating observed.

Twenty years later in 2009, the NASA Innovative Partnership Program sponsored additional gas cycling experiments to investigate the anomalous heat observed in the 1989 experiments. More experiments performed in 2014 and 2018 repeated the anomalous heat results and in addition, surface transmutations were discovered on the surfaces of the PdAg alloy tubing used in the gas cycling experiments [18].

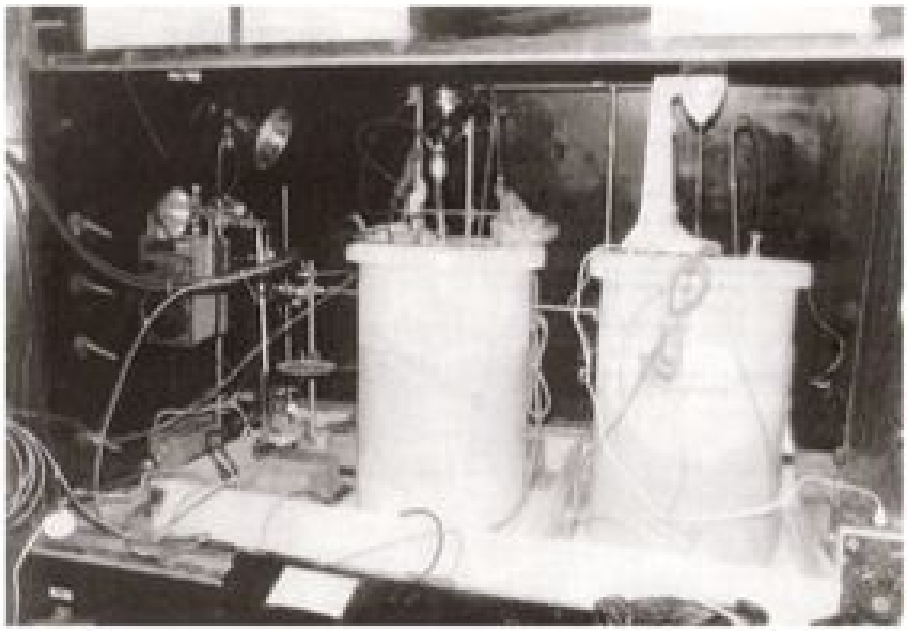

Figure 3. Two 28-liter electrolytic cells.

6. Early Electrolytic Wet Cell Experiments

In 1996, Niedra et al [3] intended to replicate experiments performed by Mills and Kneizys [20]. They used an electrolytic solution of H_2O-Ni-K_2CO_3. They discovered an apparent current-dependent excess heat consistent as heat from hydrogen-oxygen recombination. The experiment consisted of two 28-liter electrolytic cells; one active cell for electrolytic tests and one inactive cell for reference thermal measurements. Figure 3 shows the setup of the experiment. The experiments were conducted at several DC currents and a pulse mode current. Although there was excess heat production with a possible anomalous power gain of ~1.7 at the lowest current (5 A) in the NASA 1996 experiments, it was not as large as other experiments reported in literature (gain > 10). This gain was achieved without a recombiner, but Faradaic efficiency calculations and water loss measurements attempted to take recombination into account.

7. Multi-Bubble Sonoluminescence Investigation

These sonoluminescence experiments [4] were inspired by Stringham's work [21] and sponsored by NASA's Low Emissions Alternative Power (LEAP) Project and Breakthrough Propulsion Physics (BPP) Project. The experiments investigated energy of ultrasonic-generated multi-bubble sonoluminescence (MBSL). The sonoluminescence was achieved with palladium chromium (PdCr) alloy thin films over platinum (Pt) traces on alumina. When light water (H_2O) was used, no crater was seen on the PdCr thin films. However, when heavy water (D_2O) was used, crater formation was observed. Figure 4 shows the results of the MBSL experiments. In addition, large grain features are usually seen in thin films due to mismatches in coefficients of thermal expansion at high temperature (~1000 °C). The question remains: Did this result indicate point heating in the PdCr films?

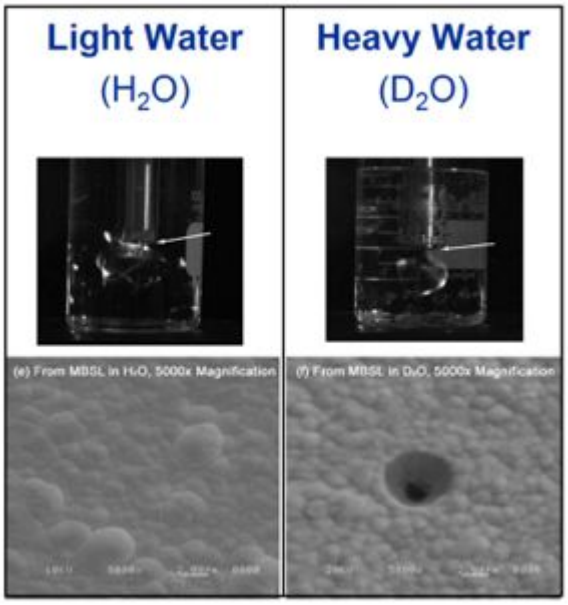

Figure 4. Surface morphology of films exposed to sonoluminescence in light water (left) and heavy water (right).

8. Scanning Electron Microscope (SEM) Energetic Electrons into Deuterated Targets

In unpublished SEM work, the objective was to investigate direct enhanced electron screening of deuterated targets via 10's of kV energetic electrons delivered by the SEM. These experiments were replications of claims by Lipson [13] of nuclear reactions under these conditions. The AEC Team exposed titanium deuteride disks to electron beams with energies of 4 to 30 kV from late 2013 into 2014. The exposure of TiD_2 targets resulted in novel nuclear effects when exposed to electron beam energies under 30keV. In approximately 20% of the cases with freshly polished TiD_2 disks, the team measured beta activation of the disks after the beam exposure. In contrast, undeuterated titanium disks did not show any evidence of nuclear reactions. Figure 5 shows the SEM and closeup photo of a TiD_2 sample surrounded by CR-39 SSND track detectors, and neutron detection foils.

9. Volumetric Electron Screening with X-ray Photons

In the goal of scaling up the reactions observed with the SEM experiments, the team investigated volumetric electron screening of deuterated targets exposed to x-ray photons. Figure 6 shows the x-ray with one of the many samples irradiated during the experiments. Titanium deuteride (TiD2) plus deuterated polyethylene (DPE), DPE alone, and for control, hydrogen-based polyethylene (HPE) samples and non-deuterated titanium samples were exposed to x-ray irradiation. These samples were exposed to various energy levels from 65 to 280 kV with prescribed electron flux impinging on the tungsten braking target from 500 to 9000 μA, with total exposure times ranging from 55 to 280 min. Alpha and beta activities were measured using a gas proportional counter and for select samples, beta activity was measured with a liquid scintillator spectrometer. Most of the deuterated materials subjected to the microfocus x-ray irradiation exhibited post-exposure beta activity above background and several showed short-lived alpha activities. The HPE and non-deuterated titanium control samples exposed to the x-ray showed no post-exposure alpha or beta

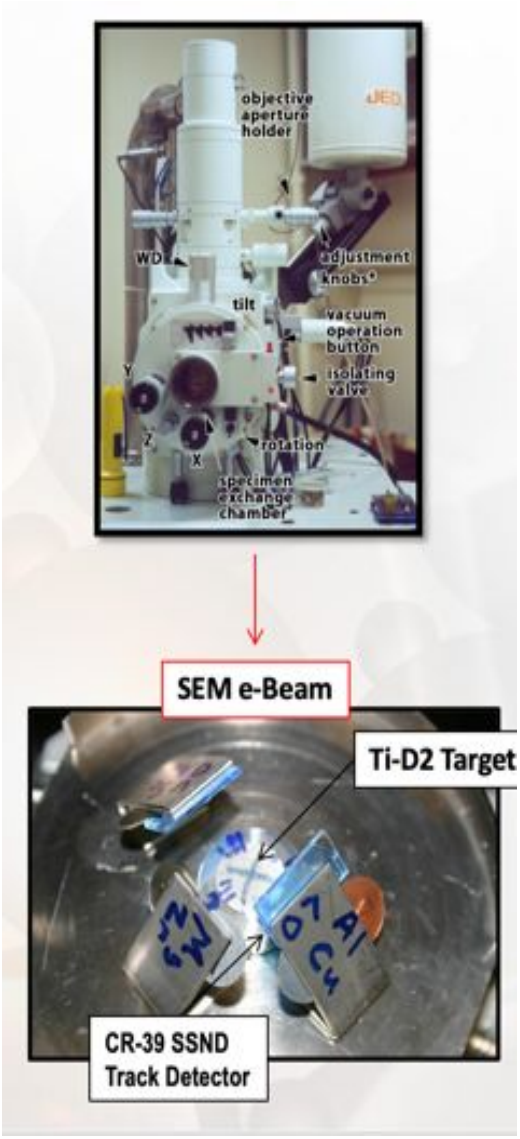

Figure 5. SEM apparatus and photo of deuterated titanium target surrounded by nuclear diagnostics materials.

activities above background. Several of the samples (SL10A, SL16, SL17A) showed beta activity above background with a greater than 4 sigma confidence level, months after exposure. Portions of SL10A, SL16, and SL17A samples were also scanned using a beta scintillator and found to have beta counts in the tritium energy band, continuing without noticeable decay for over 12 months. Beta scintillation investigation of as-received materials (before x-ray exposure) showed no beta counts in the tritium energy band, indicating the beta emitters were not in the starting materials. Full details of the x-ray irradiation experiments are documented in Benyo's NASA Technical Memorandum [7].

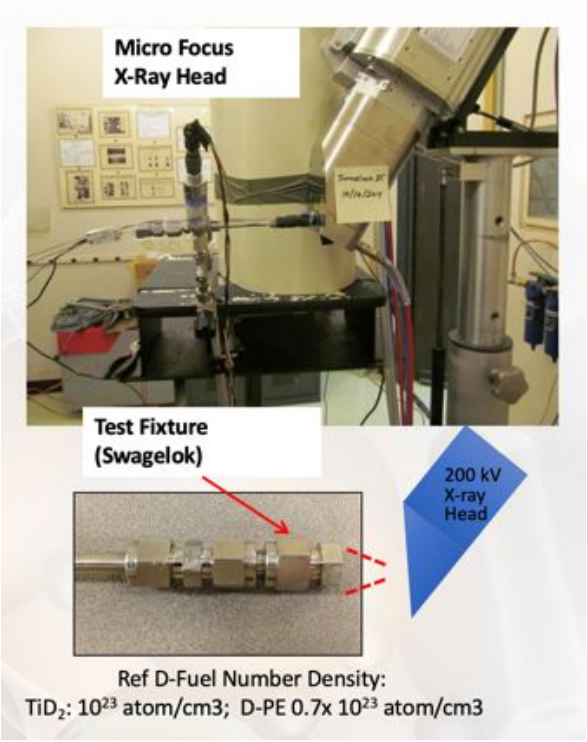

Figure 6. Photo of x-ray head (top) and test fixture containing the sample to be irradiated.

10. Linear Accelerator (LINAC) Volumetric Electron Screening Via Gamma Photons

Linear Accelerator (LINAC) bremsstrahlung irradiation of deuterated material was inspired by the work of Didyk [10]. The objective of this set of irradiation experiments was to investigate volumetric electron screening of deuterated targets exposed to gamma-ray photons at sub-threshold energies less than 2.226 MeV which is the energy at which deuterium photo-dissociates. A LINAC Model LS200 manufactured by Varian was used to expose the samples to photon energies of < 2.2 MeV (Figure 7). This industrial LINAC allowed specimens to be positioned very close to the braking target. For this study, the specimens were positioned within approximately 7.4 mm (0.29 in.) from the exit plane of the tungsten-braking target. No flattening filter was used in these tests. At 7.4 mm it is estimated that the samples saw a radiation dosage of 2.4 x 10^6 rad/min at the nominal 2-MV beam energy. An ion gage (RadCal PN 10X6-0.6) radiation detector was set-up below the test samples at the iso-center (~100 cm from the braking target). The radiation level as well as reflected power, gun current (voltage), and target current (voltage) were used to monitor beam operation to ensure that the beam flux was not changing with time.

Exposure of highly deuterated materials to a low-energy (<2.225-MV) photon beam resulted in activation of both the parent metals of hafnium and erbium and witness materials (e.g., molybdenum) mixed with the reactants. Gamma spectral analysis of all six of the deuterated materials $ErD_{2.8}$+D-Para+Mo and all six of the HfD_2+D-Para+Mo showed that nuclear processes had occurred as shown by unique gamma signatures. For the deuterated erbium specimens, post-test gamma spectra showed evidence of unstable isotopes of erbium (e.g., ^{163}Er, ^{165}Er, ^{171}Er)

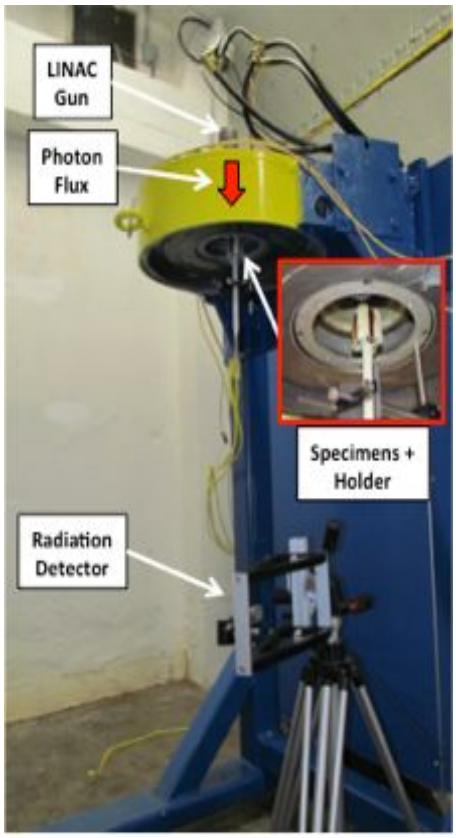

Figure 7. Varian 2-MV LINAC system with specimens positioned just below braking target and ion chamber radiation detector positioned 100 cm below target.

and of molybdenum (^{99}Mo) and by beta decay technetium (^{99m}Tc). For the deuterated hafnium specimens, post-test gamma spectra showed evidence of unstable isotopes of hafnium (e.g., ^{180m}Hf, ^{181}Hf) and molybdenum (^{99}Mo), and by beta decay, technetium (^{99m}Tc). In contrast, when either the hydrided or non-gas loaded erbium or hafnium materials were exposed to the gamma flux, the gamma spectra revealed no new isotopes. In those hydrided or non-loaded specimens, the gamma spectra peaks showed only background decay lines. Although the deuterated materials showed gamma activation lines like those resulting from activation by neutron capture, no sources of conventional neutrons have been identified that can account for this activation. Details of the LINAC experiments at NASA GRC are documented in Steinetz's NASA Technical Memorandum [8].

11. IBA Dynamitron Photoneutron Initiated Fusion with Gamma-Induced Electron Screening

The initial set of experiments performed by the AEC team did not include neutron spectroscopy and therefore, did not offer conclusive evidence of d-d nuclear fusion reactions. The most promising method triggering d-d fusion reactions at the time was the LINAC-based experiments. However, using organic scintillators for neutron spectroscopy under the high gamma and/or EMI background from the Varian LINAC proved to be almost impossible. Another type of LINAC

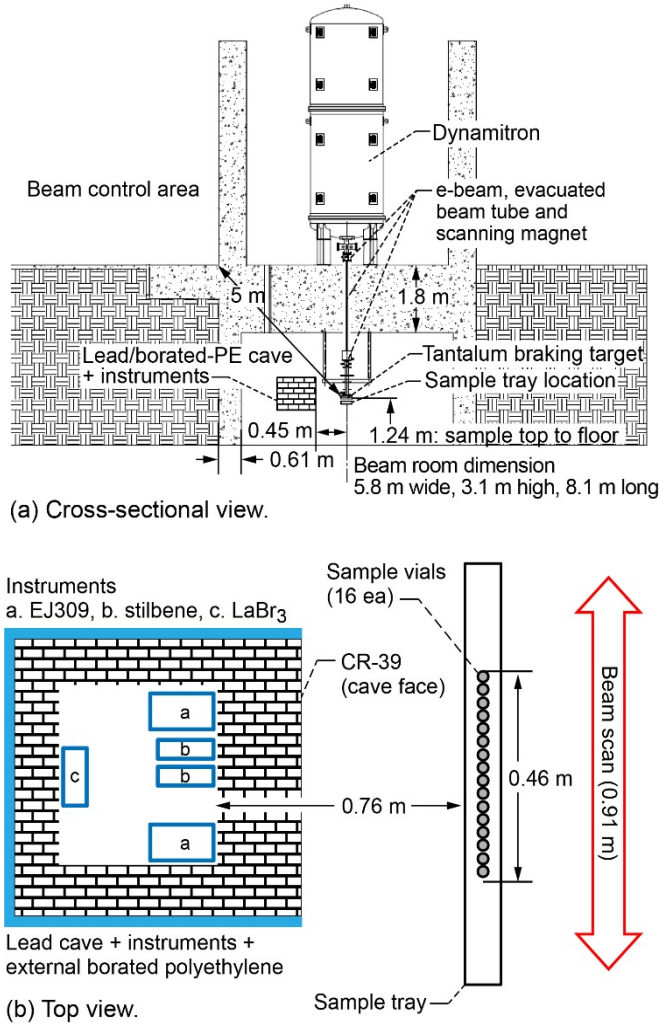

Figure 8. Schematic of beam, samples, cave, and instruments. (a) Overall cross-sectional view of setup; (b) Top view of test samples, cave (top removed), instruments, and beam scan.

needed to be used for the next generation of experiments. A Dynamitron LINAC was located and leased for additional bremsstrahlung irradiation of deuterated metals where the high gamma and EMI background was much less.

As a result, d-d nuclear fusion events were observed in an electron-screened, deuterated metal lattice by reacting cold deuterons with hot deuterons (d*) produced by elastically scattered neutrons or electron screened fast protons originating from bremsstrahlung photodissociation.

Tests were performed using a Dynamitron electron accelerator having independent control of beam energy (450 keV to 3.0 MeV) and beam current (10 μA to 30 mA), as shown in Figure 8(a). The direct-current accelerated electron beam enters the beam room via an evacuated tube and is scanned over the braking target, utilizing the scanning magnet ~1 m above the target. The beam was operated in photon mode for the current tests, utilizing a 1.2-mm-thick tantalum

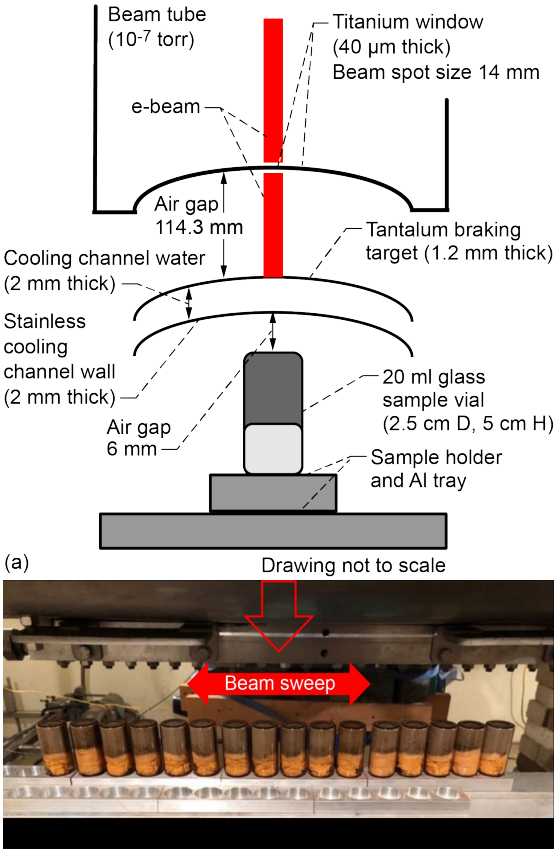

Figure 9. (a) Cross section of electron beam, titanium vacuum window, tantalum braking target, stainless steel cooling channel, and sample; (b) Photograph of specimens in glass vials.

braking target. Samples in glass vials were placed on an aluminum exposure tray close to the tantalum braking target and were exposed while the electron beam scanned at a frequency of 100 Hz over the length of 0.91 m. Figures 8(a) and (b) show the relative position of the 16 samples (total length 0.46 m) and the lead cave, which housed the neutron detectors and will be described below. Figure 9(a) illustrates the proximity (11.2 mm distance) of the 20-ml sample vials relative to the braking target, which was cooled with ambient-temperature water flowing spanwise in a stainless-steel cooling channel. Figure 9(b) illustrates how the beam scanned back and forth over the 16 glass vials.

Specifically, exposure of deuterated materials including ErD_3 and TiD_2 to bremsstrahlung photon energies (~2.9 MeV) resulted in both photodissociation-energy neutrons and neutrons with energies consistent with $D(d,n)^3He$ fusion reactions, and demonstrated process reproducibility. This study [9] and its analyses [14] identified several key ingredients required for fusion reactions. Deuterated metals present a unique environment with high fuel density (10^{22} to 10^{23} D-atoms/cm^3), which further increases the fusion reaction probability through shell and lattice electron screening, reducing the d-d fusion barrier. Exposing deuterated fuels to a high photon flux enhanced screening conditions near the cold D-fuel. This additional screening further increases the Coulomb barrier transparency and further enhances fusion reaction rates. In these tests, deuterons were initially heated by photoneutrons with an average

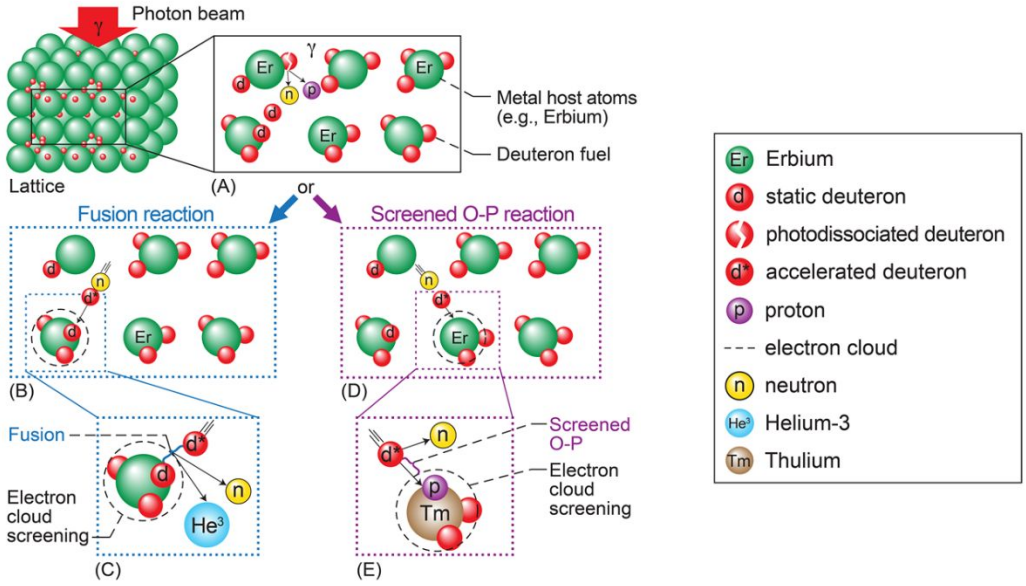

Figure 10. Illustration of reactions detected in the Gamma-Induced Electron Screening experiments. (A) lattice of erbium is loaded with deuterium atoms. Upon irradiation with a photon beam, a deuteron dissociates, and the neutron and proton are ejected. The ejected neutron collides with another deuteron, accelerating it as an energetic "d*" as seen in (B) and (D). The "d*" induces either screened fusion (C) or screened Oppenheimer-Phillips (O-P) stripping reactions (E). The fusion reaction depicted in (C) releases either a neutron and helium-3 (shown) or a proton and tritium. These fusion products may also react in subsequent nuclear reactions, releasing more energy. In (E), a proton is stripped from an energetic "d*" and is captured by an erbium (Er) atom, which is then converted to a different element, thulium (Tm). If the neutron instead is captured by Er, a new isotope of Er is formed (not shown).

energy of 145 keV from the 2.9-MeV beam energy to initiate fusion. However, other neutron sources would also provide the necessary deuteron kinetic energy.

Neutron spectroscopy revealed that both d-d 2.45-MeV fusion neutrons and other processes occurred. Figure 11 shows a comparison GRC-observed d-d fusion neutrons during these experiments with the Italian Tokamak neutron spectra. The data indicates that the significant screening enabled charged reaction products hot d* or ^{3}He* to interact with the host metal. These interactions may produce the ~4- and ~5-MeV neutrons where Oppenheimer-Phillips stripping processes occurred in the strongly screened environment, capturing the proton, and ejecting the neutron (Figure 10). The current work demonstrates the ability to create enhanced nuclear reactions in highly deuterated metals with the deuteron fuel in a stationary center-of-mass frame. This process eliminates the need to accelerate the deuteron fuel into the target with implications for several practical applications.

12. Plasma Reactor: Delivery of Ions/Energetic Electrons into Deuterated Targets

The objective of the plasma reactor experiments was to investigate dynamic loading of D+ with screening electrons into deuterated targets with a customized microstructure.

A reactor [12] was designed and constructed to generate a plasma and expose various materials to this plasma. The reactor could heat the plasma chamber and supply a gas to the chamber at pressures from vacuum levels to 200 psi. A calorimeter was constructed around the plasma chamber to accurately monitor the thermal power exiting

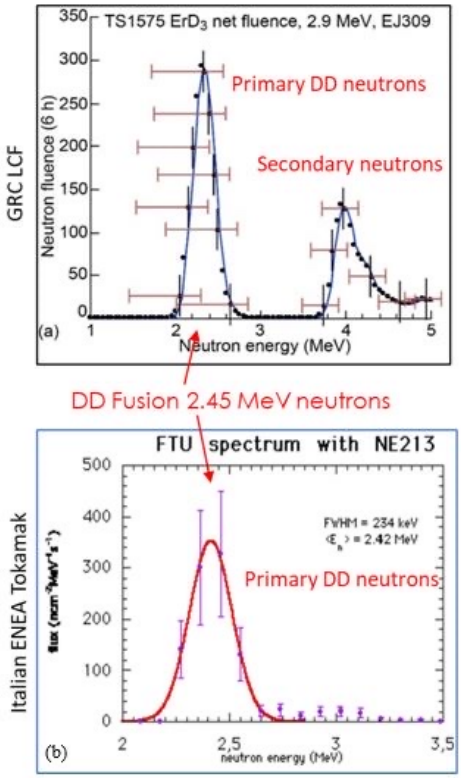

Figure 11. Comparison of neutron spectra from (a) bremsstrahlung radiation of deuterated erbium samples (TS1575 6 h exposure) and (b) fusion neutrons from the Italian ENEA Fusion Tokamak.

the plasma chamber. A steady state or pulsed plasma could be generated. The input and output electrical power for creating the plasma was monitored, and the current and voltage waveforms were observed and recorded using a series of oscilloscopes. The results of initial experiments showed the accuracy of measuring the plasma input power and of the calorimeter in measuring the total heat output of the system. It was determined that the system had a total power measurement accuracy of ± 1.36 percent. A schematic of the plasma reactor is shown in Figure 12.

The plasma reactor test rig was designed with standard anode and cathode electrode pair contained inside of a stainless-steel reaction chamber. The entire system was designed to operate with pulsed direct current (DC) plasma at pressures from integer torr to several atmosphere gas pressures. The system was designed to handle most gas types but was mainly used with hydrogen, deuterium, or inert gases. The stainless-steel reactor is wrapped in a water-cooled calorimeter capable of dissipating upwards of 2,500 W of power. The calorimeter removes the total power input into the chamber as either heat or electrical power and any heat generated within the chamber. Any heat generated within the chamber is measured by calculating the difference in the total output heat (determined by the measured temperature rise for the metered water flow) less the total input power (strap on heaters plus plasma electrical power). For materials testing, a range of powders and metal foam combinations were used. Tests that utilized hydrogen or deuterium gas also introduced the possibility of gas loading into the materials. Some disks contained powders made of materials that had no hydrogen or deuterium loading and others contained hydrogen or deuterium at high atomic number density (e.g., 10^{21} atoms/cm^3).

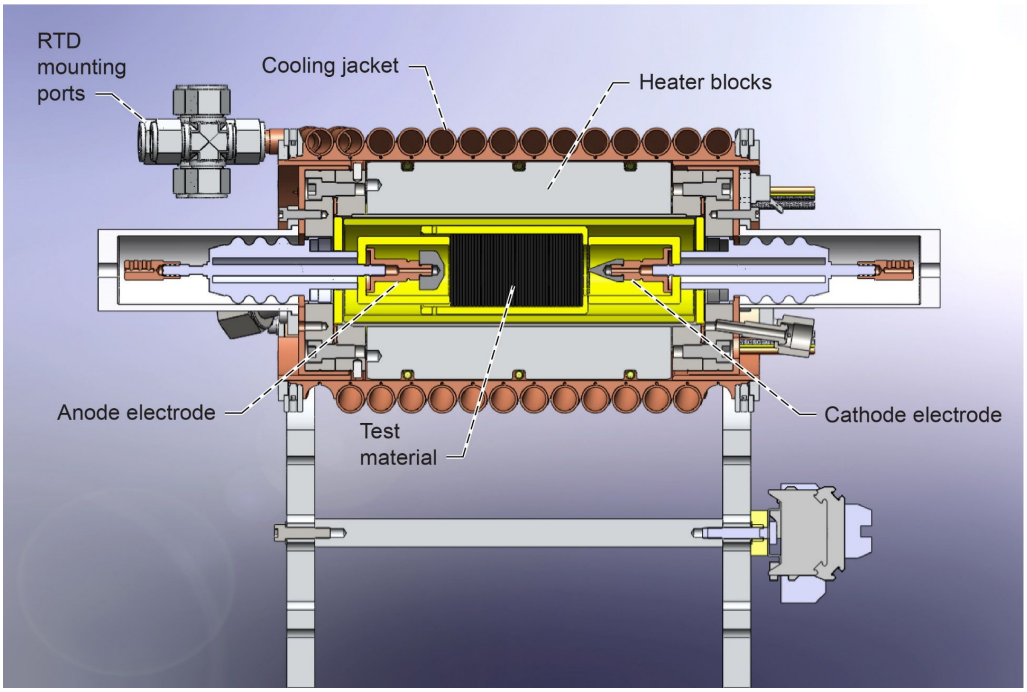

Figure 12. Plasma reactor internal layout.

The results of these plasma reactor experiments showed that tests with TiD_2 powder and PdAg indicated excess power. However, it was difficult to accurately know the input power, hence the excess thermal power was questionable despite an accurate calorimeter measuring the output power.

There were also RF emission losses during these experiments. The production of possible excess thermal power repeated with, on average, ~20–30% of the experimental runs. The team also observed anomalous gas changes which were measured during the test; growth of AMU-2, 3, 5, 6 and a decline in AMU-4 (presumed to be D_2) as shown in Figure 13.

Unbeknownst to our group, the Lawrence Berkeley National Laboratory under Dr. Thomas Schenkel's group with Google Research Funding also conducted plasma loading experiments and detected fusion neutrons [22].

13. Electrochemistry: Dynamic In-Situ Creation of High-Density Deuterated Microstructure

The objective of conducting electrolytic wet cell experiments is to investigate high current (900mA) D+ along with Pd and Li co-deposited on a metal wire. The approach for these types of experiments is either a slow [5] or fast [23] Pd/D/Li co-deposition protocol consisting of using heavy water (D_2O) or light water (H_2O) in the electrolytic solution during multi-hour runs. Calorimetry is used to measure the amount of heat produced during the experiment. The NASA Advanced Energy Conversion Project supported excess heat producing electrolytic co-deposition experiments at the Naval Surface Warfare Center (NSWC), Dahlgren Division and Density Functional Theory (DFT) modeling of hydrided materials by Dr. Louis DeChiaro. This work led to the DARPA funded HIVER effort at NSWC, Indian Head replicating these results. The NASA Lattice Confinement Fusion Project funded additional DFT results at Indian Head also by DeChiaro.

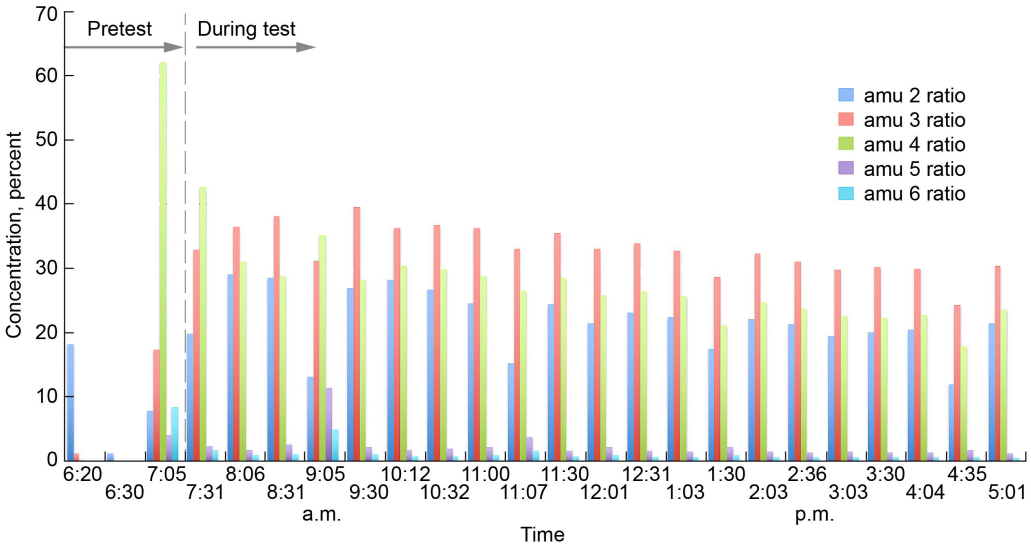

Figure 13. Residual gas analyzer (RGA) scan results taken periodically during a test.

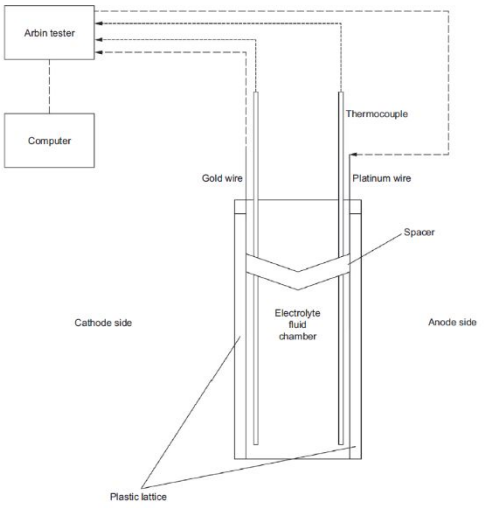

Figure 14. Test system diagram for a single electrolysis cell. A single bubble detector was placed outside the cell behind the electrolyte chamber as shown in this view.

Co-deposition [6] electrochemical cells are a simple means to examine novel nuclear reactions. In the 2016 study by our team, electrolytic cells were built as illustrated in Figure 14. During the experiments, palladium and deuterium atoms were co-deposited on a cathode at stoichiometric densities, forming dendritic morphologies. Bubble detector neutron dosimeters were used to measure equivalent dose levels during electrolytic deposition. Cells expected to

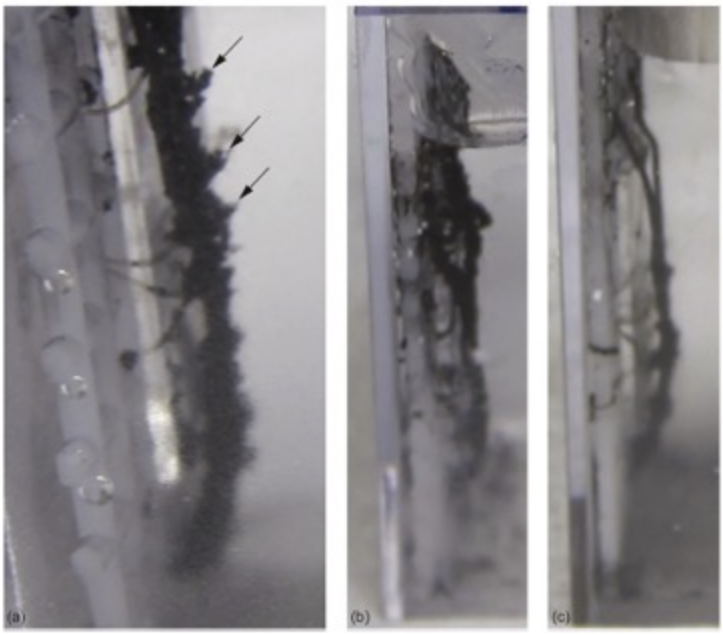

Figure 15. Close-up images of (a) T-III-E1 (above-average neutron emissions), (b) T-IV-E1 (average neutron emissions), and (c) T-III-E5 (below-average neutron emissions). The height of the plastic lattice mesh that the wire is attached to shown in (b) and (c) is approximately 2.5cm.

produce excess neutrons were denoted as experimental cells and contained an electrolyte consisting of palladium(II) chloride, lithium chloride, and heavy water. The control cells used copper(II) chloride, lithium chloride, and heavy water electrolyte. Thirteen experimental and nine control cells were supplied current, increasing from 0.1 to 100.0 mA over a period of 20 days. Neutron radiation levels detected near experimental cells were, on average, greater than those measured near control cells for the entire test profile. For test days 9 through 20, the experimental cells exhibited significantly higher average neutron radiation than the controls at a 99% confidence level.

In the experiments described in the current work, there appears to be a correlation between dendritic deposits on cathodes and observed neutron activity. For comparison, post-test images of several experimental cathode cells are presented in Figure 15 that show the final palladium deposition dendritic macrostructure on the cathode prior to disassembly. Dendrites are clearly visible on the cathode surface of the T-III-E1 cell, which produced the greatest total neutron dose over 20 days of 0.069 μSv—the greatest of all observed cells. This cell is also notable for the electrolyte clarity and lack of deposits at the bottom of the cell at the end of the test run. Cell T-IV-E1 represents an average neutron-producing experimental cell at 0.043 μSv over 20 days. Although 0.031 μSv over 20 days made T-III-E5 a below average neutron-producing experimental cell, it was still above the control cell average. It may be that the higher performing cells exhibit more Pd adhering to the cathode surface and a more distinct dendritic structure.

The findings herein were compared to those of other researchers [24] who found neutron activity using similar cell and operational protocols, but who measured neutron activity with a BF_3 neutron detector. The 2016 work corroborates other research that determined the highest nuclear activity occurred when the PdD deposits resulted in stable dendritic formations on the cathode. In cells where the PdD layer exhibited poor adherence to the electrode, neutron activities were less than the highest neutron-producing cells but remained above control-cell levels. Even though there is clear

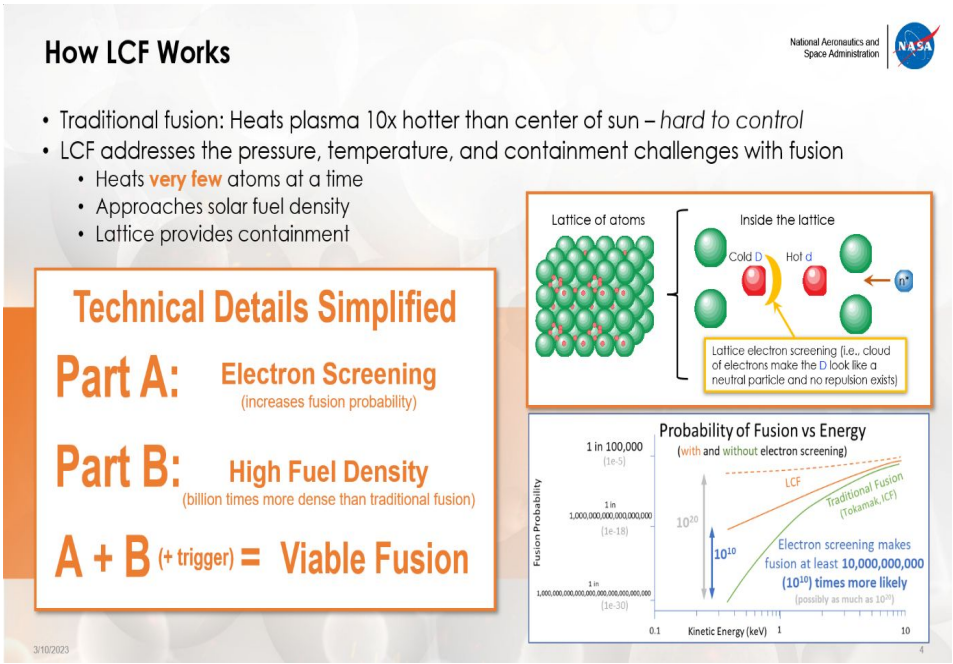

Figure 16. Lattice confinement fusion accomplished with a deuterated lattice of metal atoms, energized neutrons, and lattice electron screening.

evidence of neutron production favoring the experimental cells, the radiation produced by all individual cells was low, and the dose was the equivalent of <0.1 μSv per month adjacent to the cell wall [5].

Highlights of these experiments include:

- Bubble detector neutron dosimeters measured electrochemical cell neutron activity.
- Case control: $PdCl_2/LiCl/D_2O$ cells were compared with $CuCl_2/LiCl/D_2O$ control cells.
- Experimental cells exhibited neutron activity greater than controls: 99% confidence.
- Highest neutron-generating experimental cells produced dendritic cathode deposits.
- Neutron activity cannot be explained by chemical reactions, only nuclear processes.

14. Lattice Confinement Fusion (LCF)

Called Lattice Confinement Fusion, the method NASA revealed accomplishes fusion reactions with the fuel (deuterium, a widely available non-radioactive hydrogen isotope composed of a proton, neutron, and electron, and denoted "D") confined in the space between the atoms of a metal solid (Figure 16). In previous fusion research such as inertial confinement fusion, fuel (such as deuterium/tritium) is compressed to extremely high levels but for only a short, nano-second period, when fusion can occur. In magnetic confinement fusion, the fuel is heated in a plasma to temperatures much higher than those at the center of the Sun. In the new method, conditions sufficient for fusion are created in the confines of the metal lattice that is held at ambient temperature. While the metal lattice, loaded with deuterium fuel, may initially appear to be at room temperature, the new method creates an energetic environment inside the lattice where individual atoms achieve equivalent fusion-level kinetic energies.

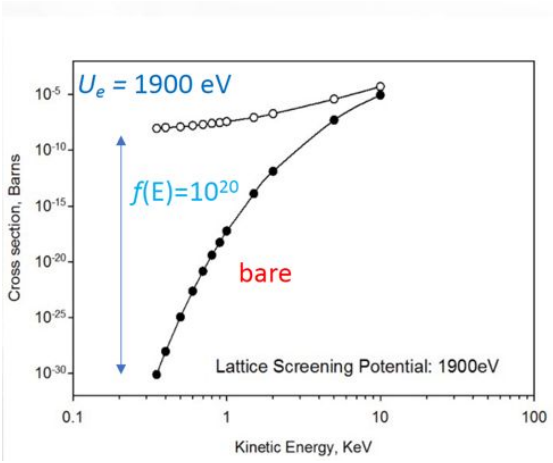

Figure 17. Screening Enhancement.

15. How LCF Works

In the current research, nuclear reactions are triggered in titanium or erbium metal lattices loaded with the hydrogen isotope deuterium—at densities approaching 10^{23} ions/cm^3. Such high fuel densities are greater than those available in current magnetic confinement (tokomak) fusion reactors, which have densities of only 10^{14} ions/cm^3 (Greenwald Limit). Also, previous deuterium (and tritium, another isotope of hydrogen) fusion research with tokamaks has relied upon temperatures 10 times the center of the Sun, yet the NASA method accomplishes the same in the loaded metal lattice. While the deuterium-loaded metal lattice may initially be at room temperature, the new method creates an environment where individual atoms achieve equivalent fusion-level kinetic energies first through electron screening and then through momentum transfer.

16. LCF Demonstrated Nuclear Fusion

Lattice Confinement Fusion uses deuterated metals at a high-density of 10^{23} ions/cm^3 where deuterons are held indefinitely in a metal lattice. The negative charge of lattice electrons screen and partially neutralize the positive deuteron charges. This neutralization effect reduces the Coulomb barrier allowing the deuterons to fuse. LCF is then triggered and controlled by bremsstrahlung [9], phonon-nuclear coupling, [25] or other means resulting in an equivalent local deuteron ion temperature of > 2.1 keV kinetic energy (24 million °C) as compared to the sun at 1.5 keV (17 million °C).

17. Electron Screening

Electron screening, noted as U_e, is where electrons 'screen' positively charged particles to approach more closely and "slip" under the Coulomb barrier. This method was applied to astrophysics by Salpeter in 1954 [26] and Hagino in 2002 [27]. Later, laboratory astrophysics experiments in 1986 [28] and later [29] using accelerated deuteron beams demonstrated electron screening effects below 10 keV that exponentially increased at lower energies as compared to the fusion of bare deuteron nuclei. As Figure 17 shows, the enhancement factor *f(E)*, can exceed 20 orders of magnitude at low kinetic energies!

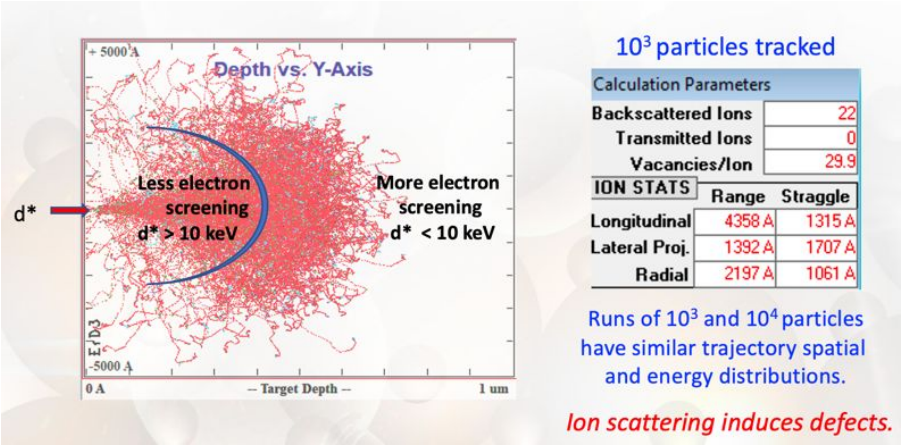

Figure 18. Ion Transport.

Remarkably, 1 keV of screening is the equivalent of 11 million degrees C where *the deuterons are locally hot but globally cold*.

Electron screening is essential for efficient nuclear fusion reactions to occur. Screening effects on fusion reaction rates as measured in deuterated materials have been demonstrated to be important.

The nuclear reaction rate includes two primary factors: the Coulomb scattering of the projectile nuclei on the target nuclei as well as nuclei tunneling through the Coulomb barrier [14]. During elastic scattering of charged projectiles on a target nucleus, such as a deuteron, some of the energy of the projectile particle is transferred to the target nucleus, hence heating it. Depending on the projectile particle energy and the efficiency of kinetic energy transfer during the scattering event, the target deuteron may become energetic enough to enable subsequent nuclear fusion reactions via tunneling through the Coulomb barrier. Electron screening plays a significant role in this process because of hot fuel interacting with lattice nuclei in the highly screened environment, as has been demonstrated in the companion experimental work reported in Steinetz et al. [8], [9].

Figure 18 shows a fast deuteron slowing in ErD_3 using the SRIM/TRIM Ion transport code [30]. Even a 64 keV deuteron will eventually slow to below 10 keV where electron screening predominates. Similar results have been shown using co-deposition with the observation of $> 10^5$ energetic protons and alpha particles with CR-39 detectors [31].

18. Summary

We have demonstrated multiple nuclear reactions initiated by various experimental techniques where detected nuclear emissions were neutrons, alphas, protons, betas, and ^{3}He. However, not all methods produce expected d-d reaction products. Transmutations, including tritium and heat release were also observed and detected. The co-deposition and LINAC photon stimulation experiments were highly reproducible by our team.

LCF electron screening theory along with astrophysics [27] and accelerator [28] experiments have provided insights in addressing the Coulomb barrier.

During our research efforts, we have developed critical concentration of expertise in multiple disciplines plus experimental and theoretical resources and are following evidence-based approach to enable timely progress. We have enlisted LANL MCNP [32], PoliMi [33] and CERN GEANT-4 [34] nuclear modeling codes, Quantum Espresso Density Functional Theory code and SRIM/TRIM [30] for modeling ions in condensed matter. It was problematic to realize that neither MCNP nor GEANT-4 can model light ions, like protons, deuterons, or alphas at energies below

1 MeV [35]. Conventional fusion occurs at energies below 100 keV whereas electron screened reactions predominate below 10 keV.

Just as important, we have learned the limitations of various hydrogen isotope loading, material triggering and diagnostic confluences. Depending upon the triggering used, these limitations can range from a high gamma ray background to electromagnetic interference. Material assays are complicated by handling and various means of contamination transportation. Nuclear diagnostics can be compromised by background gamma and alpha sources and cosmogenic neutron flux. The latter is especially problematic in identifying low level 2.45 MeV D$(d,n)^3$He fusion neutrons as the cosmogenic neutron flux also has a neutron evaporation peak at 2.5 MeV! [36].

The further development and scaling of Lattice Confinement Fusion reactions could have significant space and terrestrial applications. A NASA Innovative Advanced Concepts (NIAC) Proposal, "Accessing Icy World Oceans Using Lattice Confinement Fusion Fast Fission" was accepted and began on February 1, 2023, with a presentation to the NASA JPL Cryobot Workshop in March 2023 [37].

Appendix

NASA AEC and LCF Development Timelines

This paper is based upon an ICCF-24 Invited Session updated for submission to JCMNS at: https://www.youtube.com/watch?v=axH4kmYediQ

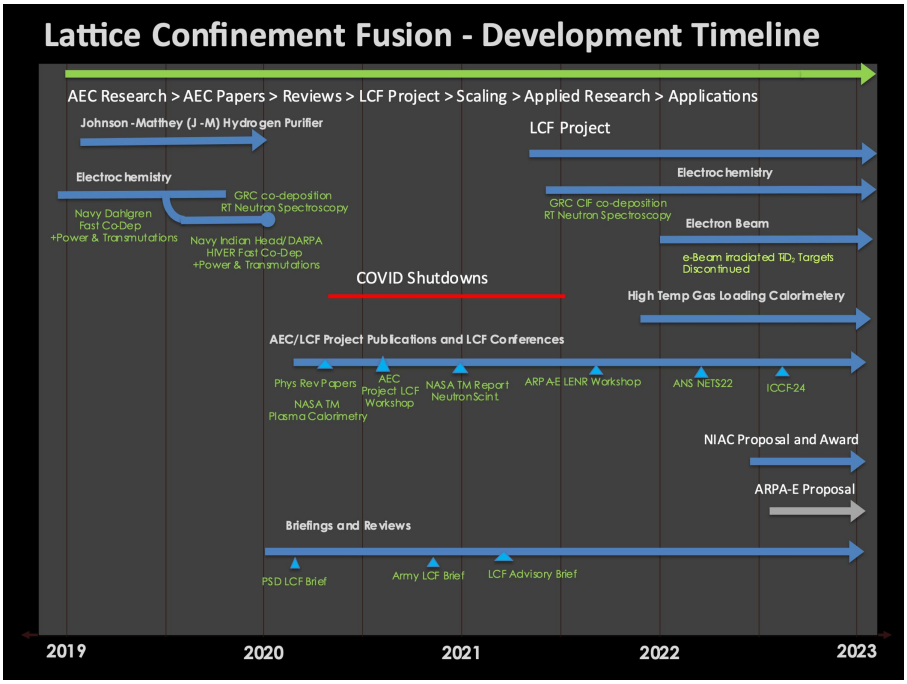

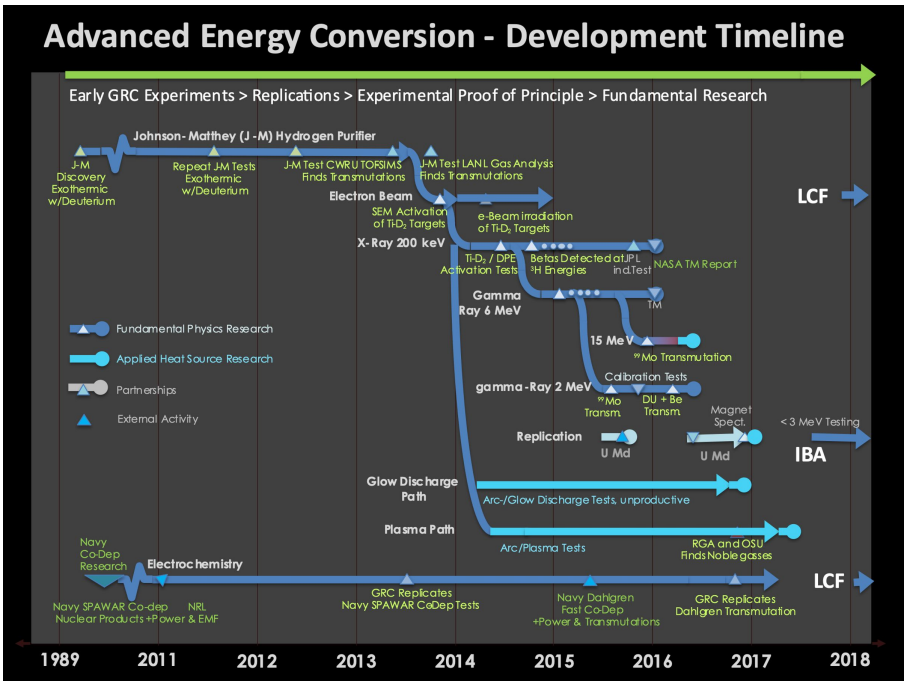

Acknowledgements

We acknowledge the support of multiple NASA Glenn Research Center Directors, the Science Mission Directorate, Planetary Science Division and Radioisotope Power Systems, and the Space Technology Mission Directorate. Further support has been provided by Global Energy Corporation under Space Act Agreements.

In memory of Dr. Marianna Pines, Senior Theoretical Physicist, NASA GRC and Pines Consulting.

References

[1] L. Forsley, "Reflections on ICCF-23: Lattice Confinement Fusion and Electron Screening", Interview, *Infinite Energy* **157** (July/August 2021)

[2] G. C. Fralick, A.J. Decker, and J. W. Blue, "Results of an Attempt to Measure Increased Rates of the Reaction ^{2}D +^{2}D --- ^{3}He + n in a Nonelectrochemical Cold Fusion Experiment", *Lewis Research Center, NASA*/TM-**102430** (December 1989).

[3] J. Niedra, I. Myers, G. Fralick, R. Baldwin, "Replication of the Apparent Excess Heat Effect in a Light Water-Potassium Carbonate-Nickel Electrolytic Cell", *NASA* **TM-107167** (1996).

[4] J. Wrbanek, G. Fralick, S. Wrbanek, N. Hall, "Investigating Sonoluminescence as a Means of Energy Harvesting," Chapter 19, *Frontiers of Propulsion Science*, Millis & Davis (eds.), AIAA (2009) 605-637.

[5] P. J. Smith, R. C. Hendricks, and B. Steinetz, "Electrolytic co-deposition neutron production measured by bubble detectors", *Journal of Electroanalytical Chemistry*, **882**, (2021) 115024.

[6] US Patent 8,419,919, "System and Method for Generating Particles".

[7] T.L. Benyo, B.M. Steinetz, R.C. Hendricks, R.E. Martin, L.P. Forsley, C.C. Daniels, A. Chait, V. Pines, M. Pines, N. Penney, T.R. Kamm and M.D. Becks, "Investigation of Deuterium Loaded Materials Subject to X-Ray Exposure", *NASA*/TM—**2015-218491/REV1** (2015).

[8] B.M. Steinetz, T.L. Benyo, V. Pines, M. Pines, L.P. Forsley, P.A. Westmeyer, A. Chait, M.D. Becks, R.E. Martin, R.C. Hendricks, N. Penney, A.M. Marsolais, and T.R. Kamm, "Experimental Observations of Nuclear Activity in Deuterated Materials Subjected to a Low-Energy Photon Beam", *NASA*/TM-**2017-218963** (2017).

[9] B. M. Steinetz, T.L. Benyo, A. Chait, R.C. Hendricks, L.P. Forsley, B. Baramsai, P.B. Ugorowski, M.D. Becks, V. Pines, M. Pines, R.E. Martin, N. Penney, G.C. Fralick and C. E. Sandifer, II, "Novel Nuclear Reactions Observed in Bremsstrahlung-Irradiated Deuterated Metals", *Physical Review C*, **101**, (2020) 044610.

[10] A. Y. Didyk and R. S. Wisniewski, "Nuclear reactions, induced by γ-quanta, in palladium saturated with deuterium surrounded by dense deuterium gas", *European Physics Letters Journal*, **99**, (2012) 22001.

[11] A.B. Karabut, "Excess heat power, nuclear products and X-ray emission in relation to the high current glow discharge experimental parameters", *9th International Conference on Cold Fusio*n, *Condensed Matter Nuclear Science*, Tsinghua Univ., Beijing, China: Tsinghua Univ. Press (2002).

[12] A.J. Colozza, T.G. Gray, B. M. Steinetz, L. G. Edwards, I.J. Jakupca, C. Castle, D. Johnson, and C. C. Daniels, "Plasma Reactor Summary", *NASA*/TM—**2020-220344** (2020).

[13] A.G. Lipson, I. Chernov, A. Roussetski, Y. Chardantsev, B. Lyakhov, E. Saunin and M. Melich, "Charged Particle Emissions Upon Electron Beam Excitation of Deuterium Subsystem in the Pd and Ti- Deuteride Targets", *ICCF-14 International Conference on Condensed Matter Nuclear Science*. Washington, DC (2008) 1–29.

[14] V. Pines, M. Pines, A. Chait, B. M. Steinetz, L. Forsley, R. C. Hendricks, G. C. Fralick, T. L. Benyo, B. Baramsai, P. B. Ugorowski, M.D. Becks, R. E. Martin, N. Penney, C.E. Sandifer, II, "Nuclear Fusion Reactions in Deuterated Metals", *Physical Review C*, **101** (2020) 044609.

[15] P.J. Smith, A.J. Colozza, I.J. Jakupca and G. C. Fralick, "Observation of Hydrogen Isotope Diffusion Through Thin Palladium-Silver Samples", *NASA/TM*-**2020-220458**. (2020) 1-60.

[16] B. Baramsai, B.M. Steinetz, L. Forsley, R.E. Martin, P.B Ugorowski, M.D. Becks, T.L. Benyo, A. Chait, R.C. Hendricks, G.C. Fralick, N. Penney, W. Pines, M. Pines, C.E. Sandifer, II., "Fast Neutron Spectroscopy with Organic Scintillation Detectors in a High-Radiation Environment", *NASA*/TM-**2020-5008493** (2020) 5-18.

[17] P.B. Ugorowski, J.C. Currie, B. Baramsai, B.M. Steinetz, L.P. Forsley, N. Penney, M.D. Becks, R.E. Martin, T.L. Benyo, A. Chait, R.C. Hendricks, G.C. Fralick, M. Pines, V. Pines, C.E. Sandifer, II, "Fast neutron spectroscopy with a volumetrically-sensitive, moderating-type neutron spectrometer in a high-radiation environment", *Nuclear Instruments and Methods In Physics Research Section A: Accelerators, Spectrometers, Detectors and Associated Equipment*, **1039**, (11 September 2022) 166982.

[18] G.C. Fralick, R.C. Hendricks, W.D. Jennings, T.L. Benyo, F.W. VanKeuls, D.L. Ellis, B.M. Steinetz, L.P. Forsley, C.E. Sandifer II, "Transmutations observed from pressure cycling palladium silver metals with deuterium gas", *International Journal of Hydrogen Energy*, **45** (2020) 32320–32330.

[19] T. L. Benyo, L. P. Forsley, L. Dudzinski and M. J. Forsbacka, "NASA GRC Hosts Lattice Confinement Fusion Virtual Workshop", *NASA GRC*, (Cleveland, Ohio) (May 21, 2020). https://ntrs.nasa.gov/api/citations/20205006546/downloads/LCF%20Workshop%20-%20May%2021%202020%20-%20Final%20Public.pdf

[20] R.L. Mills and K. Kneizys, "Excess Heat Production by the Electrolysis of an Aqueous Potassium Carbonate Electrolyte and the Implications for Cold Fusion", *Fusion Technol*., **20** (1991) 65.

[21] R.S. Stringham, "Cavitation and Fusion", *Condensed Matter Nuclear Science,* (2005) 233–246.

[22] T. Schenkel, et al., "Investigation of light ion fusion reactions with plasma discharges", *J. Applied Physics*, **126,** (2019) 203302.

[23] D. Letts and P. Hagelstein, "Modified Szpak Protocol for Excess Heat", *J. Condensed Matter Nucl. Sci.,* **6** (2012).

[24] T F. L. Tanzella, B. P. Earle NS M. C. H. McKubre, "The Search for Nuclear Particles in the Pd-D Co-Deposition Experiment", *8th International Workshop on Anomalies in Hydrogen/Deuterium Loaded Metals* Catania, Italy 13-18 October 2007.

[25] P. L. Hagelstein and I. U. Chaudhary, "Coupling between the Center of Mass and Relative Degrees of Freedom in a Relativistic Quantum Composite and Applications", *J. Condensed Matter Nucl. Sci*. **24** (2017) 114–122.

[26] E.E. Salpeter, "Electrons Screening and Thermonuclear Reactions", Australian J. Physics, **7**, (1954) 373.

[27] K. Hagino and A.B. Balantekin, "Radiation correction to astrophysical fusion reactions and the electron screening problem", *Physical Review C*, **66**, (2002) 055801.

[28] H. J. Assenbaum, K. Langanke, and C. Rolfs, "Effects of Electron Screening on Low-Energy Fusion Cross Sections" *Z. Phys. A*, **327**, (1987), 461–468.
[29] Czerski, K., et al.: Experimental and Theoretical Screening Energies for the ^{2}H(d, p)^{3}H Reaction in Metallic Environments. *Eur. Phys. J. A*, **27**, (2006) 83–88.
[30] J. F. Ziegler, M.D. Ziegler, J.P. Biersack, "SRIM - The stopping and range of ions in matter", *Nuclear Instruments and Methods in Physics Research Section B*, **268** (11-12), (2010) 1818-1823.
[31] P.A. Mosier-Boss, F.E. Gordon, L.P. Forsley and D. Zhou, "Detection of high energy particles using CR-39 detectors part 1: results of microscopic examination, scanning, and LET analysis", *Int. J. Hydrogen Energy,* **42** (2017) 416–428.
[32] J.F. Briesmeister (Ed). "MCNP"—A General Monte Carlo N-Particle Transport Code, Version 4C", *LA-13709-M*, Los Alamos National Laboratory, (April 2000).
[33] S.A. Pozzi, E. Padovani, M. Marseguerra, "MCNP-PoliMi: a Monte-Carlo code for correlation measurements", *Nuclear Instruments and Methods in Physics Research Section A*, **513**(3) (2003) 550-558.
[34] S. Agostinelli, et al, "Geant4—a simulation toolkit", *Nuclear Instruments and Methods in Physics Research Section A: Accelerators, Spectrometers, Detectors and Associated Equipment*, **506**(3) (1 July 2003) 250-303
[35] L.P. Forsley and T.L. Benyo, "MCNP Fusion Modeling of Electron-Screened Ions", *2021 MCNP® User Symposium*, Los Alamos National Laboratory July 12 – 16, 2021. https://www1.grc.nasa.gov/wp-content/uploads/MCNP-Symposium-Forsley-Accepted.pdf
[36] P. Goldhagen, "Use of Cosmic-Ray Neutron Data in Nuclear Threat Detection and Other Applications", *Neutron Monitor Community Workshop*— Honolulu, Hawaii (October 2015).
[37] T. L. Benyo and L.P. Forsley, "NIAC 23 Project: Accessing Icy Worlds using Lattice Confinement Fusion (LCF) Fast Fission", *Cryobot Workshop*, Pasadena, CA (February 21-23, 2023). https://ntrs.nasa.gov/citations/20230002343

J. Condensed Matter Nucl. Sci. 38 (2024) 42–50

Research Article

Experimental Observations on the Lattice Energy Converter

Antonio Di Stefano*
Prysmian Electronics s.r.l., Italy

Abstract

The Lattice Energy Converter (LEC) is a relatively simple gas-metal device that is able to directly generate an electric voltage and current by an unexplained mechanism, possibly related to LENR. Due to its simplicity and high reproducibility, the LEC is a very interesting experiment that may provide insights into LENR phenomena, as well as potentially being a practical new solid-state energy source. This paper describes a successful replication of a Lattice Energy Converter (LEC) and a number of experiments and observations made to investigate the nature of the effect and its electrical characteristics, and to exclude the presence of artefacts and conventional explanations. Compared to a control device, the active LEC was able to generate a stable voltage in excess of 300 mV and a current up to a few microamperes. These results are consistent with previous data published by the inventors and other replicators, so the good reproducibility of the device is confirmed. The primary and most interesting effect happening inside the device is the apparent ionization of the gas between the electrodes, allowing a significant current to flow through an otherwise insulating gap. The spontaneous voltage is instead a secondary effect, due to the presence of a bimetallic pair in contact with an ionized conductive medium, forming a kind of gas-phase battery.
 ISSN 2227-3123

Keywords: Direct Energy Converter, LENR, LEC Construction

1. Introduction

In March 2021 the author started a replication of Frank Gordon's and Harper Whitehouse's Lattice Energy Converter (LEC), as described in [1], [2] and [3]. The most interesting feature of this device was its simplicity and apparently its high reproducibility. The device was in fact already replicated by other researchers. In designing the replication experiments the first concern was to exclude any conventional effect possibly due to electromagnetic interference, noise, instrumentation drift and other common (but not obvious) effects. To this end, a series of control experiments were designed and performed before the actual replication. The second aim was to design a very simple structure that can be easily modified and reutilized in a variety of tests.

Once the device was built, the control experiments were performed, confirming the absence of conventional effects, and a satisfactory instrumentation sensitivity and noise level. Then the active electrode was made, and the actual replication was tested. Compared to other previously described implementations, the devices here reported employed

*Corresponding author: antonio.distefano@prysmiangroup.com

 ISSN 2227-3123

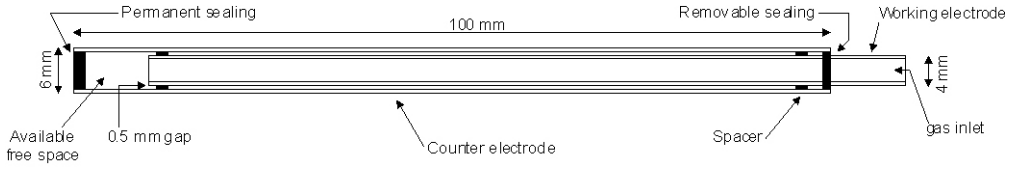

Figure 1. Design of the test LEC device.

a Fe co-deposition instead of a Pd-based one. This made the process very simple (due to the common availability of Fe and Fe-based salts, compared to Pd) and inexpensive. The results obtained were almost identical to the ones reported by Frank Gordon and Harper Whitehouse, confirming the high reproducibility of this experiment and the reality of the underlying effect. The most interesting feature of the device is not only its ability to generate electrical power, but the fact that the internal gas appears to be ionized by an unknown agent.

2. Structure of the Device

To replicate the LEC, a "laboratory" version of the device was designed, i.e., a very simple structure which can easily be modified, without the need to entirely rebuild the device for each kind of test. This structure is depicted in Fig. 1. Both electrodes are made from small diameter metal tubes (the outer tube is 6 mm OD, and the inner tube is 4 mm OD, both 0.5 mm thick). The working electrode (WE) can be electroplated, inserted in the counter electrode (CE) with a couple of rubber spacers. Then the assembly can be sealed with rubber fittings or epoxy glue. Given the device dimensions, the gap between the two electrodes is 0.5 mm. The WE tube is also used to evacuate and fill the device with the chosen gas (the 4 mm tube can be directly fitted into off-the-shelf pneumatic fittings). Different metal combinations were tested, among which: brass, copper and aluminium, as well as different gas pressures, in order to verify how the generated voltage and current were affected.

The first step was characterizing the control devices, i.e., devices with identical materials and mechanical structures as the active device, but without the co-deposition layer on the WE. This provided a clear picture of the baseline behaviour. These tests gave, among other things, a clear answer to the hypothesis of simple galvanic voltage generation or the existence of other conventional phenomena.

3. Experiments on the Control Devices

Three control devices were tested, made with a brass WE and three different metals as the CEs: brass, aluminium and copper (see Fig. 2). The first tests were performed with air at atmospheric pressure, 23.9 °C, 46% relative humidity (RH). Tests were repeated with hydrogen, then repeated again at lower pressure for both gases.

A Keithley (Tektronix) DMM6500 multimeter was used, featuring a very high precision, customizable integration time and filtering. The instrument was set to 10 MΩ input impedance and an integration time of 20 ms (the period of the local 50 Hz mains) plus averaging of 100 samples.

The capacitance of the three devices was measured, since this may affect their dynamic behaviour and it was directly related to the device geometry, so it was useful for comparing them. Results were the following:

Brass-Brass: 30 pF ± 10 pF
Brass-Aluminium: 30 pF ± 10 pF
Brass-Copper: 30 pF ± 10 pF

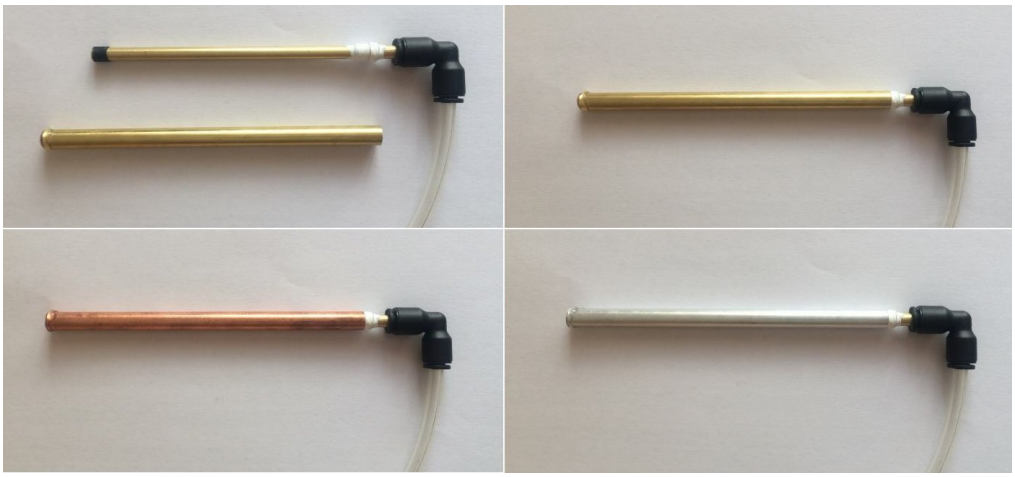

Figure 2. Some LEC devices used for the control experiments: the inner tube (WE) is the same, the outer tube (CE) can be changed in order to test different metal pairs.

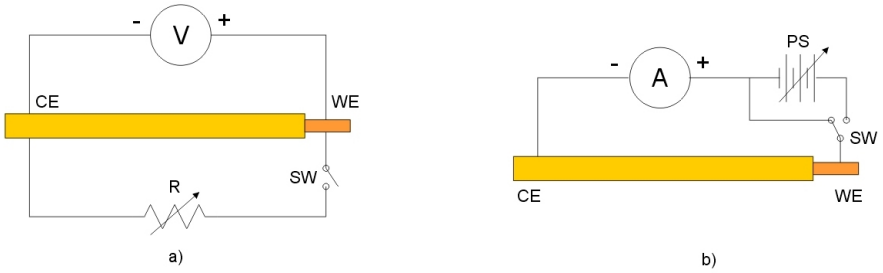

Figure 3. a) Voltage measurement: the SW switch controls the open-circuit or loaded operations through the variable resistor R. b) Current measurement: the SW switch controls the spontaneous (as in figure) or forced current mode, putting in series the variable power supply PS.

So, the geometry was consistent for the three devices, and the capacitance was in good agreement with calculations. The difference in metals was not relevant.

The second measurements were on open circuit voltage (Fig. 3a). The voltmeter was connected to the devices (WE to the positive probe, CE to the negative one), obtaining almost the same result for the three devices. The readings were the following:

- **Brass-Brass:** 0.01 mV $\pm$ 5 μV
- **Brass-Aluminium:** 0.01 mV $\pm$ 5 μV
- **Brass-Copper:** 0.01 mV $\pm$ 5 μV

This result clearly implies that the devices do not generate any spontaneous voltage, even when different metals are used together. This was a first confirmation that the voltage observed in the LEC by the inventors is not due to bimetallic, galvanic, chemical effects, or other conventional phenomena. The above-described voltages can also be considered the noise floor of the instrumentation and setup for the voltage measurement.

The third measurement was done to test the capability of the device to conduct a current when an external voltage was applied (Fig. 3b). A DC voltage ranging from −60 V to +60 V in steps of 5 V was connected to the device, measuring the flowing current. The following results were obtained, actually independently from the applied voltage:

- **Brass-Brass:** 0 μA $\pm$ 0.5 nA [from −60 V to +60 V]
- **Brass-Aluminium:** 0 μA $\pm$ 0.5 nA [from −60 V to +60 V]
- **Brass-Copper:** 0 μA $\pm$ 0.5 nA [from −60 V to +60 V]

This data essentially imply that the devices do not conduct current. This result is actually a second confirmation that the original LEC has quite different behaviour: according to the inventors, it not only generates a voltage, but it is also able to conduct a current (either spontaneous, or under an external stimulus). By increasing the amount of filtering and averaging on the instrument, it was possible to determine with good precision the residual current during this experiment; it was on the order of 100 pA.

All these measurements were repeated at a lower gas pressure (down to about 300 Torr), just to verify also the influence of this parameter. The results were essentially the same. The conclusion was that a gas pressure in this range do not significantly affect spontaneous voltage and currents. All the above-described tests on the control devices were repeated using hydrogen instead of air, obtaining the same results.

These results were very robust and lead to the conclusion that a device with the structure of the LEC, with an untreated WE electrode, does not generate a spontaneous voltage and is not capable of conducting a significant current. This behaviour is not affected by the employed metals, by the type of gas (air and hydrogen tested), and gas pressure (tested range from 300 to 760 Torr). The behaviour of the control device is exactly the one expected from the theory of electricity conduction through gases [4].

The performed measurements allowed me to assess the instrumentation sensitivity and noise level, that allow detection with high confidence voltages in the order of tens of μV and currents below of nA, that are at least 3 orders of magnitude smaller than the one expected from an active LEC.

4. Tests on the Active LEC

The device used for the active tests was exactly the same described previously as control. The only difference was the co-deposition process, involving the plating of a thin layer of Fe on the brass WE tube.

4.1. Co-deposition Process

The working electrode (WE) was gently rubbed with fine sandpaper and cleaned with alcohol, then it was placed in the electrolytic cell.

The cell was constructed with a test tube, with four 1 mm iron wires surrounding the WE. The wires were connected to the positive voltage while the WE was connected to negative (ground). The electrolyte was 1/4 HCl at 20% concentration, 3/4 tap water (so essentially about 5% HCl). No $FeCl_2$ was added since the Fe++ ions were directly obtained from the anode wires during the electrolytic process. The current was set by finely regulating the power supply voltage. The cell is shown in Fig. 4.

The current was set and maintained as follows, according to Frank Gordon's recommendations:

8:00 - 8:35:	0.7 mA	(80 μA/cm^2, 0.167 V)
8:35 - 9:05:	1.7 mA	(190 μA/cm^2, 0.254 V)
9:05 - 12:00:	16 mA	(1.8 mA/cm^2, 0.375 V)
12:00 - 16:00:	25 mA	(2.8 mA/cm^2, 0.450 V)

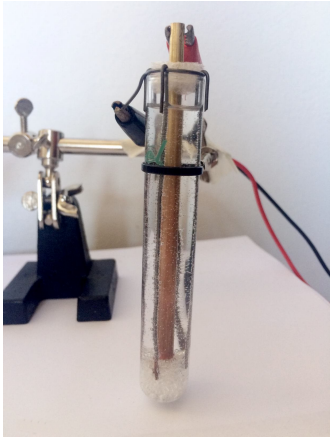

Figure 4. Electrolytic cell used for the co-deposition at the beginning of the process. This picture and the following one were taken during the first experiment. Note that the colours of the wires do not indicate the applied polarity.

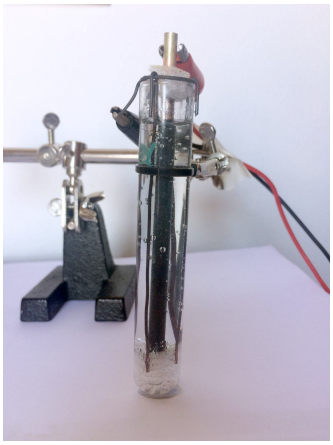

Figure 5. Appearance of the WE at the end of the co-reposition process.

Temperature was 26.4 °C, 45% RH at the beginning of the process, 26.6 °C, 51% RH at the end. At 15:30 the electrode appeared as shown in Fig. 5: it became black quite abruptly.

It can be noted that, even if this protocol proved to be effective, subsequent experiments suggested that this co-deposition method is very sensitive to a number of factors (e.g. cell dimensions, applied voltage, HCl concentration, etc), so more repeatable results can be obtained starting from a conventional solution of 0.1 M of $FeCl_2$.

4.2. Preliminary Test

The plating process was ended at 16:00, the power supply disconnected and the WE extracted, rinsed with tap water and dried with a soft paper towel. The plating appeared quite uniform, well attached to the brass substrate and with a very fine porosity. The thickness was not measurable (estimated on the order of 10 μm). An unexpected phenomenon

Figure 6. Open circuit voltage measured on the brass - brass device after about 1 hour from the co-deposition and device assembly.

was noticed while taking out the WE from the cell: the WE, as well as the iron wires, became magnetised, attracting each other. This effect may be due to the formation of magnetite nano-crystals, which also would account for the black appearance of the deposited layer.

The WE was then inserted into the brass counter electrode (CE) in air at atmospheric pressure. No hydrogen was added at this stage. The voltage was at first checked with a handheld multimeter with 10 MΩ input impedance.

The initial reading was close to 0 mV, then in tens of seconds, it started increasing and stabilizing around 242 mV. This was a clear indication that the device was generating a voltage. The device was closed but not permanently sealed, in order to allow further experiments. The following experiments were done as fast as possible, in order to prevent the oxidation of the thin Fe plating layer and/or potential hydrogen desorption.

4.3. Voltage Measurements

The first test was to accurately measure the open circuit voltage and short circuit current of the device (Fig. 3a and 3b), using the brass CE as well as the aluminium and copper ones. The positive probe of the DMM6500 multimeter was connected to the WE, the negative to the CE. The reported signs of voltages and currents reflects this choice. The voltage measured on the device with the brass CE was $-$**307 mV**, the short circuit current was $-$**2.4 μA**. The voltage of the aluminium CE was **223 mV**, and the current **1.5 μA**. The voltage of the copper CE was $-$**234 mV** with a $-$**0.69 μA** short circuit current. The voltage of the brass CE increased slowly over time, so probably also with the other two metals higher value would be obtained by extending the measurement time. During this experiment the peak voltage with brass CE was about 330 mV, as shown in Fig. 6.

All subsequent tests were done with the brass CE only.

Another test was done by loading the device with various resistors (Fig. 3a). The result is shown in Fig. 7. The behaviour is exactly the one reported in [1], showing an internal resistance in the order of 120 KΩ.

4.4. Current Measurements

The capability of the active device of conducting a current was tested as previously done with the control devices, by applying an external voltage. The result is shown in the Fig. 8. The device was apparently able to conduct a significant amount of current, so the external voltage range was limited to $\pm$10 V, in order to avoid damaging the device (e.g., by desorbing the hydrogen or damaging the co-deposited layer). Maximum current at 10 V was about 136-140 μA. Compared to about 100 pA measured on the control device, the active device showed a 6 order of magnitude increase in

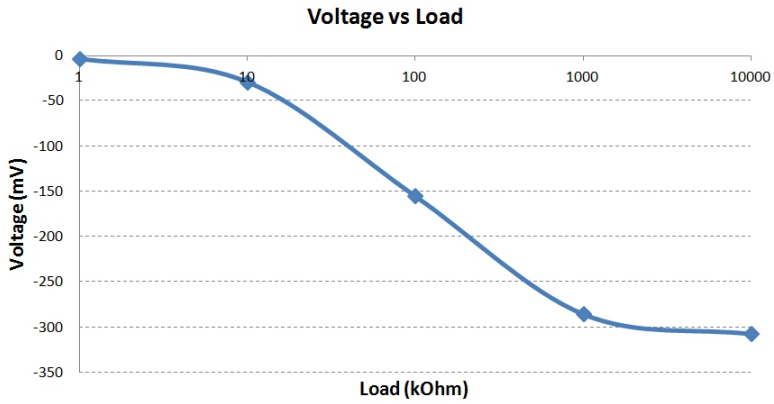

Figure 7. Voltage generated by the brass-brass LEC when a variable resistive load was applied.

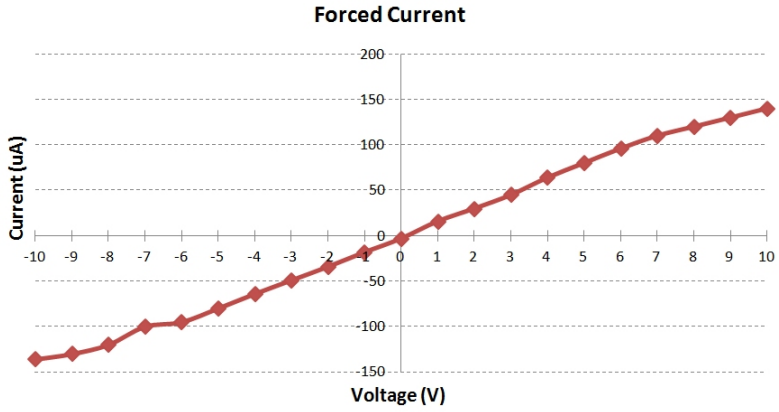

Figure 8. Current through the device by applying an external voltage ranging from −10 V to +10 V.

conductivity. It can be noted from the plot that the current tends to saturate at higher voltages: this is important because it is indicative of a true gas conduction phenomenon with limited charge carriers and not other type of conduction (e.g., through Ohmic material).

4.5. Additional Experiments

In order to verify the capability of the device to generate useful power/energy, the LEC was connected to a 100 μF electrolytic capacitor, and the charging process was monitored. The result is shown in Fig. 9. The capacitor was fully charged in about 90 seconds. It was then disconnected and the charge was measured. The stored voltage was 309 mV, so the stored energy was 4.7 μJ. The time constant of the charging curve was 15 s. Since the time constant is equal to

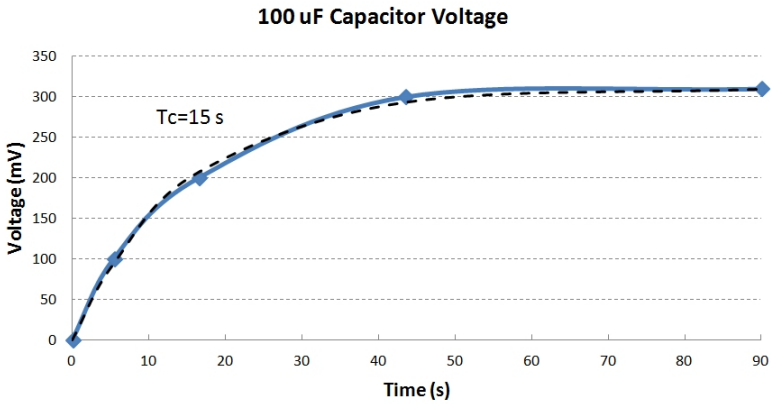

Figure 9. Results for the capacitor charging experiment.

the RC product of the circuit, the internal R of the LEC can be evaluated as about 150 kΩ. This is in good agreement with the load plot.

Another test was done on the naked WE (in air), with a Geiger-Muller counter (LND712 tube, mica window, alpha sensitive), in order to detect potential radiation. The counts for background, for the sample and for the sample plus a plastic shield, during an integration period of 10 minutes were: 9.4 CPM, 11.4 CPM and 11.6 CPM respectively. So, no significant evidence of radiation was found.

Lastly, the naked CE was left in air and in darkness for about 1 hour, in contact with a glow-in-the-dark plastic strip containing ZnS(Ag) and some fluorescent substances to test for low energy photons in the range of far UV. No fluorescence or phosphorescence visible to the naked eye was excited in the materials.

4.6. Final Considerations

All of the tests were limited by the short time available before signs of oxidation (rusting) appeared on the iron WE co-deposited layer. This effect can be reduced when the WE is sealed with hydrogen inside the CE. The day after the experiment, the condition of the WE was as shown in Fig. 10, where visible oxidation can be noted. In this condition the LEC performance decreases (the measured voltage was 50 mV or less). It is not clear if this effect was due to oxidation, hydrogen desorption or both.

All the experiments were repeated a number of times, by employing air, hydrogen or a mixture of the two. In all cases the results were very similar.

5. Conclusions

A working LEC device was successfully replicated. The entire process was not difficult or critical in any way. The capability of the LEC to conduct a current can only be explained by the emission or generation of ions by the active WE. The kind of emission of the WE and its properties remains unknown and requires further investigation. The capability of the device to conduct a current in both directions implies that the same amount of charge of both signs are present in the gas. These are most probably generated in the gas itself by an unknown source of radiation. In order to ionise the gas this radiation must have an energy at least on the order of some tens to some hundreds of electron volts. The generated

Figure 10. Oxidation appearing on the WE after exposure to air (oxidation is mainly on the left side).

voltage varied with the employed metal pairs, and changed its sign when aluminium was used. This is in accordance with electrode potentials (considering iron for the WE). This may imply that the voltage generation can be explained by some relatively conventional process (even if the environment and conditions are not conventional). A very similar effect has previously been described in a similar configuration, but with the gas ionized by an external radioactive source [5]. The ionization in the LEC cannot be explained with conventional (electro)chemical processes, requiring an energy that is generally beyond the chemical range. So, the ability to ionise the gas is the most surprising and interesting characteristic of the LEC and suggestive of the possible involvement of LENR phenomena. With reference to this, the observed phenomena are in good accordance with the ones described by Rout and Srinivasan on deuterated palladium samples [6].

Further studies are needed to understand the root phenomena observed in the device, in particular the mechanisms and the agent of the gas ionization. However, it is interesting to note that the device, even without a satisfactory explanation, can be prospectively and quite easily scaled-up and used as a practical energy source for some low power applications.

References

[1] F. Gordon, H. Whitehouse, "*Lattice Energy Converter*", Journal of Condensed Matter Nuclear Science (JCMNS), Vol. 35, pp. 30–43, 2022.
[2] F. Gordon, H. Whitehouse, "*Lattice Energy Converter II*", Journal of Condensed Matter Nuclear Science (JCMNS), Vol. 36, pp. 1–24, 2023.
[3] J.P. Biberian, "*LEC Replication Presentation*", IWAHLM 14 Conference, Assisi, 2021.
[4] J.J. Thomson, "*Conduction of Electricity Through Gases*", Cambridge University Press, 1903.
[5] P.E. Ohmart, "*Method and Apparatus for converting Ionic Energy Into Electrical Energy*", US patent US3152254, Oct. 1964.
[6] R.K. Rout et al., "*Reproducible, Anomalous Emissions from Palladium Deuteride/Hydride*", Fusion Technol., n. 30, p. 273, 1996.

J. Condensed Matter Nucl. Sci. 38 (2024) 51–77

Research Article

Energetic Ion Emission from TiD_x in Low-Energy Ion Beam Experiments

Sadie Forbes, Peter L. Hagelstein and Florian Metzler

Massachusetts Institute of Technology, Cambridge, MA, USA

Abstract

Low-level energetic ion emission has been reported previously in many low-energy nuclear reactions (LENR) experiments including electrolysis, gas-loading and ion beam experiments. The corresponding reports present evidence for MeV-level charged ions and neutrons associated with deuterium-deuterium fusion reactions, and also particles at higher energy that would be expected to originate from other processes. A study of low-level energetic nuclear particles has the potential to shed light on nuclear processes relevant to excess heat production and other LENR anomalies, which provides motivation to focus on such observables. In some of the referenced earlier experiments a small number of very energetic charged particle emissions near 20 MeV have been reported, which is of particular interest to us in connection with the involved mechanisms. We developed an ion beam experiment in which thick (1.59 mm) and thin (5 μm) Ti foils were initially loaded with deuterium by ion beam implantation and then bombarded with argon ions at 950 eV. A small number of counts in high-energy detector channels were recorded in eight different experiments, corresponding to particle energies estimated to be between 32-40 MeV, based on a calibration at lower energies with an ^{241}Am calibration source. Experiments with the 5 μm Ti foil also resulted in dozens of counts below about 11 MeV.
 ISSN 2227-3123

Keywords: Ion Emission, LENR, Charges Particles, Beam Experiments

1. Introduction

In the early days of research on low-energy nuclear reactions (LENR), many approaches were used to load palladium and other metals with deuterium including electrochemistry and gas loading, as well as loading with ion beams. A perceived advantage of ion beam implantation was that it was potentially possible to develop a D/Pd loading in excess of unity, especially at low temperature where deuterium diffusion is inhibited [1]. Early experiments done at Sandia National Laboratories [2], [3], and at the United States Naval Research Laboratory (NRL) [4] showed no anomalies, even under conditions with very high D/Pd loading ratios. Electron screening of dd-fusion reactions has been studied using accelerators at low energy, where evidence for anomalously large screening energies has been obtained [5]–[10].

There have been reports of LENR anomalies in ion beam experiments. Low-level charged particle emission near 20 MeV was reported from D implantation in PdD_x in [11]. A charged particle peak near 5 MeV was observed from D bombardment of TiD_x [12], [13]. And a small number of charged particles were seen near 8.6 MeV in ion beam experiments with proton bombardment of Li [14].

 ISSN 2227-3123

We obtained support to explore potential alpha particle emission from proton bombardment of Li, motivated by claims of p+^{7}Li fusion in glow discharge experiments by Lipinski and Lipinski [15], [16]. However, the planned campaign was interrupted by the Covid-19 pandemic, before all equipment was fully operational. In light of the positive result reported in [14] we would like to resume this campaign in the future.

In initial exploratory experiments (herein referred to as the "2019 experiments") with the ion beam experimental setup, we conducted some runs with D implantation of Ti, which resulted in several counts of interest with a charged particle detector and with a neutron detector (as discussed below in this article). In more recent experiments that sought to build on those initial findings (the "2022 experiments"), we have observed more counts of interest from TiD_x, all of which has provided motivation for documenting the experimental work to date in this article. We recognize that the presented results to date can be—and should be—improved in many ways. The purpose of this article is to share the experimental work that has been conducted thus far, to discuss the issues that have emerged, to share lessons learned, and to lay out plans for the continuation of this work.

There are quite a few issues to be considered in connection with ion beam based LENR experiments. One experimental issue concerns the lack of reproducibility associated with earlier ion beam experiments, and the need to develop a protocol that can result in comparatively high degrees of reproducibility of reported anomalies. In our recent experiments, low-level energetic ion emission is observed with an improved degree of reproducibility over earlier experiments; however, there is much room for further improvement. Another issue concerns the origins of the observed effect, and the question more generally of whether and how charged particle emission from metal deuterides may occur in LENR experiments. Related to this is the identification of the particles emitted, as well as the precise characterization of the particle energy. Looming large is the question of the origin of the energetic particles, and what conditions are required to produce them. In the remainder of this article, we will engage with these questions in the context of presenting data from the 2019 and 2022 experiments with TiD_x. We will begin with a brief review of related reports in the literature.

2. Brief Review of Reports of Low-level MeV Nuclear Product Emissions in LENR Experiments

The majority of LENR experiments over the years have focused on excess heat measurements, which would be the biggest effect in terms of corresponding reaction rates, and which may eventually lead to commercial applications. There have been fewer experiments that focus on low-level nuclear emissions. In this section, we discuss past LENR experiments, in which neutron spectra were observed and recorded, and in which charged particle spectra were observed and recorded (and in some cases particle identification carried out).

2.1. Low-level Neutron Spectra

Recall that following the announcements of 1989 by Fleischmann and Pons a great deal of work was done by many research groups around the world looking for nuclear signatures from metal deuterides, and most of the results were negative. A small subset of experiments, in which low-level neutron emission was sought and not observed, are documented in [17]–[26]. The large number of negative results published at the time has been interpreted by many as proof that there are no nuclear anomalies in metal deuterides—an interpretation that is, however, not in agreement with other publications. A better interpretation is that for one reason or another, these groups were not able to reproduce earlier claimed experimental results due to a lack of understanding of the experiments and conditions needed to obtain such results.

Even with imperfect reproducibility (as in the Frascati experiment, where TiD is cycled in gas), it has been possible to detect low-level neutron emission, and also to accumulate spectral information. A summary of published results, in which spectral information was obtained is given in Table 1. Most of the neutron spectral measurements on LENR experiments are consistent with 2.45 MeV emission from the reaction

Table 1. LENR experiments with reported neutron spectra. Note that the metal deuterides are indicated generically in the form of MeD, without an attempt to indicate specific loadings reported.

Author	Year	Ref.	MeD	Type	Detector	Peaks (MeV)
Jones	1989	[27]	TiD	electrolysis	BC-505 recoil	2.5
Bertin	1989	[28]	TiD	electrolysis	NE-213 recoil	2.5
Shani	1989	[29]	PdD	gas loading	NE-213 recoil	2.5
Wolf	1990	[30]	TiD,PdD	electrolysis, gas	NE-213 recoil	2.5
Takahashi	1990	[31]	PdD	electrolysis	NE-213 recoil	2.45,4.5,7
Bressani	1991	[32]	TiD	cycling in gas	NE-110 TOF	2.5
Bressani	1991	[33]	TiD	cycling in gas	NE-110 TOF	2.5
Takagi	1991	[34]	PdD	electrolysis	NE-110 TOF	2.5
Takahashi	1991	[35]	PdD	electrolysis	NE-213 recoil	2.45,4.5,6
Botta	1992	[36]	TiD,PdD	cycling in gas	NE-110 TOF	2.5 and above
Nakada	1993	[37]	PdD	electrolysis	NE-213 recoil	2.45, 3-7
Bittner	1993	[38]	PdD	electrolysis, degassing	NE-213 recoil	2.5
Long	1993	[39]	many	glow discharge	recoil	up to 10.5
Lipson	2000	[40]	Au/PdD/PdO	electrolysis	NE-213, recoil	2.5
Steinetz	2020	[41]	TiD,ErD	gas-loading, x-ray	EJ-309, others	2.45, 4-5

$$d + d \rightarrow n(2.4497\ \text{MeV}) + {}^{3}\text{He}(0.8193\ \text{MeV})$$

In all of these papers, evidence for emission near 2.5 MeV is reported, consistent with dd-fusion. We draw attention to the fact that in some cases, significant emission is reported at higher energies, indicative of nuclear processes other than dd-fusion. The early measurements of Takahashi et al. [31], [35] are particularly relevant in this regard. We have chosen to include the recent NASA experiment [41] as a LENR experiment closely related to earlier experiments, recognizing that not all would agree with such an interpretation.

Note that CR-39 has been used for the detection of energetic neutrons above 9.6 MeV, where the neutron energy can be inferred from triple tracks that result from ^{12}C(n,n′)3α carbon breakup [42]–[45].

2.2. Low-level Charged Ion Spectra

Also following the 1989 announcements by Fleischmann and Pons, experiments were conducted seeking charged particle emission in LENR experiments, in which, however, no evidence for anomalous charged particles was found [46]–[48]. A conclusion is that simply loading deuterium into a metal does not guarantee that reported LENR effects can be observed.

The observation of low-level neutron emission in LENR experiments near 2.5 MeV would suggest that there should also be a charged particle emission effect based on the 0.82 MeV ^{3}He from the n+^{3}He dd-fusion channel, as well as from the other main dd-fusion channel

$$d + d \rightarrow p(3.0226\ \text{MeV}) + t(1.0100\ \text{MeV})$$

In an experiment by Jones and coworkers [49] with TiD, protons were observed near 2.6 MeV based on dE-E measurements with plastic and glass scintillators. Also described is a coincidence experiment, in which samples were placed between two large-area silicon charged particle detectors, and coincidence measurements were done for protons and tritons of this branch of the dd-fusion reaction.

A list of publications, in which charged particle spectral information is reported, is presented in Table 2. Low-level charged ion emission in these experiments appears to be a weak effect, and the number of reported counts tends to be small. Nevertheless, counts are seen both with active detectors (silicon and diamond-based) as well as with passive detectors (CR-39 based), with modest to good signal-to-noise ratio.

Table 2. LENR experiments with reported charged particle spectra.

Author	Year	Ref.	MeD	Type	Detector	Energies (MeV)	Particle(s), if identified
Taniguchi	1989	[50]	PdD	electrolysis	SSB	< 3	
Aiello	1990	[51]	PdD	gas loaded	SSB	1.8	^{1}H
Cecil	1990	[52]	PdD	ion beam, current	SSB	3,5	^{1}H, ?
Chambers	1990	[11]	PdD	ion beam	SSB	21	^{3}He or ^{4}He ?
Chambers	1991	[12]	TiD	ion beam	SSB	$\sim$5	^{3}H ?
Chambers	1991	[13]	TiD	ion beam	SSB	5-6	^{3}H ?
Cecil	1991	[53]	TiD	gas loaded, current	SSB	1-10	^{3}He, ^{4}He ?
Taniguchi	1991	[54]	PdD	electrolysis	SSB	< 3	
Mo	1991	[55]	TiD,PdD	gas loaded	SSB	> 5	
Tsarev	1991	[56]	TiD,PdD	ion beam	SSB	< 4	^{1}H,^{3}H,^{3}He
Karabut	1992	[57]	PdD	glow discharge	SSB	< 20	^{4}He
Yamaguchi	1993	[58]	PdD	gas loaded	SSB	3-6	^{1}H, ^{4}He
Taniguchi	1994	[59]	PdD	electrolysis	SSB	< 10	
Karabut	1995	[60]	PdD	glow discharge	SSB	≥ 10	$\geq$ ^{4}He
Lipson	2000	[40]	PdD	electrolysis	SSB, CR-39	1-3	^{1}H, ^{3}H
Lipson	2002	[61]	PdD	electrolysis	CR-39	≤ 22	^{1}H, ^{4}He
Lipson	2003	[62]	PdD	electrolysis	SSB, CR-39	1-3	^{1}H, ^{3}H
Jones	2003	[49]	TiD	gas loading	plastic, glass	2.6	^{1}H
Roussetski	2004	[63]	PdD	electrolysis	CR-39	< 10	^{4}He
Lipson	2005	[64]	PdD	electrolysis	CR-39	≤ 16	^{1}H,^{4}He
Kitamura	2011	[65]	PdD	gas loading	SSB	2-8	
Mosier-Boss	2014	[66]	PdD	electrolysis	CR-39	≤ 20	^{1}H, ^{4}He
Lukosi	2014	[67]	PdD	gas loading	diamond	< 14	
Weaver	2015	[68]	PdD	gas loading	diamond	< 8	
Zhou	2015	[69]	PdD	electrolysis	CR-39	< 15	^{1}H, ^{4}He
Ziehm	2022	[70]	PdD	glow discharge	CR-39	0.14	^{4}He

To some observers it was apparent early on that there was more to the spectrum than could be accounted for by dd-fusion reactions (see the prescient comment at the end of Ref. [50]). Particle identification with silicon surface barrier (SSB) detectors with dE-E detection is reported in Ref. [62], and illustrated in Figure 1. Alpha particles are identified with energies between about 9 MeV and 12 MeV. This is consistent with many of the observations of energetic alphas reported in Table 2. In some experiments, a small number of very energetic charged ions are reported; as in Ref. [11] (21 MeV); Ref. [57] (18 MeV); and Ref. [66] (10-20 MeV).

2.3. Discussion of Prior Experiments and Associated Challenges

In general, the reported levels of energetic nuclear particles are not commensurate with reported levels of excess heat production, or with reported tritium production, which historically has hindered understanding of what nuclear processes may be involved and which has limited the usefulness of standard nuclear diagnostics in such experiments. Early on in LENR research, there were claims of observed neutron emission, which provided motivation to carry out measurements aimed at dd-fusion products. However, while at times observing such products, the deployment of nuclear diagnostics for such measurements has also suggested that neutrons and energetic ions are present at energies that are not commensurate with conventional dd-fusion reactions.

In the neutron spectra reported in the papers listed above, 2.45 MeV neutrons that correspond to dd-fusion are detected near the expected energy. Note that neutrons interact weakly with the experimental environment prior to detection, therefore the recorded neutron energy can be expected to be near the neutron energy at their origin. Energetic charged ions, in turn, interact with the experimental environment more strongly, losing energy as they traverse the

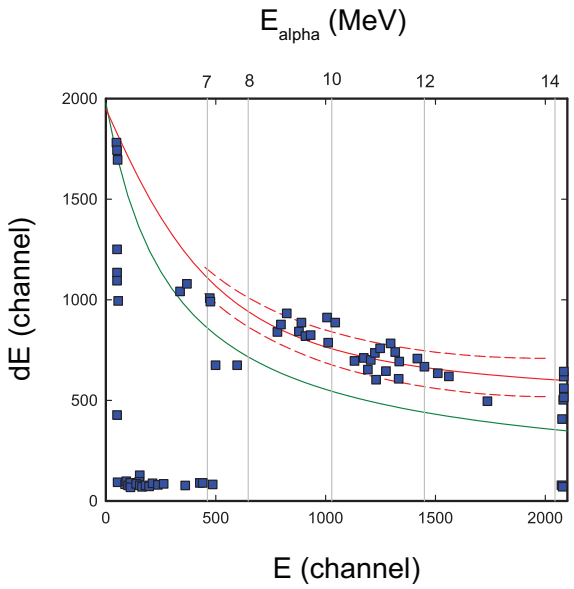

Figure 1. Data redrawn from Lipson et al (2003): blue squares; alphas fall within the red dotted lines around the solid red line; protons fall around the green line; alpha energies are indicated by the grey vertical lines.

sample. Protons from dd-fusion are born with 3.02 MeV and could show up in detectors around 2.6 MeV in [49] due to this energy loss. At present, we do not know with certainty what nuclear processes may lead to alpha emission in LENR experiments at precisely what energies. The degradation of alpha energy in the sample further complicates the situation.

The above issues point at the need for further experiments, where some of these challenges are addressed. This has been the goal of the experiments reported on below.

3. Equipment and Samples in Our Experimental Campaigns

The vacuum chamber used in the experiments reported here is a spherical chamber 304 SST model SP1800SEP from Lesker, with a primary 400 L/s turbo-molecular pump from Edwards model nExt-400, and a 15 cubic feet per minute scroll pump from Edwards model nDds-15.

The ion gun is model DC-25 from Oxford Applied Research. The ion gun specifications give the beam energy as 100-1000 eV, a beam current up to 40 mA (the collected current on target is less by on the order of 10x per our measurements) and a beam diameter of 25 mm.

The deuterium gas used is 99.8% pure from Sigma-Aldrich product number 361860. The Ar gas used is ultra high purity grade 5.0 from Airgas.

A schematic of the ion gun, vacuum chamber, sample, and charged particle detectors is shown in Figure 2. A photograph of the basic system in 2019 is shown in Figure 3.

Since we were interested in the detection of energetic alpha particles (such as the 21 MeV He ions from PdD reported by Chambers [11], the energetic alphas near 20 MeV reported by Karabut [57], and also by Lipson [61]), thick silicon surface barrier (SSB) detectors were used. We worked with two Ortec/Ametek charged particle detectors: one

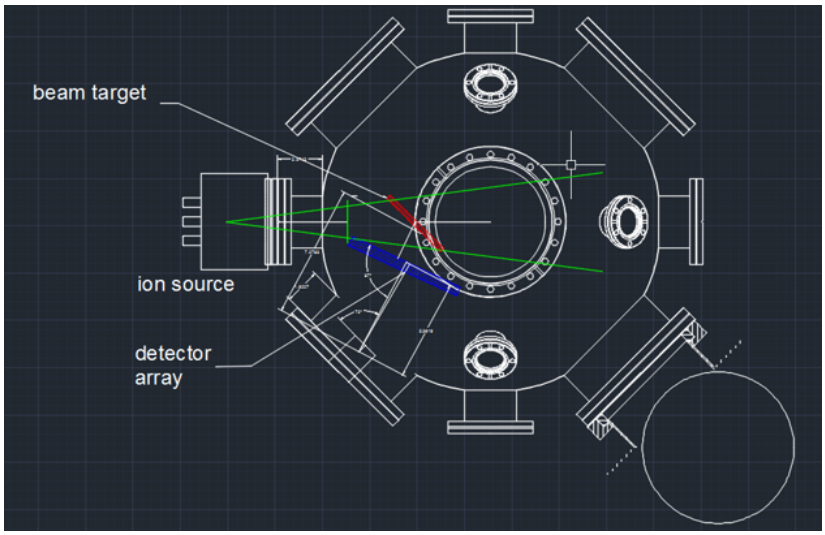

Figure 2. Experimental setup for the 2019 experiments. The ion beam cone is shown in green, the target in red, and the detector mount in blue.

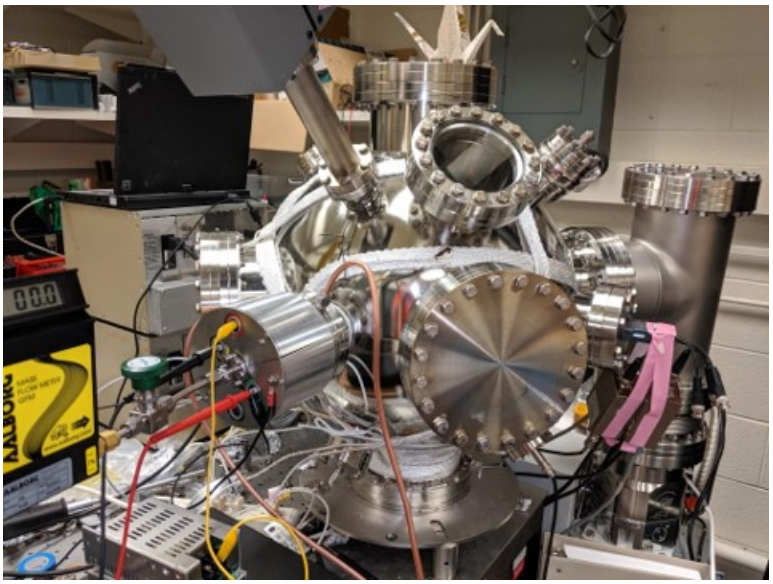

Figure 3. Chamber and ion gun (left front).

is a 500 μm thick ruggedized charged particle detector model number BR-015-050-500 (R-series) with area 50 mm^2; the other is a 2000 μm thick detector model number BA-017-050-2000 (A-series) also with area 50 mm^2.

The R-series detector was used in the 2019 experiments and its bias voltage is -180 V. The larger A-series detector was used in the 2022 experiments and its bias voltage is +250 V. The detectors were calibrated using an ^{241}Am source,

with the 5.486 MeV peak in vacuum centered on channel 1730 (out of 16000 channels), following the procedure outlined in Experiment 4.1 of the documentation on the Ortec/Ametek website [71]. A calibration spectrum obtained in 1 atm He at 2 mm distance is shown in Figure 4. For reference, the expected range of energetic alphas and protons at normal incidence in silicon is shown in Figure 5 (based on the SRIM code [108]).

We used a Wendi-2 neutron detector from Thermo Fisher Scientific (formerly Thermo Eberline) model FHT 762 with a 2 bar ^{3}He counter tube and FHT 642 P preamplifier.

For the 2019 experiments, we used a 1.59 mm thick Ti foil with area 50 mm $\times$ 100 mm made of commercially pure (grade 2, ASTM B625) Ti from McMaster-Carr. For the 2022 experiments, we used 0.005 mm thin Ti foils with area 25 $\times$ 25 mm and with purity 99.6+% from Millipore/Sigma (part number GF16653696).

4. Experimental Protocols

The topic of experimental protocols is critical to LENR experiments in general, and to the ion beam experiments discussed below in particular. At issue are the questions of exactly what conditions are sought in an experiment, and why. Much of the discussion about LENR experiments in previous years has avoided focusing on what features of an experiment are deliberately sought and for what reasons. In our experimental campaigns, the employed conditions were motivated by a concrete theoretical picture, which will be briefly reviewed below (and has been discussed in more detail elsewhere [72], [84], [101]).

Historically, there has been no generally agreed upon theoretical model for LENR anomalies, so this discussion of protocol reflects our viewpoint on the hows and whys under consideration. In the model we have advanced, excitation is transferred from D_2/^{4}He transitions to nuclear molecule states in host lattice nuclei, as described in [72]. We then need molecular D_2 species in intimate contact with an acoustic (preferably compressional) lattice vibrational mode. Although deuterons are relatively close in molecular D_2 in gas (on the order of 74 pm), there is no coupling in a gas to other nuclei via shared vibrational modes that exist in a solid.

Molecular D_2 can exist as molecules in some insulators, but the thought is that significant screening occurs in metals, which motivates how to get D_2 molecule-like species to form inside a metal. The basic problem is that in bulk metals in general the background electron density is sufficiently high that anti-bonding orbitals become occupied, pushing the deuterons further apart [73]–[75]. This directs attention to the lower electron density regions that can occur near host lattice metal atom vacancies and in other defects [76], [77].

Palladium stands out from other metals in that a single atom can bind with molecular H_2 or D_2 to form a dihydrogen or dideuterium complex. In such a complex, the metal atom binds to the (spherical) hydrogen or deuterium molecule, and not to the individual atoms of the molecule [78]–[80]. The ground state of the PdD_2 molecule is palladium dideuterium. Metal dideuterium states are low lying (but not the ground state) for other noble metal atoms [81]–[83]. The conjecture is that deuterium atoms in monovacancies in PdD_x spend some of their time in dideuterium complexes near Pd atoms of the lattice [84], where screening may be enhanced, and where substantial coupling to vibrational modes can occur. A similar picture applies to D_2 and HD in monovacancies in nickel deuteride and in a mixed deuteride/hydride. The supposition here is that a similar picture also applies to monovacancies in TiD_x.

The vacancy formation energy in Pd is over 1.5 eV [85], [86] which means that there are few vacancies in thermal equilibrium near room temperature. Hydrogen isotopes in Pd and in Ni generally occupy octahedral sites (O-sites) in bulk material [87], where the background electron density is substantial, and where the binding is not as strong as in a trap (with lower background electron density) [88], [89]. This means that if a Pd atom is removed in PdH_x, the H atoms become trapped (and hence more strongly bound), which lowers the vacancy formation energy of the Pd vacancy. At high H/Pd loading, vacancy formation becomes more probable over a wide range of temperatures (including room temperature), so that in time spontaneous vacancy formation is surmised to lead to a high vacancy concentration (up to 25%, depending on how highly loaded) [90]. Vacancy diffusion from the surface is slow near

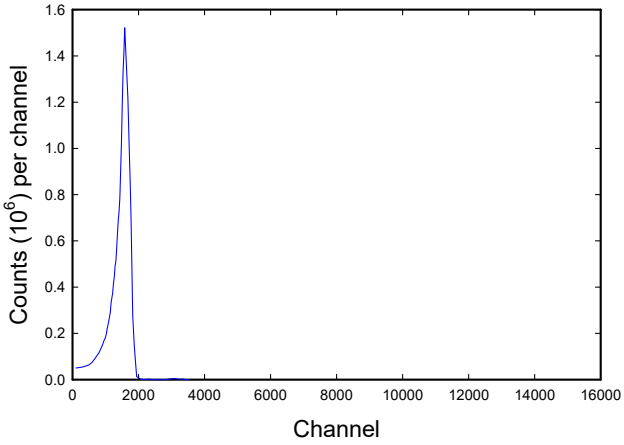

Figure 4. Calibration spectrum in 1 atm helium from ^{241}Am calibration source. The counts at the peak correspond to alphas with energies of about 5.5 MeV.

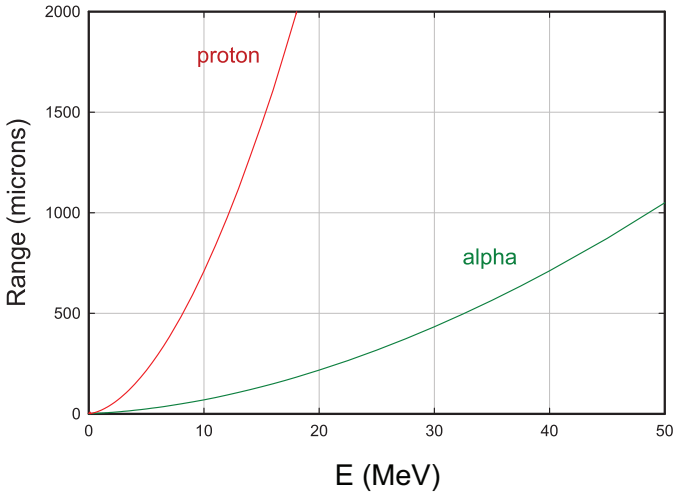

Figure 5. Alpha (dark green) and proton (red) range in silicon as a function of ion energy, based on the SRIM code [108].

room temperature, so some stimulation (such as elevated temperature) can facilitate massive vacancy formation on short (hour) time scales [91], [92]. The argument is that, when the D/Pd ratio is high in a LENR experiment, vacancy formation is favored thermodynamically, and that in some experiments, there are mechanisms available to greatly speed up vacancy formation such that di-deuterium complexes can form in the resulting low background electron density regions. In the 1990s, Szpak and coworkers reported the rapid onset of excess heat in a PdD co-deposition experiment [93]. We had conjectured that in this experiment Pd co-deposition at high current density resulted in a high D/Pd ratio near the surface, which resulted in substantial vacancy formation, since newly formed PdD layers would naturally tend toward the thermodynamically favored configuration [94]. The good reproducibility of excess

heat with the subsequently developed Letts co-deposition protocol supports this notion [95], [96]. Low-level energetic charged particle and neutron emission is observed in Pd co-deposition experiments with the related SPAWAR protocol [97]–[99]. The conjecture here is that the current density is lower in this co-deposition configuration, resulting in fewer vacancies so that the coherent dynamics contemplated in [72] are incomplete and low-level nuclear emissions occur instead of excess heat.

The background electron density in Ti is lower compared to Pd so that H and D are more strongly bound, which raises the question to what extent the same conjectures apply. Transferring the intuition about Pd to Ti suggests that what is needed to create sample conditions of interest is the use of deuterium implantation with the ion beam to develop high D/Ti loading, and then the use of D or Ar bombardment to create vacancies near the surface. The same high loading is then expected to result in occupation of the vacancies and formation of dideuterium complexes in contact with Ti atoms at the surfaces of monovacancies.

There has been much discussion of triggering of LENR experiments over the years. In the case of excess heat, in experiments of the early years following the 1989 Fleischmann-Pons announcement, a palladium cathode with high loading might sit and not exhibit any effects for extended periods of time, or might produce excess heat spontaneously. In experiments at SRI, it had been noted that a current ramp could "trigger" excess heat [100], which was thought to be connected with optical phonon generation associated with deuterium flux through the PdD_x [101], during which deuterium chemical potential energy may be converted to optical phonon energy (from our point of view, optical phonons were thought to stimulate the coherent nuclear dynamics then as now). Other related approaches to triggering are conceivable [102], including laser stimulation and electrical current stimulation. Our models suggest that strong excitation of acoustic vibrational modes allows for Dicke enhancements and optical phonon model excitation and plasmon excitation allow for energy exchange during coherent transitions; which implies that a combination of triggers is needed.

In the 1990s at SRI International, there was discussion that loading and triggering were separate functions, even though in early experiments, deuterium loading would be accompanied by deuterium flux which was a trigger (loading and trigger were mixed together), and that this could be used to advantage. This notion served as the foundation for the experiments of [103], in which cathodes were initially highly loaded and cooled, and then triggered using an electrical current pulse to heat the cathode and drive a strong deuterium flux for triggering. Yamaguchi and Nishioka worked with a loaded PdD_x sample with a blocking oxide layer that was then heated and outgassed, resulting in the observation of excess heat, neutron emission, and charged particle emission at different times [58], [104], [105]. Similar ideas were explored in the experiments by Lipson and coworkers [40], [62].

With this as preamble, in our ion beam experiments the idea was to initially load with D (and make some vacancies near the surface in the process), and then to make more vacancies and to trigger LENR reactions using Ar ion bombardment. We also considered stimulating vibrations (especially in the optical phonon modes) with the Ar beam; however, the results of our experiments lead us to conclude that triggering by outgassing is likely a bigger effect.

5. Thick TiD_x Samples in 2019 Experiments

In early tests of the system, we carried out exploratory experiments and observed counts on the R-series charged particle detector (the A-series detector was not yet operating during these early experiments), when a Ti foil was used as the ion beam target. Our principal focus at the time was on high-energy charged particles, and in one experiment, a small number of counts near 30 MeV were seen with the 500 μm 50 mm^2 R-series detector. An example is shown in Figure 6.

In this set of experiments, a 1.59 mm thick Ti foil was used, and kept in the chamber for multiple D loading and Ar bombardment cycles. In the experiment of Figure 6, D ions were implanted at 950 eV with a beam current near 0.5 mA for 1.7 hours, then near 0.63 mA for about 2.75 hours. Ar ion bombardment at 950 eV was then used for 0.25

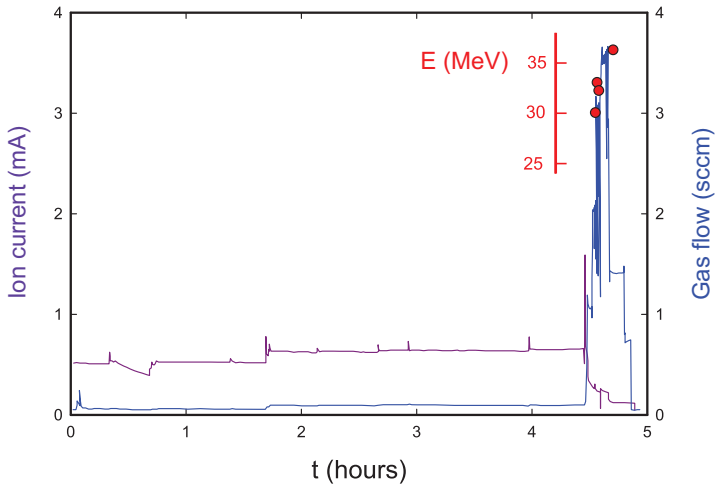

Figure 6. Ion beam current (purple) as a function of time (left y-axis); gas flow (blue) out of the chamber as a function of time (right y-axis); energetic ion counts (red circles) as a function of time (inset y-axis). The ion energies are estimated based on the calibration described in the text.

hours for driving vibrational modes and facilitating defect formation. An initial Ar ion current spike up to 1.5 mA can be seen in the figure (in purple), after which the current on target decreases to below 0.5 mA. Outgassing of the D in the sample is stimulated by the Ar ion bombardment as shown in blue. About 5 minutes after the Ar ion bombardment started, four very energetic charged particles were observed over a period of about 9 minutes on the R-series detector. This detector was located on the front side of the Ti target, 80 mm away from the center of the beam on the sample), so that the detection efficiency is 6.2×10^{-4} (assuming unit detection efficiency for particles that hit the detector).

While the charged particle detectors could not be calibrated at high energy near 30 MeV (due to the absence of radioactive calibration sources with emission in that range), the response of a thick SSB detector is expected to be reasonably linear with particle energy for low-Z charged particles (see Figure 7 and references therein), which suggests that the calibration of the detector at low energy has benefit in connection with high energy particles. We can be certain that the energy of such particles is high (more than 25 MeV), but it is difficult without dedicated calibration in this energy regime to be precise.

The particles cannot be protons (or deuterons or tritons) since their stopping range near 30 MeV is much larger than the R-series detector thickness (500 μm). The range of a 32.5 MeV alpha at normal incidence in silicon according to the SRIM code is 500 μm. At higher energies, alphas pass through the detector with incomplete energy deposition. Monte-Carlo calculations done with the SRIM code indicate that the energy deposited decreases at higher energies, as shown in Figure 8. It is possible that the use of a low-energy calibration leads to an over-estimate in the high-energy range on the order of 15%, resulting in an estimate near 37 MeV in a detector incapable of registering more than 32.5 MeV for alphas at near normal incidence, assuming that the observed counts originate from alpha particles.

A burst of counts on the Wendi-2 neutron detector was recorded starting just before the first energetic charged particle was registered, as shown in Figure 9. We plan to discuss the obtained neutron data in more detail in further reports and will focus here on data from the charged particle detectors.

Next, we report a run carried out two days later, in which a count was observed in a high-energy channel also during the Ar ion bombardment following loading via D bombardment (see Figure 10). The protocol used was similar (with less D implantation since the sample still had D from previous loading cycles without breaking vacuum) and this time, a single very energetic charged particle was observed during the Ar bombardment.

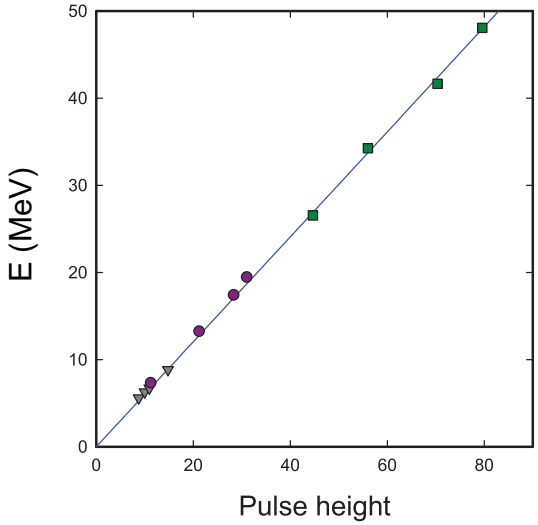

Figure 7. Calibration data of Elliott (1961) for a 3.38 mm lithium drifted silicon detector. Data for Th-228 alphas (grey triangles); data for energetic deuterons (purple circles); data for energetic alphas (dark green squares); linear calibration (blue line).

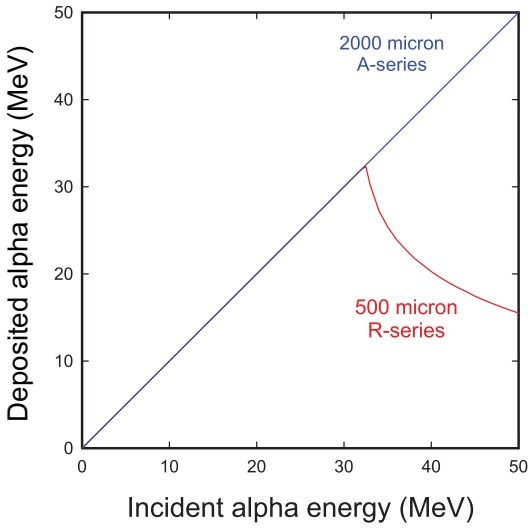

Figure 8. Results of SRIM calculations for incomplete energy deposition for alphas at normal incidence on a 500 μm thick silicon detector (red), relevant for the R-series detector; and for complete energy deposition (blue), relevant for the A-series detector.

6. Thin TiD_x Samples in 2022 Experiments

Following a prolonged interruption due to the pandemic, and also due to using the apparatus for experiments with H on Li targets, we returned to experiments with D on Ti targets in 2022. For these runs, the experimental setup was

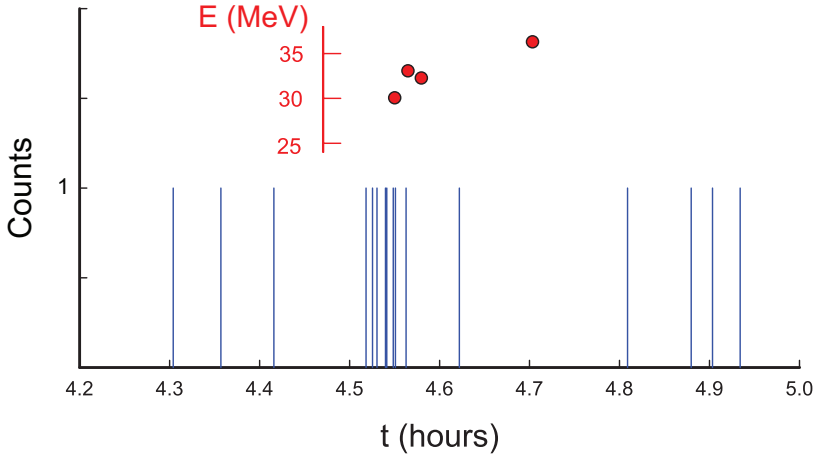

Figure 9. Neutron counts (blue) correlated in time with charged particle counts (red).

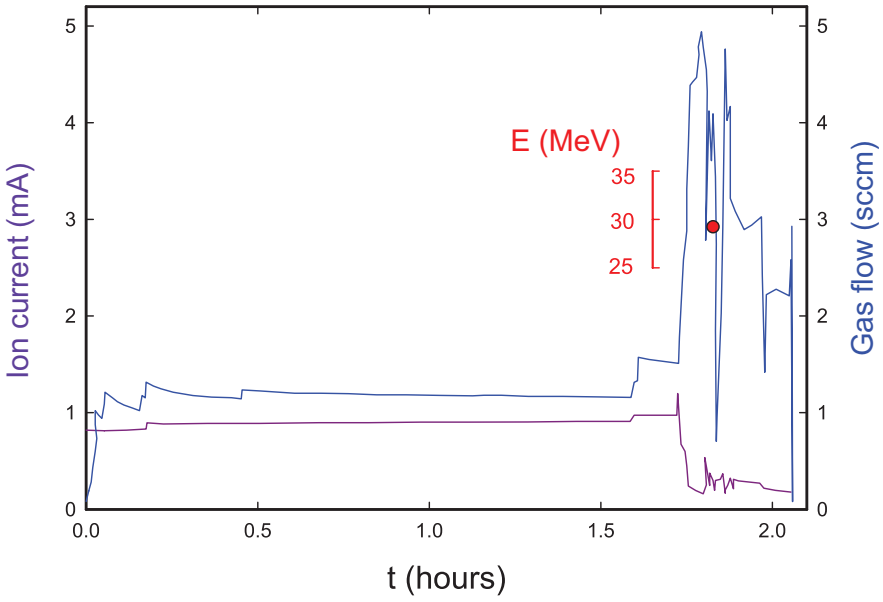

Figure 10. Ion beam current (purple); gas flow (blue) out of the chamber as a function of time; and an energetic ion count (red circle); all similar to what is shown in Figure 6.

reconfigured and the 50 mm^2 A-series detector (2000 μm thick) was positioned close behind the Ti foil, as illustrated in Figure 11. This was done to increase the solid angle relative to the 2019 configuration, where the charged particle detectors were mounted further away. However, upon implementing this change, we recognized that it also affected the experiment in unforeseen ways. The use of thinner Ti foils reduces outgassing, which had become sufficiently small

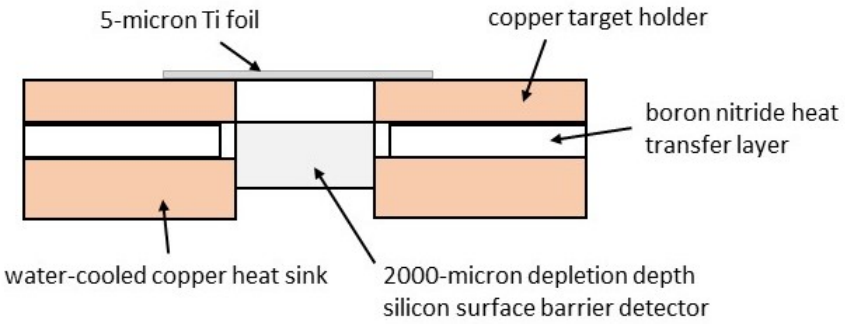

Figure 11. Sample holder, charged particle detector (both in rotational symmetry) and sample cross section (not exactly to scale). For reference, the Ti foil dimensions are 25 mm $\times$ 25 mm and the detector area is 50 mm^2.

to be unmeasurable in the 2022 experiments. There was in addition some degradation of the ion gun during the H-Li experiments, which limited the deuterium beam current compared to the 2019 experiments. As a result, with the new large-solid-angle detector configuration, we have yet to achieve again experimental conditions comparable to the 2019 experiments.

Energetic particles in the 5-6 MeV range of the spectrum from TiD samples are assumed to be alpha particles in the discussion that follows in this section. According to the SRIM code [108], 6 MeV alpha particles have a range of 20 μm in Ti, which motivated us to work with a thin 5 μm Ti (free-standing) foil in these experiments.

Results from one experiment are shown in Figure 12, where counts from the thick 2000 μm A-series detector behind the sample are shown as a function of time, with a short time window on the left focusing on the Ar bombardment, and a much longer time window on the right focusing on the absence of counts at later times in this experiment. Following previous experiments, where the sample was loaded with deuterium, in this experiment the sample was loaded with deuterium for two hours at 0.20 mA beam current and 950 eV beam energy (the last part of the D implantation is indicated in the figure). Then the Ar beam was run at up to 1.5 mA and at 950 eV for 10 minutes, then turned off.

Note that by design SSB charged particle detectors record noise in the lowermost channels. The cut-off channel for such noise can vary, depending on the experimental configuration. In particular, a temperature increase of the detector predictably leads to a higher noise cut-off channel. Although the sample and detector are water-cooled in this configuration, the detector temperature increases when the Ar beam is on, which moves the low-energy noise to higher channels and raises the noise cut-off channel (as can be seen in Figure 12). The high cut-off corresponds to a charged particle energy near 1 MeV, and the lower cut-off corresponds to about 0.36 MeV.

Also note that throughout these experiments, no counts have been registered in the channels above the noise cut-off channel, except for the counts reported in the figures. The absence of high-energy counts across prolonged periods of time (e.g., across about 25 hours in Figure 12) leads to the conclusion that the background of high-energy charged particles is very low.

We do not have particle identifications for these counts in our experiment. An estimate for the energy loss

$$\delta E = \frac{dE}{dx}\delta x \tag{1}$$

from the SRIM code [108] for an alpha going through 5 μm of Ti (at normal incidence) is shown in Figure 13. This suggests that if an alpha was born near the front surface, it would lose at least 1 MeV traversing the Ti foil. In Figure 14, the average energy of a 6.6 MeV alpha that traverses a 5 μm Ti foil is shown as a function of angle. These considerations provide a first estimate of the initial alpha energy within this scenario, but we would need a spectrum

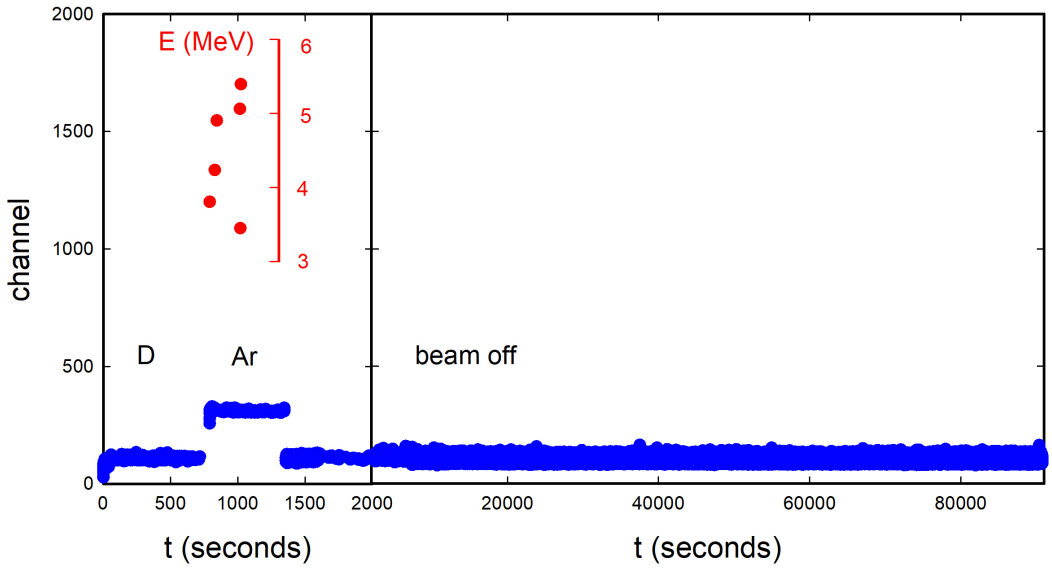

Figure 12. Counts as a function of channel from the A-series detector (Experiment 5j). The uppermost channels with low-channel noise are shown in blue; charged particle counts are shown in red. Corresponding particle energies are indicated by the inset axis in red. Note that different time scales are used for the 33 minutes around the time of the Ar bombardment (in the part of the figure on the left) and for the more than 25 hours of data taken after the Ar bombardment (in the part of the figure on the right).

from both sides of the sample in the same experiment, along with particle identification, to be certain of the precise particle energies.

Data from a later loading/bombardment cycle on the same sample (done in the same experimental configuration and on the same sample without breaking vacuum) is shown in Figure 15. In this case, a single energetic count appears near the end of the 10-minute Ar bombardment, after which counts are recorded that correspond to particle energies up to 11 MeV in a 42-hour-long burst event. Of interest is that these later counts were measured when the ion beam was already off. This further supports the notion that there is no possibility of interference with detector operation in the high-energy range due to the ion beam.

Analogous to the R-series detector of the 2019 experiments, the A-series detector was not directly calibrated above 30 MeV, so the extrapolated energies are estimated based on the low-energy calibration done with ^{241}Am. Six very energetic particle counts are seen above 37.5 MeV (estimated based on the low-energy calibration) across five different experiments in the 2022 experimental campaign. Based on these observations, and taking into account the earlier front-side measurements with the R-series detector in 2019, we expect these counts to correspond to alpha particles in the 32-40 MeV range.

7. Nuclear Reactions Directly Associated with the Ar Beam

Incoming Ar ions at 950 eV would not be expected to result in nuclear reactions based on binary collisions, due to the large associated Coulomb barriers. Fusion reactions between ^{40}Ar and ^{48}Ti have been observed in Ref. [109] with Ar ions at 325 MeV. Fusion excitation cross sections in the lab frame for the closely related ^{40}Ca+^{40}Ca reaction are given in Ref. [110] near threshold in the vicinity of 100 MeV.

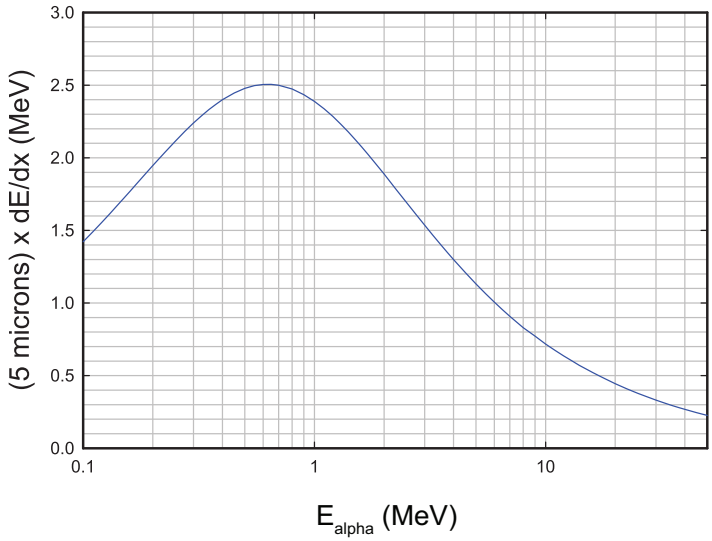

Figure 13. Energy loss for an alpha particle normal through 5 μm of Ti as a function of energy.

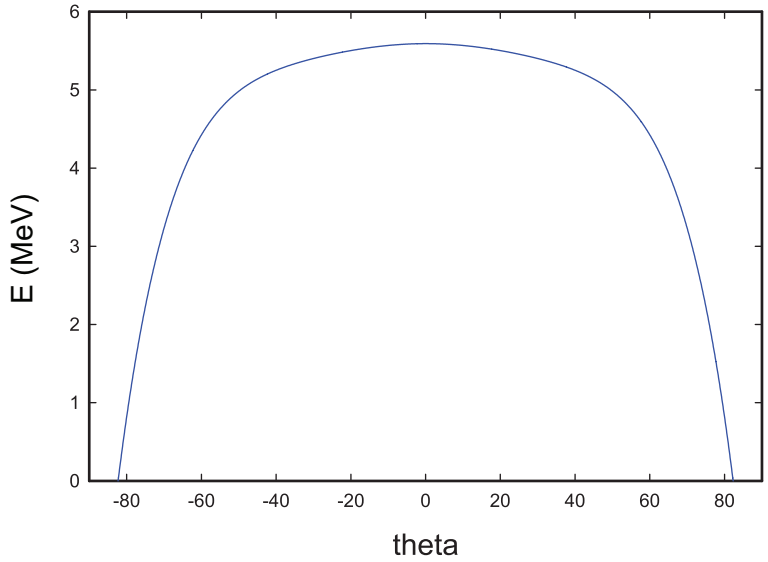

Figure 14. Energy of a 6.6 MeV alpha particle passing through 5 μm of Ti as a function of angle.

Ar ions could in principle interact with deuterons to cause nuclear reactions. Such reactions were studied in Ref. [111]. Of interest might be cross sections for the (d,p) and (d,α) reactions. According to the ENDF nuclear data library [112], the cross sections for these processes are at the μ-barn level at 1 MeV relative energy, and

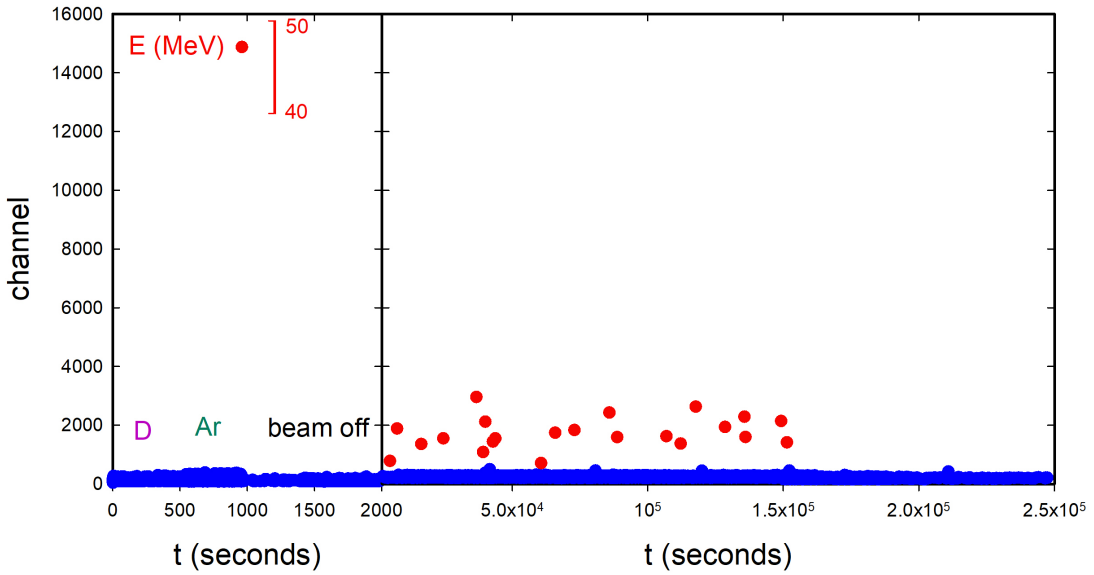

Figure 15. Counts as a function of channel from the A-series detector (Experiment 5k). The uppermost channel for the low-channel noise is shown in blue; charged particle counts shown in red. Corresponding particle energies indicated by the inset axis in red.

fall exponentially to lower values as the relative energy decreases. Based on such considerations, no reactions are conventionally expected with incident Ar ions at 950 eV.

It could be argued that incoming Ar ions could transfer energy directly to deuterons through collisions. It is possible to estimate the maximum D energy in an elastic collision leading to:

$$E_d = \frac{4M_d M_{Ar}}{(M_d + M_{Ar})^2} E_{Ar} \tag{2}$$

where E_{Ar} is the energy of the incident Ar ion, and where E_d is the maximum outgoing deuteron energy possible. In the case of a 950 eV ^{40}Ar ion, this evaluates to:

$$E_d = 0.18 \cdot E_{Ar} = 172 \text{ eV} \tag{3}$$

The deuteron-deuteron fusion cross section for a 172 eV deuteron on a deuteron at rest is negligible, even with the strong screening seen in low-energy deuteron beam experiments [5]–[10]. Hence, no knock-on dd-fusion reactions would be expected from the Ar bombardment.

8. Discussion

Low-level MeV ion emission from metal deuterides has been reported previously [11]–[13], [49]–[70]. In experiments with TiD_x, deuterium loading was done using gas loading [52], [49] or an ion beam [12], [13], [56]. Triggering of the charge emission was in our view likely achieved either by outgassing [12], [13], [56], [49] or by driving with an electrical current [52]. In the experiments reported on in this paper, the Ti foils were loaded by ion beam implantation, and we surmise that D outgassing provides the trigger, when the Ar ion beam is on (with much more outgassing occurring with thicker samples than with thinner samples). It may be that outgassing is also responsible for triggering

low-level charged particle emission after the Ar ion bombardment, while it is also possible that mechanical relaxation acts as a trigger.

While dd-fusion products were reported in the Jones experiment [49], evidence for higher energy particles from TiD_x is claimed in the experiments of Chambers [12], [13] and Cecil [53]. Our results so far support the notion of particles not emitted due to conventional dd-fusion reactions. Based on reported data from these previous experiments, the observed counts there likely correspond to low-mass ions (perhaps tritons in [13], and protons through alpha particles in [53]). While we have also reported on detector counts that correspond to particle energies below 11 MeV, our experimental configuration does not allow for particle identification in this energy range.

Energetic ion emission at very high energy (near 20 MeV) has been claimed with PdD_x samples [11], [57], [66], which motivated our experiments. PdD_x has been studied more than TiD_x, and there are few reports of very energetic particles in this range from TiD_x (one exception are some CR-39 counts at very high energy on one slide from Lipson's ICCF13 talk at Sochi in 2007). We are not aware of earlier claims of low-level energetic charged particles in the 32-40 MeV range from TiD_x. This is a new (and preliminary) result of our experiments presented in this paper.

High multiplicity events in the case of low-level neutron emission were often discussed in the early days of LENR research (such as in [113]), which suggests that they might occur also in charged particle emission (as reported in [54]). We reported on data that suggest the occurrence of a high multiplicity neutron emission event, although we will need to continue to monitor for such potential effects in future experiments with upgraded neutron detection configurations.

An important question is: what should be done next to improve the experiment and results to date? We consider the detector counts that correspond to very energetic particles in the 32-40 MeV range as the most important lead, since such purported signals can provide valuable information about mechanisms at play (as further discussed below). So future research should emphasize clarification of this issue in our view.

A major goal is the increase of the conjectured energetic charged particle emission flux. If low-level charged particle emission is triggered by outgassing in these experiments (which is consistent with the larger count rate seen from thicker Ti foils), then we would like to increase the thickness of the Ti foils used. Since deuterium diffusion in TiD_x is slow and increases with temperature [114], we then expect a higher count rate if external heating were provided during and/or after the Ar bombardment.

The observable particle count rate could also be increased if we increased the solid angle of the charged particle detector by using a larger area detector. To this end, we are procuring a 450 mm^2 2000 μm thick A-series detector. Arranging for dedicated detector calibration in the high-energy range of 40 MeV and higher has been challenging. Recently we became aware of a cyclotron available at the Crocker Nuclear Lab associated with UC Davis that operates in this regime and that can be used for detector calibration.

The very energetic 32-40 MeV charged particle counts have been observed in our experiments with two different detectors so far (the R-series and the A-series detectors). However, detecting them with a CR-39 detector would add further confidence. For this, it would be important to establish a calibration with alphas at high energy on CR-39; ideally this could be done at the same time as calibrating the SSB detectors.

Particle identification of these very energetic particles could be conducted using dE-E detection. A "thin" dE detector in this case could be a 100 μm thick SSB detector, which would provide for a substantial dE measurement. Particle identification could also be made using a foil to degrade the particle energy. Thicker titanium foils would be useful for increasing outgassing, and could make a minor contribution to energy loss, as shown in Figure 16. Given the low rate of diffusion for deuterium in TiD_x, there is little motivation to go to samples thicker than 100 μm unless the sample is heated to well above room temperature.

Observed energetic particle counts in the 1-11 MeV energy range are also of interest, but requires a different strategy to be pursued. What is of interest ultimately in this regard is the determination of the charged particle identity and particle energy when created, which prompts us to work with thin foils to minimize energy loss through the foil. As discussed above, we saw some counts in this energy range with a 5 μm thick Ti foil, which results in energy loss on

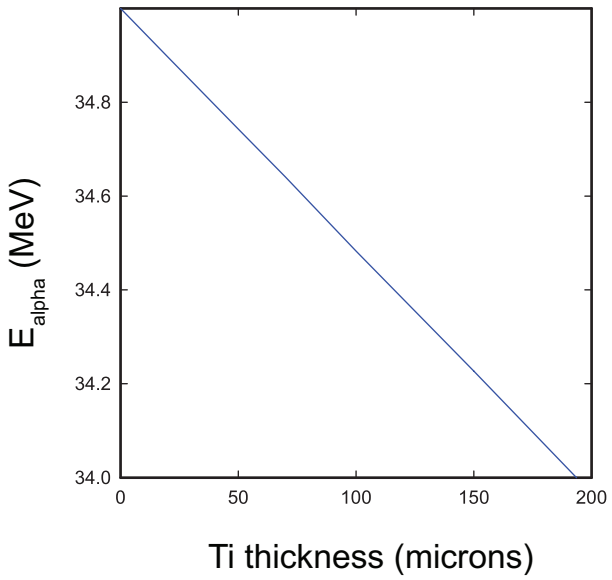

Figure 16. Energy of a 35 MeV alpha after transit at normal incidence through Ti foils of different thicknesses.

the order of 1 MeV for a 6 MeV alpha at normal incidence, less at higher particle energy, and more at lower particle energy (see Figure 13). However, from our experience so far, the thinner foils gave fewer counts of interest. Ideally, a way might be found to work with thinner foils while arranging for enough counts from which a useful spectrum can be acquired. The count rate could be increased with a large area SSB detector placed close behind the foil. Based on the early observations of Cecil [53], we expect that different low-mass charged ions contribute to the spectrum. Consequently, dE-E charged particle spectroscopy would be ideal to achieve further clarification. A large area dE-E detector could in principle be placed close behind a thin foil sample. However, this would allow for charged particles to enter the detector at arbitrary angles, making particle identification much more difficult. Moving the dE-E detector back away from the foil improves the ability to identify particles, but reduces the particle count.

As seems clear from this discussion, different tradeoffs need to be considered in preparation for the next phase of this research. If we accept these limitations, then under consideration is an experiment in which a small area dE-E detector well away from the sample captures counts from a sample emitting at low count rate, which implies the need for long runs so as to build up good statistics. On the other hand, if it were possible to arrange for a μm-scale Ti surface layer (with lots of vacancies) on a thick Pd deuterium reservoir (with no vacancies), then it may be possible to arrange for a substantial sustained D flux moving through the Ti sample, with the goal of causing sustained charged particle emission at a comparatively high level, so that a small-area dE-E detector well away from the front surface could accumulate a useful spectrum in a reasonable amount of time. The latter setup requires mindfulness about the possibility of induced charged particle emission from the PdD substrate, which could confound the TiD results. Another possibility is to attempt triggering with an electrical current through a loaded TiD_x thin film.

Also of interest is the implementation of a version of the experiment with PdD_x and other metal deuterides. One aspect that is peculiar to TiD_x is the low diffusion coefficient. This suggests that working with PdD_x at low temperature initially is appropriate, and that triggering with an even higher D flux would be possible during heating with the Ar ion bombardment.

Another conceivable improvement is the use of a more efficient neutron detector and the use of shielding for the neutron detector to improve signal-to-noise ratio. This is planned for future work.

Finally, the central question concerns mechanisms that predict and can explain low-level energetic particles emitted from TiD under the given conditions. A brief consideration of theory and candidate particles and energies is given in the Appendix.

Appendix: Energetic Charged Particle Candidates

Historically, there has been no generally accepted theory for LENR anomalies, and most attention has been focused on energetic dd-fusion products and possible rate enhancement mechanisms that may explain them. We have over many years developed comprehensive theoretical models for reported anomalies, which are based on known collective quantum effects such as Dicke enhancement applied to systems of coupled nuclei. Here we provide a brief overview of energetic charged particle candidates that can be expected from these models as candidates to account for the observations. The basic approach is outlined in Ref. [72].

Sufficiently stable nuclear molecule states in Ti

At the core of this picture is the nonradiative transfer of excitation energy from deuteron pairs to resonant or near-resonant excited states of nearby metal nuclei. The coherent nuclear dynamics involved require a great many reasonably stable nuclear excited states, for sequential excitation transfer processes starting from $D_2/^4He$ transitions near 23.86 MeV. In canonical nuclear databases, there are no known stable excited states listed near 23.86 MeV, which has long hindered the development of this kind of model. Recently, we proposed to consider long-lived cluster-based nuclear molecule states as candidate receiver states for the kind of nuclear excitation transfer under consideration. A growing literature exists on nuclear cluster states and some molecule-like formations promise to be particularly long-lived. We considered liquid drop model calculations for cluster-based nuclear states consistent with fission barrier calculations, but had to conclude that the states described by such models are very unstable in the mass and charge regime of interest.

However, calculations in the literature for $^{12}C+^{12}C$ and $^{16}O+^{16}O$ nuclear states show a potential minimum for daughter nuclei that are separated, which suggests that a kind of nuclear molecule is possible where the daughters act as separated clusters (in contrast to highly deformed states in liquid drop model calculations where the clusters nevertheless remain connected). We developed a simple model to estimate the energy for ground state nonrotational nuclear molecules [72]. Nuclear molecule excitation energies for the stable Ti isotopes, as predicted by this model, are shown in Figure 17 as a function of the decay rate of the corresponding state (which does not include radiative or internal conversion decay processes, the rates for which are yet undetermined). The lower energy nuclear molecules are highly asymmetric involving a low mass and charge daughter. Such states, occupied upon receipt of transferred excitation and subsequent tunneling decay, are candidates for low-level charged particle emission. Above about 30 MeV are a great many nuclear molecule states that can participate in the nuclear dynamics. Note that energy levels can shift in quantum systems that are affected by strong coupling, as can be the case due to collective effects such as Dicke enhancement [72], [84], [101].

Very energetic alphas above 30 MeV

The observation of very energetic alphas above 30 MeV appears consistent with the occupation of very high nuclear molecule states above 30 MeV (note that the nuclear molecule excitation energy is indirectly related with the emitted alpha energy).

According to the coherent nuclear dynamics model, the first step is a transfer of the 23.86 MeV quantum from the $D_2/_4He$ transition to a resonant receiver state. With sufficient accumulation of excited state population, subsequent

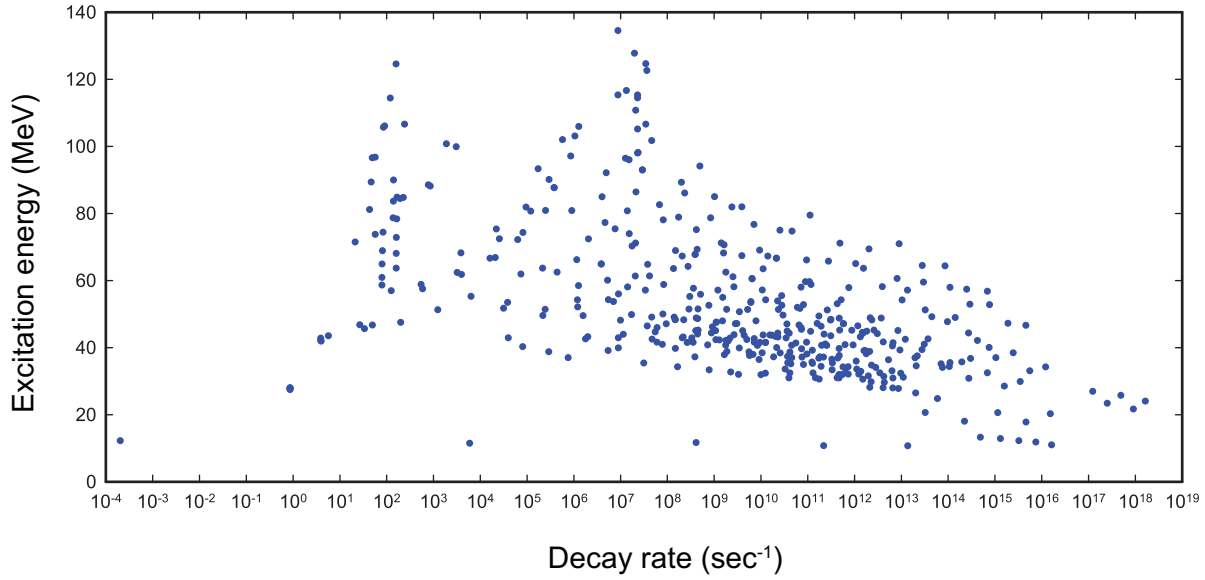

Figure 17. Nuclear molecule state energies as a function of decay rate for the stable Ti isotopes ^{46}Ti, ^{47}Ti, ^{48}Ti, ^{49}Ti, and ^{50}Ti.

third-order transitions occur leading to the accumulation of nuclear molecule population near 47.72 MeV. Depending on the details of the relative nuclear molecule energies, as well as the amount of coherent energy exchange possible with phonons and plasmons, occupation of nuclear molecule states over a range of excitation energies is expected. If the coherent dynamics are frustrated in the sense of not returning the nuclear molecule population back to the Ti isotope ground states, then one would expect energetic decay processes. We have proposed that the decay of these excited states is responsible for reported transmutation effects. Here we note that the ejection of a low-mass fragment (such as an alpha particle) would also be expected as a possible decay path (by analogy with Auger decay in atoms, where an excited electron is ejected interacting with a second electron which is de-excited).

If the energy exchange with vibrations and plasmons is minimal, then the ejected alpha energy depends only on the isotope and excitation transfer from the fusion transition. Candidates to account for the signals in our experiments above 30 MeV include:

$$^{46}\text{Ti} + 2(23.86\text{ MeV}) \longrightarrow (^{Z_b}A_b + {}^{Z_c}A_c) \longrightarrow {}^{42}\text{Ca}(3.45\text{ MeV}) + \alpha(36.2\text{ MeV})$$
$$^{47}\text{Ti} + 2(23.86\text{ MeV}) \longrightarrow (^{Z_b}A_b + {}^{Z_c}A_c) \longrightarrow {}^{43}\text{Ca}(3.30\text{ MeV}) + \alpha(35.4\text{ MeV})$$
$$^{48}\text{Ti} + 2(23.86\text{ MeV}) \longrightarrow (^{Z_b}A_b + {}^{Z_c}A_c) \longrightarrow {}^{44}\text{Ca}(3.19\text{ MeV}) + \alpha(35.1\text{ MeV})$$
$$^{49}\text{Ti} + 2(23.86\text{ MeV}) \longrightarrow (^{Z_b}A_b + {}^{Z_c}A_c) \longrightarrow {}^{45}\text{Ca}(3.06\text{ MeV}) + \alpha(34.5\text{ MeV})$$
$$^{50}\text{Ti} + 2(23.86\text{ MeV}) \longrightarrow (^{Z_b}A_b + {}^{Z_c}A_c) \longrightarrow {}^{46}\text{Ca}(2.96\text{ MeV}) + \alpha(34.0\text{ MeV})$$

Where the notation $(^{Z_b}A_b + {}^{Z_c}A_c)$ is intended to indicate that there are many reasonably stable nuclear molecule intermediate candidates possible. With thick detector calibration between 30 MeV and 40 MeV, particle identification, and with enough counts, it should be possible to either confirm or rule out these candidates in future experiments.

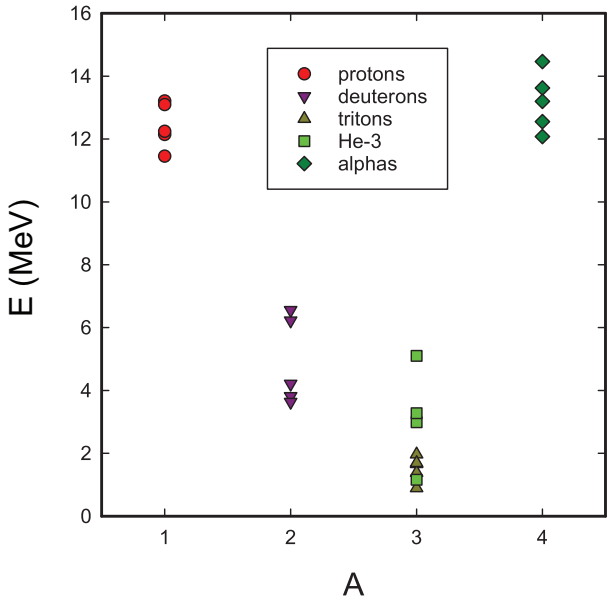

Figure 18. Candidates for low-level energetic particle emission from Ti nuclear molecules near 23.86 MeV.

Low-mass Candidates at Lower Energies

For low-level energetic charged particle emission at lower energy, the same basic approach is proposed, except with only a single fusion quantum exchanged instead of two. If energy exchange with phonons and with plasmons is minimized, then we would expect decay products and energies as illustrated in Figure 18.

In Figure 18, we see that protons and alpha particles are candidates for the higher energy counts, and deuterons, tritons and ^{3}He ions are candidates for the lower energy counts. With a thin foil sample, with a dE-E detector reasonably distant from the foil (so that particle trajectories are near normal incidence), and with a sufficiently high energetic ion emission rate, we expect it to be possible to test for these candidates to be represented in experiments that are weakly driven (to avoid complications due to double excitation and energy exchange).

A highly idealized schematic for the (generalized) excitation transfer processes and nuclear molecule tunnel decays are illustrated in Figure 19. In the nuclear dynamics proposed, the excitation transfer can lead to the occupation of Ti nuclear states near 23.86 MeV and—via up-conversion—states near 2×23.86 MeV, the latter of which are expected to lead to low-level emission of more energetic ions as described above. Excitation transfers among the different nuclear molecule states near $2 \times \Delta$E allows for coherent energy exchange with vibrations and electrons, which then leads to the possibility of down-conversion to nuclear molecule states in the vicinity of ΔE. The much simplified scheme of Figure 19 is intended to convey the essence of this more complicated picture. Lastly, transfer of excitation back to ^{4}He nuclei can lead to the excitation of unstable ^{4}He states and subsequent decay with the known 3+1 fusion products.

Observability of Nuclear Molecule Energies

Within the model, the nuclear molecule energies are key parameters, which we would like to know accurately. Over the past year we had been optimistic that such information might be gleaned from careful measurements of charged ion

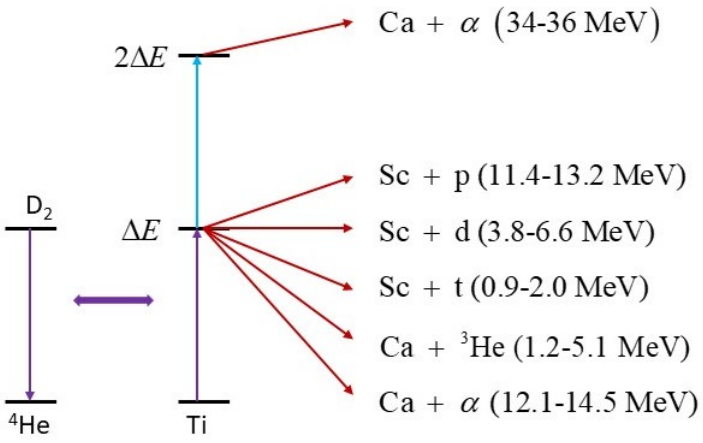

Figure 19. Idealized schematic for excitation transfer to nuclear molecule states and highly asymmetric decay pathways under consideration, where ΔE is the $D_2/^4He$ transition energy of 23.86 MeV. The energies listed are for the low-mass daughters.

energies and particle identifications. However, after some thought, it has become clear that the emitted particle energies are determined by the parent and daughter mass energies, and by the energy transferred from the fusion system, as long as there is not significant energy exchange with plasmons and phonons. The nuclear molecule energy does not come into this calculation.

We have remarked elsewhere [72] that a weak radiative decay of the nuclear molecule states is expected, such that it might be possible to provide further clarification with a very thick NaI gamma detector. Whether or not this would be successful in experiments similar to those described in this paper is not clear at present (since the emission rate is likely small). In any event, we will consider experiments of this sort on different samples in the future.

Acknowledgments

Technical assistance from Jessica Kedziora is much appreciated. Helpful discussion with Igor Jovanovic on the problem of dE-E detection is also much appreciated. Carlotta Barone-MacDonald, Jonah Messinger, and Nicola Galvanetto provided very helpful comments on the manuscript. Financial support (greatly appreciated) for this work came from the Minhas H. Family Fund, and from the Anthropocene Institute.

References

[1] W. Möller, F. Besenbacher and J. Bottiger, "Saturation and isotope mixing during low-temperature implantations of hydrogen into metals," *Applied Physics A* **27** (1982) 19–29.

[2] S. M. Myers, D. M. Follstaedt, J. E. Schirber and P. M. Richards, "Search for cold fusion at D/Pd $>$ 1 using ion implantation," *Journal of Fusion Energy* **9** (1990) 263–268.

[3] S. M. Myers, P. M. Richards, D. M. Follstaedt and J. E. Schirber, "Superstoichiometry, accelerated diffusion, and nuclear reactions in deuterium-implanted palladium," *Physical Review B* **43** (1991) 9503.

[4] G. P. Chambers, J. M. Eridon, and K. S. Grabowski, "Upper limit on cold fusion in thin palladium films," *Physical Review B* **41** (1990) 5388.

[5] F. Raiola, P. Migliardi, L. Gang, C. Bonomo, G. Gyürky, R. Bonetti, C. Broggini, N. E. Christensen, P. Corvisiero, J. Cruz, and A. D'Onofrio, "Electron screening in d(d,p)t for deuterated metals and the periodic table," *Physics Letters B* **547** (2002) 193–199.

[6] F. Raiola, L. Gang, C. Bonomo, G. Gyürky, M Aliotta, H. W. Becker, R. Bonetti, C. Broggini, P. Corvisiero, A. D'Onofrio and Z. Fülöp, "Enhanced electron screening in d(d,p)t for deuterated metals," *The European Physical Journal A – Hadrons and Nuclei* **19** (2004) 283–287.

[7] F. Raiola, B. Burchard, Z Fülöp, G. Gyürky, S. Zeng, J. Cruz, A. Di Leva, B. Limata, M. Fonseca, H. Luis and M. Aliotta, "Electron screening in d(d,p)t for deuterated metals: temperature effects," *Journal of Physics G: Nuclear and Particle Physics* **31** (2005) 1141.

[8] A. Huke, K. Czerski and P. Heide, "Accelerator experiments and theoretical models for the electron screening effect in metallic environments," *Proc. ICCF11* (2006) 194–209.

[9] A. Huke, K. Czerski and P. Heide, "Measurement of the enhanced screening effect of the d+ d reactions in metals," *Nuclear Instruments and Methods in Physics Research Section B: Beam Interactions with Materials and Atoms* **256** (2007) 599–618.

[10] K. Czerski, A. Huke, L. Martin, N. Targosz, D. Blauth, A. Górska, P. Heide and H. Winter, "Measurements of enhanced electron screening in d+d reactions under UHV conditions," *Journal of Physics G: Nuclear and Particle Physics* **35** (2007) 014012.

[11] G. P. Chambers, J. E. Eridon, K. S. Grabowski, B. D. Sartwell and D. B. Chrisey, "Charged particle spectra of palladium thin films during low energy deuterium ion implantation," *J Fusion Energy 9* (1990) 281–285.

[12] G. P. Chambers, G. K. Hubler and K. S. Grabowski, "Search for energetic charged particle reaction products during deuterium charging of metal lattices," *AIP Conference Proceedings*, American Institute of Physics **228** (1991) 383–396.

[13] G. P. Chambers, G. K. Hubler, and K. S. Grabowski, "Evidence for MeV particle emission from Ti charged with low energy deuterium ions," Naval Research Lab Memorandum Report 6927 (1991).

[14] S. Bartalucci, V. I. Vysotskii and M. V. Vysotskyy, "A search for correlated quantum states in nuclear reactions: First exciting results from an experimental test," *J. Condensed Matter Nucl. Sci.* **36** (2022) 130–136.

[15] S A Lipinski and H U Lipinski, "Hydrogen-lithium fusion device, methods and applications," *United States Patent Application Publication* US 2009/0274256 A1 (2009).

[16] S A Lipinski and H U Lipinski, "Hydrogen-lithium fusion device," *WIPO/PCT Patent Application Publication* WO 2014/189799 A9 (2014).

[17] N. S. Lewis, C. A. Barnes, M. J. Heben, A. Kumar, S. R. Lunt, G. E. McManis, G. M. Miskelly, R. M. Penner, M. J. Sailor, P. G. Santangelo and G. A. Shreve, "Searches for low-temperature nuclear fusion of deuterium in palladium," *Nature* **340** (1989) 525–530.

[18] R. B. Campbell and L. J. Perkins, "A study of cold fusion in deuterated titanium subjected to high-current densities," *Fusion Technology* **16** (1989) 383–387.

[19] G. C. Fralick, A. J. Decker and J. W. Blue, "Results of an attempt to measure increased rates of the reaction ^{2}D+^{2}D yields ^{3}He+n in a nonelectrochemical cold fusion experiment," NASA Technical Memorandum 102430 (1989).

[20] K. I. Thomassen, J. F. Holzrichter, F. T. Aldridge, B. Balke, J. Bowers, D. B. Bullen, M. D. Cable, M. Caffee, R. B. Campbell and C. Colmenares, "Lawrence Livermore National Laboratory (LLNL) research on cold fusion," *Lawrence Livermore National Laboratory Report UCID-21809* (1989).

[21] P. B. Price, S. W. Barwick, W. T. Williams and J. D. Porter, "Search for energetic-charged-particle emission from deuterated Ti and Pd foils," *Physical Review Letters* **63** (1989) 1926.

[22] H. S. Bosch, G. A. Wurden, J. Gernhardt, F. Karger and J. Perchermeier, "Electrochemical cold fusion trials at IPP garching," *Journal of Fusion Energy* **9** (1990) 165–186.

[23] D. Albagli, R. Ballinger, V. Cammarata, X. Chen, R. M. Crooks, C. Fiore, M. P. Gaudreau, I. Hwang, C. K. Li, P. Linsay and S. C. Luckhardt, "Measurement and analysis of neutron and gamma-ray emission rates, other fusion products, and power in electrochemical cells having Pd cathodes," *Journal of Fusion Energy* **9** (1990) 133–148.

[24] J. D. Porter, A. A. Shihab-Eldin, H. Bossy, F. J. Echegaray, J. M. Nitschke, S. G. Prussin, J. O. Rasmussen and M. A. Stoyer, "Limits on electromagnetic and particle emission from palladium-D_2O electrolytic cells," *Journal of Fusion Energy* **9** (1990) 319–327.

[25] H. Wiesmann, "Examination of cathodically charged palladium electrodes for excess heat, neutron emission, or tritium production," *Fusion Technology* **17** (1990) 350–354.
[26] S. L. Rugari, R. H. France, B. J. Lund, S. D. Smolen, Z. Zhao, M. Gai and K. G. Lynn, "Upper limits on emission of neutrons from Ti in pressurized D_2 gas cells: A test of evidence for cold fusion," *Physical Review C* **43** (1991) 1298.
[27] S. E. Jones, E. P. Palmer, J. B. Czirr, D. L. Decker, G. L. Jensen, J. M. Thorne, S. F. Taylor and J. Rafelski, "Observation of cold nuclear fusion in condensed matter," *Nature* **338** (1989) 737–740.
[28] A. Bertin, M. Bruschi, M. Capponi, S. De Castro, U. Marconi, C. Moroni, M. Piccinini, N. Semprini-Cesari, A. Trombini, A. Vitale and A. Zoccoli, "Experimental evidence of cold nuclear fusion in a measurement under the Gran Sasso Massif," *Il Nuovo Cimento A* **101** (1989) 997–1004.
[29] G. Shani, C. Cohen, A.. Grayevsky and A. Brokman, "Evidence for a background neutron enhanced fusion in deuterium absorbed palladium," *Solid State Communications* **72** (1989) 53–57.
[30] K. L. Wolf, N. J. C. Packham, D. Lawson, J. Shoemaker, F. Cheng and J. C. Wass, "Neutron emission and the tritium content associated with deuterium-loaded palladium and titanium metals," *Journal of Fusion Energy* **9** (1990) 105–113.
[31] A. Takahashi, T. Takeuchi, T. Iida and M. Watanabe, "Emission of 2.45 MeV and higher energy neutrons from D_2O–Pd cell under biased-pulse electrolysis," *Journal of Nuclear Science and Technology* **27** (1990) 663–666.
[32] T. Bressani, D. Calvo, A. Feliciello, C. Lamberti, F. Iazzi, B. Minetti, R. Cherubini, A. M. T. Haque and R. A. Ricci, "A study of the neutron emission from Ti loaded with D in gas phase by means of a time-of-flight spectrometer," *Proc. ICCF2* (1991) 105.
[33] T. Bressani, D. Calvo, A. Feliciello, C. Lamberti, F. Iazzi, B. Minetti, R. Cherubini, A. M. I. Haque and R. A. Ricci, "Observation of 2.5 MeV neutrons emitted from a titanium-deuterium system," *Il Nuovo Cimento A* **104** (1991) 1413–1416.
[34] R. Takagi, H. Numata, I. Ohno, K. Kawamura and S. Haruyama, "Neutron emission during a long-term electrolysis of heavy water," *Fusion Technology* **19** (1991) 2135–2139.
[35] A. Takahashi, T. Takeuchi, T. Iida and M. Watanabe, "Neutron spectra from D_2O–Pd cells with pulse electrolysis," *AIP Conference Proceedings* **228** (1991) 323–340.
[36] E. Botta, T. Bressani, D. Calvo, A. Feliciello, P. Gianotti, C. Lamberti, M. Agnello, F. Iazzi, B. Minetti and A. Zecchina, "Measurement of 2.5 MeV neutron emission from Ti/D and Pd/D systems," *Il Nuovo Cimento A* **105** (1992) 1663–1671.
[37] M. Nakada, T. Kusunoki and M. Okamoto, "Energy of the neutrons emitted in heavy water electrolysis," *Proc. ICCF3* (1993) 173.
[38] M. Bittner, A. Meister, D. Seeliger, R. Schwierz and P. Wüstner, "Observation of dd fusion neutrons during degassing of deuterium-loaded palladium," *Fusion technology* **23** (1993) 346–352.
[39] H. Q. Long, S. Sun, H. Liu and R. Xie, "Anomalous effects in deuterium/metal systems," *Proc. ICCF3* (1992) 447.
[40] A. G. Lipson, B. F. Lyakhov, A. S. Roussetski, T. Akimoto, T. Mizuno, N. Asami, R. Shimada, S. Miyashita and A. Takahashi, "Evidence for low-intensity DD reaction as a result of exothermic deuterium desorption from Au/Pd/PdO: D heterostructure," *Fusion Technology* **38** (2000) 238–252.
[41] B. M. Steinetz, T. L. Benyo, A.Chait, R. C. Hendricks, L. P. Forsley, B. Baramsai, P. B. Ugorowski, M. D. Becks, V. Pines, M. Pines and R. E. Martin, "Novel nuclear reactions observed in bremsstrahlung-irradiated deuterated metals," *Physical Review C* **101** (2020) 044610.
[42] P. A. Mosier-Boss, S. Szpak, F. E. Gordon and L. P. Forsley, "Triple tracks in CR-39 as the result of PdD Co-deposition: evidence of energetic neutrons," *Naturwissenschaften* **96** (2009) 135–142.
[43] P. A. Mosier-Boss, J. Y. Dea, L. P. G. Forsley, M. S. Morey, J. R. Tinsley, J. P. Hurley and F. E. Gordon, "Comparison of Pd/D co-deposition and DT neutron generated triple tracks observed in CR-39 detectors," *The European Physical Journal-Applied Physics* **51** (2010) 20901.
[44] P. A. Mosier-Boss, J. Y. Dea, F. E. Gordon, L. P. Forsley and M. H. Miles, "Review of twenty years of LENR research using Pd/D co-deposition," *J. Condensed Matter Nuclear Science* **4** (2011) 173–187.
[45] P. A. Mosier-Boss, L. P. G. Forsley, P. Carbonnelle, M. S. Morey, J. R. Tinsley, J. P. Hurley and F. E. Gordon, "Comparison of SEM and optical analyses of DT neutron tracks in CR-39 detectors," *Radiation Measurements* **47** (2012) 57–66.
[46] J. F. Ziegler, T. H. Zabel, J. J. Cuomo, V. A. Brusic, G. S. Cargill III, E. J. O'Sullivan and A. D. Marwick, A.D., "Electrochemical experiments in cold nuclear fusion," *Physical Review Letters* **62** (1989) 2929.

[47] K. D. Schilling, P. Gippner, W. Seidel, F. Stary and D. Wohlfarth, "Search for charged-particle emission from deuterated palladium foils," *Zeitschrift fÃijr Physik A Atomic Nuclei* **336** (1990) 1–4.
[48] V. B. Brudanin, V. M. Bystritsky, V. G. Egorov, S. G. Stetsenko I. A. Yutlandov, "Search for the cold fusion d(d,^{4}He) in electrolysis of D_2O," *Physics Letters A* **151** (1990) 543–546.
[49] S. E. Jones, F. Keeney, A. Johnson, D. B. Buehler, F. E. Cecil, G. K. Hubler, P. L. Hagelstein, J. Ellsworth and M. Scott, "Charged-particle emissions from metal deuterides," *Proc. ICCF10* (2003).
[50] R. Taniguchi, T. Yamamoto and S. Irie, "Detection of charged particles emitted by electrolytically induced cold nuclear fusion," *Japanese Journal of Applied Physics* **28** (1989) L2021.
[51] S. Aiello, F De Filippo, G Lanzanó, S. L. Nigro and A. Pagano, "Nuclear fusion experiment in palladium charged by deuterium gas," *Fusion technology* **18** (1990) 115–119.
[52] F. E. Cecil, D. Ferg, T. E. Furtak, C. Mader, J. A. McNeil and D. L. Williamson, "Study of energetic charged particles emitted from thin deuterated palladum foils subject to high current densities," *Journal of Fusion Energy* **9** (1990) 195–197.
[53] F. E. Cecil, H. Liu, D. Beddingfield and C. S. Galovich, "Observation of charged particle bursts from deuterium loaded thin titanium foils," *AIP Conference Proceedings* **228** (1991) 375–382.
[54] R. Taniguchi, T. Yamamoto and S. Irie, "Fine structure of the charged particle bursts induced by D_2O electrolysis," *Bull. Univ. Osaka Prefect., Ser A* **39** (1991) 233–240.
[55] W. Mo, Y. S. Liu, L. Y. Zhou, S. Y. Dong, K. L. Wang, S. C. Wang and X. Z. Li, "Search for precursor and charged particles in cold fusion," *Proc. ICCF2* (1991) 123.
[56] V. A. Tsarev, "Cold fusion studies in the USSR," *Proc. ICCF3* (1992) 319.
[57] A. B. Karabut, Y. R. Kucherov and I. B. Savvatimova, "Nuclear product ratio for glow discharge in deuterium," *Physics Letters A* **170** (1992) 265–272.
[58] E. Yamaguchi and T. Nishioka, "Direct evidence for nuclear fusion reactions in deuterated palladium," *Proc. ICCF3* (1993) 179–188.
[59] R. Taniguchi, "Characteristic peak structures on charged particle spectra during electrolysis experiment," *Proc. ICCF4* (1994) 18-1.
[60] A. B. Karabut, S. A. Kolomeychenko and I. B. Savvatimova, "High energy phenomena in glow discharge experiments," *Proc. ICCF5* (1995) 241.
[61] A. G. Lipson, A. S. Roussetski, G. H. Miley and C. H. Castano, "In-situ charged particles and X-ray detection in Pd thin film-cathodes during electrolysis in Li2SO4/H2O," *Proc. ICCF9* (2002).
[62] A G Lipson, G H Miley, A S Roussetski, and E I Saunin, "Phenomenon of an energetic charged particle emission from hydrogen/deuterium loaded metals," *Proc. ICCF10* (2003) 539–558.
[63] A S Roussetski, "CR-39 track detectors in cold fusion experiments: Review and perspectives," *Proc. ICCF11* (2004) 274–280.
[64] A G Lipson, G H Miley, A S Roussetski, B F Lyakhov, and E I Saunin, "Reproducible nuclear emissions from Pd/PdO:Dx heterostructure during controlled exothermic deuterium desorption," *Proc. ICCF12* (2005) 293–313.
[65] A. Kitamura, Y. Sasaki, Y. Miyoshi, A. Taniike, A. Takahashi, R. Seto and Y. Fujita, "Heat evolution from Pd nano-powders exposed to high-pressure hydrogen isotopes and associated radiation measurements," *J. Condensed Matter Nuclear Science* **4** (2011) 56.
[66] P. A. Mosier-Boss, L. Forsley and P. McDaniel, "The Use of CR-39 Detectors in LENR Experiments," *J. Condensed Matter Nuclear Science* **14** (2014) 29.
[67] E. Lukosi, M. A. Prelas, J. Shim, H. Kasiwattanawut, C. Weaver, C. Mathai, S. Gangopadhyay and K. Preece, "Diamond-based radiation sensor for LENR experiments. Part 2: Experimental analysis of deuterium-loaded palladium," *J. Condensed Matter Nuclear Science* **13** (2014) 329.
[68] C. Weaver, M Prelas, H. Kasiwattanawut, J. Shim, M. Watermann, C. J. Mathai, S. Gangopadhyay and E. Lukosi, "Progress in development of diamond-based radiation sensor for use in LENR experiments," *J. Condensed Matter Nuclear Science* **15** (2015) 305.
[69] D. Zhou, C. Wang, Y. Sun, J. B. Liang, G. Zhu, L. Forsley, X. Z. Li, P. A. Mosier-Boss and F. Gordon, "Energetic particles generated in earlier Pd + D nuclear reactions," *J. Condensed Matter Nuclear Science* **15** (2015) 33.
[70] E. Ziehm, *An experimental investigation of low energy nuclear reactions in a DC glow discharge* PhD Thesis UIUC (2022).

[71] "Experiment 4: Alpha spectroscopy with silicon charged-particle detectors," Ortec/Ametek.
[72] P. L. Hagelstein, "Possibility of coherent LENR dynamics with nuclear molecules," to appear in *J. Condensed Matter Nuclear Science*.
[73] Z. Sun and D. Tomanek, "Cold fusion: How close can deuterium atoms come inside palladium," *Phys. Rev. Lett.* **63** (1989) 59.
[74] O. B. Christensen, P. D. Ditlevsen, K. W. Jacobsen, P. Stolze, O. H. Nielsen and J. K. Norskov, "H–H interactions in Pd," *Phys. Rev. B* **40** (1989) 1993.
[75] S.-H. Wei and A. Zunger, "Instability of diatomic deuterium in fcc palladium," *J. Fusion Energy* **9** (1990) 367.
[76] P. Nordlander, J. K. Norskov, F. Besenbacher and S. M. Myers, "Multiple deuterium occupancy of vacancies in Pd and related metals," *Phys. Rev. B* **40** (1989) 1990.
[77] P. L. Hagelstein, "Molecular D_2 near vacancies in PdD and related problems," *J. Condensed Matter Nuclear Science* **13** (2014) 138.
[78] C. Jarque and O. Navaro, M. E. Ruiz and J. Garcia-Prieto, "On the stability of the PdH_2 molecule," *J. American Chemical Society* **108** (1986) 3507.
[79] O. Novaro and C. Jarque, "Potential energy surface for the Pd-H_2 system: Comparison with matrix isolation experiments," *Theor. Chim. Acta* **80** (1991) 19.
[80] L. Andrews, L. Manceron, M. E. Alikhani and X. Wang, "Observed and calculated infrared spectrum of $Pd(H_2)$ in solid argon: A ligand-free side-bonded molecular hydrogen complex," *J. American Chemical Society* **122** (2000) 11011.
[81] M. R. A. Blomberg and P. E. M. Siegbahn, "An important bound singlet state of NiH_2," *J. Chem. Phys.* **78** (1983) 986.
[82] J. A. Platts, "Theoretical electron densities in transition metal dihydrides," *Journal of Molecular Structure (Theochem)* **545** (2001) 111.
[83] L. Andrews, "Matrix infrared spectra and density functional calculations of hydrides and dihydrogen complexes," *Chem. Soc. Rev.* **33** (2004) 123.
[84] P. L. Hagelstein, "Models based on phonon-nuclear coupling," *Cold Fusion: Advances in Condensed Matter Nuclear Science*, J. P. Biberian, editor, Elsevier (2020) 283–300.
[85] A. Khellaf, R. M. Emrick, and J. J. Vuillemin, "Slow quenches of high-quality single crystals of platinum and palladium," *Physical Review B* **37** 6717.
[86] T. R. Mattsson and A. E. Mattsson, "Calculating the vacancy formation energy in metals: Pt, Pd, and Mo," *Physical Review B* **66** (2002) 214110.
[87] J. E. Worsham Jr, M. K. Wilkinson and C. G. Shull, "Neutron-diffraction observations on the palladium-hydrogen and palladium-deuterium systems," *Journal of Physics and Chemistry of Solids* **3** (1957) 303–310.
[88] F. Besenbacher, J. Böttiger and S. M. Myers, "Defect trapping of ion-implanted deuterium in nickel," *Journal of Applied Physics* **53** (1982) 3536–3546.
[89] F. Besenbacher, B. B. Nielsen, J. K. Norskov, S. M. Myers and P. Nordlander, "Interaction of hydrogen isotopes with metals: Deuterium trapped at lattice defects in palladium," *Journal of Fusion Energy* **9** (1990) 257–261.
[90] J. Mao and R. B. McClellan, "Vacancy concentrations in metals in equilibrium with H_2 at high pressures," *Journal of Physics and Chemistry of Solids* **64** (2003) 527.
[91] Y. Fukai and N. Okuma, "Formation of superabundant vacancies in Pd hydride under high hydrogen pressures," *Phys. Rev. Lett.* **73** (1994) 1640.
[92] Y. Fukai, M. Mizutani, S. Yokota, M. Kanazawa, Y. Miura and T. Watanabe, "Superabundant vacancy-hydrogen clusters in electrodeposited Ni and Cu," *Journal of Alloys and Compounds* **356-357** (2003) 270.
[93] S. Szpak, P. A. Mosier-Boss and J. J. Smith, "On the behavior of Pd deposited in the presence of evolving deuterium," *J. Electroanalytical Chemistry* **302** (1991) 255.
[94] P. L. Hagelstein and I. U. Chaudhary, "Arguments for dideuterium near monovacancies in PdD," *Proc. ICCF15* (2009) 282–287.
[95] D. Letts, "Codeposition methods: A search for enabling factors," *J Condensed Matter Nuclear Science* **4** (2011) 81.
[96] D. Letts and P. L. Hagelstein, "Modified Szpak protocol for excess heat," *J Condensed Matter Nuclear Science* **6** (2012) 44.
[97] S. Szpak, P. A. Mosier-Boss and F. E. Gordon, "Further evidence of nuclear reactions in the Pd/D lattice: emission of charged particles," *Naturwissenschaften* **94** (2007) 511–514.

[98] P. A. Mosier-Boss, L. P. G. Forsley and P. K. McDaniel, *Investigation of nano nuclear reactions in condensed matter*, DTRA Final Report (2016).
[99] P. A. Mosier-Boss, F. E. Gordon, L. P. Forsley and D. Zhou, "Detection of high energy particles using CR-39 detectors Part 1: Results of microscopic examination, scanning, and LET analysis," *Int. J Hydrogen Energy* **42** (2017) 416.
[100] M. C. H. McKubre, S. Crouch-Baker, M. C. Rocha-Filho, S. I. Smedley, F. L. Tanzella. T. O. Passell and J. Santucci, "Isothermal flow calorimetric investigations of the D/Pd and H/Pd systems," *J. Electroanalytical Chemistry* **368** (1994) 55.
[101] P. L. Hagelstein, "Bird's eye view of phonon models for excess heat in the Fleischmann-Pons experiment," *J Condensed Matter Nuclear Science* **5** (2012) 169.
[102] M. McKubre, F. Tanzella, P. L. Hagelstein, K. Mullican and M. Trevithick, "The need for triggering in cold fusion reactions," *Proc. ICCF10* (2003) 199–212.
[103] F. Tanzella, J. Bao, M. McKubre and P. Hagelstein, "Stimulation of metal deuteride wires at cryogenic temperatures," *J Condensed Matter Nuclear Scienc* **12** (2012) 176–186.
[104] E. Yamaguchi and T. Nishioka, "Cold nuclear fusion induced by controlled out-diffusion of deuterium in palladium," *Japanese Journal of Applied Physics, Part 2* **29** (1990) L666.
[105] E. Yamaguchi and T. Nishioka, "Nuclear fusion induced by the controlled out-transport of deuterons in palladium," *AIP Conference Proceedings* **228** (1991) 324.
[43] A. G. Lipson, G. H. Miley, A. S. Roussetski and E. I. Saunin, Phenomenom of an energetic charged particle emission from hydrogen/deuterium loaded metals, Proc ICCF10 (2003). (Available from LENR-CANR.org)
[106] J. H. Elliot, "Thick junction radiation detectors made by ion drift," *Nuclear Instruments and Methods* **12** (1961) 60–66.
[107] B. D. Wilkins, M. J. Fluss, S. B. Kaufman, C. E. Gross and E. P. Steinberg, "Pulse-height defects for heavy ions in a silicon surface-barrier detector," *Nuclear Instruments and Methods* **92** 381–391.
[108] J. F. Ziegler, "SRIM-2003," *Nuclear instruments and methods in physics research section B: Beam interactions with materials and atoms* **219** (2004) 1027–1036.
[109] J. Barreto, L. Tassan-Got, C. Stephan, J. P. Garron and M. Langevin, "Absence of closed shell effect in the fusion reaction ^{40}Ca+^{48}Ca at 330 MeV," *Physical Review C* **25** 1641.
[110] J. Barreto, G. Auger, M. Langevin and E. Plagnol, "Fusion of the ^{40}Ca+^{40}Ca system," *Physical Review C* **27** 1335.
[111] J. W. Engle, G. W. Severin, T. E. Barnhart, L. D. Knutson and R. J. Nickles, "Cross sections of the ^{36}Ar(d,α)^{34m}Cl, ^{40}Ar(d,α)^{38}Cl, and ^{40}Ar(d,p)^{41}Ar nuclear reactions below 8.4 MeV," *Applied Radiation and Isotopes* **70** (2012) 355–359.
[112] A. J. Koning, D. Rochman, J. C. Sublet, N. Dzysiuk, M. Fleming and S. Van der Marck, "TENDL: complete nuclear data library for innovative nuclear science and technology," *Nuclear Data Sheets* **155** (2019) 1–55.
[113] H. O. Menlove, M. M. Fowler, F. Garcia, M. C. Miller, M. A. Paciotti, R. R. Ryan and S. E. Jones, "Measurement of neutron emission from Ti and Pd in pressurized D_2 gas and D_2O electrolysis cells," *Journal of Fusion Energy* **9** (1990) 495–506.
[114] K. Mizuno, Y. Furuya, K. Hirano and H. Okamoto, "Hydrogen diffusion in titanium-hydride observed by the diffraction-enhanced X-ray imaging method," *Physica Status Solidi (a)* **204** (2007) 2734–2739.

J. Condensed Matter Nucl. Sci. 38 (2023) 78–88

Research Article

Microscopic Insights into the Anomalous Heat Effect that Unify Disparate Experimental Results

Graham K. Hubler*

The Medical School, University of Missouri, Columbia, MO USA

Abstract

The anomalous heat effect (AHE) has many embodiments including hydrogen loading by electrolysis, high and low hydrogen pressure over elevated temperature nanostructures, ultrasound, and glow discharge loading. The AHE was triggered by variable charging current, temperature fluctuations, high voltage pulses, laser pulses, ultrasound, and electrolysis time. Pd materials for which the AHE has been reported include wires, cylinders, foils, and nanoparticles. Ni materials for which the AHE has been reported include constantan wires, Ni in zeolites, and Ni nanostructures. It is highly likely that the same AHE mechanism underlies all these embodiments despite their seemingly wide differences. Many investigators involved in research on the anomalous heat effect (AHE), including this author, are of the opinion that phonons in Pd and Ni play a role in generating and sustaining the AHE. Here it is hypothesized *that the AHE requires a specific frequency optical phonon resonance that couples to electromagnetic radiation of the same frequency. If it can be arranged to sustain this specific, resonance, then the AHE is produced.* It is demonstrated how this one assumption, coupled to several recent experimental results, can lead to useful microscopic insights that unify disparate experimental results under one umbrella and that may also be useful to guide further experiments.
 ISSN 2227-3123

Keywords: Anomalous heat, Phonons, Pd deuteride, Ni hydride

1. Introduction

It *is hypothesized that the AHE requires a* ***specific frequency*** *optical phonon resonance that couples to electromagnetic radiation of the same frequency. If it can be arranged to sustain this specific resonance, then the AHE is produced.* In this paper it is demonstrated how this one assumption can lead to useful microscopic insights that unify disparate experimental results under one umbrella. The ideas that led to this model came from perturbed angular correlation (PAC) results on palladium hydrides recently obtained by this author at CERN [1], recent x-ray diffraction data on superconducting palladium hydrides [2], and 40-year-old internal friction data on PdH [3].

*Corresponding author: hublerg@umsystem.edu

 ISSN 2227-3123

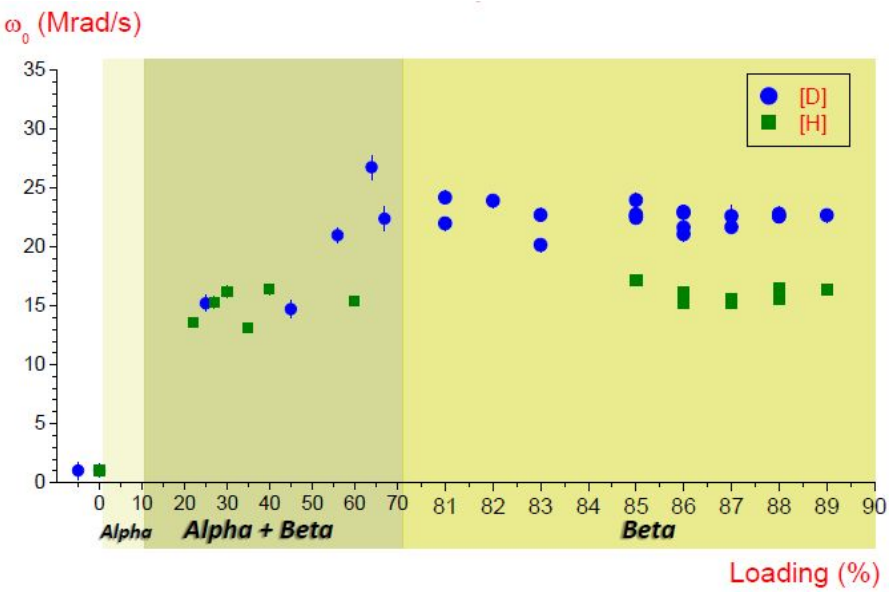

Figure 1. Precession frequency in Megaradians/s versus H or D loading fraction for dilute ^{181}Ta in a Pd host lattice. Precession is caused by an electric field gradient at the Ta nucleus site [1].

2. Underpinnings of Model

A perturbed angular correlation (PAC) experiment was conducted at the ISOLDE facility at CERN where radioactive Hf (^{181}Hf, 42 day half-life decays to ^{181}Ta + Beta, 11 ns half-life) was ion implanted into Pd foils and the gamma cascade decay of the daughter Ta nuclei were employed to measure, in situ and at room temperature, the local electric field gradient (EFG) around the nucleus as a function of the electrochemically loaded fraction of D or H [1]. A nucleus that possesses a quadrupole moment precesses in an EFG. The precession frequency of the nucleus due to the coupling of the nuclear excited state quadrupole moment with the EFG at the nucleus is a measure of the local strain around the atom. Figure 1 shows the precession frequency (strain) versus the loading fraction for both D and H. Note that the strain around the Ta atom that substitutionally replaced a Pd atom is 43% larger for D in Pd than H in Pd above ~0.5 concentration - a surprising result.

Syed et al. [2] prepared PdD_x by soaking Pd in 100 bar pressure of deuterium at a temperature of 300 C, followed by quenching to 77 K and continued cooling to 40 K. A superconducting phase was found with a superconducting transition temperature, Tc, of 61 K (Fig. 2), another very surprising result since it has been known for 50 years that $PdD_{>0.9}$ has a Tc of 11 K. What's more, the nearly flat resistivity change with increasing temperature in Fig. 2 shows the phase was stable up to room temperature since the resistivity change for a normal metal increases sharply with temperature according to the Drude model. Since there was no concomitant crystal phase transition there must be an electronic phase transition to account for this result. X-ray diffraction determined that the quench froze in a ~30% tetrahedral site occupation of D that is not present in room temperature loaded Pd that has 100% octahedral site occupation. Noting that the tetrahedral position has 1/3 the volume of the octahedral position, Syed conjectured that a significant fraction of D occupation in the tetrahedral site would expand the spacing between Pd atoms which then alters the electronic band structure to provide the Tc of 61 K. The maximum T occupancy occurs where the flux of diffusing atoms is a maximum, all of which must pass through T sites. The authors state, "At high concentrations, the

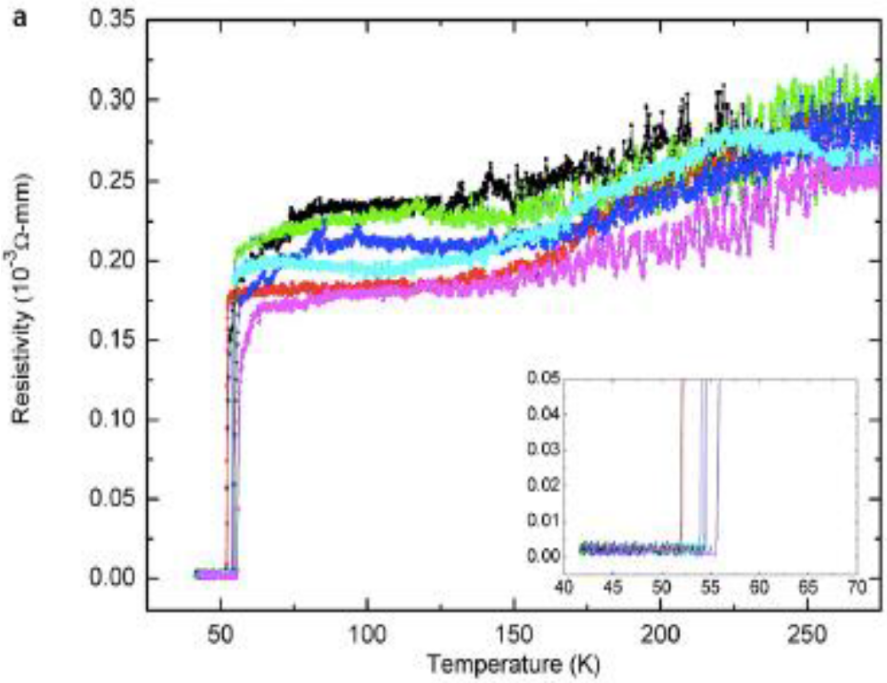

Figure 2. Resistivity versus temperature for 6 samples of Pd loaded with D at 300C and then quenched [2].

O sites are nearly filled, thus blocking the diffusion pathways. In the middle range, therefore, the diffusive flux and potential for T occupancy is greatest". For another example, the stretching of superconducting MgB_2 increases the Tc by a factor of two [3].

Figure 3 plots the internal friction data of Mazzola et al. [4] for PdH_x from x = 0 to 0.89. Internal friction is a measurement of the mechanical coupling to lattice defects by noting the damping as a function of temperature of a resonator (1/Q, the resonator quality factor) made from the material of interest. The two internal friction peaks in Fig. 3 are for mechanical coupling to H diffusion and to dislocation motion. Note that the diffusion peak has a maximum at ~0.64 and then rapidly declines because diffusive jumps are blocked since the adjacent sites are occupied. A conclusion from this data is that if H diffusion dynamics are desirable for the AHE, then the loading should be less than ~0.64. To populate the tetrahedral site, diffusive jump dynamics are desired so, operating at reduced loading helps. Ed Storms has been saying for years that the AHE exists for loading as low as 0.3 [5]. Figure 3 supports this notion. A second conclusion is that dislocations are locked above about 0.55 loading.

Returning to the PAC experiment, the Hf was ion-implanted at 80 KeV energy so all Hf atoms are less than 20 nm from the surface where the D diffusion in and out of the surface and electron current dynamics are maximized. Therefore, it is reasonable to assume that electromigration could provide the energy necessary to elevate substantial D into the tetrahedral site so that the material synthesized by the quench of PdD from 300 C and the PdD in the surface created in the PAC experiment are *one and the same material*. Coming full circle, the larger strain measured in the PAC experiment is explained by surmising that ~30% tetrahedral occupation of D expands the Pd interatomic spacing which produces the measured strain. The larger zero-point motion of the hydrogen makes it less stable in the tetrahedral site than deuterium in the dynamic surface region so only deuterium shows the increase in strain.

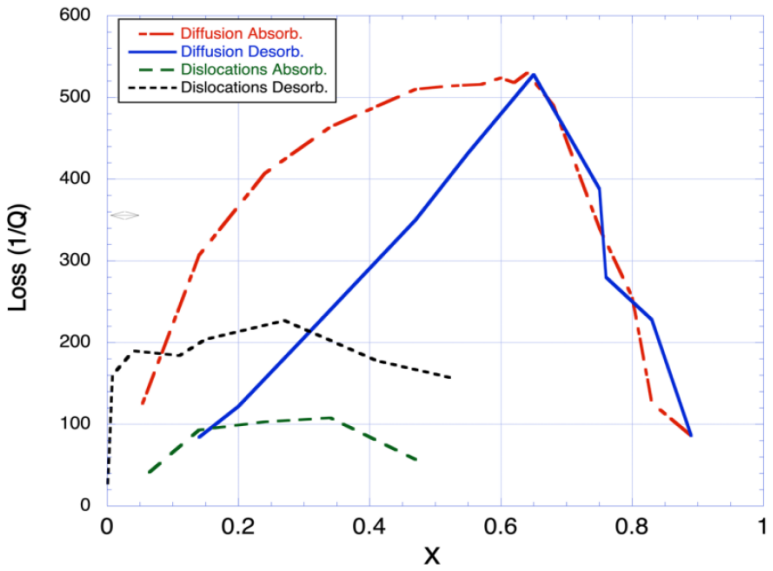

Figure 3. Internal friction loss as 1/Q versus H loading fraction in Pd at 114 K. Loss from H diffusion and dislocation motion are presented [4].

To summarize the significance these 3 experiments, the work of Syed (Fig. 2) simply proves that stable (or metastable) ~30% occupation of tetrahedral sites can exist at room temperature in PdDx and that he surmises, without measurement, that the presence of D in these sites increases strain due to the 3x smaller volume of tetrahedral sites and this strain changes the electronic band structure to yield increased Tc. The internal friction work of Mazzola (Fig. 3) indicates that the dynamics of H diffusion, where H must pass through tetrahedral sites to jump to the next octahedral site, is greatest at a H/Pd loading of 0.6, and this agrees with the conjecture of Syed that this is why he gets the highest tetrahedral occupancy for intermediate loading when soaked in H at 300 C. Now, it is conjectured here that the PAC results of 43% higher strain for PdDx (Fig. 1) is the same strain surmised by Syed and internal friction also agrees with the conjecture of Syed as to why he gets maximum loading ai D/Pd of intermediate loading. So, these three materials science measurements are related and tell us potentially important microscopic information about the Pd hydride system. The fact that the PAC method involves nuclear decay, and the 30% occupancy of tetrahedral sites was found through superconductivity measurements have nothing to do with LENR, but the microscopic facts uncovered by the measurements are related to LENR.

How would these facts apply to the AHE? The Hypothesis is modified to: *The AHE requires a specific frequency optical* ***phonon*** *resonance that is only attainable when there is* ***significant D occupation of tetrahedral sites***.

3. Palladium

As stated in the introduction, it is hypothesized that phonons in Pd and Ni play a role in generating and sustaining the AHE. *The AHE requires a specific frequency optical phonon resonance that couples to electromagnetic radiation of the same frequency.* This phonon resonant frequency in PdD_x is a complicated function of the D concentration (cannot get right frequency with H), defect concentration of the right type, interstitial site occupancy (*fraction of octahedral vs tetrahedral*), temperature, polycrystalline texture, surface micro-topology. Why is the AHE so difficult to produce? Because only a specific set of conditions outlined in the previous sentence will produce the effect and the *fraction of*

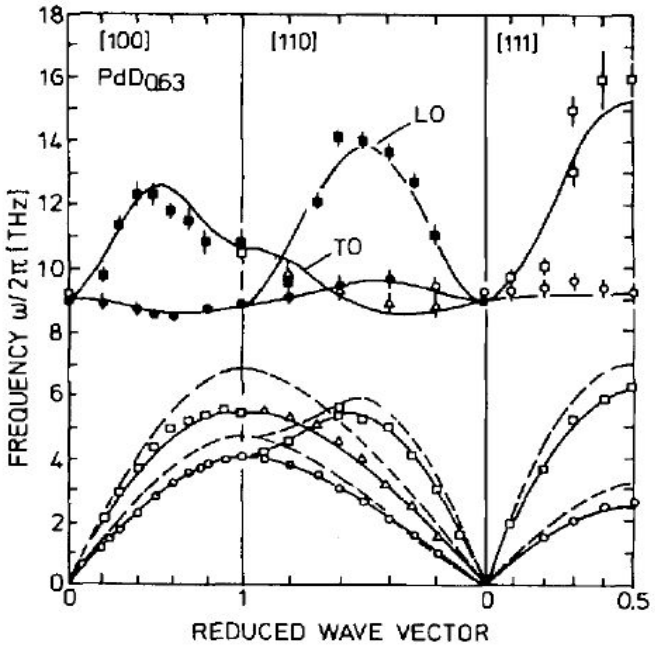

Figure 4. Measured phonon frequency dispersion versus major crystallographic axes in $PdH_{0.63}$ [6].

octahedral vs tetrahedral may be a critical one. Figure 4 shows the experimental optical and acoustic phonon spectra for $PdD_{0.63}$ [6] where phonon frequency in THz is the ordinate and the abscissa is different major axes in the crystal. Figure 5 takes the gamma <100> crystal direction and places a data point for the phonons on the plot for 6 different models of phonon frequencies [6], i.e., for Pd, $PdD_{0.63}$, PdH(oct), PdH(tet), Pd_3VacH_4(oct), Pd_3VacH_4(tet) where oct and tet stand for octahedral and tetrahedral sites, respectively, and Vac stands for vacancy. The first 2 are experimental and the last 4 are theory. Experiments can only be done for D and theory can only be done for H. Nevertheless, Figure 5 shows that the unique frequency could be over a wide range from 2 to 40 THz. In general, the addition of hydrogen increases the frequency of hydrogen sub-lattice modes and decreases the frequency of Pd sublattice modes.

Here it is conjectured that the special phonon frequency is not possible in Pd loaded with D where it is known that 100% is in the octahedral site, but promotion of significant D into the tetrahedral site will alter the phonon frequencies and one will overlap with the special frequency and heat is produced. Figure 5 demonstrates there is a second possible mechanism to achieve the special frequency – by insertion of vacancy defects into the Pd lattice. Keep in mind that the frequencies for any of the configurations will vary with changes to H concentration, temperature, crystal major axes. In this model, H will not produce the AHE because it's possible phonon frequencies never overlap with the required **specific frequency**. Figure 5 is not complete enough to try and pinpoint the specific frequency using the fact of exclusion of H and acceptance of D frequencies. Note that inelastic neutron diffraction found an 80 millielectron volt (20 THz) phonon in 8 nm $PdH_{.43}$ nanoparticles that is not in bulk PdH that is a candidate for the **specific frequency** [7].

The notion that a **specific phonon frequency** induces the AHE, leads to a straightforward mechanism that sustains the effect. Once triggered, the AHE mechanism itself produces either the right frequency phonon or the right frequency electromagnetic radiation that provides *the positive feedback to sustain the AHE mechanism*. A phonon resonance will

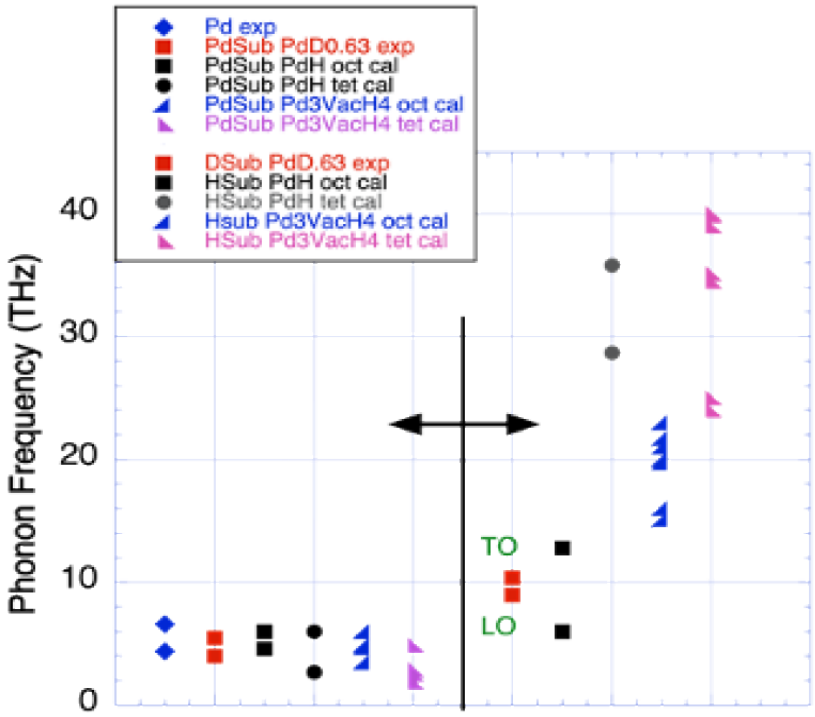

Figure 5. Phonon frequencies for the Pd and H sub lattices along the 100 axes for various configurations of H or D in Pd. Exp means experimental data and cal means calculated [6].

emit photons of the same frequency since the phonons are oscillating charges [8], [9], and electromagnetic radiation of the same frequency as the phonons will be resonantly absorbed, reinforcing the phonons.

Pd nanoparticles can play a role in producing the right frequency. It is calculated that 8 nm Pd nanoparticles have 30% occupation of the tetrahedral site [10]. The fact that nanoparticles may play a role dove tails well with experimental data. Start with Fleischman-Pons who often found that it took weeks before the excess heat effect began [11]. During electrolysis, the surface undergoes large modifications, dissolving Pd and reforming constantly and with incorporation of electrolyte impurities in the surface. Frequently there are deposits on the cathode surface after successful AHE runs. It is possible that over time, nanoparticles developed on the surface of the cathodes, and vacancies were inserted from the surface [12] and diffused in and caused the delay in the onset of the AHE. Figure 6 shows the deposits on a cathode that produced 730,000 Joules of excess energy over a period of 54 days [13]. Resonating nanoparticles on the surface from surface plasmon resonance or mechanical shape resonance, excited by charge exchange, will emit RF radiation and may not only cause the AHE in the nanoparticles but also stimulate phonons deeper into the bulk and engage a greater volume in the AHE process. Violante worked out in detail how nano-surface features on Pd could emit RF from MHz to THz [14].

Also, it was found that the addition of $\leq$ 9 nm Pd nanoparticles to an electrochemical cell increased the probability of observing excess heat [13]. Arata found the AHE using Pd nanoparticles in a heated, closed cell under D_2 pressure [15] as did Yan Kucherov in 1998 [16]. Cravens and Gempel used Pd and Au nanoparticles deposited on activated charcoal in D_2 atmosphere enclosed in a brass ball with a magnetic field [17]. The latter two

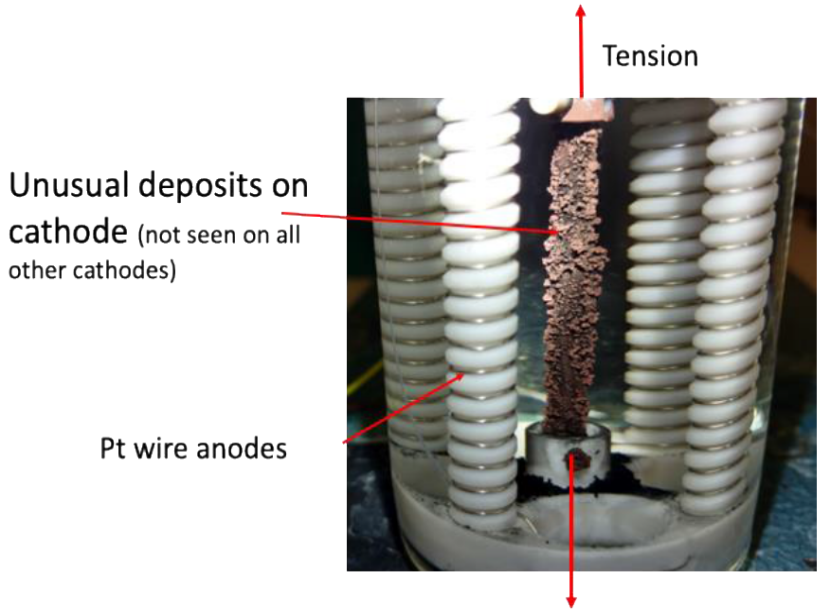

Figure 6. A Pd cathode that produced significant excess heat after 58 days of electrolysis showing deposits on surface [12].

emphasized a temperature gradient to encourage diffusion dynamics. Triggering can substitute for nanoparticles as shown by Staker [18] and Godes [19] who used electrical current pulses to stimulate the AHE in Pd rods. In this case electromigration could populate the tetrahedral site. D. Letts et al used lasers to generate THz radiation on the surface and obtained the AHE. The radiation could have provided the energy to populate the tetrahedral site with D [20]. Acoustic shock may promote D to the tetrahedral site. Energetics obtained the AHE using ultrasound stimulation [21]. It is sensible that both acoustic stimulation loading and glow discharge loading should be done gently since both may destroy triggering nanostructures formed on the surface. The polycrystalline morphology of the Pd cathodes can also play a role since a textured foil would benefit from phonon dispersion being the same across the volume of the foil or wire. This dove tails with the work of Violante who obtained evidence that the AHE is optimized for Pd highly textured in the 100 direction and for ~0.1 μm featured surface morphology [22], [23], [24]. To summarize this section, the special frequency is obtained by simple rules.

In bulk Pd

-a) Significant population of D in tetrahedral site (~30%), or
-b) High vacancy concentration

Either a or b provides the special phonon frequency that produces the AHE

-Deposit <10 nm Pd nanoparticles on surface

In nanoparticle Pd

- Use < 10 nm size
- Maximize volume of nanoparticles with access to deuterium
- Heat the nanoparticles

In general

- Stimulate this phonon to resonate by a trigger
- Sustain the stimulus to keep resonance active

*A 100 textured material will maximize heat (V. Violante) [25].

4. Nickel

Experiments using Pd are run below the Pd Debye Temperature and so phonons are possible excitations in the solid. For Ni, experiments are run at elevated temperatures that exceed the Debye temperature (450K) where phonons are not possible. However, the boundary conditions extant in nanostructured materials recover the ability of Ni-based materials to support phonons and phonon-like, size-based excitations at elevated temperatures [7]. Ni-based AHE embodiments all use nanostructured materials and Ni and Pd share the same crystal structure and similar band structure.

The experiments of Parkhamov (Ni powder, $LiAlO_2$) [26], Celani (NP coated constantan wires) [27], Swartz (ZrO_2PdNi powder) [28], Godes (Ni wire) [19], Kitamura (Ni powder) [29], Mizuno (Ni mesh) [30], Focardi (Ni powder) [31] all use Ni-based nanoparticle formulations in their reactors or coated wires. Iwamura [32] and Kasagi [33] use nm thin-film multilayers containing Ni. In the case of Ni:

- Nanostructures are preferred over bulk materials on the order of 10 nm. This may be due to the facts that experimental temperatures exceed the Debye temperature and the very low solubility of H in Ni
- Since temperature thermally drives the phonons, there is no need for a trigger
- Maximize volume of nanoparticles with access to hydrogen
- Since H produces heat, the NiH_x nanostructures produce the **special** phonon frequency
- AHE with Ni is more reproducible than with Pd (no need to kick D into T-site or produce high a vacancy concentration and the trigger is simply thermal).

5. Discussion

This model was developed by noticing that nanostructured materials are a commonality among different AHE methods, by noting experiments that exposed real microscopic differences between PdH and PdD, and by the application of common-sense organization to the data. For Pd, nanoparticles play a role of generating excess heat themselves and in addition serve to excite bulk phonons if the bulk phonons are prepared with some fraction of tetrahedral occupation or vacancy concentration. Only loading with D results in the AHE. For Ni-based materials, nanostructured materials seem to be active and bulk materials less so. Loading with H will result in the AHE and perhaps with D, but this is not well established. While this phonon resonance model seems to unify the many different AHE results, *this resonance-phonon model is agnostic as to what the actual AHE mechanism is.* Therefore, the physics of the actual AHE energy source must be mapped onto this model by devising either a source of specific frequency E&M radiation or a mechanism to drive energy into atomic motion of specific frequency phonons, keeping in mind that the only signatures of the AHE are *heat production*, *RF emission*, *no nuclear emissions.*

Some lessons from this model to guide experiments are:

- Work with Pd nanoparticles with size 9 nm or less
- For good hydrogen dynamics, stay below D/Pd ≤ 0.64
- Triggering of Pd to promote D to the tetrahedral site helpful – electric pulse has been demonstrated
- Use highly textured Pd – 100-orientation preferred – likely for Ni also Work with Ni nanostructures with size 14 nm or less. Much less determined than for Pd

- Ni does not need trigger – just heating is enough
- Glow discharge and ultrasonic loading should be done gently so as not to destroy surface nanofeatures
- Model implies that the AHE is a bulk phenomenon, not a surface phenomenon.
- The Ni-based materials at elevated temperature yield more reproducible AHE results than PdD_x materials in electrolytes.

Some suggestions for future fundamental experiments include:

- Perform the internal friction measurement for D loading in Pd instead of H and repeat the loading/deloading cycle several times on the same specimen.
- Examine the Tc = 61 K PdD_x material in an AHE apparatus with triggering
- Characterize RF emissions
- Diffuse radioactive ^{57}Co into Pd foils or Ni nanostructures and perform Mossbauer spectroscopy during excess heat events. Look for changes in decay rate or energy shift when producing heat (injects nuclear physics into experiment at 14 keV level)
- I recommend the Iwamura-Kasagi method since it is done in hard vacuum where many diagnostics become possible [32], [33]
- Add 2% Ni to Pd which renders Pd Ferromagnetic and do electrolysis with magnetic field
- Place Pd and/or Ni in fast neutron flux from a nuclear reactor to introduce high concentration of vacancies and perform AHE experiments.

A word about the well-known equation reported by McKubre which states that to obtain the AHE the D loading in Pd must be >0.88 and that the excess energy is proportional to $[X - 0.88]^2$ where x is the deuterium concentration D/Pd [34]. Also, that the current density must be 250 to 500 mA/cm^2. This is huge current density, causing a region of dynamical instability near the surface. While electromigration may populate T sites, vigorous electromigration will also depopulate the T sites and higher temperature of the cathode due to IR heating also reduces stability of D in T site. We speculate that for a cathode that will readily load to D/Pd >0.9, the large fugacity at 500 mA/cm^2 still forces D into the surface so when D/Pd gets to ~0.88 then D jumps to T site and has fewer paths to depopulate so concentration in T site begins to grow (see Fig. 1). Once this happens, the T-site population will grow as the square of the concentration above 0.88 which is what McKubre observed.

The anomalous heat effect is, to first order, a fundamental a solid-state physics problem – not a nuclear physics problem. There are unknown excitations occurring in the solid that produce heat. A survey of the several hundred named solid-state phenomena provide no clues. We need measurements that reveal phenomena at the scale of the atom in relevant material systems as represented in this work. This is a bottom-up approach where we search for the unknown excitations and then try to map them onto an energy generating process.

Finally, I offer suggestions that may lead to a mechanism. Hagelstein's theory is phonon based where a particular optical phonon in the few to 40 THz region of frequency undergoes coherent resonance and couples to virtual 2 nucleon energy levels and the energy from fusion to ^4He is dissipated by ~E8 atoms in the phonon field, and the mechanism solves the problem of the lack of energetic emissions [37]. The model presented here dovetails with Hagelstein's theory. Another place to look for an excitation that may relate to the AHE mechanism is as follows. Density Functional Theory (DFT) teaches us that the electronic band structure is *very sensitive to the interatomic spacing*. Imagine two atoms in an optical phonon at the extremity of excursion away from their equilibrium positions (equivalent to strain). For the few femtoseconds at the extreme position, an entirely different electronic band structure can evolve due to a different atomic spacing. A few fs is a long time from the electron's point of view. We can have metal to insulator, metal to semiconductor, new superconductor, non-ferromagnetic to ferromagnetic, etc., transitions [35], [36]. Such a dynamic effect is difficult to explore experimentally and may require fs timing methods. To emphasize this point, the

Tc of 61 K in PdDx and the 50% increase in Tc in MgB_2 mentioned above are both caused by static tensile strain that changes the interatomic spacings. These nonequilibrium electron configurations may cause, for example, colossal crystal fields to momentarily emerge.

The struggle to uncover the mechanism(s) that produce the anomalous heat effect continues. Perhaps the insights described in this paper will help in that endeavour.

Acknowledgements

I wish to thank Vittorio Violante, James Hirvonen and JingHao He for critical reading of the manuscript and fruitful discussions, and Mr. Sidney Kimmel for partial support of this work.

References

[1] J. He, G.K. Hubler, E. Bernardo da Silva, João G.M. Correia, J. Schell, V. Violante, I. Teles de Matos, I. Souza Ribeiro Jr., A.W. Carbonari, M. Thioye, J. Gahl, M. Zoghby, "Hyperfine interactions in palladium foils during deuterium/hydrogen electrochemical loading", Talk at ICCF20, Sendai, Japan 2020, https://www.researchgate.net/publication/359350803_Hyperfine_Interactions_in_Palladium_Foils_during_Electrochemical_Loading_of_Deuterim_and_Hydrogen

[2] H.M. Syed, T.J. Gould, C.J. Webb, E.MacA. Gray, "Superconductivity in palladium hydride and deuteride at 52-61 kelvin", arXiv:1608.01774v1 [cond-mat.supr-con] 2016.

[3] E. Johansson, F. Tasnádi, A. Ektarawong, J. Rosen, B. Alling, "The effect of strain and pressure on the electron-phonon coupling and superconductivity in MgB2—Benchmark of theoretical methodologies and outlook for nanostructure design", Journal of Applied Physics, 2022; 131 (6): 063902 DOI: 10.1063/5.0078765

[4] F.M. Mazzola, P.G. Bordoni, F.A. Lewis, "Elastic energy dissipation effects in $\alpha + \beta$ and β phase composition ranges of the palladium hydrogen system", J. Phys. F: Metal Phys., **11**, pp. 337-52, 1981.

[5] E. Storms, "How basic behavior of LENR can guide. A search for an explanation", J. Condensed Matter Nucl. Sci. 20, pp. 100-138 2016.

[6] S.S. Setayandeh, C.J. Webb, E. MacA. Gray, "Electron and phonon band structures of palladium and palladium hydride: A review", Prog. in Sol. State Chem. 60, 100285, 2020.

[7] M. Kofu, N. Hashimoto, H. Akiba, H. Kobayashi, H. Kitagawa, K. Iida, M. Nakamura, O. Yamamuro, "Vibrational states of atomic hydrogen in bulk and nanocrystalline palladium studied by neutron spectroscopy", Phys. Rev. B 96, p. 054304, 2017.

[8] T. Dekorsy, H. Auer, C. Wasehke, H. J. Bakker, H. G. Roskos, H. Kurz, V. Wagner and P. Grosse, "Emission of submillimeter electromagnetic waves by coherent phonons", Phys. Rev. Lett. 74 p. 738, 1995.

[9] M. Tani, R. Fukasawa, H. Abe, S. Matsuura, K. Sakai, S. Nakashima, "Terahertz radiation from coherent phonons excited in semiconductors", J. Applied Phys., 83, p. 2473, 1998.

[10] Hiroshi Akiba, Maiko Kofu, Hirokazu Kobayashi, Hiroshi Kitagawa, Kazutaka Ikeda, Toshiya Otomo, and Osamu Yamamuro, "Nanometer-Size Effect on Hydrogen Sites in Palladium Lattice", J. Am. Chem. Soc. 138, pp. 10238-10243, 2016.

[11] M. Fleischmann and S. Pons, "Electrochemically induced nuclear fusion of deuterium", J. Electroanal. Chem., 261 pp. 301-308, 1989.

[12] H. Akiba, M. Kofu, H. Kobayashi, H. Kitagawa, K. Ikeda, T. Otomo, O. Yamamuro, "Nanometer-Size Effect on Hydrogen Sites in Palladium Lattice", J. Am. Chem. Soc. 138, pp. 10238-10243, 2016.

[13] G.K. Hubler, D. Pease, A. El Boher, O. Azzizi, J. He, K.K. Katti, K.V. Katti, "Long term anomalous heat from 9 nm Pd nanoparticles in an electrochemical cell", Condensed Matter Nucl. Sci. 23 (2022) 38.

[14] V. Violante, E. Castagna, F. Sarto, G. Hubler, D. Knies, K. Grabowski, "Methodology of production of materials which allow a high reproducibility of the production of excess power when electrochemical loaded with deuterium", Italian Patent N0001391275 (in Italian).

[15] Y. Arata, Y.C. Zhang, "The establishment of solid nuclear fusion reactor", J. High Temp. Soc. 34 pp. 85-93, 2008.

[16] Y. Kucherov, 1998, private communication.

[17] D. Cravens, R. Gimpel, "Cold fusion at NI week 2013", Infinite Energy, Issue 111, September/ October 2013.

[18] M.R. Staker, “Coupled calorimetry and resistivity measurements, in conjunction with an emended and more complete phase diagram of the palladium-isotopic hydrogen system”, J. Condensed Matter Nucl. Sci. 29 pp. 129-168, 2019.
[19] R. Godes, R. George, F. Tanzella, M. McKubre, “Controlled electron capture and the path toward Commercialization”, https://www.researchgate.net/publication/268410824.
[20] P.L. Hagelstein, D. Letts, D. Cravens, "Terahertz difference frequency response of PdD in two-laser experiments", J. Condensed Matter Nucl. Sci. 3 pp. 59-76, 2010.
[21] I. Dardik, T. Zilov, H. Branover, “ Report on electrolysis experiments at Energetics Technologies”, In Proc. of the 13th International Conf. on Condensed Matter Nuclear Science (ICCF-13), Dagomys, Sochi, June 2007, pp. 325–347.
[22] V. Violante, F. Sarto, E. Castagna, M. Sansovini, S. Lecci, D.L. Knies, K.S. Grabowski, G.K. Hubler, “Material science on Pd-D system to study the occurrence of excess power”, Proc. 14th International Conf. on Condensed Matter Nuclear Science and 14th International Conf. on Cold Fusion (ICCF-14) Washington, DC, 2008.
[23] F. Sarto, E. Castagna, M. Sansovini, S. Lecci, V. Violante, D.L. Knies, K.S. Grabowski, G.K. Hubler, “Electrode surface morphology characterization by atomic force microscopy”, Proc. 14th International Conf. on Condensed Matter Nuclear Science and 14th International Conf. on Cold Fusion (ICCF-14) Washington, DC, 2008.
[24] E. Castagna, M. Sansovini, S. Lecci, A. Rufoloni, F. Sarto, V. Violante, D.L. Knies, K.S. Grabowski, G.K. Hubler, M. McKubre, F. Tanzella, “Metallurgical characterization of Pd electrodes employed in calorimetric experiments under electrochemical deuterium loading”, Proc. 14th International Conf. on Condensed Matter Nuclear Science and 14th International Conf. on Cold Fusion (ICCF-14) Washington, DC, 2008.
[25] V. Violante, F. Sarto, E. Castagna, G. Hubler, D. Knies, K. Grabowski, M. McKubre, A. Godfrey, “Methodology of production of materials which allow a high reproducibility of the production of excess power when electrochemical loaded with deuterium”, Italian Patent N0001391275 (in Italian).
[26] Parkhomov AG 2015 Journal of Emerging Areas of Science 3 (8): 34, in Russian.
[27] F. Celani, G. Vassallo, E. Purchi, F. Santandrea, S. Fiorilla, A. Nuvoli, M. Nakamura, P. Cirilli, A. Spallone, B. Ortenzi, S. Pella, P. Boccanera, L. Notargiacomo, “Observation of macroscopic current and thermal anomalies, at high temperature, by hetero-structures on thin and long Constantan wires under H2 gas”, International Conf. Cold Fusion 19,
[28] M.R. Swartz, G.M. Verner, J.W. Tolleson, P.L. Hagelstein, “Dry, preloaded NANOR®-type CF/LANR components”, Current Sci., 108, No. 4, pp. 25, 2015.
[29] H. Kitamura et al., Effect of minority atoms of binary Ni-based nanocomposites on anomalous heat evolution under hydrogen absorption, J. Condensed Matter Nucl. Sci. 19 pp. 135–144, 2016.
[30] T. Mizuno, “Observation of excess heat by activated metal and deuterium gas”, J. Condensed Matter Nucl. Sci. 25 pp. 1–25, 2017.
[31] S. Focardi, V. Gabbani, V. Montalbano, F. Piantelli, S. Veronesi, “Large excess heat production in Ni-H systems”, Il Nuovo Cimento vol. 111A, pp. 11, 1998.
[32] Yasuhiro Iwamura, Takehiko Itoh, Jirohta Kasagi, Shoichi Murakami, Mari Saito, “Excess Energy Generation using a Nano-sized Multilayer Metal Composite and Hydrogen Gas”, J. Condensed Matter Nucl. Sci. 33 (2020) 1–13.
[33] J. Kasagi, T. Itoh, Y. Shibasaki, T. Takahashi and Y. Iwamura, “Anomalously large heat generation in NiCu multilayer foil during H2 gas desorption measured by radiant calorimetry, 2022, to be published.
[34] McKubre, M.C.H., et al. “Excess Power Observations in Electrochemical Studies of the D/Pd System; The Influence of Loading”, in *3rd International Conf. on Cold Fusion, "Frontiers of Cold Fusion"*, 1992, Nagoya Japan: Univer. Acad. Press, Inc., Tokyo, Japan.
[35] J.D. Rameau, S. Freutel, A.F. Kemper, M.A. Sentef, J.K. Freericks, I. Avigo, M. Ligges, L. Rettig, Y. Yoshida, H. Eisaki, J. Schneeloch, R.D. Zhong, Z.J. Xu, G.D. Gu, P.D. Johnson, U. Bovensiepen, “Energy dissipation from a correlated system driven out of equilibrium”, Nature Comm. 7, 13761 (2016) DOI: 10.1038/ncomms13761.
[36] N. Poccia, T.I. Baturina, F. Coneri, C.G. Molenaar, X.R. Wang, G. Bianconi, A. Brinkman, H. Hilgenkamp, A.A. Golubov, V.M. Vinokur, “Critical behavior at a dynamic vortex insulator-to-metal transition”, 11 Sept. 2015, 349 ISSUE 6253.
[37] P.L. Hagelstein, "Recent Progress on Phonon-Nuclear Theoretical Models." JCMNS 36 (2022) 210-246.

J. Condensed Matter Nucl. Sci. 38 (2024) 89–95

Research Article

Synthesis of Silicon in the Interaction of Aluminum With a Quasi-Neutron and Estimation of the Contribution of the Aluminum Hydride Complex

Mikhail P. Kashchenko[1,2*], Maxim A. Kovalenko[1], Vladimir I. Pechorsky[2], Anatoly Ya. Kupryazhkin[1], Nadezhda M. Kashchenko[1]

[1] *Ural federal university, Yekaterinburg, Russia*

[2] *Ural state forest engineering university, Yekaterinburg, Russia*

Abstract

Among the nuclear fusion reactions of new elements, the simplest reaction refers to the capture of a proton p by the nucleus of the original element ${}_ZX^A$ with the formation of the ${}_{Z+1}Y^{A+1}$ nucleus (Z and A are the charge and mass number of the element X). In the case of cold fusion, the occurrence of such a reaction is associated with the existence of quasi-neutron ($p+e$) states in which the proton is "escorted" by the electron e: ${}_ZX^A + (p+e) \rightarrow {}_{Z+1}Y^{A+1} + e$. For example the synthesis of zinc from copper was established. It is important to note that the ratios of the proportions of synthesized isotopes in most cases should differ significantly from natural ratios, which would certainly confirm their artificial origin. The data of preliminary mass spectrometric measurements for the synthesis of zinc from copper, gallium from zinc, and rhenium from tungsten are consistent with this conclusion. However, for relatively heavy elements, the masses of daughter atoms with ${}_{Z+1}Y^{A+1}$ nuclei are difficult to distinguish from the masses of hydride complexes of parent atoms with ${}_ZX^A$ nuclei and hydrogen atoms H formed in the course of mass spectrometric measurements. In this regard, the problem of estimating the contributions of daughter atoms and hydride complexes is topical. The solution of this problem was carried out for the case of silicon synthesis from aluminum. In an air environment with water vapor, an electric arc was ignited between an aluminum anode and a tungsten cathode. Aluminum has one stable isotope ${}_{13}Al^{27}$; therefore, the synthesis of only one of the three stable silicon isotopes ${}_{14}Si^{28}$ was expected, which was observed in the mass spectrum of the powder formed on the anode surface (peak at ≈ 27.977 a.m.u.). The AlH complex corresponds to a peak at ≈ 27.989 a.m.u. This peak has a height approximately 2.5 times less than the height of the peak for the mass distribution of silicon atoms. Thus, the relatively low intensity for the mass distribution of the AlH complex suggests that it is the isotope ratios of the synthesized daughter nuclei that make the main contributions to the observed isotope mass ratios in the cases of parent atoms having several stable isotopes.
 ISSN 2227-3123

Keywords: Cold fusion, quasi-neutron, mass spectrum, aluminum, silicon, aluminum hydride

*Corresponding author: mpk46@mail.ru

© 2023 ICCF. All rights reserved. ISSN 2227-3123

Table 1. The expected difference between the mass ratios of synthesized isotopes (exp) and their ratios in nature (nat).

Z (X)	Z + 1 (Y)	Z, A_1, A_2	Z + 1, A^*_1, A^*_2	$f(A^*_2)/f(A^*_1)_{exp}$	$f(A^*_2)/f(A^*_1)_{nat}$
22 (Ti)	23 (V)	Ti, 49, 50	V, 50, 51	0,95749	399
29 (Cu)	30 (Zn)	Cu, 63, 65	Zn, 64, 66	0,446	0,56
30 (Zn)	31 (Ga)	Zn, 68, 70	Ga, 69, 71	0,03306	0,66367
74 (W)	75 (Re)	W, 184, 186	Re, 185, 187	0,92787	1,6738

1. Introduction

Among the nuclear fusion reactions of new elements, the simplest reaction refers to the capture of a proton p by the nucleus of the original element ${}_ZX^A$ with the formation of the ${}_{Z+1}Y^{A+1}$ nucleus (Z and A are the charge and mass number of the element X). In the case of cold fusion, the occurrence of such a reaction is associated with the existence of quasi-neutron ($p + e$) states [1], [2] in which the proton is "escorted" by the electron e:

$$ {}_ZX^A + (p + e) \rightarrow {}_{Z+1}Y^{A+1} + e. \tag{1} $$

The essence of the quasineutron concept is simple. As is known, there is the stationary bound state of the electron and proton in the form of a hydrogen atom ($\sim 10^{-10}$ m in size). In the concept of quasi-neutrons, the existence of non-stationary states is allowed, when an electron "escorts" a proton, screening its positive charge. Additional remarks on quasi-neutron states are given in Section 4.

In experiments [3], the synthesis of zinc with the participation of copper was observed:

$$ {}_{29}Cu^{63} + (p + e) \rightarrow {}_{30}Zn^{64} + e, {}_{29}Cu^{65} + (p + e) \rightarrow {}_{30}Zn^{66} + e, \tag{2} $$

which is consistent with the concept of quasineutrons.

2. Expected Ratios of Synthesized Isotopes and a Problem of Estimating the Contributions of Daughter Atoms and Hydride Complexes

In this regard, the problem naturally arises of determining the ratios of the synthesized isotopes $f\ (A^*_2)$ / f $(A^*_1)_{exp}$, which should be specified by the natural ratio of the initial isotopes $f\ (A_1)$ / f $(A_2)_{nat}$. Here $A_{1,2}$ are the mass numbers of the initial isotopes, $A^*_{1,2} = A_{1,2} + 1$. As a result, the ratio of the synthesized isotopes may differ markedly from their natural ratio $f\ (A^*_2)/f\ (A^*_1)_{nat}$, as follows from the data in Table 1.

The results [4] of mass spectrometry for the synthesized isotopes of zinc (with electrolysis of water using copper electrodes) and gallium (using zinc electrodes) are generally consistent with the expected results. The observed deviations from the expected values are due to the contribution of additional reactions other than proton capture.

Note that the ratio of the synthesized isotopes is always much closer to the expected value (exp) than to the natural value (nat), and the degree of similarity increases for small fractions of the synthesized powder.

For relatively heavy elements, the masses of daughter atoms with ${}_{Z+1}Y^{A+1}$ nuclei are difficult to distinguish from the masses of hydride complexes of parent atoms with ${}_ZX^A$ nuclei and hydrogen atoms H formed in the course of mass spectrometric measurements. In this regard, the problem of estimating the contributions of daughter atoms ${}_{Z+1}Y^{A+1}$ and hydride complexes ${}_ZX^A\ H$ is topical.

3. Experimental Results

The solution of this problem was carried out for the case of silicon synthesis from aluminum. Figure 1 shows a scheme of a simple experiment carried out at the Department of General Physics of the Ural Forest Engineering University.

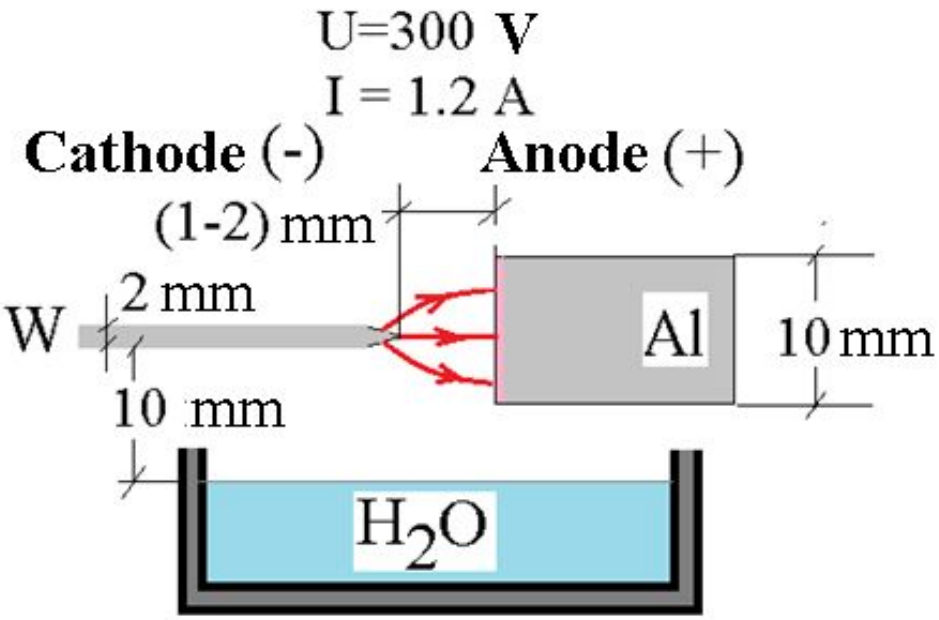

Figure 1. Experiment scheme: arc discharge in air. Conventionally, a thin surface layer of the aluminum anode is marked.

In an air environment with a high content of water vapor, an arc discharge was created between the tungsten cathode and the aluminum anode. At a typical potential difference U $\approx$ 300 V, the current I was $\approx$ 1.2 A. The geometric parameters are shown in the figure.

A small container of water led to an increase in the content of water vapor. The presence of water vapor should have promoted, in particular, the simplest nuclear reaction for the synthesis of rhenium isotopes Re - 185, 187, respectively, from tungsten isotopes W - 184, 186 during the capture of a proton escorted by an electron [5]. However, here we restrict ourselves to data on the synthesis of silicon and the possibility of separating Si-28 and aluminum hydride AlH, which are close in mass.

The analysis of the mass spectrum was carried out at the Department of Technical Physics of the Institute of Physics and Technology of the Ural Federal University. We used a Phi Trift V nano TOF time-of-flight secondary ion mass spectrometer (see Fig. 2) with a resolution R = m / Δm $\leq 10^4$ and a sensitivity up to 10^7 at/cm^2 (10 ppb).

It is clear that for reliable detection of silicon synthesis, it is expedient to use initial aluminum samples with a low silicon content. Then we can hope that the amount of synthesized silicon will exceed its initial content. The mass spectrum of the original aluminum sample in the actual region near 28 a.m.u is shown in Figure 3. The large peak in Figure 3 corresponds to aluminum hydride AlH, the region to the left of the peak may contain a contribution from a small amount of Si-28.

Aluminum has one stable isotope $_{13}Al^{27}$; therefore, the synthesis of only one of the three stable silicon isotopes $_{14}Si^{28}$ was expected. Figure 4 shows the result for $_{14}Si^{28}$ which was observed in the mass spectrum of the powder formed on the anode surface (peak at $\approx$ 27.977 a.m.u.). You can also see a small peak for AlH ($\approx$ 27.989 a.m.u.).

A comparison of Figures 4 and 3 unambiguously indicates the increase in the number of silicon isotope $_{14}$Si ^{28} during an arc discharge in the presence of water vapor. Aluminum hydride peak has a height approximately 2.5 times

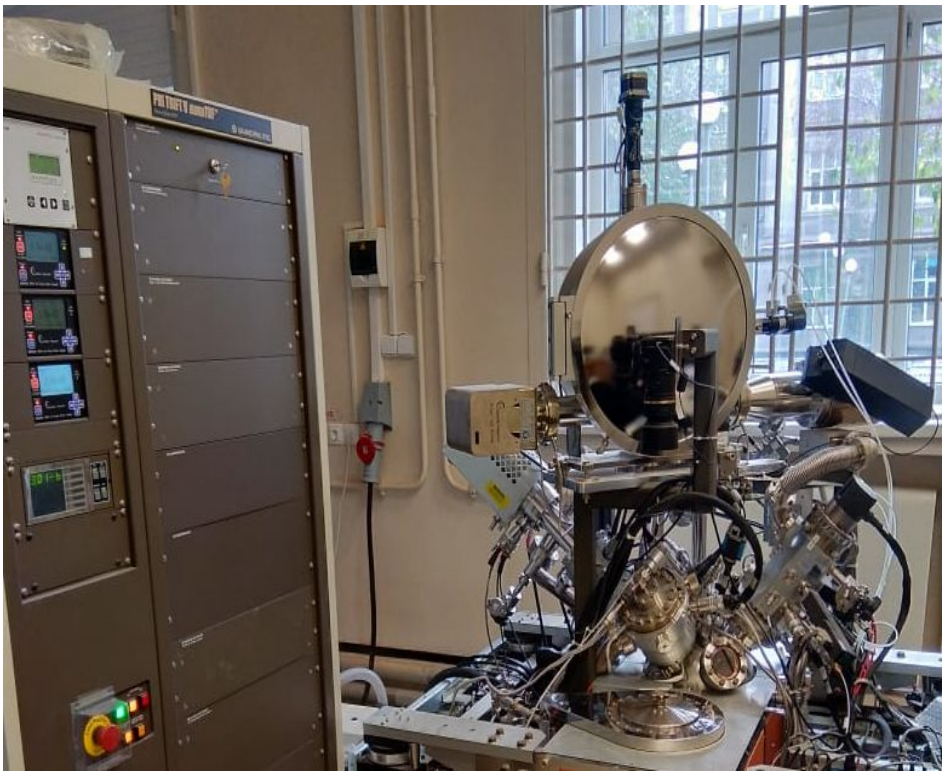

Figure 2. General view of the mass spectrometer.

less than the height of the peak for the mass distribution of silicon atoms. Thus, the relatively low intensity for the mass distribution of the *AlH* complex suggests that it is the isotope ratios of the synthesized daughter nuclei that make the main contributions to the observed isotope mass ratios in the cases of parent atoms having several stable isotopes. The results obtained indirectly testify in favor of the concept of quasi-neutron states in the implementation of cold fusion of nuclei in reactions (1).

Note that the appearance of the $_{14}$Si ^{28} isotope can give rise to the $_{14}$Si^{29} isotope, and the appearance of $_{14}$Si^{29} can give rise to the $_{14}$Si ^{30} isotope. Indeed, the capture of a proton by the $_{14}$Si ^{28} isotope leads to the unstable $_{15}$P^{29} isotope with a half-life of ≈4.1 s. Positron emission leads to $_{14}$Si^{29}. Similarly, the positron decay of the $_{15}$P^{30} isotope (half-life ≈ 2.5 min) leads to $_{14}$Si^{30}. Direct fixation of the $_{14}$Si^{29} isotope is prevented by the superposition of the $_{14}$Si ^{28}H silicon hydride peak, as can be expected from the data in Figs. 5.

It is clear that the mass of the $_{14}$Si^{29} isotope corresponds to the value (≈28.9765 a.m.u.) lying to the left of the $_{14}$Si ^{28}H peak (≈28.9847 a.m.u.). However, silicon hydride does not interfere with the identification of the $_{14}$Si^{30} isotope. The corresponding mass spectrum is shown in Figure 6.

4. Final Remarks

1. Note that the experimental results obtained in this work on increasing the content of the Si-28 isotope, as well as the observed synthesis of zinc and gallium isotopes [3], [4], are consistent with the concept of quasi-neutrons.

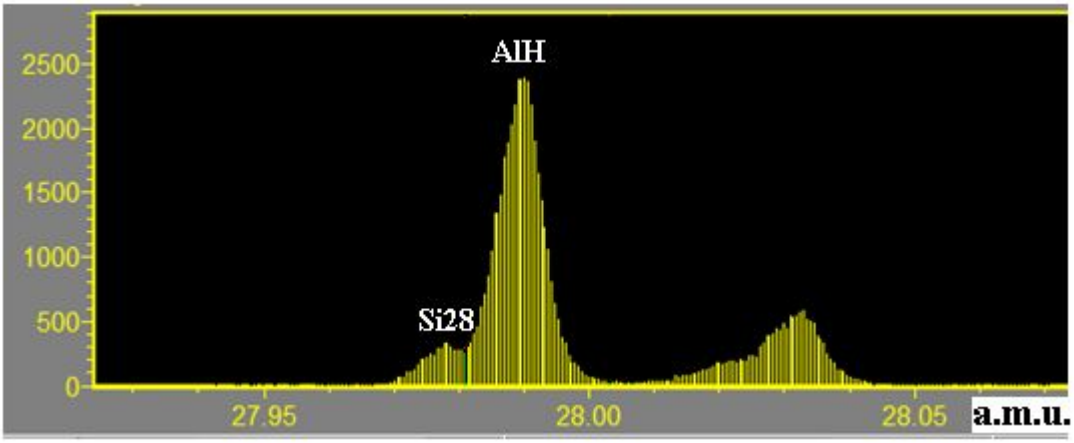

Figure 3. Mass spectrum of the initial aluminum sample in the vicinity of 28 amu. A small peak is close to the mass of the Si28 isotope (≈27.9769 amu).

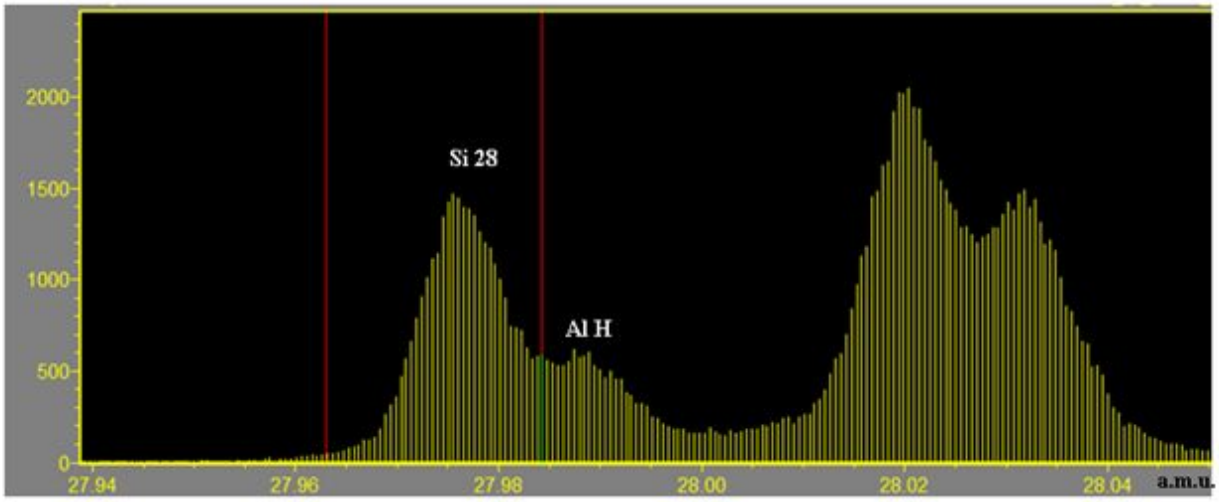

Figure 4. Mass spectrum showing the differentiation of silicon isotope Si - 28 (27.97693 a.m.u.) from aluminum hydride AlH (27.98936 amu).

2. According to the authors, the following additional arguments can be given in favor of the existence of quasi-neutron states:

i) The well-known quantum mechanical solution for the hydrogen atom (detailed, for example, in [6]) demonstrates that the probability of finding an electron is nonzero not only on atomic but also on nuclear scales.

ii) The penetration of electrons to nuclear scales is explicitly taken into account when calculating the isomer shift in the Mössbauer effect [7] and has been reliably confirmed experimentally.

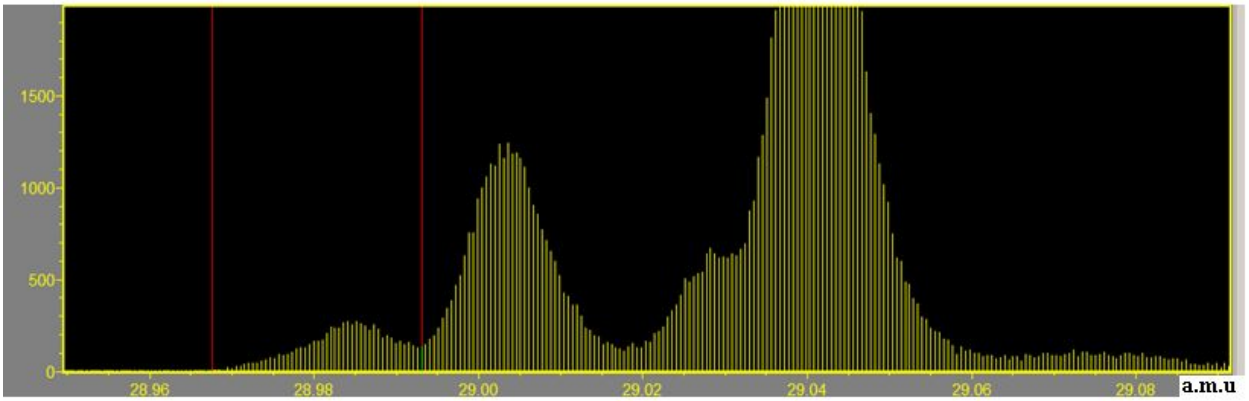

Figure 5. Mass spectrum showing the silicon гидрид $_{14}Si\ ^{28}H$ ((≈28.9847 a.m.u.).

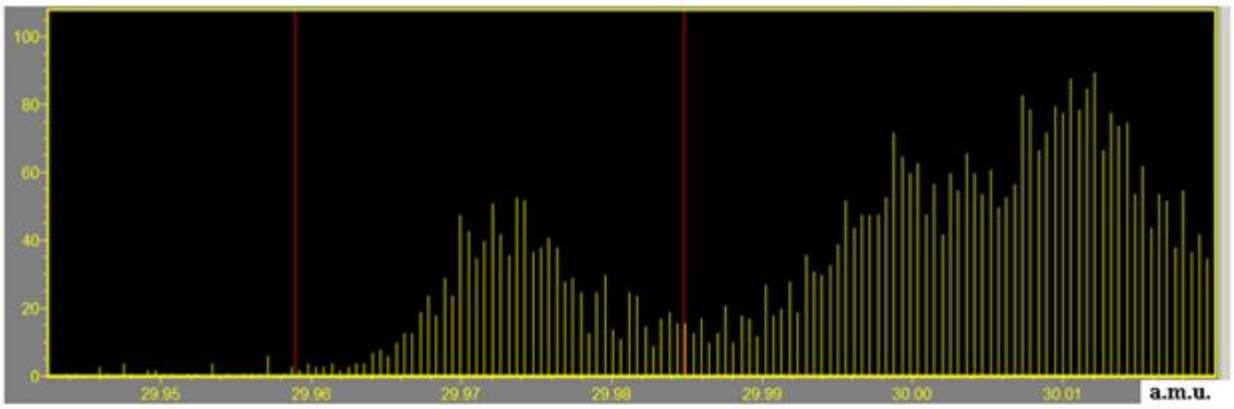

Figure 6. Mass spectrum showing the silicon isotope Si - 30 (29.97377 a.m.u.).

iii) The phenomenon of electron capture by a nucleus is also well known. This capture is associated with a weak interaction, the radius of which is about 10^{-18} m.

3. Therefore, it is natural to assume that there are states in which the electron “accompanies” the proton until the moment the proton is captured by the nucleus (during the exchange of pions according to the Yukawa mechanism).

4. It is appropriate to note that the data from modeling (by the molecular dynamics method) of the states of hydrogen atoms in a flow of free electrons in metals testify in favor of the concept of quasi-neutrons. Indeed, according to [8], there are non-stationary states in which electrons move around protons (or deuterons) in varying orbits up to $10^{-11} - 10^{-12}$ cm in size.

5. Of course, it is expedient to continue both experimental and theoretical studies on the topic of quasi-neutron states.

References

[1] M. Kashchenko, N. Kashchenko, On the Mechanism of Bismuth Transmutation in a BiPb Melt under the Influence of Nanosecond Electromagnetic Pulses, Letters on materials, vol. 9, no. 3, pp. 316–321, 2019. DOI: 10.22226/2410-3535-2019-3-316-321

[2] M. Kashchenko, N. Kashchenko, Low-temperature Nuclear Fusion: an Introduction to the Problem and its Conceptual Solution, Ural State Forestry University, Yekaterinburg, 2022, 180 p.

[3] M. Kashchenko, V. Balakirev, N. Kashchenko, M. Smirnov, Yu. Chepelev, V. Ilyushin, N. Nikolaeva, V. Pushin, The Concept of Quasineutrons and the Synthesis of Zinc from the Extraction of a Part of the Material of Copper Electrodes During Electric Current Discharges in an Aqueous Solution of NaCl, Letters on materials, vol. 10, no. 4, pp. 486–490, 2020. DOI: 10.22226/2410-3535-2020-4-486-490

[4] M.P. Kashchenko, M.A. Kovalenko, A.Ya. Kupryazhkin, N.M. Kashchenko, M.B. Smirnov, V.V. Ilyushin, Yu.L. Chepelev, V.I. Pechorsky, S.A.Krayukhin, The concept of quasineutrons and characteristic relations of the isotope content of the synthesized elements, Abstracts of the 14th International Ural Seminar “Radiation Physics of Metals and Alloys", published by IPM Ural Branch of the Russian Academy of Sciences, Yekaterinburg, abstracts, pp. 65–66. https://radiation.imp.uran.ru/Eng/AbstractBook_14.pdf

[5] M.P. Kashchenko, V.I. Pechorsky, N.M. Kashchenko, N.V. Nikolaeva, V.G. Pushin, Formation of Rhenium and Tantalum During Electrolysis of Distilled Water Using Tungsten Electrodes and the Expected Isotope Ratio, Aspects in Mining & Mineral Science , v. 8, No. 3, 2022. DOI: 10.31031/AMMS.2021.08.000688

[6] H. A. Bethe, E.E. Salpeter, Quantum mechanics of one- and two electron atoms, Springer-Verlag, Berlin, 1957, p. 564.

[7] G. K. Wertheim, Mössbauer effect. Principles and applications, Academic Press, New York and London, 1964, p 172.

[8] Kirkinsky V. A. Theory of Cold Nuclear Transmutation: problems and Solutions // Abstracts of the XXVII Russian conference on cold nuclear transmutation of chemical elements and ball lightning (Moscow 2022), pp. 44–45. https://disk.yandex.ru/i/X_7D1faIKfb3w

J. Condensed Matter Nucl. Sci. 38 (2024) 96–107

Research Article

Estimation of the Heat Generation of the Metal Composite Powder Absorbing the Pulsed Flow of Hydrogen Gas

Tomotaka Kobayashi, Ken Naitoh, Daiki Okada, Ryuki Nakagawa, and Yuta Toba

Faculty of Science and Engineering, Waseda University, Tokyo, Japan

Masaharu Uchiumi and Daisuke Nakata

Muroran Institute of Technology, Hokkaido, Japan

Abstract

Anomalous heat generation during the exposure of nickel or palladium powder to hydrogen or deuterium gas injected with pulse flow is reported here. In our previous report in ICCF23, a temperature rise of about 10 K was observed after the absorption of 0.5 MPa hydrogen gas by Pd-Ni-Zr composite powder at 244 °C. In these tests hydrogen gas was injected slowly. In this research, we added a solenoid valve to our reaction system with a small chamber, and we conducted a hydrogen gas absorption experiment with pulsed flow generated by a solenoid valve, up to 295 °C and 5 MPa. As a result, a temperature rise of over 100 K was observed. We also estimated the energy generated in the experiments. As a result, the heat release rate estimated is about 30 W, for a very small reaction chamber with only 3 g of Pd-Ni-Zr composite powder, even though we have done experiments during a very short period of fewer than ten minutes for absorption. The result indicates that the pulsed flow of hydrogen gas increases the amount of heat generation.
 ISSN 2227-3123

Keywords: anomalous heat, gas absorption, estimation, pulse flow

1. Introduction

Anomalous heat generation from the exposure of nickel or palladium powder to hydrogen or deuterium gas were reported in previous papers [1]–[2]. It was also reported that anomalous effects occur when mixed oxides of Pd and Zr absorb hydrogen (or deuterium) gas [3].

We have focused on anomalous heat generation in hydrogen (or deuterium) gas absorption at higher pressure conditions, using the metal composite powder reported in previous research. In our previous report [4], we developed a small constant-volume reaction system (shown in Fig. 1) and conducted fundamental experiments of anomalous heat generation with hydrogen gas absorption. To inject hydrogen gas gradually (slowly), a hand-operated valve is included between the safety valve and the gas supply device. In the experiments, about 10 K ΔT temperature rise was observed

 ISSN 2227-3123

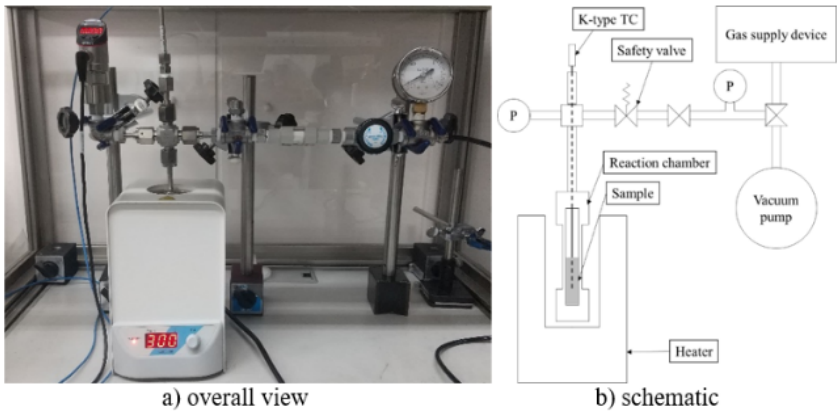

Figure 1. Reaction system developed in our previous report [4].

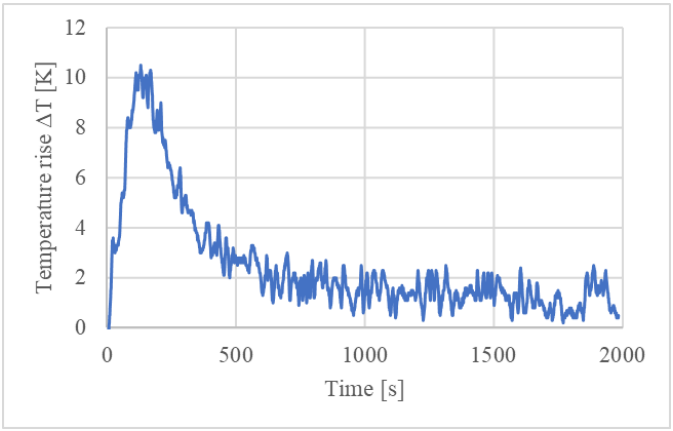

Figure 2. Experimental result in our previous report [4].

with the absorption of 0.5 MPa hydrogen gas by Pd-Ni-Zr composite powder (PNZ10r, provided by Technova Inc.) [5] at 244 °C (Fig. 2).

In this report, we added a solenoid valve to generate a pulse flow of hydrogen gas into the reaction chamber (Fig. 3). We conducted experiments on anomalous heat generation during hydrogen gas absorption. Our goal was to confirm whether the collision of the pulse jet flow on the PNZ powder surface produces increased pressure and temperature [6], which may lead to more anomalous heat generation. We also estimate the energy generated in the experiments, based on how much the sample temperature increases.

2. Experimental Device

Figure 4 shows a schematic of the reaction system. The reaction system consists of a heater, reaction chamber, K-type thermocouple, gas supply device, two pressure gauges, solenoid valve, hand valve, three-way valve, vacuum pump, and a safety valve.

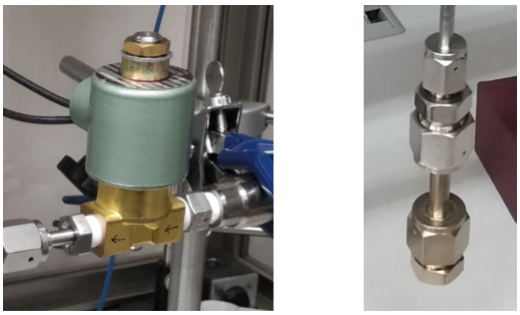

a) solenoid valve b) reaction chamber

Figure 3. Details of reaction chamber system and a solenoid valve in this report.

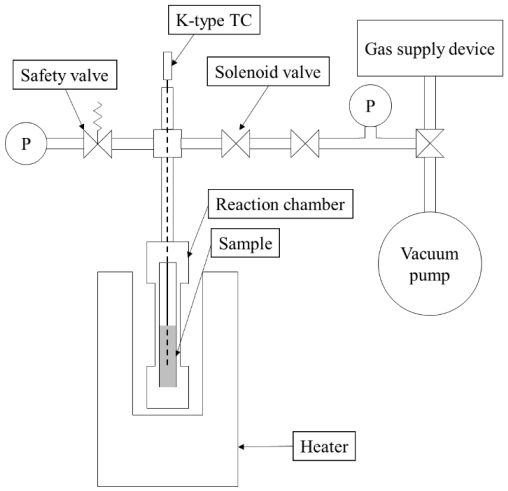

Figure 4. Schematic of the reaction system.

The reaction chamber volume is about 2 mL. The chamber is made of stainless steel (SUS316L). The heater (GBSD-300, As One Corporation) was used to preheat the reaction chamber to a range of 100 - 300 °C. The space between the heater and the reaction chamber is filled with glass beads. The K-type thermocouple (HTK0227, Hakko Electric Co., Ltd.), whose tip is embedded in the sample, is used to measure the sample temperature. The gas supply device provides hydrogen (or nitrogen) gas (1.0 MPa maximum) while performing experiments. (In experiment No. 5, a high-pressure hydrogen gas tank was used instead). The pressure of gas in the reaction chamber and the pressure of gas source are measured by two pressure gauges. In the experiments, the solenoid valve makes a pulse flow of hydrogen gas, and the hand valve regulates its flow rate. The three-way valve is used for switching gas loading and evacuation. The scroll pump (ISP-250C, Anest Iwata Corporation) is used for evacuation. The ultimate pressure (the lowest pressure that can be reached within a realistic evacuation time) of the vacuum pump is 1.6 Pa. The safety valve (RAT2V-1000, IBS Inc.) is installed to avoid fracturing the reaction chamber. The safety valve opens when the pressure in the reaction chamber exceeds 1.0 MPaG (In experiment No. 5, a relief valve that allowed up to 10 MPaG of pressure was used instead.)

Table 1. Specifications of the reaction system.

Material of reaction chamber	SUS316L
Volume of reaction chamber	2 mL
Reaction chamber internal diameter	7.40 mm
Reaction chamber external diameter	9.52 mm
Height occupied by the sample	30.6 mm
Ultimate pressure of vacuum pump	1.6 Pa
Maximum pressure of loading gas	1.0 MPa (5 MPa at experiment No. 5)
Maximum temperature of heater	300 °C
Cracking pressure of relief valve	1.0 MPaG (10 MPaG at experiment No. 5)

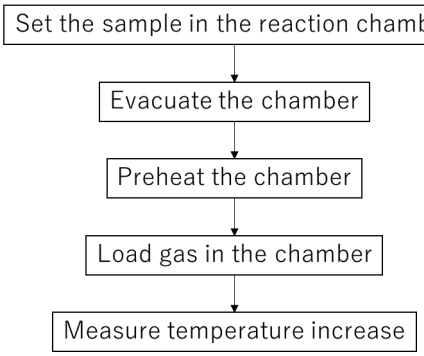

Figure 5. Experimental procedure.

Specifications of the reaction system are shown in Table 1.

3. Experimental Procedure

The experimental procedure is shown in Fig. 5. First, the sample of Pd-Ni-Zr composite powder, (designated PNZ10r [5]) is placed in the reaction chamber. Then, the reaction chamber is evacuated with the vacuum pump. After that, the chamber is preheated with the heater. After the preheating, hydrogen gas (or nitrogen gas for a control experiment) is loaded to the upstream side of the solenoid valve. The solenoid valve then opens, and the pulse flow of hydrogen (or nitrogen) gas enters the chamber (Fig. 6). A temperature increase of the sample is measured by the K-type thermocouple. At the end of the experiment, the chamber is evacuated again, so as not to leave the loaded gas in it.

4. Results

4.1. Experimental Conditions

Experimental conditions are shown in Table 2. In experiments, 3.0 g of Pd-Ni-Zr composite powder (PNZ10r, provided by Technova Inc.) [5] was used as a sample. Experiments were conducted using hydrogen gas, and nitrogen gas as the control experiment. (The control experiment using nitrogen gas is done before using hydrogen gas.) The experiments were conducted in the range of gas pressure 0.12 - 5 MPa, and initial temperature of sample 95 - 295 °C.

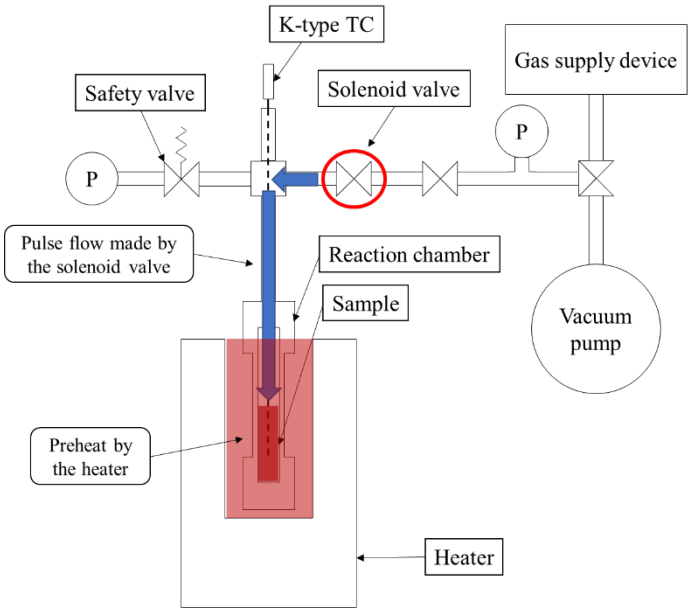

Figure 6. Schematic of the latest experiment, with pulse flow valve and preheating added.

Table 2. Experimental conditions.

Sample	Pd-Ni-Zr composite powder
Sample mass	3.0 g
Kind of gas	Hydrogen or Nitrogen (control experiment)
Gas pressure	0.12 - 5 MPa
Initial temperature	95 - 295 °C

4.2. Method of Estimating Energy

In this report, we roughly estimated the energy generated in the experiments. For simplicity, three assumptions are made for the estimate.

1. The sample temperature is uniform during the experiment.
2. The sample and the chamber absorb the generated heat.
3. The temperature on the outer surface of the chamber is the same as the sample temperature.

First, the heat absorption by the sample is considered. According to assumption 1, the heat amount absorbed by the sample Q_{sample} is calculated from Eq. 1.

$$Q_{\mathrm{sample}}\,[J] = \Delta T_{\mathrm{max}}\,[K] \times C_{\mathrm{sample}}[J/K] \tag{1}$$

where ΔT_{max} denotes the maximum temperature rise in the experiment and C_{sample} $(= 1.38\ [J/K])$ denotes the heat capacity of the sample.

Next, the heat absorbed by the reaction chamber is considered. To simplify, it is assumed that the temperature distribution in the reaction chamber wall is uniform and equals the temperature in the powder because the time constant of the wall is small compared to the time constant of the powder.

Table 3. Results of the experiments without pulse flow.

No.	Sample	Gas pressure	Initial temp.	Temp. rise	Heat generation	
1	Pd-Ni-Zr 3.0 g	0.12 MPa	95 °C	1.2 K	5.47 J	0.01 W
2	Pd-Ni-Zr 3.0 g	0.9 MPa	240 °C	12.4 K	56.5 J	0.72 W

Table 4. Results of the experiments with pulse flow.

No.	Sample	Gas pressure	Initial temp.	Temp. rise	Heat generation	
3	Pd-Ni-Zr 3.0 g	0.12 MPa	95 °C	9.1 K	41.5 J	1.06 W
4	Pd-Ni-Zr 3.0 g	0.9 MPa	240 °C	35.0 K	159 J	17.7 W
5	Pd-Ni-Zr 3.0 g	5 MPa	295 °C	115 K	524 J	105 W

As a further simplification we assume that the heat loss through the insulation is negligible. According to assumption 3, the heat amount absorbed by the chamber wall Q_{wall} is calculated from Eq. 2.

$$Q_{\mathrm{wall}}\,[J] = \Delta T_{\max}\,[K] \times C_{\mathrm{wall}}[J/K] \tag{2}$$

where $C_{\mathrm{wall}}\,(= 3.17\,[J/K])$ denotes the heat capacity of the chamber wall.

Thus, the energy is estimated from Eqs. 3 and 4 derived from the above assumptions.

$$Q\,[J] = Q_{\mathrm{sample}} + Q_{\mathrm{wall}} \tag{3}$$

$$P\,[W] = Q\,[J]/t[s] \tag{4}$$

where t denotes the time from the start of the experiments to the sample temperature becoming maximum.

4.3. Summary of Experimental Results for Heat Release Rates

Table 3 shows the results and conditions of the experiments without pulse flow, whereas Table 4 shows results from the experiments with pulse flow.

To bolster these results, let us assume that only the center of the sample is $\Delta T_{\max}$, the adiabatic assumption is close to the true condition, so in that case we should assume that the sample absorbs all the generated heat. In this case, Q is calculated using only Eq. 1 and the estimated heat is 159 J in experiment No. 5. The true value of generated heat is somewhere in between those.

4.4. Details of Experimental Data for Conditions No. 1 and No. 3 (Pd-Ni-Zr 3.0 g, 95 °C, 0.12 MPa)

In Fig. 7 in condition No. 1 without the pulse flow, time-dependent experimental temperatures are demonstrated with 3.0 g of Pd-Ni-Zr composite powder, 0.12 MPa of gas pressure, and 95 °C initial temperature. In Fig. 7, the orange line is for nitrogen gas loaded, whereas the blue line is for hydrogen gas. Figure 8 shows the temperature rise from the control experiment with nitrogen gas, i.e., the temperature difference between cases of hydrogen and nitrogen. In this experiment, the temperature rise begins just after hydrogen gas loading. However, there is no obvious difference from the control experiment. The estimated energy and power generated in the experiment are very small, 5.47 J and 0.01 W.

In Fig. 9 in condition No. 3 with the pulse flow, time-dependent experimental temperatures are demonstrated with 3.0 g of Pd-Ni-Zr composite powder, 0.12 MPa of gas pressure, and 95 °C initial temperature. The orange line shows results for nitrogen gas, and the blue line for hydrogen gas. Figure 10 shows the temperature difference between cases of hydrogen and nitrogen.

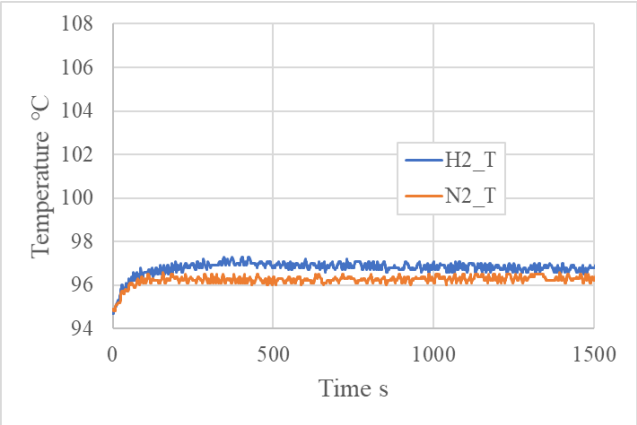

Figure 7. Result of the experiment (No. 1) [7].

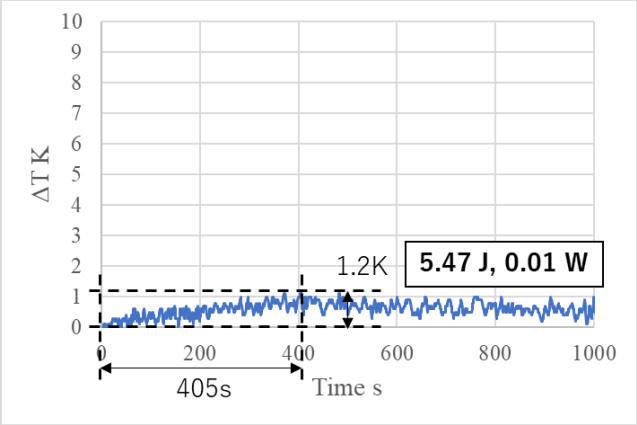

Figure 8. Temperature rise ΔT with estimation of heat generation (No. 1).

A temperature rise of 9.1 K is observed 39 seconds after the beginning. The estimated energy and power generated in the experiment are 41.5 J and 1.06 W.

A larger temperature rise and more heat generation rate for Condition No. 3, pushed by pulse flow, are observed in comparison with No. 1 having no pulse flow, while Condition No. 3 shows earlier timing of the largest temperature.

4.5. Details of Experimental Data for Conditions No. 2 and No. 4 (Pd-Ni-Zr 3.0 g, 240 °C, 0.9 MPa)

In our recent experiments we increased the initial pressure of the hydrogen gas. In Fig. 11, in condition No. 2, without the pulse flow, time-dependent experimental temperatures are demonstrated with 3.0 g of Pd-Ni-Zr composite powder, 0.9 MPa of gas pressure, and 240 °C initial temperature. Figure 12 shows the temperature rise from the control experiment for nitrogen gas, i.e., the temperature difference between the cases of hydrogen and nitrogen. A temperature

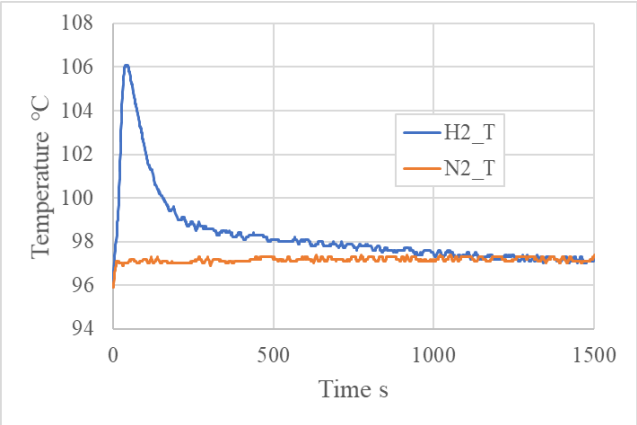

Figure 9. Result of the experiment (No. 3) [7].

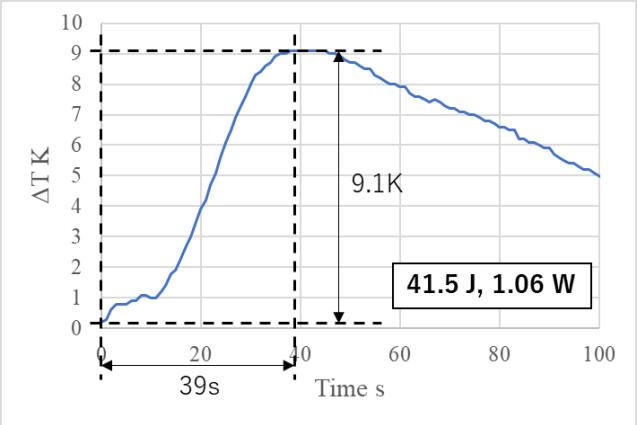

Figure 10. Temperature rise ΔT with estimation of heat generation (No. 3).

rise of 12.4 K of temperature rise is observed 79 seconds after beginning. The estimated energy and power generated in the experiment are 56.5 J and 0.72 W.

In Fig. 13 in condition No. 4 with the pulse flow, time-dependent experimental temperatures are demonstrated with 3.0 g of Pd-Ni-Zr composite powder, 0.9 MPa of gas pressure, and 240 °C initial temperature. Figure 14 shows the temperature difference between cases of hydrogen and nitrogen. A temperature rise of 35.0 K is observed 9 seconds after the test begins. The estimated energy and power generated in the experiment are 159 J and 17.7 W.

It is stressed that the higher pressure of hydrogen gas brings larger temperature gain due to absorption.

4.6. Details of Experimental Data for Condition No. 5 (Pd-Ni-Zr 3.0 g, 295 °C, 5 MPa, with the Pulse Flow)

In Figs. 15 and 16 at condition No. 5 with the pulse flow, time-dependent experimental temperatures are demonstrated with 3.0 g of Pd-Ni-Zr composite powder, 5 MPa of gas pressure, and the initial temperature of 295 °C. In Fig. 15,

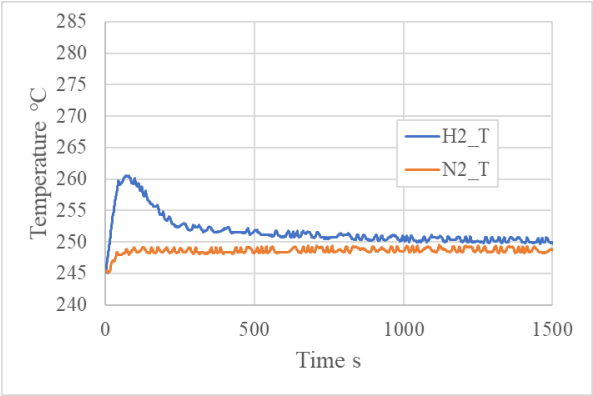

Figure 11. Result of the experiment (No. 2) [7].

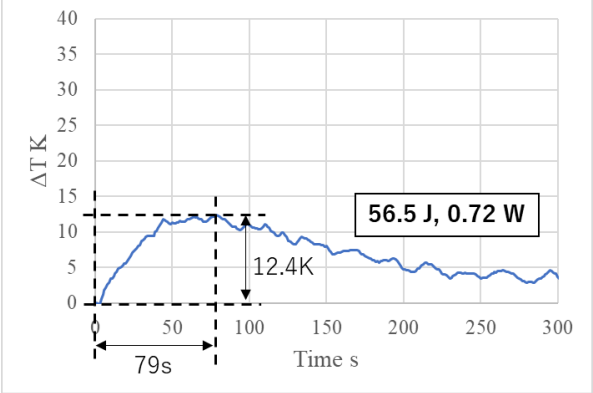

Figure 12. Temperature rise ΔT with estimation of heat generation (No. 2).

a yellow line shows the time history of the pressure in the reaction chamber, and the blue line shows the time history of the sample temperature. The temperature rise begins just after hydrogen gas loading. After the temperature rise begins, it increases by 115 K in 5 seconds. The estimated energy and power generated in the experiment are 524 J and 105 W (In this experiment, the control experiment with nitrogen gas was not conducted. Energy is estimated from the temperature rise from the start of the experiment and the time to reach the maximum temperature.)

Because we have no control experiment with nitrogen gas for this test, we had to carefully calibrate the measured value of temperature rise to estimate the heat accurately. When hydrogen gas is loaded in the chamber without the sample, a temperature rise of about 20 K is observed. From this, the actual temperature rise with the sample is estimated to be 95 K. In this case, the estimated energy and power generated in the experiment are 433 J and 86.6 W.

It should be noted that the estimated heat generation in this experiment is much larger than the predicted heat generation by a chemical reaction. The principal exothermic chemical reactions are palladium hydration and hydrogen oxidation. (In this experiment, zirconium oxide cannot be reduced by hydrogen, and nickel oxide is hardly reduced.)

First, the heat generated by the palladium hydration is predicted to be about 20 J at most (assuming the palladium absorbs hydrogen until H / Pd = 1). The 3.0 g of the sample contains about 0.1 g of palladium [5] and the heat release by

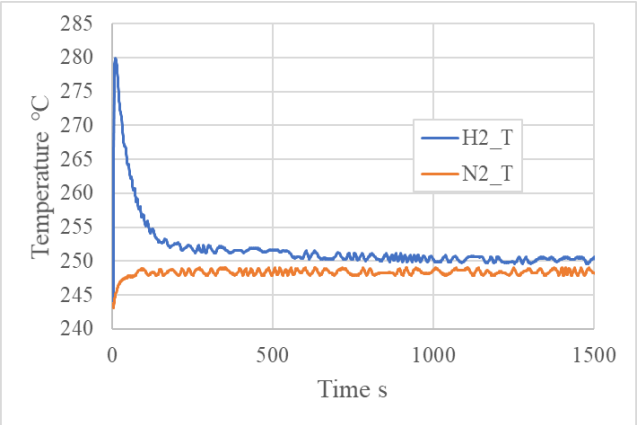

Figure 13. Result of the experiment (No. 4) [7].

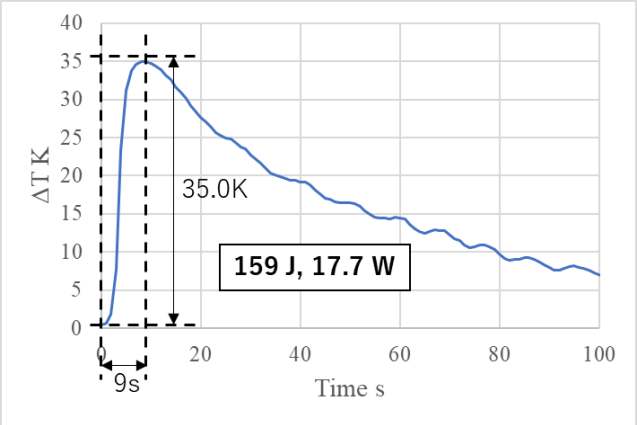

Figure 14. Temperature rise ΔT with estimation of heat generation (No. 4).

palladium hydration is 19.1 kJ/mol H [8]. On the other hand, the heat generated by the hydrogen oxidation is predicted about 3 J at most (assuming 1 kPa of air remains when the hydrogen gas is loaded), where the heat generation by hydrogen oxidation is 241.83 kJ/mol O [9] and the inner volume of the reaction system (including reaction chamber and the surrounding pipes) is about 50 mL. Even the sum of the maximum heat generation of these reactions (about 23 J) is much smaller than the estimated energy generated in the experiment (433 J). This result may show the anomalous heat generation that occurred in experiment No. 5 (Pd-Ni-Zr 3.0 g, 295 °C, 5 MPa, with the pulse flow). In the near future, we plan to conduct further experiments and improve measurement (and estimation) accuracy to ascertain what the heat generation observed in the experiment consists of.

In addition, these results may show that heat generation in the hydrogen gas absorption by the Pd-Ni-Zr sample has a positive pressure dependence. While the sample temperature is higher than the heater temperature, outward heat flow occurs. However, the estimated heat flux is about 0.7 W at maximum (where the temperature rise is 115 K), assuming the heat transfer from the reaction chamber (9.52 mm diameter × 30.6 mm high cylinder) to the heater. (Our method

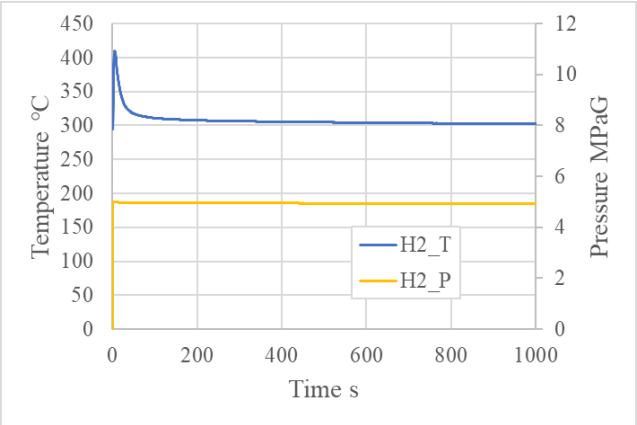

Figure 15. Result of the experiment (No. 5).

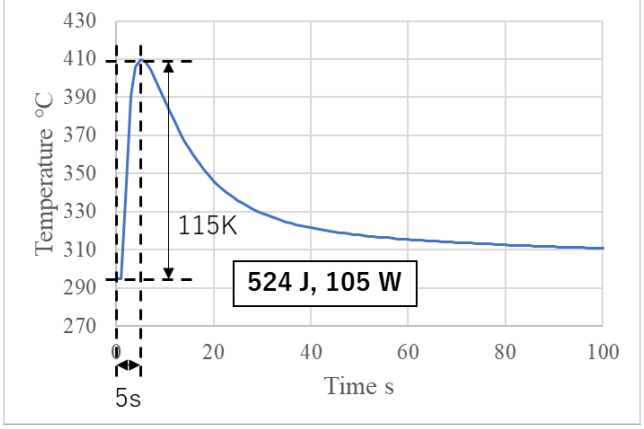

Figure 16. Estimation of heat generation (No. 5).

of estimating the heat transfer is described in section 4.2). Thus, it can be said that heat generation in the experiment has a positive pressure dependence.

5. Conclusion

We first conducted experiments on anomalous heat generation in hydrogen gas absorption with the pulse flow of hydrogen gas to confirm the effect of the pulse flow on anomalous heat generation, while with higher pressures of hydrogen gas loaded. The results obtained show that the pulse flow and higher-pressure conditions produce more heat in hydrogen gas absorption by Pd-Ni-Zr composite powder.

Next, we also tested at a very high-pressure condition of about 5 MPa, which leads to a much larger heat release of about 524 J. This is also larger than the maximum heat generation from a chemical reaction (23 J). This result apparently shows anomalous heat generation occurred in the experiment. In the near future, we will conduct further

experiments and improve measurement (and estimation) accuracy to ascertain what the heat generation observed in the experiment consists of.

Credit Authorship Contribution Statement

Mr. Tomotaka Kobayashi and Prof. Dr. Ken Naitoh mainly executed the plans, theoretical and computational studies, developments of constant chamber reactors, and their experiments at Waseda University and the Shiraoi engine test research center of Muroran Institute of Technology. Prof. Dr. Masaharu Uchiumi, Prof. Dr. Daisuke Nakata, and Mr. Tomoyuki Takano made important contributions to the setup and operation of experiments with heat generation due to high-pressure hydrogen gas and metal particles at nanometer size in constant-volume chamber, at the Shiraoi engine test research center of Muroran Institute of Technology.

Acknowledgements

This work was supported by Grant-in-Aid for JSPS Fellows (21J21973) and the grant of The Thermal & Electric Energy Technology Foundation (TEET). The experiments on anomalous heat generation in hydrogen gas absorption at higher than 1 MPa were performed at Shiraoi engine test research center of the Muroran Institute of Technology with Pd-Ni-Zr composite powder made by Technova Inc. We appreciate Technova Inc. for the useful discussion and for providing the sample of Pd-Ni-Zr powder. Sincere thanks are also due to the other members of the Naitoh Laboratory for their help.

References

[1] A.G. Parkhomov, V.A. Zhigalov, S.N. Zabavin, A.G. Sobolev, T.R. Timerbulatov, "Nickel-hydrogen heat generator continuously working for 7 months," *22nd International Conference on Condensed Matter Nuclear Science (ICCF22) Book of Abstracts*, Assisi, p. 77, 2019.

[2] Y. Arata, Y. Zhang, "The Establishment of Solid Nuclear Fusion Reactor," *J. High Temp. Soc.*, vol. 34, pp. 85–93, 2008.

[3] Kitamura, A., Nohmi, T., Sasaki, Y., Taniike, A., Takahashi, A., Seto, R., & Fujita, Y. (2009). Anomalous effects in charging of Pd powders with high density hydrogen isotopes. *Physics Letters A, 373*(35), 3109–3112. https://doi.org/10.1016/j.physleta.2009.06.061

[4] T. Kobayashi, J. Shigemura, K. Naitoh, Y. Mori, R. Seto, J. Hachisuka, "Temperature and pressure dependence of anomalous heat generation occurring in hydrogen gas absorption by metal powder," *J. Condensed Matter Nucl. Sci*. vol. 36, pp. 318–326, 2022.

[5] A. Takahashi, H. Ido, A. Hattori, R. Seto, et al., "Latest Progress in Research on AHE and Circumstantial Nuclear Evidence by Interaction of Nano-Metal and H(D)-Gas", *J. Condensed Matter Nucl. Sci.*, vol. 33, pp. 14–32, 2020.

[6] Konagaya, R., Naitoh, K., Kobayashi, T., Isshiki, Y. et al., "Two Prototype Engines with Colliding and Compression of Pulsed Supermulti-Jets through a Focusing Process, Leading to Nearly Complete Air Insulation and Relatively Silent High Compression for Automobiles, Motorcycles, Aircrafts, and Rockets," SAE Technical Paper 2020-01-0837, 2020, https://doi.org/10.4271/2020-01-0837.

[7] T. Kobayashi, K. Naitoh, J. Shigemura, D. Okada, Y. Nomura, "Heat generation of metal composite powder caused by the pulse flow of hydrogen gas," *Proceedings of the* 22^{nd} *Meeting of Japan CF Research Society JCF 22*, pp. 40–49, 2022.

[8] T. B. Flanagan, W. Luo, and J. D. Clewley, "Calorimetric enthalpies of absorption and desorption of protium and deuterium by palladium," *Journal of the Less-Common Metals*, 172–144, pp. 42–55, 1991.

[9] Chase, M.W., Jr., NIST-JANAF Themochemical Tables, Fourth Edition, J. Phys. Chem. Ref. Data, Monograph 9, 1998, 1–1951.

J. Condensed Matter Nucl. Sci. 38 (2024) 108–120

Research Article

More About Why Cold Fusion Will Lower the Cost of Energy ICCF24

Jed Rothwell
LENR-CANR.org

Abstract

Cold fusion will lower the cost of energy because:
The fuel costs far less than any other.[1]
Generators will be optimized for low cost.
It can be decentralized with no distribution grid.

With a decentralized system, consumers will purchase their own home generator instead of using electric power company equipment. Subtracting the cost of power company equipment and fuel, and adding in the cost of the home generator, cold fusion should reduce the cost of energy by a factor of 21.

Ultimately, the cost of generators is likely to fall by a factor of ~200, from $2,000/kW to $10/kW, which is the cost difference between a power company generator and a mass produced automobile engine. I wrote a paper about this in 2016 [1]. This is an expanded look at the subject.
 ISSN 2227-3123

Keywords: Cold fusion, economics, future, energy cost, decentralized energy

1. INTRODUCTION

Let us start with some assumptions. With enough R&D, cold fusion will become –

- Controllable
- With high enough power density for reasonably compact heat engines.
- With reasonably good Carnot efficiency.

That much seems certain. The following is likely:

- Cells will be fully controlled.

[1] D-D fusion with heavy water costing $1,000/kg is roughly 2,100 times cheaper than gasoline. H-H fusion with ordinary water is millions of times cheaper. Most of the cost of heavy water is for the energy it takes to separate it from ordinary water, so with cold fusion it would cost much less than $1,000.

 ISSN 2227-3123

- Cells will be inexpensive. Unless palladium is needed, the materials are inexpensive. They do not require high precision manufacturing. They should be no more expensive per watt of capacity than batteries.
- Cells will be safe. Tritium will either be absent or fully contained the way it is contained in wristwatches and hallway exit signs today. Cold fusion cells will be fully sealed, even more than today's batteries, to avoid contamination, and because there is no need to open them to replenish the hydrogen or deuterium. Enough hydrogen will be added during manufacturing to last for the life of the device.
- The COP (coefficient of production) will be high, or infinite. It is already infinite with some gas loading methods.

The COP is the ratio of input power to output power. [2] This is a big problem with experimental devices today. Electrochemical cells sometimes need much more input power than they produce as excess heat. On the other hand, some gas loaded systems produce excess heat with no input power. The COP is infinite. I assume input power will be reduced to a minimum or eliminated.

Cold fusion energy density is millions of times greater than any chemical reaction because it is nuclear fusion. This was confirmed by measuring the ratio of helium to heat, 24 MeV per helium atom, the same as one of the D-D fusion paths [2]. Each gram of deuterium releases 345,000 megajoules [3].

Needless to say, cold fusion cells are far from commercialization today. They cannot be controlled. They are very difficult to replicate. Most produce only a fraction of a watt, although a few have produced 50 to 100 W. How will we make them into a practical source of energy? As I see it, here is what must happen. First, it must become generally known that cold fusion is real and that it will probably replace other sources of energy. Once that happens, large industrial corporations will invest huge sums in R&D. Perhaps this will cost $10 million per day for 5 years, ~$18 billion total. This will include money spent on peripheral technologies needed to implement cold fusion, such as improved thermoelectric devices. Corporations have spent about $19 billion on self-driving automobiles so far, so this is not an unreasonable sum.

Will this R&D succeed? Probably. In modern history we have made astounding progress in science and technology. Consider other inventions such as internal combustion engines, transistors, masers, and lasers. The initial laboratory prototypes took years to produce, and they were unreliable. The first maser prototype took three years to make [4]. Today we manufacture millions of them, and all are extremely reliable.

Can cold fusion produce high temperatures and steady power? Can it produce power density high enough for practical use? Yes, we know it can, because it has already done so in a few experiments. One produced 100 W continuously for 30 days [5]. If something can happen once in a laboratory, we can learn to make it happen millions of times a day in the real world.

Finally, will corporations spend $18 billion on cold fusion? Yes, they will, because if they do not, their competition will put them out of business. That is the same reason automobile companies are spending billions to develop self-driving cars.

The other reason companies will spend $18 billion is that revenues to first movers will be roughly $10 trillion over 30 years. Here is the basis for this estimate. I expect that when the market matures, we will spend $340 billion per year on cold fusion generators, water heaters and other equipment. This value is discussed below. That $340 billion will go to the industrial companies that make the equipment. Most will go to the first movers, because once you take the lead in something like this, you keep it for a long time, the way Ford and GM dominated the automobile business for decades, and IBM dominated computers. $340 billion for thirty years is $10.2 trillion.

[2]The term COP is borrowed from heat pump technology, where it means the ratio of input electric power to the heat transferred by the compressor. A heat pump does not create energy, whereas cold fusion does, so arguably this term is inaccurate.

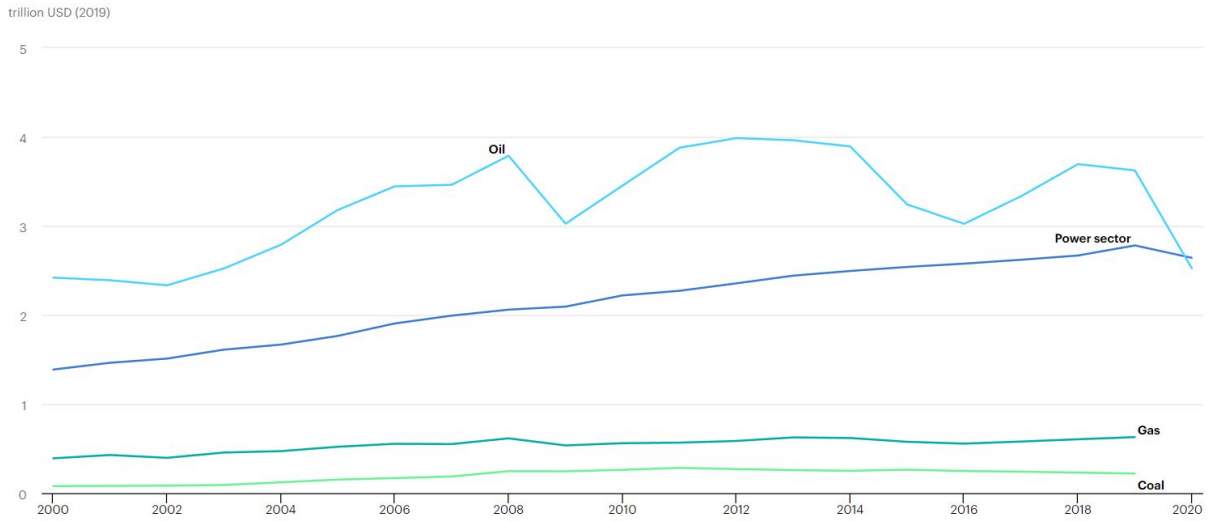

Figure 1. Global end-use spending on energy, 2000-2020, IEA, Paris https://www.iea.org/data-and-statistics/charts/global-end-use-spending-on-energy-2000-2020. The cost of coal and natural gas used in the Power sector is included in that sector. The Gas and Coal shown below that are used in other sectors. 2019 totals are: Oil $3.7 trillion, Power sector $2.8 trillion, Gas $0.6 trillion, Coal $0.2 trillion, grand total $7.3 trillion.

The $10.2 trillion will come out of the pockets of energy companies. GE will divert a fraction of ExxonMobil's revenue to itself, the way automobile companies transferred revenue from railroads to themselves in the 1920s, when many people began driving cars instead of taking trains.

End users worldwide now pay $7.3 trillion for fossil fuel and electricity (Figure 1). $340 billion is 21 times less. Such a drastic cost reduction is irresistible. People will stop buying gasoline and electricity. Energy companies will go bankrupt.

After 20 years, patents will expire, competition will increase, and cold fusion will become a commodity. Profits will be lower. Still, over 30 years the first movers will make trillions of dollars in revenue.

"Becoming a commodity" means competition drives down the cost until it approaches the cost of production. We can estimate the cost of production from the materials, the degree of precision manufacturing, and so on. No doubt the first cold fusion generators will sell at a large premium. But the cost of production will be low. A cold fusion cell should cost roughly as much as a large battery. The heat engines will cost about as much as today's models. From this, we can predict cold fusion generators will eventually be much cheaper than power company generators. Here is the basis for the estimated cost. Figure 2 shows an electric power bill. In many cities the bill now shows two main items: supply, and delivery.

1. SUPPLY. This is the cost of the generator and the fuel. It is around two-thirds of the total bill, where the generator and fuel are each about one third.
2. DELIVERY. The cost of delivering the power over the grid. This is usually around one third of bill.

The balance is somewhat different in this sample bill, with 40% going to the grid Delivery portion.

Cold fusion does not need fuel, or the grid, which leaves only the cost of the generator. How much will a cold fusion generator cost? To estimate that, let us look at a 58 MW LM6000 gas turbine generator from GE (Figure 3). It costs about $50 million, around $960/kW of capacity. The "overnight cost" comes to $1,376 per kilowatt. This is a

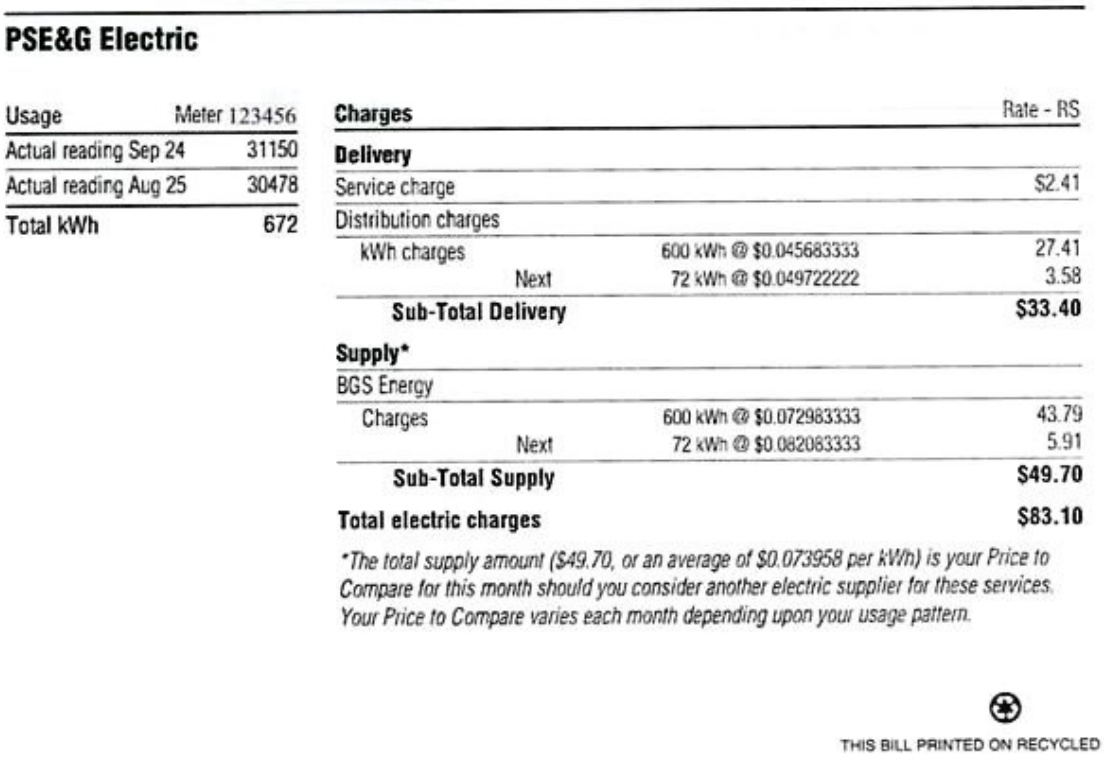

PSE&G Electric

Usage	Meter 123456
Actual reading Sep 24	31150
Actual reading Aug 25	30478
Total kWh	672

Charges		Rate - RS
Delivery		
Service charge		$2.41
Distribution charges		
kWh charges	600 kWh @ $0.045683333	27.41
Next	72 kWh @ $0.049722222	3.58
Sub-Total Delivery		**$33.40**
Supply*		
BGS Energy		
Charges	600 kWh @ $0.072983333	43.79
Next	72 kWh @ $0.082083333	5.91
Sub-Total Supply		**$49.70**
Total electric charges		**$83.10**

*The total supply amount ($49.70, or an average of $0.073958 per kWh) is your Price to Compare for this month should you consider another electric supplier for these services. Your Price to Compare varies each month depending upon your usage pattern.

THIS BILL PRINTED ON RECYCLED PAPER

Figure 2. A sample electric bill from New Jersey. Supply is 60% of the cost, which is probably about 30% for the generators and 30% for fuel. Delivery is 40%. Bills are split into Supply and Delivery because in New Jersey and other states, customers can choose which company will supply electricity, but there is only one distribution grid. As noted on this bill, customers can select another company for Supply.

masterpiece of 21st century technology. It is remarkably efficient. It has to be, because otherwise the fuel would end up costing much more over the life of the generator. This generator is optimized for efficiency.

Figure 4 shows a Chevrolet automobile engine, 145 kW. It is abominably inefficient (Figure 5). However, it costs only $1,460, with Free Shipping. That comes to $10 per kilowatt. That is 130 times cheaper than the GE generator. It is 600 times cheaper than some other power company generators. It is cheaper because it is mass produced and because it is optimized for low cost. Since cold fusion energy costs nothing, we will optimize the equipment for low cost. It will eventually be about 200 times cheaper than today's power company generator.

Granted, an automobile engine is not a generator. You have to add an alternator to make it into a generator, but this does not cost much. You also need a cold fusion cell. As noted, this should cost roughly as much as a battery. There are other differences between a mass produced heat engine and the GE generator, such as the duty cycle, and the longevity of equipment. I discussed these in the previous paper [1].

Cold fusion energy is free, but so is wind and sunlight. Why should cold fusion be cheaper than wind or solar? The equipment will be optimized for low cost, but so are wind and solar. However, these sources have problems that will never allow them to be as cheap as cold fusion, including:

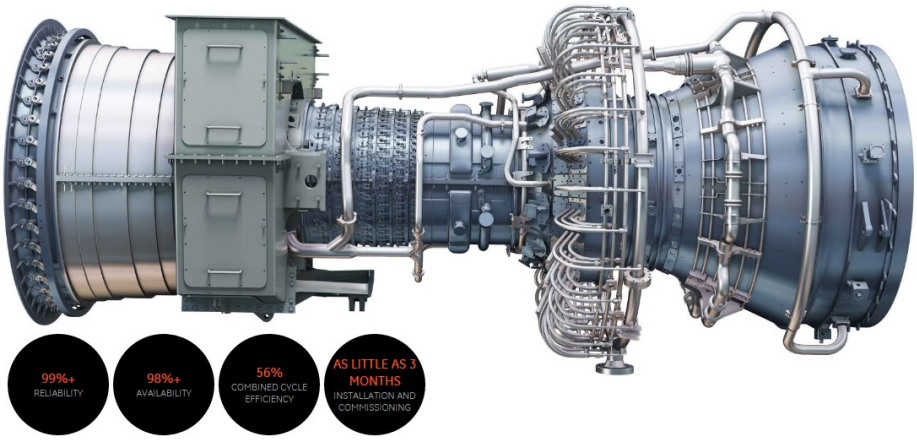

Figure 3. General Electric LM6000-PF gas turbine generator (GE Power Generation).

Figure 4. Chevrolet Goodwrench 350ci engine (www.jegs.com).

- Low power density.
- Intermittency.
- Limited availability (you need a lot of sunlight or wind).
- Wind needs a distribution grid, because it only works with gigantic machines, most of them far from major cities.
- Solar needs a grid because power density is low.

Solar power density is so low that in many parts of the U.S. such as the Midwest, even if you cover a large roof with panels (Figure 6, left), they produce only about 612 kWh per month. The average US house consumes 911 kWh per month, so you need supplemental electricity from the grid. You have to pay for the grid even when you have solar. Figure 6

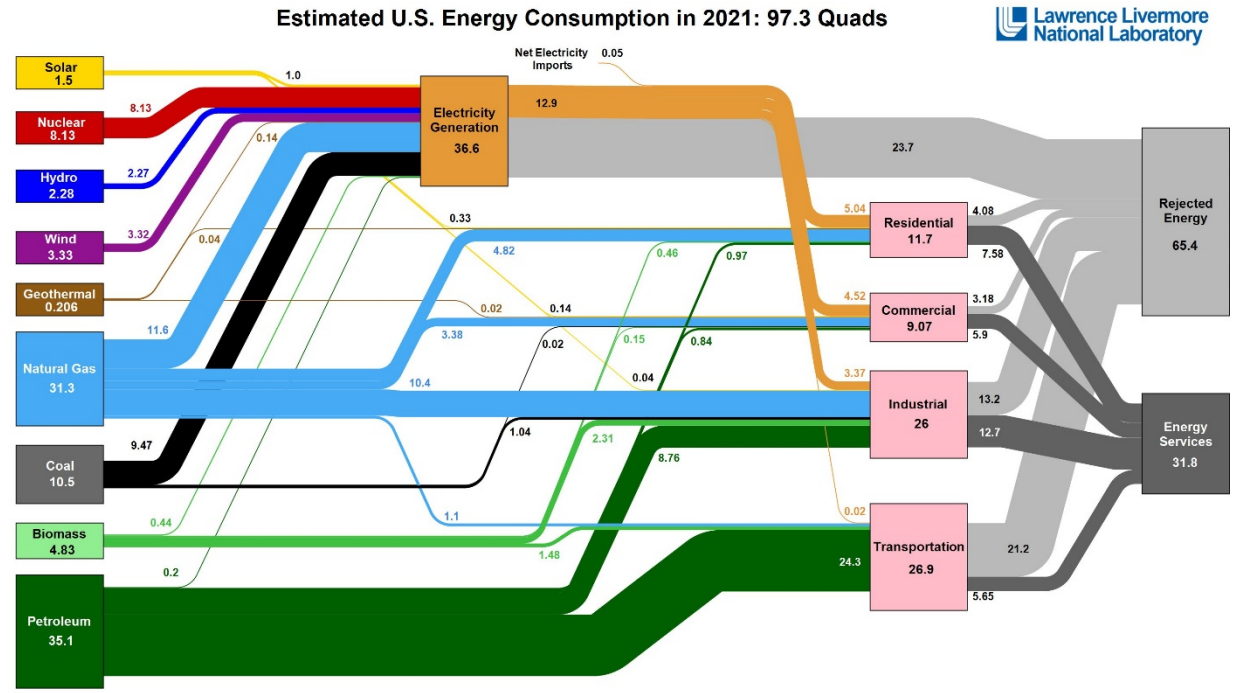

Source: LLNL March, 2022. Data is based on DOE/EIA MER (2021). If this information or a reproduction of it is used, credit must be given to the Lawrence Livermore National laboratory and the Department of energy, under whose auspices the work was performed. Distributed electricity represents only retail electricity sales and does not include self-generation. EIA reports conception of renewable resources (i.e., Hydro, wind, geothermal and solar) for electricity in BTU-equivalent values by assuming a typical fossil fuel plant heat rate. The efficiency of electricity production is calculated as the total retail electricity delivered divided by the primary energy input into electricity generation. End use efficiency is estimated as 65% for the residential sector, 65% for the commercial sector, 21% for the transportation sector and 49% for the industrial sector, which was updated in 2017 to reflect DOE's analysis of manufacturing. Totals may not equal the sum of components due to independent rounding. LLNL-MI-410527

Figure 5. Estimated U.S. Energy Consumption in 2021, Lawrence Livermore National Lab. (https://flowcharts.llnl.gov/sites/flowcharts/files/2022-04/Energy_2021_United-States_0.png) Most petroleum is used in automobile engines in the transportation sector. 21% converts to Energy Services and 79% is wasted. Other sectors convert 35% to 66% to Energy Services.

(right) shows a 20 kW deluxe standby generator (Generac, Guardian model). It will produce up to 14,600 kWh a month. It is much smaller than the solar array. It is also far smaller than your share of power company equipment, because that includes the generator, high-voltage power lines, the poles, wires, the round transformers in your neighborhood, plus the coal mines, the railroads that bring the coal, natural gas pipelines, and so on. You do not see all those things, so you do not realize how big they are, or how expensive.

The Generac generator is 122 cm × 63.5 cm × 74 cm, or 109 L. A 20 kW cold fusion home generator heat engine will be about this big. This generator has an internal combustion piston engine. A first generation cold fusion version would probably be a steam piston engine with a boiler powered by cold fusion.

Figure 6. Left: solar panels on roof. Right: a 21 kW standby generator (Generac, Guardian model).

Table 1. Generator cost per kilowatt of capacity for home generators (Lowe's retail)

Generator size	Cost per kilowatt
5300 W	$113
3500 W	$151
800 W	$230
21,000 W deluxe standby	$305

2. ROUGH ESTIMATE OF COST OF A 20 KW COLD FUSION GENERATOR

The 21 kW natural gas fired standby generator in Figure 6 costs $6,400 retail at Lowe's. A standby generator is more expensive than an ordinary gasoline generator because it includes control electronics and equipment to switch off the power company electricity and turn on the generator in the event of a power failure. An ordinary 21 kW gasoline generator costs about $4,200. Costs per kilowatt range from $113/kW to $305/kW (Table 1). The "overnight" cost of power company generators per kilowatt of capacity ranges from $676/kW for natural gas generators up to $6,599 for advanced coal plants (Table 2). (EIA definition: "The term 'overnight' refers to the cost of the project as if no interest were incurred during its construction.")

Some generator equipment is expensive to purchase, but inexpensive to operate. This is especially true of solar photovoltaic, because the fuel cost is zero. The cheapest natural gas generator is a combustion turbine – industrial frame, but combined cycle units are more efficient, so they are cheaper over the life of the equipment. The unsubsidized, levelized cost of a megawatt hour of electricity from various generators is shown in Table 3.

Assuming the cold fusion cell itself is not expensive, with today's equipment a home generator would be 5 or 10 times cheaper than a power company generator.

Mass production will bring down the cost. We should manufacture 170 million devices per year, about twice as many as the number of automobiles we make. This would meet worldwide demand for energy, except for the transportation sector. [3] Most devices would be generators, but some would be things like water heaters and pumps. The

[3]Cold fusion would greatly reduce primary energy consumption and costs in the transportation sector. Details are not covered in this paper because transportation has a very different profile from other energy applications.

Table 2. Power company generator cost per kilowatt of capacity ("overnight" cost). (Energy Information Agency) [6]

Generator type	Cost per kilowatt
Natural gas. Combustion turbine—industrial frame	$713
Wind (Great Plains)	$1,265
Solar photovoltaic—tracking	$1,313
Natural gas. Combined-cycle with 90% CCS	$2,481
Coal. Ultra-Supercritical coal (USC) (cheapest)	$3,676
Coal. USC with 90% CCS (most expensive)	$5,876

Table 3. Unsubsidized, levelized cost of a megawatt hour of electricity from various generators. (Lazard) [7]

Generator type	Lowest cost	Highest cost
Solar photovoltaic, Thin Film Utility Scale	$28	$37
Wind, Onshore	$26	$50
Natural gas, Combined cycle	$45	$74
Coal	$65	$152
Natural gas, Peaking	$151	$196

average size would be 20 kW. This is how much an average First World house needs, estimated by online programs to configure 'whole home' standby power generators. Some would be smaller for portable power, while others would be much larger, to power factories and the like.

20 kW generators now cost $4,200, but manufactured in large numbers I expect the price will fall to around $2,000 including the cold fusion cell. (This is still well above the cost per kilowatt of an automobile engine, alternator and battery.) Suppose we make 170 million per year. Suppose they last fifteen years, which is about how long internal combustion engines or refrigerator compressor motors last. The cost would be $340 billion, which is 9% of what we now pay for automobiles, or 5% of what we now pay for energy. [4]

Worldwide capacity would be 51,000 GW of electricity. Since cold fusion generators will be about 33% efficient, worldwide primary energy capacity would be 153,000 GWt (gigawatts thermal). [5] That is 7 times more generating capacity and 9 times more primary energy capacity than we have today. That does not mean we would consume 7 times more electricity. It means we would have that much on tap, to use if we want. People do not run small generators or space heaters at full capacity 24 hours a day. The point of making far more capacity than we now have, or than we would actually use at any given moment, is to give everyone access to all the energy they want without the expense of a distribution grid.

$340 billion per year is what it would cost at first, but costs would gradually fall. Think about the development of personal computers in the 1980s. They began with the microprocessor chip. That is the heart of a computer, but it also needs RAM, a keyboard, a screen, a hard disk, and a printer. When personal computers were introduced, these things were expensive. They were manufactured in small numbers for the minicomputer market. There was no such thing as a small hard disk for the home market.

[4] Global automobile sales 2022, $3.8 trillion. (https://www.ibisworld.com/global/market-size/global-car-automobile-sales/ and Stastica).

[5] 170 million generators × 15 years = 2.550 billion generators. 2.550 billion generators × 20 kW = 51,000 GWe capacity; ~153,000 GWt. World generator capacity is now 7,172 GW. World primary energy is 557.10 exajoules/year according to BP. 153,000 GWt run full time, 8760 hours per year = 1.3 trillion GWh per year, or 4,825.01 exajoules. Again, no one would run generators and other equipment at full capacity every hour of the year. https://www.americangeosciences.org/critical-issues/faq/how-much-energy-does-person-use-year

Personal computers began selling in the thousands, and then millions. Engineers worked frantically to make small, cheap hard disks and printers. Prices fell rapidly. When the cost of core technology falls – the microprocessor in this case – it creates an opportunity to invent low cost peripherals. There would be no point to developing a $300 printer in 1975. You could not sell more than a few hundred. But, when the market for printers explodes and millions are sold, it is worth developing a new type of cheap, small printer.

The first implementation of a 20 kW cold fusion generator would use a conventional mechanical heat engine. It would be better to develop thermoelectric devices, because they have no moving parts, and they last longer, around 30 years. These are far more expensive per kilowatt today, but with R&D they can probably be made cheaper, the way photovoltaic cells were.

3. ESTIMATED SAVINGS PER HOUSEHOLD

I expect all home cold fusion generators will be cogenerators, also known as combined heat and power generators. The waste heat from a cogenerator is used for space-heating in winter, eliminating the need for a home furnace. A small generator is inefficient, requiring 60 kWt to generate the 20 kWe needed for the average house, with 40 kW of waste heat. The average house space heating furnace produces 18 kW (60,000 BTU), so there would be more than enough waste heat. A cogenerator is simple. It resembles the cabin heater in an automobile. This heats the cabin with waste heat from the engine by directing fresh air through a heat exchanger connected to the engine radiator. This is why you get no heat until the engine warms up. A home cogenerator would bring some waste heat into the house in winter, or vent all heat outside in summer.

Cogenerator waste heat might also be used to heat water.

For several years, cold fusion cogenerators will probably sell at a premium, perhaps much more than a middle class family can afford. They might cost $50,000. They would resemble modern electric cars such as the Tesla, which began as luxury items and are now falling to a price that middle class people can afford. When electric cars become commodities, they should be cheaper than gasoline models, because they are simpler with fewer parts, and they are easier to assemble. Cold fusion cogenerators may eventually be cheaper than the furnaces they replace, but not at first.

Here is an estimate of the price at which it would be economical to replace a conventional gas-fired furnace with a cold fusion cogenerator. The cost of today's energy sources and equipment in the U.S. are as follows:

3.1. Equipment for Heating, Ventilation and Cooling (HVAC)

A gas fired home furnace costs $2,200 for a small house, and up to $4,000 for a large house. The average is $3,900 including installation.

The average water heater costs $1,200

The average central air conditioner costs $5,651, but an early model cogenerator would probably not replace it. A cogenerator would power a conventional electric air conditioner, so the cost would not change. Decades from now thermal air conditioners powered directly by cold fusion or by cogenerator waste heat may become cheaper than electric models.

Equipment total: $5,100. Most HVAC equipment lasts about 15 years, so the cost is $340/year

3.2. Energy

Average residential energy costs are:

$115/month electricity, $1,380/year

Natural gas costs ~$100/month gas, $1,200/year. Much of this is used for space heating.

Electricity and gas total: $2,580/year. (Incidentally, this is close to what we pay at our house in Atlanta, Georgia. Electricity $1,164, natural gas $1,333.)

A cold fusion cogenerator would eliminate the electric bill, and greatly reduce the natural gas bill, because most natural gas is used for space heating.

Today's cost of energy plus equipment: $2,920/year, $43,800 over the 15-year life of the generator.

When the cost of a cogenerator falls substantially below $43,800, most people will buy a cogenerator when their old furnace wears out. The electric power and gas companies will gradually go bankrupt. They cannot afford to lose most of their customers. Their generators and network are not designed for a much smaller customer base. When the power and gas companies go out of business, remaining holdout families will be forced to buy a cogenerator. The transition will be complete.

4. LOW AND MEDIUM POWER DEVICES

One of the reasons cold fusion R&D may cost $18 billion is that we need to invent many new things to take advantage of cold fusion. To make full use of personal computers, we needed new kinds of hard disks and printers. To make full use of cold fusion we will need many new inventions, especially better, cheaper heat engines. The companies that invent cold fusion cells will not be the only ones who make money. Whoever comes up with a better heat engine will also make large profits.

I assume that thermoelectric heat engines will be used with small devices, such as wristwatches and cell phones. To illustrate the challenges of developing cold fusion – challenges other than cold fusion itself – here is a problem with small devices.

Any small heat engine is inefficient. Present day thermoelectric devices are particularly inefficient. This makes them too hot for cell phones and laptop computers. They generate too much waste heat. Commercial thermoelectric devices today are only 15% efficient. Laboratory devices are up to 40% efficient. A cell phone draws 3 W when it is online. At 15% it would produce 20 W of waste heat. That is too hot to keep in your pocket. 40% efficiency would produce 7.5 W, which is probably cool enough.

But there is another problem. Like all heat engines, thermoelectric Carnot efficiency is better at higher temperatures. You can only get 15% today, or 40% in the future, when the hot side temperature is 1230 K (928°C). That would be fine for something like a home generator, but how could you put such a hot object in your pocket?

Perhaps something like the following would work. Imagine a gas loaded cold fusion cathode the size of an incandescent lightbulb tungsten filament that is kept at 930°C. It is encased in ceramic which is surrounded by thermoelectric devices. The heat is radiated evenly from the surface of the phone. At 7.5 W it would be a moderate temperature. But, if you drop the phone, or run over it with a car, the ceramic may crack open and expose the incandescent core. I suppose the reaction would stop and it would rapidly cool, but it might be dangerous. For that matter, a conventional cell phone battery can be dangerous. Run over one with a car and it might discharge quickly, and ignite or explode.

I do not know whether a hot ceramic core would work, but I expect someone will come up with a solution.

5. CARDIAC PACEMAKERS AND OTHER LOW POWER DEVICES

One of the best potential uses of cold fusion would be for a cardiac pacemaker. A cold fusion thermoelectric pacemaker that lasts for 50 years would be a great benefit to patients, because today's battery-powered ones have to be replaced from time to time.

An incandescent core might be acceptable in a cell phone, but you would not put one in a pacemaker battery. No one would implant that in a patient's chest. Fortunately, that will not be necessary. It turns out that for very low power levels, inefficient heat engines are fine. As long as the COP is very high, or infinitely high with no input power, cold fusion will work.

Figure 7. A plutonium powered pacemaker. The plutonium has been removed; it fit into the slot on the top left. See technical details at: https://www.orau.org/health-physics-museum/collection/miscellaneous/pacemaker.html.

Figure 7

shows a thermoelectric nuclear-powered pacemaker from the 1970s. It was powered by plutonium-238, which produces heat without significant radiation (5 to 15 mrem per hour gamma rays and neutrons). This device produced 0.13 W of heat, which converted to about 50 μW of electricity. Conversion efficiency was 0.04%. That was acceptable. The 0.13 W of waste heat did not cause a problem in the patients' chests.

Incidentally, some of these pacemakers were still implanted and functioning after 30 years, which shows that a nuclear powered pacemaker is robust and can last a long time.

There is one marvelous possibility on the horizon. Frank Gordon and Harper Whitehouse have developed and experimentally demonstrated a device they call a Lattice Energy Converter (LEC) which produces both a voltage and a current through a load [8]. Several people have independently replicated these results. Whitehouse claims to have a device that is still operating after 7 years. The LEC has two outstanding features:

1. It does not need input power; the COP is infinite. It self-initiates (spontaneously starts up on its own), and self-sustains.
2. It outputs mainly electricity, so it does not need a heat engine.

Power is very low, at the microwatt level, about the same as a wristwatch battery. Some people still wonder whether this is some sort of chemical battery. Gordon and several people who replicated the device point out that it is producing ionizing radiation in conditions where this should not happen without a nuclear process.

Gordon thinks that for general use, power output needs to be increased by nine orders of magnitude to the kilowatt level. That sounds unlikely, but laboratory science often accomplishes such things. The first fission reactor, the Chicago Pile 1, produced 0.5 W. The first power reactor a few years later produced 236 MW (8 orders of magnitude). At ICCF24, Gordon described many promising methods that might increase power by 1 or more order of magnitude, such as raising the operating temperature, or increasing surface area by a factor of 10. If power can be raised to 1 W, this will make it easier to measure the output, and allow a test showing that it lasts far longer than a 1 W battery or any other chemical device. This would also make it easier to look for helium when deuterium gas is used, to see if this is D-D fusion.

A LEC outputting 1 to 3 W would also have important practical uses, such as lighting an LED lamp or charging a cell phone. This would be a great benefit in the Third World.

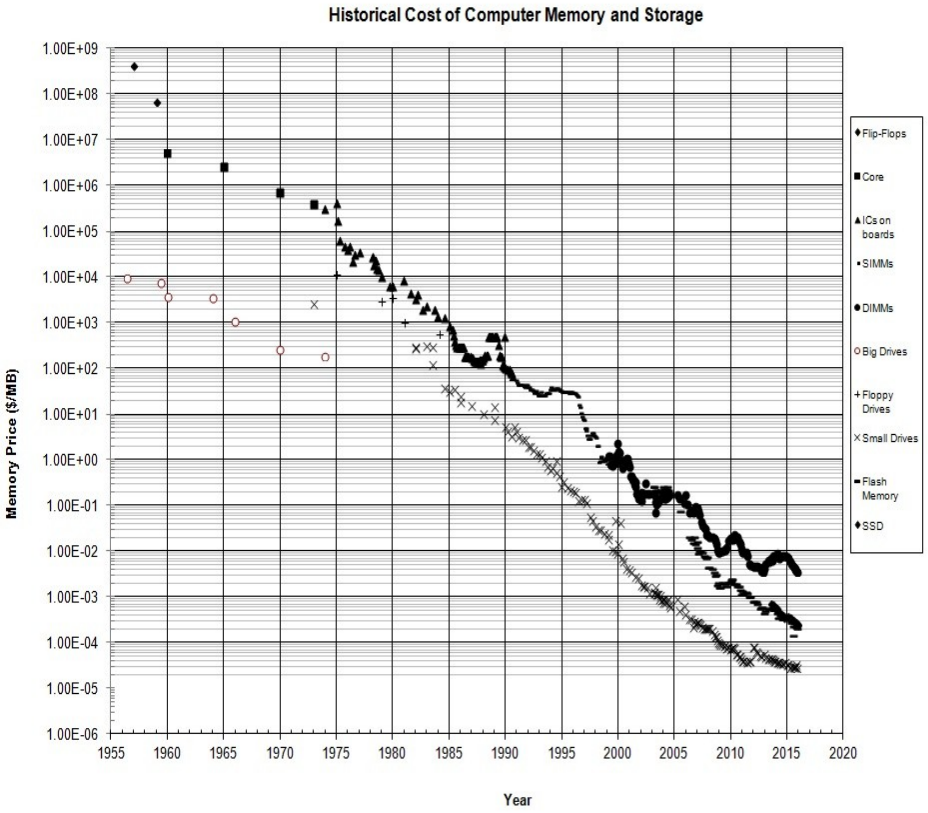

Figure 8. J. C. McCallum, National University of Singapore, Graph of Memory Prices Decreasing with time (1957 – 2015). https://www.researchgate.net/publication/227349575_Seven_Centuries_of_Energy_Services_The_Price_and_Use_of_Light_in_the_United_Kingdom_1300-2000.

6. ENERGY MAY BECOME THOUSANDS OF TIMES CHEAPER

The notion that energy might be made thousands of times cheaper may seem ridiculous to some people. These people have not read history. The cost of food and many other things has fallen dramatically since the Industrial Revolution began. In particular, intangible things such as travel, lighting, and information are cheaper. Energy is an intangible.

The cost of lighting from 1800 to 2000 fell by a factor of 3,300, while efficiency increased 700 times [9].

Over the last 50 years, the cost of information, data storage, and computation fell more than any other commodity in human history. From 1962 to 2000 the cost of computer memory fell by 8 orders of magnitude (Figure 8). I personally own more terabytes of disk storage than existed in the entire world in 1964.[6] [10] Disks are cheaper partly because

[6]I have 13 TB of storage including backups. Sanders [8] estimated there were approximately 15,000 computers in 1964 just before the introduction of the IBM 360. Looking at the specifications for the most common type, the IBM Model 1400 and the model 1301 disk storage unit, and adding in the well-known supercomputers at that time, I estimate there were ~1.7 TB of disk storage in the world. If every one of the Model 1400 computers had the maximum number of disk drives it could support (250 MB), there would be 3.75 TB total. Actually, many were equipped with tape drives only.

they became much smaller. Cold fusion will also be cheaper partly because the equipment will be smaller. It will not need the high voltage power lines, poles and transformers, or the coal mines and railroads, gas pipelines, and the rest of the unseen infrastructure we must have for today's energy sources.

References

[1] Rothwell, J. *Cold Fusion Will Lower the Cost of both Energy and Equipment*. in *ICCF20 International Conference on Condensed Matter Nuclear Science*. 2016. Sendai, Japan.
[2] Hagelstein, P.L., et al. *New Physical Effects in Metal Deuterides*. in *Eleventh International Conference on Condensed Matter Nuclear Science*. 2004. Marseille, France.
[3] Borowski, S.K., *Comparison of Fusion/Antiproton Propulsion Systems for Interplanetary Travel*. 1996, NASA.
[4] Townes, C.H., *How the Laser Happened - Adventures of a scientist*. 1999: Oxford University Press.
[5] Roulette, T., J. Roulette, and S. Pons. *Results of ICARUS 9 Experiments Run at IMRA Europe*. in *Sixth International Conference on Cold Fusion, Progress in New Hydrogen Energy*. 1996. Lake Toya, Hokkaido, Japan: New Energy and Industrial Technology Development Organization, Tokyo Institute of Technology, Tokyo, Japan.
[6] *Capital Cost and Performance Characteristic Estimates for Utility Scale Electric Power Generating Technologies*. 2020, Energy Information Administration, U.S. Department Of Energy https://www.eia.gov/analysis/studies/powerplants/capitalcost/.
[7] *Levelized Cost of Energy Comparison—Unsubsidized Analysis* 2021, Lazard https://www.lazard.com/media/451905/lazards-levelized-cost-of-energy-version-150-vf.pdf.
[8] Gordon, F. and H.J. Whitehouse, *Lattice Energy Converter.* J. Condensed Matter Nucl. Sci., 2022. **35**: p. 30–48.
[9] Fouquet, R. and P.J.G. Pearson, *Seven Centuries of Energy Services: The Price and Use of Light in the United Kingdom (1300-2000).* The Energy Journal, 2006. **27**(1): p. 138–178.
[10] Sanders, D., *Computers in Business, an Introduction*. 2 ed. 1972: McGraw-Hill.

J. Condensed Matter Nucl. Sci. 38 (2023) 121–129

Research Article

How to Fix Global Warming With Cold Fusion

Jed Rothwell
LENR-CANR.org

Abstract

Cold fusion can eliminate the threat of global warming two ways:

1. Cold fusion does not produce carbon dioxide so if it replaces other sources of energy carbon emissions would stop.
2. Cold fusion can enhance the removal of carbon from the atmosphere by reforestation.

Large scale reforestation projects have been proposed to remove carbon from the atmosphere and sequester it in trees. Cold fusion technology would greatly enhance such projects, increasing the amount of carbon by a factor of ten and reducing the cost of the project by a large factor. Cold fusion can be used to stop the natural boom and bust cycle of forest carbon, by burying charcoal made from deadwood underground. In effect this would speed up the formation of coal by a factor of a million. Conventional energy sources cannot do this.
 ISSN 2227-3123

Keywords: Global warming, future, carbon sequestration, reforestation, economics

1. Introduction

Cold fusion is not a chemical reaction. It is not any form of combustion. Like nuclear fission or plasma fusion, it adds no carbon dioxide to the atmosphere. So, if all energy were produced with cold fusion, carbon dioxide would stop increasing. However, the carbon dioxide already in the atmosphere would remain, possibly for centuries, unless we take active steps to remove it.

Many biologists, forestry experts and climatologists have advocated sequestering carbon by growing more trees. That is, by reforesting parts of North America, Europe and China that have lost forest in the last 300 years. This would be a megaproject in which trillions of trees are planted, in millions of square kilometers. Cold fusion would enhance this project. It would make the project far cheaper and faster, and it would remove ~10 times more carbon per square kilometer than the projects that have been proposed.

2. Engineering Basis for These Claims

Cold fusion researchers may feel that the predictions in this paper have no engineering basis, and they are mere speculation. I believe data from the most successful experiments justify these predictions. To use cold fusion for nearly all applications you need six things:

 ISSN 2227-3123

Table 1. Cold fusion cathodes from the best experiments compared to fission reactor fuel pellets.

	Volume	Operating Temperature	Power Density by Volume	Power Density by Area
Cold fusion cathode	0.3 cm^3	100°C	300 W/cm^3	16 W/cm^2
Fission reactor fuel pellet	1.0 cm^3	300°C	180 W/cm^3	32 W/cm^2

1. Sufficiently high power density.
2. High Carnot efficiency.
3. High energy density.
4. Perfect safety with no tritium, or at least no tritium leaks.
5. Reasonably low cost materials and manufacturing.
6. Control over the reaction.

High power density and Carnot efficiency are needed to make reasonably compact devices. If power density is low, a cold fusion generator would be too large for direct use, like a solar panel array. An array can power an electric car, but it is far too large to fit on the roof of the car.

One of the most successful experiments on record was performed by Roulette, Roulette and Pons [1]. Their tests produced 17 to 100 W, for up to 70 days continuously, in boiling cells. Experiment 3 produced 294 MJ from 3.6 g of palladium. This is comparable to the power density of a nuclear fission core fuel pellet (Table 1). A fission reactor core by itself is compact. The reactor as a whole needs a great deal of shielding, so it is not compact. If the core were safe without shielding, it would be compact enough for nearly any application.

A fission reactor runs at 300°C, giving Carnot efficiency of around 30%. The experiment by Roulette *et al.* was in unpressurized cells so the temperature was 100°C. It could easily be pressurized to 300°C or more, so it could also achieve 30% efficiency with most types of heat engines.

Cold fusion devices do not produce dangerous radiation. A few have produced tritium. Perhaps this can be prevented. If not, tritium is safely contained in today's wristwatches and hallway exit signs. Since a cold fusion cell will be tightly sealed tritium can probably be contained in them.

High energy density is assured. With Pd-D cold fusion, the ratio of energy to helium is 24 MeV, the same as one path in plasma fusion.

Materials in most cells are abundant and manufacturing processes should not be particularly expensive.

Complete control over the reaction obviously has not been achieved. I believe that with enough research funding it will be. This is shown by the history of other inventions such as internal combustion engines, transistors, masers and lasers. The initial laboratory prototypes took years to produce, and they were unreliable. The first maser prototype took three years to make [2]. Today we manufacture millions of these devices, and they are so reliable you can bet your life on them. As you do whenever you fly on an airplane.

3. How to Remove Carbon Dioxide With Cold Fusion

With cold fusion we would stop adding carbon dioxide to the atmosphere. We can also remove the carbon we have already added. We put it back underground where it came from. We do this by growing billions of trees. When they are old, we cut them down and bury them underground in abandoned coal mines.

Growing trees to sequester carbon is not a new idea. Biologists, forestry experts and climatologists have recommended this in many project proposals (Table 2). In this paper, I describe how to enhance these projects with cold fusion. Cold fusion would make carbon removal far cheaper, faster, and 10 times more effective per square kilometer.

Table 2. Recent examples of proposals to sequester carbon with reforestation.

Reforest Action, Contribute to the Global Carbon Neutrality . . . by Funding the creation and preservation of Forests, https://www.reforestaction.com/en/contribution-climate, 19 million trees planted
University of Aukland, Can reforestation help reverse the extinction crisis? https://www.thebigq.org/2019/06/12/can-reforestation-help-reverse-the-extinction-crisis
Congressional Research Service, U.S. Tree Planting for Carbon Sequestration, https://sgp.fas.org/crs/misc/R40562.pdf
Forest Service, U.S. Department of Agriculture, Planting trees to mitigate climate change: Policy incentives could lead to increased carbon sequestration, https://www.fs.usda.gov/treesearch/pubs/61873
YOUNG TREES ARE BETTER! World Resources Institute, Young Forests Capture Carbon Quicker than Previously Thought, https://www.wri.org/insights/young-forests-capture-carbon-quicker-previously-thought
NO! OLD TREES ARE BETTER! Pacific Forest Trust, E&E: Old trees store more carbon, more quickly, than younger trees, https://www.pacificforest.org/ee-old-trees-store-more-carbon-more-quickly-than-younger-trees/ Most other sources say that younger trees store more carbon per year. See also Figure 1 caption.
100 YEARS TO STORE 10 YEARS OF EMISSIONS (I say 100 years to sequester all anthropogenic emissions) Frontiers in Forest and Global Change, Forests and Decarbonization – Roles of Natural and Planted Forests, https://www.frontiersin.org/articles/10.3389/ffgc.2020.00058/ The authors do not consider growing field crop indoors; irrigating deserts; or burying deadwood anaerobically in abandoned coal mines, OR cold fusion.

4. Carbon Sequestration Project Outline

The project would begin by expanding forests with two technologies that are not related to cold fusion: indoor farms, and "cultured meat" grown from animal cells. These two greatly reduce the amount of land devoted to agriculture.

Indoor farms are already common in many parts of the world. They take up much less space than outdoor farms, and they use less water, no pesticides, and in some climates, less energy. The Netherlands is a small country, yet it is now the second largest agricultural exporter by value, after the United States, because they grow huge quantities of food indoors. One-third of the fresh tomatoes sold in the U.S. are grown indoors [3], [4]. Cold fusion would enhance indoor farms (Ref. [5], p. 130).

Cultured meat is still under development. This is not plant-based imitation meat such as the Impossible Burger. It is actual meat, grown *in vitro* from animal cells. If this pans out, it will reduce the land devoted to agriculture, because 80% of land is used for livestock production [6].

The land no longer used for agriculture can be used for living space, but much of it should be returned to nature. It should be reforested, partially restoring the North American ecosystem to the way it was before European colonization. Forests should also be expanded in Europe, especially in places such as Scotland, where hills are now barren that were forested in the 18^{th} century [7].

Cold fusion can help do this in a cost effective manner. It can do much more. Over the last 3,000 years, people expanded the Sahara and Gobi deserts by over-farming. This can be reversed with cold fusion powered desalination plants, and tap-root irrigation, which uses less water than conventional techniques. We could build roughly as many desalination plants as there are automobile assembly plants now. In fifty years, we could convert 3.5 million square kilometers of desert into verdant land, the way it was before human civilization. This is about a third of the Sahara and Gobi. It is also about a third of the land area of the United States. We would plant trees on the new land. After about fifty years the desalination plants would wear out, but we would not need to build many new ones because once the forests are established, natural rainfall increases. Reforestation of desert areas with minimal irrigation has been done successfully in Israel. Over the last 60 years, Israel has greatly increased forested land in arid and desert areas. The 3,000 hectare Yatir Forest in the Negev Desert is a good example.

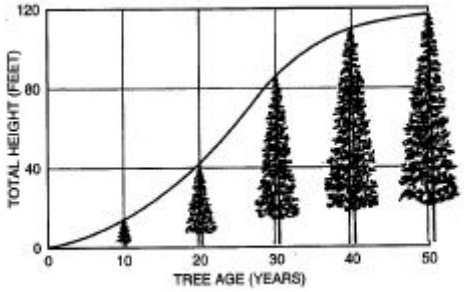

Figure 1. Tree growth patterns. Culmination in mean annual growth occurs after 40 to 50 years. Some experts think old growth forests continue to sequester carbon. "[W]hether carbon accumulation continues or peaks when net additional wood growth is minimal (in "old-growth" forests) is disputed." Ref. [8].

The desert areas would become more livable for humans and other species. The population would increase. Towns and cities would be built, increasing land values. I do not think the land will be needed for agriculture because I assume indoor farming will be superior. But if outdoor farming continues, the new verdant land will greatly increase worldwide production of food.

This is a grand reforestation megaproject to reduce carbon in the atmosphere. With cold fusion, it is larger and more ambitious than anything proposed by the experts. The tree planting and forestry management part of the project is also hundreds of times cheaper. Bringing the deserts back to life would be expensive, but it would produce ancillary benefits worth trillions of dollars.

Cold fusion would enhance this megaproject in ways that would remove at least 10 times more carbon per square kilometer than the experts think is possible. Here is why. The new trees in North America, the Sahara and the Gobi deserts would capture vast amounts of carbon dioxide as they grow. But experts point to two problems. First, when the trees mature into a climax forest, they largely stop capturing carbon dioxide, according to most experts. (Some dispute this, as noted in Table 2 and the caption for Figure 1.) Second, when there is a forest fire, or when the trees die and decompose, much of the carbon dioxide returns to the atmosphere. This is called the natural boom & bust cycle of forest carbon (Figure 2).

We need to stop this cycle before the carbon release phase (Figure 3).

To interrupt the cycle, we harvest the deadwood (fallen trees and branches). The deadwood should be cut into chips, which are then baked into charcoal with cold fusion. The charcoal is taken to abandoned open-pit coal mines and buried underground, in anaerobic conditions. In other words, these pits would become reverse coal mines. We now dig up coal from a few mines, and send it to 230 power plants scattered around the country. With this project, we would collect solid carbon from many locations around the country, ship it to the mines, and put it back underground. In effect, this is speeding up the natural formation of underground coal by a factor of a million.

The wood is cut into chips to make it easier to transport. It is made into charcoal because charcoal has less mass to transport and bury, and it is less likely to rot.

If this project were done with fossil fuel, the baking and transport of the chips would add far more carbon dioxide to the atmosphere than the project removes. This is easily estimated from the caloric content of wood, 20 MJ/kg (about as much as 435 g of gasoline). Chipping 1 kg of wood, baking it into charcoal, transporting it to North Dakota, and burying it would take far more than 20 MJ. If this project were done with wind, solar and other renewable energy, it would cost vast amounts of money. It is only technically feasible and economically possible with cold fusion.

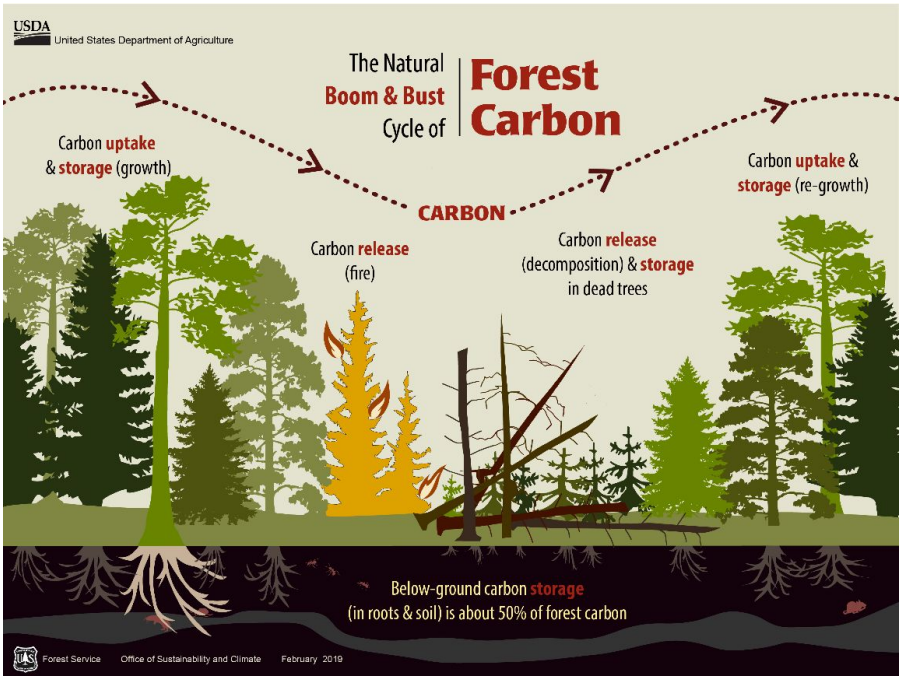

Figure 2. The natural boom & bust cycle of forest carbon. U.S. Forestry Service.

After about a century of burying carbon underground, we would sequester roughly as much carbon as we have added to the atmosphere since the beginning of the industrial revolution (Figure 4). The cumulative total is 1,710 billion tons. Suppose we put carbon back underground at the rate we emitted it in 1966, 15 billion tons. In 114 years, we would bury the excess carbon.

Charcoal is 60% to 80% carbon, so we need to bury about 21 billion tons of charcoal per year to sequester 15 billion tons of carbon. Worldwide coal extraction was 7.9 billion tons in 2019 [9]. So, we put the carbon back at about 2.6 times the rate we now mine coal.

Wood is approximately 50% carbon, so we need to chip 30 billion tons of deadwood a year. This goal cannot be met without new forests in irrigated deserts. If the deserts are not irrigated, the project will take about 200 years.

Worldwide production of lumber is approximately 1.3 billion tons per year (2.2 billion m^3). So, we increase forestry by a factor of 23.

Removing excessive deadwood improves the health of the forest overall, and reduces severe forest fires. Not all deadwood should be removed. Rotting wood is essential to the ecology, but there is too much in many forests today. Removing deadwood need not be done often. This would disrupt fauna and bother people living nearby. Deadwood could be removed every 10 years or so, in a cleanup that lasts a few days to a week.

To make 30 billion tons of wood chips, I think it would be best to use small, flying, cold fusion powered robots, the size of woodpeckers. Woodpeckers and insects demolish millions of fallen trees without much disruption.

A flying robot the size of a woodpecker may seem implausible, or risible. It may seem that such a small machine would take far too long to demolish an entire tree. However, large numbers of these machines working in coordinated groups could do this in a reasonable amount of time. Figure 5 shows a pileated woodpecker making a hole. Holes are

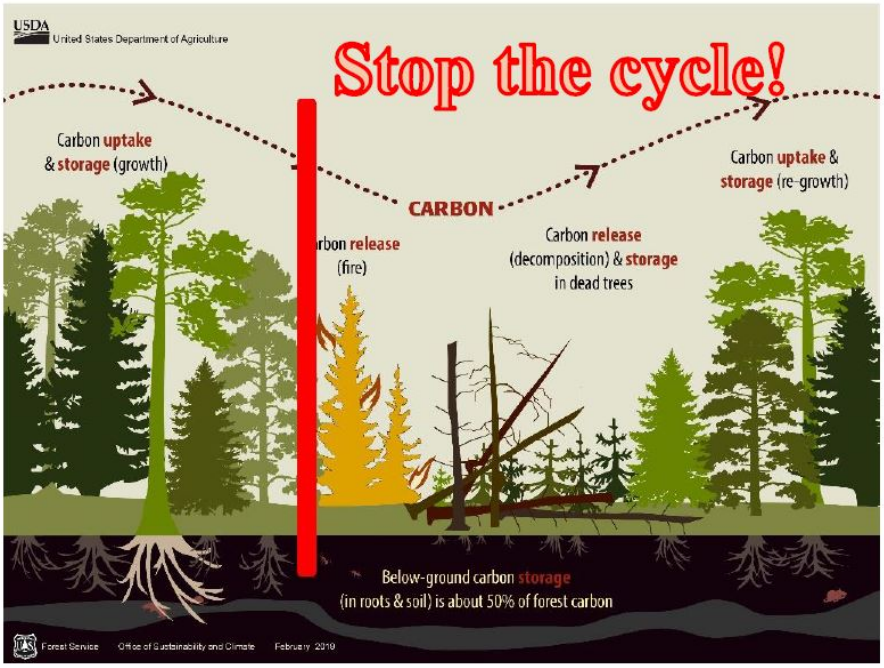

Figure 3. Interrupting the natural boom & bust cycle of forest carbon before the carbon release phase.

rectangular. The larger ones are 10 cm × 14 cm, perhaps 4 cm deep: around ~500 ml. The birds can make 2 or 3 holes a day, roughly ~1 L. The birds weigh 300 g, and their metabolism is ~1.4 W (28.31 kcal/24 hour) [10]. Larger 1 kg flying robots, with 140 W of thermoelectric power, and cutting blades that make 53 L of wood chips per day should be possible. They would be a combination of a flying drone, a cell phone, and a Dremel cutting tool. A tree service company would use about 20 of them to demolish a 15 m pine tree in one day. You would need a fleet of 3.1 billion of them to remove 30 billion tons of wood per year. 3.1 billion may seem like a large number, but it is not. If the robots last 10 years, we need to manufacture 310 million per year. Compare this to the number of cell phones we make, 1.3 billion per year.

The robots can be made quieter than today's drones and cutting tools by using electroactive polymers (EAP). They would also be longer lasting, requiring less maintenance and replacement parts. An EAP resembles an artificial muscle. It contracts when electricity is passed through it. An EAP-powered flying drone would have flapping wings, rather than the propellors used in today's drones. Small, flapping wing drones are more complicated than propeller aircraft, but the engineering problems are being solved and such machines will be perfected soon. Wings are much quieter than propellers because they move slower, pushing a larger volume of air with each stroke. This is why a hawk can fly low and silently across a field to snatch a squirrel off the ground. I have seen hawks do this. One flew just over my head and landed on a fence a meter away from me before I noticed it.

An EAP cutting blade might pinch, like an insect taking a bite out of wood. This should be quieter than a rapidly spinning circular blade.

Why use miniature flying robots? Why not make human sized chainsaws and woodchippers like the ones we have now, only powered by cold fusion? There are several good reasons to make them smaller: They can fly up into the

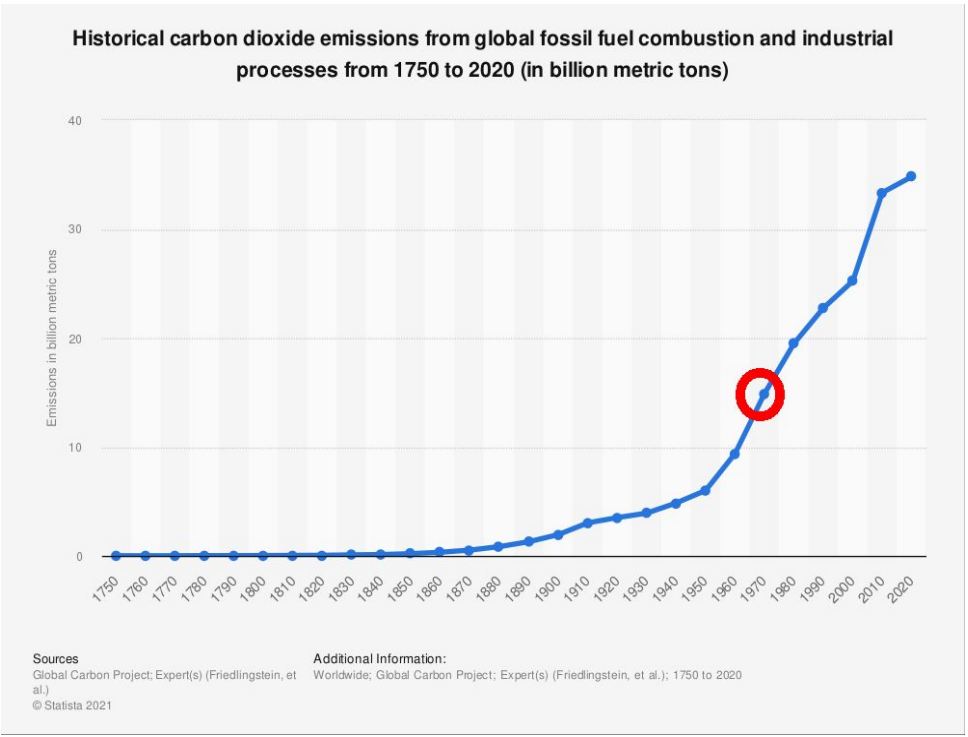

Figure 4. Graph of carbon dioxide emissions since 1750.

tree, rather than climbing. If they fall out of the tree, they cause no damage. They would be quieter than chainsaws. They would not need logging roads. They could fly into wilderness areas in California to remove deadwood without roads and without disturbing the environment. This would reduce wildfires. They do not need human operators, so they would be much cheaper and safer. Climbing trees and cutting with chainsaws is dangerous work.

If these are such good reasons, why don't we make small gasoline or battery-powered robots now? Because they would not be practical. You would have to refuel or recharge them a dozen times a day. They could not fly into the California wilderness; they would run out of fuel. Cold fusion machines run for years on a drop of fuel, so they do not need fuel tanks, and they can be any size. You pick the best size for the application, rather than being hemmed in by the limitations of the technology.

When you think about future cold fusion technology, you should rethink the size of machines. Think small. Cold fusion robotic machines do not have to be made on a human scale, the way chainsaws are. Rethink everything. The scale, the methods, the economics should all be considered anew.

This global warming reversal project would be a continental-scale megaproject. But so is the flow of coal from under the ground to coal-fired generators today. We hardly notice that. This project is no more complicated than today's forestry and coal mining. The project as a whole, including bringing the deserts back to life, would be the most profitable enterprise in history. For a trivial cost we would create trillions of dollars in wealth.

I estimate the reforestation in North America and Europe would cost roughly 100 times less than the experts do, because the work will be done by cold fusion robots. I also estimate it can remove all of the carbon in 100 years, whereas most experts say it can only remove 10 years' worth of emissions (Table 2). They are pessimistic mainly

Figure 5. Pileated woodpecker making a feeding hole. https://ebird.org/species/pilwoo

because of the boom and bust cycle. A climate researcher wrote an op-ed in the New York Times on June 4, 2022 titled, "Let's Not Pretend Planting Trees Is a Permanent Climate Solution" [11]. The gist of it was that because of the boom and bust cycle, carbon in trees eventually returns to the atmosphere:

> Trees can quickly and cost-effectively remove carbon from the atmosphere today. But when companies rely on them to offset their emissions, they risk merely hitting the climate "snooze" button, kicking the can to future generations who will have to deal with those emissions. . . .

That is true. But with cold fusion we would stop the cycle. This author did not consider the possibility of burying the carbon in abandoned coal mines. He never thought of irrigating deserts to produce 5 million square kilometers of new forest. Or having miniature robots do the work. He did not think of these things because he has never heard of cold fusion. He did not imagine these things because without cold fusion *they are unimaginable*.

When modern electric lights began replacing inefficient incandescent lights in the late 20th century, they reduced both energy costs and equipment costs, because they last much longer. One expert said: "this is not a free lunch; it is a lunch you are paid to eat" [12]. That should be the motto of cold fusion.

References

[1] Roulette, T., J. Roulette, and S. Pons. *Results of ICARUS 9 Experiments Run at IMRA Europe*. in *Sixth International Conference on Cold Fusion, Progress in New Hydrogen Energy*. 1996. Lake Toya, Hokkaido, Japan: New Energy and Industrial Technology Development Organization, Tokyo Institute of Technology, Tokyo, Japan.

[2] Townes, C.H., *How the Laser Happened - Adventures of a scientist*. 1999: Oxford University Press.
[3] *The Netherlands is the second-largest agricultural exporter after US*, in *DutchNews.nl*. 2018. https://www.dutchnews.nl/news/2018/01/the-netherlands-is-the-second-largest-agricultural-exporter-after-us/.
[4] Alexander, W., *Indoor Farming Is a 'No-Brainer.' Except for the Carbon Footprint*, in *New York Times*. 2022.
[5] Rothwell, J., *Cold Fusion And The Future*. 2004: LENR-CANR.org.
[6] https://ourworldindata.org/agricultural-land-by-global-diets
[7] Trees for Life, Deforestation https://treesforlife.org.uk/into-the-forest/habitats-and-ecology/human-impacts/deforestation/
[8] Gorte, R.W., *U.S. Tree Planting for Carbon Sequestation*. 2009, U.S. Congress: Congressional Research Service.
[9] *Statistics report, Coal Information, Overview*. 2020, International Energy Agency (IEA). https://iea.blob.core.windows.net/assets/a5f208e9-f66b-4d31-b5af-87d581b70c18/Coal_Information_Overview_2020_edition.pdf.
[10] Long, C.A., *Exponential Relations of Standard Metabolic Rates of Birds and Weights of Eggs.* The Wilson Bulletin, 1973. **84**(3).
[11] Housfather, Z., *Let's Not Pretend Planting Trees Is a Permanent Climate Solution*, in *New York Times*. 2022.
[12] Fickett, A.P., C.W. Gellings, and A.B. Lovins, *Efficient Use of Electricity.* Scientific American, 1990. **263**(3): p. 64-75 http://www.jstor.org/stable/24996931.

J. Condensed Matter Nucl. Sci. 38 (2023) 130–146

Research Article

The Nature of Cold Fusion (Cold Fusion Made Simple)

Edmund Storms*

Kiva Labs, Santa Fe, NM

Abstract

The cold fusion process is explained using a new understanding of the observed behavior that shows how many of the behaviors are related to each other and to the mechanism causing cold fusion. A mechanism is described that can guide a more reliable initiation of the nuclear process. Methods are suggested by which the model can be tested. The need for a new understanding of nuclear interaction is identified.
 ISSN 2227-3123

Keywords:

1. Introduction

Thirty-three years have passed since Profs. Martin Fleischmann and Stanley Pons (The University of Utah) discovered that a fusion reaction could be made to occur at ordinary temperatures in ordinary materials[1]. Initially, the behavior was called cold fusion. Now the preferred name is Low Energy Nuclear Reaction (LENR) because the process involves more than fusion. However, only the fusion process will be discussed here. Although much information has been discovered about how the process works, why it works is still unknown.

The distinction between HOW something works and WHY is important and needs to be understood. An example might help clarify the difference between these two concepts. When a person intends to fly an airplane, learning how the machine responds to the controls is important. This knowledge reveals HOW the machine works. Nothing needs to be known about the mechanism of lift, which is the WHY. Likewise, the LENR process can be made useful even when only the HOW is understood. The WHY does not need to be known at present. But, as is the case when flying an airplane, a flaw in understanding the HOW can cause failure. This paper describes a model based on HOW LENR behaves using the observed behavior as the teacher. Many papers supporting the idea can be accessed at www.LENR.org, only a few of which are cited here. More detail can be found in the book by Storms [2].

The role of impurities is important. Their effects were studied very early in the history because the nuclear process was thought to occur in the crystal structure where the impurities would be located. The fact that impure Pd worked

*Corresponding author: storms2@ix.netcom.com

 ISSN 2227-3123

more often than pure Pd supported the importance of impurities. How certain impurities might affect the occurrence of LENR is discussed.

Over the years, people realized that the LENR process appeared to require the creation of a special but rare condition in the host material. The question addressed here is, "Where in the material would this special condition form and what role would it play in causing LENR?"

The major nuclear product is thought to be ^{4}He because this element is found in the environment after excess energy is made when deuterium is used. In addition, tritium is occasionally produced without the expected number of neutrons. A nuclear process is described that can explain how these two observed nuclear products are produced.

2. GENERAL SUMMARY OF THE MODEL

The fuel for the fusion reaction can be any isotope of hydrogen. For simplicity, the word "hydrogen" or H is used when the comment applies to all hydrogen isotopes. This hydrogen is proposed to exist in a sequence of three different chemical relationships in a solid material before LENR can occur. These are as follows:

1. The crystal structure describes the conventional arrangement of the atoms in the material and provides a source of hydrogen to the two additional structures when they form. The crystal structure is face-centered-cubic (fcc) when Pd is used. The nuclear process does not occur in this structure because the rules governing this atomic arrangement require the atoms to be too far apart for the nuclei to interact. A violation of this requirement would require more energy than is available in the crystal arrangement. Nevertheless, this structure plays an indirect role in causing LENR as is described in Section II.1.

2. Next, a rare condition, called the Nuclear Active Environment (NAE), must form within the material. This condition is physically outside of fcc structure and chemically independent of the conditions that caused the crystal structure to form. The hydrogen atoms in the NAE have a conventional chemical relationship with each other, but one that is different from the chemical relationship on which the crystal structure is based. This process is described in Section II.2.

3. Finally, the H in the NAE interacts with electrons to form a unique chemical structure at a few random locations within the NAE. Although this process follows the rules governing chemical interaction, a shared wave function results with the ability to release mass-energy by a fusion-type nuclear reaction. As a result, this assembly, called the Nuclear Active Structure (NAS), has the unique ability to overcome the Coulomb barrier. It's proposed characteristics are described in Section II.3. The process of forming this structure and its ability to cause nuclear interaction is the great mystery revealed by LENR.

The nuclear process is not anticipated as the NAE and the NAS form. Instead, the nuclear process is the unintended result of a series of conventional chemical reactions, each of which obeys the laws of thermodynamics. After fusion takes place within the NAS, radiation, nuclear products, and energy are suddenly released as result of its destruction. Although these three different conditions have an important relationship to each other, each needs to be understood separately, starting first with the crystal structure.

2.1. Characteristics of the Crystal Environment and the NAE

Although the hydrides of palladium are most often used, this material is not the only one with the ability to cause this nuclear process. Therefore, the unique properties of PdH cannot be used to describe the universal mechanism. Instead, the general nature of the environment that can form in all materials needs to be understood and applied.

Crystal structures form because this arrangement of atoms and electrons has the lowest chemical energy compared to any other relationship for the applied conditions. Crystal structures cannot support nuclear fusion because the

nuclei are too far apart for them to interact. Any effort to force the nuclei into a closer relationship would require the application of enough local energy to overcome the chemical forces as well as the Coulomb barrier. This energy is normally not available, although many efforts have been made to justify a closer approach between the atoms based on various theories. [3]–[5] For example, the idea that enough energy to cause a fusion reaction could concentrate at a particular location by random chance is in conflict with what would happen if such a universal mechanism were to take place in a chemically unstable material. The stability of explosives demonstrates that this kind of energy concentrating mechanism does not happen in Nature. Therefore, this mechanism is an unlikely explanation for LENR.

Even the proposed metal atom vacancy model, called superabundant vacancies (SAV) [6], is not consistent with the observed behavior because the conditions required to form the SAV are not present when LENR is produced [7]. Indeed, if the proposed vacancy structure could be created within a crystal structure, this condition would be expected to occur throughout the crystal structure, thereby making LENR much more common and uniform at its locations in the material than is the case.

In addition, the ability to cause LENR is sensitive to how the material is manufactured, at least when Pd is used. The ability of a crystal structure to form metal atom vacancies would not be expected to be sensitive to the fabrication process. Therefore, for LENR to occur, the hydrogen nuclei in the host material must form a relationship that is independent of the behavior and chemical limitations characteristic of a crystal structure, which includes being independent of vacancy formation.

2.2. Nature of the NAE

The NAE has two important features. First, a physical condition able to acquired H must form physically outside of the crystal structure. Then, the NAE needs to be populated with H as a result of a conventional chemical process. The formation process is described first.

2.2.1. *How is the NAE Created?*

The conditions needed to form a suitable NAE are very limited, with flaws or gaps, sometimes called cracks, being the most likely possibilities. These can be created by chance or they can be created on purpose. Several occasions when the chance occurrence might have operated can be suggested. Suitable gaps might have formed when the Pd nanopowder used by Arata and Zhang [8] sintered into a solid mass during their study, as observed by McKubre et al. [9]. This process cannot be avoided and would quickly eliminate the initial small particles as active sites. Case [10] used coconut charcoal on which small particles of Pd were deposited. Random gaps located in the charcoal might have provided suitable sites, as suggested by the failure to produce excess power when different charcoal was used. Takahashi et al. [11] might have created gaps by ball-milling a brittle alloy containing Pd, Zr, and Ni after oxidation. When Pd is codeposited [12], suitable gaps are visible between the complex assortment of crystallites in the electroplated deposit. The Pd deposited on CaO by Iwamura et al. [13] would be $_2$. Extended electrolysis of PdD, as practiced by Fleischmann and Pons, is observed to create gaps at the surface as a result of changes in the surface purity and the creation of stress in the Pd cathode. In other words, many successes can be explained by the creation of the same unique condition. This possibility suggests that gap formation be consideration as a requirement for LENR to occur.

In addition, the gap or flaw must have a critical size or dimension because the rare occurrence of LENR demonstrates that all possible sizes are not nuclear active. An estimate of the gap width can be suggested. It needs to be greater than the distance between the H atoms in the crystal structure but smaller than the size required for the H_2 molecule to form because this reaction would compete with the ability to form the less stable NAS. A method is suggested in Section II.2.3 that describes how the critical gap width might be formed on purpose.

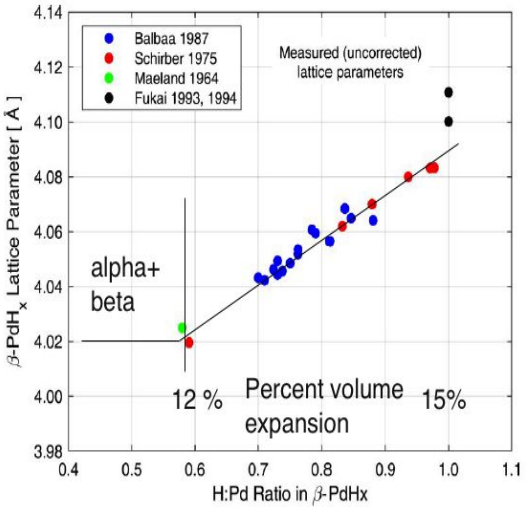

Figure 1. Change in lattice parameter when Pd reacts with hydrogen. The lattice parameter of pure Pd is 3.8916 Å.

2.2.2. *How is the NAE Populated With H?*

The process of populating the NAE with H would involve a chemical process as the H moves from its normal positions in the crystal and into this new atom arrangement. For the hydrogen to move, it must experience a loss of Gibbs energy. The resulting new chemical relationship between the H would then make possible the formation of a unique kind of chemical arrangement that is identified as the NAS. When theoreticians want to explain the nuclear process, they need to focus on the NAS because all of the processes are chemical and without novelty before the NAS forms.

The gap must have another characteristic for it to be consistent with the observations. The NAE would become stable after it has become populated with H because the removal of the H would require the return of the lost Gibbs energy. This energy is not normally available. As a result, the LENR process would be independent of the hydrogen content after the NAE has formed, as described in Section II.6.

2.2.3. *How can the NAE be Created on Purpose?*

Nano-machining of suitable grooves or holes in a metal sheet could be used to create a controlled number of active sites. This method has the advantage of providing total control of the power density and the amount of power. But first, the size of the gap needs to be known.

Another method involves the addition of small inert particles having a critical dimension to Pd. Such particles will become surrounded by a gap when the Pd is reacted with hydrogen. This effect occurs because the dissolved hydrogen causes the Pd to expand without changing the size of the particle. The magnitude of this expansion can be calculated using the lattice parameter shown in Fig. 1. The process of physical expansion has been studied [14-17] and found to be complex.

A cartoon in Fig. 2 shows an example of a gap formed around a particle of an arbitrary shape with a NAS present at an arbitrary location in the NAE. The magnitude of the gap width can be calculated using the fraction of expansion shown in Fig. 3. If the gap is assumed to be uniform around the particle, the gap (G) width can be calculated using the fraction expansion (F), times the dimension of the particle (D) divided by 2, as shown in the equations.

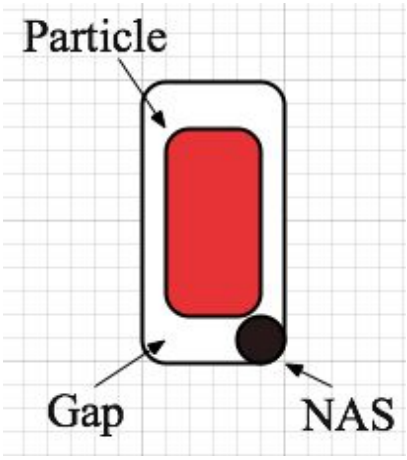

Figure 2. Cartoon of an embedded particle of inert material in the PdH structure around which a gap has formed as the result of the expansion after the Pd has reacted with H. The shape is arbitrary. A possible location of a NAS is shown. Many NAS would be expected to form in the same gap. The hydrogen atoms in the gap and the surrounding crystal structure are not shown. The figure is not drawn to scale.

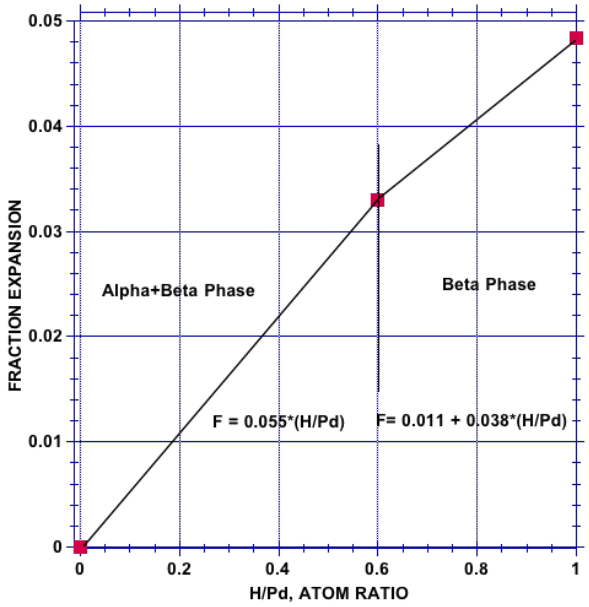

Figure 3. Fraction expansion of Pd when H is added as a function of the H/Pd atom ratio. The fraction produced by D would be similar.

$G = F*D/2$
$F = 0.055*(H/Pd)$ for H/Pd = 0.0-0.6
$F = 0.011 + 0.038*(H/Pd)$ for H/Pd = 0.6-1.0

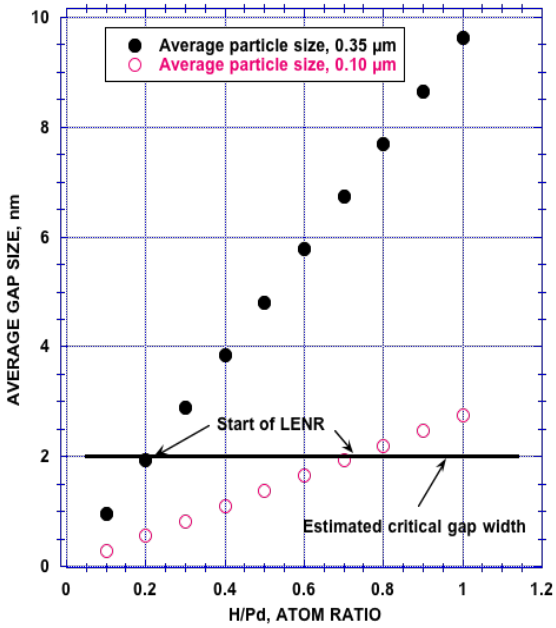

Figure 4. Example of how the particle size affects gap width as the H/Pd ratio is changed. The size needed to produce LENR is estimated to show how the H/Pd atom ratio might affect the onset of LENR.

However, the expansion will not be uniform unless the particle is a perfect cube. The actual particles will show a greater gap forming in the direction of their long axis than in the direction of the short axis, with the gap at other locations having values between these two extremes. While this behavior complicates the interpretation, it does not distract from the understanding of how the gap-forming process operates to form the NAE.

The rate of expansion changes when all of the alpha-phase has converted to the beta-phase, which is assumed to happen at H/Pd = 0.6 for this example. The actual composition at which this change in slope occurs will depend on temperature and hydrogen pressure. Nevertheless, this approximation is useful to show how the process is expected to work.

If the particle size were 0.35 μm and the active gap size is assumed to be 2 nm, the material would be expected to become active when the H/Pd ratio had reached 0.2, as shown in Fig. 4. When a particle with an average dimension of 0.1 μm is used, the H/Pd ratio would have to reach 0.8 before the material would become active. The challenge is to determine the required gap size so that a material could be made active at a known and easily obtained H/Pd ratio.

How do observations support this explanation? Two observations apply. According to Martin Fleischmann, Johnson-Matthey used cracked-ammonia to maintain a reducing atmosphere over the molten Pd while calcium boride was added to remove any oxygen during the purification process. The CaB_6 would react with oxygen to produce particles of CaO and a liquid consisting of the boron oxides. Some small particles of CaO would be expected to remain in the Pd after it had solidified. These would allow gaps to form when the Pd was later reacted with D or H. A relatively uniform distribution of these particles throughout certain batches of Pd metal would explain why, when LENR occurred, it was found to be produced by the entire batch regardless of its physical form, whether as wire or flat plate. After the Pd was further purified, for example by zone melting, it was never found to be active.

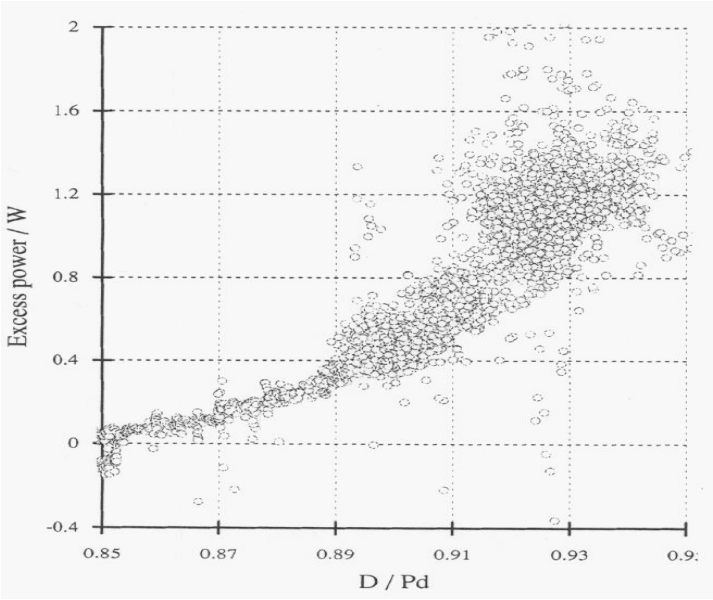

Figure 5. Relationship between the amount of power and the D/Pd atom ratio *[18]*.

McKubre et al. [18] found that the amount of power produced at 20°C when a particular batch of Pd was used increased when the D/Pd ratio was increased, as shown in Fig. 5. A similar behavior was reported by Kamimura et al. [19] Two features shown by the behavior are important. The power-composition relationship shows a wide variation in values and a nonlinear increase as the D/Pd ratio is increased. How do these two behaviors relate to the proposed role of gaps created by embedded particles?

If the particles had a size distribution as shown in Fig. 6, some power would be produced when the D/Pd ratio reached 0.8, based on the values shown in Fig. 5. However, the number of particles being activated would be too small to produce enough power for it to be detected. As the D/Pd ratio was further increased, an increasing number of smaller particles would become active, thereby causing more power to be generated. If the distribution had the form shown in Fig. 6, the amount of power would increase with a nearly exponential relationship as the data in Fig. 5 shows. The observed wide scatter in values can be partly explained by the distribution of particle size not being uniform throughout the batch of material.

This description is used only as an example of how the particle size might affect the amount of power. The critical particle size is still unknown and needs to be determined. Meanwhile, studies are underway to study the effect of adding various high melting compounds having particles of various sizes to Pd. Particles of CaO, SiO_2, and BN have been found to produce behavior consistent with this explanation.

Because the gap becomes chemically stable after it has been populated with hydrogen, LENR will not be affected by the D/Pd ratio after the LENR process starts. This behavior is discussed in Section II.6. Nevertheless complete removal of H by using either high vacuum or high temperatures would be expected to stop the LENR process from occurring even after the D had been replaced because the gap size would have become too large to become active. This expectation has been tested and found to be true. This behavior might account for the occasional failure to replicate excess power after a sample has been allowed to lose too much D. That remelting has been found to reactivate a previously active material supports this explanation.

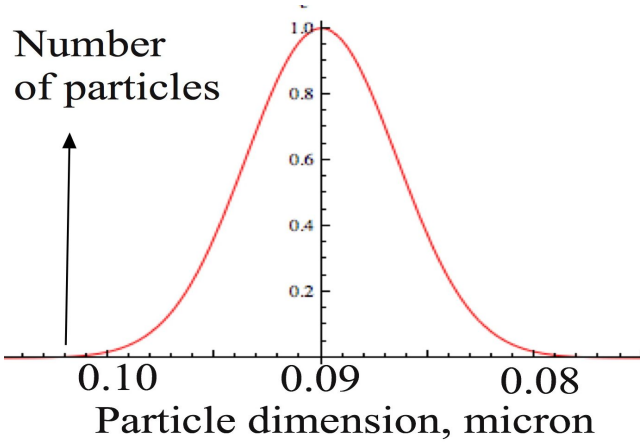

Figure 6. A hypothetical particle size distribution.

2.3. Creation of the NAS[1]

For a nuclear process to occur, the nuclei must get close enough for their nuclear energy states to interact. This requires the strong repulsion created by the Coulomb Barrier to be overcome. However, the required energy is not present in a chemical structure. Because nuclear reactions are now known to occur without the need for applied energy, the mechanism now needs to be identified. A plausible mechanism involving the ability of the electron charge to offset the positive charge of the nuclei can be suggested. This kind of shielding has been studied by applying extra energy, which triggers the hot fusion mechanism. Although electron shielding is now known to occur, it has only a very small effect [20], [21]; not nearly enough to account for the LENR behavior. Some people have suggested either neutron formation, an interaction with unusual exotic particles, or the accumulation of phonons as the source of the required energy. The flaws in these mechanisms are too complex to discuss here.

Instead, a new kind of nuclei-electron interaction is suggested, perhaps similar to that operating in the EVO, as discovered by Shoulders and replicated by Fox [22]–[24]. A similar but larger-scale process called ball lightning is suggested by Lewis. [25] These clusters are described as consisting of a collection of positive ions and electrons with about 10^6 electrons for each positive ion. [24] Although these structures are obviously real, their common feature is difficult to understand. Nevertheless, the possible relationship of this common feature to LENR makes their understanding more urgent.

Because this structure is normally made in air, it would be based on the nuclei of oxygen and nitrogen. Perhaps, the Coulomb Barrier is too large in this case to allow a nuclear reaction to take place. But, what might happen when the nuclei are those of the hydrogen isotopes? Might the presence of these nuclei allow the structure to experience a nuclear interaction as a consequence of a relatively smaller Coulomb Barrier being present?

In addition, the nature of the radiation emitted from LENR suggests the process involves a cooperative relationship between many nuclei, which would require the formation of a complex structure involving many components. The need to conserve momentum when nuclear energy is released also requires a cooperative interaction between many

[1] I called the structure that supports fusion the Hydroton in my book [2]. At the time the book was written, I suggested a linear interaction between the electrons and nuclei. Further consideration suggests, instead, a symmetrical and highly localized interaction as described here.

Table 1. Proposed reactants and resulting nuclear products and energy

(D+e+D) = ^{4}H = ^{4}He + e (fast decay) + ν	23.8 MeV
(H+e+D) = ^{3}H = ^{3}He + e (slow decay) + ν	4.9 MeV
(H+e+H) = ^{2}H (stable)	1.9 MeV
(T+e+D) = ^{4}H + **n** = ^{4}He + e (fast) + ν	<19 MeV
(T+e+H) = ^{4}H = ^{4}He + e (fast decay) + ν	<21 MeV

components. This paper is not designed to explore the nature of this assembly. Nevertheless, some words about how it might be created are warranted.

After the NAE forms, the formation of the NAS would require the electrons and hydrogen nuclei to spontaneously concentrate at the same location. Laws of thermodynamics must guide this process because the process occurs in a chemical environment. The nuclear process would not be anticipated by the atoms and would occur as an unexpected consequence of forming an unusual assembly by normal chemical interaction. In other words, the assembly process must shed Gibbs energy as it forms, perhaps as the detected X-ray emission. Only later after the assembly process is complete, does nuclear interaction take place followed by the release of the nuclear products along with the nuclear energy. Amazingly, Nature has found a new method to cause nuclear interaction but only after the required chemical conditions have been satisfied.

The process of forming the NAS might be accelerated by passing a high current through the material, as done by Godes [26], [27], or by using laser light of certain frequencies, as Letts and others have reported. [28]–[31] The presence of certain elements in the NAE might also provide a greater than normal supply of electrons. Even the electron current used to cause electrolysis might play a role instead of an ion flux [32] being the important variable. Nevertheless, some NAS seems to form spontaneously without additional effort after the NAE has formed.

The fusion reaction destroys the NAS, after which it reforms as hydrogen is resupplied first from the local NAE [33] and then from the surrounding crystal structure. In other words, this process rapidly repeats at the same locations. Because each NAE can contain many such assemblies, the amount of generated power is determined by how many NAS form in each NAE and how rapidly the H can be replaced after it has been converted to a different isotope. When the local concentration of NAS is too large, local melting would be expected, as has been observed [34].

2.4. The Nature of the Nuclear Reaction

The process is observed to produce at least helium and tritium as well as several kinds of energetic emissions. The production of transmutation products is not discussed here. If we assume all the fusion reactions take place as a result of the same mechanism, what nuclear products can be expected to result from each combination of hydrogen isotopes?

When this assumption is applied, the observed nuclear products can be explained ONLY when an electron is added to each fusion product. This electron-proton interaction does not take place outside of the NAS, hence does not produce a free and independent neutron. Addition of an electron to the final nuclear product is plausible because electrons are involved in lowering the Coulomb barrier, which would increase the probability of their capture by the final nuclear energy state.

Table 1 [2] summarizes the suggested reactions, their products, and the resulting energy. The fusion of hydrogen isotopes is proposed to make other isotopes of hydrogen, several of which then decay by beta emission to form isotopes of helium. The antineutrino (ν) is assumed to carry a small but unknown fraction of the nuclear energy. Besides being consistent with the observations, as described below, the fusion products have a satisfying symmetry to each other. Although being novel and not generally accepted, this idea allows many behaviors to be explained and many predictions to be tested, as follows.

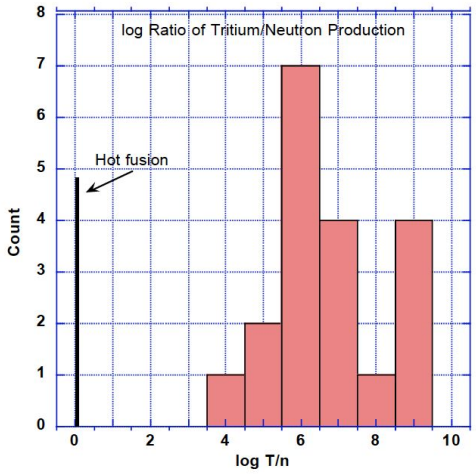

Figure 7. Relationship between the number of reported values and the log of the measured tritium/neutron ratio. The ratio resulting from the hot fusion mechanism is well established at a value near unity or log T/n = 0.

When tritium is produced by the fusion between H and D, a small number of neutrons are formed that are correlated with the amount of tritium, as shown in Fig. 7. The large difference between the T/n ratios produced by cold- and hot-fusion demonstrates that these two nuclear reactions are caused by entirely different mechanisms. Instead of many neutrons resulting from the fragmentation of the helium nucleus, a few neutrons result when tritium fuses with deuterium. The large variation in the reported values would result from a different T/D ratio being present during each measurement. A comparison of the T/n ratio to the T/D ratio when future measurements are made would test this idea.

Please note, the equations in Table 1 only identify the reactants and the products. They do not describe the mechanism or imply that only three reactants are involved. In fact, conservation of momentum when the energy is dissipated requires many carriers of the energy and momentum to be ejected from the site of the nuclear reaction. As noted previously, these energy carriers appear to come from a novel and complex nuclear process.

In summary, the combined energy state consisting of hydrogen nuclei and electrons decomposes by emitting the nuclear products along with many electrons, each containing part of the resulting energy. The nuclear products consisting of photons and ions have been detected. Emission of energetic electrons has also been observed [35]. Anti-neutrino emission is expected to carry some energy that would not be captured in the calorimeter. This radiation has not been observed although it has been considered [36].

2.5. Evidence Supporting the Formation of ^{4}H.

The ^{4}H isotope, when made by bombarding T with D at high energy, is found to decompose immediately by ejecting a neutron. The model suggested here assumes that when ^{4}H is made at low energy, the nucleus remains stable and eventually loses its energy by beta emission to produce ^{4}He. What observed behavior supports this assumption?

Karabut et al. [37] measured the ion spectrum emitted during gas discharge in D_2 using a silicon barrier detector and confirmed the presence of energetic ions using CR39. The spectrum is shown in Fig. 8. Three behaviors are important. The spectrum consists of separate ion energies having about the same energy separation; the intensity decreases as the energy increases, and most of the energy lies between about 1 and 6 MeV. They concluded some of the ions were ^{4}He.

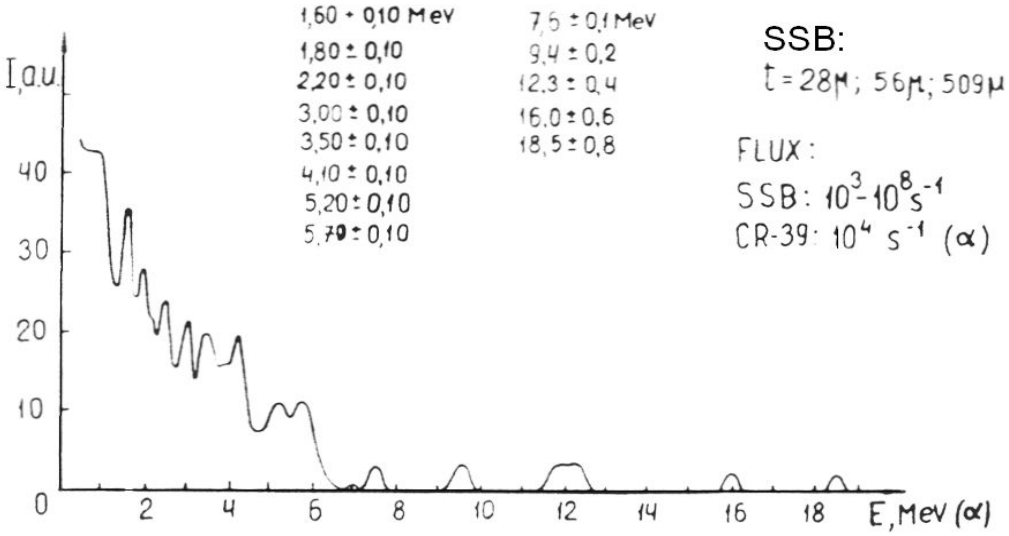

Figure 8. Ion spectrum was measured as the result of gas discharge in D_2 while using a silicon barrier detector located within the apparatus [37].

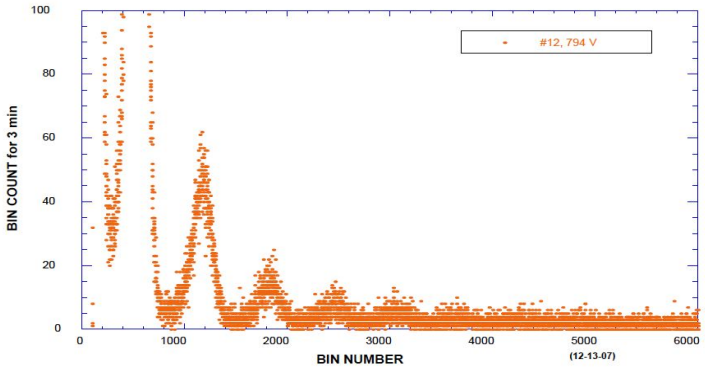

Figure 9. The typical spectrum produced during gas discharge when either H_2 or D_2 is used.

Eight years later, Storms and Scanlan [38] measured the spectrum produced during gas discharge using a silicon barrier detector, shown in Fig. 9. As can be seen in Fig. 10, the different energies all have the same energy separation equal to 0.417 MeV. The values in Fig. 11 show that the decrease in intensity can be fit by an exponential relationship. Also, the energy range falls in the same range found by Karabut et al. In other words, these two measurements that were made using different detectors and done at different laboratories show very similar behavior. Also, the same spectrum was produced by Storms and Scanlan when either H_2 or D_2 were used. The same spectrum would result because ^4H would be produced after the fusion of H had created enough D to allow some D+D fusion to take place. The D ions emitted when H+H+e fusion occurred would not have enough energy to be detected, although a similar spectrum would be expected.

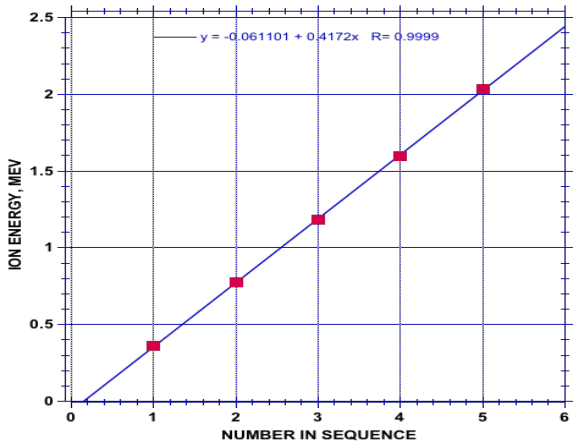

Figure 10. The relationship between the sequence in the spectrum and the ion energy when the first peak is given a value of 1.

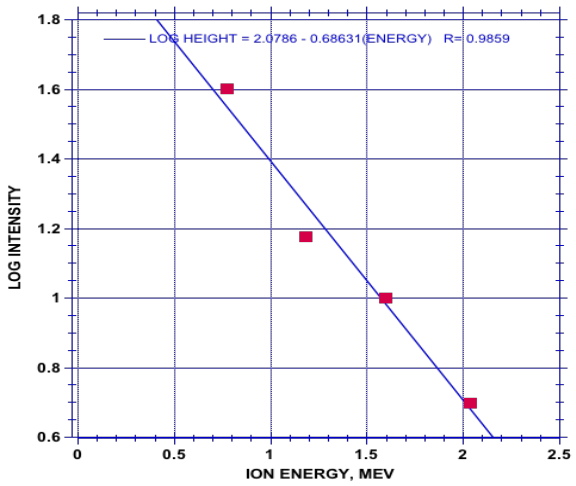

Figure 11. The relationship between log intensity and ion energy. The intensity is given a relative value.

Unlike, Karabut et al., Storms and Scanlan determined the nature of the ions by determining the change in energy produced when various absorbers were inserted. The change in energy was compared to that described in the NIST tables (NSRDS-NBS29) to identify the element being emitted. They determined that the emissions were consistent with the ions of a hydrogen isotope, not helium! However, at the time the work was done, emission of ^{4}H, which is also consistent with the behavior, was not considered.

An important question remains unanswered. If the ions are ^{4}H, approximately 23.8 MeV would have been released when each was created. The ions in the spectrum shown in Fig. 9 have, on average, much less energy than the amount released by their creation. Where is the missing energy? The missing energy is not in the antineutrino because a nearly correct total energy is measured using a calorimeter. The answer requires several possibilities to be considered, starting with the behavior shown in Fig. 10.

For the ions to have an equal separation of energies, all of the ions must result from a single fusion reaction occurring at the same location in the material. An unknown amount of energy would be removed as the ions passed through the material between the source and the detector. As a result, the measured energy of the ions would be a lower limit compared to the actual energy released at their creation. In addition, the difference in energy shown by the two spectrums suggests that the depth was slightly greater during the Storms and Scanlan study compared to the depth when Karabut et al. measured the ion energy.

On the other hand, significant absorption of energy as a result of the ions passing through different amounts of material would cause the values not to extrapolate to zero in Fig. 10 and cause much greater smearing of the energy in the spectrum shown in Fig. 9. The absence of these expectations suggests the ions resulted from events happening very near the surface.

Because absorption is not likely to have subtracted significant energy, perhaps the missing energy is emitted as photons [39]–[41] and electrons [42]. The photon energy has been measured. A measurement of the energy contained in the emitted electrons and that resulting from beta emission should be the next step in solving the mystery of the nuclear process.

What implications result from this description?

1. The ^{4}H would escape much more rapidly and more completely from the Pd compared to helium. This means the LENR process would not need to occur near the surface, as has been assumed based on the limited diffusion ability of helium to escape from the Pd structure. Consequently, the LENR reaction could take place throughout the sample with most of the ^{4}He forming after the ^{4}H had diffused out of the material. Future studies of helium production need to measure both the helium content of the gas and the Pd.

2. The failure to detect the expected fragmentation of the energetic ^{4}He nucleus would not have to be explained.

3. Use of pure D would not produce tritium.

4. Fusion of pure ^{1}H would very gradually produce an increasing amount of tritium. This nuclear product would gradually produce ^{4}He as the tritium fused with ^{1}H.

5. Tritium would be produced immediately when a mixture of D and H is used with active material, with the rate being related to the D/H ratio. The slow onset of tritium formation in previous studies using D_2O would result from the slow contamination of the D_2O with H_2O.

6. Increased numbers of neutrons would be produced as the T/D ratio approached unity.

These expectations can be tested by future measurements. These implications also have to be considered when a large energy generator is designed using LENR because a potentially large amount of dangerous tritium could be created along with a smaller neutron flux when ^{1}H is used.

2.6. Effect of Temperature and D/Pd Atom Ratio

The amount of power is increased when the temperature is increased, with a linear relationship being produced between log power and 1/T. This relationship is shown in Fig. 12 for four separate samples of solid Pd having different D contents, with the electrolytic method used during each study.

Each study has the same slope above a critical temperature even when different amounts of power are produced. For example, the sample designated B was measured while the current was applied, which produced a D/Pd ratio of 0.85. The current was then turned off and the sample was again heated several times, which resulted in a steady loss of D. Nevertheless, the values all fell on the same line. In other words, the amount of power and the effect of temperature were not affected by the D content. The activation energy that affects the power production is 0.303 eV/atom, which can be compared to the activation energy for the diffusion of D in PdD which is equal to 0.230 eV/atom [43].

A sample was made by pressing powdered Pd with CaO powder and studied using electrolysis (Fig. 13). Electrolytic current was applied during the first heating and then it was turned off. A greater amount of excess power

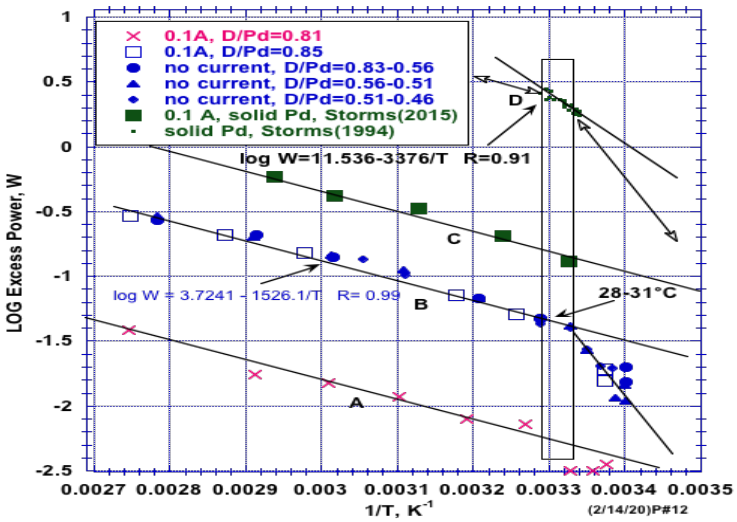

Figure 12. Relationship between log (excess power) vs 1/T for solid samples heated in an electrolytic cell. The studies labeled A, B, C, and D were made at different times using different materials.

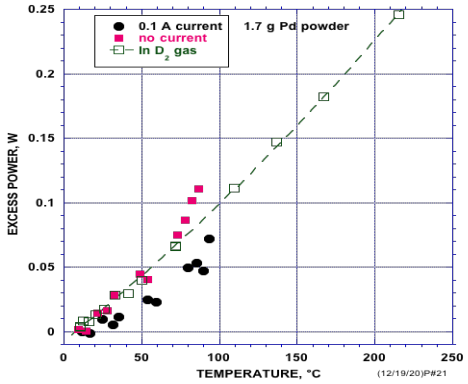

Figure 13. A sample of activated Pd powder was first heated in an electrolytic cell to 90°C. The sample was then transferred to a cell containig D_2 gas and heated to 225°C. The values are taken when the temperature is increased and then when it is decreased with a delay of 110 min between the values.

was produced even though the D content had decreased. Then the sample was removed from the electrolytic cell and placed in a cell containing only D_2 gas while using the same calorimeter. This cell was heated to higher temperatures, as shown in Fig. 13. Notice that the temperature effect

was largely unchanged and similar amounts of excess power were produced at the same temperatures. In other words, the amount of power produced by the LENR process was not affected by the change from electrolysis to gas loading. In addition, the effect of temperature remained unchanged even though the D/Pd ratio had changed. Other

studies have shown that the slope of log (Excess Power) vs 1/T of samples exposed to gas loading is less than the slope produced when electrolysis is used perhaps because the gas can more easily access the NAE.

The slope is related to the activation energy of the process that controls the amount of excess power. This activation energy is similar to the activation energy for the diffusion of D through PdD. [43], [44] Consequently, the temperature appears to be affecting the diffusion process that allows the D to travel from its location in the surrounding crystal structure to the NAE and replace the D lost as a result of fusion. Some samples show similar behavior when heated in D_2 gas at temperatures up to at least 500° C.

Notice that the amount of power produced at 20°C, the temperature used during many reported studies, is very small. Significant power is only produced when the material is heated. Perhaps many of the failures to make detectable energy might have been successful if a higher temperature had been used.

3. SUMMARY

A model is proposed that describes a series of events required for spontaneous nuclear fusion to occur in a material. The model identifies the mechanisms unique to LENR including the final event that requires a new understanding of nuclear interaction. The description is logically consistent with observed behavior and the laws that govern chemical behavior. Predictions are made that can be used to test the validity of the model.

The LENR process is proposed to take place in gaps. The gaps can be formed by several methods, including around embedded particles when the Pd expands as it reacts with H or D. The addition of the properly sized particles to Pd can be used to cause LENR with improved reliability.

These gaps have a critical width in which nuclei and electrons can assemble by a chemical process to produce a structure that can create a common energy state between all the nuclei and electrons. As a result, fusion can happen between any of the hydrogen isotopes to produce another isotope of hydrogen as a result of electron capture by the assembly.

Tritium results from the fusion between H and D. Fusion involving only D does not make tritium. Instead, ^{4}H is formed and rapidly decays to ^{4}He as the final product. Fusion involving only ^{1}H will slowly make tritium, deuterium, and ^{4}H, with ^{4}He being the final nuclear product.

All of these reactions dissipate their energy by the emission of energetic ions, electrons, and X-rays with each being unable to pass through the walls of the apparatus. Very few free neutrons are produced.

The rate of the fusion reaction is determined by the number of nuclear active structures (NAS) that form in the nuclear active environment (NAE) and by the temperature. The temperature controls the rate at which the hydrogen is replaced in the NAE after it has been converted to a nuclear product in the NAS.

ACKNOWLEDGEMENT

I'm grateful to Jed Rothwell, Thomas Grimshaw, and Robin Carter for finding most of the typos and encouraging me to explain my ideas with greater clarity. This work would not have been possible without the past financial support of Brian Scanlan.

References

[1] M. Fleischmann, S. Pons, M.W. Anderson, L.J. Li, M. Hawkins, Calorimetry of the palladium-deuterium-heavy water system, J. Electroanal. Chem. 287 (1990) 293.
[2] E.K. Storms, The explanation of low energy nuclear reaction, Infinite Energy Press, Concord, NH, 2014.
[3] G. Preparata, Cold fusion '93': Some theoretical ideas, Trans. Fusion Technol. 26 (1994) 397–407.
[4] A. Meulenberg, K.P. Sinha, Composite Model(s) for Low Energy Nuclear Reactions in the solid state: II, (2020).

[5] P.L. Hagelstein, I.U. Chaudhary, Phonon models for anomalies in condensed matter nuclear science, Current Science 108 (2015) 507–13.
[6] M.R. Staker, A model and simulation of lattice vibrations in a superabundant vacancy phase of palladium–deuterium, Modeling Simul. Mater. Sci. Eng. 28 (2020) 0650066.
[7] Z.M. Geballe, M. Somayazulu, N. Armanet, A.J. Mishra, M. Ahart, R.J. Hemley, High-pressure synthesis and thermodynamic stability of PdH1$\pm\varepsilon$ up to 8 GPa, Phys. Rev. B 103 (2021) 024515.
[8] Y. Arata, C. Zhang, Presence of helium ($^2He_4$, $^2He_3$) confirmed in highly deuterated Pd-black by the new detecting methodology, J. High Temp. Soc. 23 (1997) 110 (in Japanese).
[9] M.C.H. McKubre, F. Tanzella, P. Tripodi, V. Violante, Progress towards replication, in: X.Z. Li (Ed) The 9th International Conference on Cold Fusion, Condensed Matter Nuclear Science, Tsinghua Univ. Press, Tsinghua Univ., Beijing, China, 2002, pp. 241.
[10] L.C. Case, Catalytic fusion of deuterium into helium-4, in: F. Jaeger (Ed) The Seventh International Conference on Cold Fusion, ENECO, Inc., Salt Lake City, UT, Vancouver, Canada, 1998, pp. 48.
[11] A. Takahashi, H. Ido, A. Hattori, R. Seto, A. Kamei, J. Hachisuka, T. Yokose, Y. Mori, A. Taniike, Y. Furuyama, Latest Progress in Research on AHE and Circumstantial Nuclear Evidence by Interaction of Nano-Metal and H(D)-Gas, J. Cond. Mater. Nucl. Sci. 33 (2020) 14-32.
[12] P.A. Mosier-Boss, L.P. Forsley, F.E. Gordon, Overview of Pd/D Co-deposition, J. Cond. Matter. Nucl. Sci. 29 (2019) 34–40.
[13] Y. Iwamura, T. Itoh, N. Yamazaki, J. Kasagi, Y. Terada, T. Ishikawa, D. Sekiba, H. Yonemura, K. Fukutani, Observation of low energy nuclear transmutation reactions induced by deuterium permeation through multilayer Pd and CaO thin film, J. Cond. Matter Nucl. Sci. 4 (2011) 132-44.
[14] E.K. Storms, The nature of the energy-active state in Pd-D, Infinite Energy #5-6 (1995) 77–81.
[15] R. Griessen, R. Feenstra, Volume changes during hydrogen absorption in metals, J. Phys. F: Met. Phys. 15 (1985) 1013.
[16] O. Beeri, D.C. Dunand, Transformation mismatch plasticity in Pd induced by cyclic hydrogen charging, Mater. Sci. and Eng. A 532 (2009) 178–83.
[17] N. Armanet, M. Bonnard, Lattice volumic expansion of Palladium vs Hydrogen concentration : classical trend questioned, 2015.
[18] M.C.H. McKubre, S. Crouch-Baker, A.M. Riley, S.I. Smedley, F.L. Tanzella, Excess power observations in electrochemical studies of the D/Pd system; the influence of loading, in: H. Ikegami (Ed) Third International Conference on Cold Fusion, "Frontiers of Cold Fusion", Published by: Universal Academy Press, Inc., Tokyo, Japan, Held at: Nagoya Japan, 1992, pp. 5.
[19] H. Kamimura, T. Senjuh, S. Miyashita, N. Asami, Excess heat in fuel cell type cells from pure Pd cathodes annealed at high temperatures, in: M. Okamoto (Ed) Sixth International Conference on Cold Fusion,Progress in New Hydrogen Energy, New Energy and Industrial Technology Development Organization, Tokyo Institute of Technology, Tokyo, Japan, Lake Toya, Hokkaido, Japan, 1996, pp. 45.
[20] K. Czerski, Enhanced electron screening and nuclear mechanism of cold fusion, in: V. Violante, F. Sarto (Eds), 15th International Conference on Condensed Matter Nuclear Science, ENEA, Italy, Rome, Italy, 2009, pp. 197-202.
[21] E.N. Tsyganov, V.M. Golovatyuk, S.P. Lobastov, M.D. Bavizhev, S.B. Dabagov, Registration of energy discharge in D + D =4He* reaction in conducting crystals (simulation of experiment), Nucl. Instr. and Meth. in Phys. Res. B 309 (2013) 95–104.
[22] K. Shoulders, EV, A Tale of Discovery, www.LENR.org, 1987.
[23] K. Shoulders, Projectiles from the dark side, Infinite Energy 12 (2006) 39–40.
[24] H. Fox, J.S. X., Low-energy nuclear reactions and high-density charge clusters, Infinite Energy 4 (1998) 26–30.
[25] E.H. Lewis, Evidence of microscopic ball lightning in cold fusion experiments, in: J.-P. Biberian (Ed) 11th International Conference on Cold Fusion, World Scientific Co., Marseilles, France, 2004, pp. 304.
[26] F. Tanzella, R. George, R.E. Godes, Nanosecond Pulse Stimulation in the Ni–H2 System, J. Cond. Matter. Nucl. Sci. 29 (2019) 202–10.
[27] R.E. Godes, D. Correia, R.D. Gremban, Control of low energy nuclear reactions in hydrides, and autonomously comtrolled heat generation module, 2015.
[28] P.L. Hagelstein, D. Letts, D. Cravens, Terahertz difference frequency response of PdD in two-laser experiments, J. Cond. Matter Nucl. Sci. 3 (2010) 59–76.

[29] L. Holmlid, Heat generation above break-even from laser-induced fusion in ultra-dense deuterium, AIP Advances 5 (2015) 087129.
[30] V. Violante, M. Bertolotti, E. Castagna, I. Dardik, M.C. McKubre, S. Moretti, S. Lesin, F. Sarto, F. Tanzella, T. Zilov, Progress in excess power production by laser triggering, in: A. Takahashi, K. Ota, Y. Iwamura (Eds), Condensed Matter Nuclear Science, ICCF-12, World Scientific, Yokohama, Japan, 2005, pp. 55–64.
[31] M.R. Swartz, Photo-induced excess heat from laser-irradiated electrically polarized palladium cathodes in D_2O, in: P.L. Hagelstein, S.R. Chubb (Eds), Tenth International Conference on Cold Fusion, World Scientific Publishing Co., Cambridge, MA, 2003, pp. 213–25.
[32] M.C.H. McKubre, F.L. Tanzella, Flux Effects in Metal Hydrogen Loading: Enhanced Mass Transfer, J. Cond. Matter Nucl. Sci. 15 (2015) 1-10.
[33] S. Szpak, P.A. Mosier-Boss, J. Dea, F. Gordon, Polarized D+/Pd-D_2O system: hot spots and "mini-explosions", in: P.L. Hagelstein, S.R. Chubb (Eds), Tenth International Conference on Cold Fusion, World Scientific Publishing Co., Cambridge, MA, 2003, pp. 13.
[34] D. Nagel, A.E. Moser, High Energy Density and Power Density Events in Lattice-enabled Nuclear Reaction Experiments and Generators, J. Cond. Mater. Nucl. Sci. 19 (2016) 219–29.
[35] F.E. Gordon, H.J. Whitehouse, Lattice Energy Converter, JCMNS 35 (2022) 30–48.
[36] Z.M. Dong, C.L. Liang, B. Liu, Q.-M. Wei, J. Tian, S.X. Zheng, J.Z. Yu, X.Z. Li, Studies on Anomalous Phenomena of D/Pd Systems using a Gas-loading Process – A Stride Towards Neutrino Detection, J. Cond. Matter Nucl. Sci. 4 (2011) 119–31.
[37] A.B. Karabut, Y.R. Kucherov, I.B. Savvatimova, Nuclear product ratio for glow discharge in deuterium, Phys. Lett. A 170 (1992) 265–72.
[38] E.K. Storms, B. Scanlan, Detection of radiation from LENR, in: D.L. Nagel, M.E. Melich (Eds), 14th International Conference on Condensed Matter Nuclear Science, www.LENR.org, Washington, DC, 2008, pp. 263–87.
[39] A.B. Karabut, E.A. Karabut, P.L. Hagelstein, Spectral and temporal characteristics of X-ray emission from metal electrodes in a high-current glow discharge, J. Cond. Matter Nucl. Sci. 6 (2012) 217–40.
[40] A.B. Karabut, E.A. Karabut, Research into spectra of X-ray emission from solid cathode medium during and after high current glow discharge operation, in: D.L. Nagel, M.E. Melich (Eds), 14th International Conference on Condensed Matter Nuclear Science, www.LENR-CANR.org, Washington DC, 2008, pp. 362–7.
[41] A. Karabut, Research into powerful solid X-ray laser (wave length is 0. 8–1.2 nm) with excitation of high current glow discharge ions, 11th International Conf. on Emerging Nuclear Energy Syst., Albuquerque, NM, 2002, pp. 374.
[42] A. Meulenberg, J.L. Paillet, Nature of the Deep-Dirac Levels, JCMNS 19 (2016) 192–201.
[43] E. Storms, The Nature of the Fusion Reaction in Palladium and Nickel, ICCF-23, Xiamen, China, 2021.
[44] E. Storms, Anomalous Energy Produced by PdD, J. Cond. Matter. Nucl. Sci. 20 (2016) 81–99.

J. Condensed Matter Nucl. Sci. 38 (2023) 147–160

Research Article

Synchronization of Vacancy-Loaded Deuterons Enables Successful LANR Mass-Energy Transfer

Mitchell R. Swartz

JET Energy, Inc., Wellesley Hills, MA, USA

Abstract

Unlike hot fusion, LANR is relational and productive rather than confrontational and destructive. Rather than one D hitting the other as a target, there is no conventional "coulomb barrier", but instead synchronous interaction(s) follow application of an electric field intensity. Analysis of the pulsing coupled atomic deuteron oscillators is difficult, and here we have used equivariant bifurcation theory. A mathematical solution of this, such as a toroidal breather mode, reveals much. Most importantly, such synchronization of deuterons may obviate, i.e. circumvent, the function of the 'coulomb barrier'. We have observed that successfully driven LANR components emit unique RF emissions, with sidebands and pulsations which may herald energy-mass interactions. The final product of these processes is fusion of two deuterons with production of *de novo* helium-4, and generation of the observed "excess heat".
 ISSN 2227-3123

Keywords: Deuteron fusion, synchronization fusion, toroidal breather mode, deuteron synchronization, coupled oscillators, equivariant bifurcation theory, coulomb barrier elimination.

1. Introduction: Energy-Matter Redistribution

In successful LANR (lattice assisted nuclear reactions), pairs of loaded deuterons -located in periodic vacancy sites- combine synchronously. Unlike hot fusion, this is relational and productive rather than confrontational and destructive. Thus, here, rather than one D hitting the other as a target, there is no conventional "coulomb barrier", but instead synchronous interaction(s) follow application of an electric field intensity.

LANR/CF is quite real [Figure 2]. There are thirty-four years of solid sterling evidence heralding that the excess heat in CF/LANR is real AND comes from a nuclear origin [Figures 2, 3, 4, 5]. By the reactions described herein the important result is successful fusion of two deuterons within the lattice, with local production of *de novo* helium-4, and generation of the observed "excess heat". We previously observed unique radiofrequency ["RF"] emissions, sidebands and pulsations [1], [2], [3] from successfully driven [4], [5], [6], [7], [8], [9] lattice assisted nuclear ["LANR/CF"] components and systems. This paper will show further how successful LANR occurs by deuteron ion synchronization using analysis of the pulsing coupled atomic deuteron oscillators made using equivariant bifurcation theory.

These pulsing RF sidebands at the deuterium line [D-L] reveal interactions between them, and since ICCF-21 we have attempted to examine if a video or mathematical solution exists. One solution involves the toroidal breather

 ISSN 2227-3123

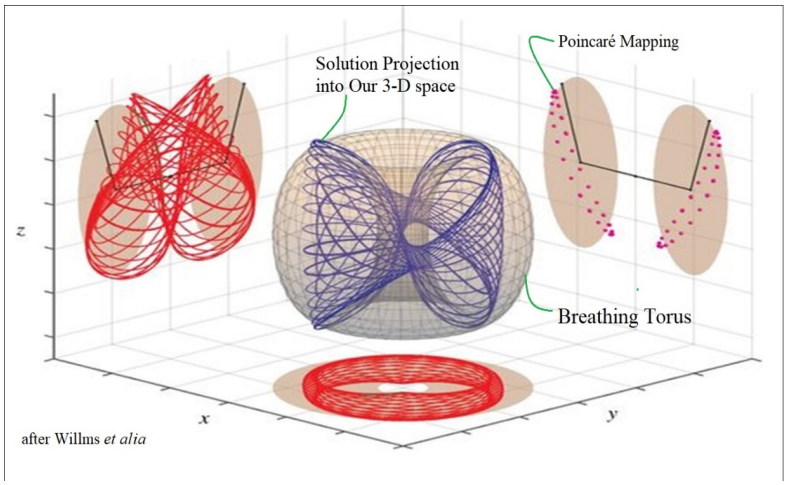

Figure 1. Toroidal Breather Mode Shows Path of Synchronized Deuterons.
Shown is a mathematical analysis of how the coulomb barrier is avoided; this is the "Synchronous deuteron fusion phase space". Projections are shown on the left and bottom side walls which are the stable solutions; two planar projections which are red colored. The Poincaré map for y=0 is magenta; on the right coordinate plane is a one-dimensional closed curve.

mode, which is revealed by equivariant bifurcation theory. This solution may explain how these systems circumvent the coulomb barrier which they clearly do and have done for more than three decades. Such an explanation transforms what is (wrongly) expected, leaving many of the skeptics' arguments essentially moot.

Deuteron synchronization is the process which enables mass-energy transfer resulting in the observed excess heat for LANR. The deuteron synchronizations are heralded by the unique antiStokes spectra [Figure 3, bottom] and by these unique RF emissions at 327.37Mhz or these reactions [Figures 4, 5]. These spectra and RF emissions occur only during observed real LANR.

Most importantly, it is proposed in this paper that the appearance of successful excess heat ["XSH"] only occurs after deuteron ion synchronization which leads to subsequent mass/energy transfer within the highly loaded metal lattice.

These curves in Figure 3, on the bottom, confirm that there are two driven LANR states, but only one (1) gives excess heat. The figure is the overlaid coherent Raman Spectra of the same preloaded ZrO_2PdD NANOR®-type CF/LANR component in three different electrical drive modes [NANOR ® type component 7-6]. The spectra are dual wavelength coherent electric-driven volume-enhanced reflection spectroscopy. The plots show the reflected optical intensity as a function of wavelength, initially from two incident coherent optical beams but also with reflected backscatter from the core along with the initial optical beams. The three modes (responses) shown are the not driven ["off"] state, the unwanted electrical avalanche mode, and the optimal operational state, the "Desired Active Mode", where "excess" energy is being released. Attention is directed to the fact that these curves confirm that there are two (2) electrically driven LANR states - but only one (1) gives excess heat.

2. Background – CF/LANR is Absolutely Real

2.1. Background – Successful LANR is Heralded by Deuteron-Line Sidebands

As previously reported, electrically driven lattice assisted nuclear reaction (LANR) systems, both aqueous and dry preloaded nanomaterial, emit very narrow bandwidth hyperfine radiofrequency (RF) emission peaks at 327.37 MHz,

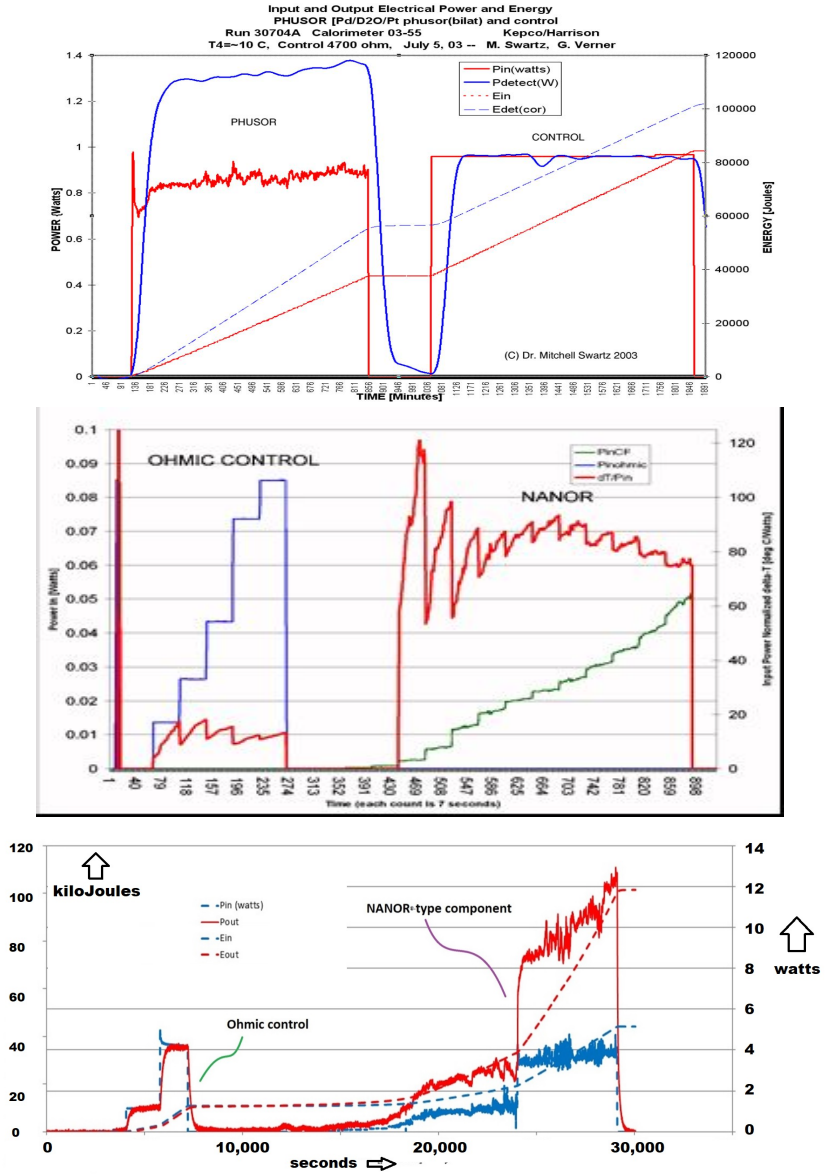

Figure 2. Successful LANR Excess Heat.
This figure shows results of two successful aqueous and dry, preloaded LANR experimental runs. To prove they are real, these demonstrations have both ohmic controls, and time integration. Reproducible Excess heat (XSH) results are shown with clear comparisons to ohmic controls. The ohmic control was second in the aqueous run, and preceded the input to the dry two preloaded NANOR® - type components, below it.
Excess heat was not seen in any of the electrically driven ohmic controls.

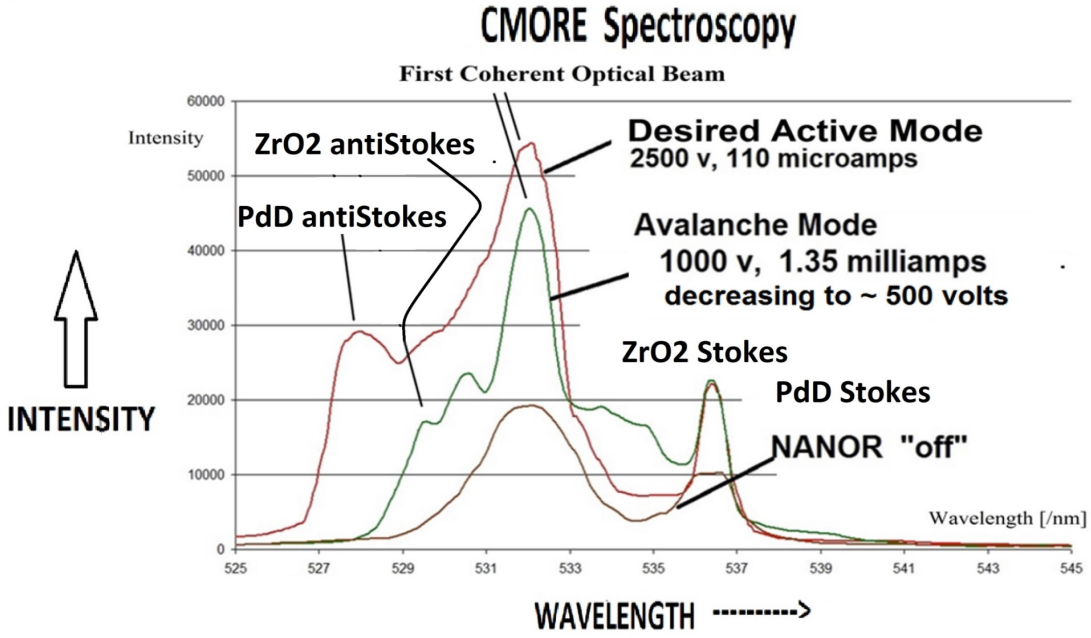

Figure 3. Successful LANR Excess Heat and the use of Coherent Raman Spectroscopy to Prove the Presence of a Working Active LANR system.
Results from preloaded NANOR®-type LANR component before, during, and after XSH. Shown for the single dry preloaded component – in two electrical drive states and "off" – are the unique antiStokes signatures, including the one that ONLY appears with active LANR systems.

located very close to the theoretical Deuteron-Line (DL; 327.348 MHz) region [Figures 4 and5]. They exhibit a large $Q > 1.2 \times 10^6$.

Figure 5 shows a radiofrequency [RF] Deuterium Line [DL] spectrum of a nickel cathode LANR system, driven at ~40 volts, 200 milliAmperes. The 'waterfall' plot shows intensity as a function of frequency. The largest amplitude pulsatile RF line on the right hand side, marked by a star.

The deuterons in the highly-loaded lattice couple together to form a phased array which is then perceived as a very high Q radiofrequency (RF) emission near the deuterium line (DL). At higher applied driving voltages, a superhyperfine line structure of sidebands appears, and that reveals the active site and much more.

Most relevant here, at least some of their emitting RF radiation superhyperfine line peaks, heralding the inverted population, were observed to be pulsing with periods of several minutes (star, above right). Their appearance is unlike everything else examined over the last six years from Earth or galactic origin. It is ONLY associated with an active XSH-producing CF/LANR system.

A close up of this is seen of some of the sidebands shown in Figure 5. These observations have been taken as a sign of possible real time mass-energy transfers within the high loaded active XSH-producing PdD lattice.

In summary, it was learned that successful cold fusion is fueled by deuterons, and in these active LANR systems this occurs by weakly coupled identical oscillators of deuteron ions located in vacancies.

It is clear that the loaded deuterons must work together from their vacancy sites to enable the desired XSH-producing reactions within the loaded Group VIII metal. It is unclear how the coupling occurs, what is its strength, whether it is uniform, and what would make them couple in phase to produce the observed maser action.

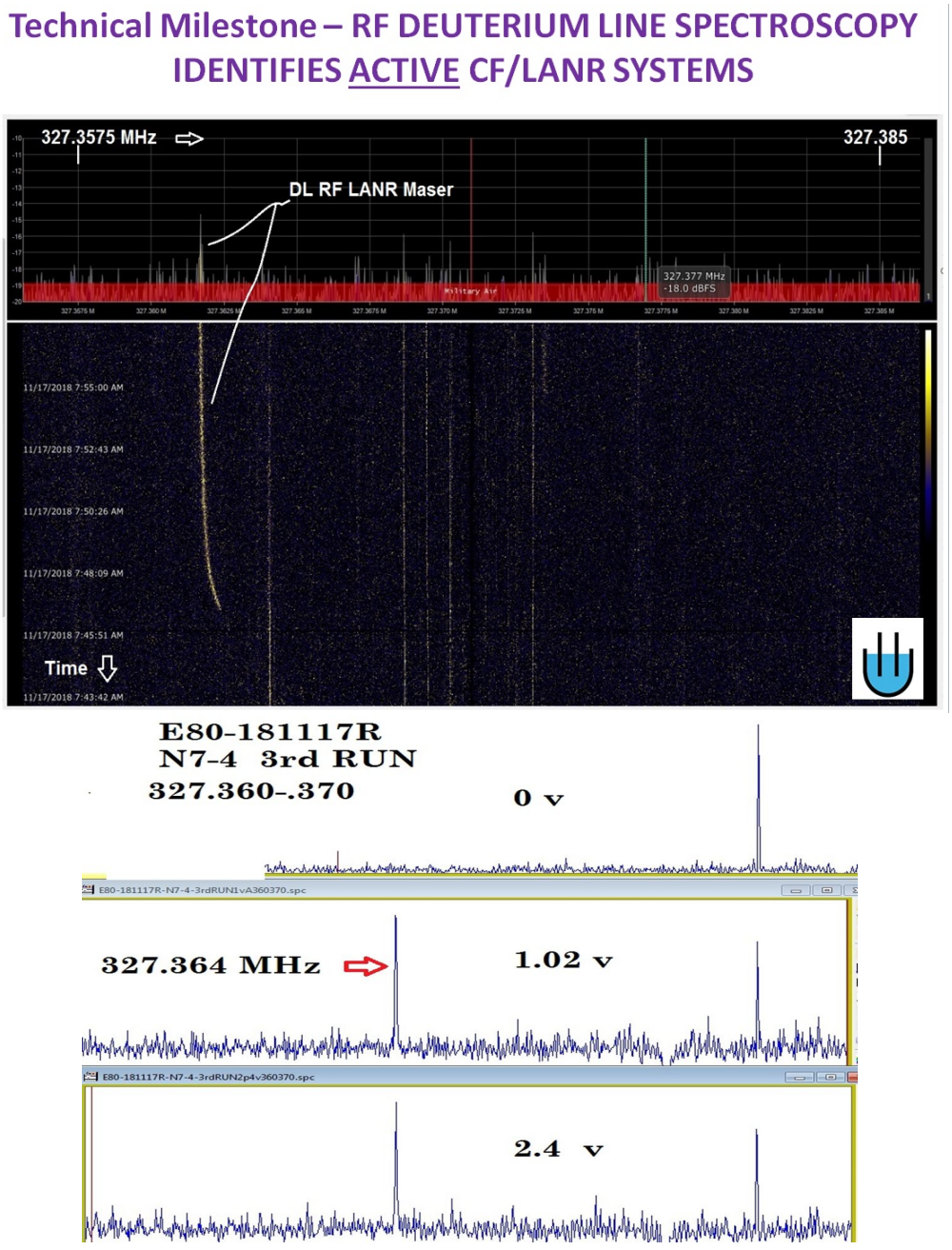

Figure 4. Successful LANR has a RF Maser Emission near 327 MHz.
Active electrically-driven LANR systems, both aqueous and dry preloaded nanomaterial, emit a hyperfine radiofrequency (RF) maser emission ~327.37 MHz [near the theoretical Deuteron-Line (DL; 327.348 MHz)]. The LANR maser exhibits a large Q > 1.2 x 10^6, and a positive Zeeman effect.

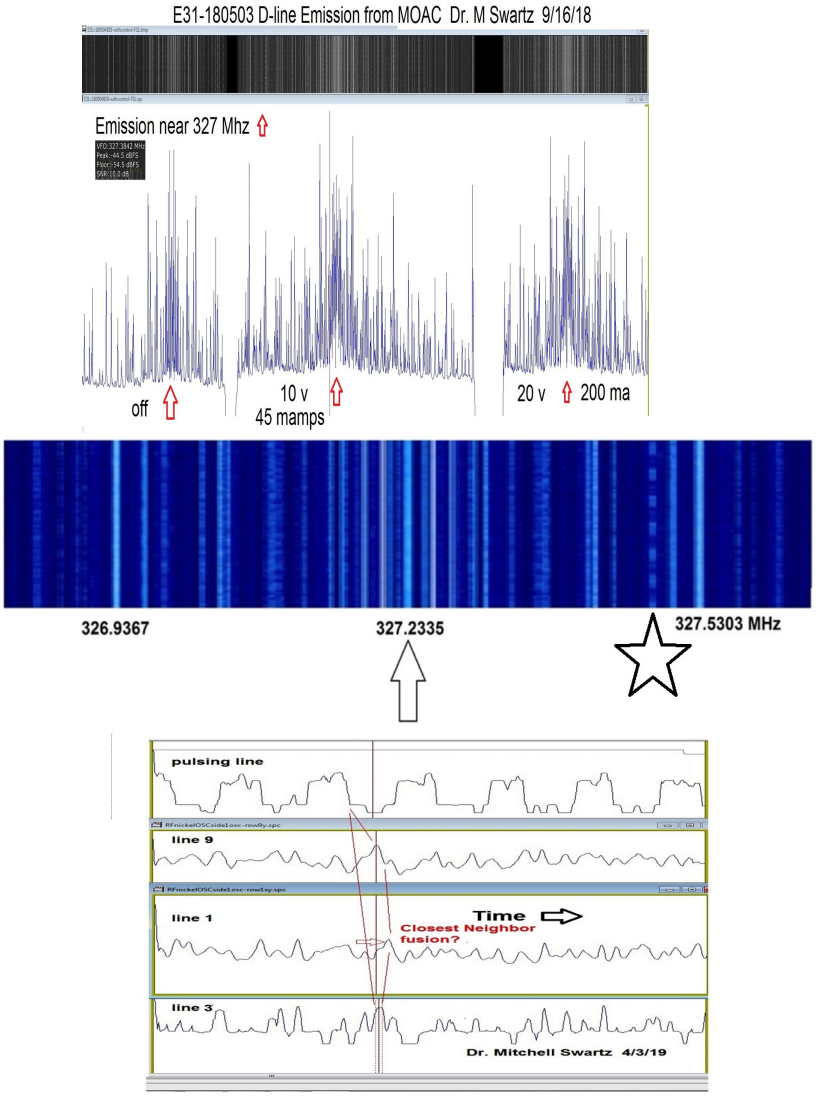

Amplitude of Pulsatile RF superhyperfine lines, time-matched from active Ni LANR.
One important implication is that in active CF/LANR systems, the loaded deuterons work together from their vacancy sites and enable the desired XSH-producing reactions within the loaded metal while emitting RF radiation at the Deuterium-line heralding the inverted population.

Figure 5. Pulsatile RF Emissions in Some Superhyperfine [“SHF”] Deuterium-Lines.
The discovery of the existence of Superhyperfine [“SHF”] Deuterium-Lines was observed at higher voltages. LANR RF maser emissions include superhyperfine lines [SHFL, or sidebands]. A very small number are pulsatile; one is marked by a star (above).
(top) – Amplitude of Pulsatile RF line and 3 other time-matched RF lines.
This figure shows the superhyperfine lines for an active working LANR system [nickel hydrogen loaded LANR system; 40 volts, 200 mA].
(middle) - This ‘waterfall’ plot (time goes down) shows intensity as a function of frequency The arrow identifies the center line; the star identifies one pulsatile line.
(bottom) – Pulsatile RF Emissions are shown, taken from a Background of the other RF Superhyperfine [“SHF”] Lines. Here, the pulsing interactions were compared, as in an ancient movie projector.

One important implication is that in active CF/LANR systems, the loaded deuterons work together from their vacancy sites and enable the desired XSH-producing reactions within the loaded Group VIII metal while emitting RF radiation at the Deuterium-line heralding the inverted population.

This can be seen in Figure 5 for CF/LANR in the aqueous system.

Is this the first intralattice "movie" of what occurs in successful LANR.

2.2. **Synchronous Behavior is Important & Ubiquitous - Localized Coupled Oscillators**

Mechanical, biological, and astronomic coupled synchronous systems have been studied for centuries [Figure 6]. Two years after Christiaan Huygens in 1663 proposed to the Royal Society that his pendulum clocks might solve the "longitude problem" in navigation; he observed that pairs of his pendulum clocks were weakly coupled through a heavy beam above them, and they synchronized to each other in about 30 minutes. Of note here, the frequency of the two pendula became identical but their displacements were opposite in direction ["anti-phase synchronization"].

3. Experimental: Solutions, Including by Hopf Fibration

Understanding these clock synchronization(s) took centuries, occurring far long after Huygens' original publication ["*Horologium oscillatorium"].* The solution(s) - even for the simplest pendula - has required understanding permutations, nonlinear engineering, Lagrangian mechanics, and the existence of numerical computations. Most difficult to explain was the anti-phase synchronization.

3.1. **Developing The Solutions for the Coupled Oscillators For/In CF/LANR**

The solutions for coupled localized oscillators such as Huygens' clocks were first characterized by non-dimensional methods to transform their conventional physical system parameters to their normal equivariant form parameters. The equivariant bifurcation theory, the equivariant center manifold theorem, and the equivariant normal solutions ["forms"] were examined as to their relevance with these coupled localized oscillator systems.

A subgroup of possible solutions is used here to better analyze what is observed with CF/LANR coupling in the loaded PdD lattice resulting from the interactions between the local oscillators in FCC vacancies. Specifically, Hopf fiber bundle topologic ["Hopf Fibration "] solutions are used in physics and medicine – from coupled oscillators to human circadian rhythms and even the sleep-wake cycle.

Here, we consider the solution of the deuteron synchronization trajectory for/to fusion for two deuterons in their periodically-located vacancies using Hopf Fibration principles. These Hopf Fibration solutions are analyzed in 4 dimensions (x,y,z, and time). In Hopf fibration, the 4D issue is simply handled by a pair of complex numbers. Simply put, Hopf fiber bundle solutions use a 4-dimensional (4D) hypersphere to map the result to inputs; the deuterons' trajectories. The "shadow" of the 4D hypersphere is mapped onto a toroid's surface which is located within our own 3-dimensions. This allows the coupled oscillators' interaction(s) to be seen, followed and studied.

****** A new Phase Space for Fusion Deuterons**

As the dynamic deuteron synchronization flows, in our 3D space, over the two-dimensional torus-shaped surface, a phase space is defined. The author calls this entire surface 3D (the shadow of the 4D processes) the "**Synchronous deuteron fusion phase space**". From the trajectory on the 3D-torus over this phase space, the deuterons can then be followed for possible quasi-periodicity, further synchronization, phase-locking, and fusion.

Mathematically, the onset of these oscillations is said to occur from their rest state. An electric field (or more) is applied for loading and to drive the desired LANR reactions. Thereafter, the synchronization is a smooth process and follows what is known as double Hopf bifurcation which can be examined as an equivariant bifurcation using normal form theory. Near the double Hopf bifurcation, the deuteron synchronization of the loaded PdD driven by the

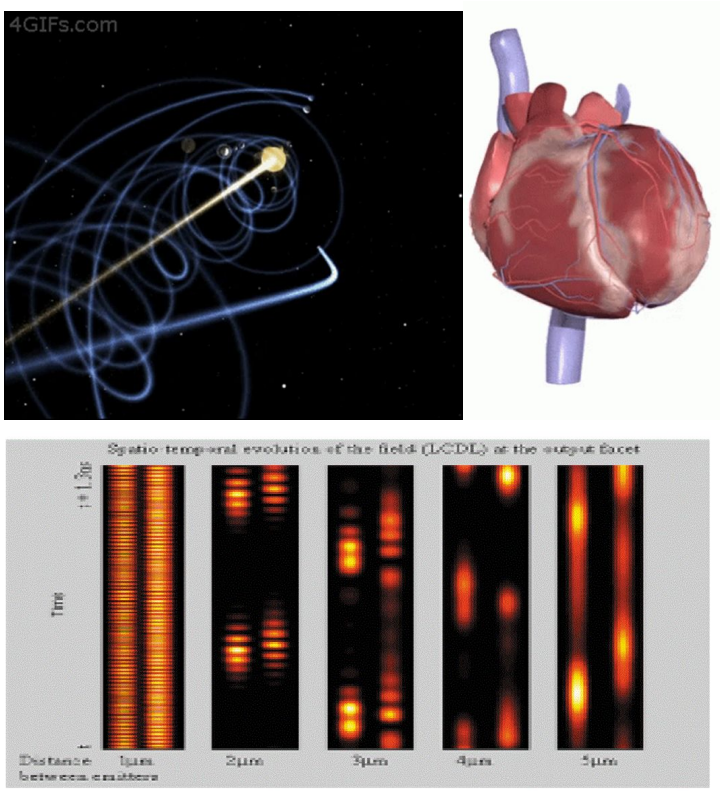

Example of spatiotemporal evolution of the field amplitude of the two laterally coupled diode lasers with five different distances between emitters [after H. Lamela]

Figure 6. Widespread Examples of Synchronous Behavior.
(top) Synchronous Behavior is seen in orbital physics, groups of animals such as fireflies, and medicine. The earliest science may habeen the study of coupled pendulum clocks.
(bottom) Shown is an example of synchronous coupling of two laterally coupled diode lasers [with five different distances between emitters; after H. Lamela, ref. 10].

applied electric field intensity, would have several emerging states including: the rest state, the in-phase and anti-phase periodic solutions, mixed-mode periodic solutions, mixed-mode 2-torus solutions, and modulo-2π and chaotic breather solutions. Most importantly, and relevant for CF, the latter three solutions, especially the breathers enable exchange energy between the two oscillators. This would indeed be the equivalent of surmounting the "coulomb barrier".

For both Huygens' clocks and CF coupling in the loaded lattice the coupling must be the same even with permutation of the clocks or deuterons if there is simultaneous reversal of the displacements and velocities. One implication is that the theoretical motions have more symmetry than the physical systems do.

Attention is drawn to the fact that in CF's highly vacancy-D-loaded Pd the deuterons are identical. They are bosons. Therefore, interchange *like the pendula* is reasonable, making the simplest of loaded ZrO_2PdD systems having a

simple permutation symmetry called Z2, also called "Huygens symmetry" when referring to his pairs of clocks. This means that the clocks, here deuterons, could be interchanged without a change in the system.

Most importantly for LANR/CF, 'permutation' symmetry can create a phase space which permits in-phase coupling (unlike Huygens' clocks which were ultimately anti-phase). In-phase periodic solutions have Huygens symmetry. Given the maser appearance and actions, there is at least some in-phase synchronization in the coupling of active CF/LANR oscillators.

Anti-phase periodic oscillations such as actually observed by Huygens have odd-Huygens symmetry. This different and now resolved 'paradox' has been better clarified by the Equivariant Hopf Bifurcation Theorem. It shows that for the Huygens' clocks, their anti-phase oscillations have a spatio-temporal symmetry which combines the permutation symmetry discussed above but with a half-period temporal phase shift.

4. Results – Superhyperfine line Pulsatile LANR Behavior Heralds A Synchronization Pathway

4.1. Successful LANR Is Driven by Forced Turbulent Deuteron Oscillator Flow

In successful LANR, deuteron fusion is initiated by electrically-forced turbulent oscillator flow. The deuterons are located in periodic vacancies in the highly loaded lattice. These ionized deuterons are identical bosons, and can interchange amongst themselves without any change in the system [a permutation symmetry called Z_2 ["Huygens (clock) symmetry"], and during successful LANR exhibit a well-defined frequency at the RF Deuterium-line.

Together, these also importantly creates the opportunity for synchronization because the deuterons are operating as a high-Q RF maser [tight range of frequency, free of noise] as required for deuteron synchronization.

STEP 1 – LOADING (a mostly reversible step)

**** Successful CF/LANR is a Multi-step process ****

The path to cold fusion (LANR) begins with loading [requiring highly-loaded vacancy-localized] deuterons, driven by the applied electric field intensity. This starts as a smooth low-level process, and continues until the "double Hopf bifurcation". This early loading of PdD is a reversible reaction. The mathematics have been covered extensively [12].

STEP 2 – Loaded Deuterons Interact on the Pathway to Cold Fusion (LANR)

Highly-loaded PdD is less reversible, because as the volume expands it changes the Pd, including forming dislocations and vacancies. The loaded deuterons interact through Band States (S. Chubb, and T. Chubb, and Kim) and other interactions (Bass, and others), and through optical interactions which provide activation energies (and more; Cravens, Letts, Swartz).

With full loading, these synchronizations of nonlinear dynamic now-coupled boson ionized oscillators in their periodic array continue. In their active state, the deuterons begin to emit antiStokes photons (Fig. 2) heralding a large acoustic phonon population ["phonon gain"].

In summary so far:

- ❑ Fusion requires highly-loaded deuterons in vacancies. So continued loading of PdD is necessary, but must be carefully done. Non-reversible reactions are wrought with changes to the lattice structure including dislocations, fractures, fissures and irreversible volume changes.
- ❑ Fusion requires highly-loaded deuterons in vacancies. So, therefore, continued loading of PdD is necessary, but must be carefully done. Non-reversible reactions are wrought with changes to the lattice structure including dislocations, fractures, fissures and irreversible volume changes.
- ❑ Deuteron Synchronization, continually driven by the applied electric field intensity, is electrically-forced turbulent oscillator flow, and initially starts as a smooth low-level process.

- ❑ In or near the active state, the deuterons can produce antiStokes photons heralding the large acoustic phonon population ["phonon gain"] and a further rise in the energy available for the synchronized deuterons.
- ❑ This process continues increasing energy of the coupled deuterons until the "double Hopf bifurcation".

4.2. **The Key Point: Fusion in Active LANR is Enabled by Deuteron Synchronicity**

STEP 3 - Toroidal Breather Mode (TBM) Enables/Solves Deuteron Synchronicity

With Hopf Fibration analysis, deuteron coupled oscillators are examined on a dynamically throbbing two-dimensional torus-shaped surface ["Synchronous deuteron fusion phase space"] as they interact.

This toroidal breather mode (TBM) solution [Figure 1] results from, and reveals, deuteron synchronicity - a *sine qua non* for fusion. The breathing torus, itself, on which the trajectories flow, is shown in Figure 1 with its cross sections which are located at x=0, y=0 and z=0 and are colored brown. The necessary 4D solutions (x,y,z,t) are handled by two complex numbers which project onto our three dimensional space as the blue central volume. It shows the deuterons' interaction trajectory.

Analysis of the Double Hopf Bifurcation . . .

At the double Hopf bifurcation, the synchronized deuterons have several possible emergent paths through it. The deuterons, most likely, can return to the original rest state. Most of the possible states examined which follow actually are not allowed. Possible paths include in-phase and anti-phase periodic solutions, mixed-mode periodic solutions, mixed-mode 2-torus solutions, and the modulo-2π and chaotic breather solutions. There are three solutions which enable exchange of energy between the coupled deuteron oscillators with these important couplings interacting in-phase with spatiotemporal symmetry. The pulsing coupled deuteron oscillators may herald the "toroidal breather mode" [TBM] which may explain successful CF/LANR systems and components.

. . . and IF/when an Excited-4He* Synchronized-State is Obtained

Once an excited-4He* State is obtained by these synchronized processes, there are several ways it can go. First, it must be seen where this is energetically. Figure 7 shows a table with present the energies of the Helium ground, and upper energy states. The CF/LANR reactions of Pd/D_2O/Pt which form *de novo* He, first involve an energy gap of between 20 MeV and 24 MeV from the ground state. This megavoltage energy difference is not "low energy", but instead is capable (under some conditions) of generating penetrating ionizing radiation. The energy is so large that it is also sufficient to create 'pair production'. There is no doubt that the result of successful CF/LANR is high energy, it is NOT 'low energy' [13].

4.3. **STEP 4 – Final Irreversible Step Culminating in Deuteron Fusion**

Any emission of penetrating gamma radiation is spin forbidden. Gamma emission IS seen in hot fusion because the spin-restriction is 'lifted' [overcome] in hot fusion because of the much higher temperature(s).

Looking at the energy map of the system [Figure 8], it becomes clear why the emission of neutrons is energy forbidden. This occurs because the neutron emission band is energetically located ~1 MeV above energy level of ^{4}He* (already at quite high energy). The large energy, compared to k_B*T, makes neutron emission not really allowed, since k_B*T is 1/25 eV ["room temperature" [13].

Normally important Bremsstrahlung emissions are not seen with CF/LANR. This occurs becase Bremsstrahlung is very Temperature-dependent [Figure 9], decreasing by 18 orders of magnitude, becoming absolutely negligible when considered at low (cold fusion, ie room) temperature [Swartz, M, G. Verner, "Bremsstrahlung in Hot and Cold Fusion", *J New Energy*, 3, 4, 90-101 (1999)].

Helium Nucleus Energy States

State	Energy (MeV)	Total Angular Momentum (J)	Parity (π)	Isospin (T)	Criteria $E < d$-d Isospin Conserved
	25.95	1	−	1	No
	25.28	0	−	1	No
	24.25	1	−	0	No
	23.64	1	−	1	No
	23.33	2	−	1	No
Third	21.84	2	−	0	[a]
Second	21.01	0	−	0	[a]
First	20.21	0	+	0	[a]
Ground	0	0	+	0	[a]

[a]States below $d + d$.

FUSION TECHNOLOGY VOL. 31 MAR. 1997

Figure 7. Energy of the Helium Ground, and Upper Energy States.
This table shows the energies of the Helium ground, and upper energy states.

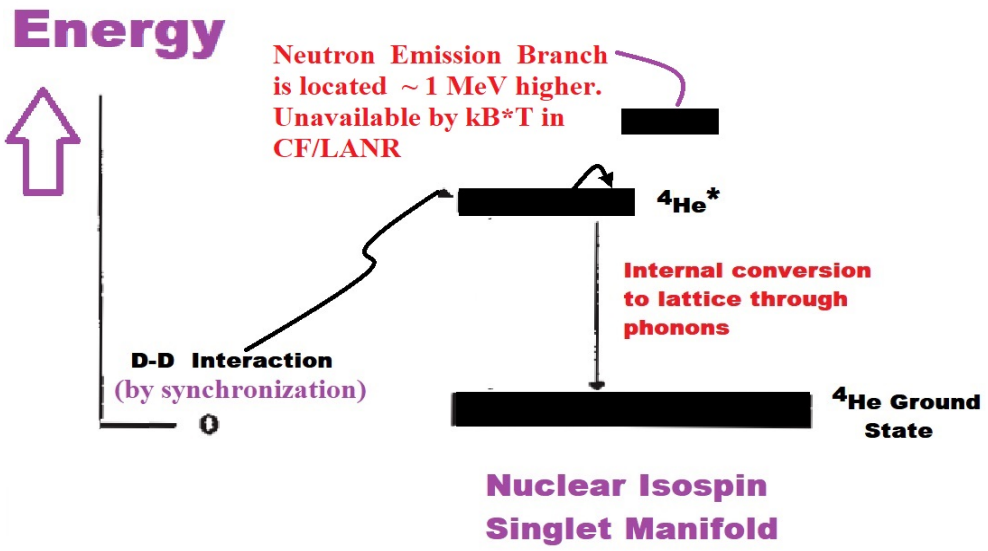

Figure 8. Energy Levels of Helium.
Shown are the energy levels of helium 4. Above the ground state, is the relevant excited state, and the neutron emission branch located 1 Mev above that.

Radiation Dose Delivered

This marked decrease in the exit of ionizing Bremsstrahlung radiation must be reflected in the radiation dose delivered. This can be calculated from the x-ray beam dose equation [20], here modified as the x-ray dose in Grays (at 1 meter) delivered per coulomb of electrical input.

$$D/Q = 1.50 * V_{max}^{2.8} * Z^{1/2} \quad \text{(Grays/Coulomb)} \tag{10}$$

V_{max} here is dominated by k_BT because the applied electrical field intensity, assuming homogeneous distribution over the system is insignificant by comparison. This most important result from equations 10 and 11 is the correct calculation of the derived value of the bremsstrahlung delivered dose at a distance of 1 meter for conventional fusion systems (Table 1). The radiation dose (Grays) per coulomb at 1 meter drops from ~3.1 x 10^{19} Grays (hot fusion) to 1.4-3.3 x 10^{-4} Grays for cold fusion.

Figure 9. The impact of lower temperature in Bremsstrahlung.
The roles of temperature have generally been ignored. However, when examined it is shown that they quite important [14].

The final critical IRREVERSIBLE (~ 20+ MeV) transition occurs coherently by PHUSON energy transfer, enabled by lossy spin bosons processes through optical phonons (Hagelstein), acoustic phonons (Swartz) and magnons (Swartz). This is what causes the observed excess heat.

4He* [via a necessary PHUSON-coherent transfer]

====> 4He + more phonons <= phonon enabled

Nota Bene: With LANR success, only *de novo* and relatively low-momentum helium nuclei are formed.

In summary, synchronous D behavior and the applied electric field intensity enable formation of ^{4}He*. Pd and D enable these processes.

The PHUSON is the quasiparticle which enables the end reaction to occur. It coherently couples the megavoltage energy of the ^{4}He* to the loaded PdD lattice. This energy transfer then appears as "excess heat", and locally yields ground state *de novo* ^{4}He. Phonons (acoustic and optical) enable the transfer of energy from ^{4}He*to the lattice [13].

5. Conclusions: Synchronous, Non-Confrontational Fusion

In successful LANR, pairs of loaded deuterons located in a periodic vacancy sites combine synchronously. Unlike hot fusion, this mechanism of fusion is relational and productive, rather than confrontational and destructive [Figure 10].

Unlike hot fusion, in LANR rather than one D hitting the other as a target, there is no conventional "coulomb barrier" because the deuterons as bosons work in synchrony. Therefore, synchronous interaction CAN – and do – occur, and XSH is observed for these working active LANR systems.

Fortunately, successfully driven lattice assisted nuclear reaction [CF/LANR] components emit unique very narrow-bandwidth hyperfine radiofrequency [RF] signals near the deuterium line [DL; ~327.37 mHz] along with informative sidebands and novel pulsations [1,2,3]. Their incredibly high Q heralds a large inverted population. The sidebands reveal much, and the pulsations portend energy-mass transfer(s).

Some of the pulsations (Figure 5, cf. star) appear coupled with periods of minutes; and when synchronized, may enable mass-energy transfer. In Ni and Pd vacancy-loaded deuterons are identical bosons, and thus can interact and interchange. This analysis requires equivariant bifurcation theory [4], [5]. The pulsing superhyperfine lines herald deuteron synchronous interactions and appear to be 2D representations of the fusing deuterons -- a "shadow" of mass-energy transfer.

Figure 10. Shown are the important differences between hot fusion and LANR.
(top) In hot fusion, one D hits the other as a target. This is brute targeting, and therefore both confrontational and destructive. Thus, there is the conventional "coulomb barrier" and 3*10**19 Grays are produced at 1 meter for 1 coulomb.
(bottom) In successful LANR, deuteron synchronization is driven by the applied electric field intensity into electrically-forced turbulent oscillator flow. From this, pairs of loaded deuterons -located in periodic vacancy sites- combine synchronously. This result is relational and productive. Thus, here, rather than one D hitting the other as a target, there is no conventional "coulomb barrier", but instead synchronous interaction(s) follow application of the electric field intensity. With cold fusion, 3*10 ** -4 Grays are produced at 1 meter for 1 coulomb.

The deuterons can return to their ground state or, as described by the toroidal breathing mode [TBM] solution, they can surmount, circumvent and make moot the imagined "coulomb barrier". The result is fusion with loss of two deuterons, production of *de novo* helium-4, and the generation of the observed excess heat.

Mathematically, synchronization of the local deuteron oscillators in FCC vacancies smoothly proceeds to the "double Hopf bifurcation" driven by the applied electric field intensity. Of the many possible states which follow, only three solutions -- especially the "toroidal breather mode" [TBM] -- enable exchange of energy between the coupled oscillators.

These important RF-detected LANR couplings, like those of the Huygens' clocks, interact in-phase with spatiotemporal symmetry. It is proposed that in LANR they combine as shown below.

Most importantly, the TBM solution is the way by which interacting vacancy-loaded deuterons in highly loaded Group VIII alloys make moot and circumvent the need for surmounting the "coulomb barrier".

Acknowledgments

The author gratefully acknowledges, and thanks, for their helpful comments, editorial assistance, ideas, suggestions, and much support for this effort: Gayle Verner, Alex Frank, Thomas Farina, Raymond Kurwzeil, Aaron Kleiner, Joshua Gyllinsky, Michael Staker, John Wallace, Andrew Meulenberg, Brian Josephson, Isidor Straus, Peter Hagelstein, Florian Metzler, Dennis Cravens, David Nagel, Dennis Letts, Frank Gordon, Pamela Mosier-Boss, Lawrence Forsley, Louis DeChiaro, Brian Ahern, Jeff Driscoll, Christy Frazier, Win Cuthbert and Carl Page. This effort was supported by JET Energy Inc. NANOR® and PHUSOR® are registered trademarks. The technology described here is protected by patents pending.

References

[1] Swartz, M. R, Active LANR Systems Emit a 327.37 MHz Maser Line, Proc. ICCF-22, J. Condensed Matter Nucl. Sci., Volume 33, pages 80-110 (2020)
[2] Swartz, M. R, FCC Vacancies in ZrO2PdD RF are the Active LANR Site, Proc. ICCF-22, J. Cond.Matter Nucl. Sci., Volume 33, pages 126-144 (2020)
[3] Swartz, M. R, Pulsatile Superhyperfine Lines at 327.37 MHz Herald LANR Activity and Possible Mass-Energy Transfer, Proc. ICCF-22, J. Condensed Matter Nucl. Sci., Volume 33, pages 111-125 (2020)
[4] Swartz, M. R., Aqueous and Nanostructured CF/LANR Systems Each Have Two Electrically Driven Modes, J. Condensed Matter Nucl. Sci. (2019)
[5] Swartz, M. R, Peter L. Hagelstein, Increased PdD anti-Stokes Peaks are Correlated with Excess Heat Mode, J. Condensed Matter Nucl. Sci. 24, 130-145 (2017)
[6] Swartz, M.R. "Optical Detection of Phonon Gain Distinguishes an Active Cold Fusion/LANR Component", JCMNS, 20, 29-53 (2016)
[7] Swartz, M. R, Increase of an Anti-Stokes Peak at the Cathode of an Electrically-Driven, Active Aqueous Nickel/H2O/Pt System, J. Condensed Matter Nucl. Sci., Vol 279, 22 (2018)
[8] Swartz M. R., Excess Power Gain using High Impedance and Codepositional LANR Devices Monitored by Calorimetry, Heat Flow, and Paired Stirling Engines, Proc. ICCF14 1, (2008), 123; ISBN: 978-0-578-06694-3, 123, (2010); www.iscmns.org/iccf14/ProcICCF14a.pdf
[9] Swartz M. R., "Survey of the Observed Excess Energy and Emissions In Lattice Assisted Nuclear Reactions", Journal of Scientific Exploration, 23, 4, 419-436 (2009)
[10] H. Lamela, M. Leones, Analysis of the dynamic behavior and short-pulse modulation scheme for laterally coupled diode lasers, Materials Science, IEEE Journal of Selected Topics in Quantum Electronics, (2001)
[11] The Huygens' clocks revisited Allan R. Willms, Petko M. Kitanov William F. Langford 06 September 2017 https://doi.org/10.1098/rsos.170777
[12] Swartz, M., "Quasi-One-Dimensional Model of Electrochemical Loading of Isotopic Fuel into a Metal", *Fusion Technology*, 22, 2, 296-300 (1992)
[13] Swartz, M., "Phusons in Nuclear Reactions in Solids", Fusion Technology, 31, 228-236 (March 1997)]
[14] Swartz, M., G. Verner, "Bremsstrahlung in Hot and Cold Fusion", *J New Energy*, 3, 4, 90-101 (1999)

J. Condensed Matter Nucl. Sci. 38 (2024) 161–170

Research Article

Deuteron Momentum and the Umweg Factor Initiate and Limit Successful CF/LANR

Mitchell R. Swartz

JET Energy, Inc., Wellesley Hills, MA, USA

Abstract

The use of dry preloaded ZrO_2PdNiD nanostructured materials in NANOR®-type components has previously demonstrated the presence of unwanted electrical avalanche behavior during successful over-driven LANR. This unwanted electrical response immediately ends the excess heat as the component returns to prosaic V*I power dissipation. This paper further examines these critical electron breakdown processes. The observed electrical breakdown in active nanostructured ZrO2PdNi LANR (lattice activated nuclear reactions) nanostructured materials and components is classically analyzed. Deuteron momentum and scattering are most important because they initiate, and then limit the success of, CF/LANR activity. We find that the deuteron momentum produces deuteron scattering, and if large enough the scattering and energy loss then limits the success of, CF/LANR activity. These collisions can create a detour ["umweg"] ruining the requisite path to deuteron synchrony needed for the desired excess heat.
 ISSN 2227-3123

Keywords: Nanor®-type components, deuteron momentum, umweg factor, successful LANR

1. Preloaded Deuterated LANR Nanomaterials

CF/LANR is very real, including with the use of dry preloaded ZrO_2PdNiD NANOR®-type components [1], [2], [3], [4]. NANOR®-type CF components have a ZrO_2-PdD or ZrO_2-PdNiD core. They are about ∼2 centimeters length, usually with ∼50-250 milligrams preloaded material. Their ability to demonstrated activity with the generation of real excess heat is easily, and repeatedly, shown (confer Figure 1).

Figure 1 shows the input electrical power to an ohmic control and then the NANOR®-type component 7–24, and the resultant output thermal power from both as a function of time. The input and output integrated energies are shown as dashed lines. The NANOR®-type component had a peak power output was ∼12.1 Watts when driven with 4 Watts. This is an incremental power gain of ∼300%, observed then the component was electrically driven below avalanche voltage [5].

2. Confirmation of Two Electrically Driven LANR States

CF/LANR is very real. The active mode is driven by the applied electric field and the enabled by the lattice vacancy-locked deuteron ions coherently interacting [6]. If adequate synchronous conditions are achieved, then cold fusion

 ISSN 2227-3123

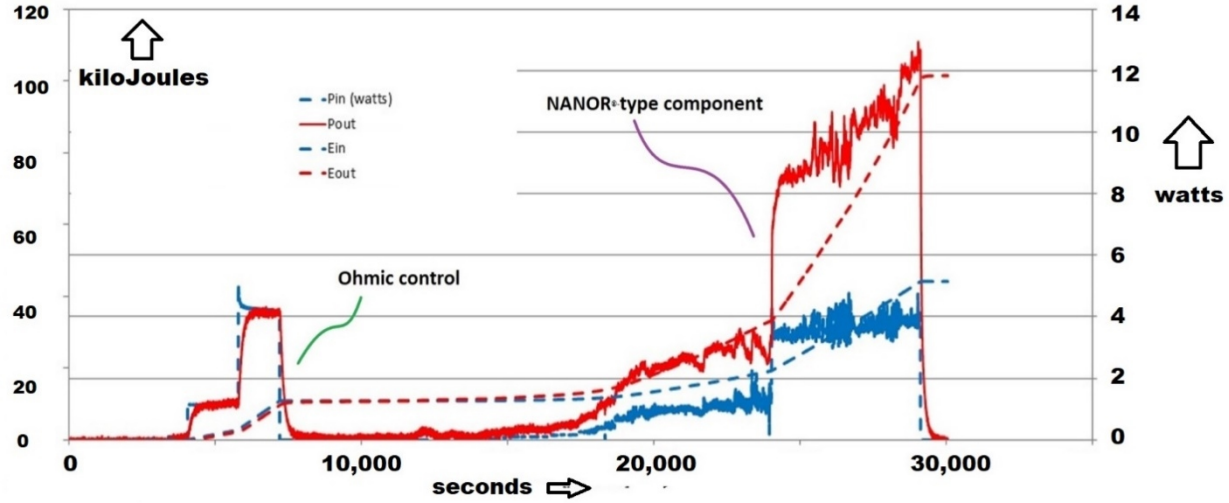

Figure 1. Calorimetry of a driven NANOR®-type component after an ohmic control to calibrate. This figure shows the input and output electrical power, and energy, to an ohmic control and then the NANOR®-type component 7–24.

(LANR) can, and does, occur. However, as shown previously, and electrically-driven LANR systems have two modes, and only one is active making the desired 'excess heat' [ref. 5; confer Figure 2]. Figure 2 presents the graphical output of a reproducible nanostructured NANOR®-type two-terminal CF electrical component, driven in both of its two different electrically driven states; and in its 'off' state and also while 'off' with an electrical ohmic control being driven. Vertical axes plot the electrical input power and the heat generated, as a function of time.

Figure 2 confirms the existence of two states. Figure 2's curves plot the temperature rise [delta-T in degrees C] of the ohmic control and the NANOR®-type LANR component, both normalized to input electrical power as a function of time so that the ratios can be used to estimate incremental power gain. There is obvious incremental power gain for the CF/LANR component until the avalanche, at which time (count ~3700) the component has no energy gain, but has a response similar to an ohmic resistor. This also saliently demonstrates that outside of the CF/LANR active state, the component acts as any other ohmic resistor, and thus this confirms that the calorimetry was calibrated, and verifies the excess heat yet an additional way. Thus, these curves confirm the existence of two states. This result also demonstrates excess heat obtained from a Ni-D nanomaterial system, as reported previously in a high impedance aqueous CF/LANR system.

In Figure 3, the curves confirm that there are two driven LANR states, but only one (1) gives excess heat. The three modes (responses) are the undriven "off"-state, the unwanted electrical avalanche mode, and the optimal operational state, the "Desired Active Mode", where "excess" energy is being released [7], [8], [9]. Shown in Figure 3 are spectra of the same NANOR®-type CF/LANR component [NANOR® 7-6] in three different electronic states, resolved by dual wavelength coherent electric-driven volume-enhanced reflection spectroscopy.

These are the overlaid Spectra of the three Different Electronic States Optical Signatures for the same preloaded ZrO_2PdD NANOR®-type CF/LANR Component in three different electrical drive modes. The plots show the reflected optical intensity as a function of wavelength, initially from two incident coherent optical beams but also with reflected backscatter from the core along with the initial optical beams. The vertical axis represents the intensity of the returned

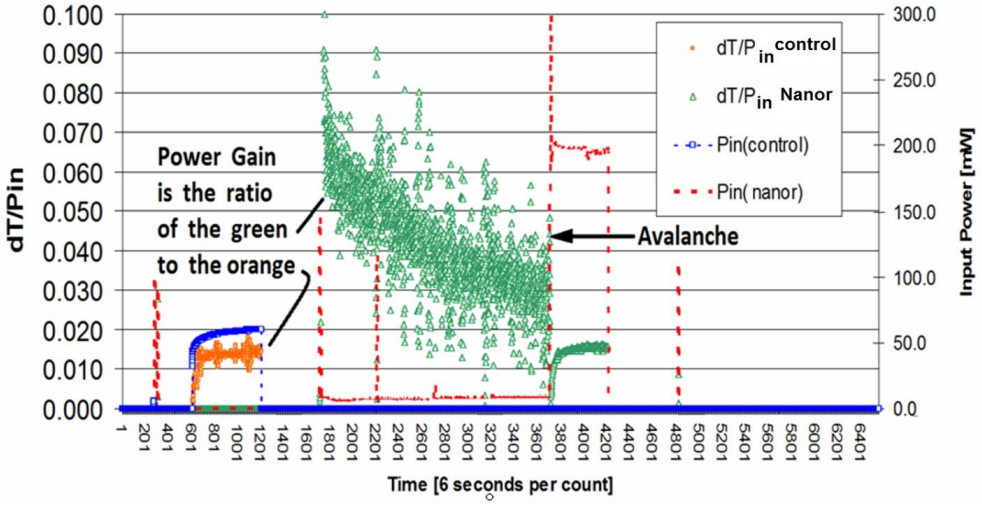

Figure 2. Demonstration of Excess Power Gain and then Sudden Loss of Activity after Electrical Avalanche for a NANOR®-type LANR component - The electrical input power and delta-T/Pin (representative of the measured instantaneous power gain) from the ohmic control and then the nanostructured two-terminal NANOR®-type ZrO_2- NiD component. The region of the Avalanche is labeled.

backscatter plotted as intensity as a function of wavelength. The horizontal axis plots the decreasing frequency to the right. The output of the first laser is shown as the peak on the left side, located at 532 nm.

3. Electrical Breakdown of Deuterated LANR Nanomaterials

When an electric field is applied, initially at low intensities, there is a region where the nanostructured LANR core acts like a very high impedance electrical resistor of several million (or several orders of magnitude higher) ohms. However, as the voltage is increased beyond a critical voltage, the electrical resistive properties of the nanostructured material core suddenly change. The component's electrical impedance post-avalanche may remain as low as only ∼8000 ohms from initially megohms to gigaohms or more.

This is a major problem for CF/LANR. Successful CF/LANR in nanomaterials is totally abolished by these electrical avalanches. In fact, this breakdown of the components resistance is what is seen above a threshold voltage. These threshold for avalanche have ranged from 30 to 1900 volts or more. Unfortunately, all ZrO_2(PdNiD) LANR nanostructured materials do, at least in some configurations, demonstrate this Zener-type avalanche behavior.

Figure 4 shows an actual avalanche electrical breakdown behavior observed in a dry preloaded, active LANR nanostructured NANOR®-type component. This occurs when the component is driven above a time-dependant threshold voltage. What is suddenly wrought is an increase of electrical current even at lower applied voltages. With the appearance of this electrical avalanche there is termination of the desired excess heat. That change with electrical avalance of the LANR component makes the component act like an ohmic resistor.

In Figure 4, note that three regions are seen; consisting of the initial plateau of electrical impedance, then the rapid fall off, and finally a sloped region at higher voltage.

Sometimes, the LANR nanomaterial electrical avalanche behavior is followed by hysteresis and partial reversibility over days. Nonetheless, optimal power gain of NANOR®-type cold fusion components is only found below the threshold breakdown.

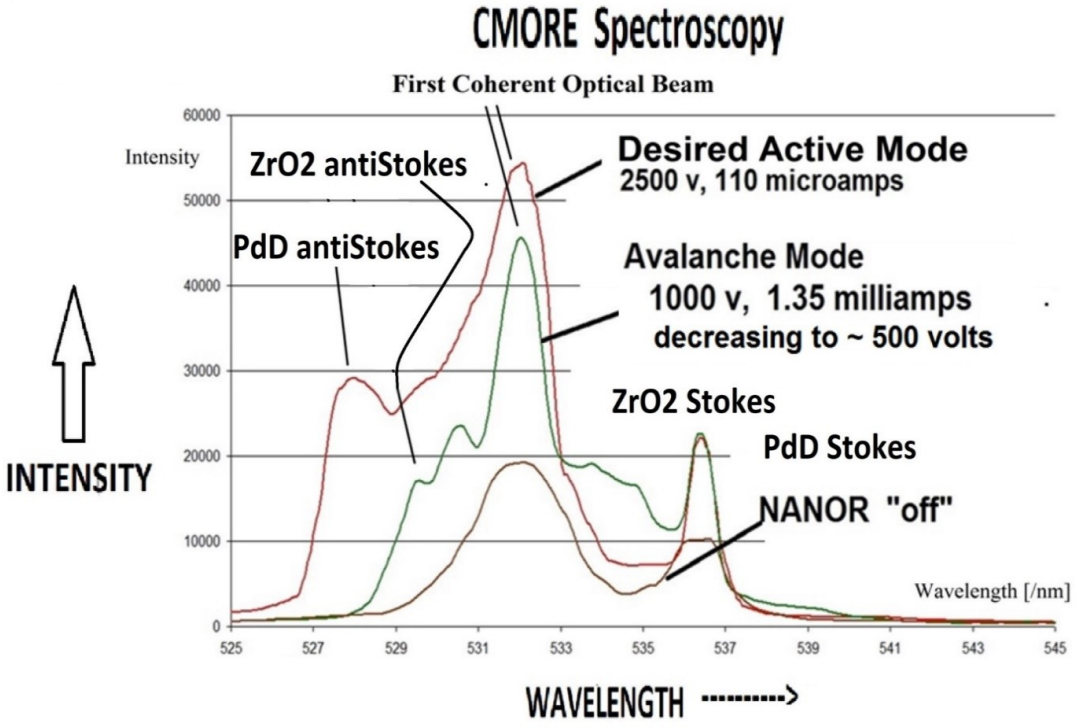

Figure 3. CMORE Spectra of ZrO_2PdD NANOR®-type CF/LANR. These are the overlaid Spectra of the three different Electronic States Optical Signatures for the same preloaded ZrO_2PdD NANOR®-type CF/LANR Component in three different electrical drive modes. Shown are spectra of the same NANOR®-type CF/LANR component [Nanor ® 7-6] in three different electronic states, resolved by dual wavelength coherent electric-driven volume-enhanced reflection spectroscopy. Labeled are the assignments of the anti-Stokes peaks to Zirconia and PdD.

Why does avalanche occur? The sudden loss of successful CF/LANR with avalanche must be better understood. In this paper, we demonstrate that it is caused by increased scattering of deuterons, producing a detour [“umweg”] in their paths. The functional result is optimal operating point (OOP) operation which has revolutionized successful CF/LANR, as shown in the graph below, and as shown by open demonstration at ICCF-10. In the next section, this breakdown will be connected to momentum and optimal operating point manifolds, which are found throughout LANR (CF/LENR/CMNS). We have generally related them to loading, and then beyond the peak to losses through unwanted pathways involving gas (D_2) evolution.

Figure 5 with its demonstration of Optimal Operating Point Operation explains many of the many “negative” results of similar systems, are the result of a failure to operate the system at the optimal operating point, which is an optimum peak in the excess heat and power gain curves as a function of input electrical power. The optimal operating point reflects the relatively narrow peak (maximum) of the biphasic production rate curve for the products obtained by the desired reactions (heat, helium-4) as a function of input electrical power [1], [2], [3], [4]. Driving with electrical input power beyond the peak optimal operating point does not improve the production of the desired product but instead yields an under desirable falloff of the production rate with increasing input power. Thus, the failure to operate similar systems at the optimal operating point, because of driving the systems inadvertently or unintentionally beyond the optimal operating point, accounts for some of the widespread difficulties in observing the desired reactions.

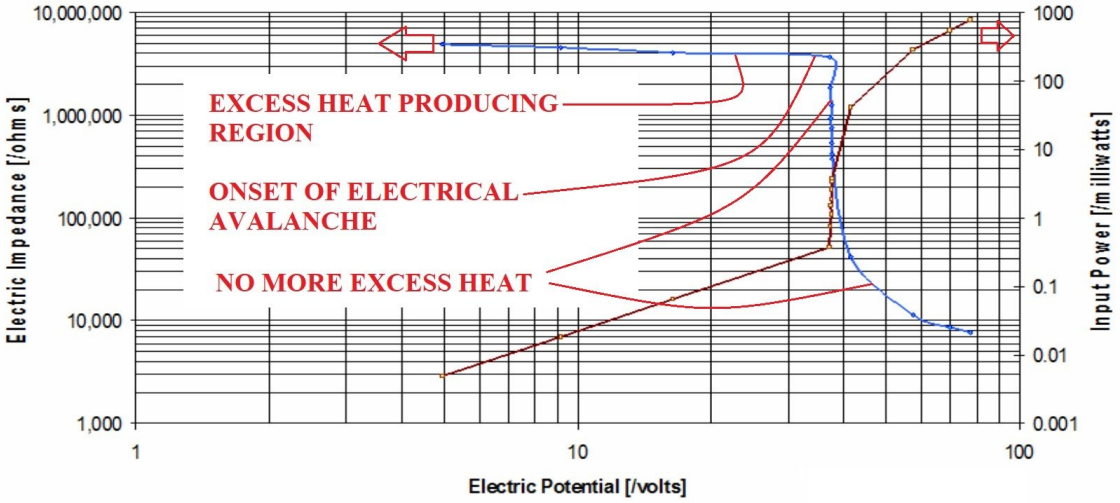

Figure 4. Impedance and Electrical current as a function of applied electric potential (volts). Shown is Avalanche (Zener-type?) Behavior in an LANR nanostructured NANOR® device containing ZrO_2(PdNiD). This figure shows the response, and particularly the Avalanche behavior with 3 distinct regions, as first observed with ZrO_2-NiH NANOR®-type component.

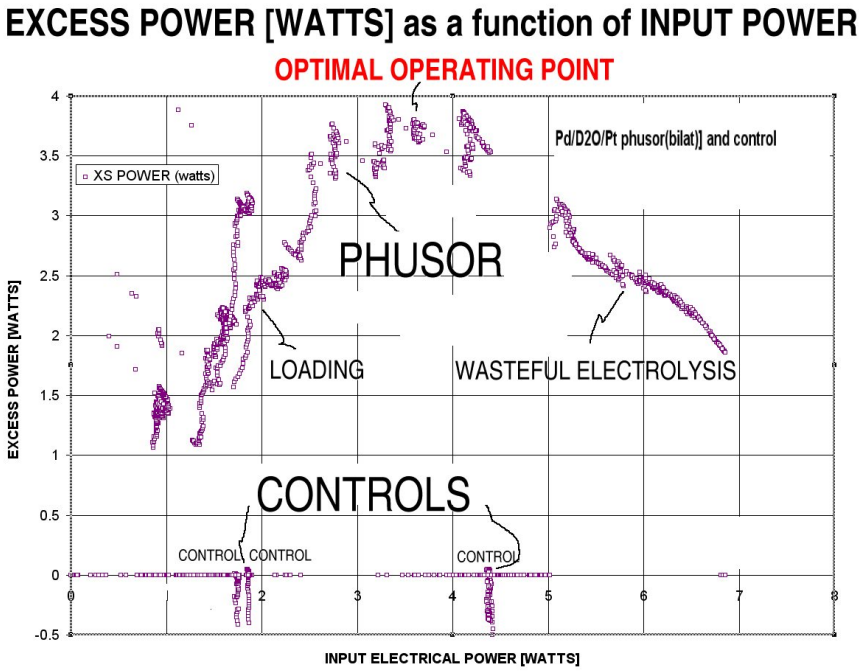

Figure 5. Optimal Operating Point Operation. The optimal operating point reflects the relatively narrow peak (maximum) of the biphasic production rate curve for the products obtained by the desired reactions (heat, helium-4) as a function of input electrical power [1], [2], [3], [4].

4. Analysis - Deuteron Momentum Initiates LANR

Deuteron momentum driven by an applied electric field first initiates, and secondary deuteron scattering then limits, active (successful) CF/LANR. These analyses of momentum and applied electrical power in LANR are important because they control LANR. Briefly, successful LANR is associated with applied electric field intensities correctly applied to loaded active palladium or nickel (or their nanostructured equivalent), followed by sustained deuteron flow through the materials, the magnitude of which can be increased by a metamaterial shape [1]. The metamaterial shape can greatly influence LANR by causing an intrapalladial current.

First, understanding how input electrical power relates to LANR is important because it dominates in the Optimal Operating Point manifolds [confer Figure 5] for all known LANR outputs in LANR including generating excess energy, tritium, and helium-4 production.

Second, it is also important to consider closer the origins, and interactions between, momentum and repeated scattering and the desired result of "excess heat". In brief summary, this analysis reveals that deuteron momentum, and then deuteron scattering, create and then limits the success of, CF/LANR activity. These collisions create a detour ["umweg"] ruining the synchrony need for the desired excess heat. With each collision, the deuteron must lose some of the energy gained from the applied electric field.

Third, the use of ZrO_2PdNi nanostructured materials has demonstrated the presence of Zener-type avalanche behavior in LANR [a]. In this paper, electrical breakdown conduction in palladium is considered in terms of the lattice during the LANR reactions, ending sometimes in electron breakdown processes.

In summary, these equations show the impact of collisions on deuteron velocity. It is noted that classical Ohm's law must fail because both the actual, and drift, velocities increase proportional to the applied E-field which further guarantees electrical avalanche.

5. Analysis - Deuteron Velocities

We next consider the movement of deuterons, and other carriers, in the loaded metal. First, let us consider the deuteron flow. Thereafter, other electrical currents involving the electrons and deuterons, and their holes, all flowing through palladium in ellipsoids related to k_B*T must be considered. These are spheroids caused by thermal background heat which are distorted by the applied electric field intensity. The quasi-1-dimensional model of isotope loading handles this and has given much success to LANR including codeposition, optimal operating points and the control of tardive thermal power. In the following, V_D is the actual velocity of a deuteron, U_D is the drift velocity of the deuteron, and τ_D is the time of free flight between collision impacts. Beginning with the Newton force equation, we can write

$$m_D \frac{d\overrightarrow{V_D}}{dt} = -q\overrightarrow{E}$$

Therefore, U_D becomes (since the drift velocity is the time averaged displacement divided by the time of flight) calculable as

$$U_D = \frac{1}{\tau_D} * \int_0^{\tau_D} \left[\frac{qE}{m_D} * t\right] dt$$

The solution of this is

$$U_D = -\frac{qE}{m_D} * \tau_D$$

Now we must consider the average number of collisions per unit length, <# collision> $_D$, which is s / $\langle \Lambda_D \rangle$.

s is the umweg (detour) factor and is the ratio of actual velocity to drift velocity.

$$< \#\text{collision} >_D = \frac{s}{\langle \Lambda_D \rangle} = \frac{V_D}{\langle \Lambda_D \rangle * U_D}$$

Therefore,

$$\tau_D = \frac{\langle \Lambda_D \rangle}{V_D}$$
$$V_D = s * U_D$$

6. Analysis - Input Electrical Power and Momentum Part 1

This is the derivation of deuteron momentum to the applied electric input power. The input power is V * I. (*****)

(***** - It is wrong to subtract the thermoneutral potential because it puts a false lower number in the denominator of a ratio used to compute putative excess power gain. It is also wrong because we have seen photographic in situ evidence of non gas evolution in early-, and mid-, loading states.)

Therefore,

$$P_{in} = V * I = qE * L * [D] * \xi_D$$

So we can compare momentum to input power as:

$$\overrightarrow{p_D} = m_D * \overrightarrow{V_D} = m_D * s * \frac{-q\overrightarrow{E}}{2 * m_D} * \tau_D$$
$$\overrightarrow{p_D} = m_D * \overrightarrow{V_D} = -s * \frac{-q\overrightarrow{E}}{2} * \tau_D$$
$$\overrightarrow{p_D} = -s * \frac{-q\overrightarrow{E}}{2} * \tau_D$$

Finally, substituting for the applied electric field intensity, and where ξ_D is the charge/deuteron.

$$\overrightarrow{p_D} = -\frac{s * \tau_D}{2L * [D] * \xi_D} * \text{Pin}$$

7. Analysis - Thermal Approximation of Velocities

In all of the time preceding, and during, LANR nuclear fusion, the energy gain per unit distance is less than $k_B * T$ so the most probable velocity is secondary to $k_B * T$.

$$\overrightarrow{\|V_D\|} = \sqrt{\frac{2 * k_B T}{m_D}}$$

One can then write the actual and drift velocities as

$$\overrightarrow{U_D} = \frac{-q}{2 * \sqrt{2 * m_D \ * k_B T}} * E = \mu_D * \overrightarrow{E}$$

In this equation, the first term of the deuteron drift velocity equation is the effective electrophoretic mobility, μ_D.

8. Analysis - Deuterium Flow Equilibrium With Collisions

Classically, with each deuteron collision, the deuteron energy loss is proportional, ℵ, to the kinetic energy.

$$\Delta\varepsilon = \aleph * 1/2 \;\; m_D * V_D^2$$

Therefore, at nanoscopic equilibrium, the deuteron energy loss per collision must balance the energy gained from the applied electric field.

$$\frac{q * E * \langle \Lambda_D \rangle}{s} = \aleph * \;\; 1/2 \;\; m_D * V_D^2$$

First, the equations show that in loaded ZrO2-PdNiD components because both the actual, and the drift, velocities must increase proportional to the applied E-field.

Such increasing drift velocity must herald BOTH further unwanted umweg behavior and ultimately loss of synchronization of the deuterons – seen by the observed electrical avalanche, coupled with the loss of all excess heat. One prediction of this derivation is that classical Ohm's law may fail in D-loaded ZrO_2PdNi nanostructures because both the actual, and drift, velocities must both increase proportional to the applied E=field, but at some voltage cannot, and are unable to do so. Instead there is avalanche behavior.

$$V_D = -\sqrt{\frac{\mathrm{q}\,\langle \Lambda_D \rangle\,\mathrm{E}}{m_D}} * \sqrt{\frac{2}{[\aleph * s]}}$$

$$s = \sqrt{\frac{4}{\aleph}}$$

$$= -\sqrt{\frac{\mathrm{q}\,\langle \Lambda_D \rangle\,\mathrm{E}}{m_D}} * \sqrt{\frac{2}{\aleph * s}}$$

$$U_D = \frac{1}{2 * [\aleph]^4} - * \sqrt{\frac{q * \langle \Lambda_D \rangle * E}{m_D}}$$

In fact, this is what is seen (Fig. 4). LANR nanostructured materials demonstrate Zener-type avalanche behavior in ZrO_2(PdNiD) above the threshold breakdown voltage.

9. Analysis - Effective Deuteron Temperature

We can determine the temperature of the deuterons within the palladium by considering them as a deuteron gas. The deuteron temperature, Θ_D, in eV, is a function of their kinetic energy. Therefore, it is important to consider ℵ, which is the relative energy loss of each deuteron per collision. Thus,

$$k_B * \Theta_D = 1/2 * m_D * \overrightarrow{\|V_D\|}^2 = \frac{q\,\langle \Lambda_D \rangle \left\| \overrightarrow{E} \right\|}{\sqrt{4\aleph}}$$

Thus, the effective deuteron temperature becomes:

$$\Theta_D = \frac{\mathrm{q}\,\langle \Lambda_D \rangle \;\; \left\| \overrightarrow{E} \right\|}{\sqrt{4\,\aleph} * k_B}$$

It can be seen from this equation that the deuteron temperature increases both with the magnitude of the applied electric field intensity, and the mean free path length for deuterons. It falls, however, as the square root of the proportion of energy lost per collision, $\aleph$.

Attention is directed to the fact that for aqueous CF/LANR systems, the loading equation demonstrates the importance of the ratio of organizing energy to thermal disorder. Here for nanomaterial CF/LANR systems, the ratio of organizing energy to thermal disorder for the deuterons goes as $\sqrt{4\,\aleph}$.

$$\frac{q * \left\| \overrightarrow{E} \right\| * \langle \Lambda_D \rangle}{k_B * \Theta_D} = \sqrt{4\aleph}$$

Note that first, as the ordering energy is increased, the energy goes to the lattice, increasingly as the energy loss proportion, $\aleph$, goes to, and approaches, 1.

Second, therefore, as an interesting corollary, we can explicitly determine the proportion of energy lost per collision from the accelerating E-field, using the effective deuteron temperature and the applied E field intensity.

$$\aleph = \frac{1}{2}\left[\frac{q * \left\| \overrightarrow{E} \right\| * \langle \Lambda_D \rangle}{k_B * \Theta_D}\right]$$

Note that if the lattice is active and energy is not "lost" but is gained, i.e. XSH from LANR reactions; then it is gained through phonons.

10. Conclusions

In summary, the deuteron momentum is controlled by the delivered electrical input power, and that determines whether there is successful LANR. This analysis reveals that the deuteron momentum produces deuteron scattering, and if large enough the scattering and energy loss then limits the success of, CF/LANR activity. The equations demonstrate that input electrical power correlates to deuteron momentum.

It is shown that deuteron velocities are first created by the electrical input power to the component. There are collisions. After the applied electric field intensity creates the movements of the deuterons within the component's lattice(s), with each collision, the deuteron lose some of the energy gained from the applied electric field.

Worse, these collisions can create a detour ["umweg"] ruining the both the requisite path and deuteron synchrony needed for the desired excess heat. As a result, it is noted that ultimately classical Ohm's law must fail because both the actual, and drift, velocities increase proportional to the applied E-field which further guarantees electrical avalanche. At a critical threshold applied voltage (which produces avalanche and ends the 'excess heat'). The functional result is optimal operating point (OOP) operation which has revolutionized successful CF/LANR, as shown in the graph below, and as shown by open demonstration at ICCF-10 [1], [4].

Acknowledgments

The author wishes to thank Gayle Verner, Alex Frank, Andrew Meulenberg, Michael Staker, Isidor Straus, Jean-Paul Biberian, David Nagel, John Wallace, Brian Ahern, Jeff Driscoll, Peter Hagelstein, Lawrence Forsley, Louis DeChiaro, and Christy Frazier for their editorial assistance, suggestions and support; and JET Energy, Incorporated and New Energy Foundation for support.

References

[1] Swartz, M.R., "Survey of the Observed Excess Energy and Emissions In LANR", Journal of Scientific Exploration, 23, 4, 419-436 (2009).
[2] Swartz. M., "Consistency of the Biphasic Nature of Excess Enthalpy in Solid State Anomalous Phenomena with the Quasi-1-Dimensional Model of Isotope Loading into a Material", Fusion Technology, 31, 63-74 (1997)
[3] Swartz. M., "Codeposition Of Palladium And Deuterium", Fusion Technology, 32, 126-130 (1997)
[4] Swartz, M., G. Verner, "Excess Heat from Low Electrical Conductivity Heavy Water Spiral-Wound Pd/D2O/Pt and Pd/D2O-PdCl2/Pt Devices", Condensed Matter Nuclear Science, Proceedings of ICCF-10, eds. Peter L. Hagelstein, Scott, R. Chubb, World Scientific Publishing, NJ, ISBN 981-256-564-6, 29-44; 45-54 (2006).
[5] Swartz, M.R., P.L. Hagelstein, G. Verner, "Impact of Electrical Avalanche on Incremental Excess Power Gain", ICCF-19, JCMNS, 19, (2016).
[6] Swartz, M.R., "Synchronization of Vacancy-Loaded Deuterons Enables Successful LANR Mass-Energy Transfer", ICCF-24 (pending).
[7] Swartz, M.R., "Optical Detection of Phonon Gain Distinguishes an Active Cold Fusion/LANR Component", JCMNS, 20, 29-53 (2016).
[8] Swartz, M.R, P.L.Hagelstein, "Increased PdD anti-Stokes Peaks are Correlated with Excess Heat Mode", J. Condensed Matter Nucl. Sci. 24, 130-145 (2017).
[9] Swartz, M.R., "Aqueous and Nanostructured CF/LANR Systems Each Have Two Electrically Driven Modes", J. Condensed Matter Nucl. Sci. , vol 29, 177 (2019).
[10] Swartz, M.R., "Optimal Operating Point Manifolds", Proc. ICCF14 2, (2008), p. 639; ISBN: 978-0-578-06694-3, 639, (2010).

J. Condensed Matter Nucl. Sci. 38 (2024) 171–178

Research Article

Impedance Spectroscopy Distinguishes Active ZrO_2-PdNiD NANOR®-type LANR Components

Mitchell R. Swartz

JET Energy, Inc., Wellesley Hills, MA, USA

Abstract

Dielectric/Impedance spectroscopy is an important nondestructive means of measuring the electrical properties of LANR materials and components as a function of frequency. An applied electric field intensity is applied to the material causing its electrical polarization. During a "relaxation" phase, the material's electrical dipoles, atoms, and electrons, all rearrange to align with the applied electrical field. The key is to de-convolve the material response, and then resolve which mechanisms contribute to polarization.
 ISSN 2227-3123

Keywords: Impedance spectroscopy, Dielectric Spectroscopy, Nanor®-type components

1. Introduction: IMPEDANCE- or DIELECTRIC SPECTROSCOPY

Dielectric/Impedance spectroscopy is an important nondestructive means of measuring the electrical properties of LANR materials and components as a function of frequency (Figure 1). An applied electric field intensity is applied to the material causing its electrical polarization. During a "relaxation" phase, the material's electrical dipoles, atoms, and electrons rearrange to align with the applied electrical field. More dielectric mechanisms add in, and are picked up, as the frequency decreases (Figure 2).

Impedance is Complex

- The actual response of any material to an applied electric field intensity is very complex (Figures 2 and 3) – and is handled by complex numbers. First, there results in electrical polarization as the charges move over some distance, and there may be many types.
- Second, there may actually be an energy-absorbing component to the response of the material which may store part of the energy delivered. And the polarization creates an electrical current (Figure 2) linked through Hilbert Space).
- Third, the material may convert the force to a new, different force in a new direction (like a gyroscope responding to a one-directional thrust).

 ISSN 2227-3123

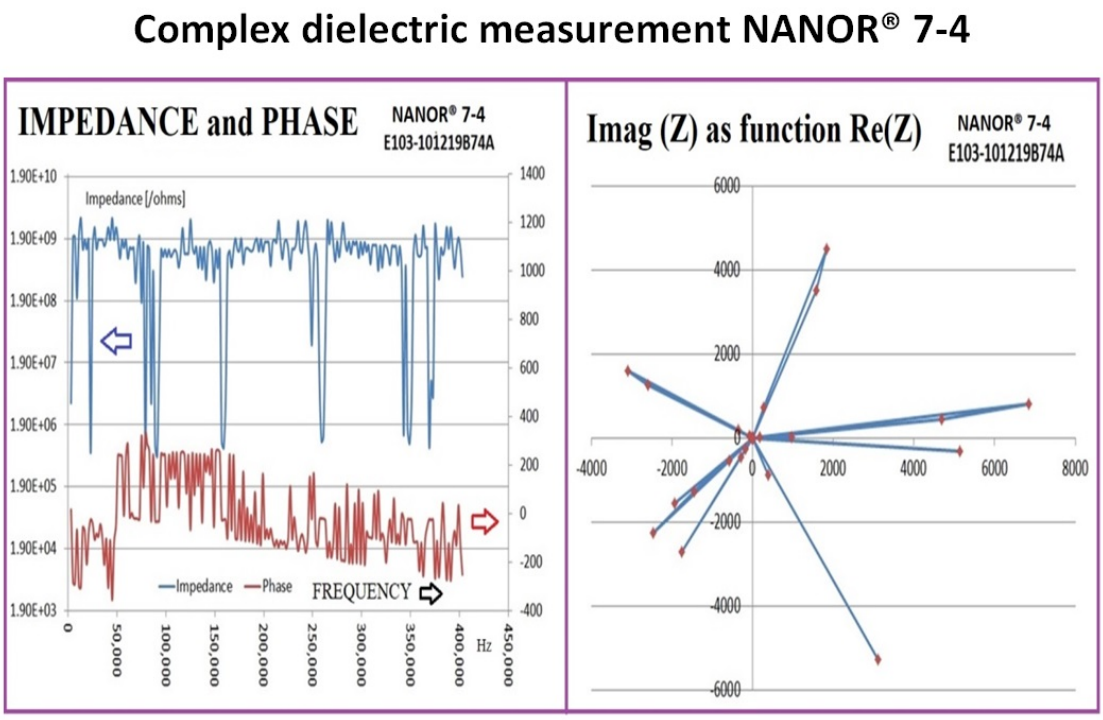

Figure 1. Dielectric Measurements of a NANOR®–type LANR Component Series 7-4. [left] Impedance and phase, as a function of frequency (a Bode plot). [right] Imaginary part of the complex dielectric impedance as a function of the real part of Impedance (Nyquist plot).

- Fourth, in a sinusoidal driving system the flow of electric charges in response to the applied E-field will create a higher-order electric fields resulting from induced (second order) magnetic field intensities. However, at low frequencies, this can be neglected.
- Fifth, in a sinusoidal driving system a phase lag results with additional impact.
- Sixth, depending on the materials, solutions, and electrodes, if irregularities are present at an electrode, for example spikes on a cathode surface, then the electric field intensity distribution can change dramatically with tens of thousands of volts per centimeter appearing over, or near, such irregularities. This has great impact. The calculated applied electric field may not be that which exists in the sample because of this and activation and concentration (space charge) polarizations and double layers, and the possible generation of bubbles (decreasing both the electrode area and adding a low dielectric constant, insulating, layer in front of the critical electrode).

2. Experimental: Presentation(s) of DIELECTRIC DATA

Dielectric data is complex (Figure 3), and can be plotted a number of ways; and all are interrelated, like a shadow to a solid object (Figure 4).

In the Bode plot, the real and imaginary components of the complex impedance, are plotted as a function of log frequency. The projection of the Bode Plot onto the k' and k" plane is the Nyquist plot. Consistent with the projection

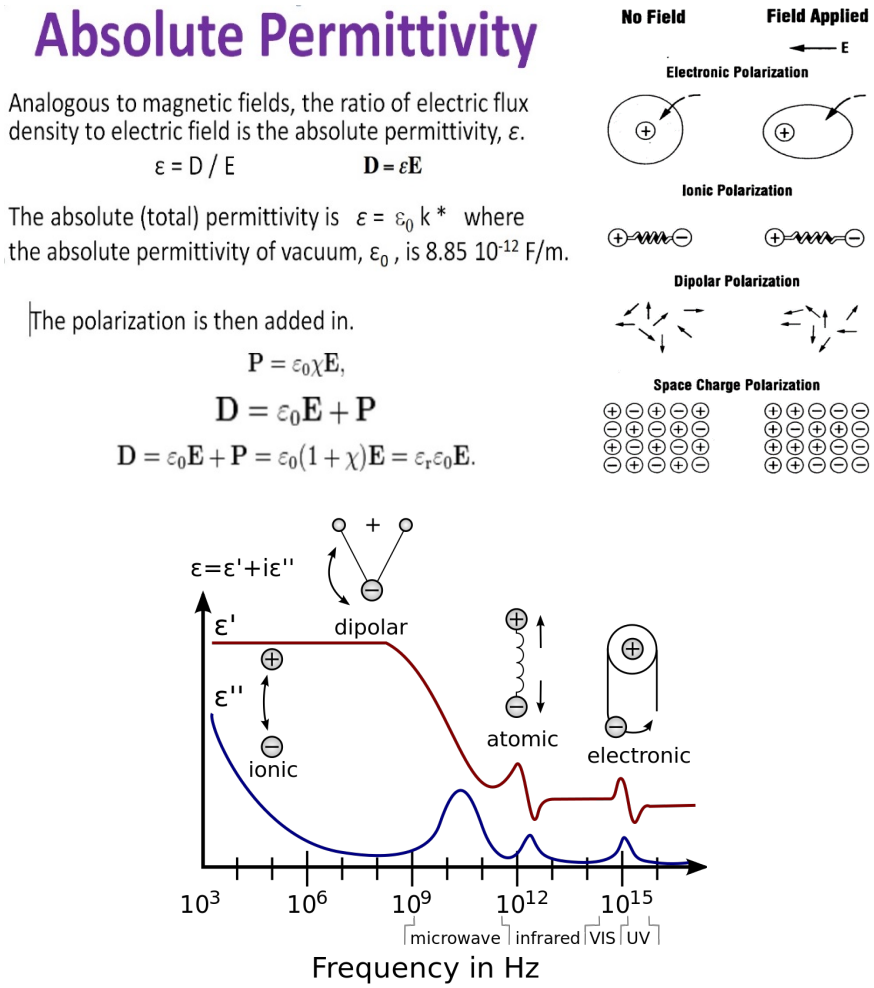

Figure 2. Dielectric Spectroscopy Examines Materials for their Polarizations. The data in Impedance Spectroscopy is presented as the "complex permittivity" which is the dielectric 'constant' and the electrical conductivity as a function of frequency.

of the Bode Plot, in the Nyquist plot, the low frequency data is on the right side of the plot, and the high frequency data is on the left. The Nyquist plot is (generally) a semicircle when the material is characterized by a single time constant.

The projection of the Bode Plot onto the k" (related to electrical conduction, or polarization loss) vs frequency plane is the Cole-Cole plot. The Cole–Cole plot is often used to examine dielectric relaxation in polymer chemistry.

3. Experimental: Impedance Analysis Using AD5933

This is how to measure this using available hardware (Figure 5). AD5933 circuit boards enable mid to high frequency analysis. It is a 12-bit impedance converter ["Network Analyzer"] with a Cortex M3 Core [programmable output to ~400 kHz with frequency control by I2C interface]. The frequency resolution is <0.1 Hz [2^7 bits], with a phase measurement accuracy ~0.5%, over a testing impedance range is ~kΩ to 10 MΩ.

Complex Relative Permittivity (real part)

Dividing out the permittivity of vacuum, the "complex relative permittivity", k* , includes both polarization and conduction components, and is written as:

$$k^* = k' - j\,k''$$

The relative polarization [k'] is the real part of the complex relative permittivity [k*].

k' is the relative permittivity which is the permittivity normalized to that of vacuum. The units are farads/meter.

k' is specifically what is called, incorrectly, the "dielectric constant". This is a misnomer because it is not a constant and is often actually time variant and actually also always changes with frequency.

Complex Relative Permittivity (imaginary part)

Continuing to the imaginary part:

the electrical conductivity of a material is mathematically the imaginary part of the complex permittivity divided by the frequency.

The units are mhos/meter-second.

$$k'' = \sigma * \omega$$

The real and imaginary components of the complex impedance arise from electrical polarization and electrical conduction, respectively. The electric field-induced dipole rotations during dielectric relaxation produce the actual electrical current. And so, the real and imaginary parts of the complex permittivity are necessarily linked through Hilbert Space.

Figure 3. Dielectric Spectroscopy uses Complex Numbers. The data in Impedance Spectroscopy is presented as the "complex permittivity" which is the dielectric 'constant' and the electrical conductivity as a function of frequency.

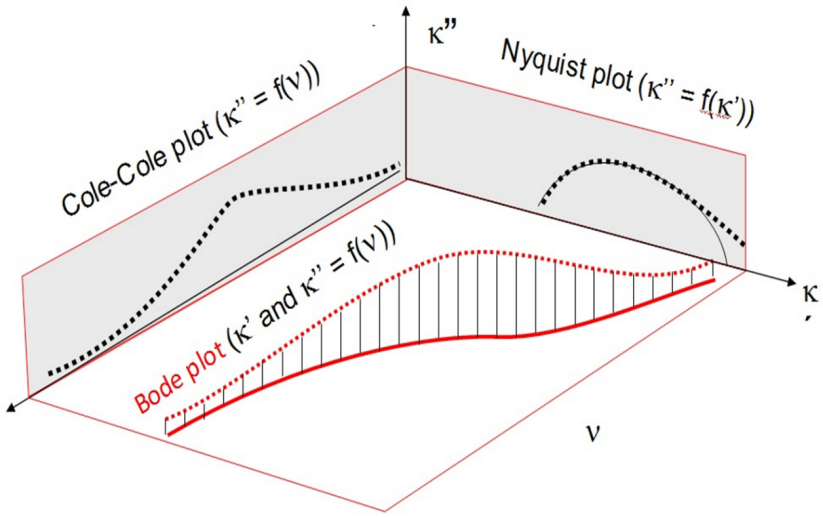

Figure 4. Phase Space of Dielectric/Impedance Spectroscopy. Impedance is complex with both real and imaginary parts. There are several different ways of viewing impedance data. The figure is adopted from, and redrawn from, http://www.gamry.com/App_Notes/EIS_Primer/EIS_Primer.htm.

4. Results: Dielectric Measurements of 3 NANOR®–type LANR Components

Impedance spectroscopy is complex with both real and imaginary parts. There are several different ways of viewing impedance data. In Figure 1 are the Dielectric Results of NANOR® –type Component 7-4. On the left is the Impedance

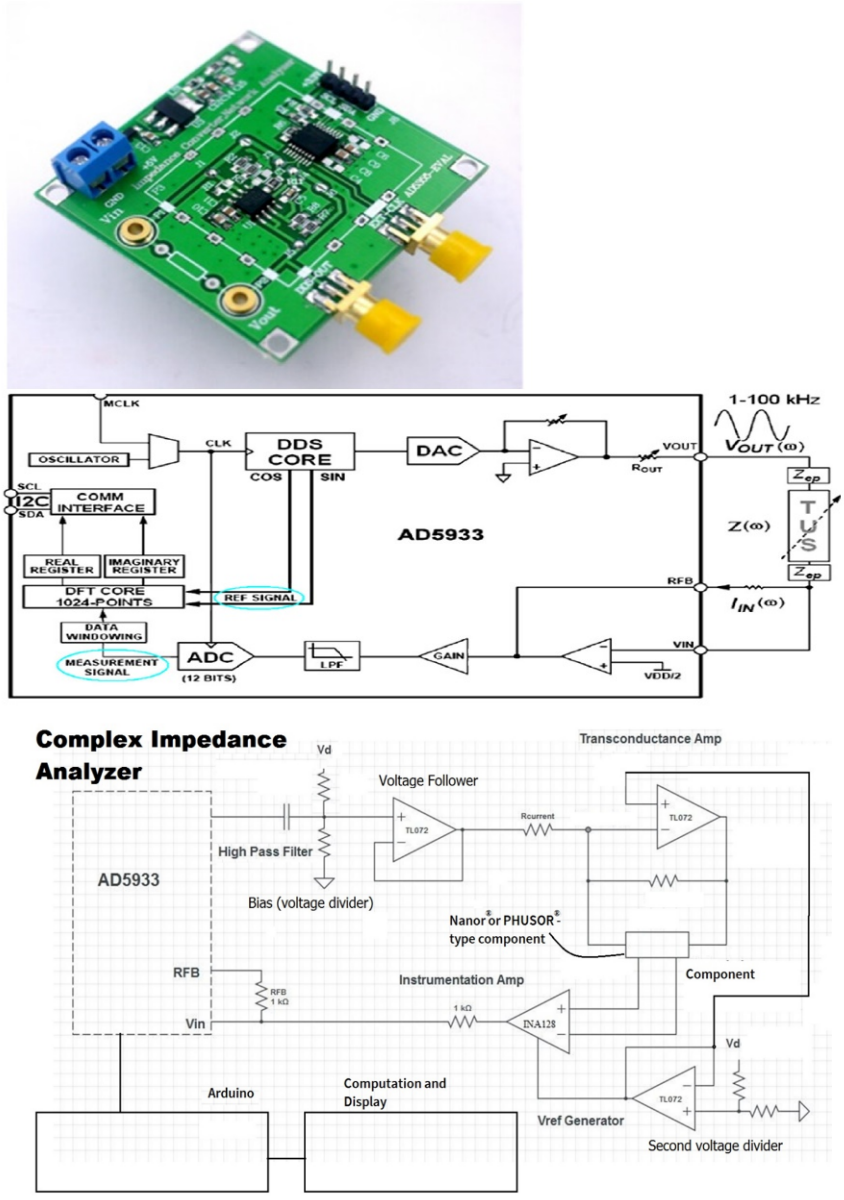

Figure 5. Inexpensive Hardware to investigate Impedance Spectroscopy. Impedance is complex with both real and imaginary parts. There are several different ways of viewing impedance data. It is made easier with available hardware and modifications. The external circuit used created a four-terminal biased and amplified front-end, connected by 12C to an Arduino microprocessor. The output is biased, and then drives an electrical current source. Constant current is sent through the component, while a four terminal conductivity measurement is first sent through an INA128 Instrumentation Amplifier before returning to the AD5933 chip for analysis by a built-in discrete Fourier transform (DFT) module. Arduino software correct quadrature errors.

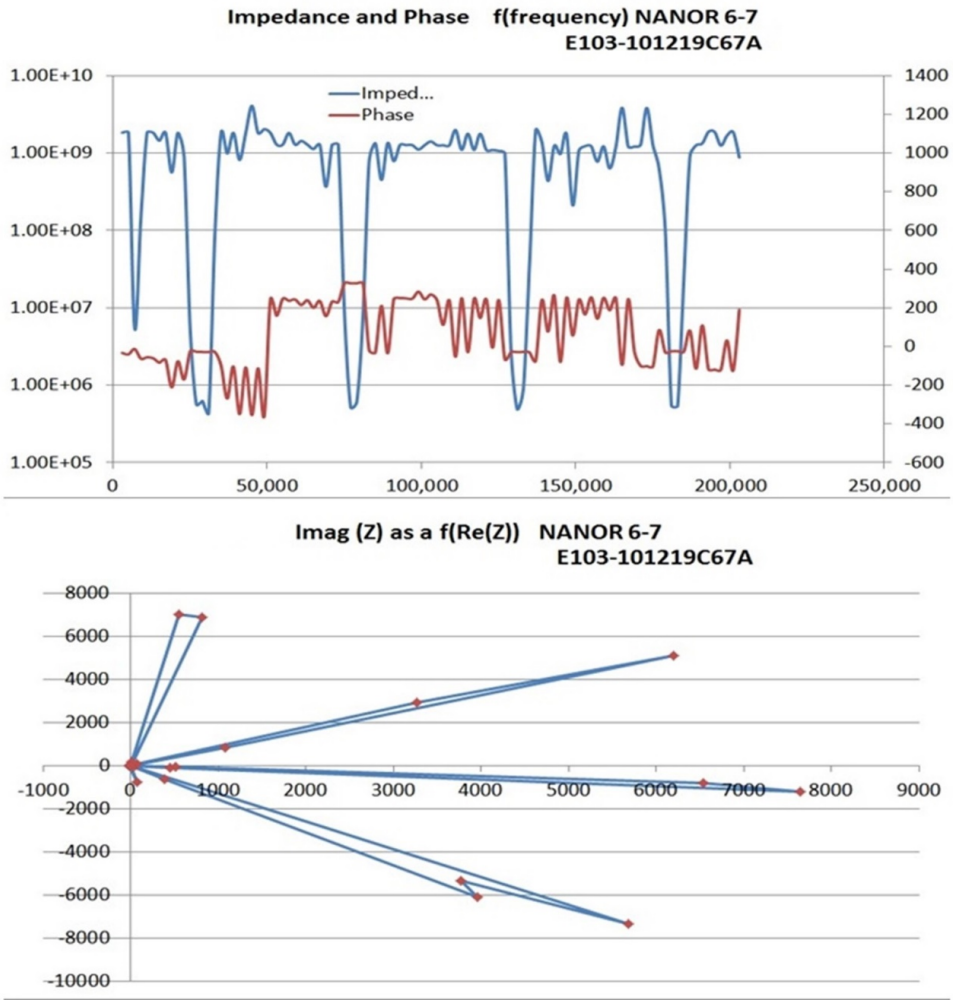

Figure 6. Dielectric Results of NANOR®–type Component Series6-7. Impedance is complex with both real and imaginary parts. There are several different ways of viewing impedance data. [above] Impedance and phase, as a function of frequency (a Bode plot). [below] Imaginary part of the complex dielectric impedance as a function of the real part of Impedance

and phase, as a function of frequency (a Bode plot). On the right is the Imaginary part of the complex dielectric impedance as a function of the real part of Impedance (Nyquist plot).

In Figure 6 are shown the Dielectric Results of NANOR® –type Component 6-7. On the top is the Impedance and phase, as a function of frequency (a Bode plot). On the bottom is the Imaginary part of the complex dielectric impedance as a function of the real part of Impedance (Nyquist plot).

In Figure 7 are shown the Dielectric Results of NANOR® –type Component 7-22. On the top is the Impedance and phase, as a function of frequency (a Bode plot). On the bottom is the Imaginary part of the complex dielectric impedance as a function of the real part of Impedance (Nyquist plot).

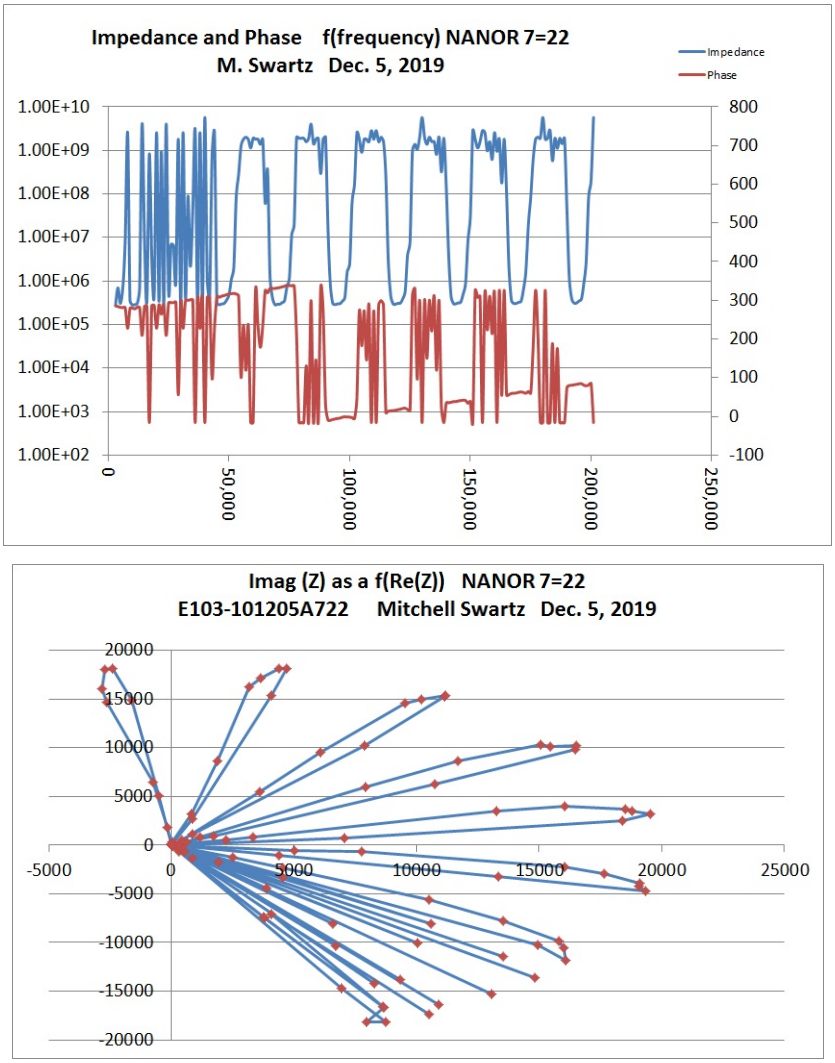

Figure 7. Dielectric Results of NANOR®–type Component Series 7-22. [above] Impedance and phase, as a function of frequency (a Bode plot). . [below] Imaginary part of the complex dielectric impedance as a function of the real part of Impedance (Nyquist plot).

5. Conclusions

5.1. Complex Impedance Measurements of NANOR®-type Components

- Active nanomaterial LANR materials have highly unusual electrical transconduction properties that accompany their excess-heat producing active states. Of particular interest and concern is that dry, preloaded nanomaterials exhibit avalanche electrical breakdown from their active XSH-producing modes which terminates the desired excess heat.

- Previously active dry preloaded LANR nanomaterial components (ZrO_2-PdD and ZrO_2-PdNiD NANOR®-type components) were examined by impedance (dielectric) spectroscopy [$\sim 10^{-4}$ Hz to $\sim$2 GHz].
- The Bode, Cole-Cole, Nyquist, and Smith-chart plots of the preloaded LANR NANOR®-type components reveal complex, and quite distinguishable, differences compared to conventional materials and ohmic controls.
- These patterns may result from many reasons including the electrical avalanches seen, and possible synchronized interactions between the loaded deuterons in vacancies, and other reasons ranging from material science to coupling and the transmission line.

Acknowledgments

The author wishes to thank Gayle Verner, Alex Frank, Andrew Meulenberg, Michael Staker, Isidor Straus, David Nagel, John Wallace, Brian Ahern, Jeff Driscoll, Peter Hagelstein, for their editorial assistance, suggestions and support, and JET Energy, Incorporated for contributing to this effort.

References

[1] Swartz, M.R., "Aqueous and Nanostructured CF/LANR Systems Each Have Two Electrically Driven Modes", J. Condensed Matter Nucl. Sci. (2019).
[2] Swartz, M.R., "Quasi-One-Dimensional Model of Electrochemical Loading of Isotopic Fuel", Fusion Technology, 22, 2, 296-300 (1992).
[3] Swartz, M.R., P.L. Hagelstein, G. Verner, "Impact of Electrical Avalanche on Incremental Excess Power Gain", ICCF-19, JCMNS, 19, (2016).
[4] Swartz, M.R, P.L.Hagelstein, "Increased PdD anti-Stokes Peaks are Correlated with Excess Heat Mode", J. Condensed Matter Nucl. Sci. 24, 130-145 (2017).
[5] Swartz. M., "Dances with Protons - Ferroelectric Inscriptions in Water/Ice Relevant to Cold Fusion and Some Energy Systems", Infinite Energy, 44, (2002).
[6] von Hippel, A. "Dielectric Materials and Applications", MIT Press (1954).
[7] Matsiev, L. "Improving Performance and Versatility of Systems Based on Single-Frequency DFT Detectors Such as AD5933", Electronics 2015, 4, 1-34.
[8] Chabowski, K, et al, "Simple Wide Frequency Range Impedance Meter Based on AD5933", Metrol. Meas. Syst., Vol. XXII (2015), No. 1, pp. 13–24.

J. Condensed Matter Nucl. Sci. 38 (2024) 179–185

Research Article

Direct Electricity Production from NANOR®-type ZrO_2-PdNiD Components Using Ultrasound

Mitchell R. Swartz

JET Energy, Inc., Wellesley Hills, MA, USA

Abstract

This paper describes new features of the NANOR®-type CF/LANR component technology. We report direct production of "excess electricity"; ∼655% higher than anything seen of any control. Thus, deuterated NANOR®-type components now appear to offer two methods of energy production. Direct LANR electric output may eventually bypass the need for thermoelectric energy conversion handicapped by Carnot inefficiency.
 ISSN 2227-3123

Keywords: Electricity production, excess electricity, NANOR®-type components, ultrasonic irradiation, LANR energy conversion

1. Introduction

ZrO_2-PdNiD nanostructured LANR (lattice assisted nuclear reaction) materials [1] contain deuterated PdNiD core islands that are electrically isolated by the zirconia (ZrO_2) dielectric. They have exquisite sensitivity to ultrasonic irradiation [2], [3], [4], including the generation of heat [5]. NANOR®-type components were examined for their ability to convert energy obtained from ultrasonic irradiation (US, or simply 'ultrasound') to DC electricity.

We report production of "excess electricity"; ∼655% higher than anything seen of any control. Deuterated NANOR®-type components now appear to offer two (2) methods of energy production. Direct LANR electric output may eventually bypass the need for thermoelectric energy conversion handicapped by Carnot inefficiency [Figure 1].

In Figure 1, the available electricity (derived from an electrometer) and the resultant temperature rise for a series of US pulses are shown for the NANOR®-type ZrO_2-PdNiD component and for ohmic controls. These are shown both with and without an additional applied magnetic field intensity. Each US pulse had the same level of power output delivered from the ultrasonic unit as described in the Experimental section. The power levels of the US irradiated was fixed, and the durations are shown along the time axis (horizontal). The left vertical axis was derived from the output of a very high-input impedance Keithley electrometer which was contacting both sides of the NANOR®-type two terminal LANR component. The colors of the pulses in the figure identify if, and when, a continuous magnetic field was added (brown) or not, or if an ohmic control was substituted for the NANOR®-type component (blue pulses), or if only US was used without an applied magnetic field (green). The green line is the output from a NANOR®-type component with US alone, and no additional magnetic field. The results of ohmic controls alone are shown as blue.

 ISSN 2227-3123

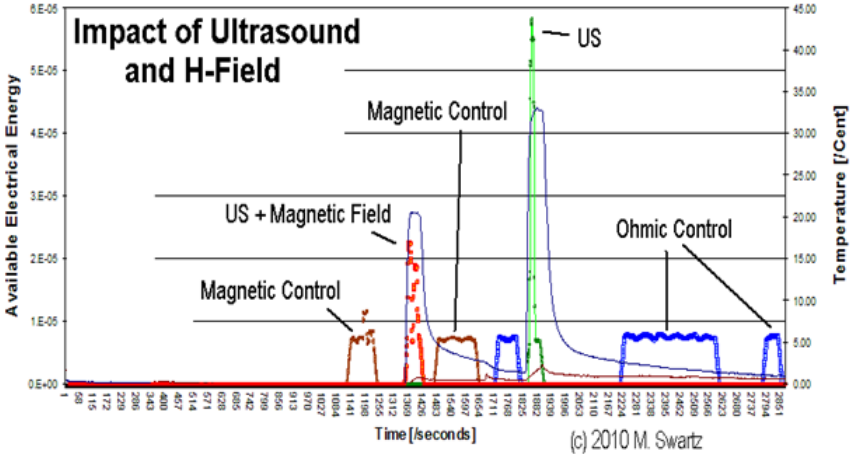

Figure 1. Direct Electricity Production from LANR using Ultrasonic Irradiation (US). The left axis show the obtained relative electrical energy available. The pulses show when ultrasonic irradiation was delivered. The key to the results follows: Brown spots, and brown line, show the Magnetic control's electrical output under an applied magnetic field with no additional ultrasonic irradiation (left axis); Red spots: NANOR®-type component electrical output under ultrasonic irradiation also with the applied magnetic field (left axis); Green line: NANOR®-type component electrical output under ultrasonic irradiation (left axis) but without the applied magnetic field; Blue lines – Electrical output of ohmic controls; Thin Blue lines: Temperature of the volume containing the NANOR®-type component and the ohmic control (right axis); Purple thin line: Temperature of the bulk aqueous tank surrounding the ohmic control and NANOR®-type component [called a 'large angle detector' (shown on the right axis).

For this run, two (2) temperature detecting probes were used. Hence there are two continuous lines showing their temperature (right vertical axis). One was a sensitive small-angle [i.e. small area subtended] detector located exactly behind the NANOR®-type component (shown as the smaller amplitude purple/red line). The other was a wider angle detector, larger and behind all of the components irradiated (blue continues line; also right vertical axis).

2. Experimental

We examined these deuterated devices for electricity output and possible heat generation during various types of activation including while being ultrasonically irradiated. These components were also examined by electric, magnetic and ultrasonic fields. In the past publications, the NANOR-type component was connected and driven by an essentially DC power supply to bring out the excess heat, to reveal the electrical avalanches, and to elicit both the antiStokes spectra and the deuterium line RF spectra near 327 MHz. These were not driven by applied electricity. Instead, the NANOR®-type component, and the ohmic controls were only attached to the electrometers terminals so that its very high impedance could be used to measure their electrical output, if any.

These devices were constructed with their two terminals only connected to the Keithley electrometer. Therefore, in none of the following cases which are shown to manifest a temperature rise is that due to an applied electric field to the NANOR component or the ohmic control.

In a similar way, the ohmic controls which are usually used for the evaluation and calibration of any excess heat released by the electrically-driven NANOR, were not used for that reason here. There was no effort here to measure the excess heat, unlike the previous papers. The temperature detectors were added only to determine the local, and regional, temperatures around the irradiated NANOR type component.

Thus, here they were used to see if they were responsive to the incident ultrasound irradiation, as a control. Therefore, they were wrapped (thermically) into a large mass with the NANOR-type component and temperature

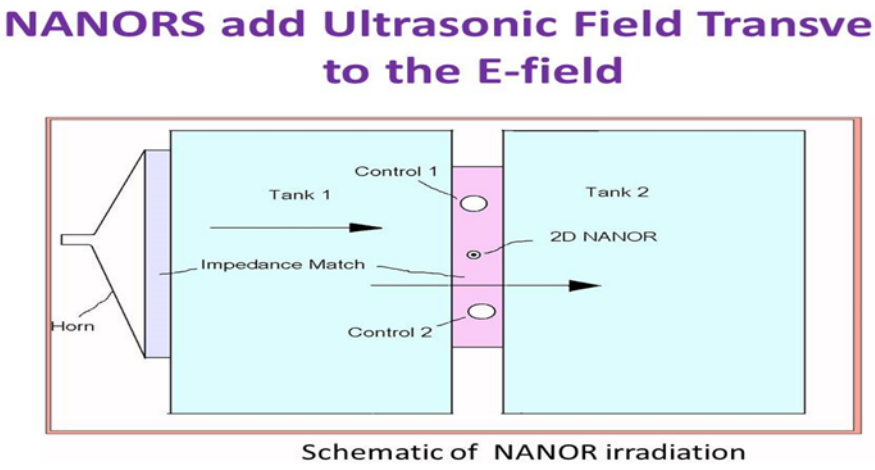

Figure 2. This is a schematic illustration/cartoon of the direction of ultrasonic radiation made through two tanks of water and the irradiated samples. The bath was larger than the irradiated area. Of more importance is that the author used quarter-wavelength impedance matches to minimize ultrasound reflectance (and this is not often done in this field). The matching impedance is obtained from the square root of the involved impedances. For palladium and heavy water, this quarter wavelength material can often be matched with a portion of red building bricks.

sensor. This larger single mass was wrapped into a larger volume with an additional metallic component acting as a local temperature sink. In fact, this tying together of their thermal masses into a larger thermal mass is commonly done in our systems and especially calorimeters, and it is also why the monitored temperatures often decreases so slowly in many of these experiments.

Temperatures (degrees C) were monitored at the LANR core, and at both ohmic controls, and at other background locations as further controls, and within two adjacent water tanks which absorbed the ultrasonic radiation and also provided thermal stabilization.

Temperature measurements were made by specialized electrically-insulated thermocouples [accuracy $+/-0.8$ deg.K, precision $+/-0.1$ deg.K]. The temperature probes were calibrated by an Omega IcePoint Cell. Peripheral temperatures were maintained by feedback control using a Yellow Spring Thermal Controller Model 72 [bandwidth of 0.2 K] within a Honeywell water circulation zone controlled room ($+/-$ 2.5 degrees K). The temperature sensors were provided to measure the local temperature of the NANOR®-type components and the other irradiated components, and to measure the regional bulk aqueous volume to which they were connected thereto (shown in Figure 2).

Calorimetry used ohmic controls and also paired water tanks for an ultrasonic control. Other controls included dry, gas deuterated, and D_2O-solvated nanomaterials, supplementing the background, magnetic, and thermal (including ohmic) controls. Two types of thermal controls were used. First, two ohmic resistors were included. The resistors were 100,000 and 10,000,000 ohms; a value selected to be in the range of the nanostructured material core. Next, the third control was a water container which surrounded the samples and controls and irradiators, minimized reflections, and was used to accumulate the heat and improve the calorimetry.

Ultrasound irradiation (0.3 to 25 W/cm^2) was delivered and subtended over an active area of $\sim$0.02 cm^2 of LANR component (Figure 2). In each case the same bath setup was used. The ultrasonic irradiator was a modified Dallons Medi-Sonic Ultrasonic generator (Model U-111). The device, and manual, state that it was operating at a nominal 1 Megahertz.

In a typical run such as Figure 1, pulses of ultrasound irradiation delivered 0.5 W/cm^2 (5 W total). For, or if there were two pulses of ultrasound irradiation; first 3 W (0.3 W/cm^2) for 5 minutes, and then 10 Watts (1 W/cm^2) for 1 minute.

Controls included thermal (ohmic) resistors also irradiated. They are seen only in cross-section.

The two ohmic resistors were designed to be included in the irradiation field so as to interact with the ultrasonic radiation. The area subtended by them is 0.35 and 0.78 cm^2. By contrast, the area subtended by the LANR nanostructured material core is 0.02 cm^2.

Electrical conductivity of the components, before, during, and after irradiation, was followed by 4-terminal electrical measurements. In addition, to measure the electricity generated (if any), the electrical output was coupled to a Keithley electrometer (Model 610A and 610B) and then a voltage follower. The system was examined at rest, during ultrasonic irradiation (such as 0.5 W/cm^2), and in the absence and presence of a continuous magnetic field intensity. Electrical conductivity of the components, before, during, and after irradiation, was followed by 4-terminal electrical measurements. The magnetic field intensity was estimated at 0.2 Tesla near the surface of the magnet, but there was not a measurement at the components, which were located about 1 to 2 cm away.

Some of these results are shown both with and without an additional applied magnetic field intensity. Most importantly, the NANOR®-type components are shown both with and without an additional applied magnetic field intensity. However, the additional control(s) of magnetic field intensities applied with the ohmic controls was not used in this run, unfortunately.

Outputs were calibrated by ohmic (thermal) controls and confirmed by adequate Nyquist sampling.

3. Results

3.1. Electricity Production

ZrO_2-PdNiD NANOR®-type LANR components are highly sensitive to sound generating both direct electrical energy and heat. Ultrasound impacting the LANR-type components does create direct electrical energy, far above the noise level. Of note, the temperature only changes with the simultaneous applied ultrasonic field.

For these results, a single NANOR®-type component was used in Figure 1 and 4. In Figure 1, the single component was irradiated along with various controls with measurement of each of their generated electricity over time.

Three different NANOR®-type components of different loadings were irradiated in the run in Figure 3. This graph shows the fundamental importance in the deuteron in these reactions.

The ultrasonic irradiation upon the NANOR®-type component in Figure 1 (and all components in Figure 3) is believed to be the sole reason for the temperature changes which are read off the right hand side of Figure 1. The more power irradiation upon all components is the reason for the temperature changes which are read off left hand side of Figure 4.

First, Figure 1 shows this direct relative electrical energy obtained from ultrasonic irradiation impacting a NANOR®-type device, and controls. The Figure also shows the impact of a magnetic field alone, ultrasound alone, and the combination of US and an applied magnetic field. Additional controls were (thermal) ohmic resistors. The marked increase in electrical energy happened only with ultrasonic irradiation of the NANOR®-type component.

Also, note that the temperature rise lasted longer than the falloff of the voltages. This demonstrates the LANR components create electricity, and it is not from the temperature rise.

Despite the marked differences in area subtended, with the LANR device having an area ratio of only 0.026 to 0.059 of the controls, it is important to note the very exquisite sensitivity of the LANR nanostructured material to ultrasonic irradiation for both electricity production and heating. The “excess electricity” was 655% higher than anything seen of any control.

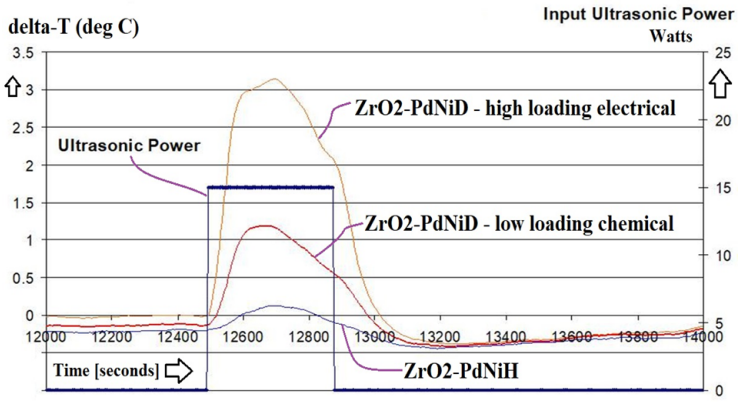

Figure 3. Thermometry of three NANOR®-type components to ultrasonic radiation (15W/cm^2), surrounded by two aqueous reservoirs for cooling. One has LANR nanomaterial, the second and third had increasing amounts of deuterons, added by heavy water and an additional electric field. This graph shows the fundamental importance of the deuteron in these reactions.

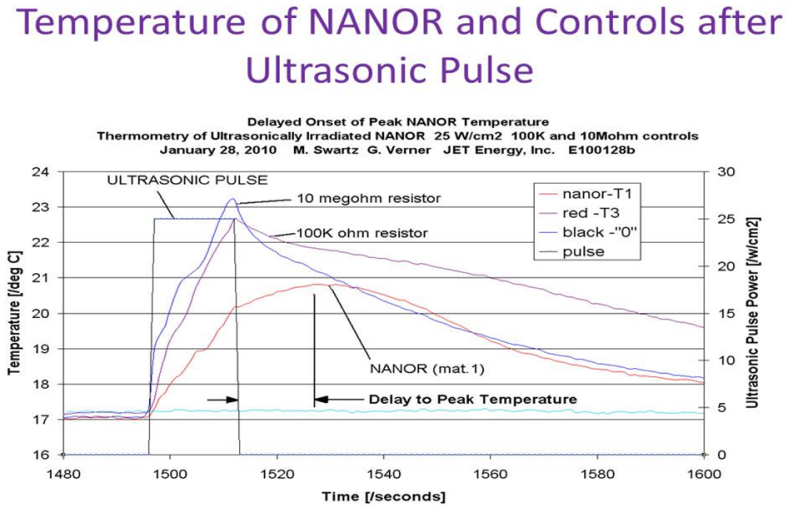

Figure 4. Thermometry of a NANOR®-type component and two additional ohmic controls. The LANR device has an area ratio of only 0.026 to 0.059 compared to the controls. Notice the delay of the peak temperature from the NANOR®-type component until after the end of the ultrasonic radiation (25W/cm^2).

Regarding impact of a magnetic field in combination with the ultrasound irradiation. As demonstrated in Figure 1, the magnitude of the electricity output was actually decreased by the applied magnetic field, applied orthogonal to the direction of induced electrical current.

3.2. Deuterons are the Fuel

Figures 3 and 4 show the temperatures (degrees Centigrade) of NANOR components and the ohmic controls, while being between two water tanks which absorb some of the ultrasonic radiation and provide thermal stabilization. They

also reveal the fuel of CF/LANR. Figure 3 also shows the secondary heat redistribution to the larger water tank, as the temperatures fall while the ultrasonic irradiator continues.

The curves in Figure 3 show the response to ultrasonic irradiation of three NANOR®-type components to a single square wave pulse of 15 watts. The lowest curve is of ZrO_2-PdNiH which shows a minimal, but clear, response. The curve above it is the response of ZrO_2-PdNiD, obtained from heavy water, chemical loading. It has a significantly greater response. The top curve, with the greatest amplitude, is the response of the ZrO_2-PdNiD, obtained from a proprietary electrical loading method,

To compare the differences between these curves, compare the integrals over time (area under the curves). Importantly, Figure 3 shows the crucial role of deuterons as the fuel of these desirable At lower input irradiation powers, there is an exquisite sensitivity of the LANR nanostructured devices by electricity output or temperature rise [degrees C] when ultrasonically irradiated. There is a sudden rapid rise in the temperature of the NANOR®-type component, exceeding that of the ohmic resistors (even though they subtend larger areas to the ultrasonic irradiation). Only at much high irradiation powers will the temperatures of the controls exceed the LANR component, such as in Figure 4.

The curves in Figure 4 show the thermometry response of a NANOR®-type component and two additional ohmic controls to ultrasonic irradiation with a square wave pulse of 25W/cm^2. In this case, notice the delay of the peak temperature from the NANOR®-type component is AFTER the end of the ultrasonic radiation (25W/cm^2). This is unlike the ohmic controls.

Notice also that these LANR components also demonstrate some late-occurring temperature responses, continuing after the ultrasound is turned off, in contrast to the control materials. This heralds secondary reactions occurring after the end of the triggering ultrasonic pulse.

4. Interpretation

NANOR®-type LANR components now offer two methods of energy production – both direct electricity production and the conventional LANR-induced excess heat. Importantly, this device for the direct production of electricity from nuclear LANR process bypasses the previous need for LANR heat generation followed by thermoelectric energy conversion, which is so handicapped by Carnot and other inefficiencies.

The "excess electricity" of the ZrO_2-PdNiH NANOR®-type LANR component is 655% higher than anything seen of any ohmic control. However, this electrical energy produced so far is microscopic in this initial system. However, the efficiency of energy conversion is small [$10^{-13} - 10^{-14}$ of the transiting ultrasonic energy] at this time. Thus, there is considerable engineering left to do, and some issues to consider.

4.1. Important Issues to Consider

It is important to consider several issues. First, why does an alternating symmetric ultrasonic wave here produces a direct electrical voltage or current. Specifically, what might be the source(s) of the dissymmetry that transforms the alternating US into a DC current. When the NANOR-type components were manufactured, i.e. including preloading, there was developed an *ab initio* inherent asymmetry because the deuterons are injected into, and enter only on one side of the component. That asymmetry from initial preloading may have been the reason why the voltage appeared on the Keithley electrometer. In the future, as a result of the question, (and in retrospect we should have looked closer) we will also add a series of electrical diodes and amplifiers to learn more, including how this electrical output could be maximized.

It is also important to consider if the small electrical output might have been an effect of the observed temperature rise. We believe that it is unlikely that the small electrical output(s) are an effect of the temperature rise. The electrical

load is at the Keithley electrometer, and it is noted that the observed voltage at the Keithley electrometer decreases and falls before the fall off of temperature. This heralds that the voltage arises from other reason than the temperature rise.

What might be the role of electrical noise? The output of the LANR component was certainly not a result of electrical noise. It is less clear regarding the ohmic controls which were irradiated. However, the very low outputs of the controls in Figure 1 may have been limited the baseline sensitivity of Keithley electrometer in our system. The US-irradiated NANORs (+ or − magnetic field intensity) far exceeded that lower possible detection limit.

It is also finally important to consider and remove a possibility that the additional heating of the NANOR®-type components might be the result of energy input from loading. That is not possible because these components were preloaded weeks before they were driven for these experiments. There could be no temperature rise here, occurring from the earlier preloading which happened long before the experimental use of the components here.

5. Conclusions

In summary, these acoustic-driven, vibration-driven PdNiD-ZrO_2 NANOR®-type components offer new methods of energy production and energy conversion from LANR systems with direct electricity production augmenting conventional LANR-induced excess heat. This discovery may add more tools to the armamentarium of CF/LANR, as well.

The incremental LANR-catalyzed induced electrical energy from vibration(s) both augments yet is dwarfed by, the induced heat. But, it has that one advantage of totally bypassing Carnot-inefficient thermoelectric energy conversion. We are developing both more robust LANR NANOR®-type components, and ancillary control systems to harvest the electricity for storage and use.

Acknowledgments

The authors wish to thank the late Charles Entenmann and Scott Chubb, and Alex Frank, Brian Ahern, Jeff Driscoll, David Nagel, and JET Energy, Incorporated and New Energy Foundation for contributing to this effort.

References

[1] Swartz, M. R, “Aqueous and Nanostructured CF/LANR Systems Each have Two Electrically Driven Modes, Proc. ICCF-21, Fort Collins, Co.6/3/18 (2018), J. Condensed Matter Nucl. Sci, Vol 29, 177 (2019).

[2] Swartz, M.R., G. Verner, “Ultrasonic Irradiation of LANR Nanostructured Material”, 2010 Colloquium on LANR at MIT, July 2010, Cambridge, MA, in Summary of 2010 Colloquium on Lattice-Assisted Nuclear Reactions (LANR), S. Chubb, T. Dolan (2010).

[3] Swartz, M.R., C.E. Entenmann, “Direct Electricity Production from Anisotropic ZrO2/PdNiD Nanostructured Devices Using Ultrasonic Irradiation”, National Meeting 241st American Chemical Society National Meeting, Anaheim, California, USA – March 27 - 31, (2011).

[4] Swartz, M.R., C.E. Entenmann, “Direct Electricity from LANR Nanostructured NANOR Devices”, 2010 Colloquium on LANR at MIT, July 2010, Cambridge, MA, in Summary of 2010 Colloquium on Latt Controls included thermal (ohmic) resistors also irradiated. ice-Assisted Nuclear Reactions (LANR), S. Chubb, T. Dolan (2010).

[5] Swartz, M.R., “Survey of the Observed Excess Energy and Emissions In Lattice Assisted Nuclear Reactions”, Journal of Scientific Exploration, 23, 4, 419-436 (2009).

J. Condensed Matter Nucl. Sci. 38 (2024) 186–195

Research Article

Excess Heat in Nanoparticles of Nickel Alloys in Hydrogen

Jean-Paul Biberian, Robert Michel
VEGATEC, France

Christophe Le Roux
CNRS France

Mathieu Valat
University of Szczecin, Institute of Physics, Poland, and also with Sart von Rohr, France

Sébastien Bucher
LIFCO France

Arnaud Kodeck
Lakoco, Belgium

Per J.R. Sjöberg
Uppsala University, Sweden

Jacques Ruer
Sart von Rohr, France

Damien Chaudanson
Aix Marseille University, CNRS, CINAM, Marseille, France

Abstract

We have developed new kinds of materials made of nanoparticles of nickel-based alloys that show production of anomalous heat in an atmosphere of hydrogen. These materials are produced starting from hydrotalcite acting as precursors of nickel and nickel alloys supported on an amorphous alumina phase. The experiments are performed in a custom-made heat-flow calorimeter having a precision of $+/-100$ mW from room temperature up to 950°C. This report shows that excess heat is produced when hydrogen is introduced into the reaction cell, however more excess heat is measured when the hydrogen is pumped out.
 ISSN 2227-3123

Keywords: Energy, hydrotalcite, nickel, high temperature calorimetry

© 2023 ICCF. All rights reserved. ISSN 2227-3123

1. Introduction

In the framework of the European Project CleanHME, we worked on experiments using nanoparticles made of nickel-based compounds. These nano particles are of prime importance because previous experiments dating back to the work of Arata [1] using palladium nanoparticles embedded in zirconium oxide in a deuterium atmosphere show excess heat production with the sole excitation of heat. Takahashi et al. [2] have shown that such nickel and copper-based nano powders produce anomalous heat in hydrogen or deuterium. To measure accurately the heat produced we used a heat-flow calorimeter of Calvet type (also known as Seebeck) to reach high temperatures using low heating power. We have also developed a new method to produce nickel-based nano particles using a much cheaper technique than the one of Arata [1] and Takahashi et al. [2], using hydrotalcites as precursors. This new method allows us to produce large quantities of materials at low cost. In addition to the work with hydrotalcite, we have also studied thin films of nickel deposited on carbon powders.

2. The Calorimeter

In a standard Calvet calorimeter [3]–[5], the hot core is surrounded by a box which has an insulated wall equipped with thousands of thermocouples in series, alternatively placed on one side of the insulated wall and on the other side. Since the insulated wall is all around the heat source, all the heat produced by the hot core must go through the wall. The voltage at both ends of the series of thermocouples is a function of the core power source. This type of calorimeter is very insensitive to the position or the temperature of the heat source in the box.

We have developed a simplified Calvet calorimeter. In our design, shown in Figure 1, the heated quartz tube is filled with the active powder. The quartz tube is placed inside a vacuum chamber (stainless steel 150 mm long $\times$ 63 mm in diameter, see Figure 1b) itself surrounded by insulating material. The heat flow produced by the cell goes through the insulation layer and creates a temperature gradient across this thermal insulation. However, our design differs from the ideal Calvet calorimeter two-fold. Firstly, since the calorimeter and the quartz cell have a cylindrical geometry, therefore, it is not necessary to have thermocouples placed in all directions. Fifty thermocouples are in one plane, because of the cylindrical symmetry, the voltage measured is proportional to the voltage measured if there were thermocouples all around the cell. Secondly, there is no thermocouple on the top flange of the calorimeter, so the heat lost by the top flange is not taken into account. This loss is minimized by putting insulating material above the flange. If the room temperature of the laboratory is constant, then by calibration, this loss is the same for a blank run as an active experiment. Therefore, after calibration, the voltage measured with the 50 thermocouples is a good representation of the heat produced.

The quartz cell is heated by a Kanthal wire wrapped around it and covered by cement, as shown in Figure 1d. Three concentric stainless-steel screens are placed around the cell, inside the vacuum chamber, to reduce the heat lost by radiation, hence limiting the heating power required to reach a high temperature. The vacuum chamber is positioned inside the double wall cylindrical aluminum vessel. The heat resistant material is crossed by 50 type-K thermocouples connected in series, alternatively sealed on each side of the insulation material. Finally, the calorimeter is placed in a constant temperature water bath, as shown in Figure 1e. Temperatures up to 950°C can be reached.

We used two types of quartz cells, 90 $\times$ 20 mm cells heated from the outside with a Kanthal heating wire, and 90 $\times$ 40 mm quartz cells heated from inside (see Figure 2). The data acquisition and control system (DACS) capture and monitors measurements in the calorimeter. The DACS is responsible for acquiring temperatures, pressures, and the Seebeck signal from the thermocouples. Additionally, the DACS controls the electrical input power from a TDK Lambda power supply. This comprehensive system ensures accurate and reliable data collection while providing seamless control over the input power for the experimental setup.

Calibration of the calorimeter was made with a quartz cell filled with alumina powder in hydrogen, see Figure 3. The heating power was increased by 10 W steps up to 70 W. The input power is plotted against the voltage measured

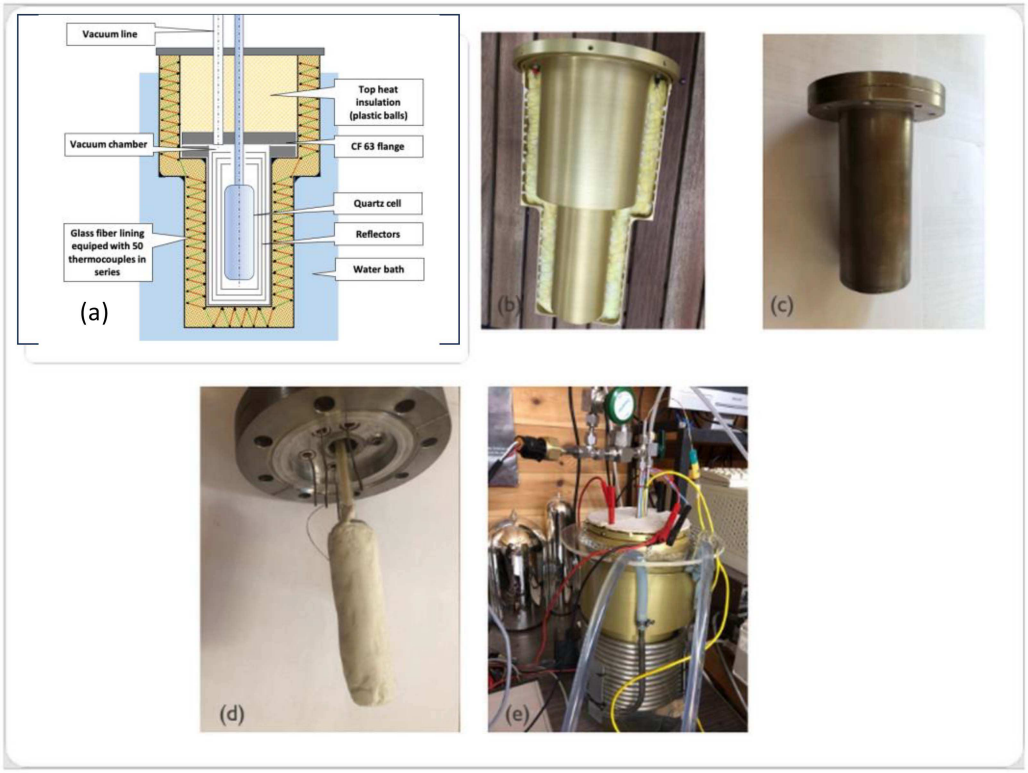

Figure 1. a) Schematic view of the calorimeter; b) Photo of the 50 thermocouples attached to the inner and outer cylinders; c) The 63 mm in diameter vacuum chamber with a CF63 flange; d) A 9 cm $\times$ 2 cm quartz cell with a Kanthal wire heater covered with a high temperature cement; e) Photo of the calorimeter in the constant temperature water bath.

by the 50 thermocouples, and a third order polynomial fit is used to determine the relation between voltage and power (Figure 3).

The formula deduced from the calibration is used to check the power measured vs. temperature. Figure 4 shows the calibration curve of Figure 3 vs temperature. It shows that the resolution is better than $+/-$ 100 mW. A limitation of the resolution of the calorimeter is due to the variations in the room temperature. The calorimeter is not a full Calvet one, since the top flange heat is not taken into account in the heat measurement, and a variation in the room temperature brings inaccuracy in the measurements. A second identical calorimeter is being tested in a constant temperature room and should produce better precision.

3. The powder

The method used by Arata [1] to produce the nanoparticles is a complex metallurgical technique. They use a melt-spinning/splat-cooling method of the desired alloy of palladium/nickel/zirconium in an argon atmosphere which produces an amorphous film. The amorphous film is then oxidized in air at 450°C. The oxidation occurs preferably on the zirconium, leaving the palladium-nickel in the form of metal nanoparticles of 5–10 nm in diameter. This technique is

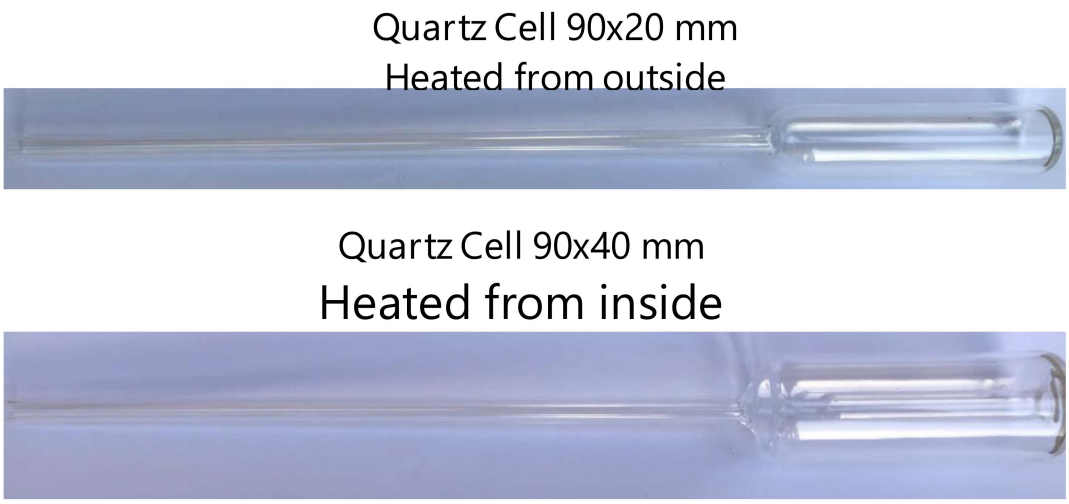

Figure 2. The two quartz cells.

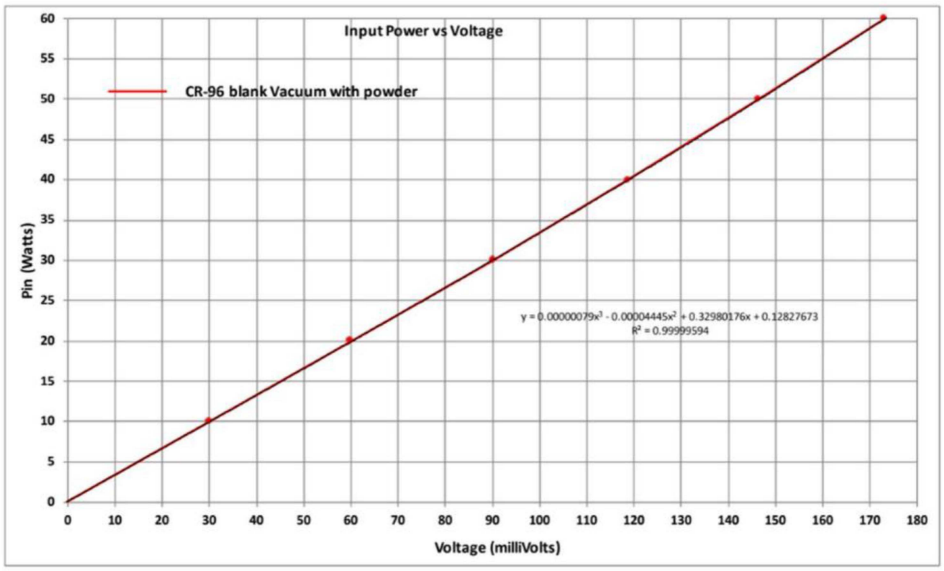

Figure 3. Input electrical power vs voltage measured with the 50 thermocouples in series.

used in the preparation of some catalysts [6]. However, these materials present some drawbacks with respect to their difficulty of preparation and/or cost.

In this study, a new method was developed to produce such metal nanoparticles supported on amorphous oxides. This method comprises the decomposition/reduction of an appropriate layered double hydroxide (LDH) [7] which is a class of minerals (natural and synthetic). The most abundant member on earth is the hydrotalcite whose formula is

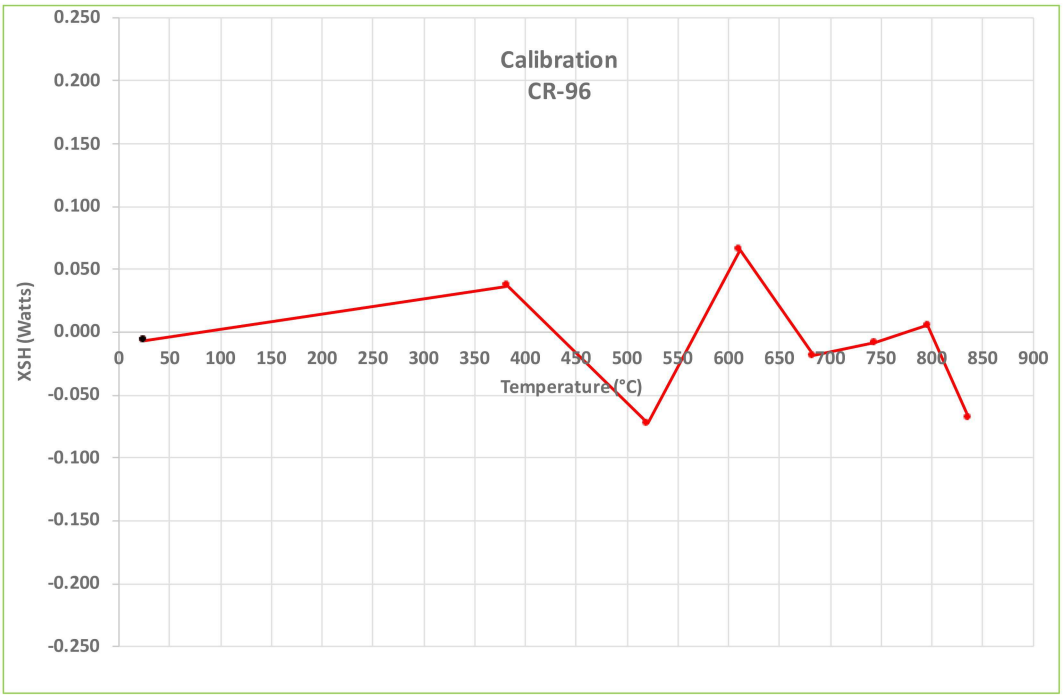

Figure 4. Calibration of the calorimeter filled with alumina powder in hydrogen up to 850°C.

$Mg_6Al_2(OH)_{16}CO_3$–$4H_2O$. Takovite, the hydrotalcite where magnesium has been replaced by nickel, has also been rarely found [8]. LDH can be represented by the general formula $[M^{II}{}_{1-x}\ M^{III}{}_x\ (OH)_2]^{x+}(A^{n-})_{x/n}$ hydrated with H_2O where i) M^{II} is a di-cation (Mg, Ni, Cu, Co, Zn, Fe, ...) and their mixtures in almost all proportions, ii) M^{III} is a tri-cation (Al, B, Ga, Fe, Y, ...) and their mixture in almost all proportions, iii) A is an anion ($CO_3{}^{2-}$, $NO_3{}^-$, Cl^-, ...), the most commonly found being carbonate. Additionally, other elements such as Zr and Ti can be incorporated in LDH crystalline structures. Under appropriate molar ratios of M^{II}, M^{III} and A, the chemical elements co-crystalize in a lamellar material called LDH. Mineral synthesis offers the unique opportunity to expand the scope of natural LDH. Thus, a wide variety of LDHs have been prepared by various methods [9], studied and designed for various applications [10], One of these applications is methanation (also known as Sabatier's reaction), a reaction involving hydrogen and CO_2 [11]. In this case, the synthetic LDH is used as a precursor to generate metal nanoparticles (mainly Ni) supported on amorphous alumina. A similar precursor has been reported to act as a pro-catalyst for the generation of hydrogen from N_2H_4-hydrate decomposition [12]. The thermal decomposition of such precursors involves successively i) a dehydration step, ii) a decarbonation step with release of CO_2, iii) a dehydroxylation step to end up with M^{II}-oxides supported on amorphous M^{III}-oxides. In the last step, conducted under hot hydrogen flow (300–700°C), the M^{II}/M^{III}-oxides are reduced to give the desired $M°/M^{III}$ metal-oxide mix (see Figure 5). Such material as prepared is then used for LENR experiments. This chemical method is easily scalable for industrial applications.

We start with synthetic hydrotalcites having the general formulas: $Ni_{5.25}Cu_{0.75}Al_2CO_3(OH)_{16}{\cdot}4(H_2O)$ and $Ni_6Al_2CO_3(OH)_{16}{\cdot}4(H_2O)$. In this work we used Ni/Cu 7/1 and pure nickel. The color of the original powder is green, and it is not magnetic (see the difference with the magnet in Fig. 5a and 5b). When the powder is heated under

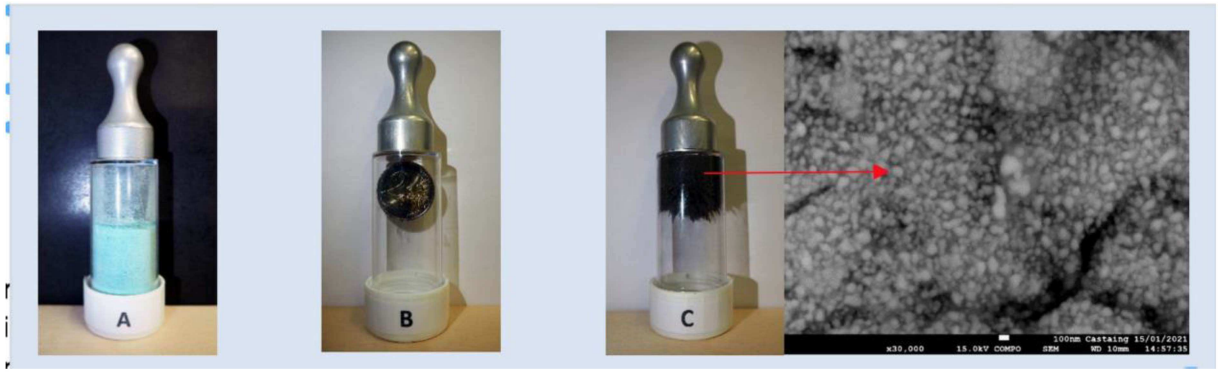

Figure 5. a) Original hydrotalcite Green not magnetic LDH $Ni_6Al_2CO_3(OH)_{16} - 4H_2O$; b) Magnet alone; c) Black Magnetic $Ni_6Al_2O_3$ attracted by the magnet, and Scanning Electron Microscopic view of nickel nanoparticles (white dots, but black at the naked eye).

vacuum up to 600°C, the color turns brown. It is still not magnetic. When the powder is heated under hydrogen, at 900°C, the powder becomes black and magnetic, as shown in Figure 5. In these conditions of operation, we did not observe any sintering.

4. Absorption of hydrogen in nickel

At room temperature, nickel does not absorb hydrogen at low pressure, because the reaction is endothermic. To introduce hydrogen in nickel, it is necessary to heat the material above 200°C [13]. Also of importance is the fact that hydrogen does not enter inside nickel if there is an oxide layer at its surface. Therefore, it is first necessary to reduce the oxide layer by heating in hydrogen before hydrogen can be absorbed by the metal nanoparticles. However, these two mechanisms are performed simultaneously. This behavior explains the procedure used in this work to produce excess power.

5. Experimental Results

5.1. Calorimetry

Experiments have been carried out in 2 cm and 4 cm diameter cells. We used hydrotalcites with Ni-Cu nanoparticles having the molar ratio 7/1 and pure nickel. The powder was either treated in a separate furnace under vacuum and hydrogen, or directly in the calorimeter. The initial powder (green) is heated under vacuum up to about 600°C (above this temperature in vacuum, there is formation of spinelles), then cooled down to room temperature. Experiments are performed at constant power with heating steps of 5 or 10 W either in vacuum or under hydrogen. The steps are continued until stabilization of the output power, typically 6 to 8 hours. At the maximum power, the cell is pumped down, and the power is lowered by steps again. The cycle of heating under hydrogen and cooling under vacuum is repeated until the excess power is stabilized. The maximum duration of an experiment at maximum temperature and under vacuum was four days, and produced close to 4 MJ of heat, with about 0.1 mole of metal.

An example of excess heat production is shown in Figure 6, with an hydrotalcite Ni-Cu with a molar ratio 7/1. The blue curve (CR-77A) corresponds to the first run under vacuum up to 390°C. At room temperature the cell is filled with hydrogen at a pressure of 1.3 Bars, and heated up to 547°C, (curve CR-77B). Most of the runs up to 600°C show excess energy of less that 200 mW. However, the green curve (CR-77C) in hydrogen shows an endothermic behavior between 330°C and 500°C. This type of behavior has been observed several times, but not systematically. It is of unknown origin at this point. We do not know if this is an artefact or a chemical or nuclear mechanism.

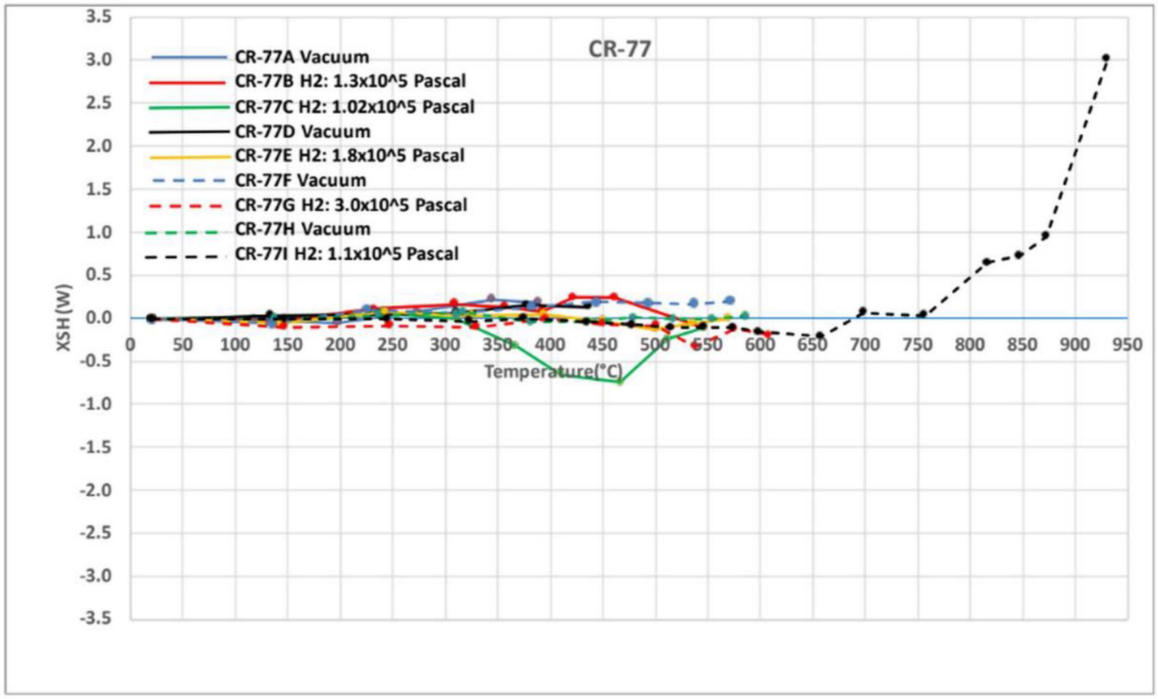

Figure 6. Experiment CR-77, example of production of excess heat with an hydrotalcite Ni-Cu ratio: 7/1 (14.6g).

Figure 7 shows the results of 7 experiments, 6 of them based on hydrotalcite, and one on nickel deposited on carbon powder. All of them show excess power at high temperatures. There are variations in the amount of excess heat observed, due to the various parameters that make each measurement unique: amount of material, preparation, and precision of the measurements. Another important point to be noted is that more excess power is measured after pumping out the hydrogen. After each cycle of loading hydrogen and pumping, the excess power increases. A saturation in the increase of excess heat happens after about four cycles.

5.2. Activation Energy

Because the experiments have been done at various temperatures it is possible to calculate the activation energy of the reactions. Figure 8 shows the various logarithmic plots of the excess energy vs 1/T. The activation energies vary from 0.6 eV to 1.8 eV. This is consistent with a diffusion of hydrogen atoms in the crystal lattices.

5.3. Transmutation?

In the experiment CR-92 with hydrotalcite and pure nickel, we have measured by SEM/EDS-X the presence of copper in the powder before and after the reaction. The ratio Cu/Ni in the before sample was 0.07% and in the after sample it was 2.05%. To determine if the copper was due to transmutation of nickel in copper, or to contamination by an unknown source, we did an ICP-MS analysis. The natural ratio ^{63}Cu / ^{65}Cu is 2.2414 while in our experimental measurement it was 2.1915. It is therefore very likely that contamination occurred from an unknown source. It is very unlikely that an unknown reaction produces copper with an isotopic ratio close to the natural one.

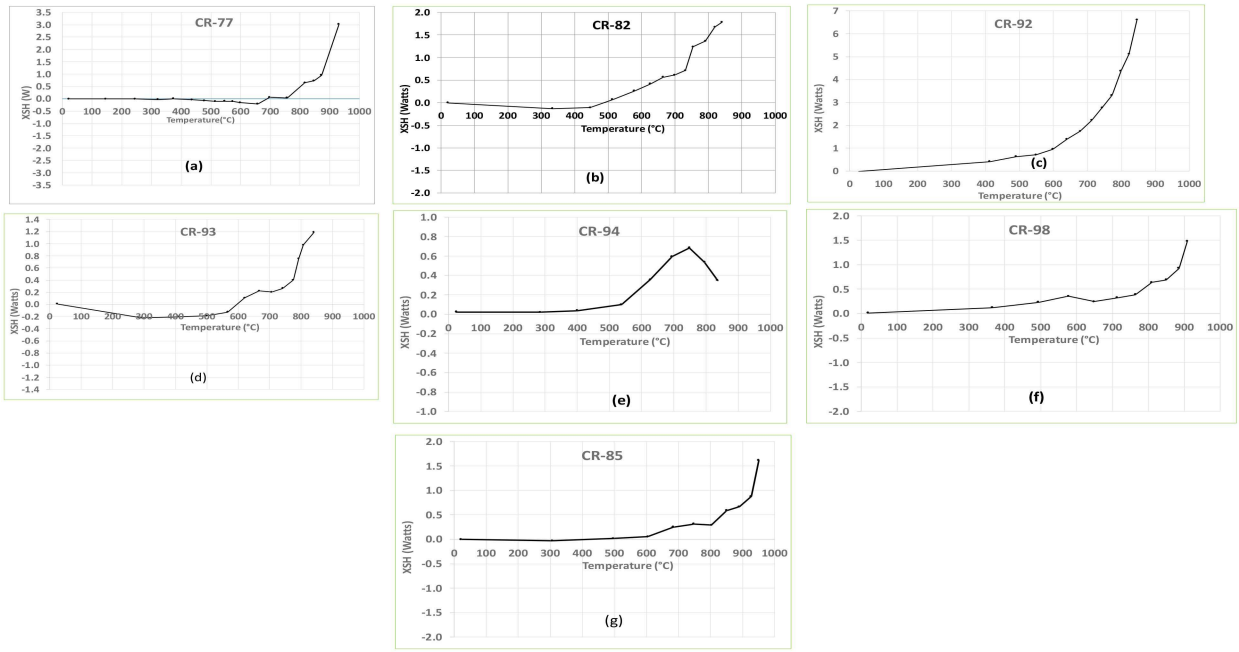

Figure 7. a) CR-77, experiment with hydrotalcite with a ratio Ni-Cu 7/1 (14.6g); b) CR-82, experiment with hydrotalcite with a ratio Ni-Cu 7/1 (30.0g); c) CR-92, experiment with hydrotalcite and pure Ni (52g); d) CR-93, experiment with hydrotalcite and pure Ni (23.3g); e) CR-94, experiment with hydrotalcite and pure Ni (12.6g); f) CR-98, experiment with hydrotalcite and pure Ni (11.9g); g) CR-85, experiment with Ni deposited on C graphite (33.5g).

6. Conclusion

We have shown that using a very precise calorimeter working at high temperatures we have found anomalous excess heat with nano-powders based on nickel alloys produced with hydrotalcites. The amount of heat produced during most of the runs exceeds the amount that can be explained by chemistry. In one experiment that lasted four days, 10 times more energy was produced that could be explained by any chemical reaction. The experiments were performed in hydrogen; we did not try using deuterium. It is important to note that the excess energy is larger during pumping of the hydrogen gas than in the presence of hydrogen at a fixed pressure. The cycling of loading and pumping hydrogen increases the excess energy. This is probably due to the reduction of the metal oxides present at the surfaces of the nano-metals, but also to the modification of the crystal structure of the metal nanoparticles: creation of: dislocations, vacancies, cracks etc. We cannot exclude the role of the interface between the nanoparticles of metals and the aluminum oxide matrix, as pointed out by Biberian et al. [14]. The excess energy is larger at high temperatures when we expect that the loading of hydrogen will decrease, but this is not the case. This behavior has been reported by Iwamura et al. [15] where excess heat is detected when hydrogen flows through multi-layers of nickel/copper at temperatures close to the ones in our experiments.

We have shown in this work the production of anomalous excess power which cannot be explained by chemical reactions. It is therefore tempting to assume that the reaction is of nuclear origin. It has been shown that in reactions with deuterium He-4 is produced at the same ratio as the d+d fusion reaction. With nanoparticles of nickel alloys in hydrogen, the p+p reaction should be much less likely to occur according to theory, so a possible reaction could be

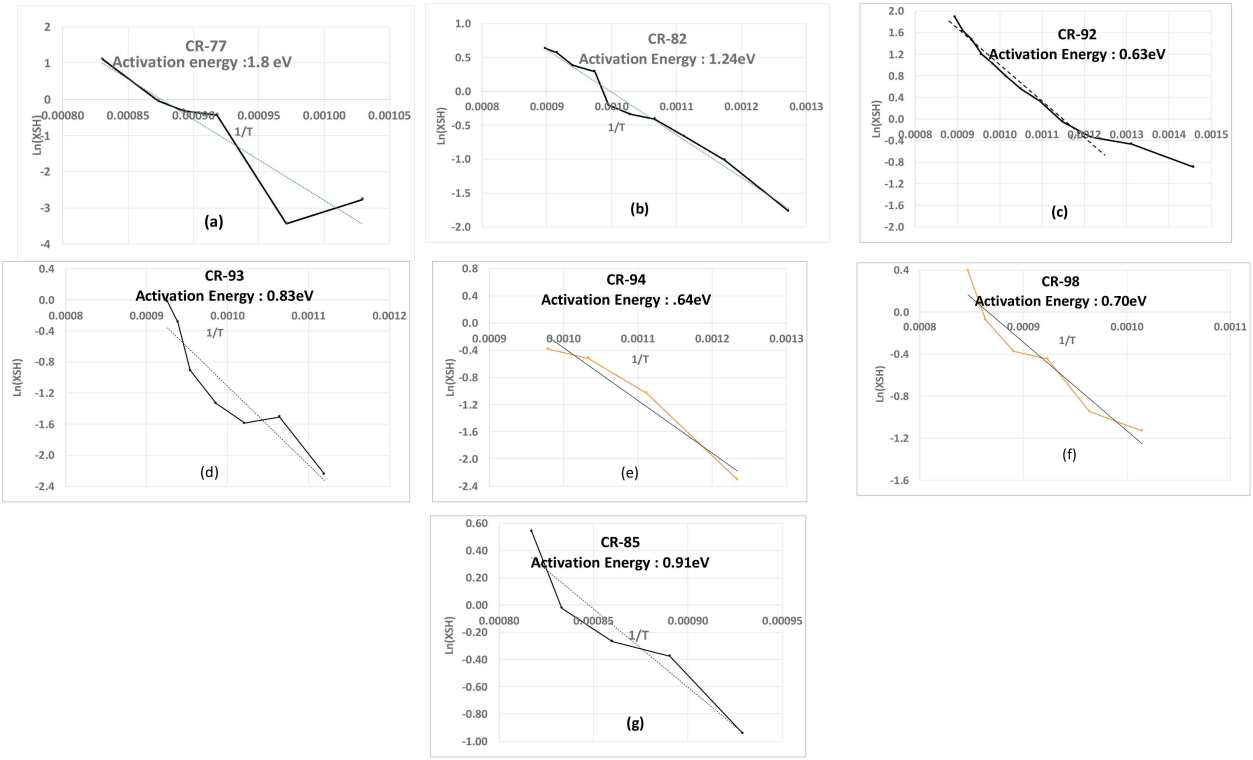

Figure 8. Activation energies for the seven experiments shown in Figure 7 calculated by plotting the logarithm of the excess energy vs 1/T.

between hydrogen and metal atoms. However, Schwinger [16], Takahashi [17] and Storms [18] have proposed other models to explain these reactions with hydrogen. We have shown in this paper that the presence of copper in a pure nickel experiment had an isotopic composition close to the natural one, indicating that this is probably contamination. More work needs to be done to discover the origin of the mechanism that produces the excess heat. For example, it will be interesting to know the loading ratio of hydrogen. This will be done in future experiments.

Acknowledgments

This study is part of the CleanHME project from the European Union's Horizon 2020 research and innovation program under grant agreement No 951974.

References

[1] Arata Y. and Y. Zhang, "*The Establishment of Solid Nuclear Fusion Reactor*", J. High Temp. Soc. 34, 85-93,2008.

[2] Kitamura A., A. Takahashi, K. Takahashi, R. Seto, T. Hatano, Y. Iwamura, T. Itoh, J. Kasagi, M. Nakamura, M. Uchimura, H. Takahashi, S. Sumitomo, T. Hioki, T. Motohiro, Y. Furuyama, M. Kishida, H. Matsune, "*Excess heat evolution from nanocomposite samples under exposure to hydrogen isotope gases*", *International Journal of Hydrogen Energy* **43** (2018) 16187-16200.

[3] Calvet, É. and Prat, H. " *Microcalorimétrie: Applications physicochimiques et biologiques* " Masson, Paris, 1956.

[4] https://en.wikipedia.org/wiki/Calorimeter
[5] https://setaramsolutions.com/app/uploads/sites/2/2020/09/Family-brochure-EN-CALVET.pdf
[6] Schwarz J.A., C.Contescu, A.Contescu - Methods for Preparation of Catalytic Materials - *Chem. Rev. 1995, 95,477-51*
[7] Cavani F., F. Trifiro, A. Vaccari, *Hydrotalcite type anionic clays: Preparations, properties and applications*, **1991**, *Catalysis Today*, 11, 173-301.
[8] Takovite: Mineral information, data and localities. (mindat.org)
[9] Wijitwongwan S., S. Intasa-ard, M. Ogawa, Preparation of layered double hydroxides toward precisely designed hierarchical organization, 2019, ChemEngineering, 3, 68; doi: 10.3390/chemengineering3030068
[10] Fan G., F. Li, D.G. Evans, X. Duan, Catalytic *applications of layered double hydroxides: recent advances and perspectives*, **2014**, *Chem. Soc. Rev.,* 43, pp 7040-7066; doi: 10.1039/c4cs00160e
[11] Huynh H.L., Z. Yu, *CO_2 methanation on hydrotalcite-derived catalysts and structured reactors: A review,* **2020**, *Energy Technol*., 8, 1901475; doi: 10.1002/ente.201901475
[12] He, L. Y. Huang, A. Wang, X. Wang, X. Chen, J.J. Delgado, T. Zhang, *A noble-metal-free catalyst derived from Ni-Al hydrotalcite for hydrogen generation from N_2H_4ůH$_2O$ decomposition*, **2012**, *Angewandte Chem. Int. Ed*., vol. 51, pp. 6191–6194; doi.org/10.1002/anie.201201737
[13] Smittenberg J., *Absorption of Hydrogen by Nickel*, Nature vol. 133, p. 81, 1934.
[14] Biberian J. P., I. Parchamazad and M. H. Miles, "*Possible Role of Oxides in the* Fleischmann–Pons Effect" J. Condensed Matter Nucl. Sci. 13 (2014) 38–43.
[15] Iwamura Y., J. Kasagi, T. Itoh, T. Takahashi, M. Saito, Y. Shibasaki, and S. Murakami, "*Progress in Energy Generation Research Using Nano-Metal With Hydrogen/Deuterium* Gas", J. Condensed Matter Nucl. Sci. 36 (2022) 285–301.
[16] Schwinger, J. (1990). "*Cold fusion: a hypothesis*." Z. Naturforsch. **45A**: 756.
[17] Takahashi, A. (2004). " *^{3}He/^{4}He production ratios by tetrahedral symmetric condensation.*" 11th International Conference on Cold Fusion, Marseilles, France, World Scientific Co.
[18] Storms, E. (2014). "Explaining Cold Fusion." J. Cond. Matter Nucl. Sci. **15**: 295–304.

J. Condensed Matter Nucl. Sci. 38 (2024) 196–210

Research Article

The Case of the Missing Tritium

Pamela A. Mosier-Boss*, Lawrence P. Forsley

Global Energy Corporation, USA

Abstract

Pd/D co-deposition experiments conducted in low and high tritiated D_2O are discussed. Four different groups, using different cathodes, electrolytes, and methodologies, performed these experiments. It was observed that when low tritiated D_2O was used, tritium was produced. However, a loss of tritium occurred when highly tritiated D_2O was employed. In this communication we explore the reactions and mechanisms that could explain this loss of tritium.
 ISSN 2227-3123

Keywords: Tritium, Pd/D co-deposition, electron screening, cross-sections, nanoparticles

1. Introduction

In the Pd/D co-deposition process, Pd is plated out onto a cathode substrate in the presence of evolving deuterium gas [1]. This results in an ever-expanding electrode surface consisting of Pd microglobules that instantly load with deuterium. Using variations of Pd/D co-deposition, researchers have reported on observing excess heat, γ- and X-ray emissions, transmutation, as well as the generation of energetic particles. Four groups of researchers have conducted Pd/D co-deposition experiments that focused on tritium production [2]–[6]. These researchers used different cathode substrates, plating solutions, and methodologies. Regardless of the experimental procedure employed, an increase in tritium was observed when low-tritiated D_2O was used, and a decrease occurred when highly tritiated D_2O was used. The decrease in tritium observed when highly tritiated D_2O was used suggests that there is a nuclear reaction(s) occurring inside the Pd lattice that consumes tritium. This loss of tritium is not observed when bulk Pd is used implying that the reaction(s) involved with the consumption of tritium is related to the high surface area of the Pd deposit and/or the vacancies present in the lattice [1]. In this communication we explore the possible reactions of tritium with Pd and Li isotopes as well as energetic particles to determine what reaction(s) can account for this loss.

*Corresponding author: pboss@san.rr.com

 ISSN 2227-3123

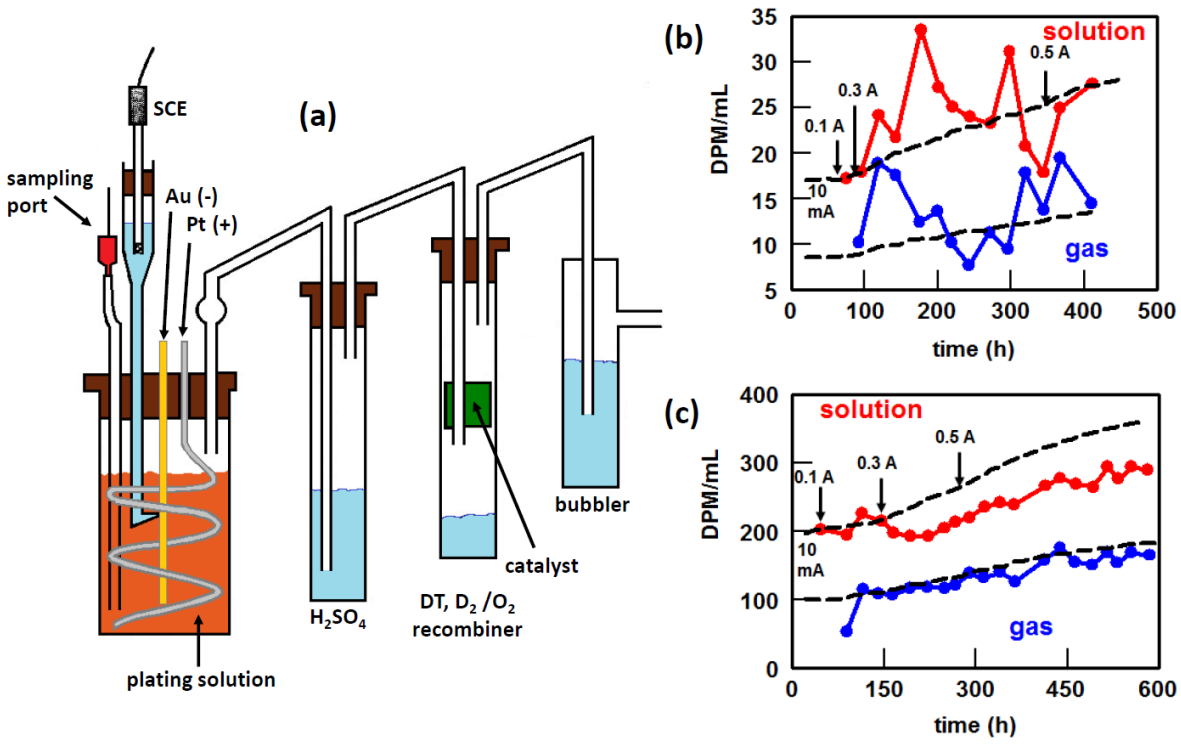

Figure 1. (a) Schematic of the experimental apparatus used by Bockris *et al.* to determine tritium content in both the gas and liquid phases [2]. Amount of tritium measured in the gas and liquid phases for experiments using (b) low tritiated D_2O and (c) highly tritiated D_2O. Current changes are indicated. Dashed lines are the expected amount of tritium based on the mass balance and isotopic separation factor, S = 0.63.

2. Summary of Pd/D Co-Deposition Tritium Results

2.1. John O'M Bockris *et al.*

Figure 1a shows a schematic of the experimental set-up for Pd/D co-deposition with simultaneous measurements of tritium in the liquid and gas phases [2]. The anode and cathode are in a concentric orientation. It is an open system using a $PdCl_2$-LiCl plating solution. The resultant Pd deposit on the Au cathode was thick and dendritic. Concentrated sulfuric acid was used as a trap for solution vapors. The D_2/DT and O_2 gases were recombined on a C-supported Pt catalyst. A bubbler at the end assured that the whole system was isolated from the atmosphere. The scintillation technique was used to measure the tritium content in both gas and liquid phases. Experiments typically ran for two weeks. Periodically fresh D_2O would be added to the electrolyte to replenish what was electrolyzed. In this methodology, a change in tritium concentration in the liquid phase occurs due to the addition of fresh D_2O containing background levels of tritium and due to the removal of tritium by electrolysis. Figures 1b and c summarize the observed results. Tritium production was observed when low tritiated D_2O was used, Figure 1b. A burst of tritium production was observed in the gas phase. At the same time, or with a slight delay, a burst of tritium would occur in the liquid phase. When highly tritiated D_2O was used, no excess of tritium was observed, Figure 1c. Instead, a loss of tritium was observed, primarily in the electrolyte. For the most part, the measured and calculated tritium values in the gas phase are in agreement. No explanation for this loss was presented.

Table 1. Summary of tritium results obtained by Miles using an open system [5].

Cathode	D_2O Consumption (mL)	Tritium (DPM ml^{-1})
D_2O	N/A	223.74 ± 0.89
Pd, cell A	161.0	361.26 ± 1.12
Pd, cell B	175.0	347.02 ± 1.11
Pd-Ce-B	248.5	336.92 ± 1.08
Pd-Ce	258.0	334.92 ± 1.07
Pd/D co-deposition cell A	7.4 ± 1.0	217.24 ± 0.87
Pd/D co-deposition cell B	7.7 ± 1.0	212.62 ± 0.87
Pd/D co-deposition cell C	8.7 ± 1.0	214.21 ± 0.89

2.2. Mel Miles

In experiments using bulk cathodes and Pd/D co-deposition, Miles used an open system with the electrodes in a concentric orientation [5]. He used highly tritiated D_2O. For Pd/D co-deposition, the cathode was copper and the plating solution was $PdCl_2$ – ND_4Cl – ND_4OD. This plating solution was chosen to produce a smooth, bright deposit; however, the resultant deposit was dark and dendritic. Liquid scintillation technique was used to measure tritium at the end of the experiment on the final electrolyte solutions after adjusting the D_2O levels to the initial volumes. Results are summarized in Table 1. For bulk cathodes an increase in tritium was observed that was attributed to enrichment as a result of electrolysis. However, the Pd/D co-deposition cells showed a decrease in tritium. It should be noted that all three of the Pd/D co-deposition cells produced excess heat and showed the positive feedback effect [1], [7].

2.3. P.A. Mosier-Boss and S. Szpak

A schematic of the apparatus used by Mosier-Boss and Szpak [4] to measure tritium in the gas and liquid phases is shown in Figure 2a. The anode and cathode are in a concentric orientation. A catalyst in a separate chamber is used to recombine the D_2 (DT) and O_2 gases. Five experiments were done using low tritiated D_2O and a $PdCl_2$-LiCl plating solution that produced a dark, mossy deposit on a Ag plated Cu cathode. Figures 2b and c show plots of the measured tritium content and the expected amount of tritium which was calculated using the following equation:

$$f(t) = f(0)\left(\frac{m(0) - r(i)t}{m(0)}\right)^{S-1} + \frac{q}{(S-1)r(i)} \bullet \left\{1 - \left[\frac{m(0) - r(i)t}{m(0)}\right]^{S-1}\right\}$$

where t = time; f = tritium mass fraction; m = mass of the electrolyte phase; $r(i) = iM_w/2F$ = the rate of change associated with the passage of cell current i; q = rate at which tritium is added/removed from the solution phase by whatever process including transport of tritium generated on the bulk electrode; and s = isotopic separation factor $= (C_T/C_D)_g/(C_T/C_D)_l$ where C is concentration, T is tritium, D is deuterium, g is gas, and l is liquid. Two experiments showed a complete mass balance as shown in Figure 2b. Three showed excess tritium, Figure 2c. Tritium production was sporadic and occurred in bursts, as was observed by Bockris *et al.* [2]. During a burst, the rate of tritium production ranged between 3000-7000 atoms s^{-1} for a 24 h period.

2.4. K.-H. Lee *et al.*

Lee *et al.* [6] used a closed system to measure changes in tritium content in cells using bulk Pd and Pd/D co-deposition, Figure 3a. The electrodes were parallel to one another. Two kinds of plating solutions were used for Pd/D co-deposition – $PdCl_2$-LiCl and $Pd(en)Cl_2$-LiCl, where en is ethylene diamine. Both low and highly tritiated D_2O were used. The scintillation technique was used to measure the tritium content of the electrolyte before and after the experiment.

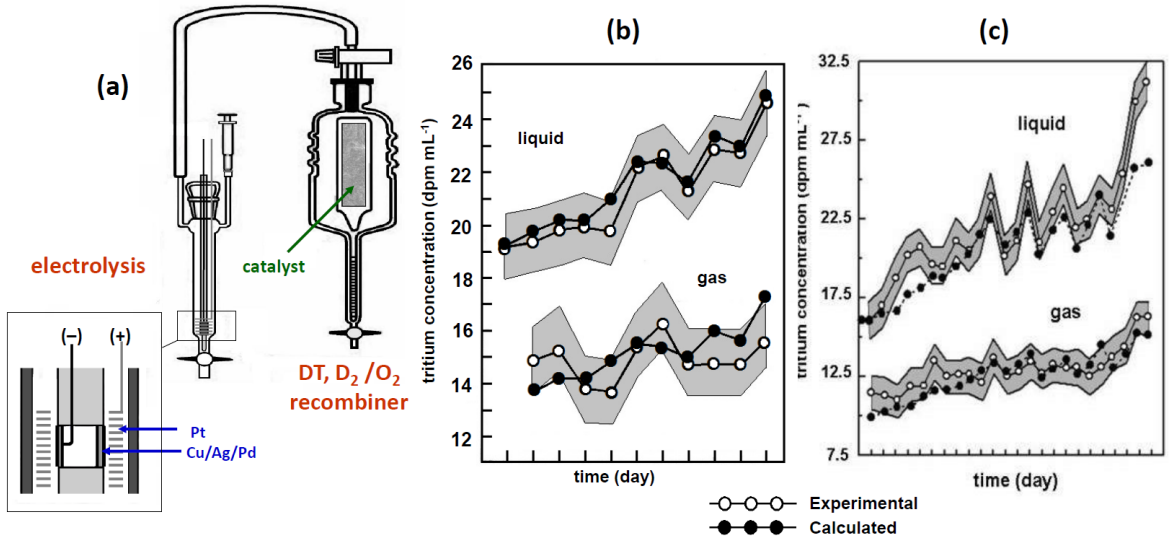

Figure 2. (a) Schematic of the experimental apparatus used by Mosier-Boss and Szpak to determine tritium content in both the gas and liquid phases [4]. Tritium content was measured using the scintillation technique. Results of two experimental runs showing (b) no tritium production and (c) tritium production occurring in bursts. The isotopic separation factor, s, was 0.68 ± 0.04, which is in agreement with the value determined by Bockris *et al.* [2].

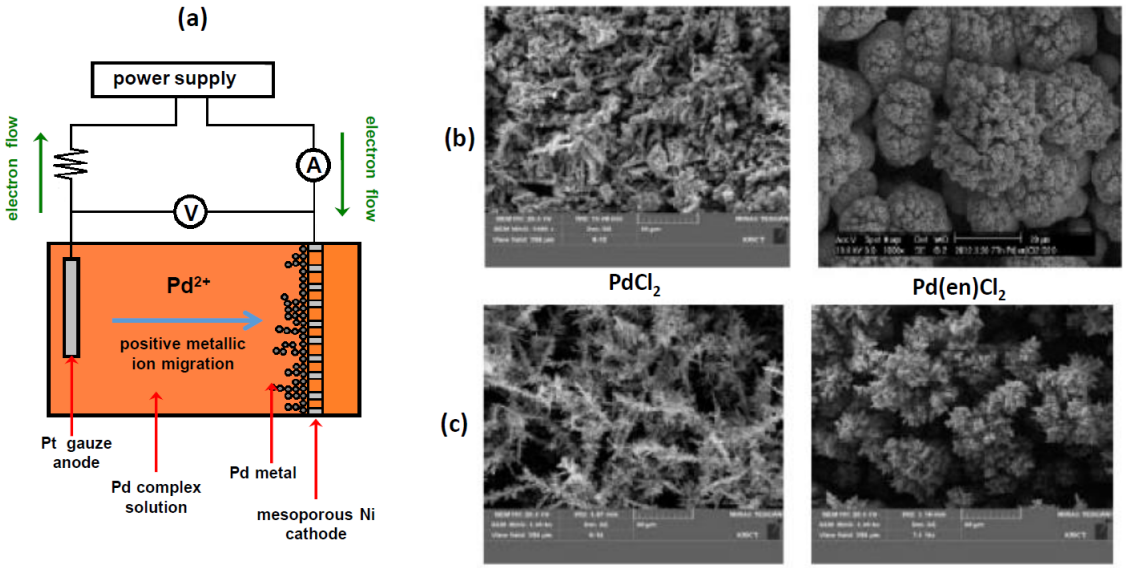

Figure 3. (a) Schematic of the experimental apparatus used by Lee *et al.* [6]. This is a closed system. Tritium content of the electrolyte was measured before and after completion of the experiment. SEM images of the deposits formed using $PdCl_2$ and $Pd(en)Cl_2$ salts when (b) highly tritiated and (c) low tritiated D_2O were used.

Table 2. Summary of tritium results obtained by Lee *et al.* using a closed system [6].

cathode, electrolyte, and cathodic charging profile[a-c]	tritium before electrolysis (CPM)	tritium after electrolysis (CPM)
Pd foil, LiCl, i = 20-400 mA for 65 h	10.00	167.00
mesoporous Ni, $PdCl_2$-LiCl, i = 1 mA for 168 h	40.00	35.00
mesoporous Ni, $PdCl_2$-LiCl, i = 20-400 mA for 65 h	28.00	314.00
mesoporous Ni, $PdCl_2$-LiCl, i = 1-300 mA for 97 h	596.00	235.00
mesoporous Ni, Pd(en)Cl_2-LiCl, i = 1 mA for 168 h	24.00	26.00
mesoporous Ni, Pd(en)Cl_2-LiCl, i = 1-300 mA for 97 h	30.00	258.00
mesoporous Ni, Pd(en)Cl_2-LiCl, i = 1-200 mA for 77 h	489.00	160.00

a. en is ethylene diamine
b. $PdCl_2$ and Pd(en)Cl_2 complexes were in ammonia water
c. All electrolytes were in D_2O.

Results are summarized in Table 2. For the bulk Pd cathode, tritium production was observed using low tritiated D_2O. No results were reported for highly tritiated D_2O. For Pd/D co-deposition, no change in tritium was observed using both complexes and low tritiated D_2O when a current of -1 mA was applied for 168 h. However, when the current was increased, excess tritium was observed which agreed with the results obtained by Bockris *et al.* [2], [3] and Szpak *et al.* [4]. Furthermore, Pd/D co-deposition produced more tritium than electrolysis using a bulk cathode. When highly tritiated D_2O was used, Pd/D co-deposition using both complexes resulted in a decrease in tritium content. These results agreed with the observations of Bockris *et al.* [2], [3] and Miles [5]. Lee *et al.* also obtained SEM images of the deposit formed using both complexes in highly tritated, Figure 3b, and low tritiated D_2O, Figure 3c [6]. It can be seen that the deposits exhibit a highly fractal surface.

3. Determining the Reactions Responsible for the Consumption of Thermal (0.025 eV) Tritium

Four groups conducted experiments measuring tritium in Pd/D co-deposition experiments. In each experiment, the Pd deposit was black and dendritic with high surface area. Different plating solutions and cathode substrates were used. Three groups had a concentric orientation for their anode and cathode while one had a parallel arrangement. Three used open systems while one used a closed one. Regardless of the experimental configuration employed, tritium production was observed when low tritiated D_2O was used. In contrast, when highly tritiated D_2O was used a decrease in tritium was observed. During electrolysis, both D and T will partition into the Pd lattice regardless of the D_2O used (low or highly tritiated). More T will enter the lattice when highly tritiated D_2O is used than low tritiated. The D and T that partition into the Pd lattice are thermalized. Under conditions of high D/Pd loading and D flux in the lattice, LENR is initiated. The exact mechanism of how this occurs is not understood and there are a number of theories. It is not the scope of this communication to elucidate what this mechanism is but rather to determine what happens after it occurs. Specifically, the decrease in tritium that occurs when highly tritiated D_2O is used suggests that there is a nuclear reaction(s) that consumes thermal tritium. In Pd/D co-deposition, we have Pd and Li salts present as well as D_2O. We began to examine nuclear reactions that can occur between T and solution components (Pd, D, ^{6}Li, and ^{7}Li) as well as reactions between T and nuclear generated particles (P, T, ^{3}He, and ^{4}He).

3.1. Possible Nuclear Reactions Between Either Li or Pd Isotopes and Tritium

The standard approach to measuring nuclear reaction cross sections is to have a beam of ions (with well-defined ion species, current, and kinetic energy) impinge on a sample that contains the target nuclei of known density. Nuclear diagnostics are used to detect/quantify reaction products normal to the beam over a 2π angle. There are no cross

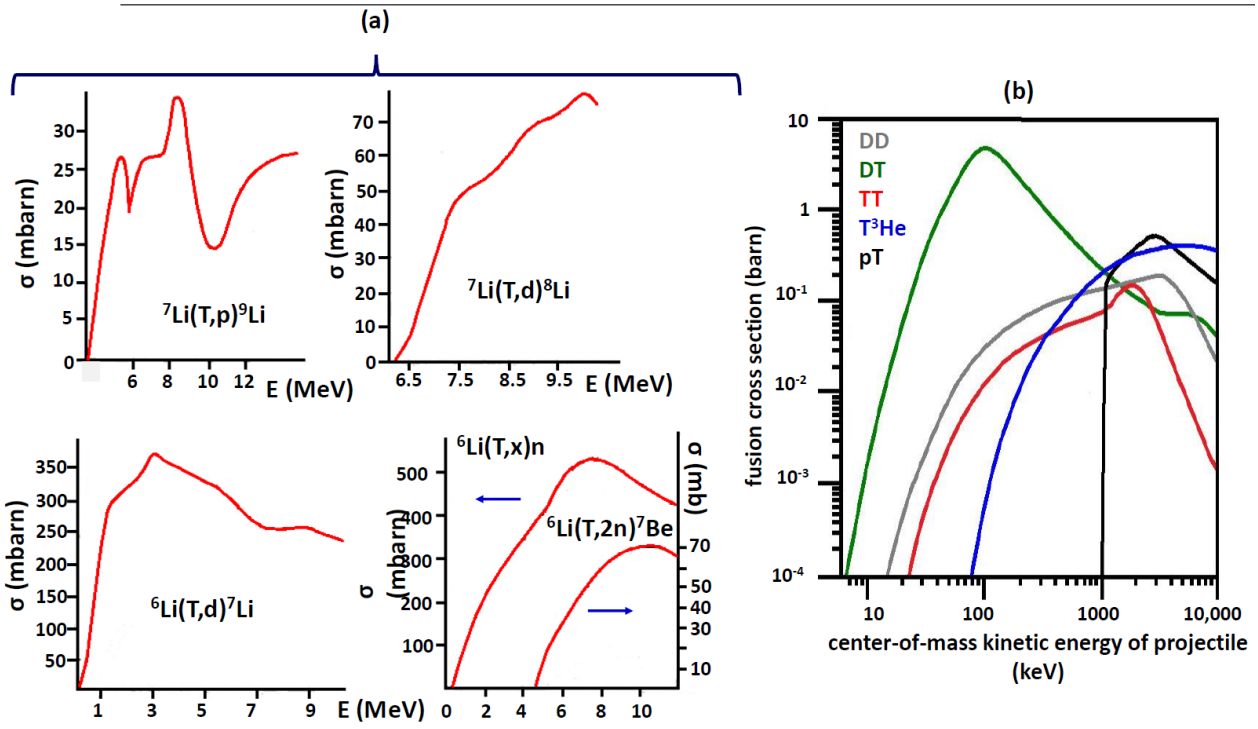

Figure 4. (a) Plots of the representative Li-T nuclear reaction cross sections [9]. (b) Standard cross-sections for the primary hot fusion reactions as a function of projectile energy [10]. Not shown is the cross section of the T-^{4}He reaction as a function of projectile energy. As shown in Table 3, the maximum cross section, σ_{max}, of this reaction is 3.58 μbarn.

sections reported for Pd(t,x)y reactions so nuclear reactions between Pd isotopes and tritium cannot account for the observed loss of thermal tritium. Also if such reactions did occur, it would involve energetic T and not thermal T.

Cyclic voltammetry measurements have shown that electrochemical incorporation of lithium into palladium can occur [8]. So nuclear reactions between Li and T may be possible inside the Pd lattice. There are a number of nuclear reactions between tritium and ^{6}Li/^{7}Li isotopes and the reaction cross sections are in millibarns [9]. Figure 4a shows plots for Li-T reactions exhibiting the largest cross sections. Although there are measurable nuclear cross sections for Li-T interactions, these interactions involve energetic T. Furthermore, Miles [5] observed a decrease in tritium content when he used highly tritiated D_2O and his electrolyte did not contain lithium salts. Therefore, it is unlikely that the reaction that consumes tritium involves Li isotopes.

3.2. Possible Nuclear Reactions Between Either ^{n}H or ^{n}He Isotopes and Tritium

Standard cross-sections for the fusion reactions between tritium and ^{n}H or ^{n}He isotopes as a function of projectile energy are shown in Figure 4b [10]. The maximum cross section, σ_{max}, and its energy, ε_{max}, for each T-^{n}H and T-^{n}He reaction are tabulated in Table 3. These cross-sections, and the screening potentials discussed below, relate to hot fusion reactions. However, in the Pd/D system, there have been reports of the production of energetic charged particles *in-situ* [16-21]. These charged particles will traverse through the Pd/D lattice, which is analogous to the charged particle projectiles used in the ion bombardment experiments to measure nuclear cross sections and electron screening.

Table 3. Fusion reactions: maximum cross section σ_{max} and location of the maximum ε_{max} [9]–[15].

Nuclear Reaction	σ_{max} **(barn)**	ε_{max} **(keV)**
D + T → α (3.52 MeV) + n (14.06 MeV)	5.0	64
D + D → T (1.01 MeV) + p (3.02 MeV) 50%	0.096	1250
D + D → ^{3}He (0.82 MeV) + n (2.45 MeV) 50%	0.11	1750
T + T → α + 2n+ 11.3 MeV	0.106	1000
T + ^{3}He → α + p + n + 12.9 MeV 57%	0.5	5000
T + ^{3}He → α (4.8 MeV) + D (9.5 MeV) 43%		
p + T → ^{3}He + n	0.6	3000
T + ^{4}He → ^{7}Li + γ	3.58x10^{-6}	1320

Consequently, use of the data summarized in Figure 4b and Table 3 are applicable to determine what reactions are responsible for the loss of thermal tritium. Looking at Table 3, the T(α,γ)^{7}Li can be ruled out as being responsible for causing the loss of tritium as the maximum cross section for this reaction is 3.58 ± 0.60 microbarns [15], which is between five and six orders of magnitude lower than the other T-^{n}H and T-^{3}He reactions.

Of the reactions summarized in Table 3, we have seen evidence of the DT reaction using a solid-state nuclear track detector (SSNTD), CR-39. This reaction has a maximum cross section of 5 barns, Table 3, and creates 14.06 MeV neutrons. Columbia Resin 39, or CR-39, is a clear, amorphous, thermoset plastic that is used to detect nuclear particles [22]. When an energetic charged particle traverses through CR-39, it creates along its path an ionization trail that is more sensitive to chemical etching than the bulk material. After treatment with a chemical etchant, tracks due to energetic particles remain in the form of holes or pits which can be examined with the aid of an optical microscope. The size, depth of penetration, and shape of the track provides information about the mass, charge, energy, and direction of motion of the particle that created the track [23]. Besides charged particles, CR-39 can also be used to detect neutrons. In particular, triple tracks are diagnostic of the 14 MeV neutrons. When a 14 MeV neutron collides with a carbon atom in CR-39, it can either cause the carbon atom to recoil or it can shatter it into three alpha particles. After etching, these three alpha particles appear in CR-39 as three particle tracks breaking away from a center point, *i.e.*, a triple track. Such triple tracks have been observed in CR-39 used in Pd/D co-deposition experiments [24]. Figure 5a compares Pd/D co-deposition generated triple tracks in CR-39 detectors with those produced by exposing detectors to an accelerated driven, DT neutron source [25]. As can be seen the Pd/D co-deposition generated triple tracks are similar to the DT neutron generated tracks. The tracks shown in Figure 5a do not have the same exact shape and the lobes making up the triple tracks do not necessarily need to have the same size. This is because the n + ^{12}C breakup reaction can proceed to the four-body final state through one or more of the reaction mechanisms shown in Figure 5b [26]. Although the DT reaction will consume tritium, the energy of the triton needs to be $\geq$ 5 keV [27] and is therefore energetic. However, the tritium lost in the highly tritiated D_2O experiments is thermal. Electron screening may lower this threshold.

Screening effects in gases, solids, and dense plasmas (metal hydrides are considered to be cold dense plasmas [28]) can increase fusion rates at low reaction energies by several orders of magnitude because screening of the repulsive Coulomb potential by plasmas or target atom electrons increases the probability for ions to tunnel through the Coulomb barrier [29, 30]. The electron screening effect can be expressed as a screening potential, U_e. The value of the screening potential strongly depends on the electronic properties of the host material [29]. The mechanism of electron screening is not fully understood and not all of the contributing factors are known. It is known that the screening potential caused by electrons in gaseous plasma is only several tens of eV for the DD fusion reaction [24], yet is as much as 20 orders of magnitude higher in deuterated metals [28]. There is a strong correlation between the screening potential and the

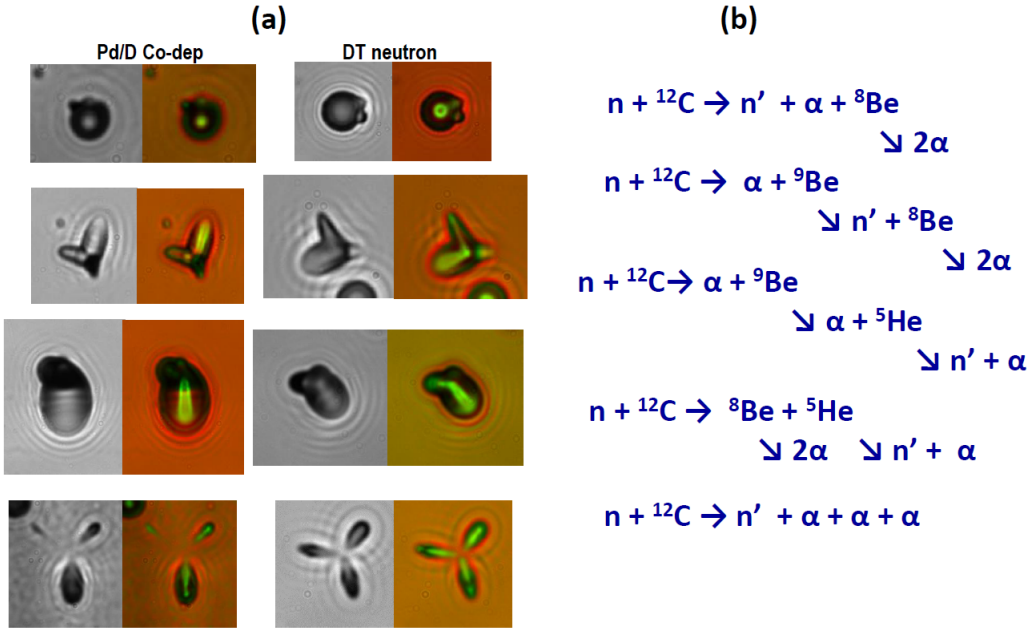

Figure 5. (a) Comparison of triple tracks observed in CR-39 detectors used in Pd/D co-deposition experiments and in detectors exposed to DT neutrons [25]. For both sets of tracks, the left-hand images were obtained with the microscope optics focused on the surface of the CR-39 detector while the right-hand images are an overlay of two microphotographs taken at different focusing depths (surface of the detector and the bottom of the pits). (b) Summary of the n + ^{12}C breakup reaction mechanisms.

deuteron density in metal during the bombardment. The deuteron density during the bombardment is inversely related to the fluidity of the deuteron. Kasagi *et al*. [31, 32] have postulated that a fluidity of deuterons in metals contributes to a reduction of the Coulomb barrier between the fusing nuclei. Pines has noted that this gives rise to plasma screening [28] likely enhanced at the Bragg Peak for the accelerated deuterons. Schenkel *et al.* [30] has argued that U_e is likely dependent on details of target loading and defect dynamics.

Table 4 summarizes screening potentials that have been measured for several Pd species. It can be seen that significantly higher enhancements have been observed for PdLi alloys. For the $PdLi_{0.1\%}$ alloy, a screening potential of ~ 4 keV has been measured for the ^{7}Li(p,α)α reaction. While Bockris *et al.* [2], Szpak and Mosier-Boss [4], and Lee *et al.* [6] used lithium salts in their electrolytes and lithium can intercalate into the Pd lattice, Miles [5] had no lithium in his electrolyte and he still observed a decrease in tritium. This would suggest that the 5 keV energy requirement is unattainable for DT fusion to occur to consume thermal tritium. However, care must be taken in using the cross sections summarized in Figure 4b and Table 3 as they have been obtained for hot fusion reactions that occur under conditions (ion density, confinement time, temperature) that make electron screening effects negligible. It is therefore very possible that, when electron screening is taken into account, the threshold energies for these reactions in metal hydrides may actually be lower than those shown in Figure 4b for hot fusion reactions. If so, then the electron screening could be sufficient to allow DT reactions to occur in the metal lattice that consume thermal tritons.

We next consider the TT and T^{3}He secondary fusion reactions. In the TT reaction, energetic tritons formed from DD reactions will consume both thermal and energetic tritium. Using NE213 neutron detectors, CR-39, and SSB detectors, Lipson *et al.* [18] obtained evidence of energetic protons, tritons, and 2.45 MeV neutrons. They attributed

Table 4. Screening potential energies for Pd species.

Target	Reaction	Screening Potential, U_e (eV)
Pd [30]	D(d,n)^{3}He	1000 ± 250
Pd [31]	D(d,p)T	310 ±20
PdO [31]	D(d,p)T	600 ± 20
Pd [32]	^{6,7}Li(d,α)^{4,5}He	1500 ± 310
$PdD_{0.2}$ [33]	D(d,p)T	296 ± 15
$PdLi_{1\%}$ [34]	^{6}Li(p,α)^{3}He	3760 ± 260
$PdLi_{1\%}$ [34]	^{7}Li(p,α)α	3790 ± 330
$PdLi_{0\cdot1\%}$ [34]	^{7}Li(p,α)α	4100 ± 650

formation of these particles to DD fusion reactions occurring inside the lattice. The group in SRI had conducted Pd/D co-deposition experiments using CR-39 detectors both immersed in the electrolyte and outside the cell [35], [36]. In the latter experiments, a 6 μm Mylar film separated the cathode and the detector. Roussetski *et al.* [36] did sequential etching analysis of these detectors. Tracks due to proton recoils caused by neutrons were detected. The energy of these neutrons was on the order of 2.45 MeV, Figure 6a. Direct detection of ^{3}He was not possible as it would be difficult to differentiate alpha and ^{3}He tracks. Consequently, in both the Lipson *et al.* [18] and the SRI experiments [35], [36], the presence of 2.45 MeV neutrons infers that ^{3}He particles were created but could not be directly detected. However, the D(^{3}He,p)α original and downscattered 14.7 MeV protons have been observed indicating the production of ^{3}He [35].

For a 1.01 MeV triton, the cross section of the TT reaction, not taking into account electron screening, is 89 mbarn. SRIM [37] can be used to calculate how far a charged particle can travel through a medium. Using SRIM, a 1.01 MeV triton will traverse 4.86 μm of PdD, which is equivalent to 11,916 unit cells. The TT reaction will result in some loss of thermal tritons but is probably not the primary reaction. The ^{3}He formed from DD reactions has an energy of 0.82 MeV. This energetic ^{3}He ion will react with thermal tritons. For a 0.82 MeV ^{3}He, the cross section of the T^{3}He reaction is 189 mbarn. However, SRIM calculations indicate that a 0.82 MeV ^{3}He will traverse only 1.15 μm of PdD, or 2,813 unit cells. The T^{3}He secondary fusion reaction forms either a 9.5 MeV deuteron and a 4.8 MeV alpha (43% of the time) or a proton, alpha, and a neutron (57% of the time). The 9.5 MeV deuteron, formed 43% of the time, can undergo more DD reactions to form more energetic ^{3}He ions and tritons. A 9.5 MeV deuteron will pass through 133.61 μm of PdD, or 327,479 unit cells. Although the T^{3}He reaction will eliminate thermal tritons, given the cross section and how far the ^{3}He ions can travel through the PdD lattice, this reaction is not the main reaction responsible for the loss of tritium.

The pT reaction involves a thermal triton and a high energy proton so thermal tritons will be consumed. There are two sources of energetic protons. One is the DD primary fusion reaction to form a 3.02 MeV proton and a 1.01 MeV triton. The other is the ^{3}HeD secondary fusion reaction that produces 14.7 MeV protons and 3.6 MeV alpha particles. Pd/D co-deposition experiments using CR-39 detectors have shown that both 3.02 and 14.7 MeV protons have been produced [35, 36]. Roussetski *et al.* [36] had subjected a CR-39 detector used in a co-deposition experiment to destructive sequential etching analysis. The results, shown in Figure 6b, showed tracks attributed to 3 MeV protons, 12 MeV alpha, and 16 MeV alphas. Prior to the destructive sequential etching analysis, this same detector had been scanned using a TASL Image system [38] to obtain quantitative information on the pits produced in the CR-39 detector [35]. Fifteen characteristic measurements of each feature in the detector are made to reliably discriminate between etched tracks and background blemishes in the plastic detectors. These measurements include track length and diameter, optical density (average image contrast), and image symmetry. Based upon the measured properties of a feature, the software algorithm determines whether or not those measurements are consistent with that

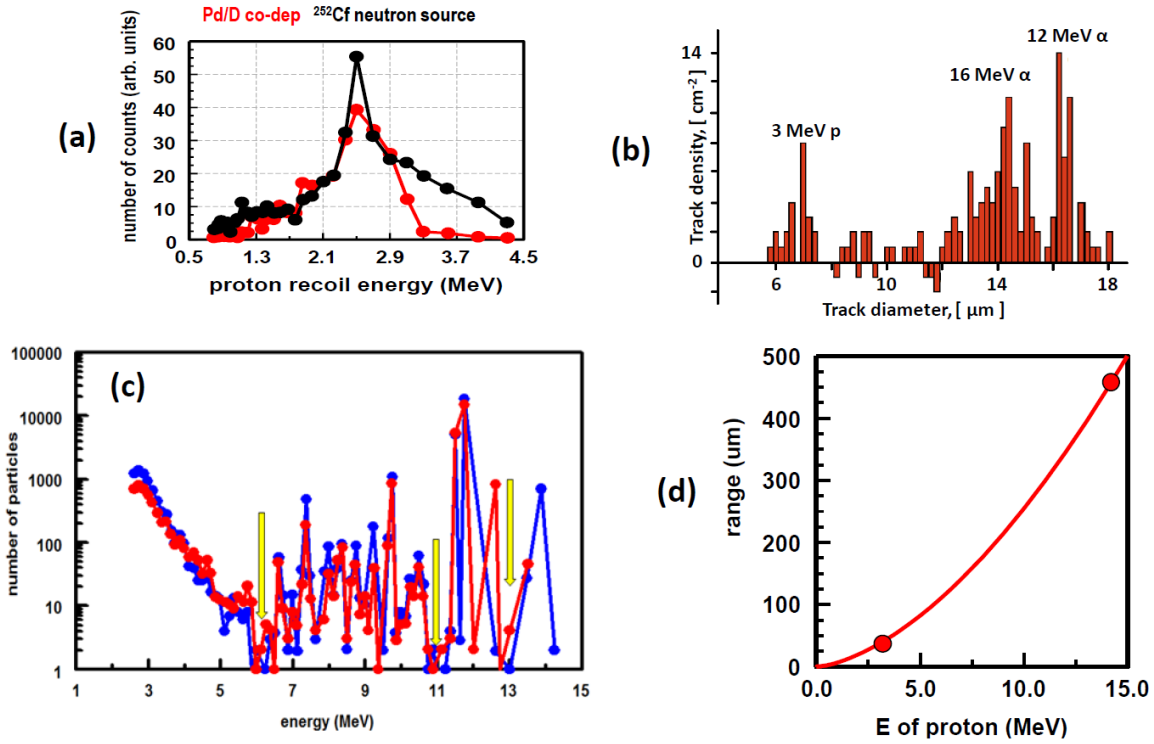

Figure 6. (a) Reconstruction of the protons recoil spectra from both Pd/D co-deposition and ^{252}Cf exposure [36]. The detector used in Pd/D co-deposition was from a non-immersion experiment where a 6 μm Mylar window separated the cathode from the detector. The detector had been etched for 14 h. (b) The difference between the nuclear track distribution on the front side of a detector in direct contact with the Ag/Pd cathode and the neutron induced proton recoil track distribution on the back side. [36]. The detector had been etched for 21 h. (c) Energy distribution of protons on the side of detectors in contact with the Ag/Pd cathodes [35]. Linear energy transfer (LET) analysis was used to determine the energies of the protons. Troughs in the energy distribution, indicated with ↓, suggest that protons with these energies are being consumed. (d) LET curve calculated for protons traversing through PdD. The 3.02 and 14.7 MeV protons are indicated (●).

of an energetic particle. LET analysis using the scanned data obtained for the detectors was done [35]. The tracks on detector surface in contact with the cathode were identified as $\geq$ 1.8 MeV protons, $\geq$ 1.8 MeV alphas, and secondary particles due to recoils from either energetic protons and/or neutrons. The energy distribution of the protons, Figure 6c, shows the presence of both 3.02 MeV and 14.7 MeV protons. Arrows indicate troughs at 6, 11, and 13 MeV which indicate that protons of these energies are being used up in additional nuclear reactions. Protons with energies between 5 and 20 MeV will cause palladium to transmute to silver [1]. SEM/EDX analysis of a cathode used in a Pd/D co-deposition experiment, Dash and Ambadkar saw evidence of Ag production [39], [40].

In the pT reaction, a 3.0 MeV proton has a cross section of 600 mbarn, which is significant. A SRIM calculation was done and the results are shown in Figure 6d. This calculation shows that a 3.02 MeV proton will pass through 34.29 μm of PdD, or 84,052 unit cells. A 14.7 MeV proton will traverse 433.43 μm of PdD. This is equivalent to 1,062,339 unit cells. Given the cross sections of the reaction and the distances the energetic protons can travel through PdD, the pT reaction is primarily responsible for the loss of tritium.

4. Conclusions

For Pd/D co-deposition, it has been demonstrated that tritium production occurs when low tritiated D_2O is used. When tritium is produced, it occurs in bursts and sporadically. In contrast, a loss of tritium is observed when highly tritiated D_2O is used. The loss of tritium indicates that reactions are occurring inside the lattice that consumes thermal tritium. Nuclear reactions involving tritons with Pd and Li isotopes were examined. No cross sections were found for T^nPd reactions. While there are a number of T^nLi nuclear reactions with cross sections in the millibarns, Mel Miles [5] did not use electrolytes containing lithium salts and he still observed a loss of tritium. Therefore, the reactions resulting in a decrease in tritium does not involve Li and Pd isotopes.

Reactions between tritium and hydrogen and helium isotopes were then explored. Because the maximum cross section for the T^4He is 3.58 μbarn, this reaction is not responsible for the observed decrease in thermal tritium when highly tritiated D_2O is used. The DT reaction has a maximum cross section of 5 barn; however, the triton has to be energetic. For hot fusion, the threshold energy for the triton is 5 keV. But the conditions (ion density, confinement time, temperature) of hot fusion are not the same as those in LENR. Metal hydrides/deuterides are essentially cold, dense plasmas [28] conducive to electron screening effects that would lower that energy threshold. It should be noted that triple tracks have been observed in CR-39 detectors used in Pd/D co-deposition experiments. These triple tracks are diagnostic of 14 MeV neutrons likely resulting from DT fusion. Given the exceptionally high cross sections for the DT reaction and electron screening, it is possible that thermal tritons are consumed. However, it is probably not the primary reaction responsible for the observed loss of tritium when highly tritiated D_2O is used.

The TT reaction will consume both thermal and energetic tritons. The T(T,2n)α is a three body reaction resulting in continuum neutron energies from 1-9 MeV, which are not observed. The DD reaction will produce 1.01 MeV tritons. For a 1.01 MeV triton, the cross section of the TT reaction is 89 mbarn and a 1.01 MeV triton can travel through 4.86 μm of PdD, which equates to 11,916 unit cells. The T^3He reaction will consume thermal tritons. The ^3He ion formed from the DD reaction has an energy of 0.82 MeV. A ^3He ion of this energy will have a cross section of 189 mbarn for the T^3He reaction. A 0.82 MeV ^3He ion will traverse 1.15 μm of PdD, or 2813 unit cells. In hot fusion, 43% of the time, the T^3He reaction will form 9.5 MeV D that will undergo additional DD reactions to generate more 0.82 MeV ^3He, 3.02 MeV p, and 1.01 MeV T that can interact with more thermal tritons. A 9.5 MeV D will go through 133.61 μm of PdD, or 327,479 unit cells. It should be pointed out that, while in hot fusion, the T/n branching ratio for the DD reactions is unity, in LENR the branching ratio is near 10^6 [41] meaning that the production of tritium is highly favoured. Although both the TT and T^3He reactions will consume thermal tritons, the TT reaction will contribute more to this loss but, based upon the cross sections of the reaction and how far a 1.01 MeV T can travel through PdD, it is unlikely to be the primary reaction responsible for the loss of thermal tritons.

The pT reaction was then examined. This reaction will react with thermal tritons. At 3.0 MeV, the cross section is 600 mbarn. Destructive sequential etching and LET analyses of CR-39 detectors used in Pd/D co-deposition experiments showed the presence of tracks due to 3.02 and 14.7 MeV protons [30], [31]. A 3.02 MeV p can travel through 23.29 μm of PdD. This is equivalent to 84,052 unit cells. In contrast a 14.7 MeV p traverses through 433.43 μm of PdD, or 1,062,229 unit cells which greatly increases the probability of a proton to encounter a triton in the lattice. Given the cross sections of reaction and the distance the protons can travel through PdD, the pT reaction is primarily responsible for the loss of thermal tritium observed when highly tritiated D_2O is used in Pd/D co-deposition experiments.

This loss of tritium when highly tritiated D_2O is used in electrolysis experiments had only been observed in Pd/D co-deposition. The difference in the behaviour of bulk Pd and the Pd deposit created as a result of co-deposition is illustrated in Figure 7, which shows photomicrographs of CR-39 obtained at 20x and 200x magnification. Figure 7a was obtained for a CR-39 detector used in a Pd/D co-deposition experiment. Not only is the density of tracks high, but tracks occur homogeneously where the Pd deposit on the Ag wire was in contact with the detector. In contrast,

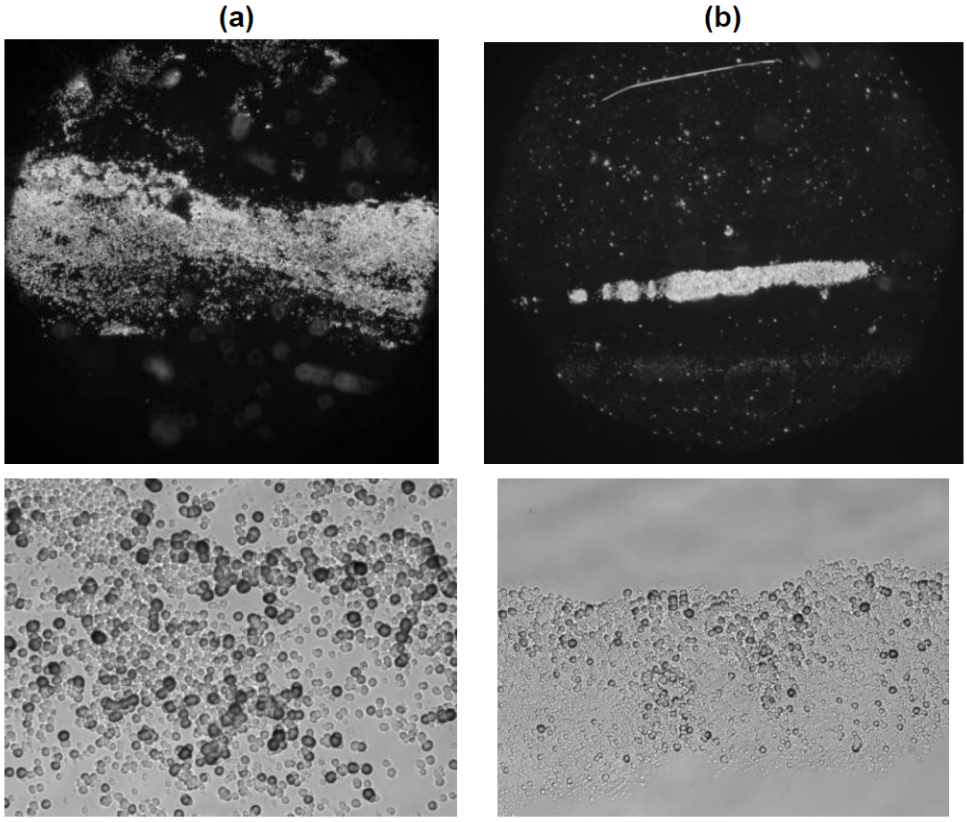

Figure 7. Photomicrographs obtained at 20x (top) and 200x (bottom) magnification for CR-39 detectors used in (a) Pd/D co-deposition in D_2O on a Ag cathode and (b) bulk Pd electrolysis in D_2O. The diameter of the Pd wire was 250 μm. The time duration of operation was the same for both experiments.

visual inspection of the CR-39 detector used in the bulk Pd wire experiment done in D_2O showed scattered cloudy areas in the detector along the length of the Pd wire. Figure 7b shows photomicrographs of one such cloudy area where the Pd wire was in contact with the detector. Although tracks are observed, the density of tracks is significantly less than that observed for the co-deposition experiment. This indicates that there are fewer active sites in bulk Pd than in the Pd deposit formed as a result of co-deposition. Figure 8a shows an SEM obtained for a Pd deposit on a Au foil cathode. The SEM is similar to those obtained by Lee *et al.* [6], Figures 3b and c. The deposit exhibits a high surface area and it will exhibit vacancies. The SEMs of the Pd deposit show that it is comprised of aggregates of Pd nm-μm sized globules. Akiba *et al*. [42] conducted neutron powder diffraction experiments on bulk and nanoparticles of palladium deuteride. Analysis showed that for nanocrystals, 30% of D atoms are located at the tetrahedral sites and 70% at the octahedral sites, shown schematically in Figure 8b. In contrast they found that only the octahedral sites of bulk Pd were occupied with D. This indicates > 1 D/Pd loadings for Pd nanoparticles. Earlier Szpak *et al.* showed high D loadings (D/Pd $\geq$ 1) in the Pd deposit using galvanostatic pulsing experiments [43]. Besides high D/Pd loadings, these vacancies will exhibit D flux [44]. Both the loading and the flux will increase the amount of electron screening [30]-[32] in the Pd deposit, compared to bulk Pd, and may account for the observed results.

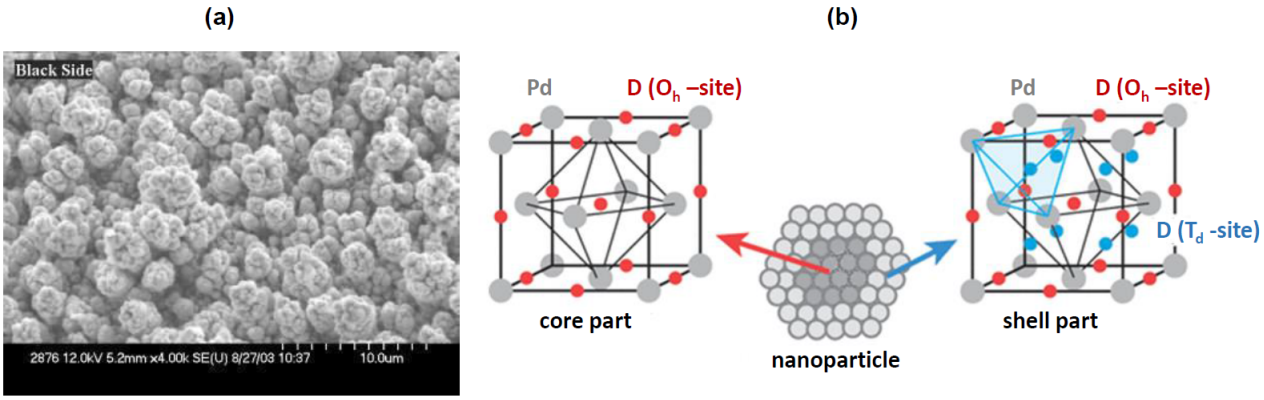

Figure 8. (a) SEM image of a Pd film deposited on Au foil. (b) Schematic showing the placement of deuterons in the lattice of a Pd nanoparticle (reproduced with permission from the J. Am. Chem. Soc. [42]).

5. Acknowledgements

The authors would like to thank the research groups who conducted Pd/D co-deposition experiments that focused on tritium measurements. They would like to thank Fran Tanzella and Ben Earle for replicating the CR-39 results and the late Andrei Lipson, Alexei Roussetski, and Dazhuang Zhou for analysing the detectors used in that replication. We are grateful to Dr. Frank Gordon for his support of the work while he was a department head at SSC-Pacific as well as the support from Dr. Jay W. Khim of GEC. Finally, we acknowledge the contributions of the late Dr. Stan Szpak for conceiving and developing the Pd/D co-deposition process.

References

[1] P.A. Mosier-Boss, L.P. Forsley, "Review of Pd/D Co-deposition" in Cold Fusion: Advances in Condensed Matter Nuclear Science, J.-P. Biberian (ed.), Elsevier Science (2020).
[2] D. Hodko, J. O'M. Bockris, "Possible Excess Tritium Production on Pd Codeposited with Deuterium," J. Electroanal. Chem., vol. 353, pp. 33–41 (1993).
[3] J. O'M. Bockris, C.-C. Chien, D. Hodko, Z. Minevski, "Tritium and Helium Production in Palladium Electrodes and the Fugacity of Deuterium Therein," Third International Conference on Condensed Matter Nuclear Science, Nagoya, Japan (1992).
[4] S. Szpak, P.A. Mosier-Boss, R.D. Boss, "On the Behavior of the Cathodically Polarized Pd/D System: Evidence for Tritium Production," Fusion Sci. Technol., vol. 33, pp. 38–51 (1998).
[5] M.H. Miles, NEDO Final Report – Electrochemical Calorimetric Studies of Palladium and Palladium Alloys in Heavy Water, University of La Verne (2004).
[6] K.-H. Lee, H. Jang, S.-J. Kim, "A Change of Tritium Content in D_2O Solutions During Pd/D Co-deposition, J. Condens. Matter Nucl. Sci. vol. 13, pp. 294–298 (2014).
[7] S. Szpak, P.A. Mosier-Boss, M.H. Miles, "Calorimetry of Pd + D Co-deposition," Fusion Sci. Technol. vol. 36, pp. 234–241 (1999).
[8] F. Dalard, M. Ulmann, J. Augustynski, P Selvam, "Electrochemical Incorporation of Lithium into Palladium from Aprotic Electrolytes," J. Electroanal. Chem. Vol. 270, pp. 445–450 (1989).
[9] S.N. Abramovich, B. Ya. Guzhovskij. V.A. Zherebtsov, A.G. Zvenigorodskij, Nuclear Physics Constants for Thermonuclear Fusion: A Reference Handbook, International Nuclear Data Committee, Moscow, U.S.S.R. (1989).

[10] R.H. Majeed, O.N. Oudah, "Achieving an Optimum Slowing-Down Energy Distribution Functions and Corresponding Reaction Rates for the (D + ^{3}He and T + ^{3}He) Fusion Reactions," AIP Conference Proceedings, vol. 1968, pp. 30048 (2018).
[11] S. Atzeni, J. Meyer-ter-Vehn, "Nuclear Fusion Reactions," in The Physics of Inertial Fusion: Beam Plasma Interaction, Hydrodynamics, Hot Dense Matter, Oxford University Press (2004).
[12] https://www.newworldencyclopedia.org/entry/Nuclear_fusion
[13] G.H. Miley, H. Towner, N. Ivich, "Fusion Cross Sections and Reactivities," Technical Report Number COO-2218-17 (1974).
[14] D. Testa, M. Cecconello, C. Schlatter, "The Dependence of the Proton-Triton Thermo-Nuclear Fusion Reaction Rate on the Temperature and Total Energy Content of the High-Energy Proton Distribution Function," Nucl. Fus., vol. 40, pp. 062004 (2009).
[15] G.M. Griffiths, J.B. Warren, R.A. Morrow, P.J. Riley, "The T(α,γ)^{7}Li Reaction," Canadian J. Phys., vol. 39, pp. 1397–1408 (1961).
[16] A.G. Lipson. A.S. Roussetski, G.H. Miley, E.I. Saunin, "Phenomenon of an Energetic Charged Particle Emission from Hydrogen/Deuterium Loaded Metals," Tenth International Conference on Cold Fusion, Cambridge, MA (2003).
[17] A.G. Lipson. A.S. Roussetski, G.H. Miley, C.H. Castano, "In-Situ Charged Particles and X-ray Detection in Pd Thin Film-Cathodes during Electrolysis in Li_2SO_4/H_2O," Ninth International Conference on Cold Fusion, Beijing, China (2002).
[18] A.G. Lipson, B.F. Lyakhov, A.S. Roussetski, T. Akimoto, T. Mizuno, N. Asumi, R. Shimada, S. Miyashita, A. Takahashi, "Evidence for Low-Intensity D-D Reaction as a Result of Exothermic Deuterium Desorption from Au/Pd/PdO:D Heterostructure," Fusion Technol., vol. 38, pp. 238–252 (2000).
[19] T. Matusomoto, "Observation of New Particles Emitted during Cold Fusion," Fusion Technol., vol. 18, pp. 356–360 (1990).
[20] R. Taniguchi, T. Yamamoto, S. Irie, "Detection of Charged Particles Emitted by Electrolytically Induced Cold Fusion," Jpn. J. Appl. Phys. Part 2 Lett., vol. 28, pp. L2021-L2023 (1989).
[21] R. Taniguchi, T. Yamamoto, S. Irie, "Fine Structure of the Charged Particle Bursts Induced by Water-D_2 Electrolysis," Bull. Univ. Osaka Prefect, Ser. A, vol. 39, pp. 233–244 (1990).
[22] B.G. Cartwright, E.K. Shirk, P.B. Price,"A Nuclear-Track-Recording Polymer of Unique Sensitivity and Resolution," Nucl. Instrum. Meth., vol. 153, pp. 457–460 (1978).
[23] D. Nikezic, K.N. Yu, "Formation and Growth of Tracks in Nuclear Track Materials," Mater. Sci. Eng. R, vol. 46, pp. 51–123 (2004)
[24] P.A. Mosier-Boss, S. Szpak, F.E. Gordon, L.P.G. Forsley, "Triple Tracks in CR-39 as the Result of Pd-D Co-deposition: Evidence of Energetic Neutrons," Naturwissenschaften, vol. 96, pp. 135–142 (2009).
[25] P.A. Mosier-Boss, J.Y. Dea, L.P.G. Forsley, M.S. Morey, J.R. Tinsley, J.P. Hurley, F.E. Gordon, "Comparison of Pd/D Co-deposition and DT Neutron Generated Triple Tracks Observed in CR-39 Detectors,"Eur, Phys. J. Appl. Phys., vol. 51, p. 20901 (2010).
[26] B. Antolkoviæ, Z. Dolenec, "The Neutron-Induced ^{12}C(n,n')3α Reaction at 14.4 MeV in a Kinematically Complete Experiment," Nucl. Phys. A, vol. 237, pp. 235–252 (1975).
[27] S.K. Murali, B.B. Cipiti, J.F. Santarius, G.L. Kulcinski,"Study of Fusion Regimes in an Inertial Electrostatic Confinement Device using the New Eclipse Disk Diagnostic," Phys. Plasmas, vol. 12, pp. 053111 (2006).
[28] V. Pines, M. Pines, A. Chait, B. M. Steinetz, L. Forsley, R.C. Hendricks, G. C. Fralick, T. L. Benyo, B. Baramsai, P. B. Ugorowski, M. D. Becks, R. E. Martin, N. Penney, C. E. Sandifer II, "Nuclear Fusion Reactions in Deuterated Metals", Phys Rev C, vol. 101, p. 044609 (2020).
[29] M. Lipoglavšek, U. Mikac, "Electron Screening in Metals," AIP Conference Proceedings, vol. 1377, pp. 383 (2011).
[30] T. Schenkel, A. Persaud, H. Wang, P.A. Seidl, R. MacFadyen, C. Nelson, W.L. Waldron, J.-L. Vay, G. Deblonde, B. Wen, Y.-M. Chiang, B.P. MacLeod, Q. Ji, "Investigation of Light Ion Fusion Reactions with Plasma Discharges," J. Appl. Phy., vol. 126, pp. 203302 (2019).
[31] J. Kasagi, H. Yuki, T. Baba, T. Noda, "Low Energy Nuclear Fusion Reactions in Solids," Eighth International Conference on Condensed Matter Nuclear Science, Lerici, Italy (2000).
[32] J. Kasagi, H. Yuki, T. Baba, T. Noda, J. Taguchi, M. Shimokawa, W. Galster, "Strongly Enhanced Li + D Reaction in Pd Observed in Deuteron Bombardment on $PdLi_x$ with Energies between 30 and 75 keV," J. Phys. Soc. Japan, vol. 73, pp. 608–612 (2004).

[33] K. Czerski, A. Huke, P. Heide, G. Ruprecht, "The ^{2}H(d,p)^{3}H Reaction in Metallic Media at Very Low Energies," Europhys. Lett., vol. 68, pp. 363–369 (2004).
[34] J. Cruz, Z. Fülöp, G. Gyürky, F. Raiola, A. Di Leva, B. Limata, M. Fonseca, H. Luis, D. Schürmann, M. Aliotta, H.W. Becker, A.P. Jesus, K.U. Kettner, J.P. Ribeiro, C. Rolfs, M. Romano, E. Somorjai, F. Strieder, "Electron Screening in ^{7}Li(p,α)α and ^{6}Li(p,α)^{3}He for Different Environments," Phys. Lett. B, vol. 624, pp. 181–185 (2005).
[35] P.A. Mosier-Boss, F.E. Gordon, L.P. Forsley, D. Zhou, "Detection of High Energy Particles using CR-39 Detectors Part 1: Results of Microscopic Examination, Scanning, and LET Analysis," Int. J. Hydrogen Energy, vol. 42, pp. 416–428 (2017).
[36] A.S. Roussetski, A.G. Lipson, E.I. Saunin, F. Tanzella, M. McKubre, "Detection of High Energy Particles using CR-39 Detectors Part 2: Results of In-depth Destructive Etching Analysis," Int. J. Hydrogen Energy, vol. 42, pp. 429–436 (2017).
[37] J. Ziegler, http://www.srim.org/
[38] "Track Analysis Systems Ltd. Napier House. Meadow Grove, Shirehampton, Bristol, BS11 9PJ, UK Tel: +44 (0) 117 9381172; Website: info@tasl.co.uk
[39] J. Dash, A. Ambadkar, "Co-deposition of Palladium with Hydrogen Isotopes," Eleventh International Conference on Condensed Matter Nuclear Science, Marseille, France (2004).
[40] J. Dash, D.S. Silver, "Surface Studies after Loading Metals with Hydrogen and/or Deuterium," Thirteenth International Conference on Condensed Matter Nuclear Science, Sochi, Russia (2007).
[41] E. Storms, "A New Source of Energy using Low-Energy Fusion of Hydrogen," Environmental Science: An Indian Journal, vol. 13, pp. 1–7 (2017).
[42] A. Akiba, M. Kofu, H. Kobayashi, H. Kitagawa, K. Ikeda, T. Otomo, O. Yamamuro, "Nanometer-Size Effect on Hydrogen Sites in Palladium Lattice," J. Am. Chem. Soc., vol. 138, pp. 10238–10243 (2016).
[43] S. Szpak, P.A. Mosier-Boss, J.J. Smith, "Deuterium Uptake during Pd/D Co-deposition," J. Electroanal. Chem. Vol. 379, pp. 121–127 (1994).
[44] M.R. Staker, "Coupled Calorimetry and Resistivity Measurements in Conjunction with an Emended and More Complete Phase Diagram of the Palladium-Isotopic Hydrogen System," J. Condensed Matter Nucl. Sci., vol. 29, pp. 129–168 (2019).

J. Condensed Matter Nucl. Sci. 38 (2024) 211–224

Research Article

Advancements in the Production of Anomalous Heat Effect in Constantan Wires: Developing a Robust Experimental Protocol

Francesco Celani*, C. Lorenzetti, G. Vassallo, E. Purchi, S. Fiorilla, S. Cupellini, M. Nakamura, P. Cerreoni, R. Burri, P. Boccanera, A. Spallone, and E. F. Marano

ISCMNS_L1, International Society of Condensed Matter Nuclear Science, Via Cavour 26, 03013 Ferentino-IT

Francesco Celani, G. Vassallo, A. Spallone, and P. Cerreoni

EU Project H2020: CleanHME
Istituto Nazionale di Fisica Nucleare, Via E. Fermi 56, 00044 Frascati (RM)-IT

G. Vassallo

DIDI, Univ. of Palermo, 90128 Palermo (PA)-IT

Abstract

This paper presents a comprehensive summary of a presentation delivered at the 24th International Conference on Condensed Matter Nuclear Science (ICCF24), which took place at the Computer History Museum in Mountain View, California, from July 25-28, 2022. Since 2011, our research team has been dedicated to discovering simple yet effective procedures for activating a specific material that we developed [1]. This material consists of surface-modified Constantan in the form of long and thin wires, utilizing Joule heating. Our main objective has been to generate measurable values of the Anomalous Heat Effect (AHE). In our most recent efforts, we have not only replicated our previous findings but also conducted new tests to explore potential isotopic effects. The results obtained have reinforced our interpretation of the AHE's main origin, aligning with the initial discoveries made by researchers in the United States, Japan, and Italy, some as early as 1989 [2], [3]. The impetus for this work stemmed from our desire to reaffirm the procedures we extensively discussed during the ANV8 Workshop held in Assisi, Italy, in December 2021. Our presentation at the Workshop, which garnered considerable interest within the LENR-AHE community, led to numerous inquiries, particularly regarding the reproducibility of our methods starting from the wire and its treatments. Consequently, we incorporated new experiments into our study, focusing on exploring any potential isotopic effects by employing H_2 and D_2 gases, in relation to the magnitude of AHE. The core geometry of our reactor remained consistent with the configuration we have developed since 2019, known as the "inverse coaxial coil" [4]. For energy balance calculations at various fixed input powers, we employed thermometry, which enabled faster measurements compared to conventional flow calorimetry. As reference points, we conducted preliminary experiments under helium gas conditions, maintaining similar pressures (typically exceeding 0.5 bar) to those used with the active gases (H_2, D_2). In assessing the energy balance, we relied on temperature measurements taken at the external wall of the glass reactor. This surface was covered with multiple layers of thermally conductive thick aluminum foil, with the side

*Corresponding author: franzcelani@libero.it

 ISSN 2227-3123

facing the ambient environment coated in a high-emissivity (>90%) black compound capable of withstanding high temperatures (800 °C). The recorded maximum temperatures during the experiments were 900 °C internally and 380 °C externally, with a maximum applied power exceeding 150 W. The weight of the wire employed in our tests was 0.45 g. Key Findings: We successfully reaffirmed that a straightforward procedure involving high-power DC Joule heating over extended durations (50-150 hours) remains effective in activating virgin Constantan coils, provided the thin wire surfaces are appropriately treated, primarily with Low Work Function materials. Furthermore, we observed that the measured AHE during the cooling cycles from the highest power levels is contingent upon the time the reactor's core spends at these elevated powers. Notably, we identified a form of "positive memory effect" relating to AHE, which typically persists for 10-20 hours. Additionally, we discovered that the AHE increases as the number of cycles between high and low power levels is increased. We also observed that increasing the wire resistance through suitable "pre-conditioning" treatments enhances the magnitude of AHE. We speculate that this effect might be attributed to an increased surface area resembling a spongy texture, facilitating the flow of active gases, i.e., flux, in and out of the wire. In our most recent experiments, we measured higher AHE values (9 W) when utilizing D_2 gas compared to H_2 (5 W) at an input power of 130 W. Discussion and Future Directions: The AHE observed in our experiments is directly related to the voltage drop along the wire, with larger drops yielding more pronounced effects.
 ISSN 2227-3123

Keywords:

1. Introduction

The Anomalous Heat Effect (AHE) observed in surface-modified Constantan wires has attracted significant attention due to its potential applications in energy generation and as a catalyst for further research in the field of low-energy nuclear reactions (LENR). In this article, we present the findings of our recent experiments aimed at reproducing and validating the activation procedures discussed during the ANV8 Workshop held in Assisi, Italy, in December 2021 [5]. Additionally, we investigate the influence of isotopic effects on the magnitude of AHE. By employing an "inverse coaxial coil" reactor configuration and implementing thermometry for energy balance calculations, we were able to analyze the relationship between AHE and the operational parameters of the system. Our results confirm the effectiveness of high-power Joule heating and prolonged activation times in producing measurable AHE. Furthermore, we explore the impact of wire resistance and cycling on AHE and provide insights into the potential underlying mechanisms. Through the incorporation of isotopic variations using H_2 and D_2 gases, we uncovered the influence of isotopic effects on the observed AHE values. Our study not only reinforces previous research findings but also contributes to the growing understanding of AHE and its applications in the field of LENR.

Building upon previous studies and discussions held at the ANV8 Workshop in Assisi, Italy, in December 2021, we embarked on a series of experiments aimed at reproducing and validating the activation procedures previously proposed. The Workshop provided a platform for in-depth discussions on the practicality and reproducibility of the activation process, as well as insights into potential improvements for enhancing the AHE.

In our study, we employed a reactor configuration known as the "inverse coaxial coil" which has been developed and refined since 2019 [4], [5], [6]. This setup offers advantages such as efficient heat transfer and improved control over operational parameters. To evaluate the energy balance within the system, we implemented thermometry techniques that allowed for rapid and accurate measurements. By monitoring the temperature at the external wall of the glass reactor, we were able to determine the temperature distribution and assess the overall energy transfer.

Our primary objective was to validate the activation procedures, involving high-power DC Joule heating and extended activation times, to activate virgin Constantan coils with surface modifications using Low Work Function materials. We aimed to reproduce the significant AHE observed in previous experiments and further explore its dependence on the reactor's operational history, wire resistance, and cycling behavior. Additionally, we investigated the influence of isotopic effects on the AHE magnitude by introducing H_2 and D_2 gases into the system.

The findings presented in this article contribute to the growing body of knowledge surrounding AHE and its potential applications. Furthermore, by exploring isotopic effects and their impact on the AHE, we aim to deepen our understanding of the underlying mechanisms involved. Ultimately, our research aims to pave the way for practical applications of AHE and its integration into future energy generation systems and LENR studies.

The motivation behind our research efforts is to find simple and effective procedures to activate the specific material we have developed. This material, based on surface-modified Constantan in the form of long and thin wires, exhibits the ability to produce measurable values of the Anomalous Heat Effect (AHE). Since 2011 [7], we have been working towards understanding and harnessing this phenomenon, which holds great potential for applications in various fields, particularly in the realm of low-energy nuclear reactions (LENR). In order to validate and refine our procedures, we undertook a series of experiments to reproduce the observed AHE and investigate isotopic effects. Our interpretation of the results further supports the notion that the AHE originates from specific material characteristics, which aligns with the findings of researchers from the United States, Japan, and Italy, dating back to as early as 1989.

2. Experimental Set-Up

The experimental setup utilized in our study closely resembles the configuration we have developed since 2019 [1], [6], [8], [7], [5], [9], known as the "inverse coaxial coil." This reactor geometry, depicted in Figures 2, 3, and 4, offers several advantages for our investigations. To analyze the energy balance within the system, we employed thermometry techniques, which enabled faster measurements compared to traditional flow calorimetry.

It is important to highlight that we took certain precautions to ensure the reliability of our calorimetric approach. Firstly, the laboratory temperature is maintained constant at 22°C $\pm$ 1 °C through air conditioning. Furthermore, the reactor is shielded from direct sunlight. We minimize also additional errors that may arise from convection currents or room drafts by regularly monitoring the room temperature and air current speed using a Kestrel anemometer with a resolution of 0.1 m/s. Relative air humidity, typically within the range of 40-60%, is also carefully monitored. The combined uncertainty arising from the aforementioned potential sources of error is estimated to be approximately $\pm$1 W.

In Figure 1, we present the typical thermal behavior of our reactor in vacuum and when filled at room temperature with 2 atmospheres of different inert gases. Notably, when replacing the gas from one experiment to another, the temperature behavior, both internally and externally (reactor wall), follows a consistent trend associated with the thermal conductivity of the filling gas, as expected.

As reference points for energy balance calculations, we conducted experiments under helium (He) gas at the beginning of the tests, maintaining similar pressures to those of the active gases (H_2, D_2). Our focus was on temperature measurements at the external wall of the glass reactor, as shown in Figure 2. To emulate black-body emission and account for conduction and convection phenomena, we covered the surface with multiple layers of thermally conducting thick aluminum foil, painted with a high-emissivity (>90%) black compound. This configuration enabled us to achieve maximum temperatures of 900 °C internally and 380 °C externally, while applying a maximum power of over 150 W. The weight of the wire used in our experiments was 0.45 g.

In the next sections, we will delve into the main procedures employed to induce AHE, the key results obtained, and potential explanations for the observed phenomenology, including the influence of hydrogen-induced Super Abundant Vacancies (SAV) [10], [11], [12] and the role of gas flux in specific materials. Furthermore, we will outline the direction of our ongoing experiments and the implications of our findings for the field of AHE research.

3. Reactor Design

Figures 2, 3, and 4 depict the reactor utilized in the experiment. The reactor consists of a straight tube made of thin commercial iron (magnetic) with an external diameter of 5 mm, as illustrated in Figure 3. In the innermost section of

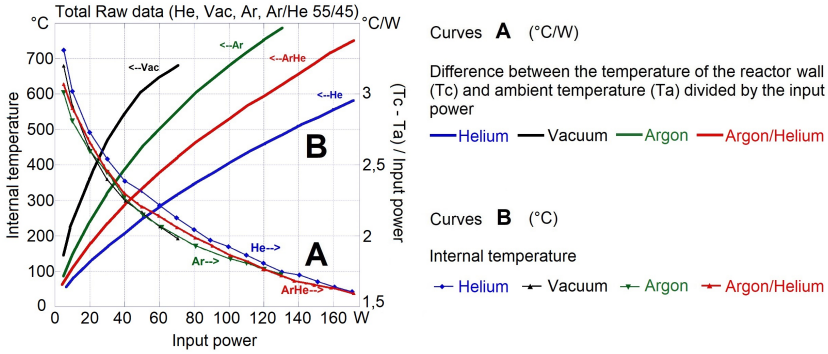

Figure 1. An overview of the internal temperature (Tint) of the reactor as a function of the input power (Pw), ranging from 5 to 170 W. This figure also presents the ratio of the temperature difference (Tc-Ta) to the input power (Pw). It is noteworthy that the internal temperature (Tint) increases as the thermal conductivity of the gases decreases, with the highest temperature observed in a vacuum. Specifically, the temperature order from highest to lowest is Vacuum > Ar > 50%Ar/50%He > He. Additionally, the ratio of temperature difference (Tc-Ta) to input power (Pin) reaches its maximum values when the reactor is in a helium atmosphere. These findings align well with accepted thermometry models, although it should be noted that our measurements do not account for potential heat losses at the extremities of the actual "reactor."

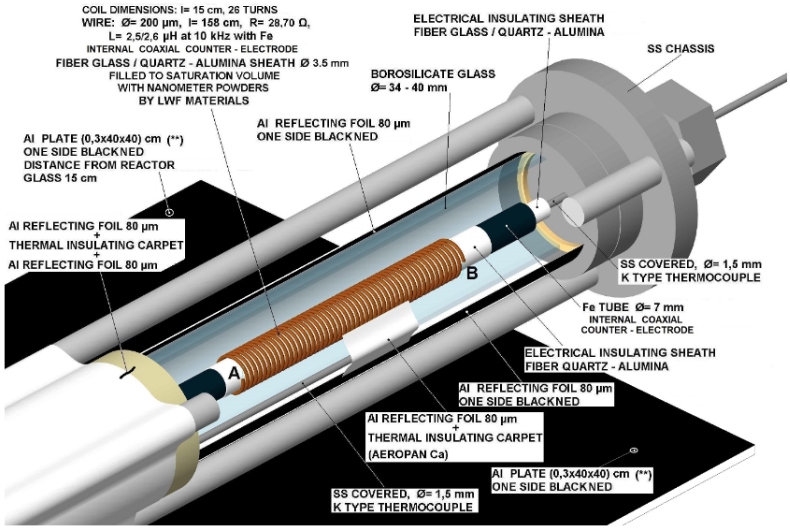

Figure 2. Schematic representation of the reactor body. The container is made of borosilicate glass with a thick wall (3.2 mm), specifically designed and tested for high-temperature mild pressure operations by Vetreria Scientifica Spaziani (Italy).

the tube, positioned at its center, a Type K thermocouple is located. The thermocouple is covered with a stainless steel (SS) layer and electrically insulated by quartz-alumina sheaths, as indicated in Figure 4. Additionally, a Constantan wire, insulated by glass sheaths (a special type known as SE-SI with a diameter of 1 mm), is coiled around the inner iron tube, as shown in Figure 4.

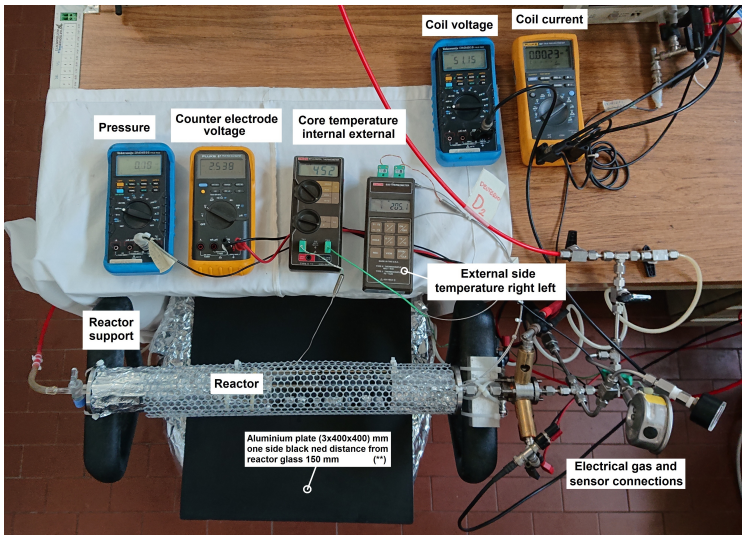

Figure 3. Photograph of the reactor, showing the protective stainless steel (SS) net used for safety purposes. The inner reactor core is our standard structure.

It is important to note that different types of insulation sheaths have been employed in the setup, each with specific characteristics, as described below:

- SE: This is a conventional glass sheath with a maximum operating temperature of 550 °C. It softens at 840 °C and undergoes fusion at 1275 °C. The composition of this glass is similar to that used in tungsten incandescent lamps, and it possesses the unique property of absorbing atomic hydrogen, as observed by Irving Langmuir in 1928. The decomposition from a molecular to atomic state is facilitated by Constantan, which is the most suitable material known for hydrogen decomposition.
- SI: This sheath is composed of quartz (80%) and alumina (20%). It can withstand continuous temperatures up to 1050 °C, remaining stable even above 1000°C.
- SE-SI: This is an unconventional sheath specially manufactured by SIGI-Favier Company based on our specific request. It combines the beneficial properties of both SE and SI sheaths. The SE and SI fibers, each with diameters ranging from 5-8 μm, are intertwined at a step of approximately 0.5 mm.

Thermocouples (Tc) are placed at the external wall of the reactor to measure temperature. Multiple layers of thermally conducting aluminum foil, with a high-emissivity black compound, cover the external surface for enhanced heat transfer and black-body emission emulation.

4. Procedures of Reactor Preparation at INFN-LNF

An innovative procedure incorporating bulk and surface treatments has been employed to induce the Anomalous Heat Effect (AHE). These procedures involve two main steps: a) the preparation of the “possibly active” material through physical-chemical processes to create a specific microstructure, and b) the activation phase. In gas phase experiments, the most extensively studied materials include Pd and its alloys, Ni, and Constantan (Cu-Ni-Mn). However, it is still possible that other transition elements and alloys may exhibit similar behaviors when suitably modified.

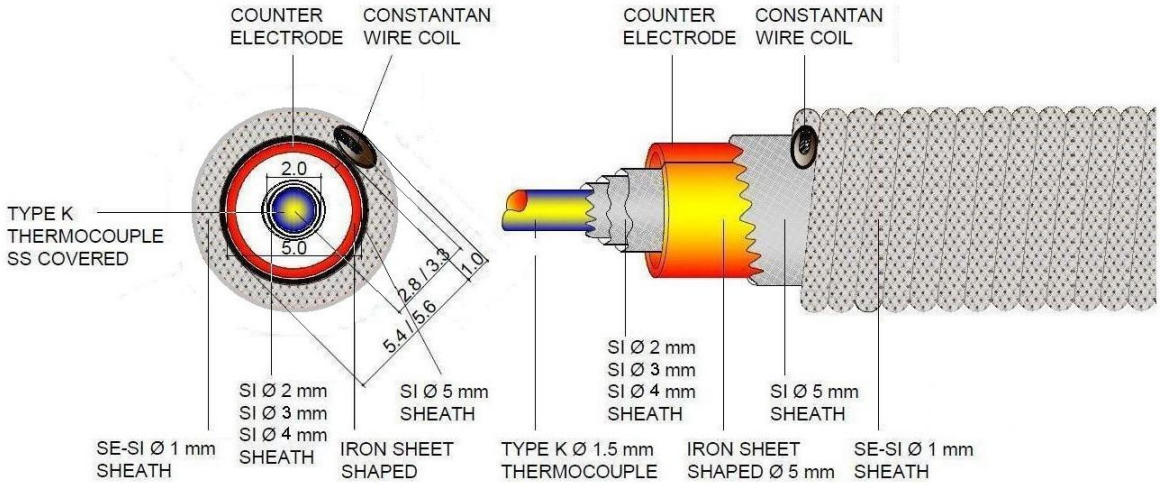

Figure 4. Detailed depiction of the inner core of the reactor. This standard and simplified configuration is utilized for pulsing tests to mitigate potential interferences arising from copper (Cu) tapes and stainless steel (SS) tubes. The schematic illustrates the coaxial coil design, featuring an inner iron (Fe) counter-electrode. The coil, with a wire length of 158 cm, typically consists of 75 turns, although it has recently been reduced to approximately 50 turns due to high voltage (HV) insulation challenges. In comparison to the ICCF23 version, the current core represents a simplified iteration that lacks infrared (IR) screening using aluminum foil and copper tapes, as well as thermal insulation.

The surface treatment of materials such as Constantan requires specific procedures to generate sub-micrometric structures, significantly increasing their surface area and resulting in a spongy-like morphology. While we have successfully addressed point a) through our expertise developed over 20 years, we have encountered challenges in developing simple and reproducible activation procedures (point b).

In previous observations, we found that our "modified" Constantan wires required prolonged conditioning at high temperatures and/or exposure to H_2 atmosphere, accompanied by a type of material stress similar to the traditional mechanical "cold-working" techniques employed mainly by Japanese researchers [13], [14], including our own work [15]. The cold worked materials used in these experiments were provided by Tanaka K. K. and IMRA Materials, both Japanese companies [14]. Similar experiments involved dynamic torsion of the electrode in situ [16], which resulted in measurable AHE.

The modified wires used in our study are composed of the Ni44-Cu55-Mn1 alloy (Constantan) and have a diameter of 200 μm. Their surfaces undergo multiple cycles of high-temperature oxidations in ambient air to obtain sub-micrometric structures resembling sponges or coral-like formations. Subsequently, the wires are coated with several layers of water solution of nitrates containing Sr, Fe, K, and Mn, which are then dried and decomposed into oxides at elevated temperatures.

Furthermore, we observed that our High Peak Power Pulses (HPPP) with peak powers reaching 10 kW/g and currents flowing along the Constantan wire (length = 160 cm; weight = 0.45 g) exceeding 12 A (current density J = 40 * 10^3 A/cm^2), with a pulse width of 10 μs and repetition rates up to 2.5 kHz, were able to activate the wire [8]. Activation was achieved when the pulsing procedure lasted 5-8 hours with a mean power of approximately 90 W. The activated state persisted for several days even after returning to DC conditions.

However, the pulsing procedure, while highly efficient [17], has proved challenging for researchers worldwide, especially for independent replication in their own laboratories, particularly in academic settings.

Additionally, in the past, the simple DC conditioning procedures were not fully understood, and the control parameters were not adequately identified. Nonetheless, we obtained "promising indications" that using solely DC conditioning for extended periods could activate the wire.

Recent experiments have been aimed at identifying potential turning points for activation based on current density and wire temperature, necessitating meticulous systematic studies. The power was adjusted in close increments (0, 1, 5, 10, 20, and later-on 10 W steps, up to a maximum of approximately 130-140 W) while using He or H_2 gases at pressures of a few bars. One potential limitation of these experiments was the possibility of underestimating AHE values if the turning point for material activation occurred during the initial experiment conducted under hydrogen gas. Typically, the data from the first loading cycle are employed as calibration and considered the zero reference, excluding measurements conducted using He gas.

Interestingly, it has recently been discovered that even the first cycle under helium (He) gas cannot be considered a true blank due to the decomposition and absorption of hydrogen content from the liquid solution into the bulk during the pre-conditioning treatments of the wires in ambient air. These pre-conditioning treatments involve subjecting the wires to currents of up to 2.8 A at approximately 900 °C, estimated using the method of "color temperature" through visual observation. It should be noted that the initial pre-conditioning, which includes oxidation and the addition of LWF (liquid with suspended solids) materials, is performed before inserting the wire into the glassy sheath. After insertion, additional LWF materials are deposited on the surface of the sheaths, followed by heating up to 500 °C to facilitate water evaporation and decomposition of the nitrates into stable oxides, such as SrO.

This effect becomes evident during measurement cycles when the power applied to the wire exceeds 120 W.

Two main types of experiments were conducted to gain control over the procedure and understand the effects on the Anomalous Heat Effect (AHE):

- The first type aimed to improve the AHE values by increasing the conditioning time at high power.
- The second type involved inducing the "degradation" of certain characteristics of the conditioned wire, for example, through high-temperature vacuum degassing, followed by attempts to restore the previous "good" conditions.

5. First type of Experiments: Increasing Activation (see Figure 5)

Initially, four cycles labeled H2#1 to H2#4 were performed following calibration with helium gas and preceding to a vacuum treatment at high temperatures lasting over 15 hours.

Throughout the cycles, the same hydrogen (H_2) gas was maintained without cleaning it by vacuum or introducing fresh H_2. Given the duration of each cycle and the relatively short reduction time, we can assume a nearly constant gas composition consisting of hydrogen and water. This approach aimed to avoid uncertainties arising from potential water production at the beginning of the first cycle, resulting from the recombination of H_2 with oxides on the material surface. By maintaining a consistent gas composition across the cycles, we ensured comparability among the different experimental runs. Additionally, by maintaining the same gas, despite the initial pressure reduction caused by oxide reduction and subsequent loading into the lattice, we sought to investigate if pressure reduction could influence the absolute value of loading and AHE values, particularly in relation to the time spent at high power under "strong" electromigration. It appears that electromigration is the dominant effect, provided that a certain gas pressure (approximately 0.5-1 bar) is present.

The main observation during these cycles was a continuous increase in AHE values (expressed in watts), on the right side of the curve in Figure 5 and a continuous decrease in R/Ro (on the left side of Figure 5). R/Ro represents the ratio of resistance (R) normalized to its initial value (Ro) under helium gas at very low power. This ratio is measured because in certain materials, such as Pd, the resistivity initially increases and then decreases with the addition and

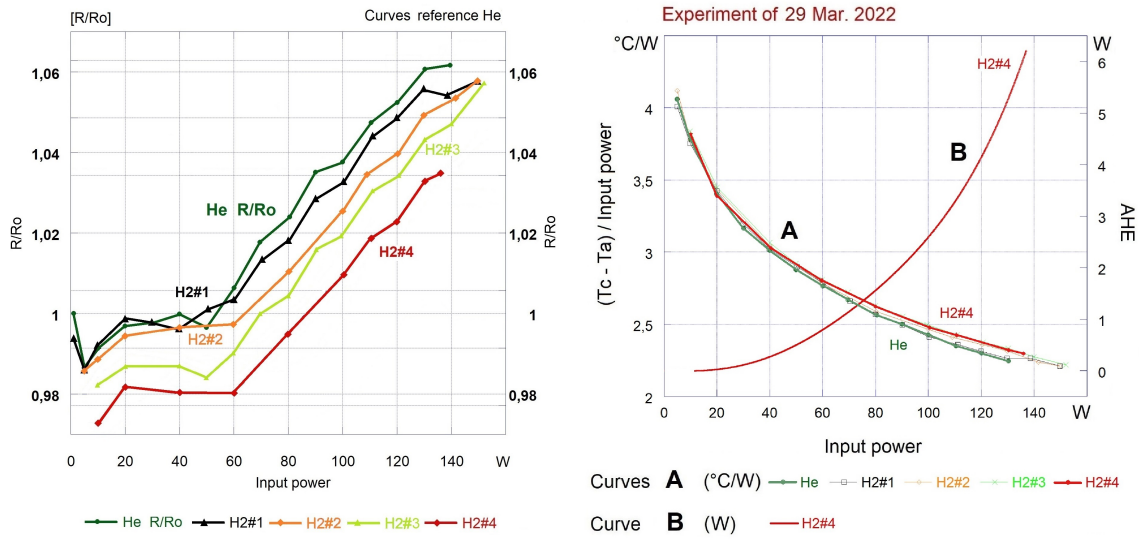

Figure 5. Activation procedure with increasing conditioning time (3 hours, 15 hours, 135 hours) at high power. The left plot depicts the progression of the electrical resistance ratio (R/Ro) of the wire across different experiments, serving as an indicator of the loading (i.e., hydrogen or deuterium absorption by the wire) compared to the initial resistance. On the right, a correlation between the Anomalous Heat Effect (AHE) and this resistance ratio is observed. These plots also illustrate the evolution of the (Tc-Ta)/(Input Power) indicating an increasing AHE based on the number of loading/unloading cycles. The AHE tends to increase until the fourth experiment cycle (H2#4), which is followed by a high-temperature degassing under vacuum at 730 °C. Subsequently, hydrogen is reintroduced in the fifth cycle (H2#5), resulting in a slightly lower AHE. The subsequent run (H2#6) was conducted after introducing fresh H2, with a wire conditioning time of 113 hours at an input power of 152 W (see Figure 6).

absorption of H or D, depending on the specific ratio of H/Pd (or D/Pd). Similar qualitative results have been observed in our experiments with Constantan wires since 2011.

- The performance, as indicated by the AHE, tends to improve with each conditioning cycle from H2#1 to H2#2, H2#3, and H2#4, suggesting a progressive increase in activation.
- Interestingly, the behavior of decreasing resistance and increasing AHE exhibited qualitative similarities to the historical observations made with palladium since 1990 [18].
- For the purpose of enhanced clarity, it is important to note that while the wire's resistance continues to exhibit an augmentation in response to the input power, there is a concurrent diminishing trend in resistance observed as one progresses from H#1 to H#4, owing to the incremental uptake of hydrogen.
- These results suggest a potential for enhancing AHE through repeated conditioning cycles and indicate the positive effect of long-term exposure to hydrogen gas on the modified Constantan wire. It appears that the dominant factor is the conditioning time at high power, which refers to the time the wire spends at high temperatures and large voltage gradients (V/cm). True AHE experiments are conducted after such conditioning times, gradually reducing the input power. The waiting time before conducting experiments is chosen to be similar to that observed under helium gas calibration to achieve temperature equilibrium, with an additional increase of 20-30% to ensure even more reliable results. Further details on conditioning time are provided in the caption of Figure 5.

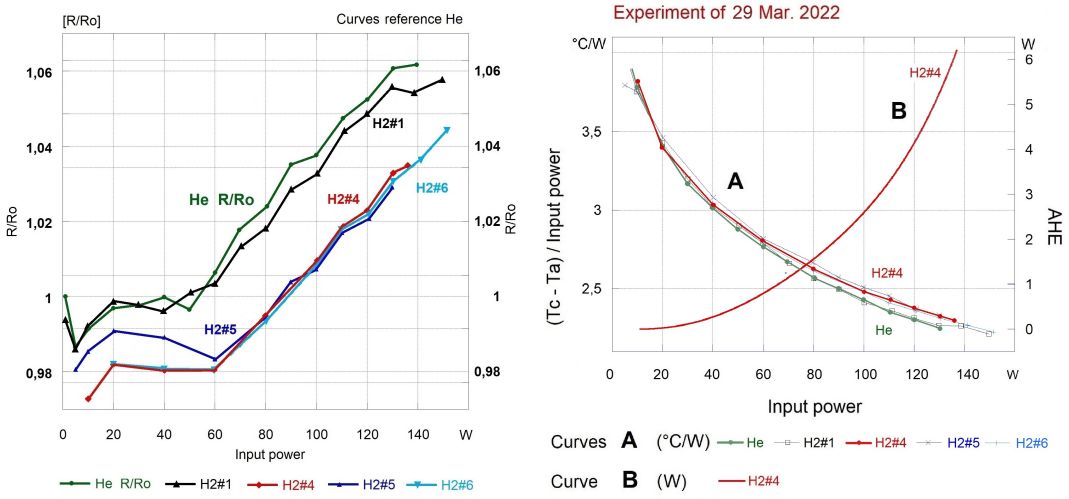

Figure 6. AHE and R/Ro Behavior with Vacuum Degassing and Refilling Cycles. This figure presents the behaviour of the Anomalous Heat Effect (AHE) and the resistance ratio (R/Ro) during cycles of vacuum degassing and refilling in the Constantan wire. The experiments involved cycles H2#4, H2#5, and H2#6. Vacuum degassing at high temperatures followed by fresh H2 refilling was performed to investigate the effects on AHE performance. The results show that the AHE of H2#5 and H2#6 is lower compared to H2#4, indicating a partial recovery of the performances. The R/Ro values provide insight into the relative change in resistance normalized to its initial value (Ro) under He gas at very low power. These findings suggest that while some recovery of performance was achieved, it was not fully restored to the level observed in H2#4.

In this study, the analysis of Anomalous Heat Effect (AHE) curves involves employing a 4th order polynomial regression model to correlate temperature measurements with input power. To ensure the robustness and accuracy of this approach, we carefully select 10-15 experimental data points for each analysis. It is essential to note that during the initial runs, the measured AHE values were relatively modest. As a result, AHE has only been reported for the most productive experiments, specifically H2#4 and D2#12. For the remaining experimental runs, we report only the temperature difference between the reactor wall (Tc) and the ambient temperature (Ta), normalized by the input power, to identify potential occurrences of AHE.

6. Second Type of Experiment: Effect of Vacuum Degassing and Refilling Cycles (see Figure 6)

Following the completion of test H2#4, a dynamic vacuum at high temperature (730 °C) was applied for 15 hours. Subsequently, fresh H_2 gas was introduced into the system at the same pressure used in test H2#1, and experiment H2#5 was conducted.

- The results of H2#5 indicated a reduction in AHE values compared to H2#4, particularly at higher input powers. The decrease in performance was most prominent at elevated temperatures.
- This reduction in AHE performance could be attributed to several factors. Firstly, it is possible that the wire's surface, which has undergone multiple treatments, may have become less effective in maintaining high AHE values at elevated temperatures. Additionally, prolonged vacuum conditions at high temperatures may have led to bulk modifications, such as diffusion of Cu and Ni within the wire's composition, given the small diameter of the wire (200 μm).

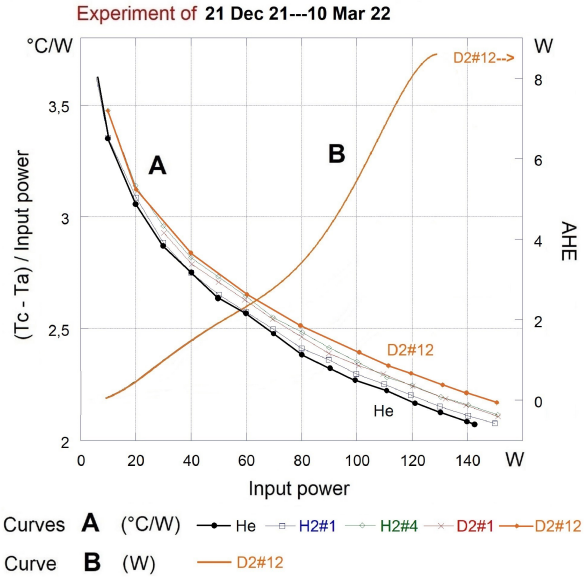

Figure 7. This illustrates the impact of substituting H2 with D2 on the behavior of the parameter (Tc-Ta)/(Input power) and AHE (anomalous heat effect). The most favorable outcomes were achieved after subjecting the system to 12 cycles of activation using high power and long durations. Specifically, the AHE under D2 (experiment D2#12) yielded an impressive power output exceeding 9 W, whereas the AHE under H2 (experiment H2#4) resulted in a power output of 5 W in the same experiment. It is important to note that the D2 experiments were conducted after the H2 experiments, potentially indicating a positive aging effect.

- An attempt was made to recover the high performance observed in H2#4 by changing the H_2 gas and subjecting the wire to a prolonged conditioning period of 113 hours at a high power of 152 W in experiment H2#6. However, this effort did not yield the desired results and further reduced the AHE performance.

In conclusion, the behavior of the low-cost material Constantan in terms of AHE and resistance variation (R/Ro) closely resembles that of the expensive material Palladium. This similarity allows us to leverage the extensive knowledge and research on Cold Fusion accumulated worldwide since 1989.

7. First Type of Experiment: Isotopic Effect (see Figure 7)

Isotopic Effect (3) (Experimental Run: 21 December 2021 - 10 March 2022).

During the extended period of operation under hydrogen and various high-power conditioning, we made a significant observation for the first time: an evident isotopic effect between hydrogen and deuterium. The specific experimental run lasted from 21 December 2021 to 10 March 2022. In previous experiments since 2011, the isotopic effects on Constantan wires after hydrogen absorption yielded inconsistent and often contradictory results, with AHE values under deuterium typically lower than those under hydrogen. In some instances, the deuterium values even fell below the calibration levels, resulting in an apparent “negative gain”.

Furthermore, we observed that the magnitude of the AHE depended on the wire’s previous “history” (resembling a memory effect), which could result in either a positive or negative impact on the AHE value. The highest recorded specific AHE value under D_2 was approximately 20 W/g of Constantan, occurring at wire temperatures ranging from

500-600 °C. The Constantan wire used in the experiment weighed only 0.45 g, and we can assume that the influence of specific glassy sheaths (several grams) and chemical coatings (<0.1 g) can be disregarded.

Taking into account these experimental findings, it becomes highly improbable to attribute the observed effects solely to unpredictable errors. The most plausible explanation is a deliberately controlled procedure, particularly in light of the consistent outcomes observed since July 2021 (as presented at ANV8, December 2021).

8. Superabundant Vacancies (SAV) as a Co-factor for Activation through Long-term Electromigration

The positive effects observed in experiments involving the flow of large current densities over extended periods, resulting in significant electromigration, can potentially be attributed to the intriguing phenomenon of Superabundant Vacancies (SAV) induced by hydrogen and/or deuterium [10], [11], [12], the primary gases employed in all Low Energy Nuclear Reactions-Atomic Hydrogen Effects (LENR-AHE) experiments. This hypothesis gains further support from the substantial increase in Anomalous Heat Effects (AHE) achieved through High Peak Power Pulses (HPPP) procedures.

Remarkably, one of our most noteworthy outcomes, published in Physics Letters A in 1996 [19], after some articles on simpler experiments [20], [21], [22], was obtained using the Pd-deuterium system, where pulsed electrolysis and electromigration were simultaneously employed. This historical finding underscores the potential role of SAV as an indirect yet potent mechanism contributing to the generation of AHE, complementing other established factors such as electromigration, Non-Equilibrium Metal Cathode Adsorption (NEMCA) [23], and the "Preparata effect" [24].

Superabundant vacancies have been identified as a novel phase that can form in various metals and alloys, including Ni, Pd, Pd-Rh alloys, Pd-Ag alloys, Ag, Rh, Pt, Au, Al, Cu, Cu-Ni alloys, Ir, Mo, Fe, Nb, Cr, Co, Mn, Ti, and Zr. These vacancies were first discovered in 1993 by Prof. Yuk Fukai and his Colleagues [25] at Tokyo University, Japan, through diverse methods such as wet electrolysis, high-temperature/high-pressure gas via anvil compression, co-deposited electrolysis, solid-state electrolysis (dry electrolyte), ion beam implantation, and plasma injection. The phenomenology of SAV, when applied to LENR phenomena, has recently undergone further development by Prof. M. Staker from Loyola University in the USA [10], [11], [12]. His studies provide confirmation that vacancies are generated through a phenomenon known as hydrogen-induced vacancy formation.

As the hydrogen activity (expressed as the D/M or H/M ratio, with M representing the metal) increases in metals and alloys, it leads to the creation and ordering of more vacancies. This state corresponds to the lowest free energy condition for the metal. Notably, this positive influence can be observed in Figure 5 and 6.

Electromigration, a phenomenon well-established since 1928 [26], also plays a role in the formation of surface-active vacancies (SAV) by facilitating the localized enrichment of the D/Pd or H/Ni ratio. When subjected to an electric current, it is believed that D+ or H+ ions migrate in the direction of the current flow. However, the counteracting influence of the "electron wind" also needs to be considered. In conclusion, further studies are necessary to validate our simplified explanation.

The attractive forces between vacancies and migrating ions lead to an augmentation of the local D/Pd or H/Ni ratio, thereby resulting in an increased presence of vacancies within that specific region.

In our research, we have utilized the same current employed for electromigration to measure the overall resistance of the PdD or NiH system, providing valuable insight into the D/Pd or H/Ni ratio. This simple methodology has allowed us to identify the optimal conditions for establishing a nuclear active environment (NAE), as defined by E. Storm. Remarkably, we have been following this procedure since 1991, unaware of the underlying phenomenology at that time.

9. Conclusions and Future Plans

In conclusion, we have successfully reconfirmed the procedure for the simple activation of surface-treated Constantan wires. As anticipated, this phenomenon is complex and has origins in both the surface and bulk properties of the

material. However, its effectiveness is limited by the requirement of prolonged operation at high power, often spanning several weeks.

Furthermore, we have identified the potential involvement of Superabundant Vacancies (SAV) as a hydrogen-enhanced co-candidate in explaining the origin of Anomalous Heat Effects (AHE). Nevertheless, in our opinion, the primary and final determinant of AHE generation remains the flux of the appropriate gas (H, D) through a suitable lattice. This finding has been consistently reported by researchers in the USA, Japan, Italy, and other countries since 1989 [3], [2], [27], [28].

It is worth noting that the gas flux is typically not spontaneous but requires external energy input. Therefore, our ultimate goal is to develop a procedure that minimizes the reliance on external energy. High Peak Power Pulses (HPPP) present a promising avenue for achieving this objective, and further optimization of this technique is warranted.

Drawing from our previous explorations of various operating points and the understanding of relevant chemical-physical conditions and phenomena (such as Child-Langmuir, Paschen/DBD, and skin effect), we aim to develop an energy-efficient reactor design suitable for practical everyday use.

Moving forward, our future plans involve conducting additional experiments to gain further insights into the underlying mechanisms of AHE and to refine our understanding of the interplay between surface and bulk effects. These efforts will contribute to the ongoing pursuit of harnessing cold fusion and anomalous heat effects for practical energy applications.

Acknowledgments

We would like to express our sincere gratitude to the Metallurgical Company in the North-Eastern part of Italy (NEMC) for their invaluable financial support and collaboration since 2011. Their independent cross-checking of our critical experiments in their own laboratories has significantly bolstered our confidence in the reported results.

We are also grateful for the ongoing collaboration with NEMC and SIGI-Favier (Italy-France) since 2017. Together, we have been working on the design and development of an original hybrid sheath (SE-SI) composed of Glass and Alumina-Quartz fibers. These sheaths, used for wire insulation in our experiments, possess exceptional thermal stability, operating continuously at temperatures up to 1050 °C. Their tailored geometry allows for the adsorption of significant amounts of Atomic Hydrogen, making them a crucial component of our experimental setup.

We would like to acknowledge Innovatiogen s.r.l. (formerly IFA, Roma-Italy) for their continued financial support, which has enabled us to cover laboratory consumables and travel expenses for conferences, workshops, and meetings, both within and outside Italy.

Special thanks are extended to the scientists involved in the CleanHME European project, led by Konrad Czerski (Szczecin University, Poland). We are particularly grateful for the fruitful collaboration with Prof. Bo Hoistad and his team at Uppsala University, Sweden, as well as Dr. Andras Kowacs from Broadbit Company. We are also indebted to Prof. Michael Staker from Loyola University, USA, for providing us with key insights into the Superabundant Vacancies (SAV) phenomenology.

Partial funding for this work has been provided by the European Union's Horizon2020 Framework Program under Grant Agreement #951974.

We deeply thank the Editor of the Journal, Prof. Jean Paul Biberian, and the Referees, because, thanks to their in-deep analysis/comments/criticisms/suggestions of our original manuscript, the paper was largely improved and is more understandable.

Disclaimer: The content and findings presented in this document are the sole responsibility of the authors and do not necessarily reflect the opinion of the entire CleanHME project.

References

[1] F. Celani and C. Lorenzetti, "Chapter 7 - Electrically induced anomalous thermal phenomena in nanostructured wires," in *Cold Fusion*, Amsterdam, Elsevier, 2020, pp. 101–113.

[2] G. C. Fralick, A. J. Decker and J. W. Blue, "Results of an attempt to measure increased rates of the reaction D-2 + D-2 yields He-3 + n in a nonelectrochemical cold fusion experiment," NASA-TM-102430, E-5198, NAS 1.15:102430 , Cleveland, 1989.

[3] F. Celani, "Talk at the "First Workshop on Cold Nuclear Fusion"," in *Summary by Richard L. Garwin, Nature Vol. 338 pg. 616-617, (1989). https://doi.org/10.1038/33861*, E. Majorana Centre for Scientific Culture, Erice (Italy), 1989.

[4] F. Celani, C. Lorenzetti, G. Vassallo, E. Purchi, S. Fiorilla, S. Cupellini, M. Nakamura, P. Cerreoni, P. Boccanera, R. Burri and A. Spallone, "Unexpected effects due to voltage waveform at anode, in gaseous LENR experiments based on sub-micrometric surface coated Constantan wires.," Researchgate. DOI: 10.13140/RG.2.2.21906.91846/1, Assisi (PG)-Italy, May 17-19, 2019.

[5] F. Celani, C. Lorenzetti, G. Vassallo , E. Purchi, S. Fiorilla, S. Cupellini, M. Nakamura, P. Cerreoni, R. Burri, P. Boccanera, A. Spallone and E. Marano, "Development of simple procedures to activate surface-coated Constantan wires and to induce AHE: the hunt for potential mistakes," Researchgate. DOI: 10.13140/RG.2.2.27006.66883, Assisi, 2021.

[6] F. Celani, C. Lorenzetti, G. Vassallo, E. Purchi, S. Fiorilla, S. Cupellini, M. Nakamura, P. Cerreoni, R. Burri, P. Boccanera, A. Spallone and E. F. Marano, "Stimulation of LENR-AHE by high power electric pulses on coiled coaxial Constantan wires at high voltage and temperature," ResearchGate. DOI: 10.13140/RG.2.2.10287.36009/2, 2020.

[7] F. Celani, E. F. Marano, B. Ortenzi, S. Pella, S. Bartalucci and S. B. F. Micciulla, "Cu–Ni–Mn Alloy Wires, with Improved Sub-micrometric Surfaces, Used as LENR Device by New Transparent, Dissipation-type Calorimeter," *J. Condensed Matter Nucl. Sci.,* vol. 13, pp. 56–67, 2014.

[8] F. Celani, C. Lorenzetti, Spallone Antonio, E. Purchi, S. Fiorilla, C. Stefano, M. Nakamura, E. Marano and P. Cerreoni, "Electromagnetic Excitation of Coaxially-Coiled Constantan Wires by High-Power, High-Voltage, Microsecond Pulses," *Journal of Condensed Matter Nuclear Science,* vol. 36, p. 408–435, 2022.

[9] F. Celani, E. F. Marano, A. Spallone, A. Nuvoli, B. Ortenzi, S. Pella, E. Righi, G. Trenta, F. Micciulla, S. Bellucci, S. Bartalucci and M. Nakamura, "Experimental results on sub-micro structured Cu-Ni alloys under high temperatures hydrogen/deuterium interactions," *Chemical Material Research,* vol. 3, no. 3, pp. 25–76, 2013.

[10] M. R. Staker, "Estimating volume fractions of superabundant vacancy phases and their potential roles in low energy nuclear reactions and high conductivity in the palladium – isotopic hydrogen system," *Materials Science and Engineering: B,* vol. 259, 2020.

[11] M. R. Staker, "How to achieve the Fleischmann-Pons heat effect," *International Journal of Hydrogen Energy,* vol. 48, no. 5, pp. 1988–2000, 2023.

[12] M. R. Staker, "The role of superabundant vacancy delta to delta prime transformation in stopping Fleischmann-Pons heat effect in palladium-deuterium," *International Journal of Hydrogen Energy,* vol. 48, no. 40, pp. 15195–15202, 2023.

[13] K. Ota, "Heat Production at the Heavy Water Electrolysis Using Mechanically Treated Cathode," in *Third International Conference on Cold Fusion, "Frontiers of Cold Fusion"*, Nagoya Japan, 1992.

[14] A. Takahashi, "Anomalous Excess Heat by D2O/Pd Cell under L-H Mode Electrolysis," in *Proceedings of the Third International Conference on Cold Fusion* , Nagoya, Japan, 1992.

[15] F. Celani, "Measurements of Excess Heat and Tritium during Self-Biased Pulsed Electrolysis of Pd-D2O," in *Proceedings of the Third International Conference on Cold Fusion*, Nagoya, Japan, 1992.

[16] C. M. D. Wan, "Repeated Heat Bursts in the Electrolysis of D2O," in *Proceedings of the Third International Conference on Cold Fusion.*, Nagoya, Japan, 1992.

[17] B. S. Ahern, "Amplification of Energetic Reactions". USA Patent US 2011/0233061, 29 9 2011.

[18] M. C. H. Kubre, "Calorimetry and Electrochemistry in the D/Pd system.," in *The First Annual Conference on Cold Fusion*, Salt Lake City, USA, 1990.

[19] F. Celani, A. Spallone, P. Tripodi, A. Petrocchi, D. Di Gioacchino, P. Marini, V. Di Stefano, S. Pace and A. Mancini, "Deuterium overloading of palladium wires by means of high power μs pulsed electrolysis and electromigration: suggestions of a "phase transition" and related excess heat," *Physics Letters A,* vol. 214, no. 1–2, pp. 1–13, 6 May 1996.

[20] F. Celani, A. Spallone, P. Tripodi, A. Petrocchi, D. d. Gioacchino, M. Boutet, P. Marini, V. D. Stefano, M. Diociaiuti and W. Collis, "Reproducible D/Pd Ratio >1 and Excess Heat Correlation by 1-μs-Pulse, High-Current Electrolysis," *Fusion Technology,* vol. 29, no. 3, pp. 398–404, 1996.

[21] F. Celani and A. Spallone, "High power μs pulsed electrolysis using palladium wires: evidence for a possible "phase" transition under deuterium overloaded conditions and related excess heat," in *Proceedings from ICCF5, 9-13 April 1995*, Montecarlo.
[22] F. Celani and A. Spallone , "High power μs pulsed electrolysis for high deuterium loading on Pd plates," in *Selected papers following ICCF4, Dec. 6-9, 1993*, Maui-Hawaii, 1994.
[23] C. G. Vayenas, S. Bebelis and S. Ladas, "Dependence of catalytic rates on catalyst work function," *Nature,* no. 343, p. 625–627, 1990.
[24] G. Preparata, "QED Coherence in Matter," 1995.
[25] Y. Fukai and N. Ōkuma, "Formation of Superabundant Vacancies in Pd Hydride under High Hydrogen Pressures," *Physical Review Letters,* vol. 73, no. 1640, 1994.
[26] A. Cohen, "Nachweis von Protonen in Metallen," *Naturwissenschaften,* vol. 16, pp. 183–184, 1928.
[27] Y. Iwamura, T. Itoh and N. Gotoh, "Characteristic X-Ray and Neutron Emission from Electrochemically Deuterated Palladium," in *Proc. 5th Int. Conf. Cold Fusion, Monte Carlo* , Monaco, 1995.
[28] Y. Iwamura, T. Itoh and M. Sakano, "Nuclear products and their time dependence induced by continuous diffusion of deuterium through multi-layer palladium containing low work function material," in *8th International Conference on Cold Fusion*, Lerici (La Spezia), 2000.

J. Condensed Matter Nucl. Sci. 38 (2024) 225–234

Research Article

Scaling up the Lattice Energy Converter

F. E. Gordon*
Inovl Inc., 2787 Curie Place, San Diego, CA, 92122 USA

H. J. Whitehouse
Inovl Inc., 6441 Del Paso Ave., San Diego, CA. 92120 USA

Abstract

Multiple Lattice Energy Conversion (LEC) devices and configurations have experimentally demonstrated the ability to self-initiate and self-sustain the production of a voltage and current through an external load impedance without the use of naturally radioactive materials. These results have been reported by the authors [1], [2], [3], [4] and replicated by independent researchers [5], [6], [7], [8], [9]. A video, [10] shows that a voltmeter and a resistance substitution box are all that is required to observe and measure LEC output which for this test produced several hundred nanowatts of power per square centimeter of working electrode surface area. Given the extraordinary nature of the LEC results, the importance of independent replications by multiple credible and respected scientists cannot be overstated. While the ability to self-initiate and self-sustain the production of a voltage and current through a load is a significant innovation, present experimental power densities are typically in the range of a few microwatts per square centimeter, output must be scaled up by 6 orders of magnitude to produce a few watts, and by 9 orders of magnitude to produce a few kilowatts. Based on a review of the literature and an analysis of experimental results, five focus areas have been identified to scale up the LEC. This paper examines each focus area and identifies possible actions to increase LEC power output.
 ISSN 2227-3123

Keywords: Direct energy conversion, contact potential difference

1. Introduction

Throughout history, many great discoveries resulted from mistakes or experiments that did not produce the anticipated results. Such is the case with the Lattice Energy Converter, (LEC). Initial experiments were designed to see if we could perform electrolysis through a dry gas by including radioactive sources to partially ionize the gas so a current could be conducted. However, analysis of these initial test results indicated that several orders of magnitude more conduction was being produced than that which the ions produced by the radioactive sources would support. Additional experimentation, in the absence of the radioactive sources, confirmed that when an electrode that had been codeposited with Pd-H was present, the gas was being ionized. This spontaneous ionization was not predicted for the gas densities,

*Corresponding author: feg@inovl.com

 ISSN 2227-3123

temperatures, and non-radioactive materials that were being used. A quote from *The Case-Book of Sherlock Holmes,* by Sir Arthur Conan Doyle states: "When you have eliminated all which is impossible, then whatever remains, however improbable, must be the truth." By following where our experiments were leading, we travelled from the improbable to the reality of the Lattice Energy Converter.

The evolution of the LEC began with experiments that produced surprising results including the realization that something was ionizing the gas between a pair of electrodes and those ions could be harvested to produce an electric voltage and current. Although the demonstrated electrical power levels were small, typically a few microwatts per square centimeter, these experiments were producing direct energy conversion.

The LEC has demonstrated the unexpected ability to spontaneously self-initiate and self-sustain the production of ionizing radiation without the use of naturally radioactive materials. This extraordinary discovery is supported by extraordinary evidence including our experimental results, peer reviewed papers [1], [2] presentations at international conferences [3], [4] and multiple independent replications by other scientists [5], [6], [7], [8], [9]. Although the demonstrated electrical power levels are small, experimental results indicate that multiple parameters can be optimized to increase the output. If successful, the LEC may address multiple critical applications including 'green' energy production, medical treatments, space applications, and applications yet to be identified.

In early experiments, JJ Thomson and E Rutherford applied an electric field between the electrodes to sweep out the ions that were being produced by a source of Röntgen rays. When there is a significant electric field, it is permissible to ignore the contribution that diffusion provides to the conductivity [11]. The first complete sets of equations known to the authors describing the gas dynamics of conduction including diffusion were "On a nearly saturated stream in an air space bounded by two concentric spheres" and "On approximately saturated currents between plane-parallel plates" by E Riecke [12], [13] and published in German. A translation of Riecke [13] is provided as an appendix to Gordon and Whitehouse, 2022 [2]. In this paper Riecke presents the equations using CGS ESU dimensions for the variables. Then, using the method of successive approximation, he calculates the distribution of the electric field withing the gas between plane-parallel electrodes. However, there is no motivation for the form of the equations or of the implication of the solution other than the results of the calculations can be used to estimate the recombination coefficient of the gas.

In 1932 Karl K Darrow, a Physicist at the Bell Telephone Laboratories, published a book, entitled *Electrical Phenomena in Gases*, [17] where he derives the gas dynamic conduction equations from first principles, including terms for the electric field and diffusion. Darrow also makes important observations of the physical implications of these equations. For convenience, an extract of this derivation and of its importance is presented as an appendix to this paper. The primary conclusion is that terms involving gaseous ion recombination and diffusion result in a pair of non-linear second order differential equations involving the electric field within the gas. This results in the electrical conduction of the gas being non-ohmic so that there can be a current through the gas even though the voltage between the electrodes is zero, *i.e*., a 'short circuit' current, or that there can be a potential difference or voltage between the electrodes even though there is no current flowing, *i.e*., an 'open circuit' voltage. This non-ohmic conduction is one of the major characteristics of self-initiating and self-sustaining LEC performance.

Neglecting the contribution of the diffusion of ions is justified when the electric field is sufficiently great so that the drift of the ions due to the electric field is much greater than the contribution to the current density by the diffusion of the ions [14]. This is the case when using the conduction of electricity through the gas as a method to measure the ionization of the gas caused by external ionizing radiation and quantifying the amount of this external radiation. However, when analyzing the performance of a LEC, diffusion of the ions must be taken into consideration when estimating the power that a LEC can deliver to an external load, and thus the distribution of the electric field becomes important. As an alternative to the use of successive approximation Tate in 1966 [24] provides multiple estimates of the electric field within the gas for different gas dynamics that can be numerically computed. He finds that even with some simplifying assumptions that the differential equation for the electric field between parallel electrodes is a 4^{th}-order non-linear differential equation.

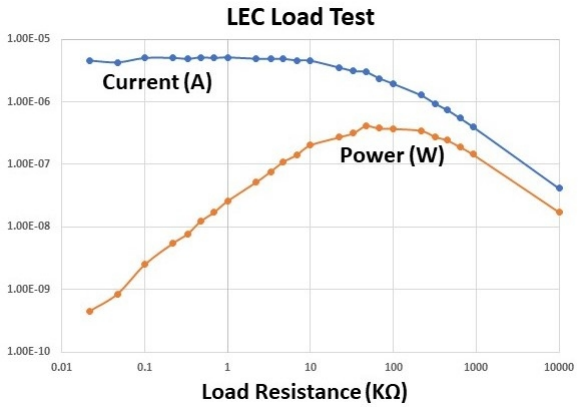

Figure 1. A typical plot of the current (A) and power (W) produced during a load test. As with most power supplies, the power peaks when the internal cell impedance matches the external load impedance

A standard way to characterize electrical power supplies is to measure open circuit voltage and short circuit current. In the case of the LEC, a 10 MΩ load resistance was used to measure the 'open circuit' voltage, and a 10 Ω load resistance to measure the 'short circuit' current. By measuring the voltage produced through intermediate resistance values, it is possible to calculate the current and power delivered to an external load as a function of resistance and temperature. Figure 1 is a typical plot of current and power as a function of load resistance for a given temperature.

Analysis of experimental results indicates that LEC performance is strongly dependent on the non-linear interactions between multiple parameters such as electrode preparation, electrode separation distance, cell temperature, and the physical properties of the gas [15], [16], [17], [18], [19]. For example, depending on the source and type of ionizing radiation, ionization is expected to increase as the number-density (fill-pressure) of the gas is increased. Thus, gas-ion dynamics is important. Ohmart [20] and RCA [21] report that the work functions of the electrodes also have a role in the performance of cells containing ionized gas even though the gas within the cell is ionized by an external source of ionizing radiation. The importance of the work function of the electrodes on the performance of a LEC is presented in Gordon and Whitehouse [2]. What is surprising is the important role that is played by the diffusion of the ions, *e.g.,* diffusion of positive ions to the positive electrode of the LEC cell. As shown in Fig. 2, electrons flow from the low work function electrode through the external load to the high work function electrode. However, to complete the circuit within the cell, more negative ions than positive ions must flow to the low work function, negative electrode, where they deposit an electron while more positive ions than negative ions must flow to the high work function, positive electrode, where they acquire an electron. Ion diffusion and gas dynamics contribute to this behavior. This is counter-intuitive since electrons normally flow to the electrode with a more positive charge, such as what happens in the electrical circuit that is external to the cell.

2. Increasing LEC Power

The big challenge with all direct energy conversion devices is the number of charge carriers that are required to produce useful power. One ampere of current requires approximately 6.24×10^{18} charge carriers per second. The number of Becquerels produced per second by one Curie of radiation which is 3.7×10^{10}. Even using unreasonably optimistic assumptions that each high energy particle emitted from a radioactive source can ionize 10^5 ions, and if all of the ions produced are collected by the electrodes before they recombine, it will still take more than 1000 Curies of radioactive material to produce 1 amp of current. One commercial atomic power source is advertised as producing

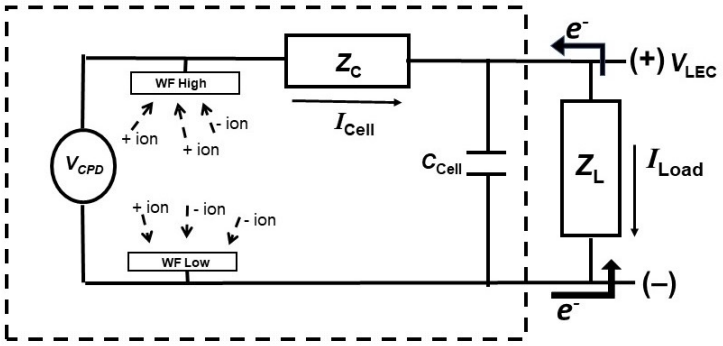

Figure 2. By convention, current flows from the positive to the negative electrode which means that electrons are flowing from the negative (low work function) electrode through the external load impedance Z_L to the positive (high work function) electrode. However, to complete the circuit, more negative ions than positive ions need to flow to the negative electrode while more positive ions than negative ions need to flow to the positive electrode within the cell. Ion diffusion and gas dynamics contributes to this behavior.

100 milliwatts of power from a 100 Ci tritium source [22]. To scale that up to produce 10 watts would require 10,000 Ci of tritium. This requirement has limited the application of direct energy conversion devices that rely on radioactive materials to produce ionized particles. On the other hand, unlike nuclear devices where the primary option is to increase the radioactivity, LECs do not require naturally radioactive materials and experimental results indicate that there are multiple opportunities to increase output power.

Based on experimental results and the equations derived by Darrow, [17] five interconnected/nonlinear focus areas, that may not be independent variables, have been identified that may increase LEC output by 6 to 9 orders of magnitudes include:

1. Improved metallurgy to increase the ionization rate to increase the gas ionization;
2. Optimize gas dynamics involving mobility, diffusivity, initial pressure, gas composition;
3. Improved LEC cell configurations such as electrode separation to increase gaseous ion harvesting efficiency;
4. Optimize temperature to increase the number of ions being produced, as well as their diffusion, leading to a corresponding increase in power output; and,
5. Increased electrode surface area.

2.1. Improved Metallurgy to Increase the Production of Ionizing Radiation

The lattice dynamics required to produce the ionizing radiation remains a subject of much discussion among LENR theorists. However, there is considerable evidence that ionizing radiation is being produced by an electrode that is codeposited with Pd or Fe that is occluded with hydrogen or deuterium. Extensive testing at the Bahaba Atomic Research Center in India by Dr. Srinivasan and others in the early 1990s showed that radiation would fog film, but even using very sensitive instruments, they were unsuccessful in detecting and identifying the type of radiation [23]. A LEC shows that the radiation being produced is sufficient to ionize a gas between two electrodes and that the ions thereby produced can be harvested to produce a voltage and current through a load. LEC experimentation suggests that the ionization is being produced by a few localized active sites. Better metallurgy to increase the number of active sites could increase the number of ions being produced, leading to increased LEC output. A target increase of the production of ionizing radiation could provide 1 to 2 orders of magnitude increase in power output.

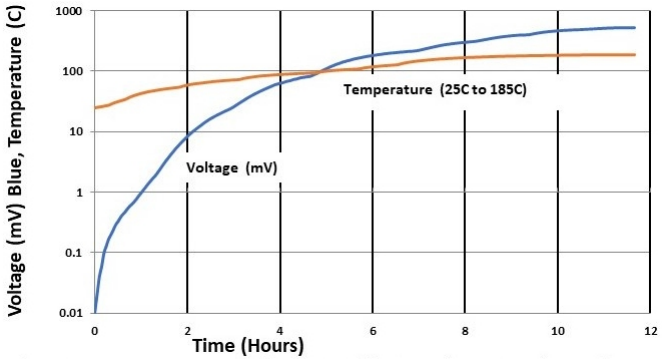

Figure 3. As Temperature increased from 25° C to 100° C, voltage increased approximately 4 orders of magnitude (Z128G22vi05 data set)

2.2. Increase Gaseous Ionization Production

Optimizing gas density (initial pressure) to ensure that the energy being emitted from the active material (Pd-H of Fe-H) will be exhausted producing ions is another way to increase the number of ions that are produced. Additionally, it is possible to use gas mixtures such as Penning gases that require fewer electron volts per ion pair produced. Optimization of gas ionization production could provide an improvement of 1 to 2 orders of magnitude.

2.3. Improved LEC Cell Configurations to Increase Gaseous Ion Harvesting Efficiency

Based on experiments where an external voltage is applied to produce an electric field that sweeps out the ions being produced before they can recombine, we estimate that in the absence of a strong electric field, the LEC is harvesting approximately 0.1% of the ions being produced with the majority of ions being recombined. Understanding the importance of electric field and diffusion on gas ion dynamics could be important to increase ion harvesting efficiency. The importance of the physical position and separation of the electrodes depends on both the type of ionizing agent or agents; as well as the distribution of the ions within the gas. For heavy particles, such as protons [25] and α-particles, [26] large electrode spacings may be appropriate while for light electrons [27] the electrodes may be closer together. Thus, it is important to determine the distribution of ions within the gas and the role that electrode shape and position have in LEC design. The authors believe that increasing the efficiency of ion harvesting can produce an improvement of 1 to 2 orders of magnitude in power output.

2.4. Optimize LEC Temperature Leading to Increase Power Output

Multiple experimental results and supporting analysis indicate that the number of ions being produced and harvested increases with temperature. As shown in Fig. 3, approximately 2 - 3 orders of magnitude increase occurred when the temperature was increased from approximately 22 °C to 80 °C and approximately 4 orders of magnitude increase when the temperature was 100 °C. This is encouraging in that even modest temperature increase will produce a significant increase in LEC output, and based on experimental results, it appears that a target of 2 – 3 orders of magnitude increase in power is reasonable with a higher temperature.

2.5. Increased Electrode Surface Area

Increasing the surface area of electrodes is the most obvious opportunity to increase LEC output. The experimental data has been normalized to power per square centimeter of electrode surface. Increasing from 1 square centimeter to

1 square meter increases the surface area by 4 orders of magnitude. In this regard, plane-parallel cell designs which will allow significant increases in surface area are being tested. Based on experimental results, a target of 3 to 4 orders of magnitude by increasing surface area is reasonable.

For each of the five focus areas, experiments and analysis are required to:

1. Identify the source and type of ionizing radiation emitted from the working electrode;
2. Identify the role that the counter electrode may play in ionizing the gas;
3. Identify gases and mixtures that optimize the production of ions; and,
4. Analyze the gas ion physics within the cell which is a 4^{th}-order nonlinear differential equation.

Supporting analysis of experimental LEC results will provide important information in LEC cell designs. Attempting to optimize a nonlinear process that involves several variables based on experimentally produced empirical information alone is a challenging problem.

3. Conclusion

Based on the experimental results and theoretical analysis, although there is much work to be done, and even though the focus areas for improvement may not all be independent, it appears that it might be possible to increase the LEC power output by the 6 to 9 orders of magnitude required to become a useful power source.

Appendix: Flow of Ions Under the Joint Influence of Fields and Concentration-Gradients

Quoting from Karl K. Darrow, Electrical Phenomena in Gases, Chapter V, (1932) 189–194

"In this section I will derive some general equations for the distribution and flow of ions through gases which are constantly being ionized by rays from without. These equations and the ways of verifying them were much considered, ten to thirty years ago; perhaps hereafter they will again be useful.

Consider a layer of gas between two infinite parallel plane electrodes a distance *L* apart; imagine that ions are being formed throughout its volume at a constant rate, *q* positive and *q* negative appearing per unit volume per unit time. Lay the axis of *x* perpendicular to the plates, with *x* increasing from anode to cathode. Consider the current-flow through a column of gas extending from unit area of the cathode to unit area directly opposite on the anode; the current this column will be the same as the current-density *i*. Everything will depend on *x* alone.

With too low a potential-difference between the electrodes and therefore too low a field strength, some of the ions will be lost by recombination (Chapter VIII) or by diffusing to the wrong electrode, positives wandering to the anode and negatives to the cathode. With too high a field strength primary ions will engender new ones (Chapter IX). If the density of the gas is not too high, there will be an intermediate range of field strengths, over which all the primary positives will be drawn the cathode and all primary negatives to the anode (Chapter IX). The current-density will then have its "saturation" value i_s:

$$is = qLe \tag{60}$$

A relation which gives a way of measuring q.

Denote by n_1 the number of positive ions per unit volume, by μ_1 their mobility, by D_1 their coefficient of diffusion, by *E* the field strength. The field causes a drift of ions over the cross-section, amounting to $n_1\mu_1 E$ of these particles per second.[10] But this is not the whole of the drift, unless the concentration is everywhere the same, which we should not assume to be the case even if the ionizing rays are everywhere equally strong. If n_1 varies with *x* there is a concentration-gradient dn_1/dx, and the drift is the sum of $n_1\mu_1 E$ and an extra term – $D_1(dn_1/_{\mathrm{dx}})$. This multiplied by *e* is the contribution of the positive ions to the current-density at *x*. Denoting by n_2, μ_2 and D_2 the concentration,

mobility, and coefficient of diffusion of the negative ions, we have for their contribution the product of *e* into the sum[11] of n_2 $\mu_2 E$ and + $D_2(dn_2/dx)$. Adding we obtain for the current-density the formula,

$$i = e[(n_1\mu_1 + n_2\mu_2)E + (D_2 dn_2/dx - D_1 dn_1/dx)] \tag{61}$$

and since it must be independent of x (otherwise there would be piling up or dwindling away of charge in various regions of the gas, contrarily to our tacit assumption that the state of affairs is unchanging) the right-hand member like the left-hand member is equal to a constant.

This differential equation, however, does not help us much by itself, for it involves the two functions n_1 and n_2, not to speak of *E* which (as we shall later see) is very likely to vary with *x*. We require a pair of equations for n_1 and n_2; and such we can obtain by invoking what is known not only about mobility and diffusion, but about generation and recombination of ions. Consider any slice of the column, between planes at *x* and *x* + *dx*. In this slice, *qdx* ions of either sign are being generated per second, and $\alpha n_1 n_2 dx$ of either sign are vanishing per second by recombination.[12] In addition, there is the possibility that more may be drifting through one side of the slice than through the other. Let us take account of the positives first. Through the side *x*, into the slice their drift per second the number ($n_1\mu_1 E$ – $D dn_1/dx$) of them, all the variables in the parenthesis being evaluated at *x*. Through the side *x* + *dx*, *out of* the slice, their drift per second a number given by the same expression, except that now all the variables are to be evaluated at *x* + *dx*; we have:

$$(n_1\mu_1 E - D dn_1/dx)x + dx = (n_1\mu 1_E - D_1 dn_1/dx)x + (\mu_1 d(n_1 E)/dx - D_1 d^2 n_1/dx^2)dx \tag{62}$$

The difference between these is the net rate at which the positive ions in the slice tend to increase because of drift. Now adding together the rate of generation of ions in *dx*, and the rate of disappearance through recombination, and the rate of increase because of drift, each with its appropriate sign according as it is gain or is loss, we have for the rate of change of the number of positives in the slice *dx*,

$$d(n_1 dx)/dx = q dx - a n_1 n_2 dx - (\mu_1 d(n_1 E)/dx - D_1 d^2 n_1/dx^2)dx \tag{63}$$

But in the steady state, n_1 must be unchanging; so, dividing out *dx*, we get a differential equation involving n_1 and n_2 and space-derivatives of n_1; there is a corresponding equation to be obtained by thinking in the same way about negative ions, and writing both of them down together, we have:

$$\begin{aligned} q - a n_1 n_2 + D_1 d^2 n_1/dx_2 - \mu_1 d(n_1 E)/dx = 0 \\ q - a n_1 n_2 + D_2 d^2 n_2/dx_2 + \mu_2 d(n_2 E)/dx = 0 \end{aligned} \tag{64}$$

I pause to point out that equation (61) may be derived from these by subtracting one from the other, and integrating once with respect to *x*.

It now seems as if everything in the discharge—the current-strength, the distribution of the ions of both signs, and so forth—is determinate once we know the rate of generation of ions, and the values of the coefficients α, μ_1, μ_2, D_1 and D_2, and the proper boundary-conditions. But there is still something new to be taken into account: the variation of field-strength *E* with *x*. Since we have been assuming that the gas is enclosed between two parallel plates, it seems natural to put E constant and equal to the quotient *V/L* of the potential-difference between the plates by the distance between them. Not so: the field strength cannot be constant in any region where the density of charge of one sign differs from that of charge of the other sign; for then there is a net density of charge different from zero, there is a space-charge which by Poisson's formula of electrostatics must entail a value of *dE/dx* different from zero. In this special case, where the net density of charge is $(n_1 - n_2)e$, Poisson's formula yields the equation:

$$dE/dx = -4\pi(n_1 - n_2)e \tag{65}$$

so that we have a family of three differential equations involving the three functions n_1, n_2, E of the independent variable x. In dealing with them we must replace the too-simple assumption that E is equal to the quotient V/L by the general statement that the integral of $E(x)$, taken across the gas from $x = 0$ to $x = L$ is equal to V.

I do not, however, wish to enter yet into the questions involving space-charge; a later chapter is to be devoted to that subject. Space-charge would play no part, of course, if n_1 and n_2 were equal; but this is a condition which the difference in mobility of the two kinds of ions makes difficult to approach—one easily sees that if carriers of both signs are generated at an equal rate, and the negatives drift faster than the positives, there will be fewer negatives than positives at any moment between the plates. However, it is interesting to simplify the equations in the way which would be permissible, were n_1 and n_2 sufficiently nearly the same. Recombining equations (64) into equation (61), making n_1 and n_2 equal and denoting each of them by n, we get:

$$i/e = n(\mu_1 + \mu_2)E + (D_2 - D_1)dn/dx \tag{66}$$

an equation easy to integrate when the mobilities and diffusion-coefficients are assumed independent of x. What is peculiarly interesting is that E and i do not necessarily vanish together. Let us put i equal to zero: then integrating (66) under the stated assumptions, we get:

$$\log n = (\mu_1 + \mu_2)Ex/(D_2 - D_1) + const. \tag{67}$$

Denoting by n_0 and n_L the values of n at the two plates, $x = 0$ and $x = L$ respectively: we get:

$$\log n_L/n_0 = (\mu_1 + \mu_2)EL/(D_2 - D_1) = (\mu_1 + \mu_2)V/(D_2 - D_1) \tag{68}$$

Recalling equation (59) [$D/\mu_e = 2U/3$] of page 188, and denoting by U_1 and U_2 the values *in equivalent volts* of the mean kinetic energy of the positives and the negatives respectively, and expressing *V in volts* (not E. S. U.), we find:

$$\log n_L/n_0 = (3/2)(\mu_1 + \mu_2)V/(U_1\mu_1 - U_2\mu_2) \tag{69}$$

These equations are to be interpreted as follows. Suppose that ions of the two signs are spread identically through a gas between two walls—by "identically" I mean that everywhere the concentrations of the two kinds are equal, though their common value varies from place to place—and that the state of affairs is stationary. Then there must be ionizing rays acting continually on the gas, and also there must be a potential-difference between the walls. For if there were no field, the negatives would diffuse along the concentration-gradient more rapidly than the positives; there would be a net current; this would result in a depletion of negatives, and an excess of positive charge would arise in the gas, in contradiction with the assumption. But suppose there is a P.D. between the walls, in such a sense as to oppose the negatives and pull the positives forward as they stream together down the gradient. A value for this potential-difference can be found, such that the field strength will retard the negatives and encourage the positives just sufficiently to annul the net current aforesaid; and that is the value determined by equation (69).

This is another illustration of the principle which we have met already and shall meet again in the chapter on diffusion. Uneven distribution of ions act like an electric field in that it tends to cause an ion-flux, a current of electricity. In other and more conventional words, a non-uniform distribution of ions entails an "electromotive force." Or, in morae conventional terms, to annul the current a real potential-difference must be applied to compensate the electromotive force.

Equation (69) provides the formula for this compensatory P.D.—we might as well say the formula for the electromotive force itself—in a special case: that in which the densities of charge of the two signs are everywhere equal. Various "test" experiments have been made in conditions where this last was not *a priori* certain: as for instance one by Wood, de Long and Compton,[13] who set up two parallel plates bounding a stratum of gas, and applied ionizing rays (X-rays) to a thin sheet of the gas near one of the plates. They measured the values n_0 and n_L of the concentrations

near each of the plates (by applying a relatively strong field for just the time required to sweep into one of the plates all the ions of one sign within a fraction of a millimetre thereof) and the voltage which had to be applied across the gas in order to bring to zero the current flowing while the rays were shining. The ratios of n_0 to n_L were of the order of four or five to one: in these experiments, the calculated values of *V* were .0050, .0053 and .0063, while the corresponding measured values were .0042, .0034 and .0067.

[10]It is assumed that the variations of *E* from place to place are so gradual, that at each point the drift-speed of the ions has sensibly the terminal value corresponding to the there-prevailing field strength.

[11]Here, as in so many other cases, it is simpler and safer to decide from "physical considerations" what the signs of the various terms should be, than to keep in mind the proper signs of all the factors. If *E* is positive, the positive ions on the one hand and the negative ions on the other are pushed each in the proper direction (the positives towards the cathode, the negatives toward the anode) to make a positive contribution to the current if dn_1/dx is positive, the positives tend to diffuse in the wrong direction (away from the cathode); if dn_2/dx is positive, the negatives tend to diffuse in the right direction (towards the anode).

[12]See Chapter VIII.

[13]E. B. Wood, O. A. de Long & K. T. Compton, **PM** (6) **32**, 499-504 (1916). Earlier work of this kind had been done by J. Zeleny and W.H. Jenkinson."

Comments: The reader should note that the unit system used for *expressing* the equations is presented using CGS ESU. Also, in equations 67, 68, and 69, log should be read as the natural logarithm, ln.

Acknowledgments

The authors would like to recognize the following: ICCF 24 organizing committee, LEC replicators, Jean-Paul Biberian, Fabrice David, Antonio Di Stefano, Andrew Erickson, and Alan Smith, as well as Ruby Carat and the organizers of the LENR Forum and the LENR Forum discussion participants.

References

[1] F. Gordon, H. Whitehouse, "Lattice Energy Converter" *J. Condensed Matter Nucl. Sci.* 35, (2022).
[2] F. Gordon, H. Whitehouse, "Lattice Energy Converter II" *J. Condensed Matter Nucl. Sci.* 36, (2022)
[3] F. Gordon, H. Whitehouse, "Lattice Energy Converter" presentation at Dr Srinivasan memorial workshop, 2021 available at: https://www.youtube.com/watch?v=J4dzTWY_aWM
[4] F. Gordon, H. Whitehouse, "Lattice Energy Converter" presentation at ICCF 23, 2021, available at: http://ikkem.com/iccf23/PPT/Invited%20Gordon%20ICCF%2023%20LEC%20T5.MP4
[5] JP Biberian, "LEC replication presentation" IWAHLM 14 Conference" 2021 available at: https://www.youtube.com/watch?v=fUsKv1af1DQ&list=PLpEPF2v_du9RtHUeW8nHusCaoC68zOMuX&t=2129s
[6] G.A. Erickson, Private Communication with Frank Gordon, Jan. 2021
[7] A. Di Stefano, "Experimental Observations on the Lattice Energy Converter." Preprint of ICCF 24, In press JCMNS
[8] A Smith, "Anomalous Electrical Output from Room-Temperature Reactors" IWAHLM 14, 2021 https://www.lenr-forum.com/attachment/18631-assisi-iwahlm-2021-presentation-final-pdf/
[9] F. David, "Direct conversion of LENR inside Solid-State Fusion Diodes" Poster at ICCF 24 July 2022. https://docs.google.com/presentation/d/1_UnVbp-M5FaQsQZdapNqjtGGM1t-azyE/edit#slide=id.p1
[10] F. Gordon, H. Whitehouse, "Lattice Energy Converter update" 2022, available at: https://youtu.be/yO-KIGKVHkI
[11] J.J. Thomson, E. Rutherford, XL. On the Passage of Electricity through Gases exposed to Röntgen Rays, *Phil. Mag*. S5 **42** (1896) 392–407.
[12] E. Riecke, "Über nahezu gesättigten Strom in einem von zwei konzentrischen Kugein begrenzten Luftraume" Annalen der Physik **317** 12 (1903) 814–819
[13] E. Riecke, "Über näherungsweise gesättigte Ströme zwischen planparallelen Platten" Annalen der Physik **317** 12 (1903) 820–827

[14] B.B. Rossi, H.H. Staub, *Ionization Chambers and Counters*, McGraw-Hill Book Co. 1949
[15] JSE Townsend, *Electricity in Gases*, Chapter III, (Oxford at the Clarendon Press, UK, 1915)
[16] J. Thomson, G. Thomson, *Conduction of Electricity Through Gases*, Vol. I, 3-rd edition, Cambridge University Press, UK, 1928, pp. 193–214.
[17] K.K. Darrow, *Electrical Phenomena in Gases*, (The Williams & Wilkins Co. Baltimore, MD, 1932). Also available online at Google Books
[18] L.B. Loeb, Fundamental Processes of Electrical Discharges in Gases, (John Wiley & Sons, 1939).
[19] L.B. Loeb, *Basic Processes of Gaseous Electronics*, (University of California Press, 1960).
[20] P. F. Ohmart, A Method of Producing an Electric Current From Radioactivity, *J. Appl. Phys.* **22** (1951) 1504.
[21] Radio Corporation of America, The Direct Conversion of Radiation into Electrical Energy, RB 3 1955.Available at http://www.one-electron.com/Archives/RCA/RCA-RB/RCA-RB.html
[22] City Labs, Nano $Tritium^{TM}$ battery, https://citylabs.net/products/
[23] R. K. Rout, *et al.,* Reproducible, anomalous emissions from palladium deuteride/hydride. *Fusion Technol.* **30** (1996) 273. Also available from http://www.lenr-canr.org/acrobat/RoutRKreproducib.pdf
[24] P.A. Tate, Effect of Diffusion on the Saturation Curve of a Plane Parallel Ion Chamber, *Phys. Med. Biol.* **11**(4) (1966) 521–532.
[25] National Institute of Standards and Technology, PSTAR https://physics.nist.gov/PhysRefData/Star/Text/PSTAR.htm
[26] National Institute of Standards and Technology, ASTAR https://physics.nist.gov/PhysRefData/Star/Text/ASTAR.html
[27] National Institute of Standards and Technology, ESTAR https://physics.nist.gov/PhysRefData/Star/Text/ESTAR.html

J. Condensed Matter Nucl. Sci. 38 (2024) 235–244

Research Article

LENR Research Documentation Initiative: What Have We Learned So Far?

Thomas W. Grimshaw*

LENRGY, LLC, 3571 Far West Blvd, Austin, Texas, 78731, USA, Ph: 512.784.1078

Abstract

Humankind desperately needs new sources of energy. Global climate change and the environmental damage caused by fossil fuels threaten the very habitability of the earth. Cold fusion (LENR) has the potential to address these issues and improve the prospects of humanity. The potential energy benefits of LENR were well understood when it was announced in 1989. Although the field was rejected by mainstream science, many capable researchers worldwide continue to pursue it to realize its potential benefits. Because many of them are now retired or dead, the LENR Research Documentation Initiative (LRDI) is underway to preserve their records while they are still available. LENR researchers and collaborators are participating in the LRDI. A site visit is usually made to survey and document records and to conduct interviews. When possible, a timeline of research activity is developed. A report is prepared, and arrangements are made for preserving and archiving records. Much has been learned in several categories in the four years since the initiative was started: 1) the participants and their LRDI projects; 2) the nature and content of the LENR records; 3) interviews and transcriptions; 4) the reports prepared for each project; and 5) the arrangements for preserving and archiving the records. The effects of continued LENR rejection have also been documented in the LRDI projects. The LRDI has many opportunities for future progress, such as expansion with new projects, extension of the findings of previous projects, and LENR advocacy through demonstration of the high quality and very large amount of research. The LRDI's ultimate objective is to advance the cause of LENR to realize its energy potential for the benefit of humankind.
 ISSN 2227-3123

Keywords: LENR Research, Research Documentation, Cold Fusion Records, LENR Energy Benefits

1. Introduction

Humanity's dependence on fossil fuels for energy has resulted in profound threats to the habitability of the earth. Major efforts and resources have been expended for over 50 years to deal with near-surface effects of energy production and use, such as smog, acid rain, water pollution, and radiation hazards. In more recent decades, global climate change – caused primarily by use of fossil fuels – has emerged as an even greater threat to our existence. It is clear that the future of humankind depends on finding new more suitable sources of energy. Alternative sources to fossil fuels, such as solar- and wind-produced energy, are helpful for addressing these critical issues.

*Corresponding author: thomaswgrimshaw@gmail.com

 ISSN 2227-3123

Cold fusion (CF) has major potential not only to displace fossil fuels, but also to provide energy in applications and areas where energy is not currently available. CF (now also called low energy nuclear reactions, LENR) was announced by Fleischman and Pons in 1989, only to be rejected by mainstream science within a year or so. People understood the immense potential energy benefit of LENR when it was announced. Despite the rejection, LENR has continued to be researched by many capable scientists around the world, and a massive amount of evidence for the reality of LENR has been accumulated.

Many of the investigators who have pursued LENR despite the rejection began their work in the early years after the announcement, and now, more than 30 years later, many are leaving the field because of old age or death. In large part because of the rejection, the researchers' records have not been systematically recorded and preserved. Because these records may eventually help understand LENR and achieve its benefits, their loss would be a tragedy not only for the field, but also for all of humankind. The LENR Research Documentation Initiative (LRDI) has been undertaken to help mitigate this loss [1], [2]. Much has been learned in the more than four years since the initiative was started.

2. Overview: What Kinds of Lessons Have Been Learned in the LRDI?

The LRDI works with investigators to document and preserve their research records and to understand their pursuit of LENR through interviews. An overall procedure [3] has been developed as shown in Figure 1.

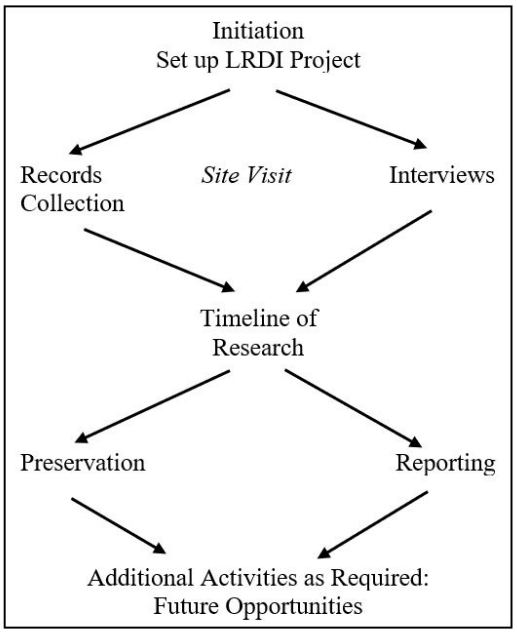

Figure 1. LRDI Procedure.

In summary, when agreement is reached with a researcher, a visit is usually made to survey and document the records and to conduct one or more interviews. Where possible, a timeline of LENR activities is developed. Interviews are usually conducted in person during the site visit. A report is prepared, and arrangements are made for preserving

and archiving the records. Information that could be added after the project is completed is identified and included in the report as "future opportunities".

The procedure was developed in a pilot project with Dr. Edmund Storms in Santa Fe, New Mexico. The initiative began in 2018 as a poster on Dr. Storms' LENR records presented at ICCF-21 [4]. Much has been learned in several categories as the LRDI has proceeded:

- Participants
- Projects
- Records
- Interviews
- Reports
- Preservation and Archiving
- Overall Status of the LENR Field

2.1. Participants

The current and previous participants are listed in Table 1. Some projects have more than one participant, such as where the researchers are collaborating. Four of the participants, Charles Beaudette, Mahadeva Srinivasan, Peter Gluck and Ludwik Kowalski, have died since their documentation projects were completed. Hal Fox and Stan Szpak had died before their projects were performed.

Table 1. LRDI Participants and Collaborators.

Beaudette, Charles*	Gordon, Frank*	Miley, George
Biberian, Jean-Paul	Hagelstein, Peter	Mossier-Boss, Pam*
Carat, Ruby*	Hubler, Graham*	Nagel, Dave
Celani, Francesco	Kowalski, Ludwik*	Passell, Tom
Claytor, Tom	Letts, Dennis	Pease, Dennis
Dolan, Tom*	Little, Scott	Rothwell, Jed*
El-Boher, Arik	Little, Marissa	Srinivasan, Mahadeva*
Forsley, Larry*	Lomax, Abd	Storms, Ed
Fowler, Malcolm	Marriott Library**	Szpak, Stan*
Fox, Hal*	Miles, Mel	Tanzella, Fran
Gluck, Peter*		

* Site visit not available or not required
** University of Utah

The interactions with the LRDI participants have resulted in many favorable subjective opinions on the part of the author. As researchers, the participants have been found to be competent, creative, conscientious, highly experienced, dedicated and driven in their work. As human beings, the strong impression is that they are professional, honest, articulate, competitive, original, opinionated, hard-working, and personable. Regarding their projects, the participants are supportive, open, cooperative, receptive, engaging, and enjoyable to work with. The overall observation is that the participants are very capable scientists are doing highly sophisticated experiments to solve the LENR riddles.

Many of the participants have laboratories for their LENR research (Figure 2). Different methods (e.g., electrolytic, gas loading), signatures (e.g., excess heat, very low levels of radiation), and facilities (ranging from small backyard labs to major university buildings) are utilized.

Figure 2. Francesco Celani (Left) and Tom Grimshaw during a Site Visit at Celani's LENR Laboratory on the INFN Campus, Frascati, Italy, September 2022.

2.2. Projects

The LRDI functions as a program with individual projects for participants. The projects are conducted in accordance with standard project management procedures. Approximately 21 projects have been performed or are ongoing under the LRDI umbrella as shown in Figure 3, where the projects are shown generally in order of initiation from left to right.

The LRDI procedure has been found to be effective in practice, but flexibility is required to meet the specific needs of each participant. It has also been found that the site visit to the participant is important to conduct a hands-on review of the records and conduct the interviews. Some projects are undertaken where the participant is no longer available, but the records are nevertheless important to the LENR field. So far, these "legacy" projects have been for describing websites or utilizing hard copy or electronic files from sources other than the author.

Relatively modest resources are needed for LRDI projects. A major cost element is the travel for site visits and to present results at conferences. The need for equipment portability for site visits is an important LRDI lesson. Several types of equipment are utilized:

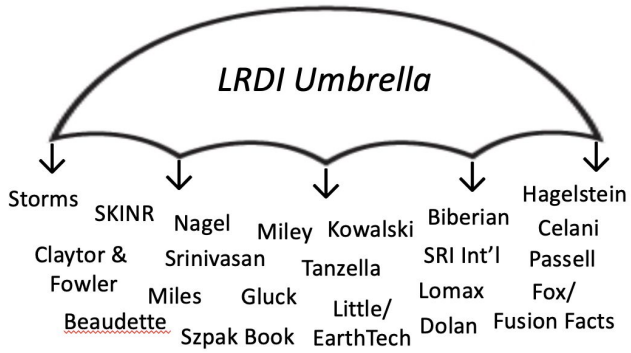

Figure 3. The LRDI Umbrella of Projects.

- Laptop computer
- External electronic files storage, such as USB flash drives and stand-alone hard disks
- Sheet-feed scanner for hardcopy files
- Printers for site visits and report preparation
- Multi-function phone for communication, taking photos, recording interviews, and hardcopy scanning (for materials not suitable for the sheet-feed scanner)

2.3. Records

A major observation in the LRDI is the very large amount of LENR records that are available. Many participants have kept the results of their investigations and activities going back to their original entry into the field. The records comprise both hardcopy and electronic files.

In general, the records fall into two categories – documents, such as publications and reports, and electronic data. Several variables determine the extent and type of records held by an LRDI participant:

- Original type of information collected – documents vs. data
- Methods of collecting and recording the information
- Completeness of the original records
- Methods and results of data analysis
- Storage media used, such as file cabinets and hard disks
- Retention and preservation

When an LRDI site visit is made, the search for records encompasses several categories:

- Publications and presentations
- Unpublished reports
- Hardcopy records in boxes and file cabinets
- Electronic files in current and legacy media
- LENR laboratory, if present, including methods, signatures, and facilities and equipment
- Lab notebooks
- LENR library, including ICCF conference proceedings, collections of books in the field, copies of journals and magazines, and virtual media (e.g., photos, tapes, DVDs)

Each time a component of the records – such as hardcopy files – is found, a memo is prepared with details of the record. The development of the digital age in the same timeframe as LENR research and other activities since 1989 has had a major impact on the participants' storage of information. Many of the electronic records have been found in legacy media, such as floppy disks (Figure 4) and obsolete stand-alone hard disks.

Figure 4. Carousel of 3 1/2-Inch Floppy Disks Containing Edmund Storms' Early Electronic Files.

2.4. Interviews

The interviews of the participants have been found to be almost as important as the records documented. They serve as a complement to the documentation and are necessary for developing a timeline of research and other LENR activities. The interviews serve as the "glue" for the records information in LRDI reports. Questions that are typically asked include:

- What were you doing at the time of the 1989 announcement?
- How did you learn about it? What was your initial reaction?
- When did you first become involved in the field?
- What have you been doing since then, and what are you doing now?
- Are you convinced that LENR is a real phenomenon? If so, what do you think is the best evidence for its existence?
- Tell me a little about yourself. Where were you born? Where did you go to school? What are your other professional interests besides LENR?

With the concurrence of the participant, the interviews are recorded using a cell phone app, and the audio files are transcribed. As noted, the interviews are normally done during the site visit. When in-person exchanges are not

feasible, the interviews are accomplished with another cell phone app for recording phone conversations. However, experience has shown that in-person interviews are superior to phone interviews because of the personal connection, lively back and forth interactions, and contributions of body language. When possible, more than one interview is conducted – separated by an significant length of time – because different events and results are recalled in each one.

Whether conducted in person or on the phone, interview audio files are submitted to an online service for transcription. Apps and services that have been found to be effective (although others may qualify also) are SmartRecorder [5] for in-person recordings; TapeACall for telephone interviews [6]; and REV.com [7] for transcription of audio files from both sources.

2.5. Reports

The memos describing the components of the records serve as the principal source for the project report. Confidentiality of the findings of the projects is required – nothing is released to others without the consent of the individuals, although some participants are willing to have their reports made public "after the fact". A consistent format of the project reports has been found to be an effective presentation of project results.

Introduction. Provides background on LENR and its rejection. Includes introduction of the participant and his or her LENR contributions. Normally includes a photo of the participant.
Research and Other Records. Generally, a section or subsection on each component of the record. Derived from memos prepared for the records. Includes lists of publications and reports.
Interviews. Recorded as audio files that are then converted to transcripts of the interviews. May also be annotated to help develop a timeline.
Timeline of LENR Activities. Prepared when sufficient information is found in the records and interviews.
Future Opportunities. Delineates findings that were uncovered but could not be included in the scope of the project. Provides framework for future additional investigations.
Project Methods. Describes the LRDI procedure used in conducting the project. Often includes a list of the memos documenting the interviews and components of the records.
Appendix. Provided as backup or extension of findings in the various sections of the report. May require a second volume of the report when voluminous.

2.6. Preservation and Archiving

Much has been learned in the LRDI about securing records and arranging for long-term archiving. The methods are quite different for hardcopy and electronic files. Fortunately, the Marriott Library at the University of Utah (Figure 5) has expressed strong interest in receiving hardcopy LENR files. A visit has been made to Special Collections at the library [8], and contact was made with the manager. A substantial LENR collection was found to already exist at the library, and arrangements were made for additional contributions from LRDI participants. So far, Edmund Storms and Tom Passell have contributed extensive materials from their research.

A solution is also being developed for long-term archiving of LENR electronic files. Currently, the files from participants are backed up on two large-capacity stand-alone hard drives. A central repository in the Cloud is being pursued to provide ready access to the files by the participants and other interested (and authorized) parties. The central issues appear to be access and security. The files must be immune from sabotage and available only to those approved by the participant. Searchability may become necessary for reanalysis of the records to help solve LENR's riddles of inadequate reproducibility and insufficient theoretical understanding.

An account has been established with Amazon Web Services (AWS) [9] for very large capacity storage at a reasonable rate. It is being used in a pilot project for storing large volumes of files from LRDI participants.

Figure 5. Reading Room of the Marriott Library Special Collections.

3. Status of the LENR Field

What has been learned in the LRDI about the status of the field is primarily verification of what is already known. LENR's rejection by mainstream science has become almost a hallmark of the field, with a multitude of adverse effects, such as highly restricted funding for research, damage to the careers of investigators, failure of mainstream journals to publish LENR papers, and barriers to younger scientists wanting to join the field. Certainly, these constraints have contributed to the lack of success in achieving reliable reproducibility and an acceptable explanation, as well as a new source of energy.

The "common cause" among the researchers of a rejected field has resulted in a strong sense of community. Although the community is held together loosely, and is often quite fractious, the sense of camaraderie persists to this day. The community has developed a separate but parallel set of practices and outlets for sharing research results. Examples of the separately developed LENR venues and outlets are shown in Table 2. (Incidentally, these sources are prime information resources for LRDI projects.)

4. Future LRDI Opportunities

A major LRDI lesson learned is the potentially very large quantity of available LENR records. The accomplishments so far seem to be "just scratching the surface". There are numerous researchers and other interested parties in the LENR field who are candidates for future projects. Also, nearly all projects completed or underway have potential for additional documentation in the future. Thus, the program can progress both by expansion with new projects and by extension with more efforts on previous projects.

Another area of opportunity is refinement of long-term arrangements for preservation and archiving, possibly beyond the Marriott Library for the hardcopy files and AWS for the electronic files. An integrated LRDI report is being prepared to describe the general characteristics of the researchers and their records, and to make observations and draw conclusions about the nature and scope of the LENR field. The ultimate objective of the report is to provide information to help understand the LENR phenomenon and secure its benefits.

Table 2. Examples of LENR Scientific Processes and Tools.

Professional Society and Awards	International Condensed Matter Nuclear Society (ISCMNS) [10]. International nonprofit organization. Preparata award.
Publications	Journal of Condensed Matter Nuclear Science (JCMNS) [11]. Issued approximately quarterly.
Magazine	Infinite Energy [12]. Published bi-monthly by the New Energy Foundation. Includes topics besides cold fusion.
Conferences	International Conferences on Cold Fusion (ICCFs). Held every one to two years. 24 meetings held since 1989.
Online Library	LENR-CANR.org [13]. Thorough collection of LENR papers going back to 1989. Easily searchable by author, title or date.
Website	LENR Forum [14]. Provides venue for communication among researchers and other interested parties.
Online Chat	CMNS Google group. Set up for posts by individuals on a full range of LENR topics. Membership is by invitation.

Another LRDI goal is to help make the case for LENR so that it will be reestablished in mainstream science, and major resources will be devoted to pursuing it. LRDI plans call for continued – or possibly expanded – communication of the positive findings of the program to persons both within and outside the current LENR field.

5. Conclusions and Acknowledgments

With the threats of current energy sources to the habitability of the earth, humankind desperately needs to pursue LENR for its energy benefits. It has been clear since the 1989 announcement that LENR is a potential source of abundant, safe, clean, and inexpensive energy. The LRDI seeks to document and preserve the LENR researcher records while they are still available. Much has been learned about the participants and their records in the four years since the initiative was started.

The LRDI is being conducted at the firm LENRGY, LLC in Austin, Texas [15]. Gratitude is expressed in particular to the participants for being willing to give interviews and grant access to their records (and in several cases also to their spouses). Thanks go to Carl Page and the Anthropocene Institute [16] for providing financial support for travel and other expenses. Gratitude is expressed to Christy Frazier of the New Energy Foundation and Infinite Energy magazine not only for providing a venue for LRDI articles [17, 18, 19] but also for assistance with tax considerations in LRDI funding. Rob Christian has provided the insight and information for setting up large-capacity storage at AWS for archiving electronic files securely.

Liz Rogers of Special Collections at the University of Utah's Marriott Library has been instrumental in arranging to receive LENR materials from LRDI participants. Jed Rothwell's LENR-CANR.org online library of LENR publications and related materials has been a great benefit as the "first stopping point" at the beginning of new projects. Finally, thanks are given to Edmund Storms, not only for serving as the pilot for LRDI projects and as the first to donate his hardcopy materials to the Marriott library, but also for being an informative and fun mentor to the author.

References

[1] Grimshaw, T., 2020. Documenting Cold Fusion Research: Preserving a Vital Asset for Humankind. Infinite Energy, Issue 150, March/April.

[2] Grimshaw, T., 2022. Mitigating the Loss of Irreplaceable LENR Research Records. Jour. Condensed Matter Nuclear Science. Vol. 36, p. 25-29.

[3] Grimshaw, T., 2019. Collection, Organization and Documentation of LENR Research Results: Guideline. Unpublished Report. January.
[4] Grimshaw, T., and E. Storms. 2018. Documentation of Dr. Ed Storms' 29-Year LENR Research Career. Poster for 21st International Conference on Cold Fusion (ICCF-21), Fort Collins, Colorado. June.
[5] Roe Mobile Development. Smart Recorder. https://www.roemobiledevelopment.com/Home.html
[6] TapeACall: The leading call recorder app for iPhone and Android. https://www.tapeacall.com/
[7] @rev Transcription Services. https://www.rev.com/
[8] Grimshaw, T., 2021, Cold Fusion Archives at the University of Utah, Unpublished LENRGY Report, October.
[9] Amazon Web Services (AWS). https://aws.amazon.com/
[10] The International Society for Condensed Matter Nuclear Science. https://iscmns.org/
[11] Journal of Condensed Matter Nuclear Science. http://www.iscmns.org/CMNS/publications.htm
[12] http://www.infinite-energy.com/
[13] LENR-CANR.org, A Library of Papers about Cold Fusion. https://lenr-canr.org
[14] LENR Forum. https://www.lenr-forum.com/
[15] LENRGY: Pursuing the Benefits of Cold Fusion Realization. http://lenrgyllc.com/
[16] Anthropocene Institute. https://anthropoceneinstitute.com/
[17] Grimshaw, T., and D. Nagel, 2020. Dr. Peter Gluck's Ego Out Blogsite: Preservation of a Major Resource for the LENR Field. Infinite Energy, Issue 151/152, May to August.
[18] Grimshaw, T., 2022. Ludwik Kowalski, Major Contributor to the Cold Fusion Field. Infinite Energy, Issue 159, November 2021 to February 2022.
[19] Grimshaw, T. and A. McElroy, 2022. "Fusion Facts" by Hal Fox: A Vital Resource for Documenting Early Progress in the LENR Field. Infinite Energy, Issue 160, March/April.

J. Condensed Matter Nucl. Sci. 38 (2024) 245–268

Research Article

Possibility of Coherent LENR Dynamics with Nuclear Molecules

Peter L. Hagelstein

Massachusetts Institute of Technology, Cambridge, MA, USA

Abstract

Excess heat in the Fleischmann-Pons experiment is generated without commensurate energetic nuclear particle emission, which has often been used to argue that the effect is not nuclear. Instead, we have argued that a better interpretation is that excess heat is not a result of quantum mechanically incoherent processes. For many years we have pursued quantum mechanically coherent models in which excess heat production is a byproduct of an underlying coherent nuclear process, of which fusion is a part of. A major difficulty with this approach has always been an inability to identify reasonably stable excited nuclear states that might support the required coherent nuclear dynamics, since only a modest number of metastable nuclei are known among all the stable isotopes. Here is proposed that nuclear molecules may provide a set of reasonably stable nuclear excited states. We use a simple cluster model based on the finite range liquid drop model to estimate excited state energies for nuclear molecules from the stable Pd isotopes. The highest density of states occurs near 50 MeV. A model is proposed in which generalized excitation transfer moves population to the high density of state region where efficient energy exchange with the lattice can occur. Excess heat is proposed to occur through a cycle in which excitation is promoted, where energy exchange occurs, followed by a multi-step return to the ground state. If this process is frustrated, then tunneling decay of highly-excited nuclear molecules results in transmutation.
 ISSN 2227-3123

Keywords: Fleischmann-Pons excess heat, coherent nuclear dynamics, theory, nuclear molecules, evolution equations

1. Introduction

We have long focused on the possibility that the anomalies in LENR are due to coherent dynamics among nuclear states driven by coupling with low energy collective degrees of freedom of the metal hydride or deuteride. A headache that has plagued this approach since the beginning is that highly-excited nuclei must be involved for any such scheme to work, but highly excited nuclei tend to be short-lived, which is problematic for coherent nuclear dynamics.

In a brainstorm in April of 2022 emerged the possibility that nuclear molecules might be involved in connection with excess heat and transmutation. An earlier naive version of the idea can be found in [1] in connection with speculations concerning lattice-induced fission in the Cardone experiments and Carpinteri experiments. Following a frantic few months of work a preliminary account of the approach was presented at ICCF24. Since then there has been some clarification of the approach, and a brief account will be given in what follows.

The notion of a nuclear molecule was introduced in response to the observation of resonances in collisions between ^{12}C nuclei [2], [3]. Two nuclei close together at the fermi scale have the possibility of forming a nuclear molecule,

 ISSN 2227-3123

by analogy at the atomic scale of molecules formed through electron bonding [4]. Earlier work on nuclear fission proposed essentially the same notion [5]. By now the notion of nuclear molecules is accepted within nuclear physics.

Bohr and Wheeler suggested the use of the liquid drop model to describe this kind of nuclear structure [5]. The basic idea in this kind of model is that the nucleus is modeled as a droplet with constant mass and charge density, with a constant (attractive) nuclear energy linear in the volume, a (repulsive) energy proportional to the surface area, and a (repulsive) Coulomb energy connected with the electric charge density. In a liquid drop model of a nuclear molecule, the volume energy is the same as in a spherical version of the nucleus, but the Coulomb energy can be decreased by the separation of charge, and the surface energy is increased due to the larger surface associated with the nuclear molecule. In this kind of model, the spherical configuration has minimum energy, but nuclear molecule states have a local minimum in energy at high excitation energies.

A significant advantage of this kind of model is that it can predict ground state energies of nuclei over a wide range of mass and charge with reasonably good accuracy [6], [7]. More sophisticated versions of the model have been developed over the years for modeling deformation associated with fission and fusion (see [8], [9], [10]).

Most nuclear molecule calculations in the literature are focused on (1) fission of heavy nuclei; (2) resonances in (heavy) nuclear collisions; and (3) resonances symmetric light systems such and C-C and O-O. Binary nuclear molecules were the focus of early research, but subsequently calculations have been published with results for ternary nuclear molecules and more complicated structures as well. At present there are no systematic studies available that provide an assessment of nuclear molecule states in Pd nuclei that might be of interest in LENR.

We draw attention to a subtle issue that will be important in the discussion to follow. Nuclear molecules with low rotational angular momentum near Pd predicted for a fission or fusion model are not expected to be stable against tunnel decay. A "nuclear molecule" made of two daughters modeled as "clusters" that nearly touch are expected in general to be much more stable against tunnel decay. In the literature such states tend to be referred to in connection with clusters, as distinct from nuclear molecules. In this paper we will use a nuclear molecule terminology in connection with both kinds of models.

A number of issues are of interest. For example, are nuclear molecule (cluster) states predicted? If so, at what energies? How stable are they? And can they be accessed through interactions with condensed matter degrees of freedom? We have recently explored models for nuclear molecules, which allows us to begin addressing some of these questions.

In Sections 2 and 3 we consider the two different models for nuclear molecules from the Pd isotopes. An important conclusion is that there reasonably stable binary nuclear molecules are not expected from liquid drop models as normally used for fission calculations. Calculations done for C-C and for O-O suggest that there should be reasonably stable nuclear molecule states which involve clusters rather than extreme nuclear deformation. We consider the possibility that reasonably stable nuclear molecules can be modeled systematically based on this picture, and we propose a simplified model for the nuclear molecule energies and tunneling decay rates. In the following sections we consider the issues involved, what kind of scheme might be involved, and what a model might look like. The conclusion is that this approach results in a model which has the potential to be closely connected to experiment. Unfortunately, the resulting model is complicated, and accurate energy levels and transition matrix elements are not available.

In Section 4 we consider issues associated with coherent energy exchange, and their impact on schemes to model excess heat production. In Section 5 we consider a candidate scheme for excess energy production in PdD_x. In Section 6 we begin thinking about modeling the associated coherent dynamics. Conclusions appear in Section 7.

2. Bohr-Wheeler Approach

The focus in the first part of this study is on a basic liquid drop model, seeking optimized surfaces and excitation energies for symmetric and asymmetric binary nuclear molecules. The idea is that since we have not worked with these

models previously, that there would be much to learn by working with the simplest relevant model. Even though the model is simple, the numerical optimization of the surface is not straightforward.

Nuclear molecules can rotate, which is important for ion-ion collisions. However, rotating nuclear molecules undergo radiative decay, which reduces their lifetime, making them perhaps less suitable for the coherent dynamics of interest in what follows. Hence, the focus here will be on non-rotating nuclear molecules.

2.1. Basic Liquid Drop Model

We worked with a Bohr-Wheeler liquid drop model based on

$$E = -B'_V \int_V d^3\mathbf{r} + B_S \oint_S d^2a + \frac{1}{2}\frac{Z(Z-1)}{Z^2}\int\int \frac{\rho_C(\mathbf{r})\rho_C(\mathbf{s})}{4\pi\epsilon_0|\mathbf{r}-\mathbf{s}|}d^3\mathbf{r}d^3\mathbf{s} \tag{1}$$

The first term on the RHS accounts for the volume and antisymmetry energy, the second accounts for the surface energy, and the third term is the Coulomb energy where $\rho_C(\mathbf{r})$ is the charge density assumed constant within the deformed nucleus. We scaled the Coulomb energy by the factor $Z(Z-1)/Z^2$ as appropriate for a nucleus made of Z discrete protons. We used values for the fitting parameters given by

$$B_V = 1.946\ \mathrm{MeV/fm^3}$$

$$B_S = 0.834\ \mathrm{MeV/fm^2}$$

$$B_A = 0.047\ \mathrm{MeV/fm^3}$$

$$B'_V = B_V - B_A = 1.899\ \mathrm{MeV/fm^3} \tag{2}$$

These correspond to the more conventional liquid drop fitting parameters

$$a_V = 14.8\ \mathrm{MeV}$$

$$a_S = 15.6\ \mathrm{MeV}$$

$$a_A = 20.3\ \mathrm{MeV} \tag{3}$$

corresponding to the more conventional liquid drop parameterization

$$E = a_V A + a_S A^{2/3} + a_C \frac{Z(Z-1)}{A^{1/3}} - a_A \frac{(N-Z)^2}{A} + \delta(N,Z) \tag{4}$$

The total energy in the spherical liquid drop model is made up of the volume energy, surface energy, Coulomb energy, symmetry (or Pauli) term and pairing term. For this model we have taken the spherical liquid drop radius to be

$$R = 1.22\ A^{1/3}\ \mathrm{fm} \tag{5}$$

The liquid drop model volume, surface and asymmetry terms were developed from least squares optimization of mass energies in the mass range near $A = 100$.

In the calculation of deformed surfaces using the liquid drop model, the nuclear volume is taken to be an invariant. Hence, the optimization in this version of the model depends on the Coulomb and surface terms, and not on the volume energy (which can be absorbed into the Lagrange multipliers in the optimization). When we optimized values of the liquid drop model parameters, the mean square error and fitting parameter for the surface energy depended only weakly on whether the pairing term was included or not. So the fitting parameters given were optimized without including the pairing energy.

2.2. Surface Parameterization

We initially developed a code to optimize a general surface characterized by cylindrical ρ_j values corresponding to z_j points. This was not straightforward as the associated Jacobian matrix for the corresponding Newton iterations is unstable, and there are headaches associated with the boundary conditions. Nevertheless, we were able to get convergence resulting in optimum solutions for a number of test problems.

From this experience we were motivated to try an approach that was closer to what is discussed in the literature. We used a parameterization given by

$$\rho(z) \;=\; \sqrt{\sum_j \rho_j^2 L_j(z)} \tag{6}$$

which involves approximating the square of the radial values in cylindrical coordinates with Lagrange interpolants. A simple version of the model was developed based on uniform spacing of points in z, from one boundary of the nuclear molecule to the other. We worked with up to 15 points, which includes two boundary points with zero fitting parameters.

2.3. Optimization

Optimization was based on the variational quantity I

$$I \;=\; E_C - B_V' V + B_S S - \lambda_b V_b - \lambda_c V_c \tag{7}$$

The optimum surface (characterized by a vector $\mathbf{c}_0$ made up of the fitting coefficients $c_j = \rho_j^2$) satisfies

$$(\nabla I)_{\mathbf{c}_0} \;=\; \mathbf{0} \tag{8}$$

or

$$(\nabla E_C)_{\mathbf{c}_0} - B_V'(\nabla V)_{\mathbf{c}_0} + B_S(\nabla S)_{\mathbf{c}_0} - \lambda_b(\nabla V_b)_{\mathbf{c}_0} - \lambda_c(\nabla V_c)_{\mathbf{c}_0} \;=\; \mathbf{0} \tag{9}$$

Around the optimum we can write

$$(\nabla I)_{\mathbf{c}} \;=\; (\nabla I)_{\mathbf{c}_0} + \mathbf{K}_I \cdot (\mathbf{c} - \mathbf{c}_0) \;=\; \mathbf{K}_I \cdot (\mathbf{c} - \mathbf{c}_0) \tag{10}$$

where $\mathbf{K}_I$ is the Jacobian of I with respect to the c_j. The formal solution for the Newton's iteration correction is then

$$(\mathbf{c}_0 - \mathbf{c}) \;=\; -\,\mathbf{K}_I^{-1} \cdot (\nabla I)_{\mathbf{c}} \tag{11}$$

We can expand this to read

$$(\mathbf{c}_0 - \mathbf{c}) \;=\; -\,\mathbf{K}_I^{-1} \cdot \Big\{ (\nabla E_C)_{\mathbf{c}} - B_V'(\nabla V)_{\mathbf{c}} + B_S(\nabla S)_{\mathbf{c}} - \lambda_b(\nabla V_b)_{\mathbf{c}} - \lambda_c(\nabla V_c)_{\mathbf{c}} \Big\} \tag{12}$$

We used an inequivalent Jacobian based on

$$\mathbf{K}_I \;\approx\; \mathbf{K}_C + B_S \mathbf{K}_S \tag{13}$$

where the Jacobians of the individual volumes are neglected (the Jacobian of the total volume vanishes). We define vectors according to

$$\mathbf{x}_C \;=\; \mathbf{K}_I^{-1}(\nabla E_C)$$

$$\mathbf{x}_S \;=\; \mathbf{K}_I^{-1}(\nabla S)$$

$$\begin{aligned} \mathbf{x}_V &= \mathbf{K}_I^{-1}(\nabla V) \\ \mathbf{x}_{V_b} &= \mathbf{K}_I^{-1}(\nabla V_b) \\ \mathbf{x}_{V_c} &= \mathbf{K}_I^{-1}(\nabla V_c) \end{aligned} \tag{14}$$

It follows that the correction is

$$(\mathbf{c}_0 - \mathbf{c}) = -\mathbf{x}_C + B'_V \mathbf{x}_V - B_S \mathbf{x}_S + \lambda_b \mathbf{x}_{V_b} + \lambda_c \mathbf{x}_{V_c} \tag{15}$$

The volumes associated with the two daughters is specified initially, and remains (approximately) constant during the iterations. For this we require that

$$\begin{aligned} (\nabla V_b)_{\mathbf{c}} \cdot (\mathbf{c} - \mathbf{c}_0) &= 0 \\ (\nabla V_c)_{\mathbf{c}} \cdot (\mathbf{c} - \mathbf{c}_0) &= 0 \end{aligned} \tag{16}$$

where $(\nabla V_b)_{\mathbf{c}}$ and $(\nabla V_c)_{\mathbf{c}}$ are the gradients of the daughter volumes with respect to the fitting parameters. These can be written as

$$\begin{aligned} (\nabla V_b) \cdot \left\{ -\mathbf{x}_C + B'_V \mathbf{x}_V - B_S \mathbf{x}_S + \lambda_b \mathbf{x}_{V_b} + \lambda_c \mathbf{x}_{V_c} \right\} &= 0 \\ (\nabla V_c) \cdot \left\{ -\mathbf{x}_C + B'_V \mathbf{x}_V - B_S \mathbf{x}_S + \lambda_b \mathbf{x}_{V_b} + \lambda_c \mathbf{x}_{V_c} \right\} &= 0 \end{aligned} \tag{17}$$

This is equivalent to the linear equations

$$\begin{aligned} \Big((\nabla V_b) \cdot \mathbf{x}_{V_b} \Big) \lambda_b + \Big((\nabla V_b) \cdot \mathbf{x}_{V_c} \Big) \lambda_c &= (\nabla V_b) \cdot \mathbf{x}_C - B'_V (\nabla V_b) \cdot \mathbf{x}_V + B_S (\nabla V_b) \cdot \mathbf{x}_S \\ \Big((\nabla V_c) \cdot \mathbf{x}_{V_b} \Big) \lambda_b + \Big((\nabla V_c) \cdot \mathbf{x}_{V_c} \Big) \lambda_c &= (\nabla V_c) \cdot \mathbf{x}_C - B'_V (\nabla V_c) \cdot \mathbf{x}_V + B_S (\nabla V_c) \cdot \mathbf{x}_S \end{aligned} \tag{18}$$

2.4. Results and Discussion

We optimized the surface in terms of the Lagrange fitting parameters, as well as the overall distance from one end to the other of the deformed nucleus. With this parametrization, we found weakly bound nuclear molecule surfaces such as shown in Figure 1 for the symmetric case, which is reasonably close to the symmetric shape near $A = 100$ shown in [9]. In Figure 2 a surface is illustrated for the asymmetric case.

The barrier energy for the symmetric case (without correcting for the fission energy, which is different in this kind of model than experiment due in part to the fact that the Coulomb energy in the liquid drop model fit is less that the Coulomb energy calculated with in the model) is near 44 MeV, which is less than 10% higher than values in the literature from more sophisticated models.

The optimizations which we carried out led systematically to a local minimum of the energy with respect to the separation of the daughters, indicative of nuclear molecule formation. It is possible that this may be an artifact of the approach, due to the fact that there are multiple solutions for the surface at a given separation. The energy minima that we found involved optimizations in which the solutions are close over the energy range considered, and we did not optimize over all possible bands of solutions permitted by the model. Even if the solutions were taken as corresponding to physical states, the potential associated with the local potential minimum is sufficiently shallow that the daughters would tunnel apart in well under 10^{-20} seconds. These solutions are unfortunately not useful for coherent nuclear dynamics modeling of the kind we are interested in.

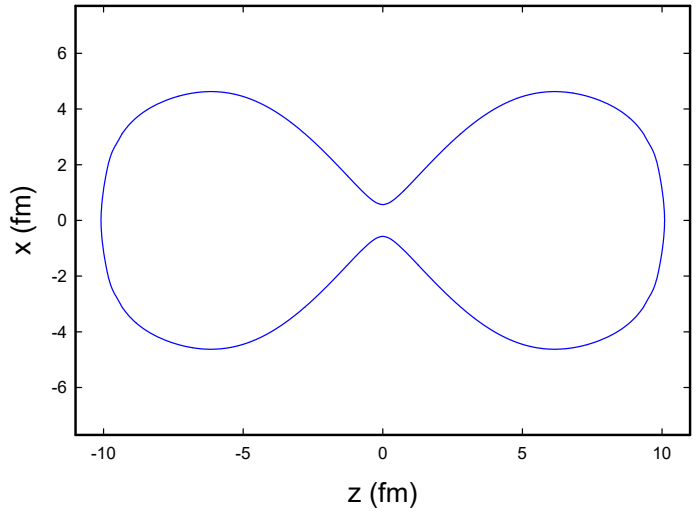

Figure 1. Liquid drop model surface for a symmetric binary nuclear molecule, where the parent $A = 106$ nucleus is split into two daughter nuclei with $A_b = A_c = 53$.

3. Finite Range Liquid Drop Model and Cluster Picture

Perhaps the most significant drawback of the Bohr-Wheeler model for describing fission and fusion processes is that the strong force interaction comes in through volume and surface energy terms, so that there is no residual strong force interaction when the daughters are separated.

A more sophisticated model that remedies this is the folded Yukawa model, such as discussed in [11]. In this model the strong force interaction is modeled through a scalar Yukawa potential between different elements of the liquid drop mass density, which leads to a short range daughter-daughter attraction as might be expected intuitively. One issue with this model is that it includes both volume and surface contributions for the strong force energy, which makes a connection with the LDM surface fit problematic. More important is that the spatial range of the Yukawa potential would be expected to be determined by the pion mass, but when compared with experiment this overestimates the range of the interactions for daughter-daughter interactions.

3.1. Finite Range Liquid Drop Model

Both of these issues are addressed in the finite range liquid drop model (FRLDM). It is possible to isolate approximately the surface contribution to the energy by subtracting an empirical exponential potential (the combination is referred to as the Yukawa plus exponential interaction, or YPE interaction), such that the contribution of the two terms to the volume energy vanishes. In this picture the Yukawa potential contribution to the volume energy is taken to be local, which greatly simplifies things. Once the surface contribution was isolated in this way, it was found that improved agreement with experiment could be obtained by allowing the range of the interaction to be a free parameter and optimizing. This resulted in a folded surface interaction with a shorter range than might have been expected based on the pion mass. The strength of the YPE interaction can be determined by matching to the surface energy of a liquid drop model optimization over the isotopic masses. This model is used with an additional charge density correction to

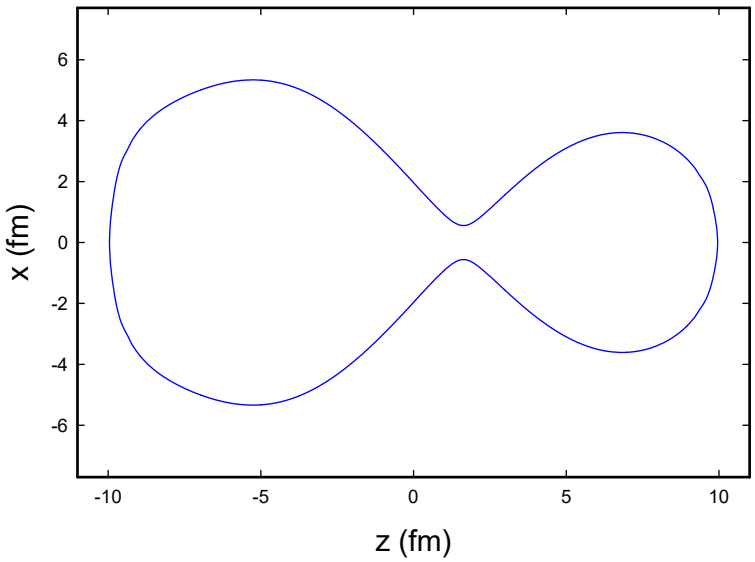

Figure 2. Liquid drop model surface for an asymmetric binary nuclear molecule, where the parent $A = 106$ nucleus is split into two daughter nuclei with $A_b = 80,\ A_c = 26$.

the Coulomb interaction, which contributes a minor correction to the shape and barrier energy. Relevant descriptions of the model are given in [8], [9].

Implementing the model into a code is greatly helped by equating the double volume integral of the folded YPE to an equivalent double surface integral (by making use of the Gauss-Ostrogradsky divergence theorem) as described in these references, and also in [12]. In our implementation we have made use of two-dimensional cubature formula in addition to Gaussian quadrature for the angular integration to evaluate efficiently the three-dimensional integrals that result. We used (older) model fitting parameters from [13].

This model was used for calculations of nuclear molecules along relevant to fission and fusion models similar to those calculated in the Bohr-Wheeler model described above. We found this more sophisticated model to be less stable than the Bohr-Wheeler model outlined above, so that useful results were not obtained with the Lagrange type of parametrization described above. We implemented a three region quadratic surface parametrization [14], along with quartic and sixth-order generalizations. Multiple branches of solutions were obtained with these models, which was a headache. The barrier energy for Pd-106 in our calculations was 40.7 MeV, in good agreement with the literature values. However, similar to the results obtained with the Bohr-Wheeler model, we did not find reasonably stable nuclear molecule solutions in connection with the fission barrier calculations.

3.2. Cluster Picture

We developed models for ^{12}C+^{12}C [15], [16], [17] and for ^{16}O+^{16}O [18], [19]. Comparisons with FRLDM nuclear molecule models appropriate for fission and fusion calculations led to the conclusion that there was no agreement with potentials from the literature. We tried instead working with models based on separated daughter nuclei, where we were able to get reasonable agreement with the potential shape and minimum.

After some consideration, this seems to be an important observation in connection with the development of a model for reasonably stable nuclear molecules. From the literature on fission models, and from a fission type of calculation with the FRLDM, one might not expect there to be a reasonably stable nuclear molecule state in these systems. Yet in the reference cited in this subsection (and in other papers as well) potential models are given which would predict a reasonably stable nonrotational nuclear molecule state. So, the question is, what is the difference in the associated physical pictures?

The conjecture here is that in these potential models, the carbon and oxygen daughter nuclei are essentially clusters which largely remain intact, and which attract one another when separated from each other but close within a few fm. The potential increases once the two nuclei begin to touch, which we might attribute to occupation of more highly excited states as the nucleons in the daughters rearrange to accommodate the deformation associated with moving into one another. In a fusion calculation at higher energy, the incoming nuclei have sufficient energy to overcome this initial barrier, and merge together as described approximately by a liquid drop model (appropriate for fission and fusion).

This suggests that there should be (at least) two basic regimes associated with nuclear molecule formation. In the higher relative kinetic energy regime, colliding nuclei come together as described in the finite range liquid drop model, with a much reduced fusion barrier. A model for fission would be essentially the same problem, but in reverse. However, in the case of much lower relative kinetic energy, the nuclei when separated look much like when they are far apart, and encounter a strong force repulsive potential barrier that keeps them separated. In this case we might consider them to interact as independent clusters, instead of as a single deformed liquid drop. There are practical issues with such a picture. In order to get the nuclei to nearly touch with vanishing relative kinetic energy in a fusion experiment, the initial relative kinetic energy would need to be large (and precise), in order to have a finite probability of tunneling through the Coulomb barrier and stopping at close range.

Note that the centripetal potential can supply repulsion at short range in a fission type of model, that could result in a well defined potential minimum for a nuclear molecule. The reason we have not focused on such nuclear molecules here is because of the possibility of (fast) radiative decay to lower energy states with lower angular momentum, and also that high angular momentum nuclear molecule states would be difficult to couple to from the (parent) ground state.

3.3. Simple Model for Reasonably Stable Nuclear Molecules

All of this suggests the possibility of developing a simple and crude model to approximate the binding energy of two clusters making up a reasonably stable nuclear molecule, as well as allowing for an estimate of the tunneling rate. It would be possible to use the FRLDM and optimize the surfaces of separated daughter nuclei as a function of the center of mass separation, which would allow us to capture the increased attraction due to the nuclear deformation that occurs in liquid drop models (for separated daughters). However, there are technical issues associated with multiple branches of solutions (which occur even for the separated problem) and the possibility of deformation sufficiently large as to be nonphysical. These headaches provide motivation to work with a simpler model based on spherical daughters, which is free of these headaches.

The model that we have studied estimates the nuclear molecule binding energy simply based on the difference between the Coulomb and YPE energies for the nuclear molecule configuration and for infinite separation. Assuming somewhat arbitrarily that the surface separation is fixed at 0.5 fm, then we can write

$$-B \;=\; E_C(R_{min}) - E_C(\infty) + E_{YPE}(R_{min}) - E_{YPE}(\infty) + E_D(R_{min}) - E_D(\infty) \tag{19}$$

where B is the binding energy of the nuclear molecule treated as two clusters, and where E_C, E_{YPE} and E_D are the Coulomb energy, Yukawa plus exponential energy, and density correction to the Coulomb energy. From this we can find the excitation energy

$$E_{bc} \;=\; M_B c^2 + M_c^2 - M_a c^2 - B \tag{20}$$

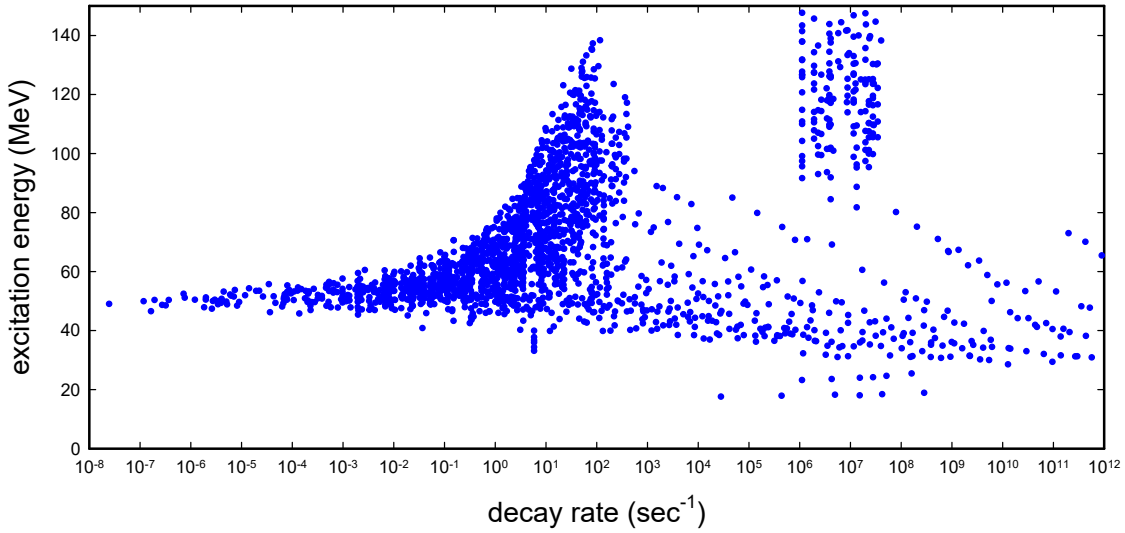

Figure 3. Energy as a function of nuclear molecule decay rate for the stable Pd isotopes.

To estimate the tunneling rate we use

$$\gamma(\text{tunnel}) \;=\; \Gamma_0 e^{-2G} \tag{21}$$

with the Gamow factor estimated using

$$G \;=\; \int_{R_{min}}^{R_{max}} \sqrt{\frac{2\mu(V(r)-E)}{\hbar^2}}\,dr \tag{22}$$

and

$$\Omega_0 \;=\; \frac{1}{2}\omega_0 \tag{23}$$

where the potential is approximated by

$$V(r) \;\rightarrow\; V_0 + \frac{1}{2}\mu\omega_0^2(r-R_{min})^2 \tag{24}$$

with the SHO potential energy taken arbitrarily to be 3 MeV at 1 fm distance from the bottom of the well.

3.4. Results for the Stable Pd Isotopes

We assembled a database for the isotopic mass energies, and used NUDAT3 for the decay rates of the isotopes. We implemented the model described above to determine approximate excitation energies and total (nuclear decay plus tunneling decay) rates for all of the "reasonably stable" nuclear molecules that resulted. Results are shown for the nuclear molecule energy as a function of nuclear molecule decay rate in Figure 3.

We see that according to this model there are hundreds of reasonably stable nuclear molecules, most of which lie above 40 MeV. This is very promising for the nuclear dynamics under consideration in this paper.

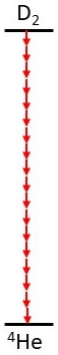

Figure 4. Schematic of naive scheme in which the fusion transition down-converts the nuclear energy to vibrational energy.

4. Coherent Energy Exchange

Excess heat in the Fleischmann-Pons experiment is observed without commensurate energetic nuclear products, which is sufficient to rule out incoherent nuclear reactions as a source. For a coherent quantum dynamics scheme to have the maximum overall transition rate, the coherent transitions must be between states that are at the same energy, so that each transition is resonant. Unfortunately, transitions between candidate nuclear states involve keV to MeV energy differences, which cannot be made up with the exchange of a few phonons or plasmons.

Consequently, there needs to be intermediate steps that involve off-resonant states. We have considered these in the context of coherent energy exchange, where interactions between nuclei and vibrations (or plasmons) are modeled in the strong coupling regime. From these models we obtain an effective interaction matrix element which describes indirect coupling between resonant nuclear plus lattice states in which a nuclear transitions occur with the energy difference matched by the change in lattice energy.

In what follows, we consider different possibilities for coherent nuclear dynamics schemes that become possible with different amounts of coherent energy exchange.

4.1. Spin-Boson Approach

Conceptually simple would be a scheme in which the $D_2/^4He$ transition was coupled to a highly-excited vibrational mode of the lattice (Figure 4), and one nuclear de-excitation would occur in combination with the (quantum coherent) sequential emission of a large number of quanta satisfying

$$(\text{nuclear energy}) \quad \Delta M c^2 \;=\; \Delta n \hbar \omega_0 \quad (\text{vibrational energy}) \tag{25}$$

Coupling of two-level system energy into oscillator energy through coherent multi-quantum exchange is known for the spin-boson system, so there is precedence for contemplation of such an approach.

Unfortunately, the coupling strength for a Coulomb-hindered fusion transition is very small, and the number of quanta Δn to be transferred is very large, so that the application of the scheme directly to fusion does not work. A modification of the scheme involving a large number of $D_2/^4He$ transitions with uniform coupling to a common vibrational mode oscillator can improve the numbers due to the appearance of cooperative Dicke factors, but even with such an enhancement the resulting coherent energy exchange rate is exponentially small.

4.2. Removal of Destructive Interference

Of interest in this discussion is what makes coherent energy exchange slow when Δn is large. One way to think about it is through perturbation theory: in the initial state is a collection of two-level systems in a Dicke state and an excited oscillator with n quanta; and in the final state is essentially the same collection of two-level systems also in a Dicke state, but with one fewer excited states, and where the same excited oscillator now has $n + \Delta n$ oscillator quanta. It is possible to enumerate all of the different pathways through off-resonant states that couple these initial and final states, as well as to sum the contributions from all the different pathways. When this exercise is completed, what is found is that roughly half of the pathways contribute to the sum with a plus sign, and roughly half contribute with a minus sign, so that the total contribution is vanishingly small (when Δn is large).

What prevents coherent energy exchange involving large Δn then is destructive interference. In models where the destructive interference is broken, a dramatic increase in the coherent energy exchange rate is seen [20]–[24].

Two approaches to implement this have been identified. One approach involves decay channels which are significant off of resonance, especially in the case where the energy of an off-resonant state is much less that the available energy (or energy eigenvalue). The energy exchange rate for an idealized model in which all off-resonant states with less energy than the eigenvalue are assumed to decay instantaneously has been quantified [24], [25], [26]. Another approach involves energy level shifts when states are driven off of resonance [27], which can reduce the destructive interference. Unfortunately, there is no such effect at second-order in excitation transfer, in contrast to the discussion given in [27]. The headache in this case was that old-fashioned perturbation theory was used incorrectly in the model discussed, leading to an incorrect conclusion. Had we used a Feynman diagrammatic approach instead, it would have been completely obvious that the nuclei were not off of resonance for second-order excitation transfer, but instead the oscillator. Off-resonant energy shifts of nuclear levels could occur for generalized excitation transfer processes at higher order. Off-resonant energy shifts of nuclear levels would be expected for neutron transfer processes at second order.

It is possible to evaluate conditions under which a great many $D_2/^4He$ transitions transfer 24 MeV to vibrations coherently using this approach (which would also be described by the scheme in Figure 4), with the result that the Dicke-enhanced coupling would only be sufficiently strong with an astronomically large number of transitions. The problem once again is that the Gamow factor associated with tunneling makes the coupling matrix element far too small.

4.3. Excitation Transfer

A much higher overall rate could be obtained if the excitation of the $D_2/^4He$ transition where transferred to produce excitation in other nuclei [27], for example through an excitation process of the form

$$D_2 + Pd \quad \longleftrightarrow \quad {}^4He + Pd^*$$

This presumes that there is a reasonably stable highly-excited Pd^* state with an excitation energy matched to the mass difference of the fusion transition. In such a scheme the excitation from a very large number of $D_2/^4He$ transitions is transferred to Pd^*/Pd transitions so that the Dicke-enhanced coupling strength is sufficiently large that the large nuclear quantum can be down-converted through coherent energy exchange (a schematic appears in Figure 5).

The models cited can be used to evaluate conditions under which this much improved scheme might work, and once again the number of transitions involved is many orders of magnitude greater than what is present in Fleischmann-Pons experiments. The problem in this case is that the number of quantum Δn is very large (on the order of 10^9 for an optical phonon mode). Even though down-conversion is greatly accelerated through off-resonant loss processes (which would be expected), it is not accelerated enough to make this approach work.

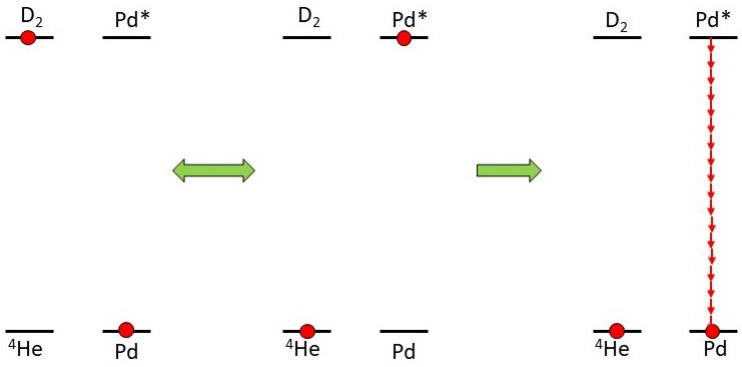

Figure 5. Naive scheme involving excitation transfer followed by down-conversion.

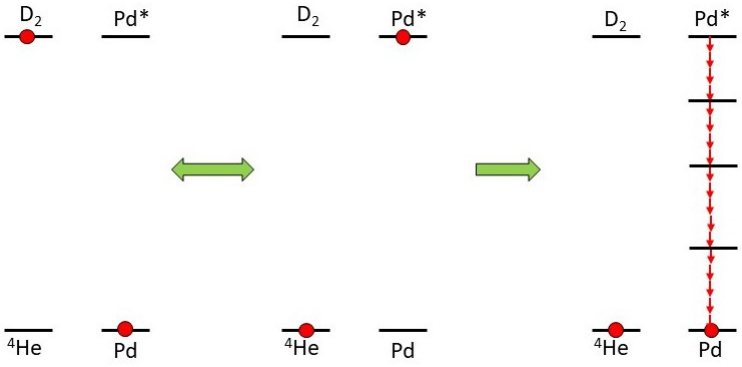

Figure 6. Scheme involving excitation transfer followed by down-conversion with intermediate states.

4.4. Smaller Steps

To address this issue, one approach is to work with smaller steps where the amount of nuclear energy transferred to vibrations is smaller. Conceptually simple (but physically improbable) is a model in which we assume that there are 10 reasonably stable nuclear states equi-spaced between the ground state and the previously assumed excited state at 24 MeV (something like the scheme illustrated in Figure 6). In this model the energy exchange associated with each individual step is $\Delta n/10$, which leads to a reduction of the coupling strength required by about three orders of magnitude.

Once again, it is possible to quantify how many $D_2/^4He$ transitions and Pd^*/Pd transitions are needed to achieve an overall coherent fusion and down-conversion rate on the order of what is seen in experiments. The result is that the number of transitions is many orders of magnitude greater than is present in the experiments.

The contemplation of this example informs us of the importance of the need for a high density of reasonably stable excited states, which motivates us to ask where the highest density of nuclear molecule states are in Pd. From the results shown in Figure 3 we find that the highest density of nuclear molecule states lies up above about 50 MeV. The average energy difference between the nearest neighbors in a naive picture in which there is only one nuclear molecule

per A_b, Z_b value can be as low as about 12 keV. This is encouraging, since the conditions required to transfer 12 keV are much more favorable than 24 MeV or 2.4 MeV.

It is discouraging that the number of transitions needed based on the cited coherent energy exchange models is still orders of magnitude more than experiment even for a down-conversion of only 12 keV.

4.5. Modeling

In preparation for ICCF24 it became clear that nuclear molecule states might offer a real opportunity for there to be reasonably stable excited states that could be used to implement coherent nuclear dynamics driven by coupling with vibrations (or other condensed matter collective degrees of freedom). This focused attention on the coherent energy transfer problem, where it became clear that the energy transfer possible to phonons from the lossy spin-boson model analyzed previously was not going to be sufficient to account for excess heat production in the Fleischmann-Pons experiment. New models that were stronger were needed.

In our ICCF24 presentation preliminary results were presented for models in which external fluctuations were introduced (to help increase the spread of the oscillator distributions in n) and combined with the off-resonant energy shift mechanism. In the calculations done prior to the meeting, this approach looked very attractive, and simulations with relatively small numbers of quanta exchanged looked very promising. Following the conference the scaling of these models was studied with more powerful tools, and it was found that they scaled poorly for large Δn.

We subsequently considered models in which fluctuations in one mode were introduced via coupling through a nonlinearity with another mode. An example of this kind of model is

$$\hat{H} = \hbar\omega_O \hat{a}_O^\dagger \hat{a}_O + \hbar\omega_A \hat{a}_A^\dagger \hat{a}_A + \Delta E \frac{\hat{S}_z}{\hbar} - i\frac{\hbar\Gamma(E)}{2} + V_O \frac{\hat{S}_x}{\hbar}\left(\hat{a}_O^\dagger + \hat{a}_O\right) + V_A \frac{\hat{S}_x}{\hbar}\left(\hat{a}_A^\dagger + \hat{a}_A\right) + K\left(\hat{a}_O^\dagger + \hat{a}_O\right)^2\left(\hat{a}_A^\dagger + \hat{a}_A\right) \tag{26}$$

In this model many two-level systems couple uniformly to acoustic and optical phonon modes that are coupled nonlinearly. Models analyzed based on this approach looked interesting, and appeared to lead to increased coherent energy exchange. After some thought, it was not obvious that there could be a dramatic increase in the coherent energy exchange of optical phonons with dynamics on a sub-picosecond times scale due to a minor interaction with acoustic phonons with dynamics on a microsecond time scale.

Under consideration then are models more closely connected to the originally lossy spin-boson model, in which the nuclei interact linearly with acoustic and optical phonons, as well as with plasmons. The interactions with acoustic phonons appear to be important in developing coherence among a large number of nuclei, while the interactions with optical phonons and plasmons are important for coherent energy exchange. The much larger energy quantum of the plasmons provides for a larger possible total coherent energy exchange.

4.6. Discussion

The conclusion for now is that with optical phonons coherent energy exchange up to on the order of 100 eV should be possible due to coupling with optical phonons, and coupling with plasmons could increase this to on the order of 10 keV. In Figure 7 is shown the density of ground state binary nuclear molecule states with combined nuclear and tunneling decay rates less than 10^{-9} sec^{-1}. The peak density of these states is near one state every 12 keV, which provides for optimism that sequential coherent transitions might be able to convert nuclear energy to plasmon and vibrational energy efficiently in a coherent nuclear dynamics scheme.

However, the situation is much more complicated. The inclusion of spin and angular momentum degrees of freedom for the daughter nuclei, then the density of states would be much larger. Similarly, the inclusion of rotational excitation

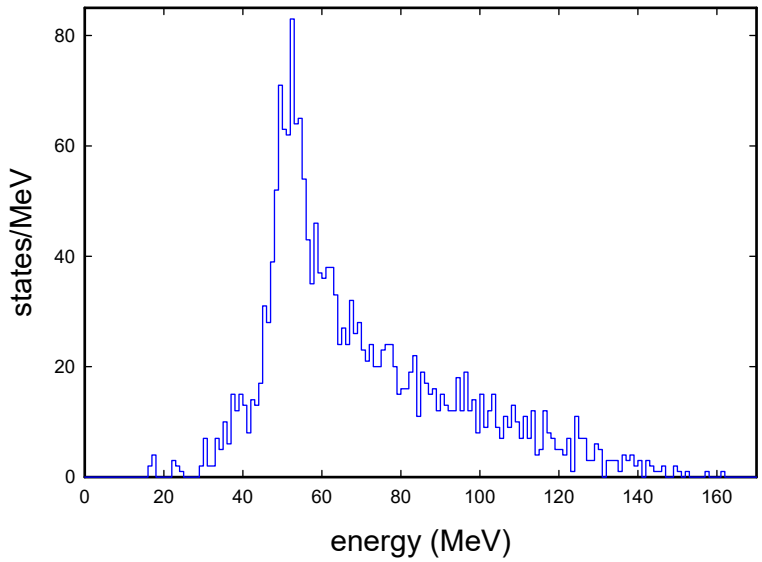

Figure 7. Histogram made from 1 MeV bins from LDM binary nuclear molecule energies from the stable Pd isotopes with decay rates less than 10^9 sec^{-1}.

and vibrational excitation of the nuclear molecule states would also greatly increase the density of states. There are also ternary and quaternary nuclear molecules, which if included would again increase the density of states. But what is important is that there can be low-order coupling from the ground states of the stable Pd isotopes to these nuclear molecule states, so that only a small fraction of these states would be expected to be relevant for the coherent dynamics schemes under consideration.

More complications arise when decay mechanisms are considered. We would expect a modification of the decay rates for the daughters when they are in a nuclear molecule configuration, as the decay energy can be changed. If there are low-order couplings from the ground state directly to these highly-excited nuclear molecule states, then we would expect fast radiative decay rates (as well as internal conversion rates), which suggests that the coupling from the ground state would have to be indirect for things to work.

It is possible that Dicke-enhanced fast excitation transfers between resonant nuclear molecule states could slow down or prevent the (local) decay of these states, by interrupting the accumulation of probability amplitude in the decay channels. In the literature there are many papers on what is called the quantum Zeno effect [28], [29], in which the decay of an excited state is interrupted through measurements. In our case, it would not be measurements that would impact the decay rate, but instead fast transitions to other states. Conceptually this is sufficiently close to the spirit of what is in the literature that it would be appropriate for us to refer to such stabilization as a quantum Zeno effect.

5. A Scenario for Excess Heat and Transmutation

Given the discussion in the sections above, it is clear that there may be a real opportunity working with nuclear molecule states to develop a coherent dynamics scheme that might be relevant to excess heat, transmutation, and other effects seen in LENR experiments. It is also clear that things are not going to be simple.

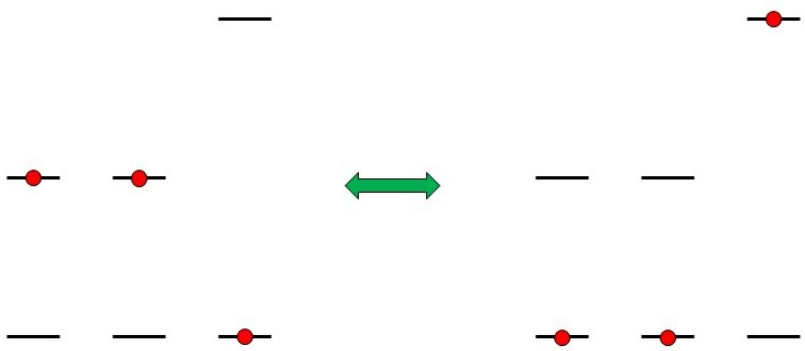

Figure 8. Schematic of a third-order excitation transfer process, where the excitation in two nuclear systems is transferred to a third.

5.1. Initial Excitation Transfer Step

To model excess heat production, the first step has to be the transfer of excitation from the fusion system to another nuclear excited state, since the coupling strength in the case of the fusion system is negligible because of hindrance due to Coulomb repulsion. We would not expect reasonably stable (undeformed) excited states in the stable Pd isotopes near 24 MeV since fast decay by proton, neutron and alpha ejection is possible. The density of nuclear molecule states near this energy is quite low (a few per MeV). A few Ru+^{6}He states are predicted in the general vicinity of D_2/^{4}He transition energy; however, the likelihood of a resonance is very small. An increased probability results if we consider nuclear molecule resonances due to impurity nuclei. Even so, it is very unlikely that a suitable resonant nuclear molecule state exists.

There is the "null" reaction which involves the transfer of excitation from the D_2/^{4}He fusion transition to a ^{4}He/D_2 transition. On the face of it, such a reaction does not seem to be useful. The issue here is that in the present context where many D_2/^{4}He transitions are present, and many ^{4}He nuclei are present to accept the excitation, that a compact D_2^* state is possible in which two deuterons created from the ^{4}He nucleus have trouble tunneling to Angstrom scale separation due to hindrance by the Coulomb barrier. Such a compact state is not expected for the 4-body system in vacuum – it is specific to an excitation transfer system. It may be that such D_2^* compact states are critical to excess heat production in PdD_x, as D_2^*/^{4}He transitions can accept excitation from D_2/^{4}He fusion transitions on resonance.

5.2. Promotion to Higher Energy States

Next, the system needs a way to promote excitation to much higher energy in order to access the high density of states above 40 MeV. Excitation transfer is a second-order process which can move excitation from an excited state at one energy to another at a nearby energy. If the Dicke-enhanced coupling is sufficiently strong, then there is the possibility that a third-order process might occur. Among the different third-order processes possible is one in which two excited nuclear molecules make transitions to the ground state, one a ground state nuclear molecule make a transition to an excited nuclear molecule state at twice the energy (as illustrated in Figure 8). This mechanism would allow promotion of excitation to twice the fusion energy (47.7 MeV) starting from nuclear molecules near the fusion energy. There are many nuclear molecule states nearby this energy. Note that if compact D_2 states are created in the initial transfer step, then low-order coupling would be very strong, favoring higher-order processes.

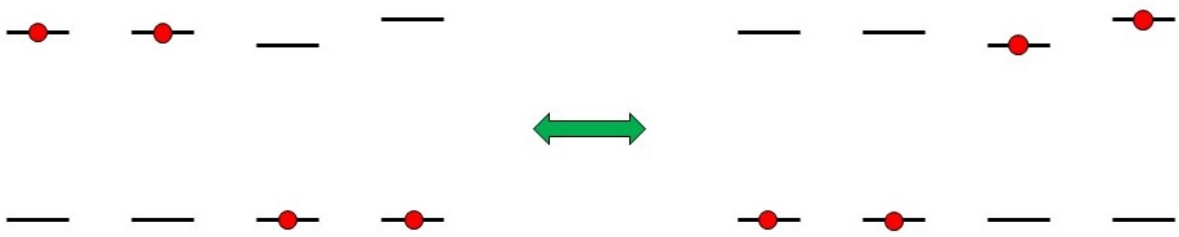

Figure 9. Schematic of a fourth-order excitation transfer process, where the excitation in two nuclear systems is transferred to two other nuclear systems.

5.3. Energy Exchange with Vibrations

With access to states at two times the fusion energy, the system has access to where the density of reasonably stable nuclear molecule states is high. If coherent energy exchange with the lattice per (nonresonant) excitation transfer step can be more than 10 keV, then it is possible that the accessible reasonably stable nuclear molecule density of states is sufficiently high to support excess heat in a scheme only requiring second-order excitation transfer. This would be the simplest possible scenario, and it looks at this point like a viable option.

In the event that coherent energy exchange transfers an energy less than the characteristic energy difference between neighboring states, then we might contemplate generalized excitation transfer processes that occur at higher order. For example, at fourth-order there are processes (illustrated in Figure 9) that can be thought of as transferring excitation between a pair of nuclear molecule states. In this case the pair density of states is much higher (see Figure 10 below), and it becomes much easier for the coherent energy exchange transfers to exceed the energy difference between neighboring states (potentially 10s of eV might be sufficient).

If excess heat is produced via simple second-order excitation transfers, then it may be that excess heat is produced more efficiently (and at a higher rate) if the system enters into a regime in which the fourth-order generalized excitation transfer process becomes dominant.

5.4. Pair Density of States for the Stable Pd Isotopes

The pair density of states can be found from the convolution

$$\rho_2(E) \;=\; (\rho_1 * \rho_1)(E) \;=\; \int_{-\infty}^{\infty} \rho_1(\epsilon)\rho_1(E-\epsilon)d\epsilon \tag{27}$$

Results for the pair density of states with single nuclear molecule decay rate less than 10^9 sec^{-1} is shown in Figure 10. There are additional issues to be considered. Due to the different spin and angular momentum states possible (and relative orientation of oblate and prolate daughters), both the density of states and pair density of states will be significantly larger. Not all of them are expected to be reachable through low-order interactions with phonons and plasmons.

5.5. End-Point of the Dynamics

Suppose now that either second-order or fourth-order (or both) excitation transfer processes are successful in allowing step-by-step transfer of nuclear energy to vibrational and plasmon energy from 3 times the fusion energy down to 2

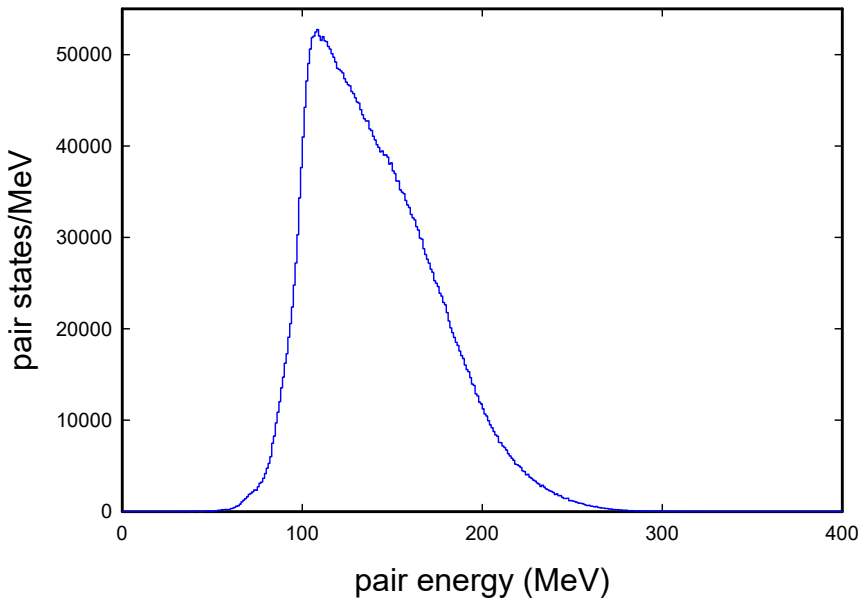

Figure 10. Histogram of the pair density of states for nuclear molecules of the Pd isotopes with decay rates less than 10^9 sec^{-1}.

times the fusion energy. In this case a return to the ground state is possible a third-order processes. The promotion of excited nuclei up to where the high density of states occurs is balanced by downward transitions, as long as there is a constant substantial excited population needed to provide sufficiently large Dicke enhancement factors. This is shown schematically in Figure 11, where for simplicity it is assumed that nearly resonant nuclear molecule states are available among the Pd isotopes for the third-order upward and downward transitions.

Sustained excess he production in this model depends on the excitation of the optical and acoustic phonons, plasmons, as well as maintaining a pool of fusion transitions upon which to draw. If for some reason these falter, and if the system loses the ability to have coherent energy exchange at the level needed for sequential transitions to neighboring nuclear molecule states, then the excess heat cycle would be expected to break. Excited nuclear molecules that are promoted would ultimately be left stranded to decay by tunneling, resulting in a transmutation effect.

6. Coherent Nuclear Dynamics

The coherent nuclear dynamics that result from the ideas outlined above is complicated, and as yet there are no simulation results which might clarify whether the scheme works or not. Nevertheless, it is possible to give a brief outline of the model.

6.1. Coherent Energy Exchange and Degenerate State Transitions

Were we to begin with a basic description of the system starting at the point of single phonon and plasmon exchange, the resulting coherent dynamics calculation would be very complicated and non-intuitive. There would be a messy

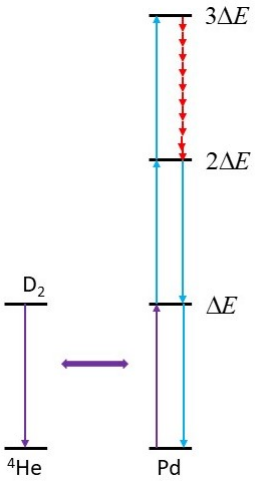

Figure 11. Schematic of excess heat production scheme in Pd. The initial (second-order) excitation transfer from the fusion transition is in purple; the upward and downward transition resulting from third-order interactions are in light blue; and the great many second-order or fourth-order transitions responsible for the primary energy exchange with the lattice are shown in red.

mix of resonant and off-resonant interactions, with off-resonant loss processes critical for the acceleration of excitation transfer processes and coherent energy exchange. Instead of working with such a complicated model, things are simpler if the problem is split into two simpler pieces.

Some years ago we analyzed coherent energy exchange in the case of a lossy spin-boson model, where the loss is asymmetric in the off-resonant energy [24], [25], [26]. What we found can be summarized according to

$$\text{direct}: \quad V_0 \quad \rightarrow \quad V_0 \frac{\Phi}{(\Delta n)^2} \quad : \text{indirect} \tag{28}$$

In essence, the direct interaction strength for a single quantum exchange V_0 leads to an indirect coupling strength between degenerate states that is reduced by a hindrance factor $\Phi/(\Delta n)^2)$, where nuclear energy is transferred to the oscillator according to

$$\Delta E \; = \; \Delta n \hbar \omega_0 \tag{29}$$

This observation is key to our thinking. It provides a way to separate the coherent energy exchange calculation from the coherent nuclear dynamics model involving transitions between a sequence of degenerate states.

Based on this observation, we can understand the much more complicated model through two separate simple models. One of these involves the calculation of hindrance factors associated with coherent energy exchange. The other involves modeling sequential coherent transitions between a sequence of resonant states that the system evolves through. In this section our focus is on the coherent nuclear dynamics between the degenerate states.

6.2. Hamiltonian

If we can separate the coherent energy exchange calculation, then we end up with a coherent nuclear dynamics calculation involving (nuclear $\otimes$ phonon $\otimes$ plasmon) states which have the same energy. The indirect coupling matrix elements involved not only describe the coupling required for the nuclear transitions of interest, but also the hindrance

that comes from coherent energy exchange that involves a great many individual interactions with the oscillators in which one quantum is exchanged at a time.

In this case, the dynamics discussed in the previous section can be described by a Hamiltonian involving only resonant terms, including transitions due to second-order interactions (for excitation transfer), as well as a subset of the third-order interactions (which promote excitation to get to the high density of states region, and subsequently bring excitation back down), and a subset of the fourth-order interactions (which takes advantage of pairs of transitions which have close initial and final states). Such a model can be expressed as

$$\begin{aligned}\hat{H} = &\sum_j \frac{1}{2}\hbar\Omega_{f,j}\left(\frac{S_+^f}{\hbar}\frac{S_-^j}{\hbar} + \frac{S_-^f}{\hbar}\frac{S_+^j}{\hbar}\right)\\ &+ \sum_{j\neq k}\frac{1}{2}\hbar\Omega_{j,k}\left(\frac{S_+^j}{\hbar}\frac{S_-^k}{\hbar} + \frac{S_-^j}{\hbar}\frac{S_+^k}{\hbar}\right)\\ &+ \sum_{j,k,l}\frac{1}{2}\hbar\Omega_{j,k,l}\left(\frac{S_+^j}{\hbar}\frac{S_-^k}{\hbar}\frac{S_-^l}{\hbar} + \frac{S_-^j}{\hbar}\frac{S_+^k}{\hbar}\frac{S_+^l}{\hbar}\right)\\ &+ \sum_{j,k,l,m}\frac{1}{2}\hbar\Omega_{j,k,l,m}\left(\frac{S_+^j}{\hbar}\frac{S_+^k}{\hbar}\frac{S_-^l}{\hbar}\frac{S_-^m}{\hbar} + \frac{S_-^j}{\hbar}\frac{S_-^k}{\hbar}\frac{S_+^l}{\hbar}\frac{S_+^m}{\hbar}\right)\end{aligned} \tag{30}$$

where the first set of terms account for the transfer of excitation from the fusion system to the compact states D_2^*, and the second set of terms account for excitation transfers between nuclear molecule states. The third and fourth set of terms account for higher-order excitation transfer processes, as discussed above. This Hamiltonian makes use of pseudo-spin operators ($\mathbf{S}^j = \sum_a \mathbf{s}_a^j$) to keep track of level populations, and treats many-level systems as if they acted as simple two-level systems for individual transitions.

6.3. Fusion to Compact State Interaction Strength

The general form of the degenerate Hamiltonian above is determined by the nuclear states involved in the scheme described in the previous section. The rate at which the nuclear coherent dynamics evolves is determined by the interaction strengths, which we consider briefly in this subsection.

The strength of the first excitation transfer step is of the form

$$\hbar\Omega_{f,j} \;=\; 2\frac{(\mathbf{a}\cdot c\mathbf{P})_f(\mathbf{a}\cdot c\mathbf{P})_j}{\Delta E_{f,j}}\left(\sqrt{\frac{V_{nuc}}{V_{mol}}}e^{-G}\right)_f \tag{31}$$

The individual transitions are assumed here to be M2 transitions mediated by the relativistic phonon-nuclear interaction [30], where the $\mathbf{a}$ are internal nuclear transition matrix elements, and where $\mathbf{P}$ is the center of mass momentum of the 4-body system for the fusion system (f) and for the compact state system (j). Note that there are quite a few molecular D_2 states possible (^{1,5}S, ^{3}P, $\cdots$), and the M2 interaction here focuses on coupling to ^{3}P molecular D_2 states. In this expression the Gamow and volume factors have been extracted from the nuclear M2 $\mathbf{a}$-matrix element to emphasize that this transition is hindered due to Coulomb repulsion. Note that the coherent dynamics rate can be on the order of the magnitude of the indirect coupling matrix element divided by $\hbar$, which means that it can be linear in e^{-G}, where incoherent fusion reactions scale as e^{-2G}. This makes explicit that the coherent dynamics can potentially be orders of magnitude faster than the rate of incoherent fusion decays. Note that indirect coupling associated with excitation transfer would have this form in the limit that off-resonant loss removes destructive interference completely, which requires that $\hbar\Gamma$ is much larger than the transition energy ΔE.

6.4. Interaction Strength for Nuclear Molecule Transitions

The simplest possible model for interactions between nuclear molecule transitions is

$$\hbar\Omega_{j,k} \;=\; 2\frac{(\mathbf{d}\cdot\mathbf{E})_j(\mathbf{d}\cdot\mathbf{E})_k}{\Delta E_{j,k}}\frac{\Phi_{j,k}}{(\Delta n)^2_{j,k}} \tag{32}$$

where we assume that transitions between the stable Pd isotope ground states and nuclear molecule states are mediated by electric dipole transitions. Also possible are magnetic dipole transitions mediated by oscillating magnetic fields associated with spin-wave modes, and M2 transitions mediated by the relativistic phonon-nuclear interaction. Once again, we assume that off-resonant loss eliminates destructive interference, leading to the form of the interaction. We expect a hindrance factor $\Phi/(\Delta n)^2$ analogous to what we found previously [24]-[26], except that a new model will be needed to evaluate it since two-quantum exchange is possible for individual excitation transfer steps (where the earlier models were analyzed for one-quantum exchange). Also, it is clear now that the calculations are going to need to extend to a range of stronger coupling than what was considered previously.

There are issues involved in connection with the evaluation of the dipole moment for these transitions. When first proposed we anticipated small dipole moments, perhaps in the range of $10^{-8}-10^{-5}$ e-fm, primarily since if the dipole moments were larger the radiative decay rates would seem to be too fast. However, more recently we have understood that to connect with experiment the dipole moments will need to be much larger. Such large dipole moments for direct transitions seem to be problematic due to the fast associated radiative decay. It is likely that the coupling would need to be indirect, so that radiative transitions directly back down to the Pd ground states are forbidden. The thought is to consider models written in terms of low-order coupling for now, and move to indirect transitions when the models are better understood.

The specification of coupling strengths for the higher-order transitions included in the Hamiltonian would work similarly.

6.5. Ehrenfest Theorem Dynamics

The dynamics of the expectation values can be determined using Ehrenfest's theorem, which might be written for a general operator $\hat{Q}$ as [31]

$$\frac{d}{dt}\langle\hat{Q}\rangle \;=\; \left\langle\frac{\partial\hat{Q}}{\partial t}\right\rangle + \frac{1}{i\hbar}\left\langle[\hat{Q},\hat{H}]\right\rangle \tag{33}$$

This approach is often used to develop equivalent classical equations of motion for a quantum mechanical model.

For the model described above, we can write for the fusion transitions

$$\begin{aligned}
\frac{d}{dt}S_x^f &= \sum_k \Omega_{k,f}\frac{S_y^k}{\hbar}S_z^f \\
\frac{d}{dt}S_y^f &= -\sum_k \Omega_{k,f}\frac{S_x^k}{\hbar}S_z^f \\
\frac{d}{dt}S_z^j &= \sum_k \Omega_{k,f}\left(\frac{S_x^k}{\hbar}S_y^f - \frac{S_y^k}{\hbar}S_x^f\right)
\end{aligned} \tag{34}$$

For the excited nuclear molecule transitions we have

$$\frac{d}{dt}S_x^n = \sum_f \Omega_{f,n}\frac{S_y^f}{\hbar}S_z^n + \sum_k \Omega_{k,n}\frac{S_y^k}{\hbar}S_z^n + \sum_{k,l}\Omega_{n,k,l}\left(\frac{S_x^k}{\hbar}\frac{S_y^l}{\hbar}+\frac{S_y^k}{\hbar}\frac{S_x^l}{\hbar}\right)S_z^n + \sum_{j,l}\Omega_{j,n,l}\left(\frac{S_y^j}{\hbar}\frac{S_x^l}{\hbar}-\frac{S_x^j}{\hbar}\frac{S_y^l}{\hbar}\right)S_z^n + \sum_{k,l,m}\Omega_{n,k,l,m}\left(\frac{S_x^k}{\hbar}\left(\frac{S_y^l}{\hbar}\frac{S_x^m}{\hbar}+\frac{S_x^l}{\hbar}\frac{S_y^m}{\hbar}\right)+\frac{S_y^k}{\hbar}\left(\frac{S_y^l}{\hbar}\frac{S_y^m}{\hbar}-\frac{S_x^l}{\hbar}\frac{S_x^m}{\hbar}\right)\right)S_z^n \tag{35}$$

$$\frac{d}{dt}S_y^n = -\sum_f \Omega_{f,n}\frac{S_x^f}{\hbar}S_z^n - \sum_k \Omega_{k,n}\frac{S_x^k}{\hbar}S_z^n + \sum_{k,l}\Omega_{n,k,l}\left(\frac{S_y^k}{\hbar}\frac{S_y^l}{\hbar}-\frac{S_x^k}{\hbar}\frac{S_x^l}{\hbar}\right)S_z^n - \sum_{j,l}\Omega_{j,n,l}\left(\frac{S_x^j}{\hbar}\frac{S_x^l}{\hbar}+\frac{S_y^j}{\hbar}\frac{S_y^l}{\hbar}\right)S_z^n - \sum_{k,l,m}\Omega_{n,k,l,m}\left(\frac{S_x^k}{\hbar}\left(\frac{S_x^l}{\hbar}\frac{S_x^m}{\hbar}-\frac{S_y^l}{\hbar}\frac{S_y^m}{\hbar}\right)+\frac{S_y^k}{\hbar}\left(\frac{S_y^l}{\hbar}\frac{S_x^m}{\hbar}+\frac{S_x^l}{\hbar}\frac{S_y^m}{\hbar}\right)\right)S_z^n \tag{36}$$

$$\frac{d}{dt}S_z^n = \sum_f \Omega_{f,n}\left(\frac{S_x^f}{\hbar}S_y^n-\frac{S_y^f}{\hbar}S_x^n\right) + \sum_k \Omega_{k,n}\left(\frac{S_x^k}{\hbar}S_y^n-\frac{S_y^k}{\hbar}S_x^n\right) - \sum_{k,l}\Omega_{n,k,l}\left(\frac{S_y^k}{\hbar}\frac{S_x^l}{\hbar}+\frac{S_x^k}{\hbar}\frac{S_y^l}{\hbar}\right)S_x^n + \sum_{k,l}\Omega_{n,k,l}\left(\frac{S_x^k}{\hbar}\frac{S_x^l}{\hbar}-\frac{S_y^k}{\hbar}\frac{S_y^l}{\hbar}\right)S_y^n - \sum_{j,l}\Omega_{j,n,l}\left(\frac{S_y^j}{\hbar}\frac{S_x^l}{\hbar}+\frac{S_x^j}{\hbar}\frac{S_y^l}{\hbar}\right)S_x^n + \sum_{j,l}\Omega_{j,n,l}\left(\frac{S_x^j}{\hbar}\frac{S_x^l}{\hbar}-\frac{S_y^j}{\hbar}\frac{S_y^l}{\hbar}\right)S_y^n + \sum_{k,l,m}\Omega_{n,k,l,m}\left(-\frac{S_x^k}{\hbar}\left(\frac{S_x^l}{\hbar}\frac{S_y^m}{\hbar}+\frac{S_y^l}{\hbar}\frac{S_x^m}{\hbar}\right)+\frac{S_y^k}{\hbar}\left(\frac{S_x^l}{\hbar}\frac{S_x^m}{\hbar}-\frac{S_y^l}{\hbar}\frac{S_y^m}{\hbar}\right)\right)S_x^n + \sum_{k,l,m}\Omega_{n,k,l,m}\left(\frac{S_x^k}{\hbar}\left(\frac{S_x^l}{\hbar}\frac{S_x^m}{\hbar}-\frac{S_y^l}{\hbar}\frac{S_y^m}{\hbar}\right)+\frac{S_y^k}{\hbar}\left(\frac{S_y^l}{\hbar}\frac{S_x^m}{\hbar}+\frac{S_x^l}{\hbar}\frac{S_y^m}{\hbar}\right)\right)S_y^n \tag{37}$$

The dynamical equations can be augmented with loss terms to account for tunnel decay of the nuclear molecules for transmutation and for low-level nuclear emissions. This involves the replacement of the time derivatives according to [31]

$$\frac{d}{dt}\mathbf{S}^n \;\rightarrow\; \frac{d}{dt}\mathbf{S}^n + \frac{\mathbf{S}^n}{\tau_n} \tag{38}$$

The pseudo-spin dynamics can be augmented with dynamical equations for the optical and acoustic phonon modes, to provide a more complete overall system description. Most of the energy transferred in this model would go into the optical phonon mode simply because the energy quantum is larger; nevertheless some goes into the acoustic mode, and how much can be determined from a coherent energy transfer model.

6.6. Discussion

To see whether the model under discussion is successful in describing excess heat, transmutation, and also low-level nuclear emissions we are going to need to solve the dynamical equations. A challenge is that on the general order of a thousand transitions would ideally need to be modeled for excess heat, which suggests that it would be appropriate to develop various reduces and simplified versions of the model that are easier to understand and analyze. A headache is that we will likely never have accurate values for the excited state nuclear molecule energies or for the transition matrix elements. So most likely we face using the models to understand what range of transition matrix element magnitudes are consistent with experiment through this kind of model.

7. Conclusions

Early models for deuteron-deuteron fusion based on the Golden Rule are conceptually simple, and reasonably straightforward to evaluate. For such a calculation one requires a specification of the initial state, the final state, and the model nuclear potential [32]. With the evaluation of the transition matrix element, and combining the square with the density of states and a prefactor, one arrives at the fusion cross section which with only modest overall effort connects reasonably well with experiment.

Contrast this with all of the various calculations that appear to be needed to evaluate the model for coherent deuteron-deuteron fusion as outlined in this paper. The conclusion is that excess heat in the Fleischmann-Pons experiment is much more complicated. It is not surprising that an appropriate theory did not emerge during the early days of the field, as the focus was on conceptually simple explanations and approaches. Nevertheless, if excess heat works as outline in this paper, then it is understandable and we can work with it.

The number of issues raised in this paper is very large, and here only a few will be considered.

It is conceptually simplest to imagine that a nuclear molecule from a Pd isotope will have a reasonably close resonance with the D_2/^{4}He fusion transition. However, there is no guarantee that the resonance will be good enough. It may be that there will be a close resonance for excitation to a reasonably stable nuclear molecule is some isotope, and perhaps this isotope is an impurity in the cathodes used. A precise resonance is guaranteed for ^{4}He/D_2^* excitation, which involves a compact D_2^* state.

The density of states is much higher in the vicinity of $2\Delta E$, so as long as sufficient coherent energy exchange is possible, these transitions should work OK.

For third and fourth-order excitation processes to become important and to play a significant role in the coherent nuclear dynamics, the coupling must be strong. In the model outlined above, this can occur if large Dicke enhancement factors occur (which means that the quantity $|\hat{\mathbf{i}}_z \times \mathbf{S}|$ associated with the relevant pseudostate $\mathbf{S}$-vectors must be large). This is consistent with a larger number of fusion transitions and relevant nuclear molecule transitions being coupled to a common highly-excited acoustic phonon mode, which could be if a larger sample is involved, and if the amplitudes of the acoustic and optical phonon mode amplitudes are large (same for the plasmon mode amplitude).

There does not seem to be anything in principle to prevent an LENR system from reaching a regime in which the coupling is sufficiently strong that fourth-order (or even higher-order) interactions become important.

We previously speculated that low-level energetic alpha decay might be due to nuclear molecules in which one of the daughters is an alpha particle. It is clear from the simple nuclear molecule model above that such states would be expected to decay rapidly, which would be consistent with a low-level emission process. The same kind of mechanism would apply to low-level emission of other light particles.

If the coupling between the Pd ground state nuclei and nuclear molecules is of low order, then we would expect low-level gamma emission above 40 MeV. Such gammas would be detectable, and if seen would provide strong confirmation of the models under discussion. More likely, the coupling to these levels would be indirectly, and gamma emission suppressed.

In the coherent reaction scheme proposed here there is a clear connection between excess heat production and transmutation. The two go hand in hand, and transmutation at low levels would be expected during excess heat production. Massive transmutation would mean that the system is close to producing excess heat, but frustrated by an increasing spacing between pairs as transitions occur further and further from the nuclear molecule band head. The model suggests that some excess heat production occurs in connection with transmutation, and that what transmutation daughters are produced depends on how much coherent energy transfer occurs. This implies that it may be possible to eventually provides some control over which transmutation daughters are produced in an experiment.

For coherent energy exchange the discussion focused on the special case involving a uniform acoustic phonon mode and a uniform optical phonon mode with nonlinear coupling, but it is clear that this is not the only possibility. It would be expected that a strongly excited uniform acoustic mode would be important (since it is easy to excite, and can couple the largest number of nuclei); however, it is probable that generalizations of the model will work for multiple optical phonon modes with less uniform interactions, as well as indirect coupling with plasmon modes (as well as other condensed matter collective modes). Intuitively, the nuclear transitions need to dump energy for the process to proceed, and the larger the quantum of the collective mode, the fewer quanta need to be exchanged, and potentially the more efficient the system can work (within the constraints mentioned previously, such as the requirement for strong Dicke-enhanced coupling).

Note that while the discussion has focused on nuclear molecule states as candidate excited states that are reasonably stable, the same ideas and approach is relevant to coupling in the case of metastable excited nuclear states, except that the coupling would involve higher multipolarity than electric dipole coupling.

Finally, it seems clear that we are going to need to develop reduced versions of the model that are more easily analyzed and worked with.

Note added in proof: It was also understood after the paper was accepted that the compact D_2^* excited states are all unstable to fast 3+1 decay, so they cannot be doorway states for promotion to nuclear molecule states at $2\Delta E$. I was also understood after the paper was accepted that the $\mathbf{a} \cdot c\mathbf{P}$ interaction leads to matrix elements orders of magnitude larger than for the $-\mathbf{d} \cdot \mathbf{E}$ interaction, so that it is likely that all important transitions in the model will be mediated by the $\mathbf{a} \cdot c\mathbf{P}$ interaction.

References

[1] P. L. Hagelstein and I. U. Chaudary, "Anomalies in fracture experiments, and energy exchange between vibrations and nuclei," *Meccanica* **50** (2015) 1189–1203.

[2] D. A. Bromley, J. A. Kuehner and E. Almqvist, "Resonant elastic scattering of C^{12} by carbon," *Phys. Rev. Lett.* **4** (1960) 365.

[3] E. Almqvist, D. A. Bromley and J. A. Kuehner, "Resonances in C^{12} on carbon reactions," *Phys. Rev. Lett.* **4** (1960) 515.

[4] E. Vogt and H. McManus, " Molecular states formed by two carbon nuclei," *Phys. Rev. Lett.* **4** 518.

[5] N. Bohr and J. A. Wheeler, "The mechanism of nuclear fission," *Phys. Rev.* **56** (1939) 426.

[6] L. G. Moretto, P. T. Lake, L. Phair and J. B. Elliott, "Reexamination and extension of the liquid drop model: Correlation between liquid drop parameters and curvature term," *Physical Review C* **86** (2012) 021303.

[7] Y. Cao, D. Lu, Y. Qian and Z. Ren, "Uncertainty analysis for the nuclear liquid drop model and implications for the symmetry energy coefficients," *Physical Review C* **105** (2022) 034304.

[8] H. J. Krappe, J. R. Nix and A. J. Sierk, "Unified nuclear potential for heavy-ion elastic scattering, fusion, fission, and ground-state masses and deformations," *Phys. Rev. C* **20** (1979) 992.

[9] A. J. Sierk, "Macroscopic model of rotating nuclei," *Phys. Rev. C* **33** (1986) 2039.

[10] P. Möller, A. J. Sierk, T. Ichikawa and H. Sagawa, "Nuclear ground-state masses and deformations: FRDM," *Atomic Data and Nuclear Data Tables* **109** (2012) 1–204.

[11] J. R. Nix and A. J. Sierk, "Potential-energy surfaces for heavy-ion collisions," *Physica Scripta* **10** (1974) 94.

[12] K. T. Davies and J. R. Nix, "Calculation of moments, potentials, and energies for an arbitrarily shaped diffuse-surface nuclear density distribution," *Physical Review C* **14** (1976) 1977.
[13] R. Bengtsson, P. Möller, J. R. Nix and J. Y. Zhang, "Nuclear shapes and shape transitions," *Physica Scripta* **29** (1984) 402.
[14] J.R. Nix, "Further studies in the liquid-drop theory on nuclear fission," *Nuclear Physics A* **130** (1969) 241.
[15] L. Satpathy and P. Sarangi, "Resonances of the bonding potential of ^{12}C+^{12}C system," *Journal of Physics G: Nuclear and Particle Physics* **16** (1990) 469.
[16] A. Diaz-Torres and M. Wiescher, "Characterizing the astrophysical S factor for ^{12}C+^{12}C fusion with wave-packet dynamics," *Physical Review C* **97** (2018)055802.
[17] K. Godbey, C. Simenel and A. S. Umar, "Absence of hindrance in a microscopic ^{12}C+^{12}C fusion study," *Physical Review C* **100** (2019) 024619.
[18] A. Diaz-Torres, L. R. Gasques and M .Wiescher, "Effects of nuclear molecular configurations on the astrophysical S-factor for ^{16}O+^{16}O," *Physics Letters B* **652** (2007) 255.
[19] C. Simenel, R. E. C. E. P. Keser, A. S. Umar and V. E. Oberacker, "Microscopic study of ^{16}O+^{16}O fusion," *Physical Review C* **88** (2013) 024617.
[20] P. L. Hagelstein and I. U. Chaudhary, "Energy exchange in the lossy spin-boson model," *J. Condensed Matter Nucl. Sci.* **5** (2011) 52–71.
[21] P. L. Hagelstein and I. U. Chaudhary, "Dynamics in the case of coupled degenerate states," *J. Condensed Matter Nucl. Sci.* **5** (2011) 72–86.
[22] P. L. Hagelstein and I. U. Chaudhary, "Second-order formulation and scaling in the lossy spin-boson model," *J. Condensed Matter Nucl. Sci.* **5** (2011) 87–101.
[23] P. L. Hagelstein and I. U. Chaudhary, "Local approximation for the lossy spin-boson model," *J. Condensed Matter Nucl. Sci.* **5** (2011) 102–115.
[24] P. L. Hagelstein and I. U. Chaudhary, "Coherent energy exchange in the strong coupling limit of the lossy spin-boson model," *J. Condensed Matter Nucl. Sci.* **5** (2011) 116–139.
[25] P. L. Hagelstein and I. U. Chaudhary, "Generalization of the lossy spinboson model to donor and receiver systems," *J. Condensed Matter Nucl. Sci.* **5** (2011) 140–154.
[26] P. L. Hagelstein and I. U. Chaudhary, "Pulse and amplitude approximation for the lossy spinboson model," *J. Condensed Matter Nucl. Sci.* **9** (2012) 30–49.
[27] P. L. Hagelstein "Phonon-mediated nuclear excitation transfer," *J. Condensed Matter Nucl. Sci.* (2018) **27** 97.
[28] C. B. Chiu, E. C. G. Sudarshan and B. Misra, "Time evolution of unstable quantum states and a resolution of Zeno's paradox," *Physical Review D* **16** (1977) 520.
[29] F. Schäfer, I. Herrera, S. Cherukattil, C. Lovecchio, F. S. Cataliotti, F. Caruso and A. Smerzi, "Experimental realization of quantum zeno dynamics," *Nature communications* **5** (2014) 3194.
[30] P. L. Hagelstein, "Lowest-order relativistic interaction between lattice vibrations and internal degrees of freedom of a nucleus," *Journal of Physics B: Atomic, Molecular and Optical Physics* **56** (2023) 195002.
[31] P. L. Hagelstein, S. D. Senturia and T. P. Orlando, *Introductory applied quantum and statistical mechanics*, John Wiley & Sons (2004).
[32] D. U. Yu, "On the question of charge symmetry in D-D reactions," *Progress of Theoretical Physics* **36** (1966) 734–744.

J. Condensed Matter Nucl. Sci. 38 (2024) 269–286

Research Article

Anomalous Heat Burst Triggered by Input Power Perturbations observed in Ni-Based Nanostructured Thin Films with Hydrogen

Y. Iwamura, T. Itoh, and Jirohta Kasagi

Research Center for Electron Photon Science, Tohoku University, 982-0826 Japan

T. Itoh, T. Takahashi, S. Yamauchi, M. Saito, S. Murakami, and T. Hioki

CLEAN PLANET Inc., 105-0022 Japan

T. Hioki

Institutes of Innovation for Future Society, Nagoya University, 464-8603, Japan

Abstract

The authors developed an innovative method to induce anomalously large heat generation phenomena that cannot be explained by known chemical processes. Ni-based nano-sized multilayer film is preloaded with hydrogen gas and heated rapidly to diffuse hydrogen and trigger the heat generation reaction. Two nano-sized metal multilayer composite samples, which were composed of Ni, Cu, and the other thin films on bulk Ni (25 mm × 25 mm × 0.1 mm), were used. Anomalous heat generations were observed during the experiments under vacuum condition ($<10^{-4}$ Pa) using nano-sized metal multilayer composites on Ni substrate, with hydrogen gas. Released energy evaluated with total amount of absorbed hydrogen reached to more than 10 keV/H. In addition to steady-state anomalous heat generation, spontaneous heat burst phenomena were sometimes observed. Based on the observation of spontaneous heat bursts, we can now trigger intentional heat bursts. The energy from even a single heat burst exceeds the energy produced by any known chemical reactions. Observation of heat bursts has improved the reliability of excess heat experiments. Samples that generated excess heat or heat bursts often show some areas of very high oxygen concentration after the experiment according to SEM-EDX and TOF-SIMS analyses.
 ISSN 2227-3123

Keywords: Anomalous heat, Heat burst, Excess heat, Nickel, Copper, Multilayer thin film, Nano-sized metal composite, Nano material, Hydrogen gas, Gas loading

1. Introduction

The authors have been studying energy generation using nano-sized multilayer metal composites with hydrogen gas. First, we briefly describe how we got started with our current research methodology. Originally, we discovered

© 2023 ICCF. All rights reserved. ISSN 2227-3123

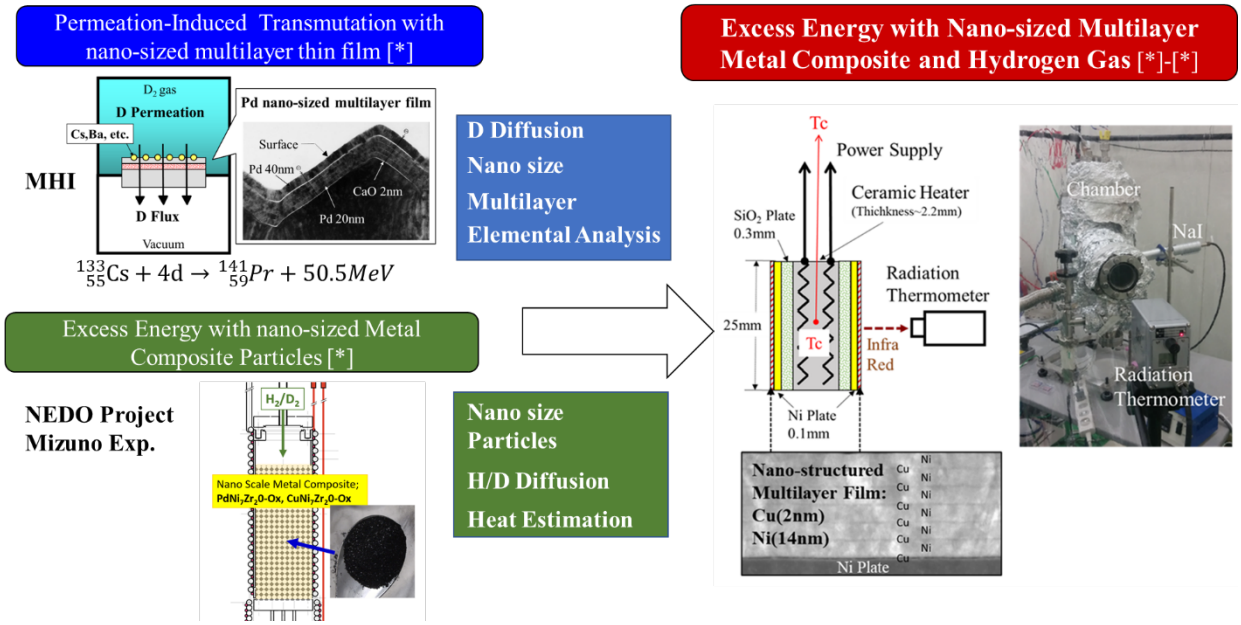

Figure 1. Background and Motivation of the Present Experimental Method.

transmutation phenomena induced by deuterium gas permeation through nanosized Pd multilayers doped with Cs and other elements [1]–[4]. We observed the transmutation of Cs into Pr by this method, which has been reproduced by other independent research institutes [5]. This study shows that the diffusion of deuterium and nano-sized multilayers are key factors in inducing the transmutation reaction [2], [4]. After moving to Tohoku University, we had a chance to participate in a national project funded by NEDO (New Energy and Industrial Technology Development Organization) to observe anomalous heat generation by deuterium or hydrogen absorption in Pd or Ni nanoparticles. We learned that anomalous phenomena occur not only with deuterium but also with light hydrogen, and that the nano-sized composite particle is one of the key factors to inducing the anomalous phenomena [6]–[8]. By combining the two methods, we have developed a new kind of experimental procedure to induce an exothermic reaction by loading light hydrogen in a nickel-based composite material with nano-sized multilayers, and then diffusing the light hydrogen through the nano-multilayers by rapid heating. This new experimental method is being used to elucidate the mechanism of the phenomenon. In addition, this method has led to a larger excess energy per hydrogen atom [9]–[16].

At present, the mechanism of this anomalous heat generation is not clearly understood. Based on observations of anomalous heating that cannot be explained by chemical reactions and nuclear transmutations, we speculate that the phenomenon may be of nuclear origin. However, since the mechanism has not yet been clearly elucidated, we have decided to call this phenomenon QHE (Quantum Hydrogen Energy) [9]. One of the reasons for this is that "nuclear" term is associated with a complicated and dangerous image that is difficult for the general public to accept. QHE can be defined as "An exothermic reaction induced by quantum phenomena during the diffusion process in a nanoscale metal composite material with hydrogen" shown in Fig. 2. The characteristics of QHE are as follows: 1) No CO_2 emission, and more than 10,000 times higher output energy than the combustion reaction of the same amount of hydrogen; 2) QHE does not emit harmful levels of radiation to the human body and has the potential to become a compact,

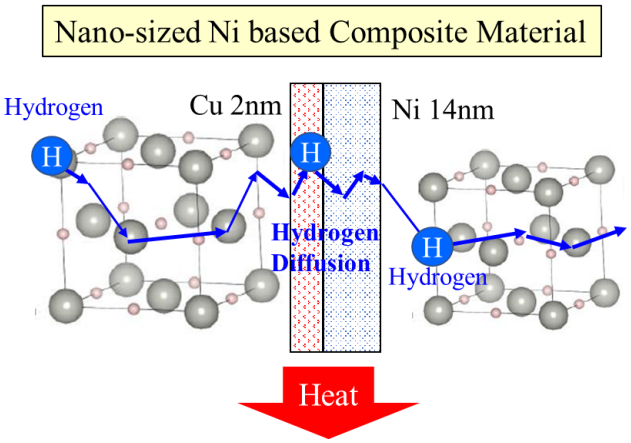

Figure 2. Quantum Hydrogen Energy (QHE)

high-power, CO_2-free energy source; 3) QHE could be used as an energy source for the production of electricity and heat.

2. Experimental

A schematic of our experimental apparatus is shown in Fig. 3(a). It is basically the same as in [9]–[10]. Two nano-sized metal multilayer composite samples, which were composed of Ni, Cu, CaO thin films on bulk Ni (25 mm $\times$ 25 mm $\times$ 0.1 mm), were placed in the center of the chamber. H_2 gas and its pressure were monitored by a Pirani gauge and a cold cathode gauge. The chamber was evacuated by a turbo molecular pump. The multilayer samples were heated up by a ceramic heater (MS-1000R; Sakaguchi E. H Voc Corp.) in which a thermocouple (TC; Pt-PtRh13%) was embedded. Surface temperatures for the two nano-sized metal multilayer composite samples were measured by two thermometers. They were made of InGaAs and dual wavelength mode, 1.55 μm and 1.35 μm, were usually used. During the surface temperature measurement, it was possible to measure the emissivity of the sample surface by switching between single wavelength mode and dual wavelength mode. Heater input power was supplied by a DC power source in constant voltage mode. The input voltage and current were measured both by voltage and current monitors provided by the power supply and an independent voltmeter and ammeter, respectively. Input power is calibrated using the voltmeter and the ammeter readings. Gamma-rays and neutrons were monitored by a NaI (Tl) scintillation counter (TCS-1172; Hitachi, Ltd.) and He-3 counter (TPS-1451; Hitachi Ltd.) during all experiments for safety reasons.

A detailed drawing of the Ni based nano-sized metal multilayer composite is shown in Fig. 3(b). It was composed of a Ni Plate (25 mm square and 0.1 mm thick) and Cu-Ni multilayer thin film (20 mm diameter circle and about 100 nm thick). These samples were fabricated by the magnetron sputtering or Ar ion beam method. The top layer of the sample is always Ni. Two nano-sized metal multilayer composite samples were heated by the ceramic heater (25 mm square and 2.2 mm thick) through SiO_2 plates (0.3 mm thick). If certain energy generation reactions occur on the surface of the samples, the temperature of the embedded thermocouple will rise. Simultaneously, infrared emission detected by the radiation thermometer, which corresponds to the surface temperature of the sample, would increase. Photos of the experimental set-ups and STEM image of Cu-Ni multilayer thin film are shown in Fig. 3.

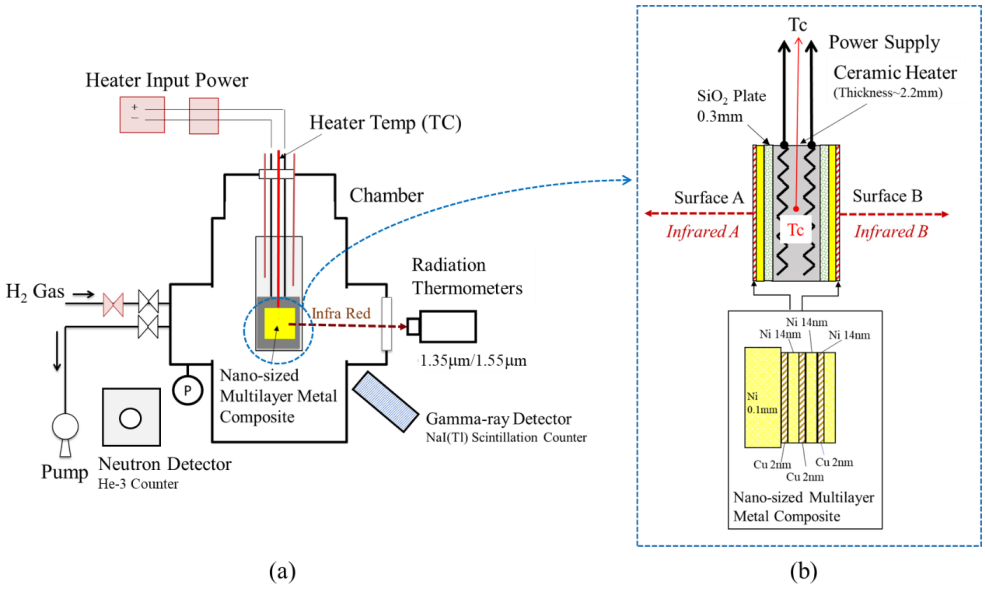

Figure 3. Experimental set-up; (a) Schematic of experimental apparatus, (b) Detail drawing around nano-sized multilayer metal composite.

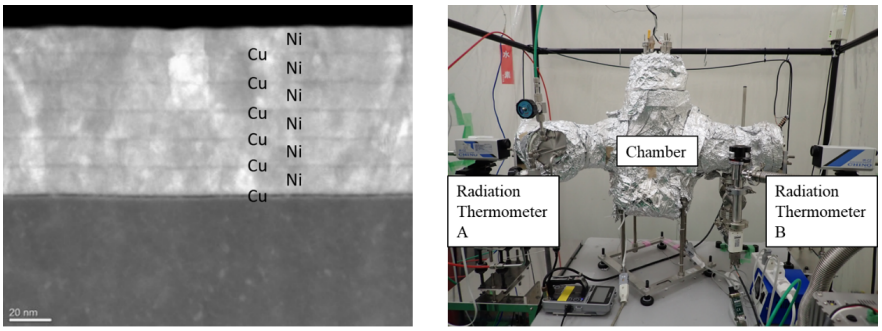

Figure 4. Photos of experimental apparatus and cross-sectional view of nano-sized metal multilayer composites; (a) STEM (Scanning transmission electron microscope) image of Cu-Ni multilayer thin film, (b) Outer view of the present experimental Set-up.

The experimental procedure is as follows. Two nano-sized metal multilayer composites were placed in the chamber and baked for 2-3 days at heater temperature 900°C to remove H_2O and other hydrocarbons from the surface under vacuum conditions.

According to general knowledge, Cu and Ni diffuse into each other during the baking process, forming a Cu-Ni alloy. However, in our multilayer film, Cu and Ni are not simply alloyed, especially when CaO, Y_2O_3, etc. are added to Ni. At present, we assume that this is due to the effect of oxygen formed on the surface during sputtering.

After the baking process, H_2 gas was introduced into the chamber up to about 200 Pa at 250°C. To change the hydrogen loading conditions, the pressure of H_2 gas was sometimes increased up to 30 kPa. H_2 gas was loaded for

about 16 hours. Then, H_2 gas was evacuated by the turbo molecular pump and simultaneously the samples were heated up by the ceramic heater up to 500∼900°C. These processes trigger heat generation reactions and anomalous heat. Typically, after 8 hours, the heater input was turned down and the samples were cooled down to 250°C. These processes (H_2 loading, heating up and cooling down samples) were repeated several times, with different heating temperatures or H_2 loading pressure.

During the above experimental procedure, hydrogen atoms are assumed to diffuse from the Ni plate through the nano-sized metal multilayer to the surface. The diffusion mechanism of hydrogen atoms is well known as "quantum diffusion" [17], although quantum diffusion is noticeable at temperatures much lower than the temperatures covered in this experiment. Hydrogen atoms are hopping from one site to another site in the metal. It is assumed that hydrogen flux is one of the key factors to induce the anomalous heat generation phenomena in the present experiments.

3. Results and Discussion

3.1. Excess Heat Evaluation

Excess Heat is evaluated based on the model described in Fig. 5(a) and the following equation (1).

$$k_{\mathrm{eff}}\frac{T_C - T_W}{L_{\mathrm{eff}}}A_{\mathrm{eff}} + A_S\sigma\left\{\varepsilon_A\left(T_{\mathrm{SA}}^4 - T_W^4\right) + \varepsilon_B\left(T_{\mathrm{SB}}^4 - T_W^4\right)\right\} + A_{\mathrm{Rloss}}\varepsilon_{\mathrm{Rloss}}\sigma\left(T_{\mathrm{Rloss}}^4 - T_W^4\right) = P_{\mathrm{in}} + H_{\mathrm{ex}}, \quad (1)$$

where k_{eff} is equivalent thermal conductivity, T_c is the thermocouple temperature embedded in the ceramic heater, T_w is the wall temperature of the chamber, L_{eff} and A_{eff} are effective length and effective surface area between the sample holder and wall, respectively. A_s is the surface area of the sample, T_S is the surface temperature, ε is the emissivity of the sample, σ is the Stefan–Boltzmann constant. subscript A and B means surface A and B, respectively. A_{Rloss}, ε_{Rloss} and T_{Rloss} are effective surface area; effective emissivity and effective surface temperature for radiation loss except from the sample surface, which is mainly derived from the sample holder. P_{in} is the electrical heater input and H_{ex} is excess power. This equation is obtained under the following assumptions.

1) Thermal conduction via H_2 gas is negligible because H_2 pressure is low.
2) Radiation from the chamber wall is negligible because T_w is room temperature.
3) The electrical input power is constant.

A blank run, in which same sized Ni bulk samples without multilayer thin films were used, was performed with the same procedure described above. Figure 5(b) shows the relationship between input power given to the ceramic heater and heater temperature detected by the thermocouple. As the radiation loss term from the sample holder is the same for Ni bulk and multilayer samples for the same temperature, generated excess heat power is evaluated based on the blank run result as shown in Fig. 3(b). Equation (1) for Ni bulk (subscript "0") is written as:

$$k_{\mathrm{eff}}\frac{T_{C0} - T_W}{L_{\mathrm{eff}}}A_{\mathrm{eff}} + A_S\sigma\left\{\varepsilon_{A0}\left(T_{SA0}^4 - T_W^4\right) + \varepsilon_{B0}\left(T_{SB0}^4 - T_W^4\right)\right\} + A_{\mathrm{Rloss}}\varepsilon_{\mathrm{Rloss}}\sigma\left(T_{Rloss0}^4 - T_W^4\right) = P_{\mathrm{in}}. \quad (2)$$

In the papers [9]–[10], excess heat analysis was done based on the assumption that ε is constant for Ni based nano-sized metal multilayer composite and Ni bulk. Emissivity ε can be measured by switching between two wavelengths mode and single wavelength mode. Actual measured emissivity was in the range of 0.1–0.2 at surface temperature 700–750°C, depending on the condition of the sample such as oxidation of surface or surface roughness, the vacuum of the experimental apparatus. However, the difference in emissivity between Ni bulk and Ni multilayer composite

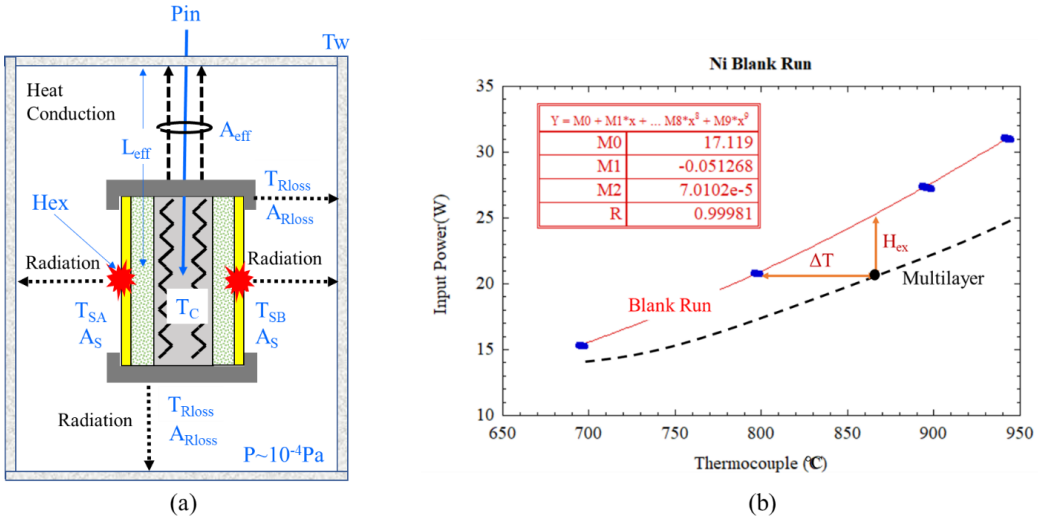

Figure 5. Excess heat evaluation; (a) Model of excess heat evaluation, (b) Relationship between input power (W) and thermocouple temperature (°C) for a blank run and a multilayer run.

samples is within 0.05, and the assumed condition is satisfied. Emissivity can be considered almost the same for the Ni bulk and multilayer composite samples.

Excess heat H_{ex} can be derived based on the equations (1) and (2). Detail formulation was described in [9]–[10]. The excess heat can be written as a function of ΔT. Therefore, excess heat evaluation by the Ni bulk calibration curve shown in Fig. 3(b) is valid under the assumptions described in [9]–[10].

3.2. Excess Heat Generation

An Example of excess heat generation is shown in Fig. 6. The used samples were covered with 6 CuNi layers (Cu=2 nm and Ni=14 nm). The red and blue lines represent excess heat and pressure of the chamber, respectively. At the beginning of the experiment, hydrogen gas was introduced to the chamber up to 200Pa and absorbed into the Ni based nano-sized multilayer metal composite at about 270°C. The pressure for each experiment gradually decreased as shown in Fig. 6. The amount of hydrogen absorbed by each sample was estimated based on the pressure change and temperature of the chamber. After about 16 hours, H_2 gas was evacuated and simultaneously each sample was heated up by the ceramic heater. After that, heat energy greater than input power was observed. The input power was stable during one cycle; for example, 19 W was applied to the ceramic heater from about 6×10^4 sec to about 1×10^5 sec.

Released excess energy per hydrogen was evaluated based on the experimental result. The amount of absorbed hydrogen, total excess energy and excess energy per absorbed hydrogen are shown in Fig. 6. The amount of excess energy was calculated as 0.76 MJ by time integration of excess power. Although it seems highly unlikely that all the absorbed hydrogen atoms reacted, we can still estimate that average released energy per absorbed total hydrogen was 12 keV/H. In the previously reported example, a total of 1.1 MJ of energy was released, and the energy released per hydrogen was 16 keV/H [9], [10], [13]. Although the released energy is somewhat lower than that, it is still definitely not at a level that can be explained by chemical reactions.

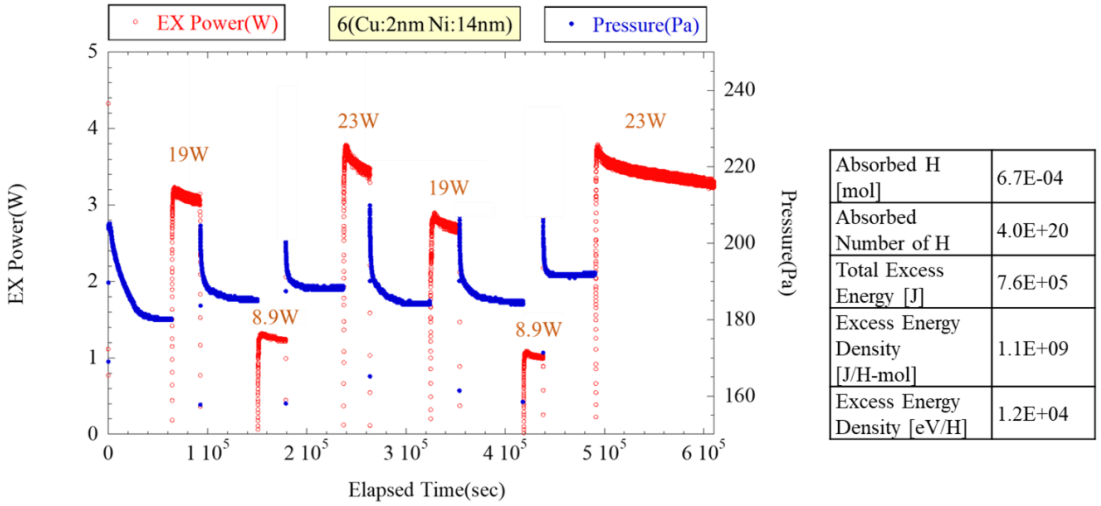

Absorbed H [mol]	6.7E-04
Absorbed Number of H	4.0E+20
Total Excess Energy [J]	7.6E+05
Excess Energy Density [J/H-mol]	1.1E+09
Excess Energy Density [eV/H]	1.2E+04

Figure 6. An example of excess heat generation

3.3. Heat Burst Phenomena

As the heat generation experiments proceeded, we began to observe a sudden increase in the amount of heat generated. In this section, we describe these heat burst phenomena, in which a rapid surface temperature increase is observed. First, examples of phenomena that cause spontaneous heat bursts are described, and then examples of intentional heat burst phenomena are described using a method devised based on observations of spontaneous heat bursts.

3.3.1. *Spontaneous Heat Burst*

Figure 7 shows an example of a spontaneous heat burst, in which temperature time variations of the temperatures for the thermocouple, surface A and B are plotted [9]–[10]. First, the temperature of surface A suddenly rises, and about 100 seconds later, the temperature of surface B rises. While these surface temperature increases are occurring, the temperature of the thermocouple embedded in the center of the heater is also gradually increasing. Detailed observations of the temperature change of the thermocouple shows that the temperature of the thermocouple increases 33 seconds after the temperature of surface A suddenly rises. Furthermore, the slope of the temperature rise of the thermocouple then increases 40 seconds after the temperature of surface B suddenly rises. From this we conclude that the heat release reaction occurred at the surface A at first and afterwards at the surface B, and heat bursts propagated to the thermocouple. Input power and room temperature were constant during these events. Therefore, these events were not caused by the change of electrical input power or heat coming in from the environment. The samples consisted of 6 layers of Cu (2 nm) and Ni (14 nm) fabricated by magnetron sputtering on Ni bulk, the same method as in [9]–[16].

Considering the material and thickness of the sample holder containing the heater, the delay time when heat is generated at the surface of the sample was roughly consistent with the observed delay time of 33 or 40 seconds [12]. Therefore, it is consistent with the interpretation that heat was generated at the sample surface and transferred to the thermocouple at the center.

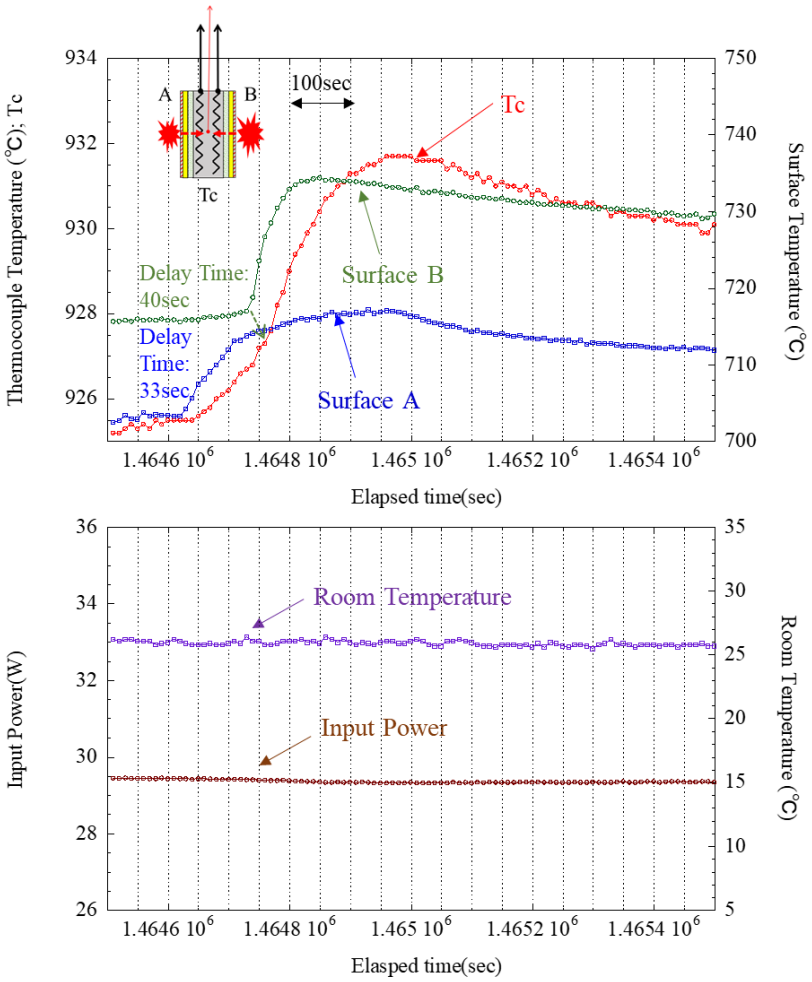

Figure 7. An example of spontaneous heat burst; Heat burst reactions occurred at surface A at first and afterwards at surface B. Their heat bursts propagated to the Tc. Input power and room temperature were constant during these events [12].

3.3.2. *Intentional Heat Burst*

When analyzing the phenomenon of spontaneous sudden heat bursts described above, it was observed that there were cases where the heat burst occurred after small changes in input power caused by fluctuations in the outside temperature, etc. Therefore, we tried to see if we could induce the heat burst by intentionally causing a small perturbation in the input power.

An example of a heat burst induced by an intentional perturbation of input electrical power is shown in Fig. 9(a). In this example, samples of 6 layers of Cu (2 nm) and Ni (14 nm) were fabricated by magnetron sputtering on Ni bulk. At the beginning, 25.8 W was input, and then decreased to 25.0 W. Then the T_C and surface temperature A and B decreased gradually. When the input was returned to the original input of 25.8 W, the surface temperature A, B, and T_c all increased and became larger than the values at the original input of 25.8 W. At maximum, T_c increased by about

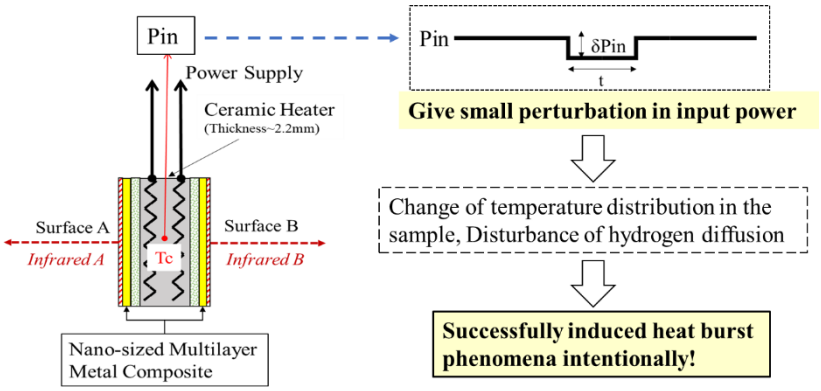

Figure 8. Intentional induction of heat burst phenomena.

9°C, surface A by about 17°C, and surface B by about 25°C. The increases in surface A and B temperatures were larger and steeper than that of T_c as shown in Fig. 9(a). We conclude that heat burst energy generated at the surface A and B, which is induced by the intentional perturbation of input power, propagated to the thermocouple.

On the other hand, an example with no heat burst phenomenon induced by a similar perturbation is shown in Fig. 9(b). In this case, Ni bulk samples were used. When the input power, which was initially 23.0 W, was reduced to 22.1 W, the thermocouple and surface temperatures A and B gradually decreased. Then, when the input power was returned to 23.0 W, the heat burst phenomenon did not occur, and the thermocouple and surface temperatures A and B returned to their original values.

Next, we examine the possibility that the observed heat burst phenomenon was caused by some chemical reactions. Figure 10 plots the change in Tc during the heat burst shown in Fig. 9(a). A heat burst induced by perturbation of input power lasted for at least 1.2×10^4 seconds. The amount of generated energy is more than the hatched region in Fig. 10. The first time in this hatched triangle corresponded to 6.0 W of excess heat, and the last time to finish the experiment was 5.6 W of excess heat. Therefore, the hatched triangle can be calculated as 5.6 to 6.0 W × 1.2E4 s = 4.8 kJ. Therefore, energy generated by a single intentionally induced heat burst is more than 4.8 kJ in this example.

Consider the following chemical reactions that may cause a heat burst:

(1) If all the residual gas is oxygen and the absorbed hydrogen is oxidized and generates heat.
(2) If the residual gas is oxygen, and the Ni metal is oxidized by it.
(3) If the residual gas consists of mixed gas (H_2:O_2=2:1), the combustion energy would give energy to the surface of the two samples.

During the heat release experimental cycle, all the hydrogen introduced for absorption was evacuated, and the degree of vacuum was less than 1×10^{-4} Pa when the heat burst phenomenon was observed. The volume of the chamber is about 9 L, so the number of moles of residual gas was less than 4×10^{-10} mol. It is known that the combustion reaction of hydrogen is about 290 kJ/mol and the heat of formation of nickel oxide is about 240 kJ/mol. Based on the number of moles of residual gas in the chamber, the heat generated in each case can be calculated as less than (1) 6×10^{-5} J, (2) 2×10^{-4} J and (3) 8×10^{-5} J. Comparing these values to the energy increased by the heat burst, 4.8 kJ, shows that they are completely negligible. This clearly shows that at least the chemical reactions (1)-(3) cannot explain the heat burst phenomenon observed in this study. Therefore, the amount of energy generated by a single intentionally induced heat burst cannot be explained by any known chemical reaction.

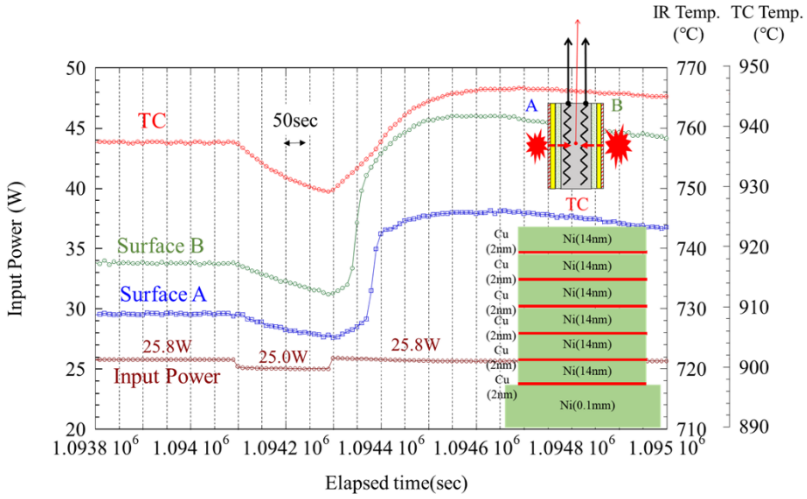

(a)

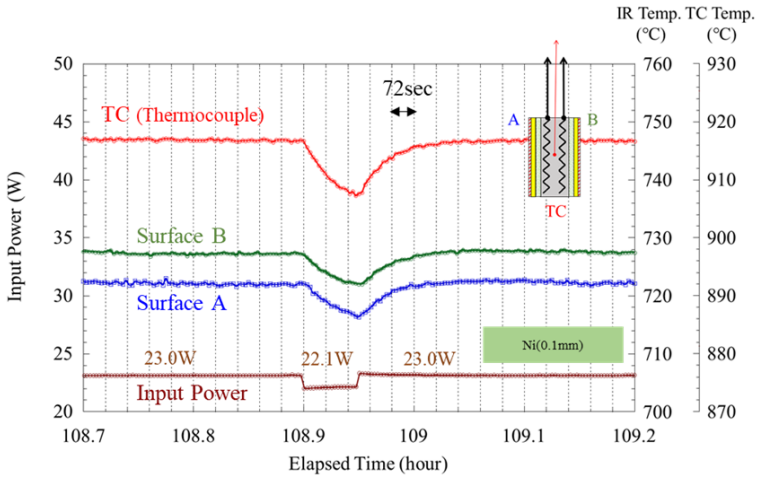

(b)

Figure 9. Different responses to intentional perturbations of input power: (a)An example of heat burst phenomenon induced by an intentional perturbation of input electrical power using CuNi multilayer samples, (b) An example where no heat burst phenomenon was induced by a similar perturbation using Ni bulk samples.

Next, we show how the intentional heat burst varies greatly, depending on sample composition and other factors. Figure 11(a) shows an example of heat burst for a 6-layer CuNi(CaO) sample with a 4.5 nm CaO layer inserted in a 14 nm Ni layer. Similar to the previous CuNi example (Fig. 9(a)), the heat burst phenomenon occurs after about 60 seconds for surface B and 120 seconds for surface A, respectively, after the input power is returned to its original value. Generated heat propagates to the heater center and the thermocouple temperature increases, similar to Figure 9(a). This type of heat burst is the most common among the experiments conducted so far.

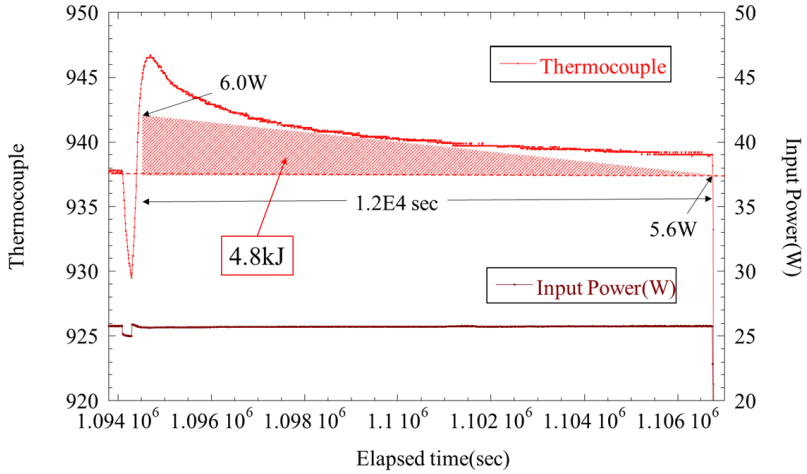

Figure 10. The amount of energy generated by an intentionally induced heat burst.

Table 1. Mill sheet for Ni bulk.

Element	Concentration (weight %)
Si	0.26
C	0.10
Mn	0.01
Mg	0.03

Figure 11(b) shows an example of a different type of intentional heat burst. After the input power was reduced from 28.4 W to 27.5 W, the heat burst phenomenon occurred on surface B before the power was increased back to 28.4 W. A weak heat burst phenomenon appears to have occurred on surface A at about the same time. Also, as before, after the input power was returned to 28.4 W, the heat burst phenomenon occurred again about 80 seconds later on surface A and about 130 seconds later on surface B. Note that the Cu thickness of this sample is thicker than usual, and the ratio of Cu to Ni is about 4.3.

It is possible to qualitatively induce this intentional heat burst phenomenon with high reproducibility in $CuNi_7$ samples of standard composition. From previous experiments, it is also known that this heat burst phenomenon depends on (1) the composition and structure of the sample, (2) the surface temperature of the sample, and (3) the magnitude and time width of the perturbation of the input power. In the experiments we are currently conducting, we are observing this heat burst phenomenon under various parameters, and we are attempting to elucidate the mechanism of the phenomenon.

3.4. Material Analysis

Various analytical methods have been applied to clarify the mechanism of the heat generation phenomenon in nano-sized multilayer metal composites. In this section, we describe the results of SEM-EDX (Scanning Electron Microscope - Energy Dispersive X-ray Spectroscopy) and TOF-SIMS (Time-Of-Flight Secondary Ion Mass Spectrometry) and discuss the obtained results.

Table 1 shows the mill sheet of the Ni bulk used for the experiments. The main impurities are Si, C, Mn and Mg. The impurities vary a little with the batch of Ni bulk, but the main impurities in Ni material are Si and Mn.

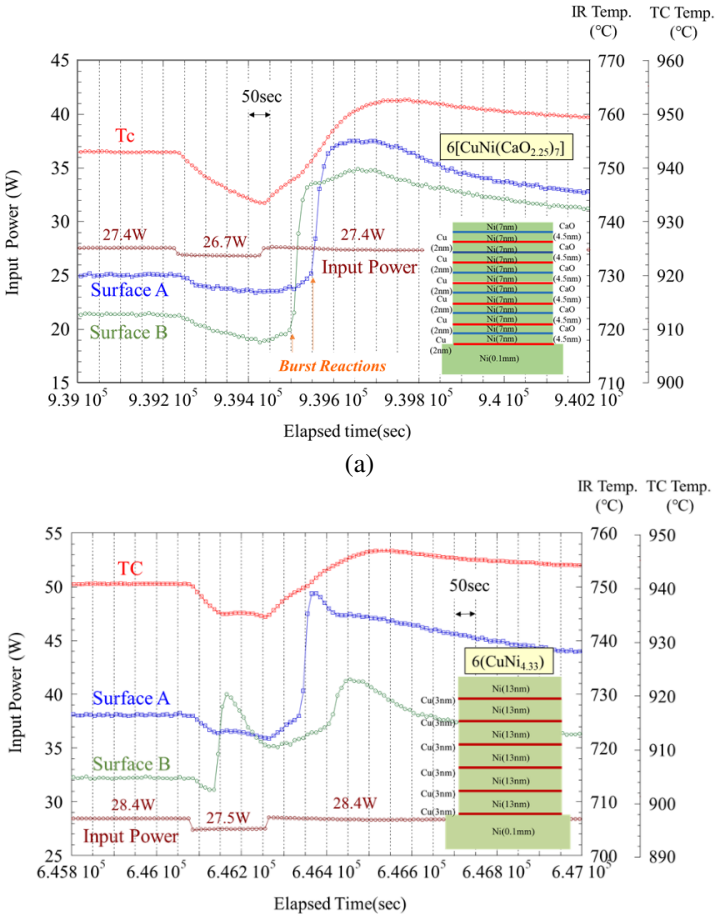

Figure 11. Variation of heat burst phenomena triggered by input power perturbation.

We normally perform SEM and EDX analysis of the sample surface for each experiment. The results of these analyses have revealed some common characteristics of the samples which produce excess heat. One example is shown in Figure 12. On the left side are the secondary electron images, and the right side are the compositional images (COMPO images) by backscattered electrons. It shows the presence of Ni crystal grains and grain boundaries ranging from several 10 μm to 100 μm. Characteristic is the presence of spotted parts in both images, which appear to be composed of elements lighter than Ni. As will be mentioned later, these black spots are areas of very high oxygen concentration.

Figure 13 shows the SEM-EDX analysis for the spontaneous heat burst sample shown in Fig. 7. Figures 13(a) and 13(b) are black spot areas, where a distinct oxygen peak is detected in the EDX spectrum, indicating a high atomic number ratio of 18% to 21%. On the other hand, Figure 13(c) is a normal area, indicating that oxygen is below the detection limit.

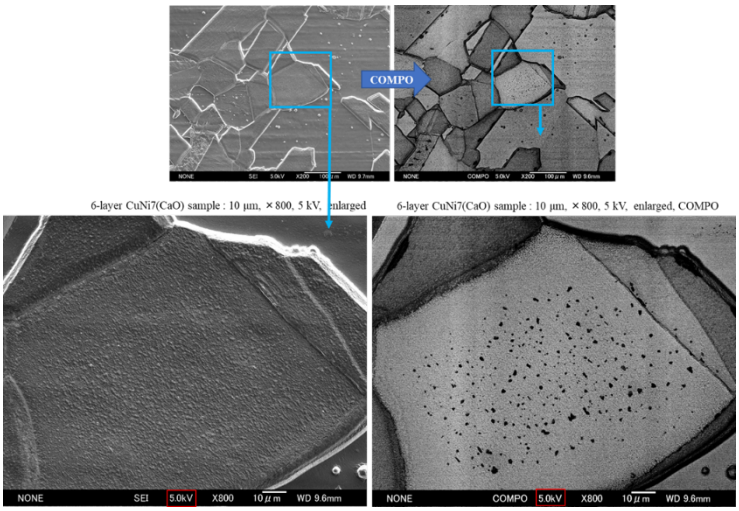

Figure 12. An example of SEM analysis after heating experiment. The spotted regions within the grains can be observed, which seems to be common to samples that observed excess heat.

Because the samples were exposed to the atmosphere after the experiment, they should be covered with NiO, however, the NiO layer is so thin that it is usually below the detection limit in the EDX spectrum, less than 1% by atomic number. Also, the Cu deposited before the experiment is not detected in the EDX spectrum because the deposited Cu was very thin, and the Cu diffused into the interior during the experiment.

Figure 14 shows SEM-EDX & TOF-SIMS analyses of the intentional heat burst sample shown in Figure 11(a). Figure 14(a) shows the result after an experiment using a sample of 6-layer CuNi7 (Cu=2nm, Ni=14nm) with 4.5nm of CaO inserted in the Ni layer: intentional heat burst phenomenon occurred. In the normal area on the left side of the figure, only Ni is detected, but in the black spot area on the right side, nearly 33% oxygen is detected by EDX.

Figure 14(b) shows the depth profile by TOF-SIMS analysis for areas with abundant black spots. Since TOF-SIMS has a larger beam diameter than EDX, we selected a region in this sample with relatively many black spots for analysis. This data is obtained using negative ion (Cs^-) and ion energy was 2 kV and ion current was 40 nA. In this TOF-SIMS analysis, the vertical axis represents the dimensionless number of counts for each ion divided by the total number of counts. As can be seen in this graph, the most abundant ion is O−, with a value of nearly 40%. Note that the orange vertical dashed line in the figure for each ion indicates the area near the interface between the surface multilayer and the Ni bulk. Although the TOF-SIMS signal is difficult to discuss quantitatively because the values vary depending on the ionizability of each element, there is no doubt that the oxygen concentration is high not only on the surface of the sample but also in the interior of the sample. Thus, for the sample in which the intentional heat burst was observed, there were spots of very high oxygen concentration by SEM-EDX, and TOF-SIMS analysis also supported the results.

An experiment was conducted to see if a black spot area of very high oxygen concentration, which was frequently observed in heat-producing samples, was caused by exposing oxygen in the air after the experiment. Figure 15 shows a selection of the highest oxygen concentration areas in the analysis results of a sample that was once removed from the chamber during the experiment, forced to oxidize at 500°C for 2 hours under atmospheric pressure, returned to the chamber, and then hydrogenated and heated again. No black spots with very high oxygen concentration were observed in this sample; Ni, Cu, Mn, Si, O, and C were observed at the grain boundary and at points 29–31, suggesting that Mn and Si are impurities in the Ni bulk and C is derived from hydrocarbons in the air. Cu, which had not been

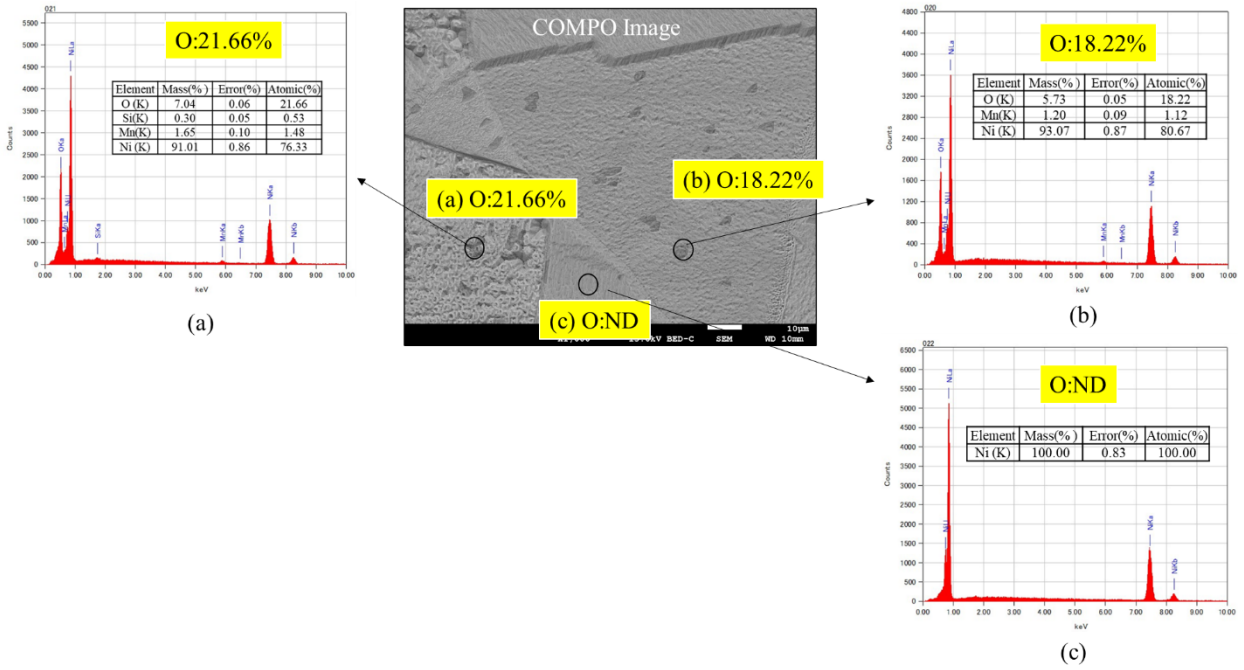

Figure 13. SEM-EDX analysis for the spontaneous heat burst sample shown in Fig. 7: (a) black spot area, (b) another black spot area, (c) normal area.

observed by EDX before, was observed in this sample. The oxygen concentration was a maximum of 4–5% at grain boundaries (31 points) and 2–3% at other points. The emissivity measured after treatment at 500°C under atmospheric pressure was almost 1, indicating that the surface was covered with a thick oxide film. Thus, once the sample has undergone forced surface oxidation, the oxygen concentration is less than 5%, even though it is mostly reduced due to the hydrogen absorption process and subsequently exposed to the atmosphere. The large number and frequency of regions with oxygen concentrations exceeding 10%, as shown in Figures 13 and 14, is an anomaly.

3.4.1. *Discussion*

In this paper, the heat burst phenomenon was described. The research implications of heat bursts are as follows. Excess heat generation is evaluated using a calibration curve. The reader may wonder whether the heat dissipation conditions are different between the time of calibration and the time of the heat generation experiment due to variations in the way the sample is mounted, etc. This is a reasonable question. However, since the heat burst phenomena were observed under the same heat dissipation conditions, it cannot be explained by the difference in heat dissipation conditions between the calibration and heat generation experiments. Therefore, it can be said that observing heat burst phenomena enhances the reliability of excess heat experiments.

The experimental results related to heat burst phenomenon were observed by the Focardi team [18]. They used Ni rods and hydrogen. They observed excess heat by once bringing the temperature of the Ni rods down to near room temperature and then abruptly returning them to their original input power level. Although the experimental

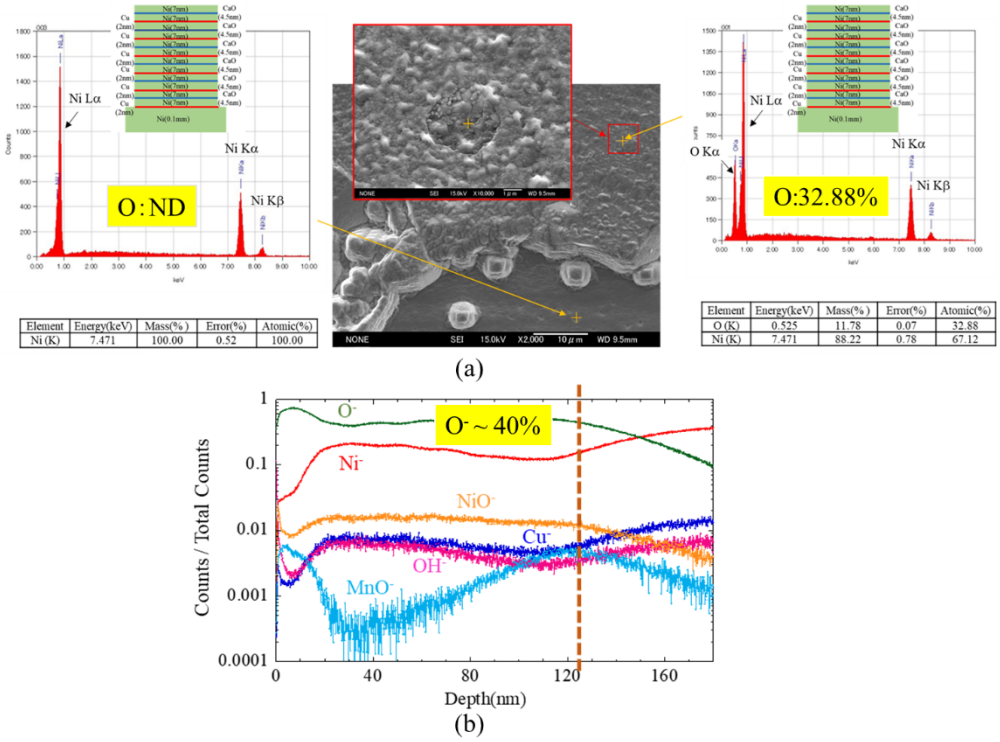

Element	Energy(keV)	Mass(%)	Error(%)	Atomic(%)
Ni (K)	7.471	100.00	0.52	100.00

Element	Energy(keV)	Mass(%)	Error(%)	Atomic(%)
O (K)	0.525	11.78	0.07	32.88
Ni (K)	7.471	88.22	0.78	67.12

Figure 14. SEM-EDX & TOF-SIMS analysis of the intentional heat burst sample shown in Figure 11(a): (a) SEM-EDX analysis results for normal and black spot areas; (b) TOF-SIMS analysis results for areas with abundant black spots.

methods are different, the same physicochemical mechanism related to the diffusion of hydrogen seems to be behind the experimental results.

Why were these described phenomena observed in CuNi multilayers? At present, we do not have a clear answer to this question. However, the NEDO project observed anomalous heating in Cu and Ni powders [6]–[8], and Celani et al. observed anomalous heating in constantan wire, an alloy of Cu and Ni [19]. Our experiments on heat generation in multilayers of CuNi were inspired by these results.

We are currently attempting to explain the phenomenon by a trapping hydrogen hypothesis as shown in Fig. 16. The hydrogen is absorbed in the bulk Ni and in the Ni/Cu mixed layer, and then the hydrogen inside diffuses by evacuation and rapid heating by the heater. Many hydrogen atoms can be trapped in the trapping sites, such as vacancy, dislocation, or voids. The perturbation of the input power causes a fluctuation in hydrogen density, which might trigger the heat burst phenomena.

4. Concluding Remarks

An innovative method to induce anomalously large heat generation phenomena that cannot be explained by known chemical processes has been developed. Ni-based nano-sized multilayer film was preloaded with hydrogen gas and heated rapidly to diffuse hydrogen and induce a heat generation reaction. Not only steady-state anomalous heat generation, but also spontaneous heat bursts were sometimes observed. Based on the observation of spontaneous heat

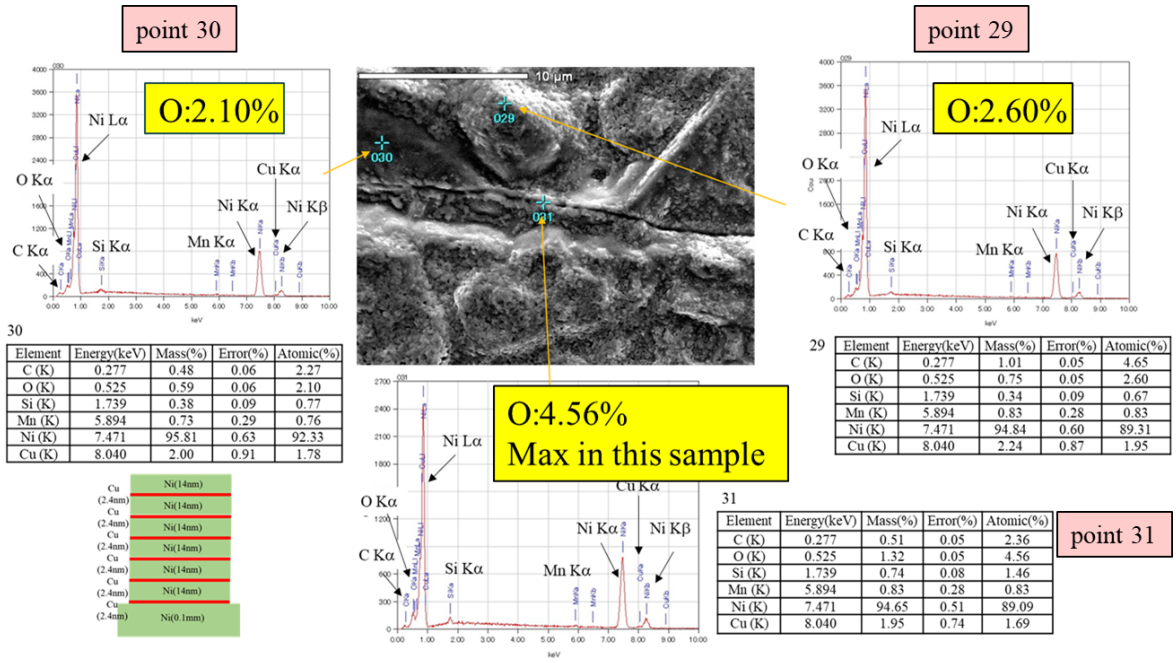

30

Element	Energy(keV)	Mass(%)	Error(%)	Atomic(%)
C (K)	0.277	0.48	0.06	2.27
O (K)	0.525	0.59	0.06	2.10
Si (K)	1.739	0.38	0.09	0.77
Mn (K)	5.894	0.73	0.29	0.76
Ni (K)	7.471	95.81	0.63	92.33
Cu (K)	8.040	2.00	0.91	1.78

29

Element	Energy(keV)	Mass(%)	Error(%)	Atomic(%)
C (K)	0.277	1.01	0.05	4.65
O (K)	0.525	0.75	0.05	2.60
Si (K)	1.739	0.34	0.09	0.67
Mn (K)	5.894	0.83	0.28	0.83
Ni (K)	7.471	94.84	0.60	89.31
Cu (K)	8.040	2.24	0.87	1.95

31

Element	Energy(keV)	Mass(%)	Error(%)	Atomic(%)
C (K)	0.277	0.51	0.05	2.36
O (K)	0.525	1.32	0.05	4.56
Si (K)	1.739	0.74	0.08	1.46
Mn (K)	5.894	0.83	0.28	0.83
Ni (K)	7.471	94.65	0.51	89.09
Cu (K)	8.040	1.95	0.74	1.69

Figure 15. SEM-EDX Analysis for the forced oxidated sample: This sample was taken out and oxidized at 500°C for 2 hours in the air. After that normal experimental process was performed.

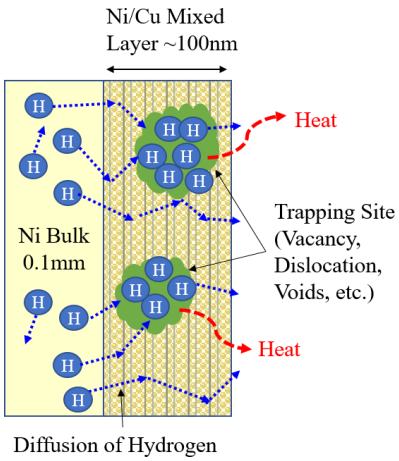

Figure 16. Trapping hydrogen hypothesis.

bursts, intentional heat bursts have also become possible. Even a single heat burst phenomenon cannot be explained by any known chemical reactions. Observation of heat bursts has improved the reliability of the excess heat experiments. Samples that generated excess heat or heat bursts often show some areas of very high oxygen concentration (higher than

in a forced oxidized sample) after the experiment according to SEM-EDX and TOF-SIMS analyses. The reason for this is currently unknown, and we would like to investigate the mechanism by assuming a trapped hydrogen hypothesis.

Acknowledgements

The authors would like to thank President H. Yoshino and all the members of CLEAN PLANET Inc. for their significant contribution. The authors also thank Mr. Y. Shibasaki and Prof. H. Kikunaga for their support. This work is supported by the Research Center for Electron Photon Science of Tohoku University, CLEAN PLANET Inc., The Thermal & Electric Energy Technology Foundation, the Iwatani Naoji Foundation and the Tanaka Kikinzoku Memorial Foundation.

References

[1] Y. Iwamura, M. Sakano and T. Itoh, "Elemental Analysis of Pd Complexes: Effects of D_2 Gas Permeation", *Japanese Journal of Applied Physics*, **41** (2002) 4642-4650.

[2] Y. Iwamura et. al, "Observation of Low Energy Nuclear Transmutation Reactions Induced by Deuterium Permeation through Multilayer Pd and CaO thin Film", *J. Condensed Matter Nucl. Sci.* **4** (2011) 132–144.

[3] Y. Iwamura, T. Itoh and S. Tsuruga, "Transmutation Reactions Induced by Deuterium Permeation through Nano-structured Pd Multilayer Thin Film", *Current Science,* **108** (2015) 628-632.

[4] Y. Iwamura, "Review of permeation-induced nuclear transmutation reactions", *Cold Fusion: Advances in Condensed Matter Nuclear Science*, Ed. Jean-Paul Biberian, Elsevier, Amsterdam, (2020)191-204.

[5] Tatsumi Hioki et al, Inductively Coupled Plasma Mass Spectrometry Study on the Increase in the Amount of Pr Atoms for Cs-Ion-Implanted Pd/CaO Multilayer Complex with Deuterium Permeation, *Jpn. J. Appl. Phys*. **52** (2013)107301.

[6] Y. Iwamura, T. Itoh, J. Kasagi, A. Kitamura, A. Takahashi and K. Takahashi, "Replication Experiments at Tohoku University on Anomalous Heat Generation Using Nickel-Based Binary Nanocomposites and Hydrogen Isotope Gas", *J. Condensed Matter Nucl. Sci.* **24** (2017) 191–201.

[7] Y. Iwamura, T. Itoh, J. Kasagi, A. Kitamura, A. Takahashi, K. Takahashi, R. Seto, T. Hatano, T. Hioki, T. Motohiro, M. Nakamura, M. Uchimura, H. Takahashi, S. Sumitomo, Y. Furuyama. M. Kishida and H. Matsune, "Anomalous Heat Effects Induced by Metal Nano-composites and Hydrogen Gas", *J. Condensed Matter Nucl. Sci.* **29** (2019) 119–128.

[8] A. Kitamura, A. Takahashi, K. Takahashi, R. Seto, T. Hatano, Y. Iwamura, T. Itoh, J. Kasagi, M. Nakamura, M. Uchimura, H. Takahashi, S. Sumitomo, T. Hioki, T. Motohiro, Y. Furuyama, M. Kishida, H. Matsune, "Excess heat evolution from nanocomposite samples under exposure to hydrogen isotope gases", *International Journal of Hydrogen Energy* **43** (2018) 16187-16200.

[9] Y. Iwamura, J. Kasagi, T. Itoh, T. Takahashi, M. Saito, Y. Shibasaki and S. Murakami, "Progress in Energy Generation Research using Nano-Metal with Hydrogen/Deuterium Gas", *J. Condensed Matter Nucl. Sci.* **35** (2022) 285–301.

[10] Y. Iwamura, T. Itoh, T. Takahashi, S. Yamauchi, M. Saito, S. Murakami and J. Kasagi, "Energy Generation using Nano-sized Multilayer Metal Composites with Hydrogen Gas; Intentional Induction of Heat Burst Phenomenon", *Proceedings of the 22nd Meeting of Japan CF Research Society*, JCF22, March 5, 2022, Online Meeting, p.27-39.

[11] T. Itoh, S. Shibasaki, T. Takahashi, M. Saito, J. Kasagi and Y. Iwamura, "Optical Observation on Anomalous Heat Generation from Nano-sized Metal Composite", *J. Condensed Matter Nucl. Sci.* **35** (2022) 274–284.

[12] Y. Iwamura, T. Itoh, M. Saito, S. Murakami and J. Kasagi, "Evidence for Surface Heat Release Reaction over Nano-sized Multilayer Metal Composite with Hydrogen Gas", *Proceedings of the 21st Meeting of Japan CF Research Society*, JCF21, December 11-12, 2020, Online Meeting, pp. 1–14.

[13] Y. Iwamura, T. Itoh, J. Kasagi, S. Murakami and M. Saito, "Excess Energy Generation using a Nano-sized Multilayer Metal Composite and Hydrogen Gas", *J. Condensed Matter Nucl. Sci.* **33** (2020) 1–13.

[14] T. Itoh, S. Shibasaki, J. Kasagi, S. Murakami, M. Saito and Y. Iwamura, "Optical Observation on Anomalous Heat Generation from Nano-sized Metal Composite", *Proceedings of the 21st Meeting of Japan CF Research Society*, JCF21, December 11-12, 2020, Online Meeting, pp. 15–25.

[15] M. Saito, T. Itoh, Y. Iwamura, S. Murakami and J. Kasagi, "Elemental Analysis for Elucidation of the Anomalous Heat Generation Phenomena", Proceedings of the 20th Meeting of Japan CF Research Society, JCF20, December 13-14, 2019, Reference Hakata Eki-Higashi Rental Room, Fukuoka, Japan pp. 74–85.
[16] S. Murakami, T. Itoh, Y. Iwamura, M. Saito and J. Kasagi, "Excess Energy Generation Experiments using a Nano-sized Multilayer Metal Composite and Hydrogen Gas", Proceedings of the 20th Meeting of Japan CF Research Society, JCF20, December 13-14, 2019, Reference Hakata Eki-Higashi Rental Room, Fukuoka, Japan pp. 86–96.
[17] Y. Fukai, Evidence for Quantum Diffusion of Hydrogen in Ta: Quench-Recovery Experiments Revisited, *Japanese Journal of Applied Physics*, Vol.23, No.8 (1984) 596–598.
[18] S. Focardi, V. Gabbani, V. Montalbano, F. Piantelli and S. Veronesi, Large excess heat production in Ni-H systems, *Il Nuovo Cimento A (1971–1996)* **111** (1998) 1233–1242.
[19] F. Celani et al., "Cu–Ni–Mn alloy wires with improved sub-micrometric surfaces used as LENR device by new transparent dissipation-type calorimeter", *Journal of Condensed Matter Nuclear Science* **13** (2014) 56–67.

J. Condensed Matter Nucl. Sci. 38 (2024) 287–294

Research Article

Highly Efficient Water Plasma Vortex Reactor for Obtaining of Extra Thermal Energy and Transmuted Chemical Elements

Klimov A., Altunin S., Kulikovskii O.

Research and Technical Centre "Prometheus", Russian Federation

Abstract

A highly efficient Water Plasma Vortex Reactor (PVR-W) was designed, manufactured and tested for the first time [1]. The groundwork obtained in plasma aerodynamics, plasma-assisted combustion and LENR physics in our Centre was used in the design of this reactor. This work is a continuation of the previous research [2]–[5]. Pulsed repetitive electric discharge was created inside an argon cavity in swirl water flow in the PVR-W. Electrodes made of clean nickel, copper (99,99% and other metals) were used in this reactor. Double-distilled water was used in our experiment. It was revealed that there is an optimal operating regime of this PVR-W reactor with a high value COP $\sim$ 2 - 10. Extra heat power in this operating regime was about 2-10 kW. Self-sustained relaxation oscillations of current and voltage were obtained in this stable operation regime. It was revealed that there are many new transmuted chemical elements in the water sediment after plasma experiments. Both light chemical transmuted elements (such as carbon, aluminium, silicon, sulphur and others) and heavy elements (such as copper, zinc, iron and others) were found in the sediment sample. Chemical analysis of these sediment dust particles was carried out by the EDS method and the optical spectroscopy method. In this paper, experimental results on the direct extraction of electrical power from a heterogeneous plasmoid created by a pulsed repetitive electric discharge in the PVR are also discussed.
 ISSN 2227-3123

Keywords: Water Plasma Vortex, Electrical Pulses, COP

1. Introduction

Experimental and theoretical studies on the creation of a highly efficient LENR reactor in our Centre have been ongoing for the past 20 years. The authors have achieved some success in this area using advanced plasma and plasmoid technologies. A special place in our research is given to the possibility of creating a plasma vortex heterogeneous reactor with water steam and a water flow reactor with a non-equilibrium energy-intensive plasmoid. Many fundamental technical difficulties identified during the operation of such power plants have been overcome [1]–[5].

The new PVR-W design has the following characteristics and parameters:

- Significantly increased output thermal power. At present, the output thermal power of PVR-W reaches about 10 kW. There is also a high coefficient of energy efficiency of this reactor, COP = 2-10 (ratio: output thermal

 ISSN 2227-3123

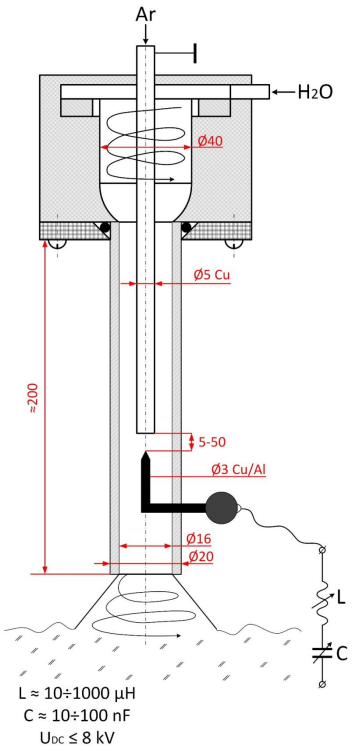

Figure 1. Schematic of the experimental setup PVR-W and additional output LC-circuit used in DC power supply.

power/input electric power). Recall that earlier the output thermal power of the older PVR models did not exceed 1-3 kW.

- For the first time, it was possible in this reactor to extract up to 200 W of electric power directly from the output plasma flow (when the total output thermal power of the reactor was about 2 kW).
- Production of cheap hydrogen. This PVR-W produces more than 10 times the hydrogen the previous PVR versions produced.
- There are significant differences in the mass and overall dimensions of the reactors. The typical dimensions of the PVR reactor was $10 \times 10 \times 100$ cm^3, and the typical dimensions of the PVR-W reached $3 \times 3 \times 20$ cm^3, with other technical characteristics of the two reactors being equal.

The PVR-W reactor does not require the use of a steam generator (unlike the PVR). The electric discharge itself evaporates water flow inside the argon cavity (near the water-argon contact boundary, Fig. 1). The presence of a steam generator certainly reduces the total energy efficiency of the PVR, due to large heat losses from the steam generator itself and the steam pipeline.

The most important distinguishing feature of the PVR-W is: the location of the water heat exchanger in the optimal place of reactor's design, which is near the plasma zone created by the electric discharge. Recall that an optimal location of the water heat exchanger was a difficult technical problem in our previous heterogeneous PVR reactor [2]–[5].

In terms of physics, the work of the PVR-W and the PVR differed significantly. In the PVR-W, a dense working medium is used – the flowing water. In the PVR argon-water steam gas mixture was used. In PVR-W, water flow is evaporated by a powerful pulsed current in the argon gas cavity. The pressure in this cavity can reach 10-100 Bar in this regime. Such hydraulic shock waves are easily measured by a hydrophone. Therefore, there is a dense working medium inside the vapour-gas cavity in the PVR-W. It is known that the productivity of any plasma-chemical reactor increases significantly with an increase in the density of the working medium (or pressure), as well as its heating. The temperature behind the SW front in the gas-plasma cavity was measured, and shown to be significantly higher than in the previous PVR reactor. The typical value of the gas temperature T_g in the plasma in the PVR-W reactor reaches $T_g \sim$ 10000 K. Recall that the typical value of the temperature T_g* in the plasma region of the PVR did not exceed T_g*<4000 K [2]–[4]. Therefore, one can suppose that the productivity of transmuted elements and hydrogen in the PVR-W increased significantly compared to the PVR.

The generation of a shock wave and many small cavitation bubbles in the discharge zone of the PVR-W led to a non-linear transformation of the electric discharge parameters due to additional charge separation at the shock wave front in a heterogeneous plasma [2]–[4]. Such an additional separation of charges on the shock wave front allowed us to extract additional electrical energy in this reactor using electric probes mounted on the discharge tube. The second method of extracting electrical power from heterogeneous plasmoid was connected with MHD - technology. Two permanent magnets with magnetic inductance B = 0.1-1T and two transverse electrodes were used in the MHD generator mounted behind the output nozzle of this reactor. Maximal electric power extracted by these two methods was about 200 W in our experiment (at typical output thermal power about 2 kW).

A closed water pipeline was used in the PVR-W. Thus, the transmuted chemical elements created in the PVR-W crossed many times in the plasma aria and were conserved in water flow. So, their concentrations increased with the duration of the reactor operation.

1.1. Experimental setup of PVR-W

A schematic of the experimental setup of the PVR-W is shown in the Fig. 1. This reactor consists of:

- Water swirl generator (1),
- Swirl concentrator-amplifier (2)
- Cathode - argon injector (3)
- Quartz tube and electric discharge chamber (4)
- High voltage anode (5)
- Water pool, (Fig. 2)
- Water pump,
- Water pipeline, (Fig. 2).

A general view of the experimental setup of the PVR-W is shown in the Fig. 2. The water consumption in this installation was 30 L/min. Argon consumption in this reactor was 1 G/s.

DC power supply with an output voltage 8 kV and an output current 2 A was used in this reactor to create electric discharge in the working chamber of this reactor. An additional LC- circuit was used in this power supply to create self-sustaining relaxation oscillation mode in argon-water plasma. Typical frequencies of these oscillations varied in the range F_i = 1000 - 10000 Hz, Fig. 3.

2. Experimental Results

The electric voltage of electric discharge was measured by a high-voltage probe (Tektronix P6015). Electric discharge current was measured by a current probe (TRC P0300).

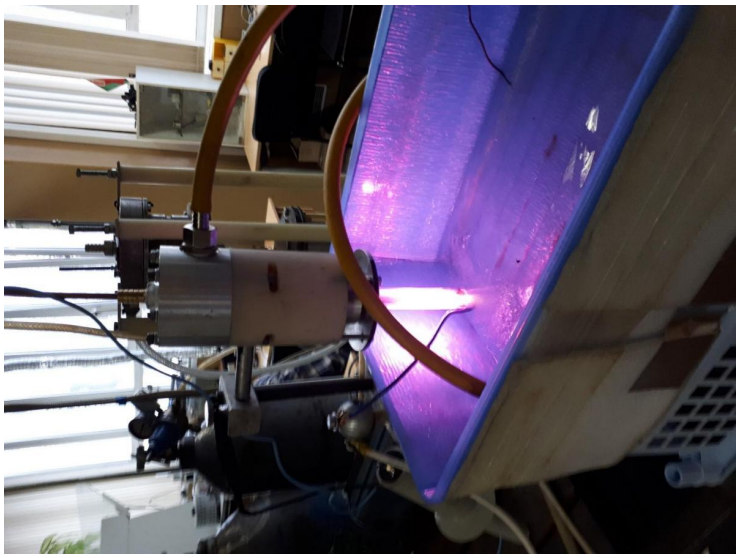

Figure 2. General view of the PVR-W setup during operation. One can see a water pool and water supply pipeline.

The initial temperature T_o and final temperature T_f in the water pool were measured by thermocouples. The water mass M_{H2O} in water pool + water pipeline was measured before and after the experiment.

The experiment was conducted by the following steps: The water pump was turned on at the beginning. Then argon flow was injected in the working chamber of this reactor. Plasma was created by electric discharge in argon cavity inside the swirl water flow. The typical experimental time was about 10 minutes. After this, the plasma was switched off and the final water temperature T_f was measured by thermocouple. After 1 hour the water sediment was collected and dried in a muffle furnace. The powder thus obtained was used in chemical analysis.

It follows from Fig. 3 that the voltage oscillations have an asymmetric form (there is an DC component in this signal's spectrum) after the breakdown of the gas discharge gap. This result can be explained by the separation of charged particles at the front of the shock wave created by a powerful pulsed discharge [2]–[4]. This result makes it possible to generate electric power directly from a heterogeneous plasmoid using electric probes with a resistive load.

The typical experimental calorimetric characteristics of the PVR-W are shown in Table 1. One can see that the value $K_x = COP$ did not exceed 0.73-0.80 in experiments No. 1, 2 where relaxation oscillations were absent (LC-circuit was absent). Production of the sediment powder with transmuted chemical elements was absent in this experiment also (see below). On the other hand, the value of the COP increased to **1.62–2.82** in these experiments No. 3-7. Production of the sediment powder with transmuted chemical elements was about 17 mG/sec in these experiments also.

Table 1, where M_{H2O}- water mass, used in the PVR-W; τ_{exp}- experimental time, N_{el} - mean electric power, Q_{H2O}- water thermal power, obtained in the experiment, Q_{el}- electric energy input in plasma, COP = Q_{H2O}/Q_{el} (without heat power losses)

It should be noted that when calculating the value of the COP, the following energy losses were not taken into account: - heating of the body of the water pool itself, connecting pipes, pump, mass of accumulated water vapour and mass of accumulated hydrogen, EM-radiation from the heterogeneous plasmoid. Taking into account these factors increases the indicated values of the COP by 1.5-2 times.

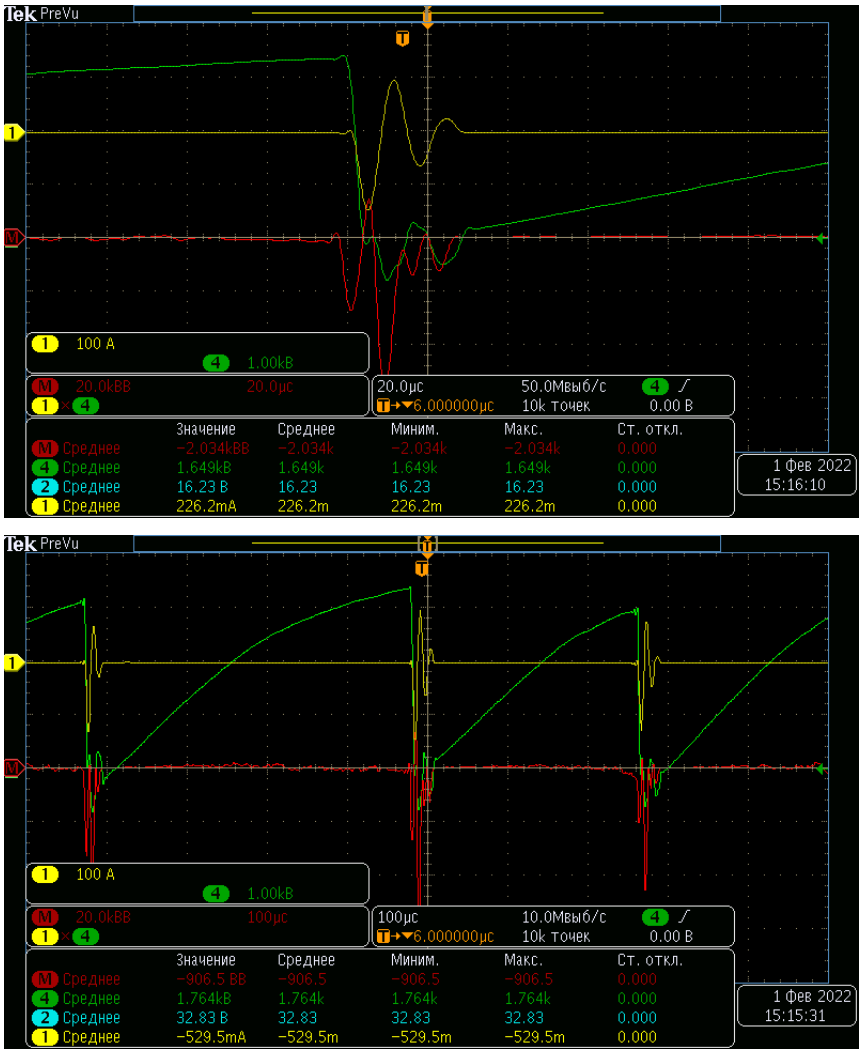

Figure 3. Volt-ampere signals obtained at the discharge gap of the PVR-W. The mode of stable relaxation oscillations. Green - voltage, yellow - current, red - electrical power. Top picture – 20 μs/div, bottom picture – 100 μs/div.

3. Transmutation of Chemical Elements in the PVR-W

Chemical analysis of the sediment powder with dust particles obtained in the PVR-W was performed using the method of EDS spectroscopy and optical spectroscopy. This powder was obtained in the process of drying the sediment of the aqueous solution accumulated in the PVR-W during the experiment. The productivity of the powder in this setup turned out to be many times higher than the one obtained in the previous PVR. Its value reached about 17-20 mG/sec (an order of magnitude higher than in the PVR). At the same time, the measured erosion of the electrodes (loss of their mass) did not exceed 1 mG/s in the PVR-W. One can conclude that the production of transmuted elements was carried out not only in eroded metal clusters, but also in the water itself. Note that double-distilled water was used in our

Table 1.

Exp, №	M_{H2O}, G	T_H,C	T_k,C	ΔT,C	τ_{exp}, sec	N_{el}, W	Q_{H2O}, kJ	Q_{el}, kJ	COP
1	4000	18,0	25,2	7,2	218	690	120,4	150,4	0,80
2	4000	23,6	29,6	6	174	790	100,3	137,5	0,73
3	5000	26,7	33,6	6,9	90	970	144,2	87,3	**1,65**
4	5000	32,2	40,4	8,2	90	700	171,3	63,0	**2,72**
5	6000	17,5	22,4	4,9	60	727	122,9	43,6	**2,82**
6	6000	26,8	31,8	5	55	1071	125,4	58,9	**2,13**
7	8000	28,2	34,9	6,7	90	1540	224,0	138,6	**1,62**

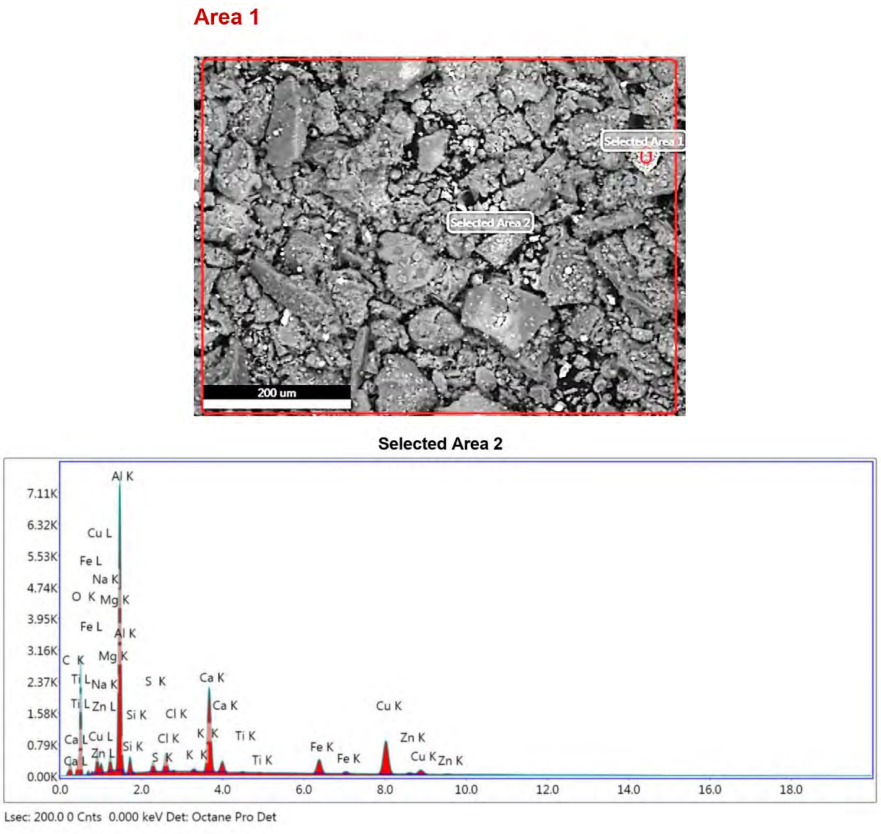

Figure 4. Typical EDS spectrum of sediment in water pool of the PVR-W (bottom) and dried powder view (top).

experiment. Therefore, it is impossible to explain the production of transmuted elements in this reactor with the help of contamination in the initial water. We use clean copper electrodes (99.99%),clean nickel electrodes (99.99%) and clean aluminium electrode (99,99%). Therefore, it is very difficult to explain the production of transmuted elements in this reactor with the help of contamination in the initial unexposed electrodes.

The chemical composition of the powder was studied by EDS spectroscopy. Typical results obtained using this method are presented in Fig. 4, 5 and Table 2. Important conclusions follow from the analysis of experimental data

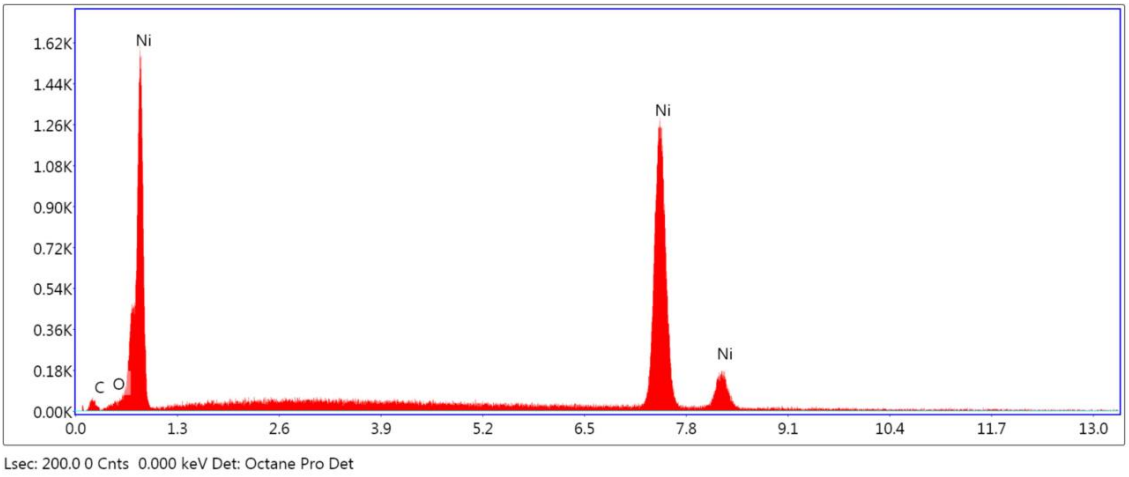

Figure 5. Typical EDS spectrum of unexposed nickel electrode before experiment.

Table 2. Composition of new transmuted elements obtained in the PVR-W. EDS-analysis.

Element	Weight %	Atomic %
CK	4.76	10.96
OK	30.86	53.29
MgK	0.98	1.11
AlK	4.67	4.78
SiK	0.51	0.50
S K	0.19	0.17
CIK	1.17	0.91
KK	0.15	0.11
CaK	1.24	0.86
TiK	0.05	0.03
MnK	0.24	0.12
FeK	52.96	26.20
CuK	1.98	0.86
ZnK	0.24	0.10

obtained using EDS spectroscopy. Both heavy transmuted elements and light transmuted elements (compared to the atomic weight of the electrode material) are measured in the powder. In the EDS spectra, the expected transmuted elements are observed, such as zinc and iron (products of a possible transmutation of copper), silicon and magnesium (products of a possible transmutation of aluminium electrode); as well as completely unexpected elements, such as carbon, calcium in large quantities, and many others. It should be noted that these transmuted chemical elements were absent in the composition of the initial electrode material and initial water before the start of the experiments. Additional analysis of these initial electrodes and initial water sample was performed by the same EDS-method before experiment, Fig. 5. One can see that there is a small concentration O-atoms in nickel oxide film on surface of a initial nickel electrode.

4. Conclusions

1. Further transmutation study requires a thorough analysis of the isotopic composition of the new elements obtained in the PVR-W. The possible difference between the composition of the transmuted elements and the their natural composition can finally confirm the hypothesis of the artificial origin of these elements.
2. The joint results of our experiments using the EDS spectroscopy method and the optical spectroscopy method clearly show that a possible source of additional thermal energy release in the reactor is associated with the process of cold transmutation of the initial chemical elements in it (but it is not associated with chemical reactions). We estimate that the value of the specific thermal energy yield per one hydrogen atom (or one atom of the electrode metal) reaches on the order of q = 1-10 keV/ atom. Note that the q value is much higher than the typical q* value released in any chemical reaction.
3. The physical mechanism of transmutation of chemical elements detected in the PVR-W reactor will be finally clarified by measuring the isotopic composition of exposed electrodes and sedimentary powder obtained during the experiment under consideration. The analysis of the optical spectra with high spatial and temporal resolution in heterogeneous plasmoid created in the PVR-W will allow us to find out the plasma-chemical kinetics of the transmutation of chemical elements. The authors believe that the physical model of a bi- nuclear atom [6] allows us to explain the transmutation of chemical elements detected in the PVR-W reactor.

References

[1] Patent RU 2 788 269 C, H02N 3/00,17.01.23 Bull #2, Method for Obtaining Thermal Energy, Extracting Electric Energy and a Device for Its Implementation.

[2] A. Klimov, N. Belov, I. Zavershinskii, N. Molevich, “High effective heterogeneous plasma vortex reactor for production of heat energy and hydrogen,” IOP Conf. Series: Journal of Physics: Conf. Series, vol. 980, no. 012040, pp. 1–6, 2018.

[3] A. Klimov, N. Belov, I. Zavershinskii, N. Molevich, “Thermal Energy Release and Hydrogen Production in Swirl Heterogeneous Plasma-Chemical Reactor,” IOP Conf. Series: Journal of Physics: Conf. Series, vol. 1112, no. 012024, pp. 1–6, 2018.

[4] V. Bitiurin, A. Klimov, O. Korshunov and V. Chinnov, “Kinetic Model of Aluminum Oxidation by Water Vapour in Heterogeneous Plasma: Gas-Phase Kinetics”, High Temp., vol. 52**,** pp. 657–63, 2014.

[5] A I Klimov, N K Belov, B. N. Tolkunov, Neutron Flux and Soft X-Radiation Created by Heterogeneous Plasmoid, Journal of Physics: Conference Series 1698 (2020) 012034, IOP Publishing, doi:10.1088/1742-6596/1698/1/012034

[6] V.L. Gurevich, M. Yu. Pogorelskii, V. P. Chaly, Bi-Nuclear Atom Is the Bound State of a Proton and a Heavy Atom, JTF, 2009, V.79 No 2, P. 1–5 (in Russian).

J. Condensed Matter Nucl. Sci. 38 (2024) 295–306

Research Article

Understanding of MHE Power Generation Patterns by TSC Theory

Akito Takahashi*, Masahiko Hasegawa, Yutaka Mori

MHE Kobe lab Technova Inc., 658–0022 Kobe Japan

Abstract

The main MHE power generation pattern can be explained by the nuclear energy release of 4H/TSC WS fusion events at T-sites of Ni nano-cores. The release occurs when dynamic 4H cluster formations of 4 protons move from O-sites under phonon excitations in GMPW (global mesoscopic potential well) of Ni-nano-islands. This is the major process of power (about 20 W in our runs). In addition, minor excess power (about 4 W) is considered to be continuously released by 4H/TSC WS fusion events at SNHs (sub-nano-holes) on surfaces of Ni-nano-cores. This minor process remains after the H/Ni ratio is saturated. We found a method of MHE power re-activation by the RCV (reaction chamber valve) close-to-open method after H/Ni loading ratio becomes nearer to saturation. When RCV is opened, pulse thermal power generation occurs from 4H/TSC WS fusions at SNHs, which induces H-gas desorption-bursts from T-sites of Ni-nano-cores. This trigger event produces empty T-sites in Ni-nano-cores and slow H-loading to T-sites restarts with relatively large generation of 4H/TSC WS fusion power (10-15 W) for a considerably long time (about one day in our trigger-trial runs). This re-activation/trigger process can be repeated in-situ. We were able to trigger pulse thermal power more than ten times. The prediction by the TSC theory seems to be working very well. Some brief historical aspects of "cold fusion" or MHE research evolution are described in a portion of the Introduction.
 ISSN 2227-3123

Keywords: Metal hydrogen energy, heat pattern, TSC theory, H-loading ratio

1. Introduction

We are convinced by our latest results [1]–[11] that we have now found a very reproducible method of generating high energy density excess thermal power in long lasting reactions, using nano-composite metal meso-catalyst and hydrogen (D or H) gas interaction at elevated temperatures. The original aspect of underlying phenomena was published in our ICCF20 paper [12].

We gave up doing the F-P type electrolysis experiments around 2000, due to the very difficult reproducibility of AHE. We thought that the FPHE (Fleischman-Pons Heat Effect) phenomenon could happen by 4D/TSC formation at arbitrary (by chance) formed surface nano-structure sites (SNH: sub-nano-holes) and/or T-sites in the FCC lattice of Pd (or Ni) metal, [13] conditions which would be difficult create artificially with electrochemical methods. The co-deposition method (P. Boss et al. [17]) surface analysis gave AT (Akito Takahashi) a hint for possible nano-structure

*Corresponding author: E-mail: akito@sutv.zaq.ne.jp

 ISSN 2227-3123

formation. Next, the Arata-Fujita idea [18] of Pd nano-particles in zirconia gave AT a more functional hint to a way to make a working material in a systematic way: the spin technique. We made spin material to do the D-gas-loading experiments with mesoscopic size catalyst powder of Pd- or Ni-core binary nano-composite islands [19]. Pure Pd samples do not have the capability to trap D(or H) particles in lattice sites or surface defects at elevated temperatures (>> 300°C) necessary for an energy source application, therefore we have concentrated on Ni-core/Pd(or Cu)-shell meso-catalyst structures [1]–[16]. According to the 4D(or H)/TSC formation on surface SNHs (or inner sub-periodic potential wells of a global mesoscopic potential well: GMPW) of a nano-island, TS clusters formation are more enhanced the higher the D-loading ratio is in meso-catalyst islands [13], [19]. (We found 3.5 loading at most for PNZ.) We have tried to design PNZ or CNZ type samples of mesoscopic catalysts.

Using our new experimental system (called D-system [9]) of MHE (nano-metal hydrogen energy) reaction, we are able to measure and to evaluate more clearly the anomalous heat effect (AHE) by the elevated temperature interaction of nano-composite metal samples and hydrogen-gas. Two findings of new characteristics of AHE excess power by the MHE reaction are reported [10]. After starting initial heating by W2 (100-160 W) heater, excess thermal power by MHE is steeply generated from around 300°C of CNZ-sample powder in the outer region. Excess power suddenly starts to increase when the H/Ni loading ratio reaches around 1.0. This timing is considered to be the time that H-loading at O-sites of Ni core become full, attaining H/Ni = 1.0 in about 20–60 minutes in our runs (Phase-1 process: Fast H-Loading). After that turning point, relatively high excess power generation continues for about 3 days, until the elapsed time region where H/Ni loading ratio saturates to be far greater than 1.0; H/Ni = 2.2 was the saturated value in some runs. This is the second phase H-loading by T-sites loading in Ni core: (Phase-2 process: Slow H-Loading).

The main MHE power generation pattern can be explained by the nuclear energy release of 4H/TSC WS fusion events at T-sites of Ni nano-cores, by dynamic 4H cluster formation of 4 protons (associating 4 electrons) moved from O-sites under phonon excitations in GMPW (global mesoscopic potential well) of Ni-nano-islands [13], [19]. This is the major process of power (about 20W in our runs). In addition, minor excess power (about 4 W) is considered to be continuously released by 4H/TSC WS fusion events at SNHs (sub-nano-holes) on surfaces of Ni-nano-cores. This minor process remains after the H/Ni ratio is saturated.

We found a method of MHE power re-activation by the RCV (reaction chamber valve) close-to-open method after H/Ni loading ratio becomes nearer to saturation [9], [10]. When RCV is opened, pulse thermal power generation happens by 4H/TSC WS fusions at SNHs, which induces H-gas desorption-bursts from T-sites of Ni-nano-cores. This trigger event produces empty T-sites in Ni-nano-cores and slow H-loading to T-sites restarts with relatively large generation of 4H/TSC WS fusion power (10-15 W) for a considerably long time (about one day in our trigger-trial runs). This re-activation/trigger process can be repeated in-situ. We have successfully triggering it more than ten times.

We have to bear in mind that our latest reports [9], [10] at the JCF-22 Meeting would be shocking to old authorities in CF/LENR studies, which were based on heavy water electrolysis with Pd cathode, and based on ideas of deuteron induced fusion reactions. We were convinced by our characteristics data of a close correlation between excess power evolution and H/Ni loading ratio exceeding 1.0, by the elevated temperature interaction of light hydrogen and mesoscopic nano-metal catalyst. We are also convinced that the results with light hydrogen take place with the same underlying physics mechanism as our former results using deuterium gas and meso-catalyst interaction at room temperature and elevated temperatures [1]–[11]. Both the light hydrogen and deuterium reactions observed appear to match very well with AT's 4H/TSC WS fusion and 4D/TSC fusion theories. The common underlying physics is the condensed cluster fusion (CCF) of hydrogen isotopes in dynamic ordering process of condensed matter (to be mesoscopic catalyst) [7], [13], [16], [20]. So, our results for light hydrogen results are theoretically consistent with the old observations of heavy water/gas and Pd metal interaction. Both results showed energy generation density of more than 1000 times conventional chemical reaction energies, leading us to conclude this is of nuclear origin. We understand we are seeing, at least, one rational solution of the "cold fusion" puzzle. We may hope that other rational solutions may emerge from other efforts. We think we can go ahead to the R&D stage for industrial application to clean portable energy devices of primary nuclear energy source.

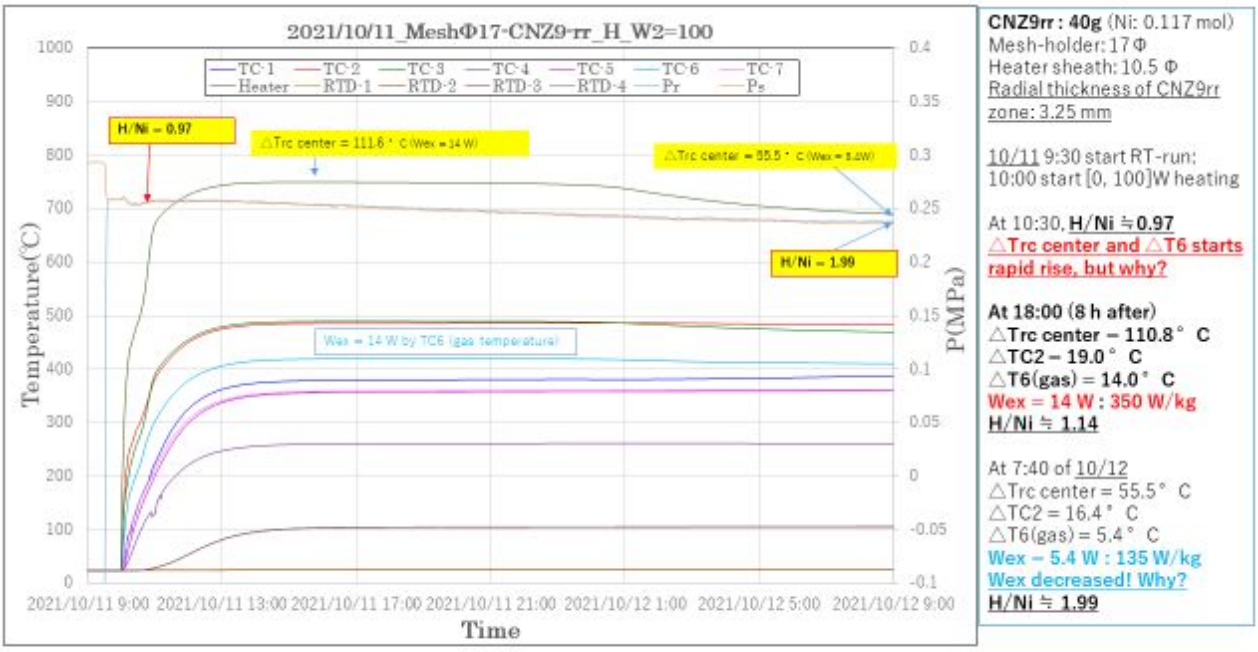

Figure 1. Typical example of raw data from the D-system MHE experiment for re-calcined sample.

2. Correlation between Excess Thermal Power and H/Ni Loading Ratio

A typical example of raw data from the new D-system MHE experiment [9], [10], [21] is shown in Fig. 1. Blank calibration runs were carried out with three dummy samples, namely zirconia beads, zirconia fine powder and a "dead" CNZ7rrr sample. To estimate excess power generation by active sample runs, we found that the blank data of the dead sample is the most accurate for estimating increased temperatures in each point of the D-system. Estimation of excess thermal power by active samples (CNZ9 series and CNZ8 series in this paper) was made by using H2-gas temperature in the reaction chamber (RC) in current data [9], [10].

We have found for every initial ET (elevated temperature) run of CNZ-type samples after re-calcination that excess power rises very steeply when the H-loading ratio (H/Ni) exceeded a value close to 1.0. Relatively high excess power levels (14 W in Fig. 1) plateaued, continuing for many hours (0.5 to 3 days, depending on sample type), and started to decay slowly after saturating H/Ni loading ratios (around 2.0 in real runs). Why did this pattern of excess power evolution occur? We have found also that temperature data at the RC center (Trc-center) was most sensitive to the evolution of excess thermal power generation. However, to estimate excess power, the increment of the H-gas temperature in the RC (ΔT6) from the "dead sample" blank data is appropriate in this study, considering that gas temperature in the RC should reflect the average trend. We have oil mass flow calorimetry data by radiation heat recovery in the D-system. Due to the very slow response of the oil outlet temperature, the present oil mass flow system does not show accurate time evolution data for excess power, but as an estimation of integrated heat over a long run, it is effective.

In Fig. 2, we show a typical example of correlation data between excess thermal power evolution and H/Ni loading ratio evolution. During H/Ni loading, the fast-loading phase reached H/Ni 0.9 in ca. 30 minutes after the W2 heater

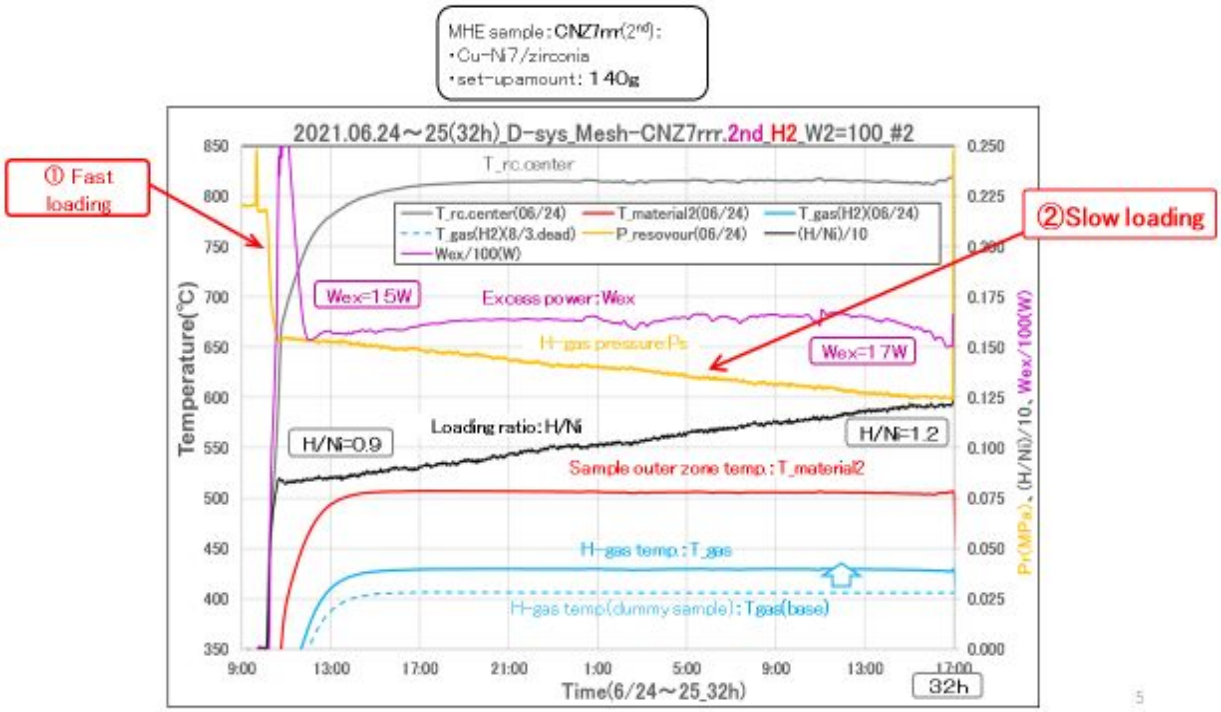

Figure 2. Typical data showing correlation between excess power (W_{ex}) evolution and H/Ni loading ratio evolution, for ET run of CNZ7rrr sample which was still active for the MHE reaction.

was turned on (100 W constant power supply in this case). Following this, the very slow H-loading phase lasting for a few days, reaching the saturated value around 2.0. As for excess thermal power evolution, we see a burst-like peak [3] after the fast H/Ni loading finished and rather plateau-like power level (15-17W) continues with the slow H/Ni loading phase for many hours. Why are such patterns of H/Ni loading and excess power in close correlation?

We have found that H-loading ratio can become very high as 3.5 when we used nano-composite metal particles of Pd and Pd-Ni binary particles in ceramics supporter flakes [19] at room temperature. Here we consider that high H-loading over H/Ni = 1.0 can be formed for Ni-core/Cu-incomplete-shell nano-composite meso-catalyst, especially at elevated temperatures, probably by the endothermic H-absorption process to Ni-core lattice, as shown in the model in Fig. 3. H_2 gas molecules may be trapped first by electron dangling bonds at sub-nano-holes (SNHs) on surface of Ni-core with Cu (defect points), and dissociated to protons to enter into Ni nano-core lattice for occupying octahedral sites (O-sites) of Ni FCC lattice. When all O-sites are occupied by protons, H/Ni loading ratio becomes 1.0. After that fast-loading phase, very slow H-loading to tetrahedral sites (T-sites) of Ni FCC core lattice goes on by excited phonon states of protons at O-sites under elevated temperature condition. As the T-site H-trapping potential is with shallow well on potential hill of FCC structure, efficient excitation of proton oscillator phonon at O-site is needed. The non-linear coupled proton oscillations to produce high phonon states can be expected in the global mesoscopic potential well (GMPW) with inner fine FCC Bloch potentials of O-sites, under elevated temperatures [19]. Maximum partial loading ratio to T-sites is 2.0. Total loading to be saturated is therefore 3.0 as sum of O-sites and T-sites H-occupations, theoretically. The experimentally observed value 0.9 in Fig. 2 can be regarded as 1.0 nominal value,

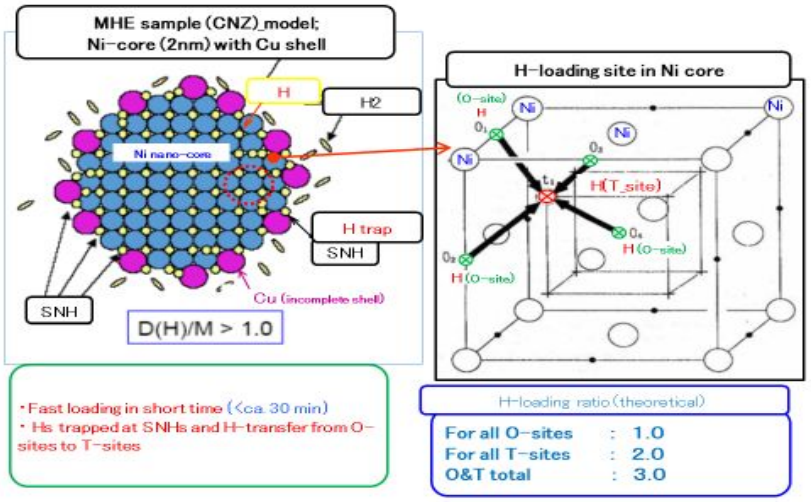

Figure 3. Model of hydrogen loading to a Ni-core/Cu-incomplete-shell nano-composite meso-catalyst particle [13], [19].

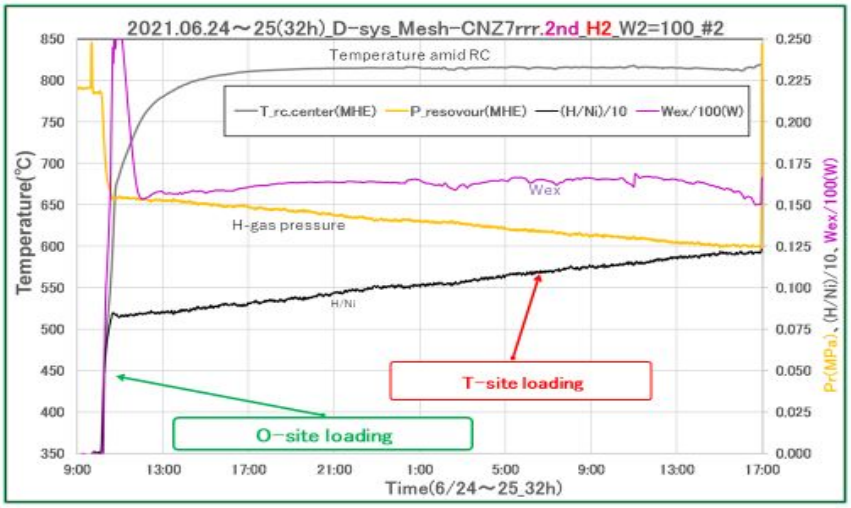

Figure 4. Explanation of two (fast and slow) phase H-loadings to Cu_1Ni_7/zirconia nano-composite sample powders, in close correlation with Wex (excess thermal power).

namely we conceive 90% meso-catalyst state of CNZ7rrr sample, and we know that bulk Ni metal sample cannot absorb Hs over 1.0.

As shown in Fig. 4, the observed H-loading patterns with excess thermal power correlation can be explained as the O-site H-loading for the fast-loading phase and the T-site H-loading for the slow loading phase. The next question is why the excess power pattern correlates closely to the evolution of H/Ni loading ratio.

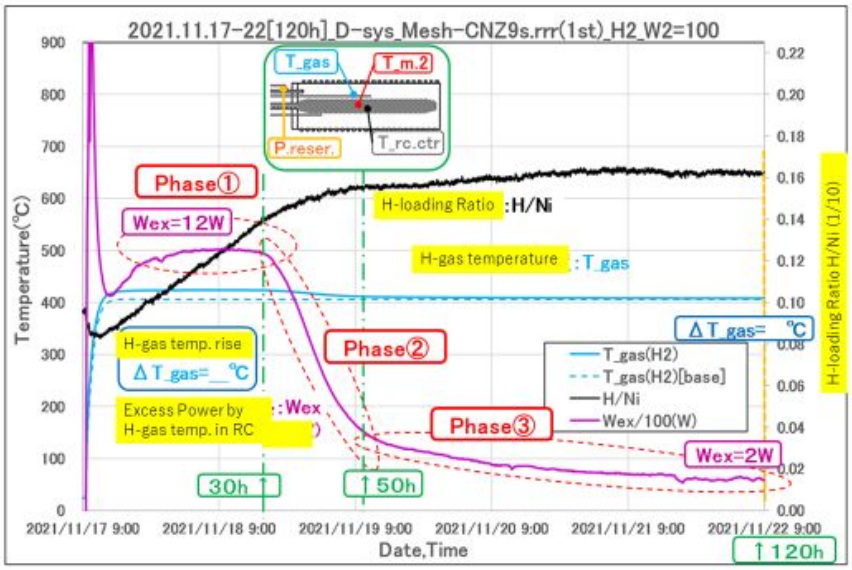

Figure 5. Evolutional correlation of H/Ni loading ratio and excess thermal power, with a typical example of a CNZ9srrr sample (140 g) after the third re-calcination (rrr).

In Fig. 5 a typical three phase pattern of excess power generation is shown in correlation with H/Ni loading ratio evolution. Explanation by the 4H/TSC WS fusion theory (7, 13, 16) is shown in the flow chart in Fig. 6. The many hours lasting plateau of relatively high power level in Phase-1 is conceived to be produced by the 4H/TSC WS fusion reactions at T-sites. Under full O-sites occupation with protons, 4H-cluster formation probability is enhanced by high order proton-oscillation phonon in GMPW of Ni-nano-core. If the end-state oscillation of 4H/TSC condensation collapse continues more than 1.0 fs, about 3% of 4H/TSC will produce the nuclear energy of WS fusion, as shown in a simple simulation scheme (Fig. 7) [16]. Detailed data of a simulation of 4H/TSC end-state oscillation is shown in [7].

When the density of remaining empty T-sites rapidly decreases as the H/Ni loading approaches saturation. 4H/TSC WS fusion rates also decrease accordingly. This is Phase-2 of Fig. 5. After the saturated occupation of T-sites, smaller level of 4H/TSC WS fusion rates may continue at SNHs of Ni-nano-cores. This is Phase-3 of Fig. 5.

In Fig. 8, we show that heat vs. H/Ni correlation patterns are reproducible for changing samples and heating conditions. Total heat energy by excess thermal power plateau by this 160 W run is 12.6 MJ/mol-H, which is equivalent to the specific reaction energy of 131 eV/H-atom-absorbed, for 70 h duration. We know that H-absorption to CNZ sample at elevated temperature is endothermic. However, even if we assume that H-absorption is an exothermic reaction, 131 eV/H-atom-absorbed is too large in 2–3 orders of magnitude to be a chemical reaction, and we must conclude it has a nuclear origin. A very important physics issue is that light hydrogen can generate fusion-like nuclear energy in a laboratory experimental system. By assuming 4H/TSC WS fusion, 68 ppm H atoms would be consumed by the nuclear reaction to produce MHE excess heat in this case.

However, why have we observed larger and longer “high-power plateau” with higher H/Ni saturated value with the 160 W heating case than the 100 W case?

For the H/Ni>1.0 condition, phonon-excited movement of protons (Hs) from 4 O-sites to a T-site has the highest probability for one H, and lower probabilities for 2H, 3H and 4H, in relative order, when the Ni-core temperature is lower. T-site occupation of Hs is most enhanced in the lower temperature condition. Fig. 9 shows the enhancement of

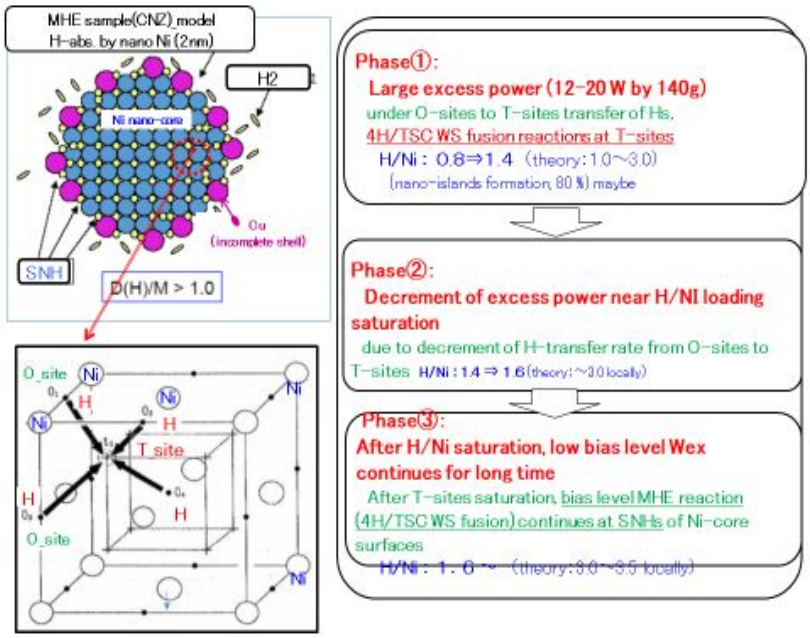

Figure 6. Explanation schematic of MHE power generation patterns with evolution of H/Ni loading ratio.

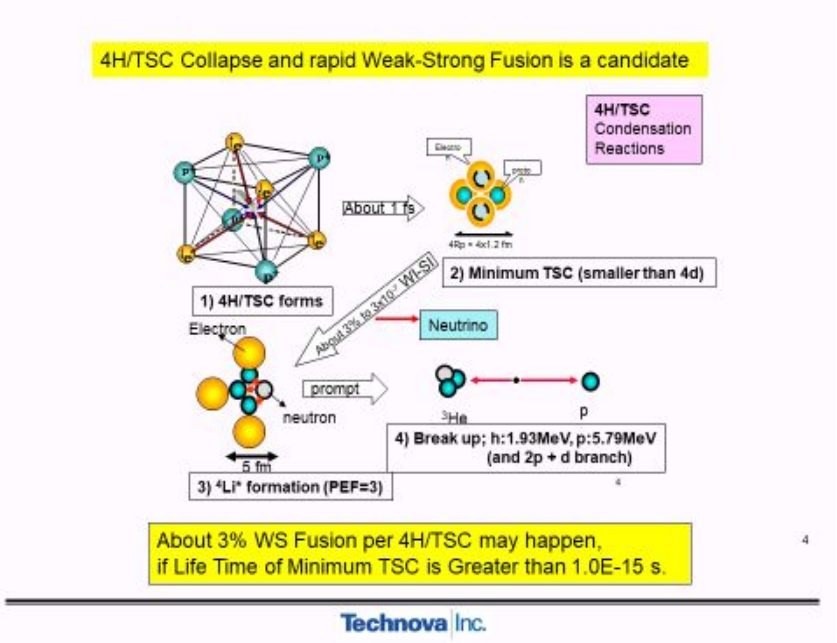

Figure 7. Simplified scheme of 4H/TSC WS fusion model [7], [16].

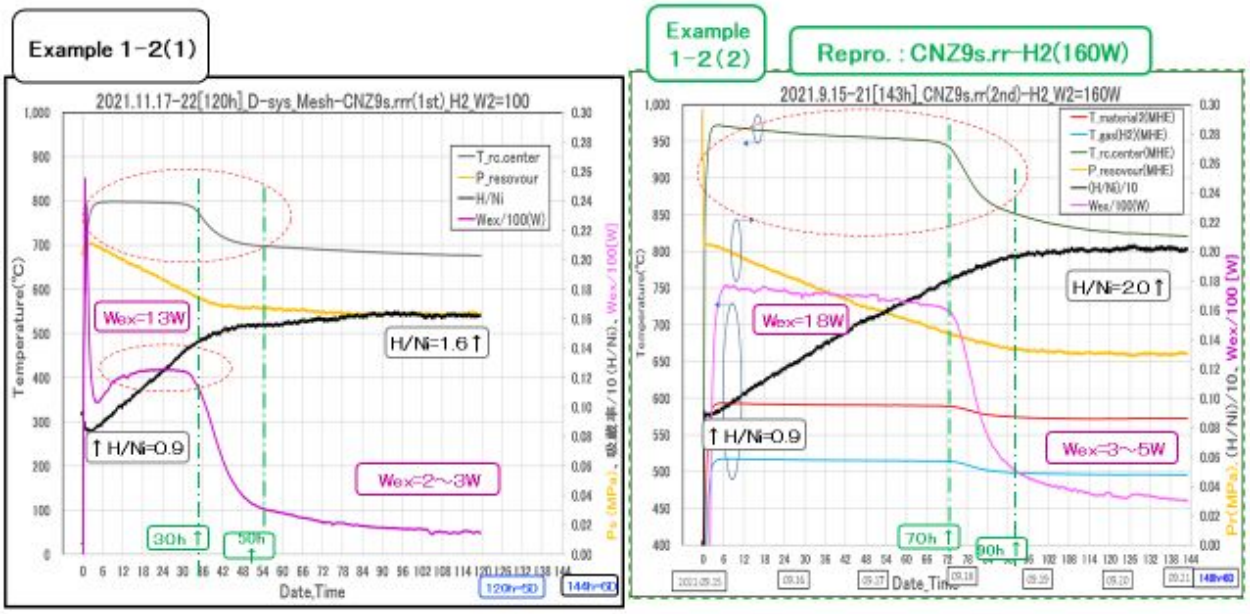

Figure 8. Comparison of power generation patterns for the lower (100 W) heating and the higher (160 W) conditions, with H/Ni loading patterns.

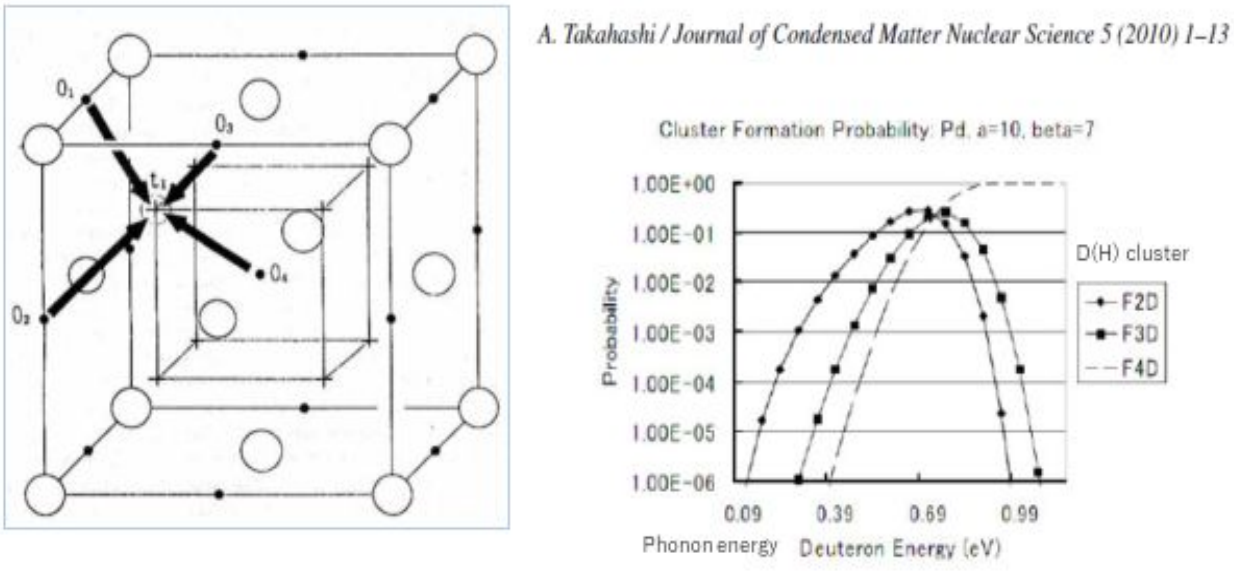

Figure 9. Competition of H-cluster formation probabilities under the FCC lattice proton phonon excitation energy [22].

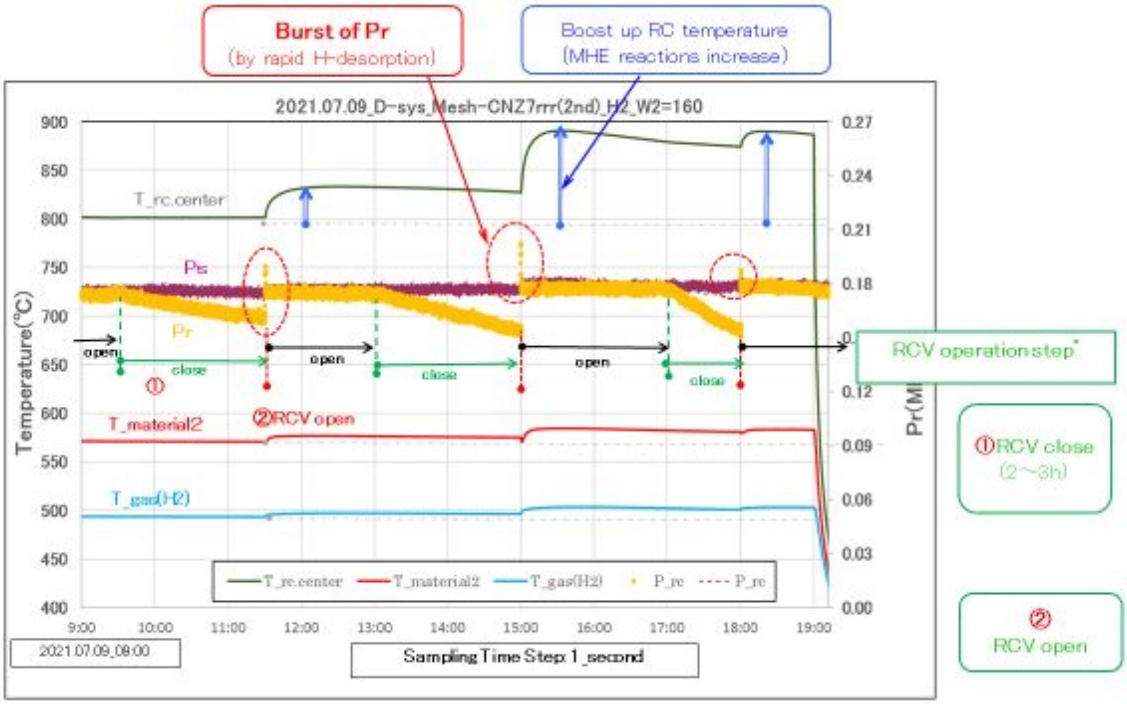

Figure 10. Re-activation data of MHE power by the RCV-close-to-open method [9], [10], [21].

the H-cluster formation probability by the phonon excitation level. Namely, 4H/TSC WS fusion rate at T-sites becomes more enhanced at higher temperatures for O-site phonon excitation, for the H/Ni > 1.0 condition. T-sites will remain empty after 4H/TSC WS fusion events. Therefore, it takes the condition that the more time for full T-site occupation with Hs needs when the 4H/TSC WS fusion rate is higher. As a consequence, integrated excess heat by MHE reactions can be enhanced by higher W2 heater condition. However, how large W2 watts can be supplied is the actual problem. However, we observed that duration of "high Wex plateau" changed by changing samples (by changing Cu/Ni atomic ratio and frequency of re-calcination) [21].

3. Triggering Mechanism of MHE Power Re-Activation

We have found the MHE re-activation method by the RCV-close-to-open method [9], [10]. Before reaching the saturation of H/Ni value (close to 2.0 in real runs), we may close the RC gas valve and wait for several hours.

We observe an H-gas pressure decrease (brown-color data in Fig. 10) during the closure of RCV (reaction chamber valve), showing slow H-absorption by CNZ sample. When we opened the RCV, a burst of Pr (H-pressure of RC) and boost-up of RC temperatures were recorded, which showed an increase of MHE power, which is to say re-activation. After the triggering by RCV-opening, the boosted-up excess power (15-10 watts in the run) continued for many hours. By repeating the RCV-close-to-open treatments, we observed a boost-up of excess power level repeatedly. What is the mechanism of this triggering/activation phenomenon?

When RCV is closed, H_2 accumulated on SNHs, moving from Ni-core inside. When RCV is opened, incoming H_2 meets accumulated H_2 to generate 4H/TSC to WS fusion, which generates a heat burst, and an H-desorption burst

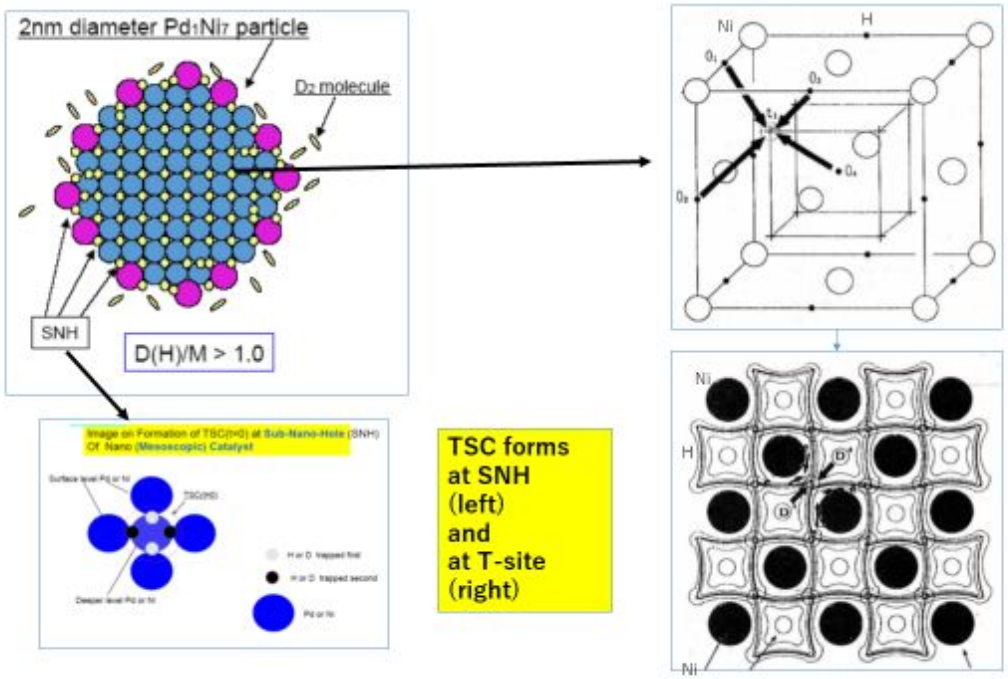

Figure 11. 4H/TSC WS fusion events can take place at surface SNHs (lower left figure) and also at T-sites of Ni-nano-core FCC lattice sites (right figure).

is induced. (See the left side of Fig. 11.) After H/Ni exceeds 1.0, absorbed Hs slowly fill T-sites by H-moving from surrounding 4 O-sites under phonon excitation (Fig. 11, right lower). The 4H/TSC WS fusion rate will be enhanced at T-sites under this process. When all T-sites will be filled with Hs, 4H/TSC formation rates will drop. By RCV-close-open triggering with H-desorption burst, empty T-sites will be generated, and the process of the slow phase H-loading at T-sites restarts, generating 4H/TSC WS fusion events.

4. Concluding Remarks

1) After starting initial heating by W2 (100 – 160 W) heater, excess thermal power by MHE is steeply generated from around 300°C outer region temperature of CNZ-sample powder.
2) Excess power suddenly starts to increase when the H/Ni loading ratio reaches around 1.0. This timing is considered to be the time that H-loading at O-sites of Ni core becomes full, attaining H/Ni =1.0 in about 20–60 minutes in our runs (Fast Loading process).
3) After that turning point, relatively high excess power generation continues for 1- 4 days, until the elapsed time region where H/Ni loading ratio saturates to be far greater than 1.0; H/Ni = 2.2 was the saturated value in some runs. This is the second phase H-loading by T-sites loading in Ni core: (Slow Loading process).
4) MHE power generation can be explained by the nuclear energy release of 4H/TSC WS fusion events at T-sites by dynamic 4H cluster formation of 4 protons moved from O-sites under phonon excitations in GMPW (global mesoscopic potential well) of Ni-nano-islands. This is the major process of power (about 20W in our experimental runs). In addition, minor excess power (about 4 W or less) is considered to be continuously

released by 4H/TSC WS fusion events at SNHs (sub-nano-holes) on surface of Ni-cores. This minor process remains after H/Ni ratio is saturated.

5) We found a method of MHE power re-activation by the RCV (reaction chamber valve) close-to-open method after H/Ni loading ratio becomes nearer to saturation. When RCV is opened, pulse thermal power generation occurs by 4H/TSC WS fusion at SNHs, which induces H-gas desorption-bursts from T-sites of Ni-cores. This trigger event produces empty T-sites in Ni-cores and the slow H-loading to T-sites restarts with relatively large generation of 4H/TSC WS fusion power (10-15 W) for a considerably long time (about one day in present trigger-trial runs). This re-activation/trigger process can be repeated.
6) Predictions by the TSC theory seem to be working very well.

References

[1] Akira Kitamura, Akito Takahashi, Koh Takahashi, Reiko Seto, Takeshi Hatano,Yasuhiro Iwamura, Takehiko Itoh, Jirohta Kasagi, Masanori Nakamura, Masanobu Uchimura, Hidekazu Takahashi, Shunsuke Sumitomo, Tatsumi Hioki, Tomoyoshi Motohiro, Yuichi Furuyama, Masahiro Kishida, Hideki Matsune; "Excess heat evolution from nanocomposite samples under exposure to hydrogen isotope gases", *Int. J. Hydrogen Energy*, **43** (2018) 16187–16200

[2] Yasuhiro Iwamura, Takehiko Itoh, Jirohta Kasagi, Akira Kitamura, Akito Takahashi, Koh Takahashi, Reiko Seto, Masanobu Uchimura, Hidekazu Takahashi,Tatsumi Hioki, Tomoyoshi Motohiro, Yuichi Furuyama, Masahiro Kishida, Hideki Matsune, "Anomalous Heat Effects Induced by Metal Nano-composites and Hydrogen Gas", *J. Condensed Matter Nucl. Sci.*, 29, 119–128 (2019)

[3] Toyoshi Yokose, Akito Takahashi, Koh Takahashi, Yuichi Furuyama, "Anomalous Heat Burst by CNZ7 Sample and H-Gas", Proceedings of JCF19, pp. 18–35, 2019

[4] Akito Takahashi, Toyoshi Yokose, Yutaka Mori, Akira Taniike, Yuichi Furuyama, Hiroyuki Ido, Atsushi Hattori, Reiko Seto, Atsushi Kamei, Joji Hachisuka, "Latest Progress in Research on AHE and Circumstantial Nuclear Evidence by Interaction of Nano-Metal and H(D)-Gas", *J. Condensed Matter Nucl. Sci.*, 33, 14–32, 2020

[5] Akito Takahashi, Toyoshi Yokose, Yutaka Mori, Akira Taniike, Yuichi Furuyama, Hiroyuki Ido, Atsushi Hattori, Reiko Seto, Atsushi Kamei, Joji Hachisuka, "Enhancement of excess thermal power in interaction of nano-metal and H(D) gas", Proc. JCF20, pp. 9–27, 2020

[6] Masahiko Hasegawa, Yutaka Mori, Akito Takahashi, Joji Hachisuka, Hiroyuki Ido, Reiko Seto, Akira Taniike, Yuichi Furuyama, "Comparison of AHE data between H2 and He runs for CNZ7rrr Sample", Presentation at JCF21 Meeting, December 2020, web conference of JCFRS: (PDF) Comparison of AHE data between H2 and He runs for CNZ7rrr sample - English version (researchgate.net)

[7] Akito Takahashi, "4H/TSC Effective Life Simulation rev2"; see (PDF) 4H TSC End State Effective Life Simulation 2rev (researchgate.net)

[8] Akito Takahashi, Fundamental of Rate Theory for CMNS, J. Condensed Mat. Nucl. Sci., 1–18, 19 (2016) (PDF) Fundamental of Rate Theory for CMNS (researchgate.net)

[9] Yutaka Mori, Akito Takahashi, Masahiko Hasegawa, Joji Hachisuka, Yuichi Furuyama; New MHE Experiments by D-System, JCF-22 Meeting, March 2022, see also: (PDF) New MHE Experiments by D-System (researchgate.net)

[10] Masahiko Hasegawa, Akito Takahashi, Yutaka Mori, Joji Hachisuka, Yuichi Furuyama, Characteristics of Excess Power Generation in MHE Experiments by D-System, JCF-22 Meeting, March 2022, see also: (PDF) Characteristics of Excess Power Generation in MHE Experiments by D-System (researchgate.net)

[11] (PDF) MHE nuclear-like thermal power generation and guiding TSC theory (researchgate.net)

[12] (2) (PDF) Anomalous Heat Effects by Interaction of Nano-Metals and H(D)-Gas (researchgate.net)

[13] Akito Takahashi, Physics of Cold Fusion by TSC Theory, J. Condensed Mat. Nucl. Science, 13, 565–579, (2013) (PDF) Physics of Cold Fusion by TSC Theory full paper (researchgate.net)

[14] Akito Takahashi, Nuclear Products of Cold fusion by TSC Theory, J. Condensed Mat. Nucl. Science, 15, 11–22, (2014) (1) (PDF) Nuclear Products of Cold Fusion by TSC Theory (researchgate.net)

[15] Akito Takahashi, The Basics of Deuteron-Cluster Dynamics as Shown by a Langevin Equation, J. Marwan and S. Krivit Ed., Low-Energy Nuclear Reactions and New Energy Technologies Sourcebook Volume 2, Chapter 11 (pp.193-217), ACS Symposium Series 1029, 2009 (1) (PDF) Basics of Deuteron-Cluster Dynamics by Langevin Equation (researchgate.net)
[16] Akito Takahashi, Chaotic End-State Oscillation of 4H/TSC and WS Fusion, Proc. JCF-16, 41–65 (2016) (1) (PDF) Chaotic End-State Oscillation of 4H/TSC and WS Fusion (researchgate.net)
[17] Pamela A. Mosier-Boss, Frank E. Gordon and Lawrence P.G. Forsley, Characterization of Neutrons Emitted during Pd/D Co-deposition, JCNMS, Vol.6 (2012)13
[18] Y. Arata and Y. Zhang, J. High Temp. Soc., Special Issue, Vol1, 2008
[19] A. Takahashi et al., Mesoscopic catalyst and D-cluster fusion, Proc. JCF11, pp. 47–52, JCFRS web-site, (2011)
[20] Akito Takahashi, Background of Condensed Cluster Fusion, Proc. JCF-15, 63–90 (2015) (PDF) Background for Condensed Cluster Fusion (researchgate.net)
[21] Masahiko Hasegawa, Akito Takahashi, Yutaka Mori, Yuichi Furuyama, MHE Reactions in New Experiments by D-System, paper to ICCF24, July 25–28, 2022, USA
[22] Akito Takahashi, Progress in Condensed Cluster Fusion Theory, JCNMS, 5, 1–13 (2010)

This paper is for Proceeding of ICCF24, July 25-28, 2022, USA, to be submitted to J. Condensed Matter Nuclear Science

J. Condensed Matter Nucl. Sci. 38 (2024) 307–312

Research Article

Evaluation of the Possibility of Using the Helium Leak Detector TI 1-14 for the Analysis of Protium H_2, Deuterium D_2, Helium-3 ^3He and Tritium T_2

Sergei A. Tcvetkov

Independent Consultant on Cold Fusion (LENR), Russia

Konstantin V. Fedko

Mass Spectrometric Analyst, Russia

Abstract

The characteristics of the TI 1-14 helium leak detector are given. The possibility of detecting fusion products based on the interaction of hydrogen isotopes with the TI 1-14 sensor is evaluated. The results of calibration of the leak detector by helium are given. The results of measuring hydrogen and the apparent products of nuclear fusion during the electrolysis of solid proton-conducting electrolytes in the deuterium atmosphere are described.
 ISSN 2227-3123

Keywords: TI 1-14 helium leak detector, nuclear fusion products, hydrogen isotopes, protium, deuterium, helium-3, tritium.

1. Introduction

We would like to draw your attention to one of the results of the first work of M. Fleishmann and S. Pons[2]. That is to say, tritium as an undeservedly forgotten product. One of the products of the D+D reaction of cold nuclear fusion is tritium.

$$\begin{array}{c} \mathbf{^2D + {}^2D \rightarrow {}^3T(1.01\ MeV) + {}^1H(3.02\ MeV)\ (v)} \\ \mathbf{or} \\ \mathbf{^2D + {}^2D \rightarrow {}^3He\ (0.82\ MeV) + n\ (2.45\ MeV)\ (vi)} \end{array} \quad \mathbf{(2)}$$

Use of eqn. (2) indicates that reaction (v) takes place to the extent of $1 \div 2 \times 10^4$ atoms s^{-1} which is consistent with the measurements of the neutron flux, bearing in mind the difference in radii. On the other hand, the data on enthalpy generation would require rates for reactions (v) and (vi) in the range $10^{11} \div 10^{14}$ atoms s^{-1}. It is evident those reactions (v) and (vi) are only a small part of the overall reaction scheme and that other nuclear processes must be involved.

 ISSN 2227-3123

Note that the amount of tritium in the first work significantly exceeds the number of detected neutrons. Isn't this the error in the discrepancy between the amount of detected helium-4 and the total excess heat discovered by other authors subsequently?

Confucius (an ancient thinker and philosopher of China, VI-V century BC) said:

Explore the past if you want to know the future.

In the development of this thesis, let us suggest that you consider the possibility of the TI 1-14 helium leak detector as an instrument to detect tritium, hydrogen and deuterium.

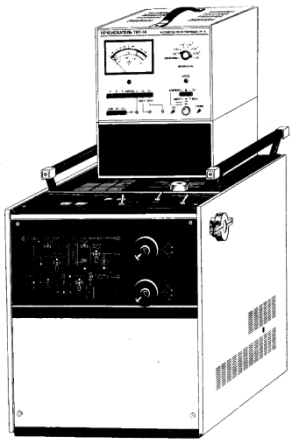

Figure 1. Leak detector produced in the 1990s.

Figure 2. Modern leak detector.

The modern upgraded helium leak detector has the ability to adjust to control gases: **helium and hydrogen**[3].

Table 1. Technical characteristics of the leak detector TI 1-14

Parameter	**Values**
Minimum helium flow recorded by the leak detector without throttling pumping	7×10^{-12} m$^3\times$ Pa/s
Minimum helium flow recorded by a leak detector with throttling pumping	7×10^{-13} m$^3\times$ Pa/s
Residual pressure in the analyzer, no more	1.3×10^{-3} Pa
Input pressure regulation P_2	$1.3\times10^{-3} \div 3\times10^{-3}$ Pa
Regulation of the accelerating voltage U_A	(150 ÷ 450) V
Suppressor voltage regulation U_S	(15 ÷ 300) V
The level of the output signal at the residual pressure in the analyzer and when U_A changes by 10% of the maximum value of the helium peak, no more	30%
Dynamic output range	(0.0002 ÷ 100) V
Fluctuations of the electric zero of an electrometric DC amplifier, no more	± 2 mV
Change in the emission current of the ion source cathode when the input pressure P_2 changes from 35 to 55 scale divisions, no more	± 0.5 scale divisions of the linear scale of the arrow device

Minimum recorded helium flux in units of the flux of helium atoms per second according to the following formula:

$$N_{\mathrm{He}}^{\min} = \frac{\mathrm{PV}}{\mathrm{RT}} \cdot N_A$$

at a temperature T = 300 K

$N_A = 6.022 \cdot 10^{23}\mathrm{atom/mol}$ - Avogadro number,
$N_{\mathrm{He}}^{\min 1} = 1.69 \cdot 10^{9}\frac{\mathrm{atom}}{s}$ - without throttling pumping,
$N_{\mathrm{He}}^{\min 2} = 1.69 \cdot 10^{8}\frac{\mathrm{atom}}{s}$ - with throttling pumping.

1.1. Operating Principle of the Leak Detector

The leak detector is a highly sensitive magnetic mass spectrometer tuned to detect helium. The leak detector consists of a vacuum system and a recording device. The main element of the leak detector is a mass spectrometric analyzer containing an ion source, an analyzer (drift space) and an ion receiver. In the ionizer, electrons collide with gas molecules entering the leak detector from the investigated volume and cause their ionization. The resulting ions are pulled out of the ionizer by an accelerating electric field acting in a direction perpendicular to the electron beam. The flow of ions through the outlet diaphragm of the ion source enters the drift space, in which the spatial separation of ions by mass takes place. Under the action of a constant magnetic field directed perpendicular to the direction of motion, the ions move along circular trajectories. The radii of these trajectories depend on the mass of the ions.

The radius of the ion trajectory in centimeters is determined by the formula:

$$R = \frac{0.576 \cdot \pi}{H} \cdot \sqrt{M \cdot U}$$

where **R -** radius of the ion motion trajectory, cm; **H** - magnetic field strength, A/m; **U** - potential difference accelerating the ions, V; **M** - effective mass of the ion, equal to ratio of its mass number to electron charge.

1.2. Possibility of Detecting Tritium

With different ratios of the effective masses of the ions and different potential differences accelerating these ions, respectively, the ion receiver is located motionless and the radii of the trajectories of different ions (tritium and helium) during detection will be equal to

$$\boldsymbol{R_T = R_{He}} = 2.5 \text{ cm},$$

Then

$$M_T \cdot U_T = M_{\mathrm{He}} \cdot U_{\mathrm{He}}$$
$$M_T = \frac{6 \text{ amu}}{e}, \qquad M_{\mathrm{He}} = \frac{4 \text{ amu}}{e}$$
$$U_T = \frac{2}{3} \cdot U_{\mathrm{He}}$$

If the regulation range of the accelerating voltage is $\mathbf{U_A}$=150÷450 V, and the accelerating voltage when tuned to a helium leak for the helium peak is U_{He} =265 V, then with the accelerating voltage U_T=177 V, tritium **can be detected**.

1.3. What can be Analyzed With This Leak Detector?

Consider all ions and their mass numbers that can be formed during ionization in the ion source of the leak detector on account of nuclear reactions of cold nuclear fusion:

Table 2. Ions and their mass numbers

Ions	**H+**	**^{3}He++**	**H_2+**	**D+**	**^{4}He++**	**HD+**	**^{3}He+**	**T+**	**D_2+**	**HT+**	**^{4}He+**	**DT+**	**T_2+**
m, amu	1	1.5	2	2	2	3	3	3	4	4	4	5	6

Obviously, the identification of chemical elements by these mass numbers is difficult. Therefore, in order to accurately identify the measured products of nuclear reactions, in addition to direct calibration of the instrument for pure gaseous components (hydrogen - H_2, deuterium - D_2, tritium - T_2, helium-3 -$_3$He, helium-4 -$_4$He) one should apply the method of chemical separation of hydrogen from helium. This method is to oxidize the hydrogen in a special reactor on a chemically pure copper oxide, followed by analysis of the remaining gaseous helium and analysis of the resulting water for tritium content.

1.4. Ions flow

Knowing the input resistance of the electrometric amplifier of the leak detector, it is possible to calculate the ions flow of a certain effective mass by the formula

$$N = \frac{U(V)}{R(Ohm) \times e(Kl)}$$

where **U** - the intensity of the peak measured by the ion receiver (*V*), **R=1014 Ohm** - the input impedance of the electrometric amplifier (*Ohm*), and **e** is the electron charge (*Kl*).

Since the value of the input resistance of the electrometric amplifier of the leak detector R is indicated in the description as its smaller limit, its real value may differ from the accepted value.

Therefore, it must be understood that the real flow values are less than the calculated values.

However, there are also factors that increase the found ion flow values:

- not all molecules that get into the flow of ionizing electrons will be ionized;
- not all ions will join the flow directed to the collector, some of them will be scattered.

Table 3. Setting for the helium leakage

Measured component	**P_2, scale divisions**	**U_A, V**	**Peak content in total, %**	**Ions flow, ions/s**	
He	42	265	100%	9.233×10^{15}	The leakage is open

1.5. Measurement Results

Mass numbers can be calculated using the formula:

$$m = \frac{R_{\mathrm{He}}^2 \times B^2 \times e}{2 \times U_A}$$

If $R_{\mathrm{He}} = 0,025$ м, B =0.187498 T - magnetic induction value of a constant magnetic field, $e = 1.6021766310^{-19}$, $U_A = 265\ V$, then

Table 4. Helium mass numbers

U_A,V	**265**
m_{He}, kg	6.64216×10^{-27}
m_{He}, amu	4.0

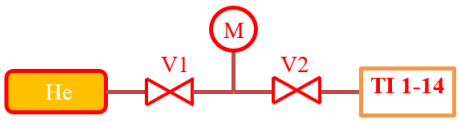

Figure 3. Connection diagram of a helium balloon to TI 1-14.

Table 5. The change in the He peak intensity depending on the pressure P_2

Measured component	**P_2, scale divisions**	**U_A, V**	**Peak intensity, mV**	**Ions flow, ions/s**
He	30	285	78	4.801×10^{14}
He	40	280	198	1.219×10^{15}
He	50	280	740	4.555×10^{15}
He	60	280	1890	1.163×10^{16}

1.6. Helium Peak Calibration

Helium peak intensity depending on the pressure P_2 has a nonlinear, close to polynomial, form.

D_2 measurements from the sample after electrolysis of solid proton-conducting electrolytes in a deuterium atmosphere.

In addition to deuterium, this sample clearly shows the presence of **tritium**, and possibly helium-3 and helium-4.

2. Conclusions

We have shown how the leak detector can be used to measure the products of nuclear reactions of hydrogen, deuterium, tritium and helium fusion. We need to develop a standard technique, combining the analysis of tritium with the transfer of all hydrogen into water and analysis of the β-activity of tritium in the resulting water. The development of this

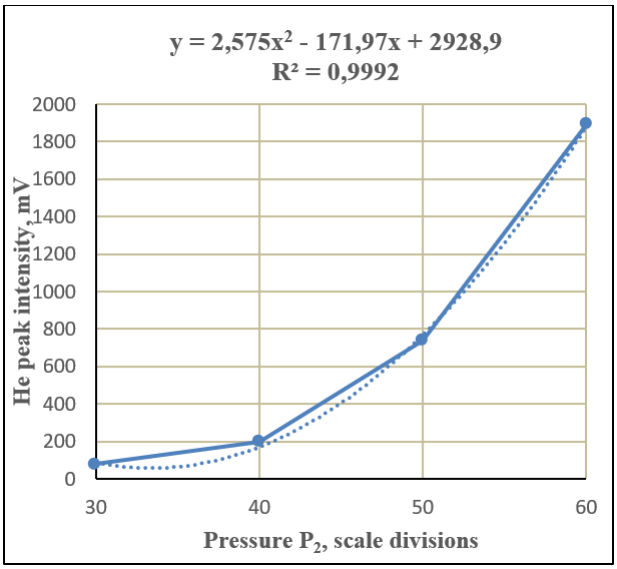

Figure 4. Helium peak intensity depending on the pressure P_2.

Table 6. Measurement results

Measured component	P_2, scale divisions	U_A, V	Peak intensity, mV	Peak content in total, %	Ions flow, ions/s	m, amu	Ions identification
D_2	45	375	55	47%	3.385×10^{14}	3.0	HD^+,$^3He^+$,T^+
		275	30	25%	1.847×10^{14}	4.1	D_2^+,HT^+,$^4He^+$
		190	33	28%	2.031×10^{14}	5.9	T_2^+
D_2	55	375	90	52%	5.540×10^{14}	3.0	HD^+,$^3He^+$,T^+
		275	40	23%	2.462×10^{14}	4.1	D_2^+,HT^+,$^4He^+$
		190	44	25%	2.708×10^{14}	5.9	T_2^+
D_2	60	375	150	34%	9.233×10^{14}	3.0	HD^+,$^3He^+$,T^+
		275	180	41%	1.108×10^{15}	4.1	D_2^+,HT^+,$^4He^+$
		190	114	26%	7.017×10^{14}	5.9	T_2^+

technique requires a strict metrological analysis of the results at all stages of such a combined hybrid method of analysis. It is necessary to modernize the leak detectors manufactured now to facilitate the detection and identification of reaction products. It is necessary to continue work on setting up a leak detector for hydrogen.

References

[1] A.L. Samgin, A.N. Baraboshkin, I.V. Murygin, S.A. Tsvetkov, V.S. Andreev, S.V. Vakarin, "The Influence of Conductivity on the Neutron Generation Process in Proton Conducting Solid Electrolytes"// Proceedings ICCF-4, December 6-9, 1993, Lahaina, Hawaii, EPRI, Palo Alto, California, Vol. 3; Nuclear Measurements Papers, p.5-1–5-7.

[2] Electrochemically induced nuclear fusion of deuterium. / Fleischmann Martin, Pons Stanley // J. of Elecroanal. Chem. -1989. - Vol. 261. - No. 2a. - pp. 301÷308.

[3] ТЕЧЕИСКАТЕЛЬ ГЕЛИЕВЫЙ МАСС-СПЕКТРОМЕТРИЧЕСКИЙ ТИ1-14М (Helium mass-spectrometric leak detector TI1-14M) https://vactron.ru/index.php/library/rukovodstva-po-ekspluatatsii/73-ti1-14-https://vactron.ru/index.php/library/rukovodstva-po-ekspluatatsii/73-TI 1-14 (in Russian).

J. Condensed Matter Nucl. Sci. 38 (2024) 313–325

Research Article

A LENR Solution for Fundamental Mysteries of the Solar Corona (Anomalously High Temperature and Anomalous He^3 Concentration)

V. I. Vysotskii* and M. V. Vysotskyy
Taras Shevchenko National University of Kyiv, Kyiv, 01601 Ukraine

Sergio Bartalucci
INFN Laboratori Nazionali di Frascati, Frascati, 00044 Italy

Abstract

The features and the method for solving of two fundamental problems of astrophysics are considered: the anomalously high temperature of the solar corona above the surface of the Sun, which is 200 times higher than the temperature of the surface itself, as well as the anomalously high concentration of the He^3 isotope (compared to He^4) in this region. It is shown that both of these effects are associated with the implementation of LENR in a low-temperature magnetized plasma in the solar atmosphere due to the self-similar formation of coherent correlated states and the generation of giant particle energy fluctuations in this region.
 ISSN 2227-3123

Keywords: Nuclear fusion, low-temperature hydrogen plasma, alternation of ionization and recombination of atoms, coherent correlated states, energy fluctuations

1. Introdution

Among the fundamental mysteries of modern astrophysics and the Sun physics, one of the most mysterious is the problem of the anomalously high temperature of the solar corona surrounding the visible Sun surface (photosphere) with the temperature 5780 K. This temperature rises slowly as we move away from the surface towards the center of the Sun. It is logical to assume that as one moves away from the surface upwards, the temperature will decrease.

However, the actual situation appears to be just the opposite. Above the surface of the photosphere there is a thin (about 10^3 km) layer of the chromosphere, near the outer surface of which (at the bottom of the solar corona) the temperature increases to $(1.5–2)\cdot10^6$K in the range of 100–300 km (Fig. 1). In this area concentration of particles is

*Corresponding author: vivysotskii@gmail.com

 ISSN 2227-3123

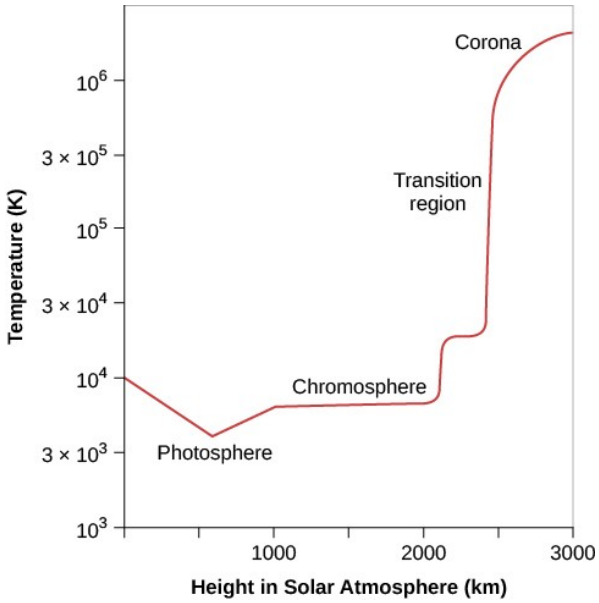

Figure 1. Altitude distribution of solar gas temperature in the lower part of the solar atmosphere [1].

about n≈10^8 cm^{-3}. In some places of this region the temperature rises to a value of $2{\cdot}10^7$ K, which is higher than in the center of the Sun.

Such features of temperature change contradict all the laws of thermodynamics.

All traditional (and unsuccessful) multiple attempts to explain these phenomena are associated with an unrealistic hypothesis about the possibility of "transit" ways of transferring energy without significant losses from the center of the Sun far beyond its surface through a much colder near-surface medium (e.g. [2]).

It has been shown that taking into account all possible "transit" mechanisms for heating the solar corona can provide no more than 3.5% of the corona energy that is recorded in numerous astronomical observations. Sources and mechanisms for the implementation of the rest of the energy are actually unknown. The greatest problem is the search for a mechanism that can stably maintain a high temperature of the corona throughout the entire solar cycle [3].

From numerous astronomical observations it is also well known that in this part of the Sun, very frequent vertical ejections of gas-plasma atom and ion magnetized substance (spicules of II type) occur from the volume of the photosphere, stimulated by fast switching (reconnections) of the magnetic field. These particles form a low-temperature plasma, which is held very firmly inside magnetic tubes and freely moves along its axis.

The process of formation of these open magnetic tubes occurs at the boundaries of photospheric supergranules of very large size, where there are opposite plasma flows, and concentrated extended zones of a strong magnetic field are generated. In these zones, the Kruscal-Schwarzshild instability conditions are satisfied [4], and the zone itself is divided into a system of magnetic tubes.

At any given time, there are about 10^6 such spicules on the Sun and they cover about 1% of Sun surface at any given moment of time. They move with an initial speed of $50{-}100\ \mathrm{km/s}$, have a diameter of 200–2000 km, an average lifetime of 5–7 min, and rise above the chromosphere to the lower part of the solar corona to a height of $(6-10)\cdot 10^3\ \mathrm{km}$. Inside the spicules, there is a circulating magnetic field $H \approx 2-3\mathrm{kOe}$ [5].

The plasma temperature in the observable part of the spicules, which exits the chromosphere, reaches $T \approx (1.5-2)\cdot 10^6$ K.

Figure 2. Photos of typical spicules on Sun surface [6], [7].

In some cases, the energy of vertical injection of such spicules is so high that these plasma flows overcome the gravitational field of the Sun and form coronal mass ejections into space, which, with the corresponding ejection direction, are registered on Earth and cause magnetic storms.

The typical photos of such spicules are presented in Fig. 2.

The scheme of magnetic field circulation and the direction of motion of the corresponding flows of low-temperature plasma forming spicules in the solar atmosphere (at the boundary of the photosphere, chromosphere and corona) are shown in Fig. 3.

The typical composition in the base of the spicule tube in photosphere is a "standard" low-temperature Sun gas (mainly hydrogen) with initial temperature $T \approx 10^4$ K and initial total hydrogen atom and ion concentration $n_{a0} \approx 10^{16} - 10^{17}\ \mathrm{cm}^{-3}$.

One of the hypothetical mechanisms of such a sharp heating is connected with the assumption of the possibility of inducing strong electric currents along very high circulating magnetic loops, vertical magnetic tubes with moving low-temperature plasma in the volume of solar spicules [7].

In this work, it is assumed that the presence of electrons in the volume of such a circulating field leads to the formation of a longitudinal electric current. It is also assumed that the collision of electrons and ions with neutral hydrogen atoms leads to a very strong heating of the moving solar gas to a temperature of $10^6 - 10^7$ K, which ultimately leads to anomalous heating of the solar corona. Such a mechanism does lead to an initial heating of the gas, but when it reaches temperature of 10–15 eV, the entire gas turns into plasma and the proposed heating mechanism becomes impossible. Based on this circumstance, it can be assumed that the initial heating of the gas can correspond to such

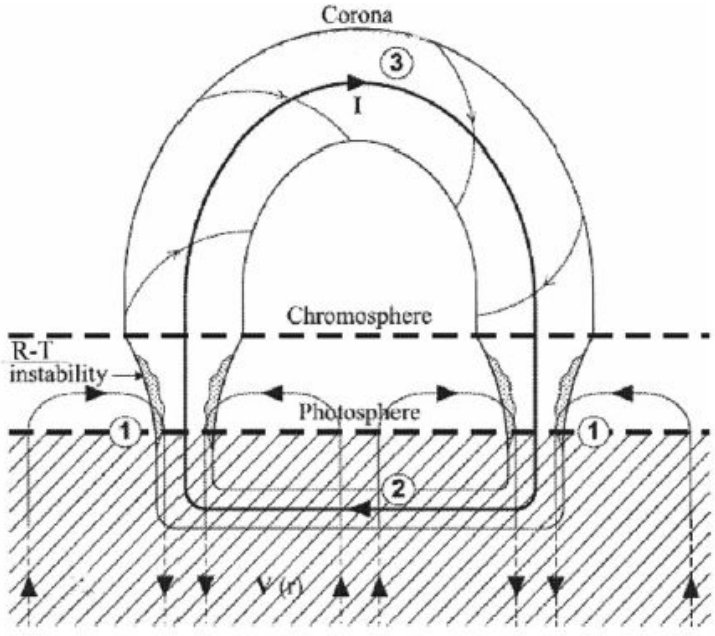

Figure 3. Scheme of spicule formation on the solar surface [8].

an electrodynamic mechanism up to a temperature of 3–5 eV, at which almost complete dissociation of hydrogen molecules occurs, but a significant part of neutral hydrogen atoms is retained. At the same time, the problem of the mechanism of further main heating of the solar gas (in fact, low-temperature plasma) to the observed high temperature of 200–2000 eV remains unresolved.

Another mystery is related to the anomalously high concentration of He^3 isotope (multiple times increase) relative to He^4 isotope in solar flares compared to the usual 0.0004 ratio. This result cannot be explained on the basis of the available data on processes on the Sun.

These anomalies are among main and fundamental problems of astrophysics.

An alternative method for solving this problem by implementing its own source of intense heating of the corona, which is not related to the transfer of heating energy from the central regions of the Sun, can be associated with the implementation of the mechanism of nuclear reactions directly in the volume of spicules. In this case, it would also be possible to find a solution to the problem of a high concentration of He^3 isotope.

Obviously, such a mechanism of self-heating of low energy matter due to the very low density of the medium and low temperature is not analogous to "standard" thermonuclear reactions, which take place, for example, in the center of the Sun. This conclusion is based on the traditional consideration of nuclear reactions under quasi-stationary conditions. An example of such a quasi-stationary system is plasma, which is usually characterized by averaged parameters that do not take into account the dynamic processes occurring at the nano-level.

The actual situation characterizing the features of nuclear interaction in locally dynamic systems is significantly different and much more optimistic. It is shown that such "nuclear solution" can be effectively implemented in low-temperature nuclear reactions optimized in self-similar process of formation of coherent correlated states of interacting particles [9]. The characteristic features of such states are the generation of giant fluctuations in the momentum and energy of these particles, which leads to a very significant increase in the cross section and the probability of nuclear

reactions. It is shown below that this process and these mysteries can be successfully solved by LENR stimulated by the combined action of a constant magnetic field and spatial nanodynamics of low-temperature solar plasma.

2. Mechanism of the Formation of Coherent Correlated States of Protons and Deuterons in Stable Low Energy Solar Plasma

It is well known that the state of a charged particle in a magnetic field corresponds to a harmonic oscillator with a standard instantaneous spectrum of energy levels $E_n = \hbar\omega(n + 1/2), \omega = eH/M_ic$. In a plasma medium, the kinetic energy of such particles does not depend on the presence of an constant external magnetic field and is determined by the plasma temperature based on the relationship $\hbar\omega(n + 1/2) \approx kT$.

The quantum state of such an ion essentially depends on its environment.

In the idealized case of a single ion, the situation is rather simple. If, for example, an isolated charged particle began to interact with a magnetic field in time $\mathrm{t} = 0$, then its state is determined by a coherent superposition of its own wave functions $\Psi_n(x)$ for each of two coordinates transverse to the direction of the magnetic field $\vec{H}$ with fixed initial phases $\varphi_n(0) = 0$ and deterministic change of these phases $\varphi_n(t) = E_nt/\hbar$ in time

$$\Psi(x) = \sum_n B_n\Psi_n(x)e^{-iE_nt/\hbar}, \Psi_n(x) = C_nH_n\left(x/x_0\right)e^{-x^2/2x_0^2},$$
$$C_n = \frac{1}{\sqrt{x_0 2^n n!\sqrt{\pi}}}, x_0 = \sqrt{\hbar/M\omega}, E_n = \hbar\omega(n + 1/2) \tag{1}$$

Here $H_n\left(x/x_0\right)$ is the Hermite polynomial.

In the optimal mode of switching on this interaction, the superposition of eigenfunctions forms a coherent correlated state (CCS) of the particle. The state of a particle in such a coherent superposition corresponds to Schrödinger-Robertson uncertainty relations [10]–[28]

$$\delta q\delta p \geq \hbar/2\sqrt{1 - r^2} \equiv \hbar^*/2,$$
$$\delta E\delta t \geq \hbar/2\sqrt{1 - r^2} \equiv \hbar^*/2,$$
$$\hbar^* = G\hbar, G = 1/\sqrt{1 - r^2} \tag{2}$$

with generation of giant fluctuations of the momentum and kinetic energy

$$\delta E_{G>1} = (\delta p)^2/2M \geq G^2\hbar^2/8M(\delta q)^2 = G^2\delta E_{G=1} \tag{3}$$

of this particle.

Here $0 \leq r < 1$ and $1 \leq G < \infty$ are correlation coefficient and correlation efficiency coefficient.

Specific values of parameters r and G depend on the mode of switching on the interaction of the ion with the magnetic field from the initial value $\omega(0) = \omega_0$, which corresponds to the initial state of the atom based on the uncertainty relation, taking into account energy fluctuations, to the final value $\omega(t \to \infty) = \omega_0 g \equiv \omega_{\max} = eH/M_ic$ with a characteristic turn-on time equal to τ for different values $g = \omega_{\max}/\omega_0$ of the final change in the frequency

$$\omega(t) = \omega_0\left\{1 + (g - 1)\left[1 - e^{-t/\tau}\right]\right\} \tag{4}$$

of the oscillator.

Here $g \approx 2\omega_i\sqrt{m_e/4\pi n_e e^2}$ is the coefficient of increase of the frequency of the magneticion oscillator during ionization of the atom, ω_i is the ionization frequency of the atom.

An analysis and direct calculation [11], [18], [22], [28] of the dynamics of the CCS formation process in such nonstationary systems show that the realistic value of the coefficient G for such a change of the frequency of the effective oscillator can reach very large values $G \geq 10^2 - 10^3$ and depends on the parameters of the nonstationary oscillator.

This lower limit corresponds to the case when the particle in effective harmonic oscillator was in the ground, lowest state with $E(0) = \hbar\omega/2$ before the switching on the interaction. In the case, when the initial state of the particle corresponded to the excited state of the oscillator with energy $E(n) = \hbar\omega(n + 1/2)$ the corresponding expression for the minimum energy of fluctuation has the following form [12], [13]

$$\delta E^{(\min)} = G^2 E(n) \tag{5}$$

This case, in particular, corresponds to the thermal energy of the medium with $E(n) = \hbar\omega(n + 1/2) \approx kT$, where such an oscillator is located, and leads to the following formula for effective thermal fluctuation

$$\delta T = G^2 T(n). \tag{6}$$

It is quite obvious that the realization of LENR in a low-temperature plasma using CCS in magnetic field is possible only during the single short time interval after CCS creation when there are large fluctuations of the kinetic energy of the particles. To repeat the considered process, it is necessary to turn off the interaction of a charged particle with a magnetic field, and then turn on such an interaction again. In laboratory conditions, such a repetitive process can be realized by frequently turning off and turning on the field.

It seems obvious that this is the only possibility for long-term quasi-stationary nuclear fusion. However, a more detailed analysis [9] shows that taking into account the nonstationary microdynamics of stationary plasma makes it possible to implement a fundamentally different process based on the natural switching on and off of the ion charge in a constant magnetic field. These processes are associated with alternating acts of ionization (charge switching on) of neutral hydrogen atoms or its isotopes and their subsequent recombination (charge switching off).

The analysis of these processes requires information on the composition and state of the gas-plasma medium.

Hydrogen atoms and ions ($\sim 94\%$) are the main elements of the solar atmosphere. To estimate the initial (molecular-atomic) state of hydrogen in the composition of solar gas, it is possible to use the Saha equation [29]–[32]

$$\frac{n_{a0}^2}{n_{m0} - n_{a0}/2} \approx 4\frac{(m_a kT/2)^{3/2}}{\hbar^3} \exp\left(-V_{diss}/kT\right) \tag{7}$$

interpreting it as an equation for determining the equilibrium ratio of the concentrations of hydrogen atoms n_a and molecules n_m taking into account the temperature and dissociation energy $V_{diss} \approx 4.5\text{eV}$ of hydrogen molecules.

A direct analysis of the solution of equation (7) at initial conditions $T = 10^4\ \text{K}(\text{kT} \approx 0.86\text{eV})$, $n_{m0} \approx 0.5 \cdot 10^{17}\ \text{cm}^{-3}$, shows that even at such a relatively low initial temperature, more than 99.99% of all hydrogen will be in a dissociated (non-molecular) state and $n_a \approx 2n_{m0}$. When the temperature increases, the probability of the existence of neutral molecules and molecular hydrogen ions becomes even less.

The subsequent analysis of the processes of ionization and recombination of hydrogen, as well as the processes of formation of coherent correlated states in the volume of magnetic tubes, will be carried out based on these results, assuming that the total concentration of hydrogen atoms and nuclei is equal to $n_{a0} \approx 2n_{m0}$. The equilibrium concentration of electrons and nuclei of the ionized part of atomic hydrogen at the beginning of the process of spicule formation (at $n_{a0} \approx 10^{17}\ \text{cm}^{-3}, T = 10^4\ \text{K}$) can be determined using the standard form of the same Saha equation. Its solution has the following form:

$$\frac{n_{i,e}^2}{n_{a0} - n_{i,e}} \approx 4\frac{(m_a kT/2)^{3/2}}{\hbar^3} \exp\left(-V_i/kT\right) \equiv N_{i,e},$$
$$n_{i,e} = \sqrt{n_{a0}N_{i,e} + N_{i,e}^2/4} - N_{i,e}/2 \tag{8}$$

In this equations $V_i = 13.6\text{eV}$ is the ionization potential of a hydrogen atom; n_e, n_i and $n_a = n_{a0} - n_{e,i}$ are concentrations of electrons, hydrogen ions (proton or deuteron) and neutral atoms.

From this solution, using the given initial parameters, we find $n_{i,e} \approx 3 \cdot 10^{16}\ \text{cm}^{-3}$. As the temperature rises, the number of ions rapidly increases to a limiting value. It is very important that the state of a stationary plasma at the microlevel is non-stationary and is characterized by alternating ionization and recombination processes.

The corresponding durations of the existence of a neutral hydrogen atom before ionization $<t_{atom}>$ and an ion before recombination $<t_{ion}>$ are determined by the laws of plasma and are equal to:

$$<t_{atom}> = 1/<\sigma_{ion}\,(v_e)\,v_e>n_e = \left\{C_H n_e\,(kT_e)^{3/2}\sqrt{\frac{8}{\pi m_e}}\left(\frac{V_i}{kT_e}+2\right)\exp\left(-\frac{V_i}{kT_e}\right)\right\}^{-1}; \tag{9}$$

$$<t_{ion}> = n_i/n_a n_e<\sigma_{ion}(v)v_e> = K_{ia}<t_{atom}>$$

$$K_{ia} = \frac{n_{i,e}}{n_a} = \frac{n_{i,e}}{n_{a0}-n_{i,e}} \approx 4\frac{(m_e kT_e/2)^{3/2}}{\hbar^3 n_{i,e}}\exp\left(-V_i/kT_e\right). \tag{10}$$

In this equations $C_H \approx 6 \cdot 10^{-18}\ \text{cm}^2/\text{eV}$ is a parameter depending on the structure of the cross section $\sigma_{ion}\,(v_e)$ of the hydrogen ionization process [30], K_{ia} is the ionization parameter (the ratio of the concentrations of ions and non-ionized atoms in the solar low-temperature plasma).

It follows from (10) that for the initial stage of evolution of spicules (at $T = 10^4$ K and $n_{i,e} \approx 3 \cdot 10^{16}\ \text{cm}^{-3}$) we have $K_{ia} \approx 0.4$. For this stage

$$<t_{atom}> \approx 0.08\ \text{s}, <t_{ion}> \approx 0.03\ \text{s}. \tag{11}$$

As the temperature increases to $kT \approx 10 - 20\text{eV}$, the ion concentration increases to a maximum value $n_{e,i} \approx n_{a0}$, and the duration of alternating intervals decreases to values

$$<t_{atom}> \approx 10^{-8}\ \text{s}, <t_{ion}> \approx 0.01\ \text{s}. \tag{12}$$

With a subsequent increase in temperature, the value $<t_{atom}> \sim 1/\,(T_e)^{3/2}$ decreases indefinitely, while the duration $<t_{ion}>$ remains approximately the same.

3. Selective Low Energy Nuclar Fussin in Sun Spicules

The dynamics of possible thermonuclear fusion processes in spicule volume

$$\begin{aligned}\frac{dn_{He^3}}{dt} &= n_p n_d<\sigma_{p+d=He^3}v>,\\ \frac{dn_{H^3}}{dt} &= n_d n_d<\sigma_{d+d=H^3+p}v>,\\ \frac{dn_{He^3}}{dt} &= n_d n_d<\sigma_{d+d=He^3+n}v>.\end{aligned} \tag{13}$$

are based on the most effective reactions

$$p + d = He^3 + Q; d + d = He^3 + n + Q, H^3 + p + Q \tag{14}$$

involving deuterium.

The base formula for the average thermonuclear reaction rate at a specific plasma temperature has the standard form [34]–[36]

$$<\sigma_{fusion}(v)v> = \sqrt{\frac{8/\pi\mu}{(kT)^3}}\int_0^\infty \sigma_{fusion}(E)Ee^{-E/kT}dE \tag{15}$$

If we use the correct expression for the reaction cross section

$$\sigma_{fusion}(E) = \frac{S(E)}{E} \exp\left(-\frac{\pi e^2 Z_1 Z_2}{\hbar}\sqrt{\frac{2\mu}{E}}\right) \tag{16}$$

taking into account the astrophysical S-factor [34]–[36], then the final expression for the rate of thermonuclear interaction takes the form

$$<\sigma_{fusion}(v)v> \equiv <\sigma_{fusion}(v)v>_v = Ae^{-B}\ \mathrm{cm}^3/\mathrm{s};$$
$$A \approx 1.3\cdot 10^{-16} S\left(T_9\right)\left[\mathrm{keV}\cdot \mathrm{bn}\right]\left(Z_1 Z_2/\mu_A\right)^{1/3}/T_9^{2/3}; B \approx 4.246\left(Z_1^2 Z_2^2 \mu_A\right)^{1/3}/T_9^{1/3} \tag{17}$$

Here $S\left(T_9\right) = S_0\left(1 + a_1 T_9 + a_2 T_9^2 + a_3 T_9^3\right)$ is astrophysical factor for dd-reactions; a_k are extrapolation parameters corresponding to a specific reaction [36]; Z_1, Z_2 are charges of interacting particles in units of proton charge; $\mu_A = A_1 A_2/\left(A_1 + A_2\right)$ is a reduced mass of interacting nuclei, expressed in mass numbers; T_9 is the plasma temperature, expressed in units of 10^9 K.

It follows from these results that in the case of standard solar plasma without CCS in the volume of lower part of spicules the rate of thermonuclear interaction for reactions (p, d) and (d, d) is very small $\sim 10^{-100}\ \mathrm{cm}^3/\mathrm{s}$. In this case any nuclear fusion is impossible.

A fundamentally different situation corresponds to the case when we take into account the real microdynamics of atoms in the volume of a magnetized plasma. In this case, the effective nonstationary temperature changes according to the replacement

$$T \to T_{eff}(t) = T\{G(t)\}^2. \tag{18}$$

At such approximation the basic formula (17) has the next form:

$$<\sigma_{fusion}(v,t)v> = A^*(t)\exp\left\{-B^*(t)\right\}\mathrm{cm}^3/\mathrm{s},$$
$$A^* = A/G(t)^{4/3}, B^* = B/G(t)^{2/3}. \tag{19}$$

In this case the final formula for the thermonuclear reaction rate has to be additionally averaged over time within the oscillation period $\pi/2\omega_H$

$$<<\sigma_{fusion}(v,t)v>> = \frac{2\omega_H}{\pi}\int_0^{\pi/2\omega_H} <\sigma_{fusion}\left(v, S\left(T_{eff}(t)\right)v\right>dt \tag{20}$$

In [9] it was shown that the formula $G(t) = G_{\max}\left|\sin\left(2\omega_H t\right)\right|$ is a very good approximation of the dependence $G(t)$ during the time interval of maintaining the coherence of the formed correlated state.

The results of such a double averaging (20) of the thermonuclear interaction rate $\sigma_{fusion}(v,t)v$ for (14) reactions with such approximation are shown in Fig. 4 for both low and high effective temperatures.

It is very important that the effective (virtual) temperature does not affect the quasistationary state of the plasma and the duration of the intervals of existence of ions $<t_{ion}>$ and neutrals $<t_{atom}>$, but it has a very significant effect on the probability of internuclear interaction.

In the idealized case such a regime can exist for an indefinitely long time. In a real material medium (in particular, in a gas or plasma), the optimal phase relationships are quickly violated due to collisions of an ion with other particles. In this case the duration of existence of such CCS with giant energy fluctuations δE is determined by the mean free path

$$\Delta t_{ion}^{(corr)} \approx <l>/<v_{ion}> \approx \sqrt{\left(kT_{ion}\right)^3 M_{ion}}/4\pi n_i e^4 \Lambda \tag{21}$$

of the ion in the plasma.

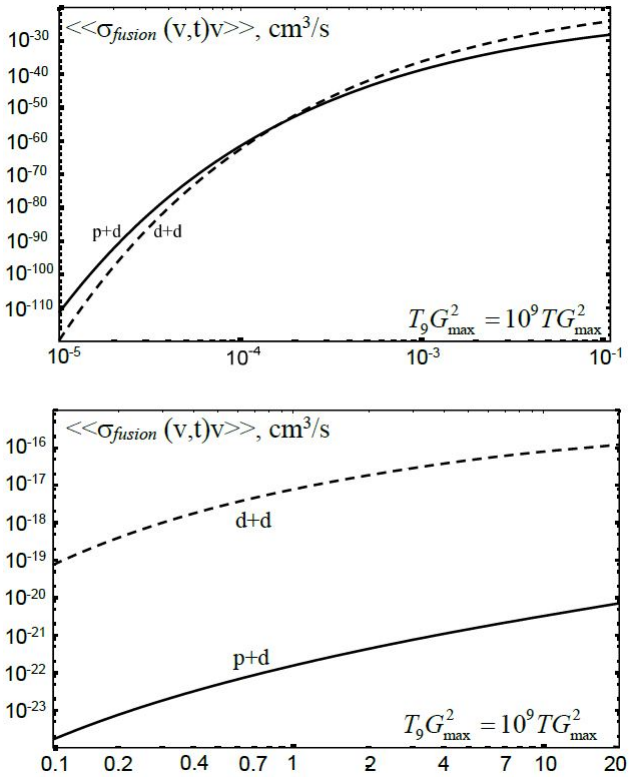

Figure 4. Dependence of double averaged thermonuclear interaction rate for (d,d) and (p,d) reactions in hydrogen low temperature plasma on the effective temperature and correlation coefficient.

The duration of the existence of such a correlated state with the accompanying giant fluctuations of the kinetic energy of a considered charged particles is equal to [30], [31]

$$\Delta t_{ion}^{(corr)} \approx <l>/v_i \approx \sqrt{(kT_i)^3 M_i}/4\pi n_i e^4 \Lambda. \tag{22}$$

Here $v_i \approx \sqrt{kT_i/M_i}$ is the isothermal velocity of a heavy ion (proton) in a given medium, $<l> \approx (kT)^2/4\pi n_i e^4 \Lambda$ is free path length, $\Lambda \approx 5 \ldots 10$ is Coulomb logarithm.

If we take into account that in the coherent correlated state the effective energy of the particle increases by a factor of G^2, then to calculate $\Delta t_{ion}^{(corr)}$ from formula (22) the replacement

$$T_i \to <T_i^{eff}(t)> = <G^2>_t T_i \tag{23}$$

should be made, which leads to a very significant increase of the lifetime $\Delta t_{ion}^{(corr)} \sim \left\{<G^2>_t\right\}^{3/2}$ of the CCS. In particular, for $kT_i = 1 - 10\mathrm{eV}$ and $n_i \approx 10^{17}\ \mathrm{cm}^{-3}$, the time $\Delta t_{ion}^{(corr)}$ increases from $\Delta t_{ion} \approx 10^{-9} - 10^{-12}$ s for the uncorrelated state to $\Delta t_{ion}^{(corr)} \approx 10^{-3} - 10^{-2}$ s for the values of $<G> \approx 200 - 1000$. This time is approximately equal to the time $<t_{ion}>$ of existence of the ionized state of an ion in a plasma and is $10^4 - 10^5$ times longer than the

oscillation period ω_H of the harmonic oscillator, which corresponds to the frequency of the proton in a magnetic field H with a strength of $1000 - 3000$ Oe.

Taking these features into account leads to the following form of equations:

$$\frac{dn_{He^3}}{dt} = \left\{n_p^* n_d + n_p n_d^*\right\} <<\sigma_{p+d=He^3} v>>, \tag{24a}$$

$$\frac{dn_{H^3,p}}{dt} = n_d^* n_d <<\sigma_{d+d=H^3+p} v>>, \tag{24b}$$

$$\frac{dn_{He^3,n}}{dt} = n_d^* n_d <<\sigma_{d+d=He^3+n} v>>, \tag{24c}$$

which determine the dynamics of thermonuclear fusion processes in low energy magnetized plasma in spicule volume.

Here $n_{p,d}^* = \eta n_{p,d}; \eta = P_{diss}\ \Delta t_{ion}^{(corr)} / (<t_{ion}> + <t_{atom}>)$ is the efficiency factor for the use of CCS for nuclear fusion in flashing low-temperature magnetized plasma; $P_{diss} \approx 0.4 - 0.6$ is the probability of dissociation of hydrogen molecules or its isotopes into atoms in the considered range of temperature and plasma density; n_p^* and n_d^* are concentrations of protons and deuterons in correlated state.

From these equations, we can find the intensities

$$\frac{dn_{He^3}}{dt} \approx 1.5 \cdot 10^9\ \mathrm{cm}^{-3}\ \mathrm{s}^{-1}, \tag{25a}$$

$$\frac{dn_{H^3,p}}{dt} \approx \frac{dn_{He^3,n}}{dt} \approx 1.9 \cdot 10^8\ \mathrm{cm}^{-3}\ \mathrm{s}^{-1} \tag{25b}$$

of three considered nuclear fusion reactions for the real value $G_{\max} \approx 300 - 1000$ of the correlation efficiency coefficient and the initial concentrations $n_p(1-\eta) = 7 \cdot 10^{16}\ \mathrm{cm}^{-3}, n_p^* = 3 \cdot 10^{16}\ \mathrm{cm}^{-3}, n_d(1-\eta) = 2.1 \cdot 10^{12}\ \mathrm{cm}^{-3}, n_d^* = 9 \cdot 10^{11}\ \mathrm{cm}^{-3}$ of protons and deuterons in uncorrelated and correlated states.

The initial rate of average heating of each particle of the substance of spicules due to the energy of these reactions is equal to

$$\frac{d(kT)}{dt}\frac{1}{n_i + n_e + (n_{a0} - n_{i,e})} = \left\{\frac{dn_{He^3}}{dt} Q_{He^3} + \frac{dn_{H^3,p}}{dt} Q_{H^3+p} + \frac{dn_{He^3,n}}{dt} Q_{He^3+n}\right\} \frac{1}{n_{a0} + n_{i,e}} \approx 0.1\mathrm{eV/s} \tag{26}$$

Such heating leads to an increase of the effective temperature $T_{eff} \sim T$, to an increase of the double averaged thermonuclear interaction rate $<<\sigma_{fusion}(v,t)v>>$, and to additional rapid ionization. In 15–20 seconds after the start of the process, the entire medium of the spicules becomes ionized, which leads to an increase of the concentration of CCS active protons n_p^* and deuterons n_d^* in the correlated state.

As a result of these processes, the intensities of fusion reactions increase to values

$$\frac{dn_{He^3}}{dt} \approx 10^{10}\ \mathrm{cm}^{-3}\ \mathrm{s}^{-1}, \tag{27a}$$

$$\frac{dn_{H^3,p}}{dt} \approx \frac{dn_{He^3,n}}{dt} \approx 6 \cdot 10^9\ \mathrm{cm}^{-3}\ \mathrm{s}^{-1}, \tag{27b}$$

and the heating rate of each particle of the spicule substance increases to

$$\frac{d(kT)}{dt}\frac{1}{n_i + n_e} \approx 0.7 - 0.8\mathrm{eV/s} \tag{28}$$

It should be noted that fast neutrons and tritium H^3 isotopes formed in these reactions are also actively involved in subsequent nuclear fusion in a dense heated plasma. In particular, tritium nuclei are actively involved in the process of CCS formation with subsequent stimulation of a very efficient reaction

$$H^3 + d = He^4 + n + 17.589\mathrm{MeV}, \tag{29}$$

the probability of which is several orders of magnitude greater than that of the main reactions $\mathrm{d} + \mathrm{p}$ and $\mathrm{d} + \mathrm{d}$.

For this reason, the final concentration of tritium in the spicule plasma after its release into the solar atmosphere will be very low. From the photo (Fig. 2) it can be seen that the length L of the base of the spicules, located in the photosphere of the Sun, is approximately equal to the height of the magnetic loop itself and is equal to $6000 - 10000\ \mathrm{km}$. The plasma medium, under the action of the magnetic field of the tube, shakes the base of the spicule and begins to move vertically through the rest of the photosphere and the chromosphere, having a temperature of about $kT_L \approx 200\mathrm{eV}$.

Assuming the initial temperature $T_0 = 10^4\ \mathrm{K}\ (kT_0 \approx 0.86\mathrm{eV})$ and taking into account the almost linear law of the increase in plasma temperature with time, it is easy to determine that the translational velocity of deuterons during the time of movement at the base of the spicule increased from $v_{od} \approx 5\ \mathrm{km/s}$ to $v_{Ld} \approx 70\ \mathrm{km/s}$. It follows from these data that the time of deuteron motion along the base of the spicule is equal to

$$\tau_{0L} \approx \frac{3L\sqrt{M_d}}{2\sqrt{2}} \frac{kT_L - kT_0}{(kT_L)^{3/2} - (kT_0)^{3/2}} \approx 3L/2v_{Ld} \approx 180 - 250\ \mathrm{s} \tag{30}$$

This result agrees well with the rate of specific heating of the spicule material (26) and with the final plasma temperature $kT_L \geq 200\mathrm{eV}$ at the end L of the horizontal part (base) of the spicule.

After changing the motion of the spicule from horizontal to vertical, it quickly passes (with little additional thermonuclear self-heating) through the thin layer of the chromosphere and moves with gravitational deceleration in the solar corona, effectively heating the surrounding atoms and ions. On this part of the trajectory, the transverse size of the magnetic tube with plasma increases rapidly, and the plasma density in the volume of the swelling spicules decreases to $n_{i,e} \approx 3 \cdot 10^9\ \mathrm{cm}^{-3}$ [37], and at an even higher height to $n_{i,e} \approx 10^8\ \mathrm{cm}^{-3}$. This process reduces greatly the probability of similar nuclear reactions taking place in the volume of the spicule on the outer part of the trajectory.

The discussed scenario for LENR realization due to the self-formation of CCSs makes it possible to substantiate the thermonuclear mechanism of giant and abnormal heating of the spicules and Sun atmosphere. An important factor is the complete synchronization of the observed heating of matter in the volume of spicules with the generation in this region of a very large amount of nuclear He^3 isotope, which is a daughter isotope of nuclear fusion reactions (14).

This result is a consequence of the specifics of the implementation of LENR and He^3 synthesis, taking into account the specifics of the formation of CCS in a low-temperature magnetized plasma for different particles:

- effective stimulation of (p, d) and (d, d) reactions, which lead to the formation of CCS and He^3 synthesis due to the alternation of complete ionization and recombination of hydrogen atoms;
- the impossibility of stimulation of similar low-energy nuclear reactions $He^3 + He^3 = 2p + He^4$ and $He^3 + He^4 = Be^7$, which can lead to a decrease in He^3 concentration, but correspond to a very low probability of CCS formation due to low probability of alternating full ionization (creation of He^3 nuclei) and full recombination (creation of neutral helium atoms).

The presence of such fundamental inequality of both types of nuclear reactions is the solution to the well-known He^3 problem: the presence of an excess amount of He^3 isotope in relation to He^4 in the composition of coronal ejections from the surface of the Sun. This problem cannot be solved on the basis of using the mechanism of standard thermonuclear fusion in the volume of stars due to the existence of alternative ways of creating and destroying of this isotope [9].

References

[1] https://commons.wikimedia.org/wiki/File:Temperature-height_graph_for_solar_atmosphere.jpg

[2] Erdèlyi R., Ballai I. Heating of the solar and stellar coronae: a review. *Astronomical Nachrichten*, v. 328(8) (2007), 726—33.

[3] Zaitsev V.V., Stepanov A.V., Kronshtadtov P.V. Type-II Spicules as Important Sources of Both Heating and Sustain the Mass Loss of Solar Corona. *Geomagn. Aeron.* V.**61 (2021)**, 1116–1121

[4] Kruscal M., Schwarzshild M. Same instabilities of a completary ionized plasma. *Proc. Roy. Soc., A,* v. 223 (1954), No 1154.

[5] G. Tsiropoula, K. Tziotziou, I. Kontogiannis, M.S. Madjarska, J.G. Doyle, Y. Suematsu. Solar fine-scale structures. 1. Spicules and other small-scale, jet-like events at the chromospheric level:observation and physical parameters. Space Sci Rev, Springer Science+Business Media B.V. 2012.

[6] https://hi-news.ru/wp-content/uploads/2017/06/solarflare-1000x415.jpg.

[7] https://encrypted-tbn0.gstatic.com/images?q=tbn:ANd9GcSkQQ2wJVmVblN7cU15ddPMFmvIKBNk6njH9w

[8] V.V. Zaitsev, A.V. Stepanov, P.V. Kronshtadtov. On the possibility of heating the solar corona by heat fluxes from coronal magnetic structures. Solar.Phys., v. **295** (2020), 166.

[9] V.I. Vysotskii, M.V. Vysotskyy. Self-controlled Flashing Nuclear fusion in Stationary Magnetized Low-temperature Plasma, *Fusion science and technology*, 2023.
doi: https://doi.org/10.1080/15361055.2022.2151284

[10] E. Schrödinger. Heisenbergschen Unschärfeprinzip. *Ber. Kgl. Akad. Wiss*., Berlin, **S24 (1930),** 296.

[11] H.P. Robertson. A general formulation of the uncertainty principle and its classical interpretation, *Phys. Rev. A*, v. **35 (1930)** 667.

[12] V.V. Dodonov, V.I. Manko. "Invariants and correlated states of nonstationary systems", in: Invariants and the Evolution of Nonstationary Quantum Systems, *Proceedings of the Lebedev Physical Institute*, Nova Science, Commack, New York, v. 183 (1988), 103.

[13] V.V. Dodonov, A.B. Klimov, V.I. Manko. Physical effects in correlated quantum states", in: Squeezed and Correlated States of Quantum Systems, Proceedings of the Lebedev Physical Institute, Nova Science, Commack, New York, v. **295,** (1993), 61–107.

[14] V.I. Vysotskii, S.V. Adamenko. Correlated states of interacting particles and problems of the Coulomb barrier transparency at low energies in nonstationary systems. *Technical Physics*, v. **55**(5) (2010), 613.

[15] V.I. Vysotskii, M.V. Vysotskyy, S.V. Adamenko. Formation and application of correlated states in non-stationary systems at low energy of interacting particles. *Journal of Experimental and Theoretical Physics*, v. **114**(2) (2012), 243.

[16] V.I. Vysotskii, S.V. Adamenko, M.V. Vysotskyy. The formation of correlated states and the increase in barrier transparency at a low particle energy in nonstationary systems with damping and fluctuations. *Journal of Experimental and Theoretical Physics*, v. **115**(4) (2012), 551.

[17] V.I. Vysotskii, M.V. Vysotskyy. Coherent correlated states and low-energy nuclear reactions in non stationary systems. *European Phys. Journal* A, v. **49**: 99 (2013).

[18] V.I. Vysotskii, S.V. Adamenko, M.V. Vysotskyy. Acceleration of low energy nuclear reactions by formation of correlated states of interacting particles in dynamical systems. *Annals of Nuclear energy*, v. **62** (2013), 618.

[19] V.I. Vysotskii, M.V. Vysotskyy. Correlated states and transparency of a barrier for low-energy particles at monotonic deformation of a potential well with dissipation and a stochastic force. *Journal of Experimental and Theoretical Physics*, v. **118**(4) (2014), 534.

[20] V.I. Vysotskii, M.V. Vysotskyy. Formation of correlated states and optimization of nuclear reactions for low-energy particles at nonresonant low-frequency modulation of a potential well. *Journal of Experimental and Theoretical Physics*, v. **120**(2) (2015), 246.

[21] V.I. Vysotskii, M.V. Vysotskyy. The formation of correlated states and optimization of the tunnel effect for low-energy particles under nonmonochromatic and pulsed action on a potential barrier. *Journal of Experimental and Theoretical Physics*, v. **121**(4) (2015), 559.

[22] V.I. Vysotskii, M.V. Vysotskyy. Coherent correlated states of interacting particles – the possible key to paradoxes and features of LENR. *Current Science*, v. **108**(4) (2015), 30.

[23] V.I. Vysotskii, M.V. Vysotskyy. Formation of correlated states and tunneling at low energy at controlled pulse action on particles. *Journal of Experimental and Theoretical Physics*, v. **125**(8) (2017), 195.
[24] V.I. Vysotskii, S.V. Adamenko, M.V. Vysotskyy. Subbarier interaction of channeling particles under the self-similar excitation correlated states in periodically deformed crystal. *Journal of surface investigation*, v. 6(2) (2012), 369.
[25] V.I. Vysotskii, M.V. Vysotskyy, S. Bartalucci. Features of the formation of correlated coherent states an nuclear fusion induced by the interaction of slow particles with crystals and free molecules. *Journal of Experimental and Theoretical Physics*, v. **127** (3) (2018), 479.
[26] S. Bartalucci. V.I. Vysotskii, M.V. Vysotskyy. Correlated states and nuclear reactions: An experimental test with low energy beams. *Phys. Rev. Accelerators and Beams,* **v. 22** (5) (2019), 054503.
[27] V.I. Vysotskii, M.V. Vysotskyy, S. Bartalucci. Using the method of coherent correlated states for production of nuclear interaction of slow particles with crystals and molecules. *Journal of Condensed Matter Nucl. Sci*. V. 29 (2019), 358–367.
[28] V.I. Vysotskii, M.V. Vysotskyy. Universal mechanism of LENR in physical and biological systems on the base of coherent correlated states of interacting particles. In Book: Cold Fusion. Advances in Condensed Matter Nuclear Science. Edited by Jean-Paul Biberian, Elsevier, 2020. CHAPTER 17, pp. 333–370.
[29] Gordon Francis. Ionization Phenomena in Gases. Academic Press, 1960.
[30] Low Temperature Plasma Technology. Methods and Applications. Edited By Paul K. Chu, XinPei Lu, CRC Press, 2020.
[31] Shi Nguyen-Kuok. Theory of Low-Temperature Plasma Physics. Springer Cham. 2017
[32] Takayoki Fueno, Henry Eyring, Taikyue Ree. Three-body recombination of gaseous ions. *Can. J. Chem*. V.38 (1960), 1693.
[33] Ferreira, C.M., Tatarova, E., Gordiets, B.F. Kinetic theory of low-temperature plasmas in molecular gases. *Plasma Physics and Controlled Fusion*; v. 42(12B) (2000), 165–188.
[34] W.A. Fowler, G.R. Gaughlan, B.A. Zimmerman. Thermonuclear Reaction Rates. *Annual Review of Astronomy and Astrophysics*, v. 5 (1967), 525.
[35] W.A. Fowler, G.R. Gaughlan, B.A. Zimmerman. Thermonuclear Reaction Rates, II. *Annual Review of Astronomy and Astrophysics*, v. 13 (1975), 69.
[36] C. Angualo et al. A compilation of charged-particle induced thermonuclear reaction rates. *Nuclear Physics A,* v. 656 (1999), 3–183.
[37] Kano R., Tsuneta S, Scaling Law of Solar Coronal Loops Obtained with YOHKOH, *Astrophys. Jour*., v. 454 (1995), 934.

J. Condensed Matter Nucl. Sci. 38 (2024) 326–337

Research Article

Mechanism and Dynamics of Quasi-Stationary Self-Supporting LENR in Low-Temperature Magnetized Plasma

V. I. Vysotskii*, M. V. Vysotskyy

Taras Shevchenko National University of Kyiv, Kyiv, 01601 Ukraine

Abstract

The physical foundations for the production of effective self-controlled low energy nuclear fusion in a magnetized deuterium or hydrogen cold plasma are considered. The LENR mechanism is associated with the features of the charge state of individual particles of cold plasma, which corresponds to the fluctuation alternation of ionization and recombination processes of each atom in such plasma with thermal energy $kT \approx 10 - 20eV$. Each act of ionization of any hydrogen atom in the presence of a constant magnetic field corresponds to the creation of a harmonic oscillator, which continues to exist until the moment of recombination of this atom. The impulsive process of creating of such an oscillator based on a proton or deuteron is accompanied by the formation of quantum coherent correlated states of these particles in created harmonic oscillator, which are characterized by giant fluctuations of kinetic energy. The magnitude of these fluctuations reaches 30 – 100 *keV* and exceeds the temperature of low-temperature plasma by 10^3 – 10^4 and more times. For particles with such energy, the probability of nuclear fusion during interaction with nearest atoms or ions is very high.
 ISSN 2227-3123

Keywords: Nuclear fusion, low-temperature plasma fusion, atoms ionization and recombination, coherent correlated states, energy fluctuations

1. Introduction

Traditional methods and mechanisms of producing nuclear reactions at low energy (LENR) are based on several basic concepts:

- controlled very essential change in the critical characteristics (heating or acceleration) of the interacting particles;
- purposeful change in the characteristics of the nearest environment of the material media in which the interacting particles are located (intense compression, change in the density of the electron or muon environment, change in the phase or physical volume etc.);
- hypothetical short-term change in the charge state of the individual protons due to its transformation into a neutron by weak interaction with accelerated electrons, which solves the problem of the Coulomb barrier.

*Corresponding author: vivysotskii@gmail.com

 ISSN 2227-3123

To implement these mechanisms, special methods are required. Each of them is a one-time phenomenon. To repeat them, it is necessary to repeat the entire cycle of external influences. Such a one-time nature of the manifestation of these methods and the associated lack of multiple regular repetitions of nuclear processes are among the fundamental reasons for the unreliability and non-optimality of the existing methods for producing LENR.

In this paper an effective mechanism of self-regulating stimulation of quasi-stationary LENR is described. This mechanism is connected with fundamental phenomena of thermal equilibrium in multiparticle systems and is produced in the cyclical natural alternation of the processes of ionization of atoms and recombination of ions occurs, lasting indefinitely.

2. Peculiarities of LENR Produced by an Impulsive Change in the Charge State of an Interacting Particle

It is obvious that the starting prerequisite for the implementation of any nuclear reaction involving charged particles is to ensure a high probability that these particles will pass through the Coulomb potential barrier. One of the most effective methods for overcoming the Coulomb barrier in the implementation of nuclear fusion at low energy is the use of coherent correlated states (CCS) of a particle.

Such states are characterized by both very large (giant) and very long (compared to uncorrelated states) fluctuations of energy and momentum of this particle. These states correspond to the modified Schrödinger-Robertson uncertainty relations [1]–[4]

$$\delta p\delta q \geq \frac{\hbar}{2\sqrt{1-r^2}} \equiv \hbar_{eff}/2, \hbar_{eff} = \hbar/\sqrt{1-r^2} \equiv G\hbar, r = \frac{<qp>+<pq>}{2\sqrt{<p^2><q^2>}};$$
$$\delta E\delta t \geq \frac{\hbar}{2\sqrt{1-r^2}} \equiv \hbar_{eff}/2, \quad \hbar_{eff} = \hbar/\sqrt{1-r^2} \equiv G\hbar, r = \frac{<Et>+<tE>}{2\sqrt{<E^2><t^2>}}, \tag{1}$$

which are the universal generalization of Heisenberg uncertainty relations at $r \neq 0$.

In these relations parameter r is the correlation coefficient the value of which corresponds to the interval $-1 \leq r \leq 1$. This coefficient characterizes the degree of mutual connection of corresponding dynamic variables p, r and E, t. An alternative characteristic of such states is the correlation efficiency coefficient $G = 1/\sqrt{1-r^2}$.

The simplest and most efficient method for creating of such states can be implemented in a non-stationary harmonic oscillator. It was shown in the works [5]–[14] that fast modulation of the parameters of such an oscillator leads to the formation of a CCS and to the generation of very large fluctuations of the momentum δp and energy δE of the particle. The same effect corresponds to the motion of a particle in a spatially inhomogeneous system of potential wells (in particular, in a channel between atomic planes in crystals [15]–[19]).

The physical basis for such processes is the in-phase mutual interference of different eigenfunctions of the same particle in this system.

From formula (1) a simple estimate for the lower limit (minimum value) of fluctuations of the kinetic energy follows:

$$\delta E^{(\min)} = (\delta p)^2/2M = G^2\hbar^2/8M(\delta q)^2, \tag{2}$$

where *M* is a particle mass and δq is the spatial interval, where the particle is localized.

It is important to note that this lower limit corresponds to the case when the particle in the parabolic potential corresponding to the harmonic oscillator in the ground state, the lowest state with $E(0) = \hbar\omega/2$ before the deformation of the potential well started. In a more realistic case, when the initial state of the particle corresponds to the excited

state of the oscillator with the energy $E(n) = \hbar\omega(n + 1/2)$ the corresponding expression for the minimal energy of fluctuation has the following form:

$$\delta E^{(\min)} = G^2 E(n). \tag{3}$$

This case also corresponds to the thermal energy of the medium with $E(n) = kT$ where such an oscillator is located and leads to the following formula for effective thermal fluctuation:

$$\delta T = G^2 T(n). \tag{4}$$

An analysis [5]–[17] of the dynamics of the CCS formation process in such non-stationary systems shows that the realistic value of the coefficient G for such a change in the frequency of the effective oscillator can reach very large values $G \geq 10^2 - 10^3$ and depends on the parameters of the nonstationary oscillator.

In the works [3]–[5] it was shown that the correlation coefficient r

$$r = \mathrm{Re}\left\{\varepsilon^* \frac{d\varepsilon}{dt}\right\} \Big/ \left|\varepsilon^* \frac{d\varepsilon}{dt}\right| \tag{5}$$

can be calculated based on the solution of the equation of a classical oscillator with a variable frequency

$$\frac{d^2\varepsilon}{dt^2} + \omega^2(t)\varepsilon = 0 \tag{6}$$

under the initial conditions

$$\varepsilon(0) = 1, \left.\frac{d\varepsilon}{dt}\right|_0 = i \tag{7}$$

In these equations $\omega(t) = 1 + f(t)$ is the dimensionless nonstationary frequency, which is normalized to the initial frequency of the oscillator $\omega_0 = \omega(0); t$ is the dimensionless (normalized to ω_0^{-1}) time; $\varepsilon(t)$ is the dimensionless (normalized to $q_0 = \sqrt{\hbar/M\omega_0}$) complex coordinate of the particle.

Let us consider the dynamics of the formation of a coherent correlated state in a pulsed (close to stepwise) mode of increasing the oscillator frequency

$$\omega(t) = \omega_0 \left\{1 + (g-1)\left[1 - e^{-t/\tau}\right]\right\} = \omega_0 \left\{1 + (g-1)\left[1 - \exp\left(-\frac{\omega_0 t}{\omega_0 \tau}\right)\right]\right\} \tag{8}$$

from the initial value ω_0 to the final value $\omega(t \to \infty) = \omega_0 g \equiv \omega_{\max}$ with a characteristic turn-on time τ for different values of the final change in the frequency of the oscillator $g = \omega_{\max}/\omega_0$.

One of the most realistic models of such an oscillator is associated with the motion of a particle with a charge Q and with a mass M in a magnetic field H [8], [9]. In such a system, all parameters of particle motion, including eigenfunctions $\varphi_n(q)$, frequency $\omega_H = QH/Mc$ and the spectrum of energy levels $E_n = \hbar\omega(n + 1/2)$, fully correspond to the mathematical model of a harmonic oscillator. With each act of a very sharp switching on of the magnetic field, a coherent correlated state of ions located in the region of action of this field forms. This problem has been considered in detail in [20].

The subsequent analysis shows that for the problem of the motion of an ion in the volume of a low-temperature plasma in a realistic (moderate in amplitude) constant magnetic field, we have the following inequality $\omega_H \tau << 1$. For the problem considered in this work, this parameter is equal to the value $\omega_H \tau \approx 10^{-8}$.

If we take into account that the time of existence of the CCS is much greater than the period of the main frequency $\omega_{\max} = \omega_H$, then the last condition actually corresponds to a purely stepwise mode of switching the oscillator frequency.

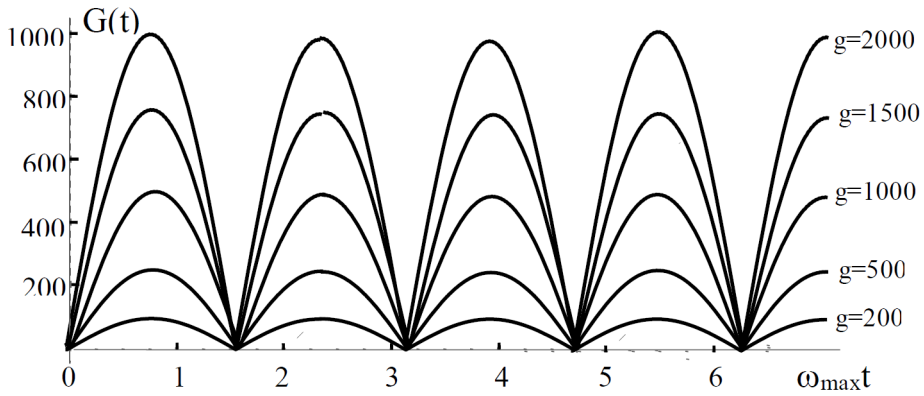

Figure 1. Non-stationary dynamics of the correlation efficiency coefficient G after increasing of the base oscillating frequency $\omega(t)$ in g times related to initial value ω_0.

The results of calculation of the correlation efficiency coefficient $G = 1/\sqrt{1-r^2}$ for different g at condition $\omega_H \tau << 1$ are presented in Fig. 1.

It can be seen that in this mode of the oscillator frequency change, a very large value of the coefficient is produced. Direct analysis shows that all these dependencies $G(t)$ are very well approximated by a simple formula $G(t) = G_{\max}(g)\,|\sin(2\omega_H t)|$.

This approximation corresponds to the relation

$$\left\langle G^2 \right\rangle = G^2_{\max}(g)/2. \tag{9}$$

At first glance, it seems that for the production and practical use of such an effect, we need a system that generates very fast and frequent changes in the magnetic field strength. The difficulties of creating such a system are obvious.

A detailed analysis shows that there is a realistic mechanism that allows this process to be generated in a completely stationary plasma! For this, it is necessary to take into account the features of the real microdynamics of multiple repeated mutual transformations of atoms and ions that occur in a stationary low-temperature hydrogen plasma. Such features of plasma microdynamics are associated with the continuous alternation of the processes of ionization and recombination of atoms and ions at a plasma temperature close to the ionization potential of its atoms and exceeding the characteristic potential of dissociation of hydrogen molecules into atoms. In such a plasma, each act of ionization corresponds to a pulsed switching on of the interaction of the formed ion with a magnetic field and the formation of a short-term CCS, and each recombination event corresponds to a pulsed switching off of the interaction and also the formation of a short-term CCS due to the interference of those spatially distributed wave functions that, before the recombination act, formed a coherent correlated superposition.

Such a fundamentally new mechanism for changing the frequency $\omega(t) = Q(t)H/Mc$ of an effective harmonic oscillator, corresponding to the process of interaction of ions with a magnetic field, is based not on the traditional change in the parameters of the magnetic field with a constant charge of the ion, but on the action of a constant magnetic field and a self-controlled change in the effective charge of the ion, when it is turned on and off in turn in the processes of ionization and recombination.

Obviously, such a process can be the most efficient in a plasma containing atoms with one electron (hydrogen or deuterium). For heavier atoms, the efficiency of this process has to be significantly lower due to two main reasons:

- the process of single ionization or recombination does not allow the interaction of a particle with a magnetic field to turn off completely, which leads to a small value of the parameter $g = \omega_{\max}/\omega_0$ and, accordingly, to a small value of the correlation efficiency coefficient,
- the presence of electrons in the ion shell after partial ionization greatly increases the probability and cross-section of scattering of these ions in the plasma volume, which leads to a rapid dephasing of coherent states and a very short lifetime of the CCS.

Of course, heavier atoms can also be present in such plasma, but they will be a "passive target" for hydrogen or deuterium atoms, which, with such a switch, will receive a very large fluctuation of kinetic energy.

In such a system the value $\tau = \tau_{ion}$ characterizes the process of switching on the ion charge, which corresponds to the duration of the process of changing the frequency of the equivalent non-stationary harmonic oscillator. The value

$$\tau_{ion} \approx R_D/v_e = \sqrt{m_e/4\pi n_e e^2} \tag{10}$$

is determined by the speed v_e of plasma electrons incident on the atom, whose energy exceeds the ionization potential, and by their distance from the atom (it can be estimated through the Debye screening radius $R_D = \sqrt{kT_e/4\pi n_e e^2}$), at which the moving electron can affect the state of the atom; and is equal to $\tau_{ion} \approx 2 \times \left(10^{-13} - 10^{-14}\right)$ sec in plasma with parameters $T_e = 10 - 20\text{eV}$, $n_e = 10^{16} - 10^{18}\ \text{cm}^{-3}$.

The initial time of "turning on the charge" $Q(t)$ of an ion during neutral atom ionization can be determined by Heisenberg uncertainty relation, according to which any atom can be in an ionized state for a time $\delta t \geq \hbar/2\delta E = \hbar/2E_{ion} = 1/2\omega_{ion}$ due to the quantum mechanical fluctuation $\delta E \geq E_{ion}$ of the electron energy. Such a fluctuating initial ionization of an atom does not lead to the excitation of a real vibrational state of the nucleus in an external magnetic field, but does allow it to establish the initial frequency ω_0 of such vibrations after the beginning of real ionization. According to such an analysis, a dynamically reliable (non-virtual) process of "switching on" the mechanism of hydrogen atom ionization actually begins after a very short time $\delta t \approx 1/2\omega_{ion} \approx 2 \times 10^{-16}$ sec.

Taking into account this circumstance and condition $\tau_{ion} \gg \delta t$, the base equation (8), which characterizes the one cycle of "turning on" the charge, can be represented in its original form

$$\omega(t) = \omega_H \left\{1 - \exp\left(-\frac{\delta t + t}{\tau_{ion}}\right)\right\}. \tag{11}$$

It is possible to prove that (11) can be reduced to (8) by the following mathematical transformation:

$$\omega(t) \approx \omega_H \left\{1 - \left(1 - \frac{\delta t}{\tau_{ion}}\right) \exp\left(-\frac{t}{\tau_{ion}}\right)\right\} = \omega_0 \left\{1 + (g-1)\left(1 - \exp\left(-\frac{t}{\tau_{ion}}\right)\right\}\right. . \tag{12}$$

Here

$$g = \tau_{ion}/\delta t \approx \omega_i \sqrt{m_e/\pi n_e e^2}, \omega_0 \equiv \omega(0) = \omega_H/g. \tag{13}$$

It can be seen from these estimates that in the case of a typical magnetic field of $H \approx 1000 - 3000Oe$ in a plasma with a density $n_e = 10^{16} - 10^{18}\ \text{cm}^{-3}$, the frequency increase parameter g of the equivalent oscillator is equal to value $g \approx 100 - 1000$, which agrees with the data presented in Fig. 1.

The duration of the existence of such a correlated state with the accompanying giant fluctuations in the kinetic energy of charged particles can be estimated as the time from the moment of creation of such a CCS to the first collision of this particle with surrounding atoms and ions

$$\Delta t_{ion}^{(corr)} \approx < l > /v_i \approx \sqrt{(kT_i)^3\, M_i}/4\pi n_i e^4 \Lambda. \tag{14}$$

Here $v_i \approx \sqrt{kT_i/M_i}$ is the isothermal velocity of a heavy ion (proton) in a given medium, $< l > \approx (kT)^2/4\pi n_e e^4 \Lambda$ - free path length, $\Lambda \approx 5...10$ - Coulomb logarithm.

During such a collision, there is a partial violation of the optimal phase relationships between different eigenfunctions of a particle in a strictly phased superposition state of a harmonic oscillator, which, of course, immediately sharply reduces the correlation coefficient.

If we take into account that in the coherent correlated state the effective energy of the particle increases by a factor of G^2, then to estimate $\Delta t_{ion}^{(corr)}$ from formula (14) the replacement

$$T_i \rightarrow < G^2 >_t T_i \tag{15}$$

should be made, which leads to a very significant increase of the lifetime $\Delta t^* \sim \left\{\left\langle G^2 \right\rangle_t\right\}^{3/2}$ of the CCS. In particular, for $kT_i = 10\mathrm{eV}$ and $n_i = 10^{16} - 10^{18}\ \mathrm{cm}^{-3}$, the time $\Delta t_{ion}^{(corr)}$ increases from $\Delta t_{ion} \approx 10^{-9} - 10^{-11}\,\mathrm{sec}$ for the uncorrelated state to $\Delta t_{ion}^{(corr)} \approx 10^{-3} - 10^{-2}\,\mathrm{sec}$ for the values of $< G > \approx 200 - 800$. This time is $10^4 - 10^5$ times longer than the oscillation period ω_H of the harmonic oscillator, which corresponds to the frequency of the proton in a magnetic field H with a strength of 1000–3000 Oe.

It should be noted that the total disintegration of the CCS takes place only after several successive collisions, which increases the time $\Delta t_{ion}^{(corr)}$ by several times and contributes to a more efficient use of the CCS.

3. Dynamics of CCS Formation and LENR Generation Under Natural Alternation of Ionization and Recombination Processes in Low-Temperature Magnetized Plasma

The process considered above, of CCS formation during the ionization of atoms in plasma, is part of one stage of the cyclic process. This process consists in the repeated alternation of the ionization and recombination of atoms in a low-temperature plasma.

Each stage of this cyclic process consists of several substages:

a) The initial part of every stage starts with the time interval (average duration $\langle t_{atom} >$) of the existence of an atom before the beginning of the ionization process

$$< t_{atom} >= 1/ < \sigma_{ion}\left(v_e\right) v_e > n_e = \left\{ C_H n_e \left(kT_e\right)^{3/2} \sqrt{\frac{8}{\pi m_e}} \left(\frac{V_i}{kT_e} + 2\right) \exp\left(-\frac{V_i}{kT_e}\right)\right\}^{-1}. \tag{16}$$

Here V_i is the ionization potential of an atom; $C_H \approx 6 \cdot 10^{-18}\ \mathrm{cm}^2/\mathrm{eV}$ is a parameter depending on the structure of the cross section $\sigma_{ion}(v)$ of the hydrogen ionization process [21].

Using this result, it is possible to determine the typical average duration of atomic state of the particle

$$< t_{atom} > \approx \left(10^8 - 10^9\right)/n_e \approx 10^{-7} - 10^{-10}\mathrm{sec}, \tag{17}$$

corresponding to the plasma temperature $kT_e = 10 - 20\mathrm{eV}$ and electron (ion) concentration $n_i = 10^{16} - 10^{18}\ \mathrm{cm}^{-3}$.

b) The substage of a neutral atom ends with the process of direct ionization. Its characteristic duration corresponds to the value τ_{ion} (10) and is equal to the short duration $\tau_{ion} \approx 2 \times \left(10^{-13} - 10^{-14}\right)$ sec in the same plasma.

c) The next parameter determines the characteristic (average) time

$$< t_{ion} >= n_e n_i / n_a n_e^2 < \sigma_{ion}(v) v_e >= K < t_{atom} >, K = n_i/n_a = n_i/\left(n_{a0} - n_i\right) \tag{18}$$

of existence of the ionized state of a hydrogen isotopes until the moment of recombination and transformation into an atom [22]–[25]. This time differs by a large factor (Saha formula)

$$K \approx 4 \frac{\left(m_e kT_e/2\right)^{3/2}}{\hbar^3 n_{a0}} \exp\left(-V_i/kT_e\right) >> 1 \tag{19}$$

from the similar average lifetime $< t_{atom} >$ of the same particle in the form of an atom.

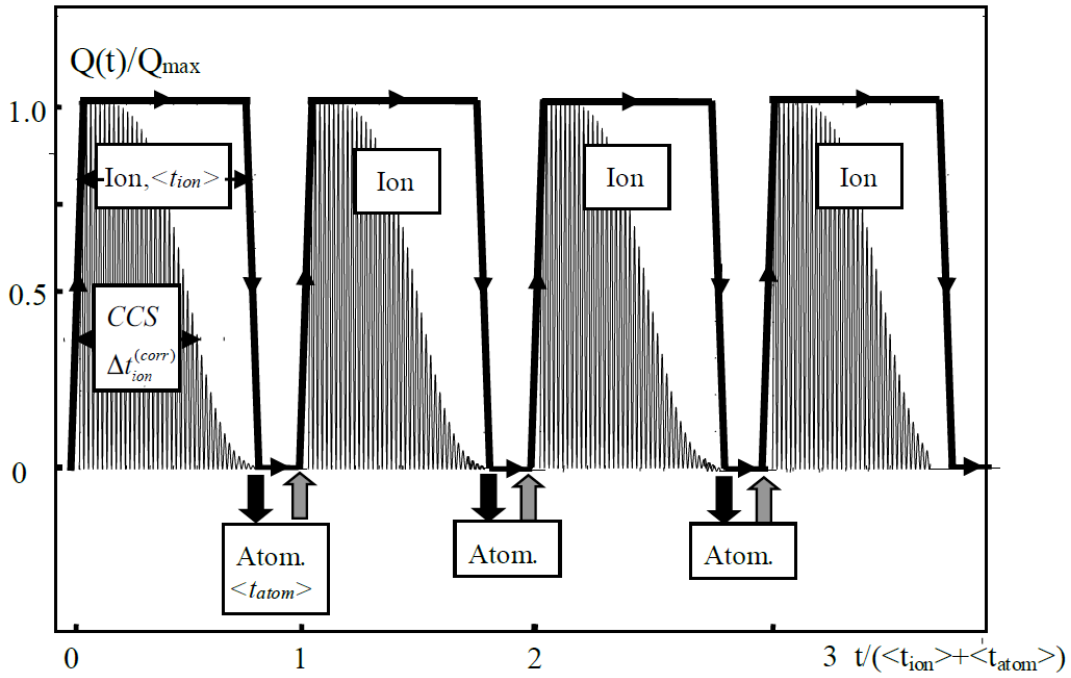

Figure 2. The sequence of existence of coherent correlated states and the dynamics of turning on and off the hydrogen effective charge Q(t).

Result (19) with $K >> 1$ is valid in the considered temperature range $kT_e \approx 10 - 20\text{eV}$ under the obvious condition that the total concentration of particles in a plasma $n_{a0} << 10^{24}\,\text{cm}^3$, i.e. much less than in a solid. From the condition $K >> 1$, it can be seen that the average time $< t_{ion} >$ of existence of hydrogen and its isotopes in the form of a free nucleus and a free electron in such a plasma is much longer than the similar time of existence of these particles in the form of atomic hydrogen, i.e. the time $< t_{atom} >$ required for the subsequent rapid ionization of atoms in the same plasma.

d) The final part of the direct recombination process is close in order of magnitude to the analogous duration τ_{ion} of the direct ionization process, and its duration is much shorter than $\langle t_{ion} \rangle$.

The given parameters may differ by several times when additional factors such as multistage ionization or ionization from a pre-excited state of the atom are taken into account. These corrections do not change the general trend: the duration of existence of the self-stimulated coherent correlated state of the hydrogen ion in a magnetized low-temperature plasma is the major part of the duration of each stage of ionization-recombination cycle.

Estimations show that in a partially ionized magnetized plasma about $\{< t_{atom} > + < t_{ion} >\}^{-1} = \{(1 + K) < t_{atom} >\}^{-1}$ full cycles of preconditions of flashing LENR every second for each of the atoms (H or D) are possible.

These processes are shown in a symbolic form in Fig. 2.

4. Features and Efficiency of Nuclear Fusion Stimulated by Energy Fluctuations in Low-Temperature Magnetized Plasma

Let us briefly consider the features of the influence of such giant energy fluctuations on nuclear dd-fusion at a low mean plasma temperature.

The dynamics of $d\left(d,He^3\right)n, d(d,T)p$ reactions is described by the equations

$$\begin{aligned}\frac{dn_{He^3}}{dt}=\frac{dn_n}{dt}=\eta n_d^2<\sigma_{d+d=He^3+n}v>,\\ \frac{dn_t}{dt}=\frac{dn_p}{dt}=\eta n_d^2<\sigma_{d+d=t+p}\nu>.\end{aligned} \tag{20}$$

Here $\eta = P_{diss}\Delta t_{ion}^{(corr)}/\left(< t_{ion} > + < t_{atom} >\right)$ is the efficiency coefficient for the use of CCS in lowtemperature magnetic plasma; $P_{diss} \approx 1$ is the probability of dissociation of D_2 molecules into atoms in the considered range of plasma temperatures $kT \approx (2-4)\varepsilon_{diss}$.

The base expression for the average thermonuclear reaction rate at a specific plasma temperature has the following form

$$< \sigma_{fusion}(v)v >= \sqrt{\frac{8/\pi\mu}{(kT)^3}}\int_0^\infty \sigma(E)Ee^{-E/kT}dE \tag{21}$$

and can be calculated taking into account the dependence of the same cross-section of both nuclear reactions on the speed of interacting particles [26-28]

$$\sigma_{fusion}(E)=\frac{S}{E}\exp\left(-\frac{\pi e^2 Z_1 Z_2}{\hbar}\sqrt{\frac{2\mu}{E}}\right) \tag{22}$$

Here μ is a reduced mass of interacting nuclei; T is the plasma temperature; $S = S_0\left(1 + a_1T_9 + a_2T_9^2 + a_3T_9^3\right)$ is the astrophysical factor for dd-reactions; a_k are extrapolation parameters [28] corresponding to a specific reaction; T_9 is the plasma temperature, expressed in units of 10^9 K.

At low energy $S = S_0 \approx 56\text{keV}\cdot\text{bn}$ and it significantly increases with the increase of energy (plasma temperature).

If we take into account the approximation $G(t) = G_{\max}\left|\sin\left(2\omega_H t\right)\right|$ presented in Fig. 1 and the replacement $T \to T_{eff}(t) = T\{G(t)\}^2$ then the formula for the thermonuclear reaction rate must be additionally averaged over time within the oscillation period $\pi/2\omega_H$

$$<< \sigma_{fusion}(v,t)v >>= \frac{2\omega_H}{\pi}\int_0^{\pi/2\omega_H} < \sigma_{fusion}(v,S(T(t)))v > dt \tag{23}$$

The results of such a double averaging of the thermonuclear interaction rate $\sigma_{fusion}(v,t)v$ for $d+d = t+p, He^3+n$ reactions are shown in Fig. 3. These graphs for both reactions visually coincide.

From these results it can be concluded that the maximum value of doubly averaged rate in the presence of correlation can reach a value $<< \sigma_{d+d}(v,t)v >>\approx 10^{-16}\ cm^3/sec$ at $T_9 = 10^{-4}(kT \approx 8.6eV)$ and $G_{\max} \approx 300$. With such a value of doubly averaged rate, the final fusion efficiency is

$$\frac{dn_{fusion}}{dt} = n_d^2\eta << \sigma_{d+d}v >>\approx 10^{16} - 10^{20}\ cm^{-3}\cdot sec^{-1} \tag{24}$$

at, respectively, the plasma density $n_d = 10^{14} - 10^{18}\ cm^{-3}$.

If we take into account that an energies of $\Delta E \approx 3.2 - 4MeV$ are released in these reactions, then the maximal specific power of energy release can have a great value:

$$\frac{dn_{He^3}}{dt}\Delta E \approx 5\ kW - 50MW/cm^3 \tag{25}$$

It should be noted that the actual power of energy release can be significantly lower due to the presence of negative feedback: a very fast and very significant increase in the local plasma temperature to the level $kT >> V_i$ leads to a

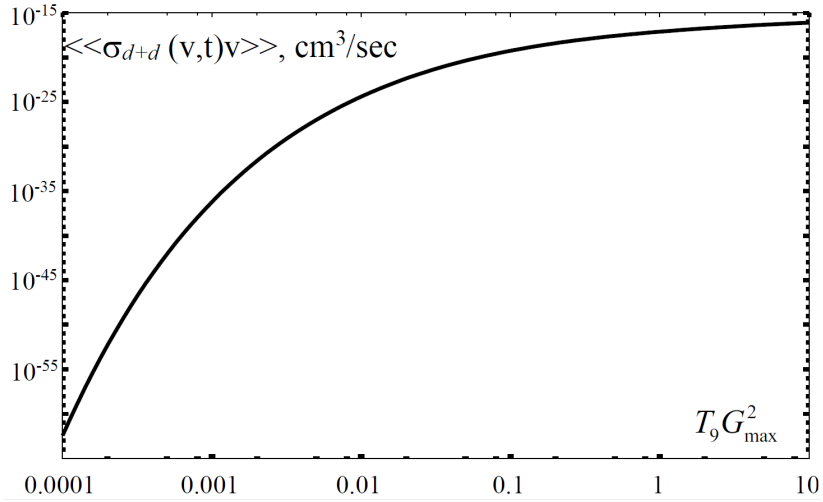

Figure 3. Dependence of the doubly averaged rate of thermonuclear interaction $<< \sigma_{fusion}(v,t)v >>$ for (d,d) reaction on the actual temperature and different maximum values $G_{\max}$ of the correlation efficiency coefficient.

slowdown in the process of ion recombination into the atomic state and, accordingly, to a decrease in the coefficient η in equations (20) and (24).

The subsequent cooling of the plasma accelerates nuclear fusion again. This is due to a very rapid increase in the intensity of the ultraviolet radiation of the heated plasma due to the Stefan-Boltzmann law $J_{rad} \approx \sigma T^4$, which leads to plasma cooling.

The combination of these processes automatically leads to a quasi-stationary regime of selfcontrolled nuclear fusion.

5. Conclusions

It is shown that taking into account of the microdynamic features of the processes of alternating ionization and recombination of hydrogen atoms and its isotopes in a magnetized low-temperature plasma makes it possible to implement the mechanism of self-controlled nuclear fusion using controlled very intense quasi-periodic fluctuations of the kinetic energy of these particles. The origin of these fluctuations is associated with the formation of coherent correlated states that are formed during each act of fast atom ionization.

A very important fact is that nuclear fusion in a low-temperature plasma can last an indefinitely long time and does not require large expenditures of energy.

Another very important advantage of CCS-based LENR reactions is connected with the possibility of a very significant increase in the pulsed effective temperature $T_i^* = \{G(t)\}^2 T_i$ with an average value $< T >_i^* = G_{\max}^2 T_i/2$, which can reach 30-100 keV and even more. This possibility makes realization of CCS stimulated fusion with the participation of heavier nuclei possible:

$$\begin{aligned} d + He^3 &= p + He^4 \\ d + Li^6 &= 2He^4 \\ p + Li^7 &= 2He^4 \\ p + B^{11} &= 3He^4, \ldots \end{aligned} \tag{26}$$

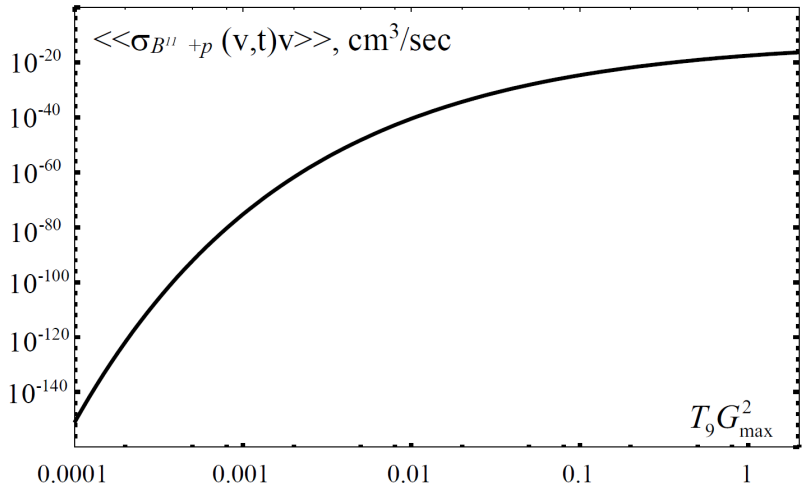

Figure 4. Dependence of the doubly averaged rate of thermonuclear interaction $<< \sigma_{B^{11}+p}(v,t)v >>$ for $\mathrm{B}^{11}\left(\mathrm{p},\mathrm{He}^{4}\right)2\mathrm{He}^{4}$ reaction on the actual temperature and different maximum values $G_{\max}$.

These heavier nuclei will be passive (not in the CCS state) targets in nuclear fusion and may be present in the hydrogen or deuterium plasma either as an admixture or as a result of previous nuclear reactions. The doubly averaged rate for $p + B^{11} = 3He^4$ reaction is presented in Fig. 4.

It can be seen from these data that the efficiency of this reaction in a magnetized low-temperature plasma in the presence of a CCS with large value of $G_{\max}$ is approximately the same as in $d + d = t + p, He^3 + n$ reactions.

The specificity and features of the implementation of LENR on the basis of the process of CCS formation in such reactions in different physical and biological systems are considered in [20], [29]–[30].

It should be noted that the optimum hydrogen plasma temperature for such the fusion is in the range of $10 - 20eV$. At a much higher temperature, the probability of ion recombination, which is necessary to start the next cycle of atomic transformations, is significantly suppressed. At a lower temperature (less than dissociation threshold energy of about $4.5eV$), the number of hydrogen molecules of the $H_2, HD, D_2, HT, DT, T_2$ type increases sharply, which do not provide an effective ionization recombination process with the alternation of a full cycle of switching on and off the charge of the particle (this is possible only for a hydrogen-like atom, but not for a molecule).

Estimates show that this optimal regime will be self-sustaining due to internal negative feedback that does not allow the temperature to rise above the optimal interval.

A very important and unique feature of the mechanism is the fact that it allows us to combine two mutually opposite requirements: a relatively low plasma temperature to ensure automatic frequent alternation of ionization and recombination, and the need for very high energy to ensure efficient nuclear fusion.

A more detailed analysis of the values and ratio of all characteristic times of each ionization and recombination cycle was carried out in [22-26, 31].

In conclusion, it should be noted, that the considered features of a self-sustaining LENR in a lowtemperature magnetized plasma will also be attained by the propagation of a correlated wave packet, the features of which were considered in [32-34].

The implementation of the considered fundamentally new mechanism of nuclear fusion at low temperatures [31] can be carried out both in an ordinary terrestrial laboratory and in also the atmosphere of the Sun and other stars, where all the necessary conditions are met.

References

[1] E.Schrödinger. Heisenbergschen Unschärfeprinzip. Ber. Kgl. Akad. Wiss., Berlin, **S24,** 296 (1930).

[2] H.P.Robertson. A general formulation of the uncertainty principle and its classical interpretation, Phys.Rev.A, **35,** 667 (1930).

[3] V.V.Dodonov, V.I.Manko. Invariants and correlated states of nonstationary systems", in: Invariants and the Evolution of Nonstationary Quantum Systems, Proceedings of the Lebedev Physical Institute, Nova Science, Commack, New York, 183, 103 (1988).

[4] V.V.Dodonov, A.B.Klimov, V.I.Manko. Physical effects in correlated quantum states", in: Squeezed and Correlated States of Quantum Systems, Proceedings of the Lebedev Physical Institute, Nova Science, Commack, New York, **295,** 61–107 (1993).

[5] V.I.Vysotskii, S.V.Adamenko. Correlated states of interacting particles and problems of the Coulomb barrier transparency at low energies in nonstationary systems. Technical Physics, **55**(5), 613 (2010).

[6] V.I.Vysotskii, M.V.Vysotskyy, S.V.Adamenko. Formation and application of correlated states in non-stationary systems at low energy of interacting particles. Journal of Experimental and Theoretical Physics, **114**(2), 243 (2012).

[7] V.I.Vysotskii, S.V.Adamenko, M.V.Vysotskyy. The formation of correlated states and the increase in barrier transparency at a low particle energy in nonstationary systems with damping and fluctuations. Journal of Experimental and Theoretical Physics, **115**(4), 551 (2012).

[8] V.I.Vysotskii, M.V.Vysotskyy. Coherent correlated states and low-energy nuclear reactions in non stationary systems. European Phys. Journal A**49**: 99 (2013).

[9] V.I.Vysotskii, S.V.Adamenko, M.V.Vysotskyy. Acceleration of low energy nuclear reactions by formation of correlated states of interacting particles in dynamical systems. Annals of Nuclear energy, **62**, 618 (2013).

[10] V.I.Vysotskii, M.V.Vysotskyy. Correlated states and transparency of a barrier for low-energy particles at monotonic deformation of a potential well with dissipation and a stochastic force. Journal of Experimental and Theoretical Physics, **118**(4), 534 (2014).

[11] V.I.Vysotskii, M.V.Vysotskyy. Formation of correlated states and optimization of nuclear reactions for low-energy particles at nonresonant low-frequency modulation of a potential well. Journal of Experimental and Theoretical Physics, **120**(2), 246 (2015).

[12] V.I.Vysotskii, M.V.Vysotskyy. The formation of correlated states and optimization of the tunnel effect for low-energy particles under nonmonochromatic and pulsed action on a potential barrier. Journal of Experimental and Theoretical Physics, **121**(4), 559 (2015).

[13] V.I.Vysotskii, M.V.Vysotskyy. Coherent correlated states of interacting particles – the possible key to paradoxes and features of LENR. Current Science, **108**(4):30 (2015).

[14] V.I.Vysotskii, M.V.Vysotskyy. Formation of correlated states and tunneling at low energy at controlled pulse action on particles. Journal of Experimental and Theoretical Physics, **125**(8),195 (2017).

[15] V.I.Vysotskii, S.V.Adamenko, M.V.Vysotskyy. Subbarier interaction of channeling particles under the self-similar excitation correlated states in periodically deformed crystal. Journal of surface investigation, V.**6**(2), 369, (2012).

[16] V.I.Vysotskii, M.V.Vysotskyy, S. Bartalucci. Features of the formation of correlated coherent states an nuclear fusion induced by the interaction of slow particles with crystals and free molecules. Journal of Experimental and Theoretical Physics, **127** (3), 479 (2018).

[17] S. Bartalucci. V.I.Vysotskii, M.V.Vysotskyy. Correlated states and nuclear reactions: An experimental test with low energy beams. Phys. Rev. Accelerators and Beams, **22** (5), 054503 (2019).

[18] S. Lipinski and H. Lipinski, Hydrogen-lithium fusion device, Patent No. WO 2014/189799 A9, 2013. https://patentimages.storage.googleapis.com/73/7e/b3/6f1ac23e29b703/WO2014189799A9.pdf

[19] V.I.Vysotskii, M.V.Vysotskyy, S. Bartalucci. Using the method of coherent correlated states for production of nuclear interaction of slow particles with crystals and molecules. Journal of Condensed Matter Nucl. Sci. v. 29, 358–367, (2019).

[20] V.I.Vysotskii, M.V.Vysotskyy. Universal mechanism of LENR in physical and biological systems on the base of coherent correlated states of interacting particles. In Book: Cold Fusion. Advances in Condensed Matter Nuclear Science. Edited by Jean-Paul Biberian, Elsevier, 2020. CHAPTER 17, pp. 333–370.

[21] Gordon Francis. Ionization Phenomena in Gases. Academic Press, 1960.

[22] Low Temperature Plasma Technology. Methods and Applications. Edited By Paul K. Chu, XinPei Lu, CRC Press, 2020.

[23] Shi Nguyen-Kuok. Theory of Low-Temperature Plasma Physics. Springer, 2017.
[24] Takayoki Fueno, Henry Eyring, Taikyue Ree. Three-body recombination of gaseous ions. Can. J. Chem. 38, 1693 (1960).
[25] C.M.Ferreira, E.Tatarova, B.F.Gordiets. Kinetic theory of low-temperature plasmas in molecular gases. Plasma Physics and Controlled Fusion; v. 42(12B); p. 165–188, (2000).
[26] W.A.Fowler, G.R.Gaughlan, B.A. Zimmerman. Thermonuclear Reaction Rates. Annual Review of Astronomy and Astrophysics, 5, 525 (1967).
[27] W.A.Fowler, G.R.Gaughlan, B.A. Zimmerman. Thermonuclear Reaction Rates, II. Annual Review of Astronomy and Astrophysics, **13**, 69 (1975)
[28] C.Angualo et al. A compilation of charged-particle induced thermonuclear reaction rates. Nuclear Physics A, **656**, 3–183 (1999).
[29] V.I.Vysotskii, M.V.Vysotskyy. Features of correlated states and a mechanism of self-similar selection of nuclear reaction channels involving low-energy charged particles. Journal of Experimental and Theoretical Physics, **128**(6), 856–864 (2019).
[30] V.I.Vysotskii, A.A.Kornilova. Microbial transmutation of Cs-137 and LENR in growing biological systems, Current Science, **108**(4), 636–640 (2015).
[31] V.I.Vysotskii and M. V.Vysotskyy, Self-controlled flashing nuclear fusion in stationary magnetized low-temperature plasma, Fusion Science and Technology, **79**, No. 5, 537–552 (2023).
[32] V.V.Dodonov, A. V. Dodonov, Transmission of correlated Gaussian packets through a delta-potential. J. Russ. Laser Res., **35(1)**, 39–46 (2014).
[33] V.I.Vysotskii, M.V.Vysotskyy. Features of the propagation, evolution, and remote collapse of a correlated wave packet. Journal of Surface Investigation: X-ray, Synchrotron and Neutron Techniques, **13**, No. 6, 1116–1121 (2019).
[34] V.I.Vysotskii, M.V.Vysotskyy. Application of correlated wave packets for stimulation of LENR in remote targets. Journal Condensed Matter Nucl. Science, **33**, 305–313 (2020).

J. Condensed Matter Nucl. Sci. 38 (2024) 338–356

Research Article

Thoughts on a Model of Vysotskii and Vysotskyy

Peter L. Hagelstein

Massachusetts Institute of Technology, Cambridge, MA, USA

Abstract

Motivated by the recent proposal of Vysotstkii and Vysotskyy of the possibility of correlated coherent state evolution of an ion wave function in a low density magnetized plasma leading to low energy nuclear reactions, we have considered the construction of a dynamical squeezed state wave packet solution for a particle with a dynamic charge in a constant magnetic field. For a z-directed magnetic field, the dynamics simplify if the wave packet is constructed to have the same dynamics in x and y. From the solution developed, evolution equations are obtained for the first and second moments. In the case of the first moments, the dynamics that result are Newton's laws for a particle in a magnetic field. The second moments evolve according to what would be expected for a squeezed state solution, except that the breathing frequency is reduced by a factor of two. The uncertainty product for the squeezed state is a Schrodinger-Robertson relation. The amount of squeezing required for the fluctuation energy to be sufficient to result in nuclear reactions is extremely large, and such a wave packet would be quite fragile in the sense that collisions with other particles would prevent organized "breathing" mode evolution except at very low plasma density. Following the proposal of Vysotskii and Vysotskyy, we constructed generalization of the squeezed state wave packet in which an excited state SHO eigenfunction is squeezed, and find that the evolution of the squeezing parameters is similar as for a squeezed state solution. The uncertainty principle is of the form of the Schrodinger-Robertson relation, but with a prefactor that substantially increases the uncertainty. An issue that was identified in the proposed scheme is localization associated with electron ionization and recombination that has the potential to spoil the delocalization and phase of the wave packet. It is noted that in a minor modification of the scheme non-classical energy exchange may be possible for charged particles traveling through a dynamic and spatially inhomogeneous magnetic field, as long as the changes in the field as seen by the particle are non-adiabatic relative to the squeezing dynamics.
 ISSN 2227-3123

Keywords: Squeezed states, correlated coherent states, non-classical heating, low-density magnetized plasma

1. Introduction

Vysotskii and Vysotskyy have proposed that sequential ionization and recombination of hydrogen isotopes in a magnetized plasma can produce correlated coherent states at a temperature (10-20 eV) that can result in nuclear reactions requiring high energy (10 keV) [1], [2] (see also [3]–[5]). Such a result is unexpected, and worth some thought. This provides motivation for the construction of a squeezed state wave function that is relevant to the problem, as well as the construction of a generalization based on the squeezing of excited eigenfunctions of the simple harmonic oscillator.

 ISSN 2227-3123

In essence, we were interested in better understanding the model. In a quantum class taught at MIT, we make use of a configuration space representation of squeezed state wave packets, as they are easy to work with and don't require operator algebra. We were interested in developing explicit wave packet solutions, in part to develop an example that might at some point be used in class, but which in the process would hopefully provide some clarity as to the physics of interest in the model.

The model that results provides for a "clean" and explicit solution. The amount of squeezing required for a proton to gain 10 keV of fluctuation energy is extreme (as noted by Vysotskii and Vysotskyy [2]), and the associated wave packet becomes very delocalized during the breathing, which makes it fragile in the sense of being quite sensitive to collisions with neighboring particles.

Following on the suggestion of Vysotskii and Vysotskyy that the squeezing of a highly excited simple harmonic oscillator (SHO) eigenstate would work better [2], in the Appendix we consider the construction of a wave packet made from the squeezing of a highly excited eigenfunction.

2. Schrodinger Equation

Vysotskii and Vysotskyy have proposed modeling ionization and recombination of a hydrogen atom through the use of a time-dependent charge [1], [2]. While it would seem better to model the system using a many-particle wave function to describe the proton and electrons involved, our focus here is on the squeezed state part of the problem. So we will follow Vysotskii and Vysotskyy and work with a time-dependent charge.

The Schrodinger equation in the nonrelativistic approximation (and ignoring spin effects) is

$$i\hbar\frac{\partial}{\partial t}\Psi(\mathbf{r},t) \;=\; \frac{|\mathbf{p}-q(t)\mathbf{A}|^2}{2m}\Psi(\mathbf{r},t) \tag{1}$$

The magnetic field is static, and is described by the vector potential

$$\mathbf{A} \;=\; \frac{1}{2}\hat{\mathbf{i}}_z B_0\times\mathbf{r} \;=\; \frac{1}{2}\begin{vmatrix}\hat{\mathbf{i}}_x & \hat{\mathbf{i}}_y & \hat{\mathbf{i}}_z\\ 0 & 0 & B_0\\ x & y & z\end{vmatrix} \;=\; \frac{B_0}{2}\left(\hat{\mathbf{i}}_y x-\hat{\mathbf{i}}_x y\right) \tag{2}$$

From this vector potential we compute the magnetic field to be

$$\mathbf{B} \;=\; \nabla\times\mathbf{A} \;=\; \begin{vmatrix}\hat{\mathbf{i}}_x & \hat{\mathbf{i}}_y & \hat{\mathbf{i}}_z\\ \partial_x & \partial_y & \partial_z\\ -B_0 y/2 & B_0 x/2 & 0\end{vmatrix} \;=\; \hat{\mathbf{i}}_z B_0 \tag{3}$$

We can use this to expand out the Schrodinger equation according to

$$\begin{aligned} i\hbar\frac{\partial}{\partial t}\Psi(\mathbf{r},t) &= \left(\frac{|\mathbf{p}|^2}{2m}-q(t)\frac{\mathbf{A}\cdot\mathbf{p}}{m}+q^2(t)\frac{|\mathbf{A}|^2}{2m}\right)\Psi(\mathbf{r},t)\\ &= \left(\frac{|\mathbf{p}|^2}{2m}-q(t)\frac{A_x p_x+A_y p_y}{m}+q^2(t)\frac{A_x^2+A_y^2}{2m}\right)\Psi(\mathbf{r},t)\end{aligned}$$

$$= \left(\frac{|\mathbf{p}|^2}{2m} - B_0 q(t) \frac{-yp_x + xp_y}{2m} + B_0^2 q^2(t) \frac{x^2+y^2}{8m} \right) \Psi(\mathbf{r},t)$$

$$= \left(-\frac{\hbar^2}{2m}(\partial_x^2 + \partial_y^2 + \partial_z^2) - i\frac{\hbar B_0 q(t)}{2m}(y\partial_x - x\partial_y) + \frac{B_0^2 q^2(t)}{8m}(x^2+y^2) \right) \Psi(\mathbf{r},t) \quad (4)$$

The goal is to study a time-dependent wave function solutions for this model.

3. Correlated Coherent States

Correlated coherent states were proposed by Dodonov and coworkers as a generalization of squeezed states [6]. Such states satisfy the Schrodinger-Robertson uncertainty relation

$$\sigma_A \sigma_B - \sigma_{AB}^2 \;=\; \sigma_A \sigma_B (1-r^2) \;\geq\; \frac{1}{4} \left| \left\langle \left[\hat{A}, \hat{B} \right] \right\rangle \right|^2 \quad (5)$$

with minimum uncertainty, where $\hat{A}$ and $\hat{B}$ are operators of interest for a particular problem. In the event that these operators are taken to be position and momentum operators, then this reduces to

$$(\Delta x)^2 (\Delta p)^2 (1-r^2) \;\geq\; \frac{\hbar^2}{4} \quad (6)$$

with r the correlation coefficient according to

$$r \;=\; \frac{\sigma_{AB}}{\sqrt{\sigma_A \sigma_B}} \quad (7)$$

In their papers, Dodonov and coworkers focus on a particular configuration space construction relevant to position and momentum operators, such as [6]–[9]

$$\Psi_\beta(x|r,\eta) \;=\; N_\beta \exp\left\{ -\frac{x^2}{4\eta}\left(1 - i\frac{r}{\sqrt{1-r^2}}\right) + \frac{\beta x}{\eta} \right\} \quad (8)$$

From our perspective, such a state could be considered to be a snapshot of a squeezed wave packet solution at a particular time, which suggests that it would be possible to develop a squeezed state wave packet solution based on

$$\Psi(x,t) \;=\; N_{\beta(t)} \exp\left\{ -\frac{x^2}{4\eta(t)}\left(1 - i\frac{r(t)}{\sqrt{1-r^2(t)}}\right) + \frac{\beta(t) x}{\eta(t)} \right\} \quad (9)$$

A big advantage of a configuration space description of a squeezed state wave packet is that it is very convenient for calculations, where the equivalent calculations based on operator algebra would be much harder.

The solution that we consider in the following sections could be considered to be a three-dimensional generalization according to

$$\Psi(x,y,z,t) \;=\; N_{\beta_x(t)} \exp\left\{ -\frac{x^2}{4\eta_x(t)}\left(1 - i\frac{r_x(t)}{\sqrt{1-r_x^2(t)}}\right) + \frac{\beta_x(t)x}{\eta_x(t)}\right\}$$

$$N_{\beta_y(t)} \exp\left\{ -\frac{y^2}{4\eta_y(t)}\left(1 - i\frac{r_y(t)}{\sqrt{1-r_y^2(t)}}\right) + \frac{\beta_y(t)x}{\eta_y(t)}\right\}$$

$$N_{\beta_z(t)} \exp\left\{ -\frac{z^2}{4\eta_z(t)}\left(1 - i\frac{r_z(t)}{\sqrt{1-r_z^2(t)}}\right) + \frac{\beta_z(t)x}{\eta_z(t)}\right\} \tag{10}$$

There would be no difficulty in principle using this representation as a starting place for solving the time-dependent Schrodinger equation for a nonrelativistic particle in a magnetic field. However, based on our previous experience with this kind of problem, calculations based on this kind of wave function written in a different form leads to dynamical equations for the parameters which are more intuitive.

4. General Squeezed State Wave Packet

We start with a general squeezed state wave packet given by

$$\Psi(\mathbf{r},t) \;=\; C(t)e^{-i\Theta(t)}e^{iP_x(t)(x-X(t))/\hbar}e^{iP_y(t)(y-Y(t))/\hbar}e^{iP_z(t)(z-Z(t))/\hbar}$$
$$e^{-\alpha_{xx}(t)(x-X(t))^2/2}e^{-\alpha_{xy}(t)(x-X(t))(y-Y(t))}e^{-\alpha_{yy}(t)(y-Y(t))^2/2}e^{-\alpha_{zz}(t)(z-Z(t))^2/2} \tag{11}$$

The center of the wave packet is located at

$$\langle \mathbf{r} \rangle \;=\; \hat{\mathbf{i}}_x X(t) + \hat{\mathbf{i}}_y Y(t) + \hat{\mathbf{i}}_z Z(t) \tag{12}$$

and the mean momentum is

$$\langle \hat{\mathbf{p}} \rangle \;=\; \hat{\mathbf{i}}_x P_x(t) + \hat{\mathbf{i}}_y P_y(t) + \hat{\mathbf{i}}_z P_z(t) \tag{13}$$

Distortion of the wave packet (or fluctuations) is modeled using the α_{xx}, α_{yy}, α_{xy} and α_{zz} parameters. For example, if the real parts of these parameters are big, then the wave packet is well localized.

To maintain normalization, we require that

$$\int \Psi^*(\mathbf{r},t)\Psi(\mathbf{r},t)d^3\mathbf{r} \;=\; 1 \tag{14}$$

The integrals can be done analytically, and we end up with

$$C(t) \;=\; \frac{1}{\pi^{3/4}}\left(\mathrm{Re}\{\alpha_{xx}(t)\}\mathrm{Re}\{\alpha_{yy}(t)\} - \mathrm{Re}\{\alpha_{xy}(t)\}^2\right)^{1/4}\left(\mathrm{Re}\{\alpha_{zz}(t)\}\right)^{1/4} \tag{15}$$

5. Independence

The x, y degrees of freedom and the z degrees of freedom are independent in this model. We can write the Schrodinger equation as

$$i\hbar\partial_t \Psi(x,y,z,t) \;=\; \Big(H_{xy} + H_z\Big)\Psi(x,y,z,t) \tag{16}$$

and the wave function as

$$\Psi(x,y,z,t) \;=\; \psi_{xy}(x,y,t)\psi_z(z,t) \tag{17}$$

Then separation can lead to

$$i\hbar\partial_t \psi_{xy}(x,y,t) \;=\; H_{xy}\psi_{xy}(x,y,t) \tag{18}$$

$$i\hbar\partial_t \psi_z(z,t) \;=\; H_z\psi_z(z,t) \tag{19}$$

These can be written out as

$$i\hbar\frac{\partial}{\partial t}\psi_{xy}(x,y,t) = \left\{ -\frac{\hbar^2}{2m}(\partial_x^2+\partial_y^2) - i\frac{\hbar B_0 q(t)}{2m}(y\partial_x - x\partial_y) + \frac{B_0^2 q^2(t)}{8m}(x^2+y^2)\right\}\psi_{xy}(x,y,t) \tag{20}$$

$$i\hbar\frac{\partial}{\partial t}\psi_z(z,t) = -\frac{\hbar^2}{2m}\partial_z^2\psi_z(z,t) \tag{21}$$

6. Evolution Equations for the z-Degrees of Freedom

Since the problem in z is much simpler, we focus on it first. Using Mathematica we plug in

$$\psi_z(z,t) \;=\; \left(\frac{\mathrm{Re}\{\alpha_{zz}\}}{\pi}\right)^{1/4} e^{-i\Theta_z(t)} e^{iP_z(t)(z-Z(t))/\hbar} e^{-\alpha_{zz}(t)(z-Z(t))^2/2} \tag{22}$$

Mathematica gives

$$\begin{aligned}
&-\frac{1}{2}i\hbar z^2\alpha'_{zz}(t) + i\hbar z Z(t)\alpha'_{zz}(t) - \frac{1}{2}i\hbar Z(t)^2\alpha'_{zz}(t) + \frac{i\hbar\alpha'_{zz}(t)}{4\alpha_{zz}(t)} + i\hbar z\alpha_{zz}(t)Z'(t) \\
&\quad - i\hbar\alpha_{zz}(t)Z(t)Z'(t) + \hbar\Theta'(t) - zP'_z(t) + Z(t)P'_z(t) + P_z(t)Z'(t) \\
&= -\frac{\hbar^2 z^2\alpha_{zz}(t)^2}{2m} + \frac{\hbar^2 z\alpha_{zz}(t)^2 Z(t)}{m} - \frac{\hbar^2\alpha_{zz}(t)^2 Z(t)^2}{2m} + \frac{\hbar^2\alpha_{zz}(t)}{2m} \\
&\quad + \frac{i\hbar z\alpha_{zz}(t)P_z(t)}{m} - \frac{i\hbar\alpha_{zz}(t)P_z(t)Z(t)}{m} + \frac{P_z(t)^2}{2m}
\end{aligned} \tag{23}$$

We can match terms proportional to z^0, z^1 and z^2 individually to get constraints.

Two of the constraints correspond to Newton's laws for propagation in free space:

$$\frac{d}{dt}Z(t) = \frac{P_z(t)}{m} \tag{24}$$

$$\frac{d}{dt}P_z(t) = 0 \tag{25}$$

We know that a wave packet spreads in free space. This is due to the uncertainty principle, where localization in space leads to a spread of momentum, which means that the wave packet spreads (there are no forces in free space to keep it localized). Within the model this is accounted for by

$$i\hbar\frac{d}{dt}\alpha_{zz}(t) \;=\; \frac{\hbar^2}{m}\alpha_{zz}^2(t) \tag{26}$$

An exact solution is possible. However, the focus of our arguments is concerned with the x, y degrees of freedom, so we will not pursue this here.

The phase Θ_z is required to satisfy the Schrodinger equation, and satisfies

$$\hbar\frac{d}{dt}\Theta_z(t) \;=\; -\frac{P_z^2(t)}{2m} + \frac{\hbar^2\alpha_{zz}(t)}{4m} \tag{27}$$

This can be solved exactly with no difficulty. However, the phase factor is not important in connection with the issues of interest.

The expectation value of the energy is

$$\langle H_z\rangle \;=\; \frac{P_z^2(t)}{2m} + \frac{\hbar^2}{4m}\frac{|\alpha_{zz}(t)|^2}{\mathrm{Re}\{\alpha_{zz}(t)\}} \tag{28}$$

This is both interesting and instructive. The expectation value of the energy is split into two pieces: one is the classical kinetic energy, and the other is the (non-classical) kinetic energy associated with the localization of the wave packet. Note also that the expectation value of the energy associated with the z-degree of freedom is constant in time, since

$$\begin{aligned}
\frac{d}{dt}\frac{|\alpha_{zz}(t)|^2}{\mathrm{Re}\{\alpha_{zz}(t)\}} &= \frac{2}{(\alpha_{zz}(t)+\alpha_{zz}^*(t))^2}\left((\alpha_{zz}^*(t))^2\frac{d}{dt}\alpha_{zz}(t) + \alpha_{zz}^2(t)\frac{d}{dt}\alpha_{zz}^*(t)\right) \\
&= \frac{2}{(\alpha_{zz}(t)+\alpha_{zz}^*(t))^2}\left((\alpha_{zz}^*(t))^2\frac{\hbar^2}{im}\alpha_{zz}^2(t) - \alpha_{zz}^2(t)\frac{\hbar^2}{im}(\alpha_{zz}^*(t))^2\right) \\
&= 0
\end{aligned} \tag{29}$$

7. Evolution Equations for the x and y Degrees of Freedom

For the next part of the problem we start with

$$\begin{aligned}
\psi_{xy}(x,y,t) \;=\; &\frac{1}{\pi^{1/2}}\left(\mathrm{Re}\{\alpha_{xx}\}\mathrm{Re}\{\alpha_{yy}\} - \mathrm{Re}\{\alpha_{xy}\}^2\right)^{1/4} e^{-i\Theta_{xy}(t)}e^{iP_x(t)(x-X(t))/\hbar}e^{iP_y(t)(y-Y(t))/\hbar} \\
&e^{-\alpha_{xx}(t)(x-X(t))^2/2}e^{-\alpha_{yy}(t)(y-Y(t))^2/2}e^{-\alpha_{xy}(t)(x-X(t))(y-Y(t))}
\end{aligned} \tag{30}$$

This is plugged into the Schrodinger equation

$$i\hbar\frac{\partial}{\partial t}\psi_{xy}(x,y,t) \;=\; \left(-\frac{\hbar^2}{2m}(\partial_x^2+\partial_y^2) - i\frac{\hbar B_0 q(t)}{2m}(y\partial_x - x\partial_y) + \frac{B_0^2 q^2(t)}{8m}(x^2+y^2)\right)\psi_{xy}(x,y,t) \tag{31}$$

As might be expected, quite a few terms are generated. It is possible to match terms to develop a set of constraints.

As expected, the first-order constraints are Newton's law equations according to

$$\frac{d}{dt}X(t) = \frac{P_x(t)}{m} + \frac{B_0 q(t)}{2m}Y(t) \tag{32}$$

$$\frac{d}{dt}P_x(t) = -\frac{B_0^2 q^2(t)}{4m}X(t) + \frac{B_0 q(t)}{2m}P_y(t) \tag{33}$$

$$\frac{d}{dt}Y(t) = \frac{P_y(t)}{m} - \frac{B_0 q(t)}{2m}X(t) \tag{34}$$

$$\frac{d}{dt}P_y(t) = -\frac{B_0^2 q^2(t)}{4m}Y(t) - \frac{B_0 q(t)}{2m}P_x(t) \tag{35}$$

It is possible to make use of the kinetic momenta variables

$$\Pi_x(t) \;=\; P_x(t) - q(t)A_x(t) \;=\; P_x(t) + \frac{B_0 q(t)}{2}Y(t)$$

$$\Pi_y(t) \;=\; P_y(t) - q(t)A_y(t) \;=\; P_y(t) - \frac{B_0 q(t)}{2}X(t) \tag{36}$$

to write these equations in terms of Newton's equations with the Lorentz force law

$$\frac{d}{dt}\mathbf{R}_\perp = \frac{\mathbf{\Pi}_\perp}{m}$$

$$\frac{d}{dt}\mathbf{\Pi}_\perp = q\frac{\mathbf{\Pi}_\perp}{m}\times\mathbf{B} \tag{37}$$

as expected.

Also from matching terms we can develop evolution equations for the squeezing parameters

$$i\hbar\frac{d}{dt}\alpha_{xx}(t) = \frac{\hbar^2}{m}\alpha_{xx}^2(t) + \frac{\hbar^2}{m}\alpha_{xy}^2(t) + i\frac{\hbar B_0 q(t)}{m}\alpha_{xy}(t) - \frac{B_0^2 q^2(t)}{4m} \tag{38}$$

$$i\hbar\frac{d}{dt}\alpha_{yy}(t) = \frac{\hbar^2}{m}\alpha_{xy}^2(t) + \frac{\hbar^2}{m}\alpha_{yy}^2(t) - i\frac{\hbar B_0 q(t)}{m}\alpha_{xy}(t) - \frac{B_0^2 q^2(t)}{4m} \tag{39}$$

$$i\hbar\frac{d}{dt}\alpha_{xy}(t) = \frac{\hbar^2}{m}\alpha_{xy}(t)\alpha_{yy}(t) + \frac{\hbar^2}{m}\alpha_{xx}(t)\alpha_{xy}(t) - i\frac{\hbar B_0 q(t)}{2m}\alpha_{xx}(t) + i\frac{\hbar B_0 q(t)}{2m}\alpha_{yy}(t) \tag{40}$$

Unfortunately, these coupled equations are sufficiently complicated in general that we are motivated to look for a simplification.

Mathematica gives a complicated evolution equation for $\Theta_{xy}(t)$ that we have not developed a simplification for, so we will not pursue the issue here.

8. Simplification

It is possible to simplify the model by focusing on a specific case. If we look at the evolution equations for the squeezing parameters, we see that if assume that

$$\alpha_{xx}(t) = \alpha_{yy}(t)$$

$$\alpha_{xy}(t) = 0 \tag{41}$$

then the evolution equations for the squeezing parameters reduce to

$$i\hbar\frac{d}{dt}\alpha_{xx}(t) = \frac{\hbar^2}{m}\alpha_{xx}^2(t) - \frac{B_0^2q^2(t)}{4m} \tag{42}$$

$$i\hbar\frac{d}{dt}\alpha_{yy}(t) = \frac{\hbar^2}{m}\alpha_{yy}^2(t) - \frac{B_0^2q^2(t)}{4m} \tag{43}$$

$$i\hbar\frac{d}{dt}\alpha_{xy}(t) = 0 \tag{44}$$

In this limit the problem simplifies and separates. For the solution we can write

$$\psi_{xy}(x,y,t) \;\rightarrow\; \frac{1}{\pi^{1/2}}\left(\mathrm{Re}\{\alpha_{xx}\}\mathrm{Re}\{\alpha_{yy}\}\right)^{1/4} e^{-i\Theta_{xy}(t)} e^{iP_x(t)(x-X(t))/\hbar} e^{iP_y(t)(y-Y(t))/\hbar}$$

$$e^{-\alpha_{xx}(t)(x-X(t))^2/2} e^{-\alpha_{yy}(t)(y-Y(t))^2/2} \tag{45}$$

The expectation value of the Hamiltonian is

$$\begin{aligned}\langle H_{xy}\rangle &= \left\langle -\frac{\hbar^2}{2m}(\partial_x^2+\partial_y^2) - i\frac{\hbar B_0 q(t)}{2m}(y\partial_x - x\partial_y) + \frac{B_0^2q^2(t)}{8m}(x^2+y^2)\right\rangle \\ &= \frac{P_x^2(t)}{2m} + \frac{P_y^2(t)}{2m} + \frac{B_0q(t)}{2m}\Big(-X(t)P_y(t) + Y(t)P_x(t)\Big) + \frac{B_0^2q^2(t)}{8m}\Big(X^2(t)+Y^2(t)\Big) \\ &\quad + \frac{\hbar^2|\alpha_{xx}(t)|^2}{4m\mathrm{Re}\{\alpha_{xx}(t)\}} + \frac{\hbar^2|\alpha_{yy}(t)|^2}{4m\mathrm{Re}\{\alpha_{yy}(t)\}} + \frac{B_0^2q^2(t)}{16m\mathrm{Re}\{\alpha_{xx}(t)\}} + \frac{B_0^2q^2(t)}{16m\mathrm{Re}\{\alpha_{yy}(t)\}}\end{aligned} \tag{46}$$

The classical contribution to the expectation value of the Hamiltonian is precisely what we would expect. The last line is the fluctuation energy, which is made up of the kinetic energy fluctuations and the potential energy fluctuations. In the event that the time dependent charge is either $q(t) = 0$ or $q(t) = |e|$ the total fluctuation energy is constant.

The fluctuation energy changes when the charge changes in this model due to the potential energy contribution to the fluctuation energy.

The classical energy (the first line on the RHS of equation (46)) is constant assuming that the magnetic field and charge are constant. Also, the fluctuation energy (the second line on the RHS of equation (46)) is also constant. This can be verified from a direct calculation of the x contribution

$$\frac{d}{dt}\left\{ \frac{\hbar^2|\alpha_{xx}(t)|^2}{4m\mathrm{Re}\{\alpha_{xx}(t)\}} + \frac{B_0^2q^2}{16m\mathrm{Re}\{\alpha_{xx}(t)\}} \right\} \;=\; 0 \tag{47}$$

which involves a fair amount of algebra, that we have verified works within this model.

9. Solution for the Squeezing Parameter

It is possible to develop solutions for the evolution equations for the squeezing parameters. For example, suppose that we start with

$$i\hbar\frac{d}{dt}\alpha_{xx}(t) \;=\; \frac{\hbar^2}{m}\alpha_{xx}^2(t) - \frac{B_0^2q^2}{4m} \tag{48}$$

with $\alpha_{xx}(0)$ given for the special case when $q(t) = q = |e|$. We can solve and write

$$\frac{\hbar\alpha_{xx}(t)}{m\omega_a} \;=\; \frac{\frac{\hbar\alpha_{xx}(0)}{m\omega_a}\cos(\omega_a t) + i\sin(\omega_a t)}{\cos(\omega_a t) + i\frac{\hbar\alpha_{xx}(0)}{m\omega_a}\sin(\omega_a t)} \tag{49}$$

where ω_a is

$$\omega_a \;=\; \frac{B_0q}{2m} \tag{50}$$

Note that squeezing in this system does not work like in a normal one-dimensional SHO, where the relevant frequency for squeezing is the same as the oscillator frequency. In this system the oscillator frequency ω_0 is the cyclotron frequency

$$\omega_0 \;=\; \frac{B_0q}{m} \tag{51}$$

and the frequency relevant to squeezing ω_a is half of this

$$\omega_a \;=\; \frac{1}{2}\omega_0 \tag{52}$$

This means that if a wave packet is localized at one point in the cycle in the $x-y$ plane, that it reforms at the same point on the next cycle (schematic in Figure 1).

The cyclotron frequencies of interest in the model of Vysotskii and Vysotskyy are

$$\omega_0 \;=\; 2\pi \;\times\; 1.54\,\mathrm{MHz} \quad (1000\,\mathrm{Oe}) \qquad \omega_0 \;=\; 2\pi \;\times\; 4.61\,\mathrm{MHz} \quad (3000\,\mathrm{Oe}) \tag{53}$$

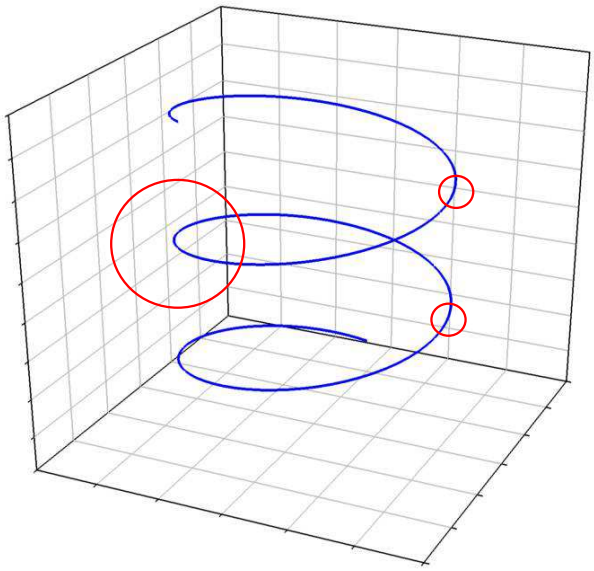

Figure 1. Schematic of squeezing in connection to particle motion in a magnetic field.

10. Wave Packet Energy

It is of interest to examine the energy of the wave packet, which is conserved when the magnetic field and charge are constant. For simplicity, we consider the situation when

$$q(t) \rightarrow q = |e| \tag{54}$$

The expectation value of the energy can be divided into classical and non-classical terms according to

$$\langle H \rangle = \langle H \rangle_c + \langle T \rangle_{nc} + \langle V \rangle_{nc} \tag{55}$$

where based on the calculation above we can write for the classical energy

$$\langle H \rangle_c = \frac{P_x^2(t)}{2m} + \frac{P_y^2(t)}{2m} + \frac{B_0 q}{2m}\Big(- X(t)P_y(t) + Y(t)P_x(t)\Big) + \frac{B_0^2 q^2}{8m}\Big(X^2(t) + Y^2(t)\Big) \tag{56}$$

The non-classical kinetic energy is

$$\langle T \rangle_{nc} = + \frac{\hbar^2 |\alpha_{xx}(t)|^2}{4m\mathrm{Re}\{\alpha_{xx}(t)\}} + \frac{\hbar^2 |\alpha_{yy}(t)|^2}{4m\mathrm{Re}\{\alpha_{yy}(t)\}} \tag{57}$$

and the non-classical potential energy is

$$\langle V \rangle_{nc} = \frac{B_0^2 q^2}{16m\mathrm{Re}\{\alpha_{xx}(t)\}} + \frac{B_0^2 q^2}{16m\mathrm{Re}\{\alpha_{yy}(t)\}} \tag{58}$$

Since the classical and non-classical degrees of freedom are independent, we can find solutions for $X(t)$ and $Y(t)$ that satisfy

$$\langle H \rangle_c \ \sim \ 20 \text{ eV} \tag{59}$$

while at the same time developing solutions for $\alpha_{xx}(t)$ and $\alpha_{yy}(t)$ that satisfy

$$\langle T \rangle_{nc} + \langle V \rangle_{nc} \ \sim \ 10 \text{ keV} \tag{60}$$

11. Localization

The fluctuation energy oscillates between kinetic energy and potential energy, as can be understood from the time-dependence of the solution for $\alpha_{xx}(t)$ given above. The kinetic energy is highest when the wave function is most localized. For the kinetic energy to reach 10 keV, the localization can be estimated starting from

$$\frac{(\Delta p_x)^2}{2m} \ = \ 5 \text{ keV} \tag{61}$$

since there are 2 degrees of freedom. Since the maximally squeezed wave packet is Gaussian in this model we have

$$\Delta x \Delta p \ = \ \frac{\hbar}{2} \tag{62}$$

The localization in x satisfies

$$\frac{\hbar^2}{8m(\Delta x)^2} \ = \ 5 \text{ keV} \tag{63}$$

This is evaluated to give

$$\Delta x \ \sim \ 3.2 \times 10^{-4} \text{ Angstrom} \tag{64}$$

12. Delocalization

After the squeezed wave packet is localized, it spreads out. Of interest is to estimate how big the spread is. To proceed we recall that

$$\frac{\hbar\alpha_{xx}(t)}{m\omega_a} \ = \ \frac{\frac{\hbar\alpha_{xx}(0)}{m\omega_a}\cos(\omega_a t) + i\sin(\omega_a t)}{\cos(\omega_a t) + i\frac{\hbar\alpha_{xx}(0)}{m\omega_a}\sin(\omega_a t)} \tag{65}$$

So, the maximum and minimum values are

$$\left(\frac{\hbar\alpha_{xx}(t)}{m\omega_a}\right)_{max} \ = \ \frac{\hbar\alpha_{xx}(0)}{m\omega_a} \qquad \left(\frac{\hbar\alpha_{xx}(t)}{m\omega_a}\right)_{min} \ = \ \frac{m\omega_a}{\hbar\alpha_{xx}(0)} \tag{66}$$

or

$$\Big(\alpha_{xx}(t)\Big)_{min} \;=\; \frac{m^2\omega_a^2}{\hbar^2\alpha_{xx}(0)} \tag{67}$$

It follows that

$$(\Delta x)^2_{min} = \frac{1}{2(\alpha_{xx})_{max}} \;=\; \frac{1}{2\alpha_{xx}(0)} \tag{68}$$

$$(\Delta x)^2_{max} = \frac{1}{2(\alpha_{xx})_{min}} \;=\; \frac{1}{2}\frac{\hbar^2}{m^2\omega_a^2}\alpha_{xx}(0) \tag{69}$$

We can use this to write

$$\frac{(\Delta x)_{max}}{(\Delta x)_{min}} \;=\; \frac{\hbar}{m\omega_a}\alpha_{xx}(0) \;=\; \frac{\hbar}{2m\omega_a(\Delta x)^2_{min}} \tag{70}$$

We recall that

$$\frac{\hbar^2}{8m(\Delta x)^2_{min}} \;=\; 5\ \mathrm{keV} \tag{71}$$

So we have

$$\frac{(\Delta x)_{max}}{(\Delta x)_{min}} \;=\; \frac{20\ \mathrm{keV}}{\hbar\omega_a} \;=\; \frac{40\ \mathrm{keV}}{\hbar\omega_0} \tag{72}$$

We can evaluate this for the two magnetic field strengths to obtain

$$\frac{(\Delta x)_{max}}{(\Delta x)_{min}} \;=\; 6.26\times10^{12} \quad (1000\ \mathrm{Oe}) \qquad \frac{(\Delta x)_{max}}{(\Delta x)_{min}} \;=\; 2.10\times10^{12} \quad (3000\ \mathrm{Oe}) \tag{73}$$

If we use our estimate from above

$$(\Delta x)_{min} \;\sim\; 3.2\times10^{-4}\ \mathrm{Angstrom} \tag{74}$$

then we end up with

$$(\Delta x)_{max} \;\sim\; 20.0\ \mathrm{cm} \quad (1000\ \mathrm{Oe}) \qquad (\Delta x)_{max} \;=\; 6.72\ \mathrm{cm} \quad (3000\ \mathrm{Oe}) \tag{75}$$

These numbers we might compare to the distance associated with the proton velocity for 5 keV (for the x-degree of freedom) at a frequency of ω_a estimated according to

$$\frac{v}{\omega_a} \;=\; 20.3\ \mathrm{cm} \quad (1000\ \mathrm{Oe}) \qquad \frac{v}{\omega_a} \;=\; 6.75\ \mathrm{cm} \quad (3000\ \mathrm{Oe}) \tag{76}$$

13. Uncertainty Product for the Wave Packet

Of interest is the uncertainty product $\Delta x \Delta p_x$ for the wave packet solution. To proceed, we can use Mathematica to evaluate

$$(\Delta x)^2 \;=\; \frac{1}{2\mathrm{Re}\{\alpha_{xx}(t)\}} \qquad (\Delta p_x)^2 \;=\; \frac{\hbar^2 |\alpha_{xx}(t)|^2}{2\mathrm{Re}\{\alpha_{xx}(t)\}} \tag{77}$$

For the $\Delta x \Delta p_x$ product we can write

$$\Delta x \Delta p_x \;=\; \frac{\hbar}{2} \frac{|\alpha_{xx}(t)|}{\mathrm{Re}\{\alpha_{xx}(t)\}} \tag{78}$$

This can also be written in the form

$$\Delta x \Delta p_x \;=\; \frac{\hbar}{2} \frac{1}{\sqrt{1 - \frac{\mathrm{Im}\{\alpha_{xx}(t)\}^2}{|\alpha_{xx}(t)|^2}}} \tag{79}$$

This is of the form

$$\Delta x \Delta p_x \;=\; \frac{\hbar}{2} \frac{1}{\sqrt{1 - r_{px}^2(t)}} \tag{80}$$

where

$$r_{px}(t) \;=\; \pm \frac{\mathrm{Im}\{\alpha_{xx}(t)\}}{|\alpha_{xx}(t)|} \tag{81}$$

This is seen to be consistent with the Schrodinger-Robertson uncertainty relation. We can write explicitly

$$r_{px}^2(t) \;=\; \frac{\sin^2(2\omega_a t) \left(\alpha_{xx}^2(0)\hbar^2 - m^2\omega_a^2\right)^2}{\sin^2(2\omega_a t) \left(\alpha_{xx}^2(0)\hbar^2 - m^2\omega_a^2\right)^2 + 4\alpha_{xx}^2(0)\hbar^2 m^2 \omega_a^2} \tag{82}$$

14. Conclusions

A primary motivation for the construction documented above was to try to help and support Vysotskii and Vysotskyy in their efforts to develop models for LENR reactions. An additional motivation was that we had worked with squeezed wave packet solutions in an academic setting, and we were interested in the application of these solutions to the particle in magnetic field problem proposed by these authors.

As can be seen, it is possible to plug the three-dimensional wave packet solution into the Schrodinger equation for a nonrelativistic particle in a constant z-directed magnetic field and obtain evolution equations from the resulting constraints with modest effort (as long as we require that the evolution in the x and y degrees of freedom match). The spread in position and momentum can be combined to construct a dynamic uncertainty product that has a minimum Schrodinger-Robertson uncertainty. This is consistent with the approach proposed by Dodonov and coworkers for the construction of correlated coherent states.

It is possible to construct states mathematically in which the fluctuation energy greatly exceeds the classical energy. In order for the fluctuation energy to reach 10 keV, the maximum localization is a small fraction of an Angstrom, which is indicative of extreme squeezing. In this case the maximum spread of the wave packet is on the cm scale, which means that it would be very fragile in the sense that interactions with neighboring charged and uncharged particles in the surrounding environment would spoil the wave packet phase and prevent subsequent localization.

Vysotskii and Vysotskyy propose working with squeezed wave packets based on excited state eigenfunctions of the SHO [2]. Due to our unfamiliarity with such states, we examined their construction in the simpler case of a one-dimensional simple harmonic oscillator in the Appendix. This construction was successful, and from the construction the dynamics of the "breathing" is the same as for the more conventional squeezed state solution based on simpler complex Gaussian wave packets. We expect independence of the classical and fluctuation energies for these solutions, and provide an expression for the expectation value of the Hamiltonian which gives the constant fluctuation energy (as expected for a constant potential). The uncertainty principle for this wave packet appears to be a generalization of the Schrodinger-Robertson relation that includes a prefactor of $(2n+1)^2$. For a highly excited eigenfunction, the uncertainty will be very large. The amount of squeezing required to boost the energy of such an eigenfunction at 10 eV to have a fluctuation energy of 10 keV is much less than the amount of squeezing needed to boost the ground state eigenfunction energy (on the order of 10 neV) to 10 keV.

Of interest is how the charged particle gains energy in this kind of scheme. In the event that the dynamics can be modeled making use of a dynamic particle charge, then we can understand the situation relatively simply making use of a one-dimensional analog. When the charge is on, the particle in one dimension sees a parabolic potential, and when the charge is off the particle sees a flat potential. However, in both cases the same squeezed state solution applies. For the basic squeezed state solution we might imagine a particle starting in the ground state of the parabolic well, where it is happy to stay so long as the potential doesn't change. When the potential is set to zero, the wave packet expands with free space dynamics, which also happens to coincide with the evolution of a squeezed state. Later on, when the potential turns back on, the expanded wave packet now extends over a larger region, and will have more energy. The subsequent wave packet dynamics are breathing mode dynamics, since a squeezed state was generated by the free-particle evolution, and we would expect subsequent localization to a width less than that of the ground state. Repeated turning on and off would be expected in this simple model to randomly increase or decrease the squeezing (and wave packet energy), resulting in an interesting non-classical mechanism for the transfer of energy from the dynamics potential to the particle. A classical analog particle in this case would sit at the origin and not notice the changes in the potential. Hence, the fluctuation energy increase in this case is a non-classical effect.

If instead the wave packet started in an excited state eigenfunction of the well, then the subsequent evolution would be qualitatively similar, but faster since much more energy is involved. As long as the potential remains following the initialization of the wave packet, the wave packet would remain localized to within the spread of the excited state eigenfunction. When the potential turns off, the wave packet would expand according to free space dynamics, which would involve a much faster expansion since the eigenfunction is that of a highly excited particle. Now when the potential turns back on, the expansion that occurred results in the wave packet extending to regions where the potential is much larger, which corresponds to net (fluctuation) energy gain. In light of the solution given in the Appendix, the wave packet will undergo generalized squeezing dynamics, which will appear as a "breathing" with the basic shape remaining intact. As before, with random switching on and off of the potential, one would expect that energy would be gained on average through the same basic non-classical energy exchange effect.

A question which remains for future work concerns whether the effect persists in a more sophisticated model in which the proton and electrons are modeled explicitly, making use of multi-particle wave packet solutions. The issue is that if an incoming electron collides with a hydrogen atom to produce ionization, then one would expect a localization of the proton with respect to the electrons at the time of the collision. Intuitively, this localization might be expected to

impact the delocalization required for non-classical energy exchange. In the worst case scenario, the processes in the scheme needed to make the charge be time-dependent also destroys the delocalization.

Should this worst case scenario play out, it might still be possible for the non-classical energy exchange proposal of Vysotskii and Vysotskyy [3] to work with a minor modification. Consider instead a situation in which charged particles (protons or other charged nuclei as well as electrons) at very low density travel through a magnetic field that is spatially varying and perhaps time varying. If the plasma density is very low (so that collisions are infrequent) then quantum coherent effects generally have a better chance of being important. At times and in regions where the magnetic field is small, then the wave packet would expand in three dimensions according to free space dynamics. When the particle enters a region with a strong magnetic field, then this is roughly equivalent to when the analog potential turns on, which means squeezing could occur. Now, what is important (as implicit in the arguments of Vysotskii and Vysotskyy) is that the change in the equivalent potential is nonadiabatic. The ionization and recombination proposed by Vysotskii and Vysotskyy are proposed to occur on a very short time scale, which makes them maximally non-adiabatic, and maximizes the energy exchange. Analogously, a moving charged particle encountering magnetic fields that change in strength and orientation can experience non-classical energy exchange if the associated dynamics are non-adiabatic.

Squeezed Wave Packet Based on an Excited SHO Eigenfunction

In this Appendix we consider the construction of a wave packet centered around the origin which is a squeezed version of an excited state eigenfunction of the simple harmonic oscillator. Since the fluctuation degrees of freedom are independent of the position and momentum degrees of freedom, we can focus on the fluctuations with the expectation that it would be straightforward to generalize in the case of a moving wave packet.

Schrodinger Equation and Wave Packet

We consider the time-dependent Schrodinger equation

$$i\hbar\frac{\partial}{\partial t}\psi(x,t) \;=\; -\frac{\hbar^2}{2m}\frac{\partial^2}{\partial x^2}\psi(x,t)+\frac{1}{2}m\omega_0^2x^2\psi(x,t) \tag{.1}$$

and assume a solution of the form

$$\psi(x,t) \;=\; \left(\frac{a(t)}{\alpha_0}\right)^{1/4}e^{-i\Theta(t)}e^{ib(t)x^2/2}\phi_n\left(\sqrt{\frac{a(t)}{\alpha_0}}x\right) \tag{.2}$$

with

$$\phi_n(x) \;=\; \left(\frac{m\omega_0}{\pi\hbar}\right)^{1/4}\frac{1}{\sqrt{2^n n!}}e^{-m\omega_0x^2/2\hbar}H_n\left(\sqrt{\frac{m\omega_0}{\hbar}}x\right) \tag{.3}$$

and

$$\alpha_0 \;=\; \frac{m\omega_0}{\hbar} \tag{.4}$$

We assume that $a(t)$ and $b(t)$ are real.

Plugging in and Simplifying

We plug in and obtain

$$\hbar\phi_n\frac{d}{dt}\Theta(t)+\frac{1}{4}i\hbar\phi_n\frac{1}{a(t)}\frac{d}{dt}a(t)+\frac{1}{2}i\hbar\sqrt{\frac{a(t)}{\alpha_0}}x\phi_n'\frac{1}{a(t)}\frac{d}{dt}a(t)-\frac{1}{2}\hbar x^2\phi_n\frac{d}{dt}b(t)$$

$$=-\frac{\hbar^2}{2m}\frac{a(t)}{\alpha_0}\phi_n''+\frac{m\omega_0}{2}x^2\phi_n-i\frac{\hbar^2}{2m}b(t)\phi_n+\frac{\hbar^2}{2m}x^2b^2(t)\phi_n-i\frac{\hbar^2}{m}\sqrt{\frac{a(t)}{\alpha_0}}x\phi_n'b(t) \tag{.5}$$

We can eliminate terms proportional to $x\phi_n'$ if we set

$$\hbar\frac{d}{dt}a(t) \;=\; -\frac{2\hbar^2}{m}a(t)b(t) \tag{.6}$$

This results in a simplification according to

$$\hbar\phi_n\frac{d}{dt}\Theta(t)+\frac{1}{4}i\hbar\phi_n\frac{1}{a(t)}\frac{d}{dt}a(t)-\frac{1}{2}\hbar x^2\phi_n\frac{d}{dt}b(t)$$

$$=\;-\frac{\hbar^2}{2m}\frac{a(t)}{\alpha_0}\phi_n''+\frac{m\omega_0}{2}x^2\phi_n-i\frac{\hbar^2}{2m}b(t)\phi_n+\frac{\hbar^2}{2m}x^2b^2(t)\phi_n \tag{.7}$$

We can make use of the evolution equation for $a(t)$ to simplify a bit further and write

$$\hbar\phi_n\frac{d}{dt}\Theta(t)-\frac{1}{2}\hbar x^2\phi_n\frac{d}{dt}b(t) \;=\; -\frac{\hbar^2}{2m}\frac{a(t)}{\alpha_0}\phi_n''+\frac{m\omega_0}{2}x^2\phi_n+\frac{\hbar^2}{2m}x^2b^2(t)\phi_n \tag{.8}$$

We can make use of operators to write

$$x^2\phi_n \;=\; \frac{1}{2}\frac{1}{a(t)}(\hat a+\hat a^\dagger)^2\phi_n\left(\sqrt{\frac{a(t)}{\alpha_0}}x\right)$$

$$\phi_n' \;=\; \sqrt{\frac{\alpha_0}{2}}(\hat a-\hat a^\dagger)\phi_n\left(\sqrt{\frac{a(t)}{\alpha_0}}x\right)$$

$$x\phi_n' \;=\; \frac{1}{2}\sqrt{\frac{\alpha_0}{a(t)}}(\hat a+\hat a^\dagger)(\hat a-\hat a^\dagger)\phi_n\left(\sqrt{\frac{a(t)}{\alpha_0}}x\right)$$

$$\phi_n'' \;=\; \frac{\alpha_0}{2}(\hat a-\hat a^\dagger)^2\phi_n\left(\sqrt{\frac{a(t)}{\alpha_0}}x\right) \tag{.9}$$

This leads to

$$\hbar\frac{d}{dt}\Theta(t)\phi_n - \frac{1}{4}\hbar(\hat{a}+\hat{a}^\dagger)^2\phi_n\frac{1}{a(t)}\frac{d}{dt}b(t)$$

$$= -\frac{\hbar^2}{4m}a(t)(\hat{a}-\hat{a}^\dagger)^2\phi_n + \frac{m\omega_0}{4}\frac{1}{a(t)}(\hat{a}+\hat{a}^\dagger)^2\phi_n + \frac{\hbar^2}{4m}\frac{b^2(t)}{a(t)}(\hat{a}+\hat{a}^\dagger)^2\phi_n \quad (.10)$$

We can expand and simplify to obtain

$$\hbar\frac{d}{dt}\Theta(t)\phi_n - \frac{1}{4}\hbar\hat{a}^2\phi_n\frac{1}{a(t)}\frac{d}{dt}b(t) - \frac{1}{4}\hbar(2n+1)\phi_n\frac{1}{a(t)}\frac{d}{dt}b(t) - \frac{1}{4}\hbar(\hat{a}^\dagger)^2\phi_n\frac{1}{a(t)}\frac{d}{dt}b(t)$$

$$= -\frac{\hbar^2}{4m}a(t)\hat{a}^2\phi_n + \frac{\hbar^2}{4m}a(t)(2n+1)\phi_n - \frac{\hbar^2}{4m}a(t)(\hat{a}^\dagger)^2\phi_n$$

$$+\frac{m\omega_0}{4}\frac{1}{a(t)}\hat{a}^2\phi_n + \frac{m\omega_0}{4}\frac{1}{a(t)}(2n+1)\phi_n + \frac{m\omega_0}{4}\frac{1}{a(t)}(\hat{a}^\dagger)^2\phi_n$$

$$+\frac{\hbar^2}{4m}\frac{b^2(t)}{a(t)}\hat{a}^2\phi_n + \frac{\hbar^2}{4m}\frac{b^2(t)}{a(t)}(2n+1)\phi_n + \frac{\hbar^2}{4m}\frac{b^2(t)}{a(t)}(\hat{a}^\dagger)^2\phi_n \quad (.11)$$

Matching Terms

Matching the $\hat{a}^2\phi_n$ and $(\hat{a}^\dagger)^2\phi_n$ terms leads to the constraint

$$-\frac{1}{4}\hbar\frac{1}{a(t)}\frac{d}{dt}b(t) = -\frac{\hbar^2}{4m}a(t) + \frac{m\omega_0}{4}\frac{1}{a(t)} + \frac{\hbar^2}{4m}\frac{b^2(t)}{a(t)} \quad (.12)$$

which can be written as

$$\hbar\frac{d}{dt}b(t) = \frac{\hbar^2}{m}a^2(t) - \frac{\hbar^2}{m}b^2(t) - m\omega_0 \quad (.13)$$

Matching terms proportional to ϕ_n leads to

$$\hbar\frac{d}{dt}\Theta(t) - \frac{1}{4}\hbar(2n+1)\frac{1}{a(t)}\frac{d}{dt}b(t) =$$

$$\frac{\hbar^2}{4m}a(t)(2n+1) + \frac{m\omega_0}{4}\frac{1}{a(t)}(2n+1) + \frac{\hbar^2}{4m}\frac{b^2(t)}{a(t)}(2n+1) \quad (.14)$$

This simplifies to

$$\hbar\frac{d}{dt}\Theta(t) = (2n+1)\frac{\hbar^2}{4m}a(t) + (2n+1)\frac{m\omega_0}{4}\frac{1}{a(t)} + (2n+1)\frac{\hbar^2}{4m}\frac{b^2(t)}{a(t)}$$
$$+ (2n+1)\frac{1}{4}\left(\frac{\hbar^2}{m}a(t) - \frac{\hbar^2}{m}\frac{b^2(t)}{a(t)} - m\omega_0\frac{1}{a(t)}\right)$$
$$= (2n+1)\frac{\hbar^2}{2m}a(t) \tag{.15}$$

Discussion

From the discussion above we see that the proposed wave packet solution satisfies the time-dependent Schrodinger equation. We can summarize the evolution equations that were obtained as

$$\hbar\frac{d}{dt}a(t) = -\frac{2\hbar^2}{m}a(t)b(t) \tag{.16}$$

$$\hbar\frac{d}{dt}b(t) = \frac{\hbar^2}{m}a^2(t) - \frac{\hbar^2}{m}b^2(t) - m\omega_0 \tag{.17}$$

$$\hbar\frac{d}{dt}\Theta(t) = (2n+1)\frac{\hbar^2}{2m}a(t) \tag{.18}$$

It is possible to combine $a(t)$ and $b(t)$ into a single complex variable $\alpha(t)$ according to

$$\alpha(t) \;=\; a(t) - ib(t) \tag{.19}$$

In terms of $\alpha(t)$ the dynamical equations become

$$i\hbar\frac{d}{dt}\alpha(t) = \frac{\hbar^2}{m}\alpha^2(t) - m\omega_0 \tag{.20}$$

$$\hbar\frac{d}{dt}\Theta(t) = (2n+1)\frac{\hbar^2}{2m}\mathrm{Re}\{\alpha(t)\} \tag{.21}$$

The expectation value for the Hamiltonian is

$$\langle\hat{H}\rangle = \left\langle -\frac{\hbar^2}{2m}\frac{d^2}{dx^2}\right\rangle + \left\langle\frac{1}{2}m\omega_0^2x^2\right\rangle$$
$$= (2n+1)\frac{\hbar\omega_0}{4}\left(\frac{a(t)}{\alpha_0} + \frac{\alpha_0}{a(t)}\right) + (2n+1)\frac{\hbar^2}{4m}\frac{b^2(t)}{a(t)}$$
$$= (2n+1)\frac{\hbar^2}{4m}\frac{|\alpha(t)|^2}{\mathrm{Re}\{\alpha(t)\}} + (2n+1)\frac{m\omega_0^2}{4}\frac{1}{\mathrm{Re}\{\alpha(t)\}} \tag{.22}$$

which is a constant for this model.

To develop an uncertainty principle for this wave packet, we can start with

$$(\Delta x)^2 \;=\; \frac{1}{2}(2n+1)\frac{1}{\mathrm{Re}\{\alpha(t)\}} \qquad (\Delta p)^2 \;=\; \frac{1}{2}(2n+1)\hbar^2\frac{|\alpha(t)|^2}{\mathrm{Re}\{\alpha(t)\}} \tag{.23}$$

We can use these to write

$$(\Delta x)^2(\Delta p)^2 \;=\; (2n+1)^2\frac{\hbar^4}{4}\frac{|\alpha(t)|^2}{\mathrm{Re}\{\alpha(t)\}^2} \;=\; (2n+1)^2\frac{\hbar^4}{4}\frac{1}{1-\frac{\mathrm{Im}\{\alpha(t)\}^2}{|\alpha(t)|^2}} \tag{.24}$$

The conclusion is that

$$\Delta x\Delta p \;=\; (2n+1)\frac{\hbar}{2}\frac{1}{\sqrt{1-r^2(t)}} \tag{.25}$$

with

$$r(t) \;=\; \pm\frac{\mathrm{Im}\{\alpha(t)\}}{|\alpha(t)|} \tag{.26}$$

References

[1] V. I. Vysotskii and M. V. Vysotskyy, "Self-Controlled Flashing Nuclear Fusion in Stationary Magnetized Low-Temperature Plasma," *Fusion Science and Technology* **79** (2023)

[2] V. I. Vysotskii and M. V. Vysotskyy, "Mechanism and dynamics of quasi-stationary self-supporting LENR in low-temperature magnetized plasma," to appear in *J. Condensed Matter Nuclear Science* (2023).

[3] V. I. Vysotskii, M. V. Vysotskyy and S. G. Bartalucci, "LENR solution for fundamental mysteries of the solar corona (anomalously high temperature and anomalous He^3 concentration)," to appear in *J. Condensed Matter Nuclear Science* (2023).

[4] V. I. Vysotskii and M. V. Vysotskyy, "Features of correlated states and a mechanism of self-similar selection of nuclear reaction channels involving low-energy charged particles," *J. Experimental and Theoretical Physics* **128** (2019) 856–864.

[5] V. I. Vysotskii, M. V. Vysotskyy, and S. V. Adamenko, "Formation and application of correlated states in nonstationary systems at low energies of interacting particles," *J. Experimental and Theoretical Physics* **114** (2012) 243–252.

[6] V. V. Dodonov, E. V. Kurmyshev and V. I. Man'ko, "Generalized uncertainty relation and correlated coherent states," *Physics Letters A* **79** (1980) 150–152.

[7] V. V. Dodonov, V. I. Man'ko and O. V. Man'ko, "Correlated coherent states and emission by quantum systems," *Journal of Soviet Laser Research* **14** (1993) 223–236.

[8] V. V. Dodonov, V.V., "Nonclassical states in quantum optics: a squeezed review of the first 75 years," *Journal of Optics B: Quantum and Semiclassical Optics* **4** (2002) R1.

[9] V. V. Dodonov, A. B. Klimov V. I. Man'ko, "Physical significance of correlated and squeezed states," *Group Theoretical Methods in Physics: Proceedings of the XVIII International Colloquium Held at Moscow, USSR, 4–9 June 1990* Springer, Berlin (2005) 450–456.

J. Condensed Matter Nucl. Sci. 38 (2024) 357–362

Research Article

Validation of Excess Energy in the H2 Loaded Palladium System

Prahlada Ramarao, Shree Varaprasad NS, Shashank G Dath,
Mohankumara PB and Suprith GC

Centre for Energy Research, S-VYASA Deemed-to-be University, Jigani, Bangalore, Karnataka, India 560 105

Abstract

The depletion of conventional energy resources necessitates the exploration of alternative energy sources, such as solar, wind, geothermal, and bio-gas. However, these renewable options have limitations in different climatic conditions and require large land areas for installation, while their output efficiency remains comparatively low. To address this challenge, the study of Low Energy Nuclear Reactions (LENR) presents a promising avenue for green, clean, portable, and sustainable energy. The Centre for Energy Research (CER) at S-VYASA University, Bangalore, India, has actively pursued LENR research for the past 9 years. Research groups have observed that the absorption of hydrogen into metal lattices is a crucial condition for LENR to occur. Various research groups, including CER, have explored metals like nickel, platinum, titanium, and palladium for high levels of hydrogen loading at controlled temperatures and pressures. In this study, two identical reactors were fabricated, one with an active fuel component and the other serving as a control unit. Both reactors underwent identical processes and hydrogen loading protocols. The active reactor consistently exhibited higher skin temperatures compared to the control reactor under the same power input, indicating the generation of excess heat. The experiment ran continuously for three months, showcasing sustained excess temperatures.
 ISSN 2227-3123

Keywords:

1. Introduction

The need to find alternative energy sources is very much a pressing demand on a global scale. Fossil fuel-derived sources are limited in availability and are not eco-friendly. On the other hand, renewable energy sources such as solar, wind, geothermal and bio-gas have their limitations such as lower efficiencies, higher costs, unfavorable geography, competing with land usage and also being very much seasonal. Alternative energy sources can be a reliable source of options if one can demonstrate energy generation at lower costs, reliable operation and environmentally safe. One such source being experimented on and researched by scientists is “Low Energy Nuclear Reactions” (LENR). Energy generated using LENR can overcome most of the limitations faced by using other non-conventional energy sources [1].

In the LENR reaction hydrogen (H2) atoms are made to undergo fusion at certain temperature and pressure conditions. The H2 gas is made to absorb into palladium (Pd) treated nickel (Ni) mesh under controlled pressure and temperature to trigger the reaction. Many countries are involved in researching LENR in different ways, either hydrogen or deuterium gas. A few countries viz, Russia, China, Japan and the USA are conducting extensive research

 ISSN 2227-3123

to demonstrate the concept and generation of excess heat energy using LENR. The Centre for Energy Research (CER) at S-VYASA University, Bengaluru has been working on this for the past 7 years. The objectives were to successfully design and develop a stand-alone, sustainable, low-cost, clean source of portable energy device. CER has conducted a series of experiments demonstrating repeatable generation of excess heat without any radiation.

Efforts are now being made to develop the device as a commercial source of heat as it is capable of generating excess heat output compared to electrical input power. There is every possibility that, the output thermal energy can be converted into other forms of energy. Presently, this source can be used as a room heater capable of heating rooms, bulidings, army bunkers over several months without any fuel replenishment.

There are many alternative explanations proposed by scientists all around the world which try to describe the LENR phenomena. Each research team has come up with their theory to describe LENR. However, there is no consensus on which of these is capable of explaining all the observations and justify quantum of excess heat. Research papers, conferences and journals on LENR must be promoted in the mainstream media for the world to acknowledge the potential of LENR.

2. Equipment Used

- Variable Frequency Supply : Aplab 8630P Input: 0-230V Single Phase AC. Output: 0-135/240 V, 0-12/24 A, 45-450 Hz, single phase AC programmable supply.
- Auto-transformer Dimmerstat : Input: 0-230 V Single Phase AC. Output: 0-230 V, 0-28 A, single phase AC.
- Compact DAQ : National Instruments cDAQ 91744 Slot, USB Compact DAQ Chassis.
- Pressure Transducer: Equinox EQ PT700A Measuring range: 0-1 bar (abs), Output: 4-20 mA, Process Conn: 1/4-inchBSP for Data Acquisition. Input 230 V AC. Output USB.
- Direct Drive Rotary High Vacuum Pump INDVAC.

3. Sample Preparation

Before starting any experiment, the reactor chamber is cleaned thoroughly to remove any impurities. Nickel meshes are cut to the desired size, cleaned thoroughly and complete care was taken to remove oil, trapped gases and oxide layers if any. Initially mesh was cleaned with sand paper, then with mild detergent, and ethanol [3]. Further the mesh was heated to 300 °C and applied vacuum simultaneously. Removal of the oxide layer was further confirmed with one of the samples with EDS analysis. The mesh was weighed soon after cleaning. Palladium is then deposited over the meshes as a thin layer (the process has a patent pending) and once it is done, the meshes were weighed again. The difference in weight of the meshes before and after Pd deposition determines the quantity of Pd deposited.

Pd-deposited meshes are positioned inside the reactor chamber. The ends of the reactor flanges are then closed and sealed air-tight. The reactor chamber is then degassed at elevated temperatures to remove moisture and any impurities (The pressure shown on display was 100 Pa, but this might be the lowest value this display can show). The heating is then turned off and the reactor is cooled down to room temperature (RT).

After the reactor reaches room temperature, the vacuum pump is turned off and the reactor is flushed thoroughly with H2 gas. It is then filled with H2 gas at low vacuum levels (H2 is filled with just 30K Pa). The absorption of H2 is done at Room temperature) [3], [4]. Since palladium-nickel mesh has a very strong tendency to absorb hydrogen gas, we see the hydrogen pressure falling. (Generally, the pressure falls 1000 to 1500 Pa pressure during H2 absorption). What we have observed is that, if there is no H2 absorption for unknown reasons, excess heat is not generated. The active experiment is started after completing the above procedures.

Figure 1. The reactor setup.

4. Experimental Setup and Procedure

The experimental setup used at CER has a stainless steel (SS) heating chamber where the active component to be heated is placed inside as shown in *Figure 1*. The reactor is a cylindrical hollow tube having a volume of 6.36×10^{-5} m^3. A cartridge heater is inserted into the reactor chamber for heating purposes. A vacuum pump is used to evacuate reactor before sealing, and a pressure transducer is used to monitor the reactor pressure.

The active materials used for the experiment are nickel mesh deposited with palladium. A calculated quantity of palladium is deposited over the nickel mesh. H2 gas under vacuum conditions is used for the experiment [6].

The reactor is electrically heated by using a sealed cartridge heater. A K-type thermocouple embedded in the heater is used to measure the temperature of the heater coil. A single-phase, variable AC power supply is used to heat the reactor to the desired temperature by varying the voltage applied, and the input power is measured using a digital power meter. The current drawn by the reactor at different voltages is also measured using a current transformer.

The temperature readings at different power levels are recorded by placing various thermocouples at different regions of the reactor. The heater temperature (core temperature) is measured by the embedded thermocouple in the heater. The reactor body temperature (surface) is also measured by embedding the thermocouple on the surface of the reactor using a high-temperature adhesive. All the experimental data are continuously monitored and recorded using a customized data acquisition system. This data is further utilized for analysis and interpretation.

In the calibration experiment, untreated Ni meshes are positioned in the reactor and H2 gas is filled to the same pressure as done in the active experiment. The experimental setup and instrumentation are maintained identical as done in the active setup. The rest of the procedure is followed as done in the active experiment and the data is logged. In one of the experiments, also employed the same reactor for both the active and calibration measurements, ensuring consistency in all parameters. This approach was adopted to minimize potential variations that could arise from using different reactors. By using the same reactor, aimed to isolate the effect of the active material and accurately assess its impact on surface temperature. The temperatures obtained in the calibration experiment are compared with the active experiment and plotted. The twin setup is shown in the Figure 2.

5. Results

At CER, two identical reactors were run in parallel having the same configuration. One was used as the active reactor and the other was used as a calibration reactor. The temperature of surface was used as an indicator for comparing the data of both the reactors. It was seen that the surface temperatures read in the active experiment was consistently higher (Graph 1) than the calibration experiment at all the power input values over several months on a 24×7 basis. The same is plotted continuously on 24×7 basis and is shown in ***Graph 2.*** The temperature readings were observed

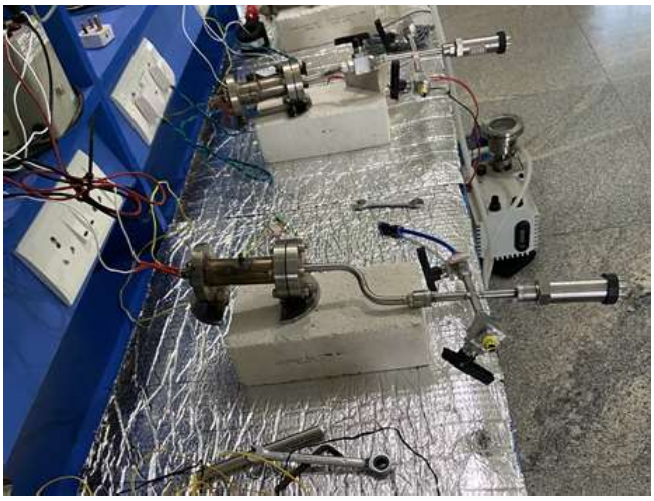

Figure 2. Parallel experiment setup.

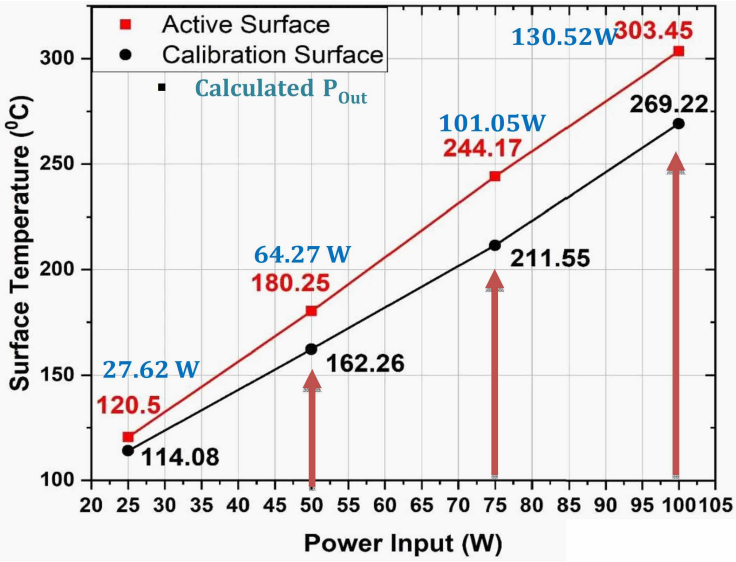

Graph 1. Graph of Surface Temperature (C) Vs Power input (W). The calculated power output for the active experiments also mentioned in the graph (quantification done by comparing with the data of calibration experiment).

for more than 2 months and the active experiment showed a higher temperature than the calibration over the r entire duration.

From Graph1, it is seen that for power inputs of 25 W, 50 W, 75 W and 100 W, the surface temperature was higher for the active reactor than in calibration reactor by 6.42°C, 17.99°C, 32.62°C and 34.23°C respectively. The power

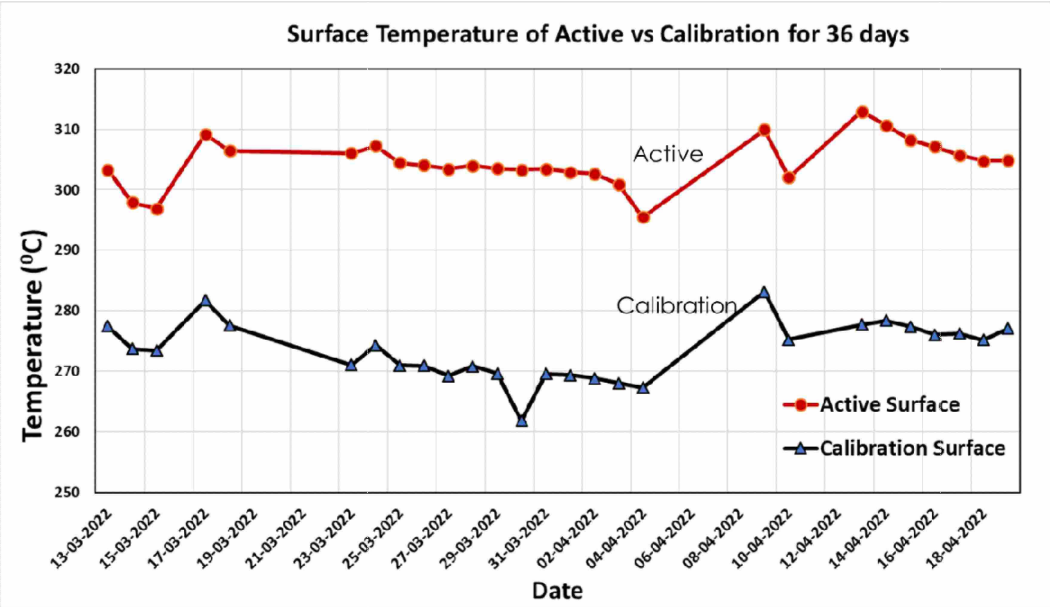

Graph 2. Surface temperature (C) (both active and calibration experiments) Vs Time for 36 days.

output was calculated with the following equation and is mentioned in the graph for different power inputs.

$$Q = \epsilon\sigma A(T_h^4 - T_c^4)$$

Where Q = Total heat energy radiated in Watts

σ = Stefan Boltzmann constant, 5.670×10^{-8} W m^{-2} K^{-4}

ε = emissivity of the reactor material

A = Total surface area of the reactor body in m^2

T_h = Surface temperature of the reactor in K (hot body)

T_c = Temperature of the surrounding air in K (cold body)

The surface temperatures for both the active and calibration experiment are also plotted in ***Graph 2*** for a period of 36 days at constant power input of 100 W. It is seen that the surface temperature of the active experiment was always higher than surface temperature of calibration over the entire duration.

6. Observations and Inferences

As seen by the results, the active experiments show higher surface temperatures than that of the calibration. One of the probable theories to explain the observed phenomenon is the possibility of tritium or helium formation causing the release of energy in the lattice of the Pd. Factors such as inter lattice crevices in the Pd, purity of the mesh and the gas play an important role in obtaining excess energy. CER is trying to simulate and develop a thermal and mathematical model of the working concept of the designed reactor. CER is constantly trying to improve the performance of the reactors by continued research and refining the experimental protocol.

7. Conclusion

Based on the experimental data and the results obtained thus-far, CER has shown that LENR is a topic of interest which should be pursued by other scientific communities around the world. The following conclusions can be drawn by CER based on the research work carried out:

- The excess heat seen in experiments is replicated in different experiments at CER, Bangalore and other cities.
- Multiple efforts are being tried at CER to improve the energy output of the reactor.
- The reactor can be used as a room heater with improved efficiency.
- Eventually the reactor with improved efficiency can be used as an energy source to generate electricity.
- CER is working on the possible theoretical explanation which can describe the experimental results.
- The heat loss is not only through radiation. It is through radiation, conduction and convection. Some experiments have also been conducted in a closed small room, by maintaining the ambient temperature a constant value. This showed the device was capable of generating excess heat.
- Switching the device OFF, and then switching it ON after a week did not disturb the performance of the device
- Using only nickel also produces excess heat but the combination of Ni and Pd given better performance, as Pd has high tendency to absorb more H_2 gas.
- The purpose of the paper is to show the repeatability, sustainability and consistency of the system.

References

[1] Prahlada Ramarao, Shree Varaprasad NS et al., Direct measurement confirming Generation of Excess Heat, 23rd International Conference on Condensed Matter Nuclear Science (ICCF-23), June 9–11 2021, in Xiamen, China

[2] McKubre, M.C.H., and F.L. Tanzella. “Using resistivity to measure H/Pd and D/Pd loading: Method and significance.” Condensed Matter Nuclear Science. 2006. 392–403

[3] Mizuno, Tadahiko. “Observation of excess heat by activated metal and deuterium gas.” J. Condensed Matter Nucl. Sci 25 (2017): 1–25; Mizuno, T. and J. Rothwell (2019). “Excess Heat from Palladium Deposited on Nickel.” J. Cond. Matter. Nucl. Sci. **29**: 21–33

[4] Nagel, David J. “Lattice-enabled nuclear reactions in the nickel and hydrogen gas system.” Current Science (2015): 646–652

[5] Stepanov, I. N., Yu I. Malahov, and Chi Nguyen Quoc. “Experimental Measurement of Excess Thermal Energy Released from a Cell Loaded with a Mixture of Nickel Powder and Lithium Aluminum Hydride.” Journal of Emerging Areas of Science 3.9 (2015)

[6] Adams, B. D., & Chen, A. (2011). The role of palladium in a hydrogen economy. Materials today, 14(6), 282–289.